Electrochemical Crosslinking Strategies using Redox-Active Units for Optoelectronic Thin Film Applications

Von der Fakultät Chemie der Universität Stuttgart zur Erlangung der Würde eines Doktors der Naturwissenschaften (Dr. rer. nat.) genehmigte Abhandlung

vorgelegt von

Claudia Malacrida

aus Carate Brianza

Hauptberichterin: Prof. Dr. Sabine Ludwigs

Mitberichter: Prof. Dr. Biprajit Sarkar

Prüfungsvorsitzender: Prof. Dr. Joris van Slageren

Tag der mündlichen Prüfung: 30.11.2022

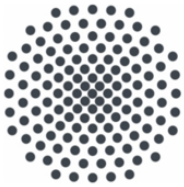

Universität Stuttgart

Fakultät 3

Institut für Polymerchemie
Lehrstuhl für Struktur und Eigenschaften polymerer Materialien

2023

Erklärung über die Eigenständigkeit der Dissertation

Ich versichere, dass ich die vorliegende Arbeit mit dem Titel

„*Electrochemical Crosslinking Strategies using Redox-Active Units for Optoelectronic Thin Film Applications*“

selbständig verfasst und keine anderen als die angegebenen Quellen und Hilfsmittel benutzt habe; aus fremden Quellen entnommene Passagen und Gedanken sind als solche kenntlich gemacht.

Declaration of Authorship

I hereby certify that the dissertation entitled

„*Electrochemical Crosslinking Strategies using Redox-Active Units for Optoelectronic Thin Film Applications*“

is entirely my own work except where otherwise indicated. Passages and ideas from other sources have been clearly indicated.

Name/Name: Claudia Malacrida

Unterschrift/Signed: _____

Datum/Date: _____

Acknowledgments

This PhD thesis represents the achievement of an important personal goal, and I would like to thank all the people who have supported me and without whom this work would have not been possible.

First of all, I would like to thank Prof. Dr. Sabine Ludwigs who allowed me to undertake the doctoral research project at IPOC and who continuously and professionally supervised me through the doctoral study. I would also like to thank you for your continuous trust, allowing me to work within different research projects and collaborations.

I would like to thank the different research partners for their support in this doctoral thesis and that allowed fruitful scientific collaboration.

I would like to start thanking Prof. Dr. Carmen Ruiz Delgado and Sergio Gàmez from the University of Malaga, thank you for your constant availability and your help to interpret and support the gathered experimental results with theoretical calculation.

I also would also like to thank Prof. Dr. Hubert Perrot, Dr. Ozlem Sel and Dr. Halim H. Mahdi for the support with EQCM and *ac*-electrogravimetry measurements and data interpretation as well as for their hospitality within the LISE laboratories at Sorbonne University.

Special thanks also go to Prof. Dr. Tiziana Benincori and Dr. Luca Scapinello from the University of Como, for their collaboration and support within the Biindole Project. Luca, I would like to especially thank you not only for being a very nice collaborator for your help during experiments but also for your positivity, determination, and support.

Thanks also to Prof. Dr. Philippe Blanchard from the University of Angers for the support and collaboration within the chromophore dimerization project.

My special thanks go to all the IPOC group, first to Dr. Klaus Dirnberger, Beatrice Omiecienski and Philipp Sliskovic for their constant support and patience during the last years. Thank you for leaving your door always open for help and constructive discussion. I would like to also thank all doctoral colleagues at IPOC: Dr. Yannic Gross, Dr. Kirsten Bruchlos, Dr. Peter Reynold, Dr. Matthias Wieland, Dr. Jochen Kuhllman, Carsten Dingler, Dr. David Gepperth, Sherri Liu, Lukas Stein and David Neusser, thank you for the nice time spent together, you have been for me in the last years not only great colleagues but also very good friends.

I want to thank the bachelor and master students for the work together: Yushi Lu, Claire Schlewitz, Michael Mueller, Lea-Sophie Hornberger and Daniel Hilscher.

Sincere thanks also go to my old colleagues from the University of Milan, Prof. Patrizia Mussini Dr. Mirko Magni, Dr. Serena Arnaboldi, Sara Grecchi for your continuous support and discussion also during the last years.

Special thanks go to my parents, my boyfriend and all my friends who have always supported me and continuously spur me to believe in myself and always aim for the best.

Summary

In this thesis, the electrochemical reactivity of different classes of redox molecules of optoelectronics interest was analyzed and exploited to crosslink precursor systems endowed with multiple dimerization sites. The so-generated electroactive films show well-defined and controlled π-conjugation and result in a well-defined redox behavior, which can be directly related to the one of the dimer of the starting redox unit. This dissertation was subdivided in two main sections, the first section focused on the oxidative electrodeposition from solution of different multimeric systems of optoelectronic interest, whereas in the second section of the thesis, electrochemically triggered dimerization was exploited to crosslink previously casted thin-films of redox-active polymers.

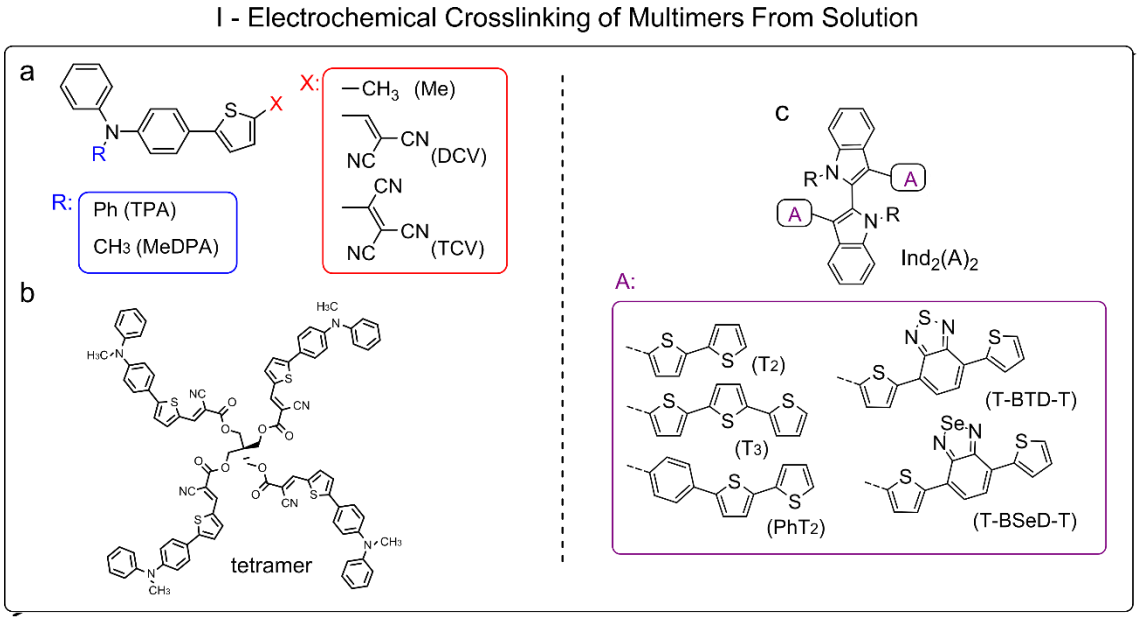

Figure 1: Structure of (a) D-π-A push-pull chromophores studied and (b) of tetramer employed for electrodeposition of highly crosslinked push-pull networks. Structure of (c) 2,2'-biindole architecture with oligothiophene terminals.

In the first section of this dissertation, the reactivity towards dimerization of a set of D-π-A push-pull molecules based on similar molecular architectures is reported (Figure 1 (a, b)). The molecules consist of a small push-pull system with an arylamine donor block, triphenylamine (TPA) and methyldiphenylamine (MeDPA), respectively, connected to an acceptor group through a thienyl linker. The aim of the study was to provide additional understanding of the electrochemical behaviour and dimerization ability of arylamine-based systems, in particular, of linear D-π-A push-pull systems, which find ubiquitous application in organic photovoltaics. The study also aimed to identify suitable dimerizing units for electrodeposition of functional films for electro-optic applications.

The structure-properties relationships in correlation to the chromophores' electrochemical behaviour were studied by electrochemical methods, *in-situ* UV-Vis spectroelectrochemical experiments and TD-DFT calculations. Experimental results indicate that the replacement of a Ph with a Me unit in the arylamine-based push-pull molecules significantly influence the reactivity of the compounds; we found that Me substituted chromophores tend to be more reactive towards oxidative dimerization than the Ph substituted ones. Dimerization of compounds TPA-T-TCV, MeDPA-T-DCV and MeDPA-T-TCV is confirmed by voltametric and *in-situ* UV-Vis-NIR spectroelectrochemical experiments.

Theoretical calculations were performed in collaboration with the group of Prof. C. Ruiz-Delgado to rationalize the reactivity observed in the chromophore series. It was found that spin-density alone (Mülliken) is not enough to predict dimerization behavior in the series, in contrast to general discussions of reactivity which can be found in the literature for dimerization of substituted arylamines and electropolymerization of conjugated monomers. For the first time correlations between the closed-shell nature of the dimeric-dication state was correlated with the dimerization ability of arylamine compounds. Finally, the dimerization ability of arylamine-based chromophores was exploited to electrodeposit electroactive films of Tetra-5, generating stable films with reversible redox and electrochromic behavior, to be developed and tested in bulk-heterojunction solar cells.[1]

As a second example of oxidation of multimers to deposit electroactive functional surfaces, the electrochemical characterization of a set of chiral molecules endowed with a 2,2'-biindole architecture and oligothiophene terminals was presented. Structure-property relationships by variation of the molecular structure through different π-spacers as oligothiophene terminals were analyzed (Figure 1 (c)). All molecules could be successfully electrodeposited generating stable electroactive films which could be repeatedly charged and discharged between their neutral and oxidized states in a highly reversible way. The analysis of *in-situ* conductance and of UV-Vis-NIR spectroelectrochemistry hints to the fact that the biindole scaffold plays only a marginal role in determining charge transport and absorption properties within the system. After analysing the charging behaviour and assigning the charge speciation as function of the potential, the enantiodiscrimination ability of enantiopure oligomeric films of compound Ind_2T_6 was demonstrated with *(S)-(−)-* or (*R)-(+)*-N,N′-dimethyl-1-ferrocenylethylamine chiral probes. A peak potential separation of ∼40 mV between the two antipodes was reproducibly measured, specularly for the two enantiomeric films. As outlook, the chiral discriminating ability of these systems and their reversible electrochromic behaviour could be exploited for developing chiral electrochromic devices.[2]

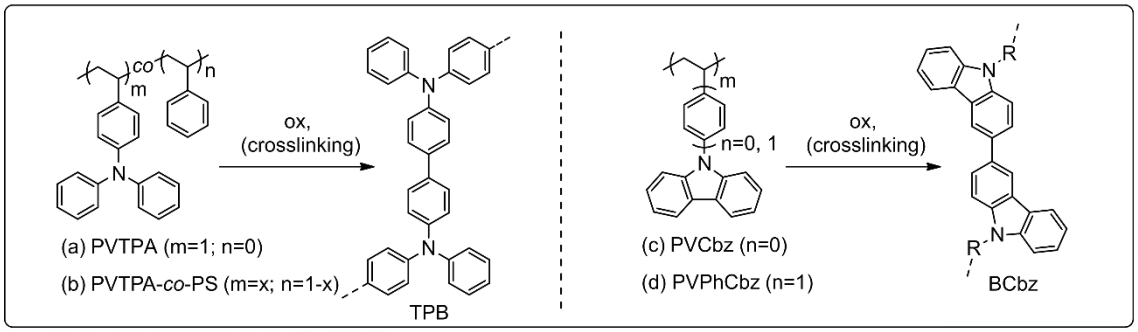

Figure 2: Structure of PVTPA, PVTPA-co-PS, PVCbz and PVPhCbz (left) and of the dimerization products tetraphenylbenzidine (TPB) (left) and biscarbazole (BCbz) (right).

In the second part of the thesis, insight into oxidative crosslinking as a post-solution deposition step to obtain electroactive films is provided. The dimerizing ability upon oxidation of triarylamine (TPA) and carbazole (Cbz) units as redox-active pendant groups on a saturated polymer backbone, resulting in crosslinking of the polymer film, was studied (Figure 2). Electrochemical and doping behaviors of the crosslinked polymer films were analyzed by *in-situ* electrochemical methods (*in-situ* conductance and *in-situ* UV-Vis spectroelectrochemistry). Additionally, in collaboration with the group of Dr. H. Perrot, electrochemical quartz crystal microbalance experiments (EQCM) and *ac*-electrogravimetry were performed upon electrochemical doping of the films, to provide information about the specific contributions and kinetics of the species involved in the charge-compensation process. The effect of variation of the polymer film composition in terms of the number of redox units with respect to electrochemical, potential dependent conductance and ion transport properties was investigated by comparing films of the PVTPA homopolymer with PVTPA-*co*-PS copolymers containing different PVTPA-PS ratios. More precisely 50-50, 30-70, 20-80 and 10-90 PVTPA-PS ratios were analyzed. Variations in the CV profiles of electrochemically crosslinked films were observed upon modification of the redox active content of the polymer films. These included a variation of the total oxidative charge and of the peak positions. The redox active films studied are characterized by a mixed valence conductivity behavior, with two maxima of conductance encountered for the oxidation TPB/$TPB^{+\bullet}$ and $TPB^{+\bullet}$/ TPB^{2+}, respectively. We could observe a direct relationship between the conductivity region (and electroactivity) of the polymers and the number of redox units in the film. The charge compensation properties upon oxidation of electrochemically crosslinked films, *ec*-PVTPA and *ec*-PVTPA-*co*-PS 50-50 in 0.1M CH_3CN/NBu_4PF_6 were also analyzed through classical and advanced EQCM, and the effect of film composition on the transfer of ions and solvents upon oxidation was analyzed. It was found that species transfer at the electrode│electrolyte interface upon p-doping is dominated by the anion PF_6^- and solvent moving in the same flux direction. In general, the homopolymer *ec*-PVTPA

shows for both electronic conductivity and ion transfer superior performance in comparison to the copolymers analyzed.

The concomitant crosslinking and doping with the strong oxidant $FeCl_3$ of spin-coated crosslinkable redox polymer films was also performed and optimized. In particular, I report a study on electronic conductivity upon chemical and electrochemical oxidation of polyvinyltriphenylamine (PVTPA) and polyvinylcarbazole (PVPhCbz and PVCbz) redox polymer films. The oxidative dimerization of the electroactive units is performed on solution-casted films and results in polymer crosslinking. Upon exposure to $FeCl_3$ solutions highly conducting films are obtained with maximum conductivities ranging from 10^{-3} to 10^{-2} S/cm. The increased chemical stability resulting from crosslinking together with the transparency of the conducting layers makes them interesting candidates for optoelectronic applications as hole transport layers or transparent electrodes.

It is found that doping of PVTPA and PVPhCbz gives bell-shaped conductivity profiles with a maximum conductivity only observed when radical cations and dications are both present with the pure neutral and fully oxidized samples only giving very low conductivities. Crosslinked and doped PVCbz films on the other hand do maintain the highest conductivity over a broad potential and concentration doping range, also when radical cation and dications are coexisting.

In-situ electrochemistry coupled with conductance and spectroscopy experiments have been performed to map the doping behavior of the films and to identify the right doping regimes to be targeted upon chemical doping. It is found that cross-communication allowing three-dimensional electronic connectivity for hopping is strongly affecting the conductivity profile, as evidenced in the case of doping PVCbz. DFT calculations hint at a pronounced tendency of the bicarbazole units to form π-stacks, and, in the case of BCbz smaller intermolecular π-stacking distances are calculated in comparison to BPhCbz. Similarly to the observation for *ec*-PVTPA-*co*-PS copolymers, neighboring interactions result in significant variations in the electrochemical and potential dependent conductivity profile of the systems.

The increased chemical stability resulting from crosslinking, together with the transparency and “high” conductivity of the resulting doped layers makes them interesting candidates for hole transport layers and transparent electrodes in optoelectronics applications. The reported crosslinking and doping procedure are currently under test for PVCbz and PVTPA thin layers used as HTLs in perovskite solar cells.[3]

References:

1. C. Malacrida, A. H. Habibi, S. Gámez-Valenzuela, I. Lenko, P. S. Marqués, A. Labrunie, J. Grolleau, J. T. López Navarrete, M. C. Ruiz Delgado, C. Cabanetos, P. Blanchard and S. Ludwigs, *ChemElectroChem*, **2019**, *6*, 4215–4228.
2. C. Malacrida, L. Scapinello, R. Cirilli, S. Grecchi, A. Penoni, T. Benincori, S. Ludwigs, *ChemElectroChem* **2021**, *8*, 3250–3261.
3. C. Malacrida, Y. Lu, K. Dirnberger, S. Gámez-Valenzuela, M. C. Ruiz Delgado and S. Ludwigs, *J. Mater. Chem. C*, **2020**, *8*, 15393-15405

Zusammenfassung

In dieser Dissertation wurde die elektrochemische Reaktivität verschiedener Klassen von Redoxmolekülen, die im Bereich der Optoelektronik von Interesse sind, analysiert und genutzt, um durch oxidative Dimerisierung Precursor-Systeme zu vernetzen, die mit mehreren Dimerisierungsstellen ausgestattet sind. Die so hergestellten elektroaktiven Filme zeigen eine genau definierte und kontrollierte π-Konjugation und führen zu einem genau definierten Redoxverhalten, das direkt auf das Dimer der Ausgangsredoxeinheit zurückgeführt werden kann. Diese Dissertation ist in zwei Hauptteile untergliedert. Der erste Teil befasst sich mit der elektrochemischen Abscheidung verschiedener multimerer Systeme in Lösung, während im zweiten Teil der Arbeit die elektrochemisch ausgelöste Dimerisierung zur Vernetzung von zuvor hergestellten dünnen Filmen aus redoxaktiven Polymeren beschrieben wird.

I - Elektrochemische Vernetzung von Multimeren in Lösung

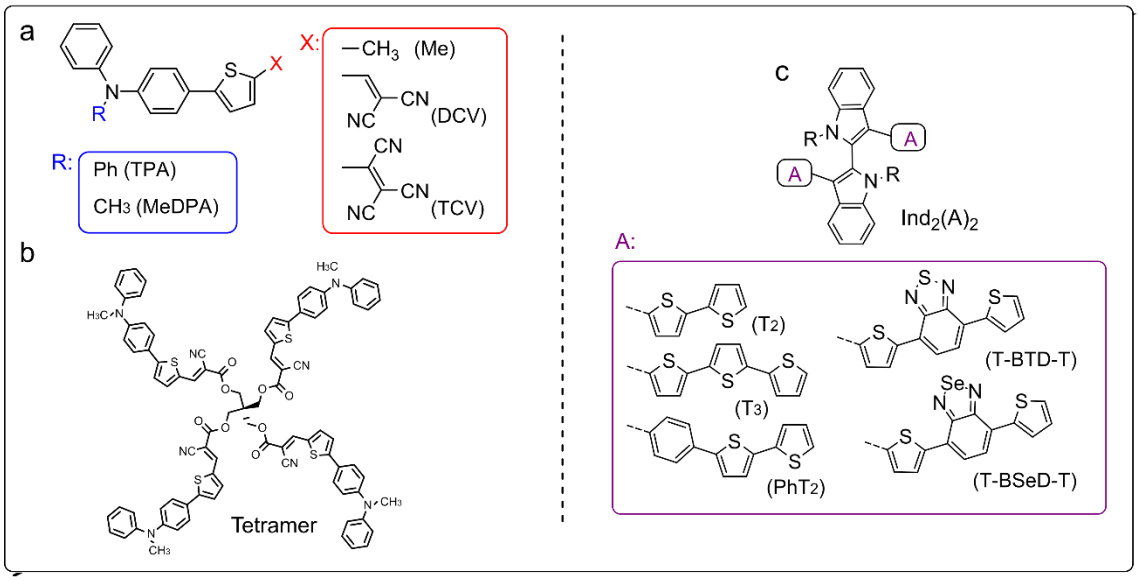

Abbildung 1: Struktur der (a) untersuchten D-π-A-Push-Pull-Chromophore und (b) des Tetramers, das für die elektrochemische Abscheidung hochvernetzter Push-Pull-Netzwerke verwendet wird. Struktur von (c) 2,2'-Biindol-Architektur mit Oligothiophen-Endgruppen.

Im ersten Abschnitt dieser Dissertation wird über die Reaktivität einer Reihe von D-π-A-Push-Pull-Molekülen berichtet, die auf ähnlichen Molekülarchitekturen basieren. Die Moleküle bestehen aus einem kleinen Push-Pull-System mit einem Arylamin-Donor-Block, Triphenylamin (TPA) bzw. Methyldiphenylamin (MeDPA), der über einen Thienyl-Linker mit einer Akzeptor-Gruppe verbunden ist (Abbildung 1 (a, b)). Ziel der Studie war es, ein besseres Verständnis des elektrochemischen Verhaltens und der Dimerisierungsfähigkeit von Systemen auf Arylaminbasis zu erlangen, die in der organischen Photovoltaik allgegenwärtige Anwendung finden. Die Studie zielte auch darauf ab, geeignete

Dimerisierungseinheiten für die elektrochemische Abscheidung von Funktionsschichten für optoelektronische Anwendungen zu identifizieren. Die Struktur-Eigenschafts-Beziehungen in Bezug auf das elektrochemische Verhalten der Chromophore wurden mit elektrochemischen Methoden, *in-situ* UV-Vis-spektrochemischen Experimenten und TD-DFT-Berechnungen untersucht. Die experimentellen Ergebnisse deuten darauf hin, dass der Ersatz einer Ph- durch eine Me-Einheit in den auf Arylaminen basierenden Push-Pull-Molekülen die Reaktivität der Verbindungen erheblich beeinflusst. Es konnte herausgefunden werden, dass Me-substituierte Chromophore tendenziell reaktiver gegenüber oxidativer Dimerisierung sind als Ph-substituierte. Die Dimerisierung der Verbindungen TPA-T-TCV, MeDPA-T-DCV und MeDPA-T-TCV wurde durch voltammetrische und *in-situ* UV-Vis-NIR-spektroelektrochemische Experimente bestätigt. Theoretische Berechnungen wurden in Zusammenarbeit mit der Gruppe von Prof. C. Ruiz-Delgado durchgeführt, um die beobachtete Reaktivität in der Chromophorreihe zu erklären. Es wurde festgestellt, dass die Spin-Dichte allein (Mülliken) nicht ausreicht, um das Dimerisierungsverhalten in der Serie vorherzusagen. Dies steht im Gegensatz zu allgemeinen Diskussionen in der Literatur über die Reaktivität der Dimerisierung von substituierten Arylaminen und die Elektropolymerisation von konjugierten Monomeren. Zum ersten Mal wurden Korrelationen zwischen der geschlossenen Schale des dimeren Dikationzustandes und der Dimerisierungsfähigkeit von Arylaminverbindungen hergestellt. Schließlich wurde die Dimerisierungsfähigkeit von Chromophoren auf Arylaminbasis ausgenutzt, um elektroaktive Tetra-5-Filme abzuscheiden und stabile Filme mit reversiblem Redox- und elektrochromem Verhalten zu erzeugen, die in bulk heterojunction solar cells entwickelt und getestet werden sollen. [1]

Als zweites Beispiel für die Oxidation von Multimeren zur Abscheidung elektroaktiver funktioneller Oberflächen wurde die elektrochemische Charakterisierung einer Reihe chiraler Moleküle mit einer 2,2'-Biindol-Architektur mit Oligothiophen-Endgruppen, die durch verschiedene π-Abstandshalter modifiziert wurden (Abbildung 1 (c)), vorgestellt. Die Struktur-Eigenschafts-Beziehungen in Abhängigkeit von den verschiedenen π-Abstandshaltern wurden analysiert. Für die verschiedenen Verbindungen wurden Modifikationen der Interaktion der beiden teilweise interagierenden Redox-Einheiten beobachtet, was zu unterschiedlichen Peak-zu-Peak-Abständen in den CV-Experimenten führte. Alle Moleküle konnten erfolgreich galvanisch abgeschieden werden, so dass stabile elektroaktive Filme entstanden, die wiederholt in reversibler Weise zwischen ihrem neutralen und oxidierten Zustand geladen und entladen werden konnten. Die Analyse der *In-situ*-Leitfähigkeit und der UV-Vis-NIR-Spektroelektrochemie deutet darauf hin, dass das Biindolgerüst nur eine marginale Rolle bei der Bestimmung der Ladungstransport- und

Absorptionseigenschaften innerhalb des Systems spielt. Nach der Analyse des Ladungsverhaltens als Funktion des Potentials wurde die Enantiodiskriminierungsfähigkeit eines enantiomeren Films der Verbindung Ind_2T_6 mit *(S)-(-)*- oder *(R)-(+)*-N,N′-Dimethyl-1-ferrocenylethylamin chiralen Sonden nachgewiesen. Eine Peak-Potential-Trennung von ~40 mV zwischen den beiden Antipoden wurde reproduzierbar gemessen. Die chirale Unterscheidungsfähigkeit dieser Systeme und ihr reversibles elektrochromes Verhalten könnten für die Entwicklung chiraler elektrochromer Systeme genutzt werden.[2]

II - Elektrochemische Vernetzung als Funktionalisierungsschritt nach Schichtabscheidung

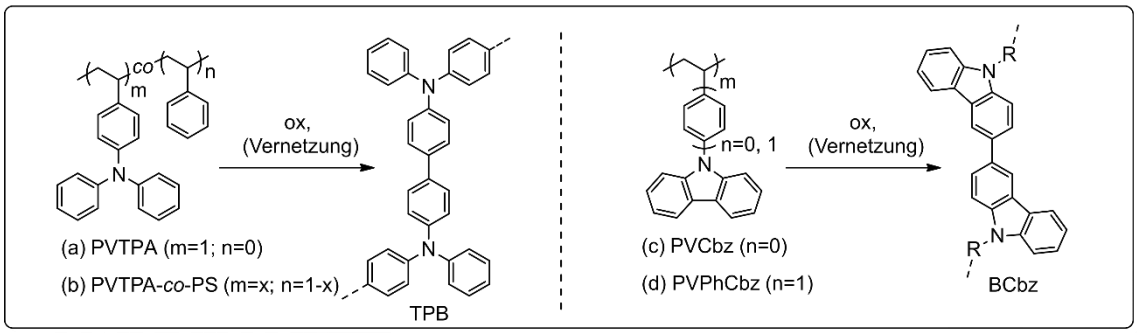

Abbildung 2: Struktur von PVTPA, PVTPA-co-PS, PVCbz und PVPhCbz (links) sowie der Dimerisierungsprodukte Tetraphenylbenzidin (TPB) (links) und Biscarbazol (BCbz) (rechts).

Im zweiten Teil der Arbeit wird die oxidative Vernetzung von, durch Spin-coating hergestellten elektroaktiven Filmen untersucht. Die Vernetzung, die durch die Dimerisierung bei der Oxidation von Triarylamin (TPA) und Carbazol (Cbz) als Seitengruppen in Redoxpolymeren entsteht, wurde untersucht (Abbildung 2). Das elektrochemische und das Dotierungsverhalten der vernetzten Polymerfilme wurde mit Hilfe elektrochemischer *In-situ*-Methoden (*In-situ*-Leitfähigkeit und *In-situ*-UV-Vis-Spektroelektrochemie) analysiert. Darüber hinaus, in Kooperation mit der Gruppe von Dr. H. Perrot, wurden bei der elektrochemischen Dotierung der Filme Messungen mit einer elektrochemischen Quarzkristallmikrowaage (EQCM) und ac-Elektrogravimetrie durchgeführt, die spezifischen Beiträge und kinetische Informationen über die am Ladungsausgleichsprozess beteiligten Spezies lieferten. Die Auswirkung der Variation der Zusammensetzung des Polymerfilms in Bezug auf die Anzahl der Redoxeinheiten auf die elektrochemischen, potenzialabhängigen Leitfähigkeits- und Ionentransporteigenschaften wurde durch den Vergleich von Filmen des PVTPA-Homopolymers mit PVTPA-*co*-PS-Copolymeren mit unterschiedlichen PVTPA-PS-Verhältnissen untersucht. Genauer gesagt wurden die PVTPA-PS Verhältnisse 50-50, 30-70, 20-80 und 10-90 analysiert. Es wurden Variationen in den CV-Graphen elektrochemisch vernetzter Filme beobachtet, die den redoxaktiven Gehalt der Polymerfilme verändern. Dazu gehörte eine Variation der gesamten oxidativen Ladung und der Peakpositionen. Die untersuchten redoxaktiven Filme

zeichnen sich durch ein gemischtes Valenzleitfähigkeitsverhalten aus, wobei zwei Leitfähigkeitsmaxima für die Oxidation TPB/$TPB^{+\bullet}$ bzw. $TPB^{+\bullet}$/ TPB^{2} auftreten. Wir konnten eine direkte Beziehung zwischen dem Leitfähigkeitsbereich (und der Elektroaktivität) der Polymere und der Anzahl der Redoxeinheiten im Film beobachten. Die Eigenschaften des Ladungsausgleichs bei der Oxidation von elektrochemisch vernetzten Filmen, *ec*-PVTPA und *ec*-PVTPA-*co*-PS 50-50 in 0,1M CH_3CN/NBu_4PF_6 wurden ebenfalls mittels klassischer EQCM und ac-electrogravimetry analysiert. Ebenfalls wurde hierbei die Wirkung der Filmzusammensetzung auf den Transfer von Ionen und Lösungsmitteln bei der Oxidation untersucht. Es wurde festgestellt, dass der Speziestransfer an der Elektroden-Elektrolyt-Grenzfläche bei p-Doping durch das Anion PF_6^- und das Lösungsmittel dominiert wird, die sich in dieselbe Flussrichtung bewegen. Im Allgemeinen zeigt das Homopolymer *ec*-PVTPA sowohl eine höhere elektronische Leitfähigkeit als auch einen schnelleren Ionentransfer als die untersuchten Copolymere.

Die gleichzeitige Vernetzung und die Dotierung mit dem starken Oxidationsmittel $FeCl_3$ von schleuderbeschichteten vernetzbaren Redoxpolymerfilmen wurde ebenfalls durchgeführt und optimiert. Insbesondere wird die elektronische Leitfähigkeit nach chemischer und elektrochemischer Oxidation von Polyvinyltriphenylamin (PVTPA) und Polyvinylcarbazol (PVPhCbz und PVCbz) Redoxpolymerfilmen untersucht. Die oxidative Dimerisierung der elektroaktiven Einheiten wird an den durch Spin-coating hergestellten Filmen durchgeführt und führt zur Vernetzung der Polymere. Nach Oxidierung mit $FeCl_3$/ CH_3CN Lösungen werden hochleitfähige Filme mit maximalen Leitfähigkeiten von 10^{-3} bis 10^{-2} S/cm erhalten. Die erhöhte chemische Stabilität infolge der Vernetzung zusammen mit der Transparenz der leitenden Schichten macht sie zu interessanten Kandidaten für optoelektronische Anwendungen, als Lochtransportschichten (HTLs) oder transparente Elektroden.
Es zeigt sich, dass die Dotierung von PVTPA und PVPhCbz zu glockenförmigen Leitfähigkeitsprofilen führt, wobei eine maximale Leitfähigkeit nur dann zu beobachten ist, wenn sowohl Radikalkationen als auch Dikationen vorhanden sind, während die reinen neutralen und vollständig oxidierten Proben nur sehr geringe Leitfähigkeiten aufweisen. Vernetzte und dotierte PVCbz-Filme hingegen weisen über einen breiten Potenzial- und Dotierungsbereich die höchste Leitfähigkeit auf, wenn Radikalkation und Dikationen gemeinsam vorhanden sind. Vor der chemischen Dotierung wurden elektrochemische *In-situ*-Untersuchungen (*In-situ*-Leitfähigkeit und *In-situ*-UV-Vis-Spektroelektrochemie) durchgeführt, um die Leitfähigkeit des Films abzubilden und festzustellen, welche Ladungsträger erzeugt werden sollten, um die höchste Leitfähigkeit der Filme zu erreichen. Es wurde festgestellt, dass die Querkommunikation, die eine dreidimensionale elektronische Konnektivität für Hopping ermöglicht, das Leitfähigkeitsprofil stark beeinflusst, wie im Falle der Dotierung von PVCbz nachgewiesen wurde. DFT-Berechnungen deuten

auf eine ausgeprägte Tendenz der Bicarbazoleinheiten zur Bildung von π-Stapeln hin, und im Fall von BCbz werden im Vergleich zu BPhCbz kleinere intermolekulare π-Stapelabstände berechnet. Ähnlich wie bei den *ec*-PVTPA-*co*-PS-Copolymeren führen benachbarte Wechselwirkungen zu erheblichen Veränderungen im elektrochemischen und potenzialabhängigen Leitfähigkeitsprofil der Systeme.
Die aus der Vernetzung resultierende erhöhte chemische Stabilität in Verbindung mit der Transparenz und "hohen" Leitfähigkeit der resultierenden dotierten Schichten macht sie zu interessanten Kandidaten für Lochtransportschichten und transparente Elektroden in optoelektronischen Anwendungen. Das beschriebene Vernetzungs- und Dotierungsverfahren wird derzeit für PVCbz- und PVTPA-Dünnschichten getestet, die als HTLs in Perowskit-Solarzellen verwendet werden.[3]

Quellen:

1. C. Malacrida, A. H. Habibi, S. Gámez-Valenzuela, I. Lenko, P. S. Marqués, A. Labrunie, J. Grolleau, J. T. López Navarrete, M. C. Ruiz Delgado, C. Cabanetos, P. Blanchard and S. Ludwigs, *ChemElectroChem*, **2019**, *6*, 4215–4228.
2. C. Malacrida, L. Scapinello, R. Cirilli, S. Grecchi, A. Penoni, T. Benincori, S. Ludwigs, *ChemElectroChem* **2021**, *8*, 3250–3261.
3. C. Malacrida, Y. Lu, K. Dirnberger, S. Gámez-Valenzuela, M. C. Ruiz Delgado and S. Ludwigs, *J. Mater. Chem. C*, **2020**, *8*, 15393-15405.

Scientific Contributions

Publications:

4. T. Benincori, S. Gámez-Valenzuela, M. Goll, K. Bruchlos, **C. Malacrida**, S. Arnaboldi, P. R. Mussini, M. Panigati, J. T. López Navarrete, M. C. Ruiz Delgado, G. Appoloni and S. Ludwigs, Electrochim. Acta, 2018, 284, 513–525.
5. P. Blanchard, **C. Malacrida**, C. Cabanetos, J. Roncali and S. Ludwigs, Polym. Int., 2019, 68, 589–606.
6. **C. Malacrida**, A. H. Habibi, S. Gámez-Valenzuela, I. Lenko, P. S. Marqués, A. Labrunie, J. Grolleau, J. T. López Navarrete, M. C. Ruiz Delgado, C. Cabanetos, P. Blanchard and S. Ludwigs, ChemElectroChem, 2019, 6, 4215–4228.
7. M. Wieland, **C. Malacrida**, Q. Yu, C. Schlewitz and L. Scapinello, Flex. Print. Electron., 2020, 5, 014016.
8. Hofmann, R. Kroon, S. Zokaei, E. Järsvall, **C. Malacrida**, S. Ludwigs, T. Biskup and C. Müller, Adv. Electron. Mater., 2020, 2000249.
9. D. Neusser, **C. Malacrida**, M. Kern, Y. M. Gross, J. Van Slageren and S. Ludwigs, Chem. Mater., 2020, 32, 6003–6013.
10. **C. Malacrida**, Y. Lu, K. Dirnberger, S. Gámez-Valenzuela, M. C. Ruiz Delgado and S. Ludwigs, J. Mater. Chem. C, 2020, DOI:10.1039/d0tc03090b.
11. P. Shiri, D. Neusser, **C. Malacrida**, S. Ludwigs and L. G. Kaake, J. Phys. Chem. C, 2020, 8, 125–536.
12. J. Ratzsch, J. Karst, J. Fu, M. Ubl, T. Pohl, F. Sterl, **C. Malacrida**, M. Wieland, B. Reineke, T. Zentgraf, S. Ludwigs, M. Hentschel and H. Giessen, J. Opt. (United Kingdom), 2020, 22, 8.
13. **C. Malacrida**, L. Scapinello, R. Cirilli, S. Grecchi, A. Penoni, T. Benincori, S. Ludwigs, ChemElectroChem 2021, 8, 3250–3261.
14. J. Karst, M. Floess, M. Ubl, C. Dingler, **C. Malacrida**, T. Steinle, S. Ludwigs, M. Hentschel, H. Giessen, Science 2021, 374, 612–616.
15. **C. Malacrida**, O. Sel, H. El. Mahdi., S. Ludwigs, H. Perrot, *Manuscript in Preparation*.
16. **C. Malacrida**, S. Gámez-Valenzuela, D. Gepperth, M. C. Ruiz Delgado, P. Blanchard, S. Ludwigs, *Manuscript in Preparation*.

Oral Presentations:

1. ECHEMs Saint-Pierre-d'Oléron (France); 21-23 May 2019: Mixed Valence Conductivity in Crosslinkable Triarylamine Redox Polymer Films.

Poster Presentations:

1. Makromolekulares Kolloquium Freiburg (Germany); 26-28 February 2020: *Electroactive Polymers, exploring conductivity behaviors and doping methods.*
2. Symposium on Progress in Organic Optoelectronics & Energy Conversion Malaga (Spain); 12-13 December 2019: *Mixed Valence Conductivity in Crosslinkable Triarylamine and Carbazole Redox Polymer Films*.
3. ECHEMs Saint-Pierre-d'Oléron (France); 21-23 May 2019: *Dimerization Study of two Small Push-Pull Chromophores based on Arylamine donor groups.*

Table of Contents

List of Abbreviations

4pp Four-point-probe

AFM Atomic Force Microscopy

a.u. Arbitrary unit

BCbz Biscarbazole

BPhCbz Bisphenylcarbazole

Cbz Carbazole

CE Counter electrode

CP Conducting polymer

CV Cyclic voltammetry / cyclic voltammogram

DCM Dichloromethane

DCV Dicyanovinyl

DSC Differencial scanning calorimetry

ec- Electrochemically crosslinked

EDOT 3,4-ethylenedioxythiophene

EQCM Electrochemical quartz crystal microbalance

Fc|Fc$^+$ Ferrocen | ferrocenium

GPC Gel permeation chromatography

HOMO Highest occupied molecular orbital

ITO Indium doped tin oxide

IDE Interdigitated electrode

LUMO Lowest unoccupied molecular orbital

MALDI-TOF Matrix-assisted laser ionization time-of-flight

MeCN acetonitrile

MeDPA Methyldiphenylamine

M_n Number average molecular weight

M_w Weight average molecular weight

NBu_4PF_6 Tetrabutylammonium hexafluorophosphate

NMR Nuclear magnetic resonance

OFET Organic field effect transistor

OLED Organic light emitting diode

OPV Organic photovoltaics

P3HT Poly(3-hexylthiophene)

$PC_{61}BM$ Phenyl-C61-butyric acid methyl ester

PDI Polydispersity index

PEDOT Poly(3,4-ethylenedioxythiophene)

PhCbz Phenylcarbazole

PS Polystyrene

PVCbz Polyvinylcarbazole

PVPhCbz Polyvinylphenylcarbazole

PVTPA Polyvinyltriphenylamine

PVTPA-co-PS Polyvinyltriphenylamine-co-polystyrene

RE Reference electrode

rpm Revolutions per minute

TCV Tricyanovinyl

TEMPO 2,2,6,6-tetramethylpiperidinyl-N-oxyl

THF Tetrahydrofuran

TPA Triphenylamine

TPB Tetraphenylbenzidine

UV/Vis (NIR) Ultraviolet / Visible (Near Infrared)

WE Working electrode

1 Introduction

The story of conducting polymers (CPs) reported in the scientific literature dates back to 1862, when the anodic oxidation of aniline generating a blue-black powder insoluble in water was reported by Letheby.[1] Back then, the ability to determine the molecular structure was lacking, and the first model on macromolecules was introduced by Hermann Staudinger many decades later (1920s). Consequently, the first reports of CPs lacked their description as macromolecules as well as the concept of redox doping. It was only in 1977 that studies on CPs started calling the interest of the scientific community with the ground-breaking discovery of the scientists Shirakawa, MacDiarmid and Heeger, who found that the exposure of poly(acetylene) to halogen vapors led to a 10^8 folded increase in conductivity.[2] This discovery revolutionized the traditional view of organic polymers from insulating plastic to (semi)conducting materials.

In the last decades, conducting polymers have found large interest in the scientific community thanks to their peculiar combination of physical properties of polymers, including low specific weight, processability, solubility, tunable mechanical properties, flexibility etc. with those of inorganic semiconductors, to obtain unique and novel materials and paving the way to new applications. Examples of such applications are large-area, flexible polymer Light-Emitting-Diodes (pLEDs) that can emit light in virtually any part of the visible spectrum, all-polymeric Field-Effect-Transistors (FETs) that give access to low-cost and high-tech plastic electronics for the simple fabrication of conductive films, e.g. for electromagnetic shielding, antistatic applications or sensing applications. One peculiarity of conjugated polymers, and more generally of organic semiconductors, is the ease of manipulation of their electronic properties by modification of their chemical structure; allowing the fabrication of materials with tailor-made electronic and/or mechanical properties.[3]

1.1 Charge Transport in Conducting Polymers

One main characteristic of conducting polymers is their ability to switch between a non-conducting and (semi)conducting state upon removal (oxidation) or injection (reduction) of electrons. This process is referred to as "*p*- or *n-doping process"*, respectively. Conducting polymers, and more in general organic semiconductors present relatively small ionization potentials and large electron affinities, resulting in a relative ease of oxidation and/or reduction. For this reason, π-electrons can be removed or added without significant destabilization of the bonds that keep the molecular structure together; as charge carriers are generated upon doping this process is also often referred to as "*charging process*".

Doping of CPs can be performed chemically, by employment of organic and inorganic oxidizing or reducing agents of both organic or inorganic nature. The majority of CPs is composed by electron-rich units and to perform their p-doping oxidants like I_2, $FeCl_3$ 2,3,5,6-

tetrafluoro-7,7,8,8-tetracyanoquinodimethane (F4TCNQ) etc., can be employed.[4–7] Despite the advantages of a large scale preparation and possibility of combination with large variety of solvents, chemical doping can be difficult to control, especially when intermediate doping levels are required. For this reason, electrochemical doping can be considered a good alternative to chemical doping, in this case the oxidization or reduction of the material can be easily achieved by fine tuning the electrode potential. Another peculiar advantage of electrochemical doping is also its intrinsic reversibility, which has made it the approach of choice for example in electrochromic applications and sensing.[8,9]

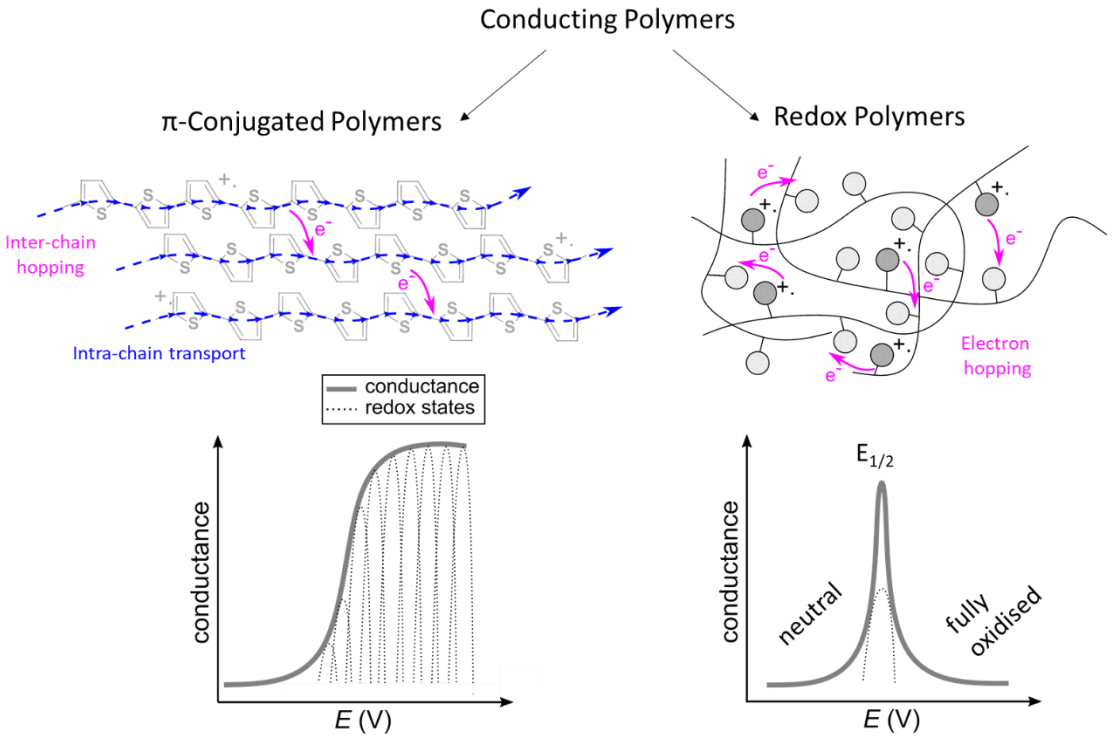

Figure 1.1: Classification of conducting polymers into π-conjugated polymers and redox polymers (top), with representation of charge transport mechanisms and conductivity profiles as function of the doping level (bottom).

Based on the nature of charge propagation, conducting polymers can be subdivided into two main categories, namely redox and conjugated polymers. In redox polymers electronic conductivity is sustained by electron hopping between localized redox active units, whereas in π-conjugated polymers, the motion of delocalized electrons occurs intra- and inter- conjugated chains and is mediated by different charge carriers. The two classes of conducting polymers present different conductivity profiles as function of the doping level (potential), as a result of their structure, with an exemplification reported in Figure 1.1. Description of the two classes of CPs and the charge transport mechanisms in the latter is provided in the following paragraphs.

1.1.1 π-Conjugated Polymers

Π-conjugated polymers consist of sp^2-hybridised carbon atoms which results in alternating π- and *σ*-bonds in the polymer backbone. The simplest molecular structure of a *π*-conjugated polymer backbone is the one of *trans*-poly(acetylene) (PA) represented in Figure 1.2 (top). *Trans*-poly(acetylene) was the first conducting polymer, for which systematic doping studies were performed. Following the studies of the scientist Shirakawa, MacDiarmid and Heeger, other polyaromatic structures were also discovered and studied (Figure 1.2). In the 80´s research was concentrated on the so called second generation of CPs, including π-conjugated polymers such as poly(aniline) (PANI), poly(thiophene) (PT) and poly(pyrrole) (PPy). These polymers were typically synthetized through anodic electropolymerization or chemical oxidative polymerization. Different synthetic strategies were later introduced to realize more reliable synthetic procedures towards the field of electronic materials, allowing important advances in this research field.

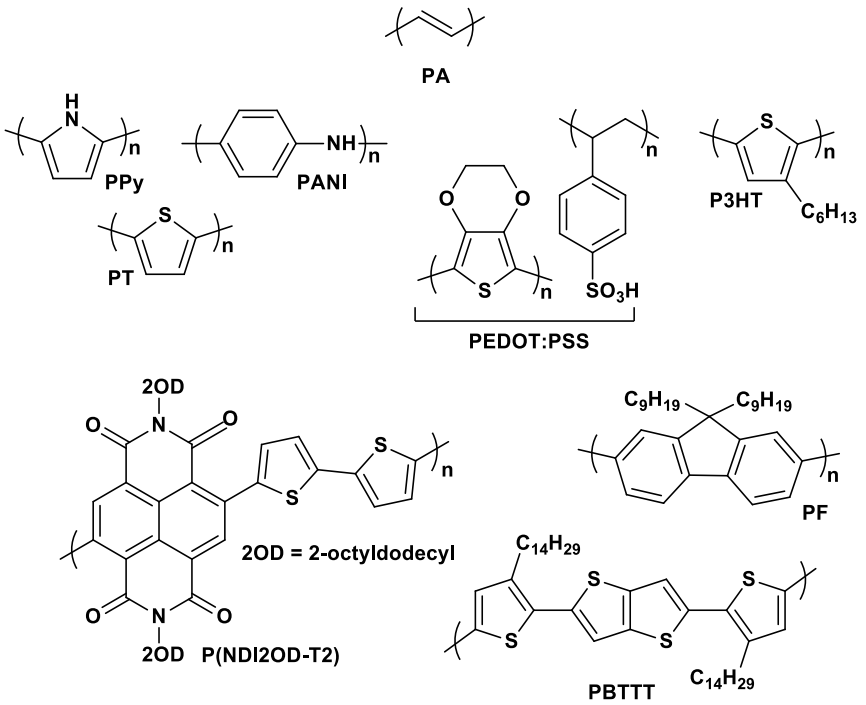

Figure 1.2: Some examples of conducting polymers: PA trans-poly(acetylene). PPy poly(pyrrole), PANI poly(aniline); PT: poly(thiophene), PEDOT:PSS, poly(3,4-ethylenedioxythiophene):poly(styrene sulfonate); P3HT, poly(3-hexylthiophene); PF, poly(9,9-dinonyl-9H-fluorene-2,7-diyl); PbTTT, poly(2,5-bis(3-tetradecylthiophen-2-yl)thieno[3,2-b]thiophene); P(NDI2OD-T2), poly{[N,N'-bis(2-octyldodecyl) naphthalene-1,4,5,8-bis(dicarboximide)-2,6-diyl]-alt-5,5'-(2,2'-bithiophene)}.

Among π-conjugated polymers, P3HT (poly(3-hexylthiophene)) and PEDOT:PSS (poly(3,4-ethylenedioxythiophene):poly(styrenesulfonate)), have shown superior electrical properties together with adequate processability and are currently the most utilized conjugated polymers and are commercially from various sources.[10][11] Molecular

engineering has also been widely exploited to synthetize new polymers and modulate their electronic properties, including for example the rigidification of the conjugated backbone such as in PF, poly(9,9-dinonyl-9H-fluorene-2,7-diyl) and PbTTT, poly(2,5-bis(3-tetradecylthiophen-2-yl)thieno[3,2-b]thiophene, or the introduction of electron-withdrawing or electron-donating side groups and the increase of the quinoid (versus aromatic) character such as in P(NDI2OD-T2), poly{[N,N'-bis(2-octyldodecyl) naphthalene-1,4,5,8-bis(dicarboximide)-2,6-diyl]-alt-5,5'-(2,2'-bithiophene)}.

Under an electronic point of view, conjugated polymers are characterized by electrons organized in bands rather than in discrete levels. This organization originates from the interaction of the p-orbitals of the repeating units throughout the chain and is exemplified in Figure 1.3 in the case of poly(thiophene), where the calculated frontier-energy-levels of oligothiophenes with n = 1 - 4 and of polythiophene are shown as a function of oligomer length. Addition of every new thiophene unit causes the hybridization of the energy levels yielding more and more levels until a point is reached at which there are bands rather than discrete levels.[12] Interaction between the p-electrons of neighboring molecules leads to a three-dimensional band structure. Similarly to inorganic semiconductors, the highest occupied band, which originates from the HOMO of a unit, is called the valence band, whereas the lowest unoccupied band, which originates from the LUMO of a single repeat unit, is called the conduction band. The difference in energy between these levels is called the band gap E_g. At the origin of the energy gap in organic semiconductors lays the so-called Peierls instability, which predicts that an equidistant linear chain structure is unstable towards a structural deformation of alternating shorter double and longer single bond, allowing to gain in electronic energy in order to compensate for the loss of "elastic" energy.[9,13] The bond length alternation gives in CPs a major contribution to the energy-gap (Eg).[14,15] One method to reduce this bond length alternation is achieved through doping.

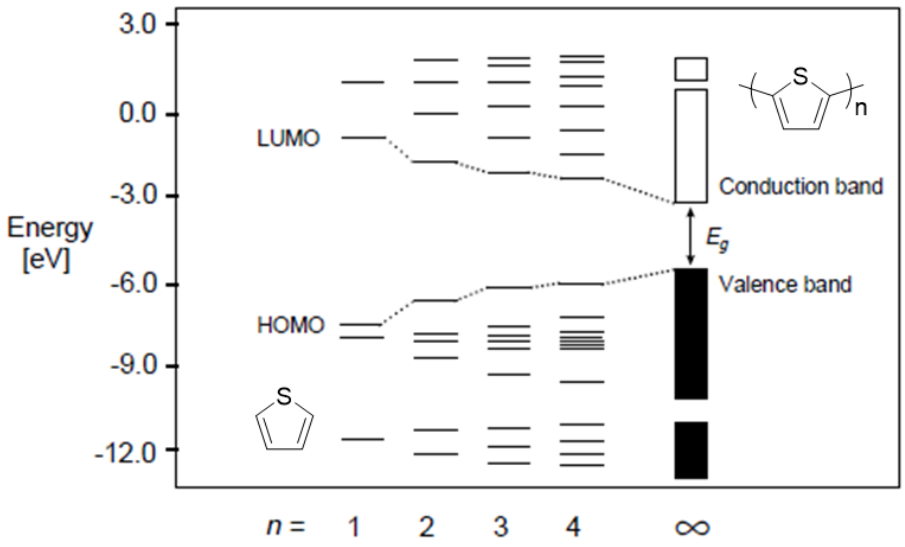

Figure 1.3: Schematization of the frontier orbitals of PT as exemplification of conjugated polymer. Effect of increasing conjugation length is shown from the left (isolated atomic orbitals) to the right (continuous valence and conducting bad in polymer chains). Picture adapted with permission from ref. [12]. Copyright Elsevier (1998).

1.1.1.1 Charge Transport Mechanism in π-Conjugated Polymers

The first generally accepted model describing charge transport in π-conjugated polymers was developed in the 80's by Bredas and coworkers.[16,17] The model is based on the ideal assumption that the chain of a well ordered polymer is infinite, resulting in the presence of a band structure. Upon oxidation or reduction, charges are generated along the polymer chain; these charges are localized due to strong electron-phonon coupling and are referred to as polarons (P) and bipolarons (B) and play a fundamental role in the charge transport mechanism of π-conjugated polymers.[16,17]

Let us consider the case of oxidation, upon generation of a positive charge $1q^+$ in the polymer; an energetically favorable situation consists in the localization of this charge with concurrent generation of a local lattice distortion around it. As consequence of this distortion, localized electronic states are formed with an up-shift of the HOMO and a down shift of the LUMO of an energy term Δε, as shown in Figure 1.4.

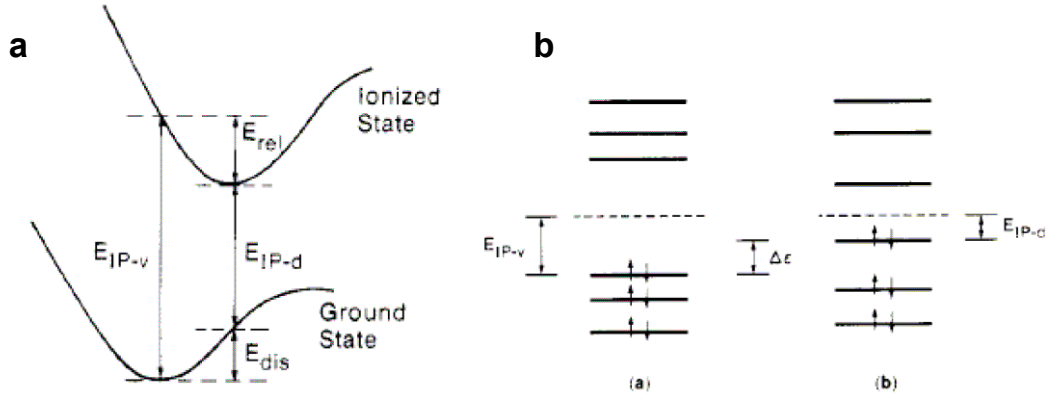

Figure 1.4: (a) Representation of the energies involved in a molecular ionization process with (b) schematization of the vertical transitions. E_{IP-v} is the vertical ionization energy, E_{rel} the relaxation energy gained in the ionized state, E_{dis} the distortion energy to be paid in the ground state in order that the molecule adopts the equilibrium geometry of the ionized state, and E_{IP}-d the ionization energy of the distorted molecule. Adapted from ref. [17]. Copyright ACS (1985).

If the energy term Δε necessary for the up-ward shift of the HOMO is larger than the energy change for the distortion, ΔE_{dis}, the polaron formation will be favorable.

Upon Bredas interpretation, considering the case of p-doping, a polaron is regarded as a radical ion correlated to a lattice distortion bearing charge $1q^+$ and spin ½ , the latter is EPR active and characterized by a full VB and an empty CB. Upon further removal of one electron, similarly to a two-folded oxidation process, a bipolaron is formed bearing $2q^+$ charge and spin 0. Bipolarons are therefore EPR silent and are also associated with a strong local lattice distortion. Polaron and Bipolarons in CPs are analogous to radical cations and dications, respectively, in conjugated oligomers. Upon the model presented from Bredas, it is found that in conjugated polymers, the formation of a bipolaron is energetically more favorable than generation of an additional polaron, because its generation is associated with a significant gain in ionization energy. The model from Bredas further claims that metallic behavior can be observed at high doping levels, when the broadening of the bipolaron states in the gap upon increasing doping concentrations leads to the merging of the VB and CB, resulting overall in an unfilled VB and metallic like behavior.

After several decades the model of polarons and bipolarons as traditionally introduced by Bredas is still widespread and generally utilized to explain spectroscopic and conductivity behaviors in conjugated conducting polymers. Different controversies are although associated with this model, which also provide only limited or incomplete description of experimental spectroscopic, EPR and conductivity data. More specifically, the main controversies to Bredas model derive from:

- the absence of experimental proof from EPR and electrochemical experiments of the stabilization of a bipolaron in comparison to two polarons expected for bipolaron generation,[18–20] and neglection of solid state phenomena,[20]
- the incomplete description of spectroscopic data;[21]
- the decrease in conductivity found at very high doping levels in different classes of CPs, contradicting the predictions of increased conductivity due to better overlap between VB and CB with increasing doping level.[20,22]

Integrations to Bredas' model have been proposed, and take mainly into consideration the interaction between charge carriers.[9,23,24] Polarons and bipolarons have until this point been described as intra-chain species, it is also not surprising that at the solid state, interactions between polymer chains will also take place. This has indeed been experimentally proved, showing that the coupling of polarons can take place between polymer chains (inter-chain interaction) in the form of weak bonds, whose formation and properties can strongly depend on the degree of delocalization of the charge for the polaron.[20,25–31]

These interacting species are indicated as π- and σ- dimers, respectively. Additionally, polaron-pairs have also been discussed as charge carriers for intermediate doping levels as additional intra-chain charge carriers. The formation of the different interacting charge-carriers is highly dependent on the structure and the doping level, they normally coexist at a specific polarization potential and are difficult to be distinguished among each other. A schematization of the charge carriers generated in poly(thiophene) as function of the doping level is reported in Figure 1.5 and complete representations of the possible structures are reported in Figure 1.6. In the following sections we will focus on each of these specific charge carriers.

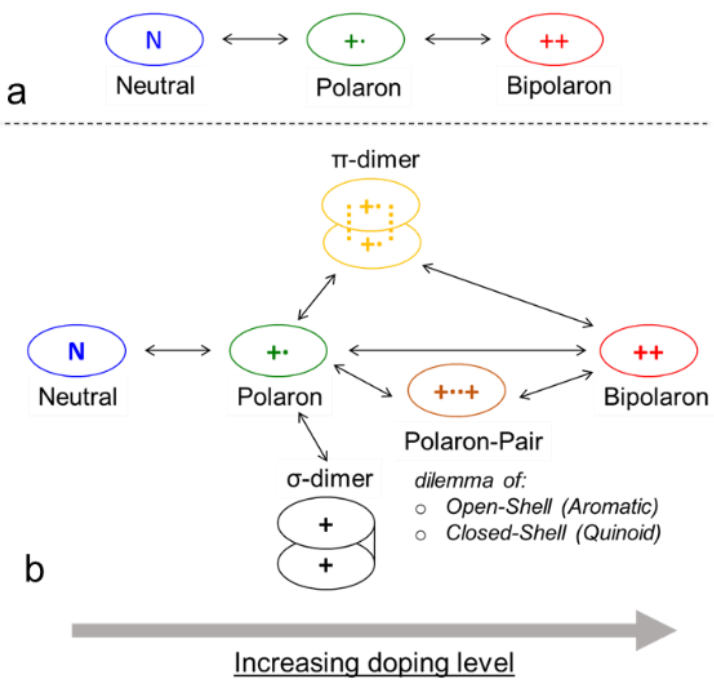

Figure 1.5: Schematic diagrams showing intrachain and interchain charge carriers.[9,32]

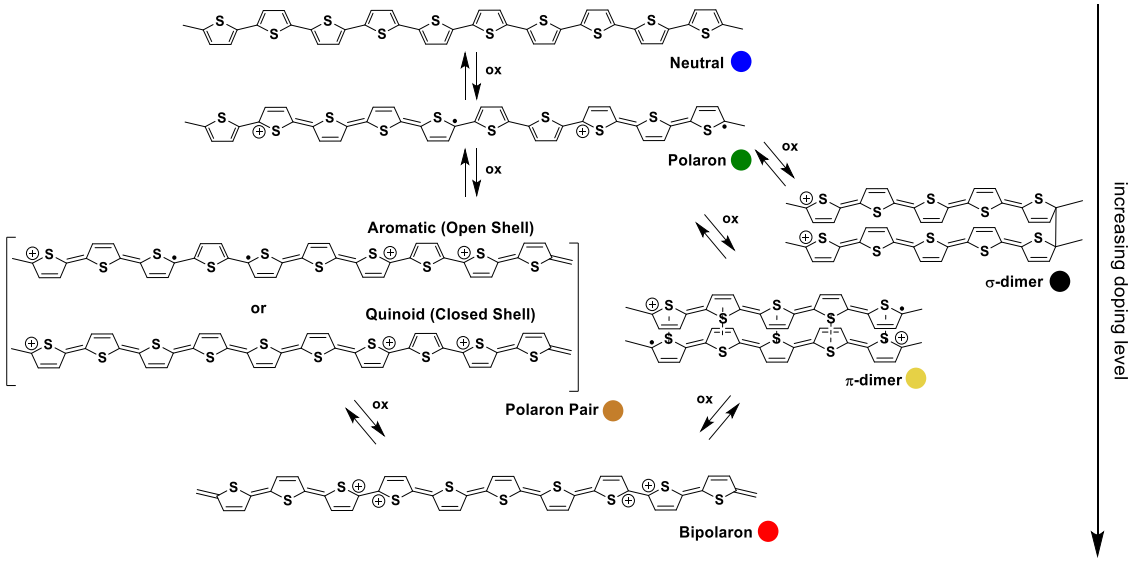

Figure 1.6: Charge carriers as function of the doping level, schematization, and exemplification for PT. [9,32]

π-dimers

The generation of π -dimers and their role in the charge transport mechanism upon oxidation of different conjugated oligomers, such as oligothiophenes, oligopyrroles etc., in analogy to role of π-dimers and stacks on the conductivity of mixed-valence salts, has been described in different works.[25,27,33] The formation of this species is entropically unfavored and is promoted at high concentration or at the solid state, as well as at low temperatures, by stabilization of the molecules by double occupation of a lower energy level generated by

the splitting of two interacting, singly occupied energy levels of the interacting units.[25–27] Π-dimers, sometimes indicated as inter-chain bipolarons, are EPR silent species. In the case of conjugated oligomers, they generally exhibit two transitions and in some cases a CT band, which are red-shifted with respect to the radical cation counterparts.[34–36] In the case of short-chain oligomers their absorption can be normally identified whereas in conjugated polymers their absorption is difficult to be differentiated from the one of "intra-chain bipolarons".[26,32,34,37,38]

σ-dimers

Charged σ-dimers have also been proposed as possible intermediate generated during the charging/discharging of conjugated conducting polymers. The formation of σ-dimers was first disclaimed by Heinze et al. to explain the reactivity of hetero-aromatic monomers during electropolymerization and the charging-discharging patterns of conjugated polymers, including the low conductivities registered at low doping levels and hysteresis phenomena.[23,30,39] The formation of σ-dimers has been proved for both radical anion and cations of different conjugated oligomers, in addition to the formation of π-dimers. [20,28–31] The chemically reversible generation of σ-bonds between two charged radical ions has been detected by voltammetric and spectroscopic experiments at different scan rates and low temperatures.[29–31] Further, the reversible formation of charged σ-dimers was also observed to take place in blocked position, when the molecule would be charged at sufficiently high oxidation potentials[20,29–31] The formation of σ-dimers is driven by the high coupling tendency of radical species which is associated to negative enthalpies of formation. The presence of σ-dimers generated at lower doping levels has also been associated to peculiar ion transport behavior; in particular, it is found that a high concentration of these species can reduce the mobility of anions during p-doping making necessary cation insertion at the polymer | electrolyte interface to allow for electroneutrality.[40]

In general, considering the experimental evidences for the formation of both interacting charge-carriers, π- and σ-dimers, it is expected that both species should be formed during charging/discharging processes of conjugated polymers. In general, it is found that the enthalpy of dimerization increases with increase in the chain length in the case of π-dimers, whereas σ-dimer formation is enhanced in systems characterized by a lower conjugation.[23,41]

Polaron Pair

Doping of conjugated polymers generates intramolecular microscopic defects, polaron and bipolarons, whose stabilization is driven by generation of quinoidal segments at expenses of aromatic moieties. For different chain lengths, the stability of a bipolaron can be very

different and is strictly dependent on the doping levels. The concept of polaron-pairs as charge carriers in CPs has been predicted by calculations by assuming a decrease of the coulombic repulsion upon separation of two positively charged polarons.[42,43] In general, in the case of shorter oligomers, quinoidization is the preferred way to accommodate two charges in a single molecule.[44–46] On the other hand, for longer oligomers, the gain in aromaticity paying the energy cost to break a double bond and to form a diradical is preferred and open shell diradicals are found (polaron pair). It is theoretically and experimentally evidenced a threshold in the conjugation length for which coulombic repulsions and energy of formation of two polarons, associated to a structural deformation, are in competition.[32,44,45] In the case of oligothiophenes it is found that shorter oligomers ($T4^{2+}$, $T6^{2+}$) present a closed shell (quinoid) dicationic state, whereas longer oligothiophenes ($T8^{2+}$, $T12^{2+}$) show an open shell (benzoid) diradical character in the dication state (polaron pairs). Upon introduction of electron-withdrawing substituents, the close shell to open shell transition is found to be easier and takes place for shorter oligothiophenes, due to decreased electron density and strength of the double bond for the quinoid form. This type of behavior, is also found for other type of conjugated oligomers.[47]

1.1.1.2 Spectroscopic Transitions in π-Conjugated Polymers

Following the traditional description by Bredas *et al.*, considering the p-doping in a non-degenerate ground-state polymer such as PT, the one electron oxidation results in a partially quinoid-like structure on the polymer chain. This geometric distortion is associated with an upward shift of the HOMO and a downward shift of the LUMO, generating polaronic levels symmetrically located with respect to the center of the band-gap (Figure 1.4 (b)). Upon further removal of one electron, either another segment of the chain could be oxidized generating another polaron or if the unpaired electron of the polaron is further removed, a bipolaron is formed. In bipolarons a further shift of the intra-gap levels toward the gap center occurs, because of the increased lattice distortion caused by the Coulombic repulsion of the two charges. Summarizing, this approach proposes that the lowest polaronic level is occupied by one electron and that the bipolaronic levels are empty, and in the case of a crystal this results in half filled polaronic bands and empty bipolaronic bands, respectively. Figure 1.7 (a) reports the energy levels and electronic transitions for polythiophene in the neutral, polaron and bipolaron state following a traditional interpretation as first reported by Bredas et al.[16,17]

In the case of the polaron state of PT two main transitions are expected, P1 and P2, which are dipole allowed; a third transition P3 is also expected but with negligible intensity as consequence to the fact that the associated electronic levels possess the same symmetry properties. Upon the same model, in the case of the bipolaron state, the possible

transitions are taking place from the top of the valence band, with the transition B1 stronger than B2. These theoretical predictions have found good feedback in experimental results with conjugated oligomers, whereas in the case of conducting polymers these theoretical results are not entirely followed[21,42] In fact, many conjugated polymers show two transitions at the energy characteristic for the polaron states, also for doping levels for which bipolarons should be already present.[20,21,48]

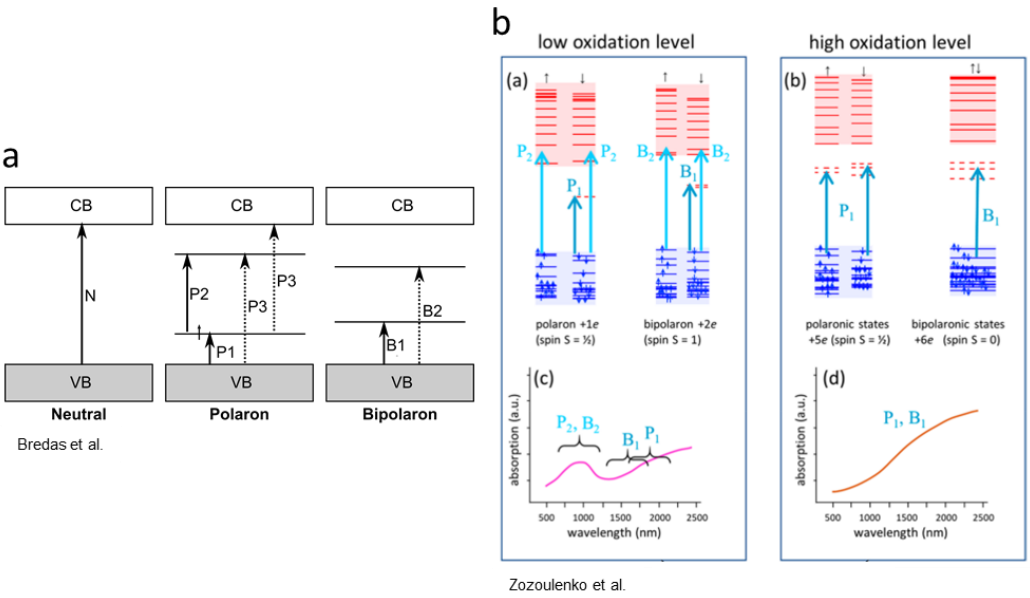

Figure 1.7: (a) Energy levels and electronic transitions in a PT and the corresponding polaronic and bi-polaronic redox states. Strongly dipole-allowed transitions are indicated with a solid arrow. Valence and conduction bands are presented in gray and white, respectively. Adapted from Bredas et al. ref. [17]*. (b) Characteristic spectroscopic transitions of PEDOT in different doping levels by TD-DFT from Zozoulenko et al. adapted with permission from ref. [21]. Copyright ACS (2019).*

Recently, a review of the classical charge carriers' classification, based on results obtained by density functional theory (DFT) and time-dependent (TD)-DFT approaches have also been used to study various electronic and optical properties of organic semiconductors. Upon these approaches, different transitions are predicted both quantitatively and qualitatively, which better correlate with the experimental results.[21] In the more recent description (Figure 1.7 (b)), for low doping levels the polaronic states ($1q^+$) are not any more treated as spin-degenerate, disregarding the lifting of the spin-degeneracy. The bipolaron's ground-state (bipolaron considered as $2q^+$) is regarded as triplet (S=1), in contrast with the traditional approach treating it as spinless (S=0). In this situation, the band diagram and the optical transitions for the bipolaron show similar features with the polaronic state. For higher doping levels instead the ground states for the polaronic states ($3q^+$,$5q^+$) are doublets (S=1/2), whereas the ones for the bipolaronic states ($4q^+$,$6q^+$) are a singlet (S = 0), also in this case the main features of the band structure are very similar for bipolaronic and polaronic states. The revisitation of the traditional description of polaronic and

bipolaronic states indicates that these charge carriers present between each other much stronger similarities and not a strong separation of the properties as traditionally proposed. From this prospective, the authors claim that considering a different transport mechanism for the two charges would be in contrast with the strong similarities these species present. The success of the interpretation from Zozoulenko *et al.* lies in the consideration of the different possibilities of interactions between charge carriers and their spin state as function of the doping level.[21]

1.1.2 Redox Polymers

In addition to π-conjugated polymers, redox polymers constitute the second class of materials into which conducting polymers can be classified. Redox polymers are characterized by the presence of redox-responsive groups or sites that are spatially localized and isolated, and which determine their electroactive and conductivity properties. Subclassification of these materials is determined by the position of the redox-active group, which could be integrated in the polymer backbone or as side chain, and by the organic or inorganic nature of the redox group. The structures of some characteristic organic redox polymers are presented in Figure 1.8, including systems with pendant redox units such a poly(9-N-vinylcarbazole) (PVCbz) (1), poly(vinyltriphenylamine) (PVTPA) and (2) poly(vinyl-p-quinone) (PVQ) (3) as well with redox units such as N-phenyl-naphthalene-diimide (PNDI) (4) and viologen (5) embedded in the polymer backbone. The absence of a π-conjugated backbone makes these systems typically characterized by superior solubilities in comparison to conjugated polymers.

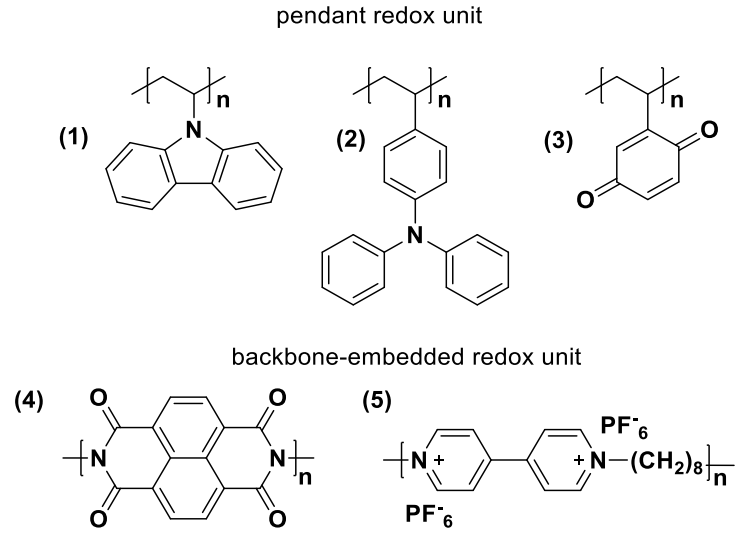

Figure 1.8: Structures of some common organic redox polymers characterized by pendant redox unit (1-3) or a backbone-embedded redox unit (4-5).

1.1.2.1 Charge Transport in Redox Polymers

In redox polymers, the redox active units can be easily oxidized and/or reduced, and will result in charge hopping between units in different states of oxidation. In general, redox polymers present in comparison to π-conjugated polymers lower intrinsic conductivities, and narrower conductivity profiles as function of the doping level. More specifically, the conductivity profiles in systems characterized by localized redox units show typically narrow windows of electroactivity and of conductivity, with maxima found in correspondence to the half-wave potential of a redox reaction (Figure 1.1). The half-wave potential corresponds to the situation in which the amount of isoenergetic states between which electron-hopping can take place is maximum.[9,23,49] This description of charge transport in redox systems is also known as mixed-valence conductivity model. In the case of redox polymers, the mixed-valence conductivity model can be considered as a localized molecular version of the half-filled band for conjugated systems, where due to the presence of weakly interacting states, a very narrow energy band is expected. Narrow bands created with little, or no delocalization can, however, have a high density of states at a particular energy. If the localized units are close enough for efficient electron tunneling and there are low reorganization energies associated with the electron transfer (redox) events, then a highly conductive state can be achieved.[9]

1.2 Electrochemistry of Conducting Polymers

In this work, electrochemical methods were employed individually or in combination to other techniques (*in-situ* electrochemical methods), for preparative or synthetic purpose, as well as for characterization of the electroactivity including reversibility, charging/discharging phenomena, HOMO, LUMO and E_g determination.

1.2.1 Electropolymerization

Electrochemical methods were employed for the preparation of electroactive surfaces by electrodeposition from both solution as well as at the solid state, i.e. performing the functionalization of solution casted films by electrochemical activation of reactive redox active units. A description of the general electroactive mechanism for a heteroaromatic unit is presented in Figure 1.15. This type of mechanism and the intermediates are also found with strong similarities in the reactivity of different oxidatively generated organic radical cations, as will be later presented in the thesis.

From a mechanistic point of view, potentiostatic, potentiodynamic or galvanostatic techniques can all lead to the electrochemical formation of conducting polymers upon generation of reactive radical cations, or anions in the case of a less common reductive electropolymerization. In general, cyclic voltammetry is often preferred to other

electrodeposition methods as it allows to easily follow the deposition process by the analysis of the current, which gives information about the amount of progressively deposited material, and of the potential, which provides information about the extent of conjugation. In this case electrodeposition is performed by repeatedly scanning the working electrode potential up to the oxidation potential of the monomer and back to the re-reduction potential of the generated oligomers/ polymer.[50,51] In general, the anodic electropolymerization from a monomer solution involves an oxidation step which generates a radical cation, this is followed by coupling and a deprotonation and re-aromatization step generating the dimer, and proceeds via nucleation and a phase-growth mechanism. Whereas potentiodynamic electrodeposition allows for a facile overview of the process, it does not provide information on nucleation and growth steps; to gather these information, potential-steps experiments are employed. Electrodeposition offers several advantages over the chemical oxidation, such as absence of catalyst, direct grafting of the polymer onto the electrode surface, easy control of the film thickness by the deposition charge, and possibility to perform *in-situ* characterization during the growing process of the film by electrochemical and / or spectroscopic techniques.[20,52]

The polymerization starts with the formation of oligomers in solution; the next general step is the deposition, which includes nucleation, growth, and additional chemical steps under solid-state conditions. In the electrodeposition of CPs, different models for layer formation have been discussed and they all refer to the deposition of metals. There are two kinds of nucleation, namely instantaneous and progressive, and three types of growth involving one- (1D), two- (2D), and three-dimensional (3D) processes. In the case of instantaneous nucleation, the number of nuclei is constant, and they grow without the formation of further nuclei. In the case of progressive nucleation, nuclei are always generated. One-dimensional growth occurs only in one direction, e.g. perpendicular to the electrode. In the bi-dimensional growth, the nuclei preferably grow parallel to the electrode, and in the three-dimensional growth, the rates for these processes perpendicular and parallel to the electrode are very similar.[20]

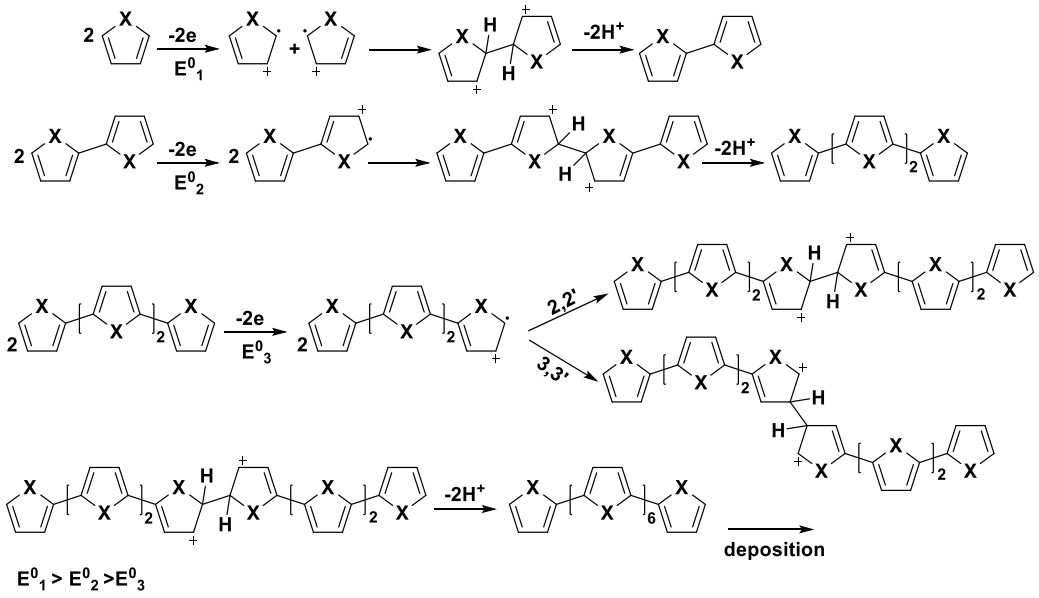

Figure 1.9: Electrodeposition mechanism for a general heteroaromatic unit, through the formation of σ-bonded intermediates. Mechanism from ref. [20].

In general, charged σ-dimers have been found to play a fundamental role in the electrodeposition mechanism, the first step of electrodeposition take indeed place through charged- σ-dimers, which stability determines the extent of proton elimination, which also constitutes the rate-determining-step for the electrodeposition process. An increase in the stability of these species, encountered by increase in the conjugation or electronic effects, causes a decrease in the rate of proton elimination. As previously mentioned, σ-dimers also cover a fundamental role in the charge / discharge processes of CPs.[30,31]

Analogously to other electrodeposition techniques, electropolymerization is characterized by strong dependence on experimental variables such as the nature of the solvent, monomer concentration, temperature, nature and geometry of the working electrodes and the applied electrical conditions.[20]

1.2.2 Cyclic Voltammetry of Conducting Polymers

Cyclic voltammetry constitutes also a powerful tool for the characterization of conjugated and redox polymers and oligomers confined on an electrode surface, allowing to gather information including for example HOMO and LUMO levels and the electrochemical band-gap E_g of the analyzed material, as well as their charge / discharge properties of the film. A theoretical description for the CV of thin films of redox polymers has been developed over 30 years ago.[20,53] The characteristic cyclic voltammograms of a thin layer polymer film presenting fast charge transfer and charge transport, is defined by completely symmetric and mirror-image voltammetric signals characterized by identical peak potentials and peak currents (Figure 1.10). In this situation, the current (I) measured at the working electrode is described by the following equation:

$$I=\frac{n^2F^2}{RT}\frac{vA\Gamma e^{(\theta)}}{\left[1+e^{(\theta)}\right]^2} \qquad (1.1)$$

with n representing the charge; *v* the scan rate, Γ the total surface concentration of redox sites, and A the covered electrode surface.

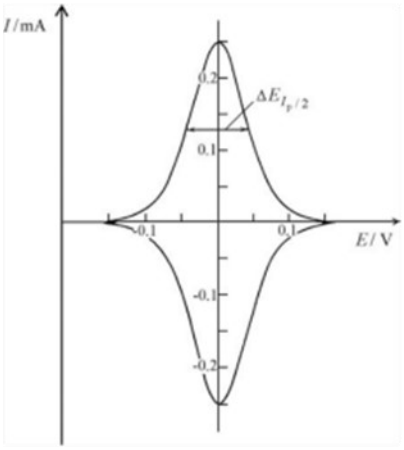

Condition	t_{film} *vs.* δ	$I_p \propto$	CV signal
Thin-Layer	$t_{film} << \delta$	*v*	symmetric, $E_{p,a} = E_{p,c}$
Finite Diffusion	$t_{film} \sim \delta$	-	loss of symmetry when increasing *v*
Semi-Infinite Diffusion	$t_{film} >> \delta$	$v^{0.5}$	asymmetric, $E_{p,a} \neq E_{p,c}$

Figure 1.10: Theoretical cyclic voltammogram for a thin-layer film with one redox center, resume of characteristic parameters for the CV of a surface confined electroactive layer as function of the film thickness. Adapted with permission from ref. [52]. Copyright Springer (2008).

One peculiarity of the cyclic-voltammograms of electroactive thin-films registered in equilibrium conditions, is the linear relationship between the peak currents (I_p) and the scan-rate (*v*) up to high scan-rate values. In principle, this linearity is valid only for monomolecular layers. In general in the case of thin polymer films deposited on an electrode, different situations for the current to scan-rate relationship can be predicted depending on the relative sizes of the thickness of the diffusion layer (δ) with respect to the film thickness (t_{film}).[50]

The thickness of the diffusion layer (δ) depends on the diffusion coefficient and the time-scale of the experiment, and, in the particular case of a voltammetric experiment, on the scan-rate. [50] In the case of polymer films two extreme situations are derived:

- a thin-layer behavior is found when the film thickness is much smaller than the diffusion layer $t_{film} << \delta$, in this condition direct proportionality between the peak-current and the scan-rate is found ($I_p \propto v$);
- the second extreme situation is the one of semi-infinite diffusion which is observed when the film thickness exceeds the thickness of the diffusion layer ($t_{film} >> \delta$). In this case the current responses are known from studies of solution redox species, showing direct proportionality between the peak-current and the square-root of the scan-rate ($I_p \propto v^{0.5}$).

In this case the voltammetric response also gradually shifts from mirror symmetrical diagrams to the classic asymmetrical voltammetric shape.

The case of finite-diffusion is considered for the intermediate situation between these two limiting cases (t_{film}~δ). Neighboring interactions between redox-active centers also result in a modification of the CV shape with possible broadening or narrowing of the CV curve.[20,52]

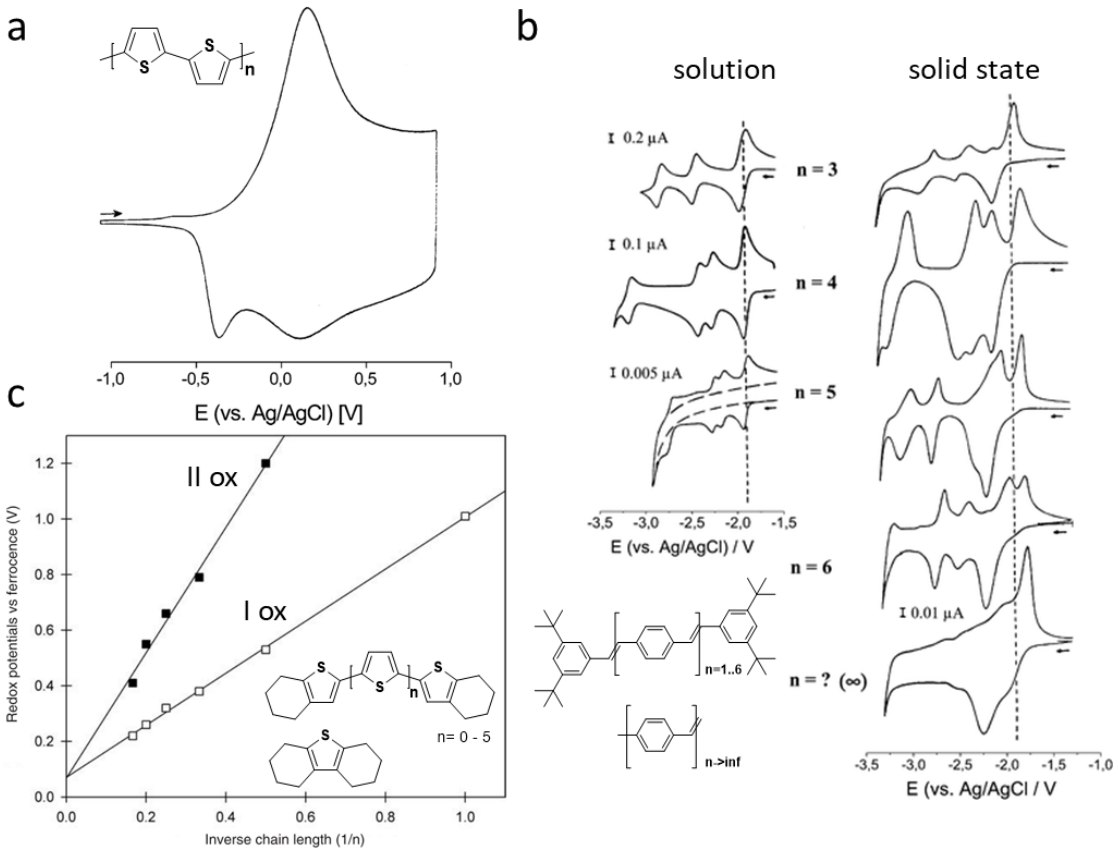

Figure 1.11: (a) CV for the oxidation of poly(4,4'-bithiophene), adapted from ref. [20] (copyright ACS 2010). (b) Cyclic voltammograms of the reduction of (left) oligo(p-phenylenenevinylenes) in solution and (right) under solid state conditions, adapted from ref. [54] (copyright Elsevier 1996). (c) Correlation of the first and second oxidation potentials of end-capped oligothiophenes vs the inverse of the chain length, adapted from ref. [55]. Copyright Wiley (1992).

In the case of films of conjugated polymers and oligomers differences in the voltammetric behavior are encountered in comparison to pure redox systems which are characterized by well-defined and limited redox states. In conjugated polymers due to the presence of multiple and subsequent electron processes the shape of the voltammogram is generally more complicated than the one of pure redox systems. For instance, the CVs of conjugated polymer generally show indeed steep anodic waves followed by a step plateau at higher doping levels, further, hysteresis between peaks in the forward and backward scans is generally encountered.

Upon studies on conjugated oligomers, the following points are established:[20,56]

- the number of accessible redox states in CPs increases by increasing the chain length;
- adding successive monomeric subunits increases the number of available redox states;
- the amount of available redox states cannot excess the amount of monomeric subunits in the chain;
- redox states present progressively lower energies (less extreme potential values) for the formation of a specific charged state by increasing the number of repeat units. The decrease in the energy of formation tends to saturate approaching a convergent limit as the number of repeat units increases.

1.2.3 Charge Compensation upon Electrochemical Doping

The generation of charge carriers in a polymer film upon doping is necessarily accompanied by ion compensation to allow electroneutrality of the charged film. In the case of a redox reaction related to electroactive molecules in a solution on a conducting electrode surface, the electron transfer step will take place at the electrode│electrolyte interface and is accompanied by transport of these electroactive species from the bulk solution to the electrode surface. On the other hand, a conducting polymer film deposited on an electrode constitutes a more complex situation and can be defined as an electrochemical system in which at least three phases are contacted successively: a first-order conductor (the working electrode), an electrochemically active polymer layer and a second-order ionic conductor (the electrolyte). The succession of interfaces in contact with each other in this case is described as follow: electrode | CP film | electrolyte.[50,52] When polarizing a non-coated electrode, the excess of charge builds up on the working electrode and the so generated surface charge is largely compensated by the diffuse double layer at the electrode| electrolyte interface.[50] In the case of electrodes coated with a CP film the polarization of the working electrode results in doping of the conducting polymer film, and the charges generated on the latter are compensated by ions that can penetrate the polymer matrix within the polymer strands.[57] In other words, upon electrochemical doping, the injection or removal of an electron at the electrode | CP-film interface requires the concurrent counterbalance of the ionic charge at the CP-film | solution interface.

Let us consider the general electrochemical doping (oxidation and / or reduction) of a conducting polymer <CP>. As previously mentioned, charge compensation will be undertaken by the counterions in the solution, a sketch is presented in Figure 1.12. The terms $<P^{n-},nC^{+},mS>$ and $<P^{n+},nA^{-},mS>$ represent “n” inserted cations and anions with “m” solvent molecules, for the general mechanisms of reduction and oxidation of a conducting polymer film, respectively. The examples listed above constitute two situations which can be found during electrochemical doping. As presented in Figure 1.12, for the more general

and simple situation the transferred ion should be the counter ion (*i.e.*, anion for a positively charged polymer, cation for a negatively charged polymer). However, in case of high ionic strength or for bulky counterions, the activity coefficients indicate that even the co-ion plays an important role, together with an equivalent amount of its counterion.[58–60]

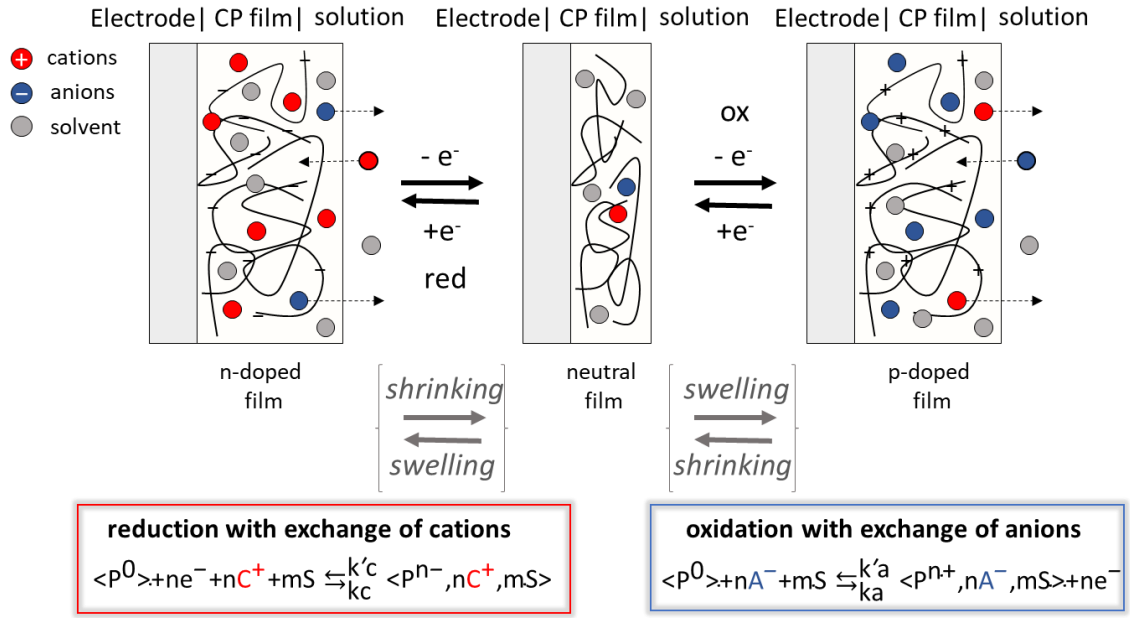

Figure 1.12: Representation of n- and p-doping processes for a CP film with charge compensation mechanism for the simple situation of (left side) reduction with exchange of cations, and (right side) oxidation with exchange of anions.

It is in general not possible to define a single mechanism that satisfies the electroneutrality prerequisite; for example, to compensate the positive charge in an oxidized film, both, entrance of anions and expulsion of cations, are also possible. Different and more complicated situations in addition to the one presented can also be encountered and are in general strictly correlated to the class of analyzed polymer as well as on the nature of the employed electrolyte. Indeed, when considering the case of conducting polymers in combination with bulky polyanions (i.e. PEDOT:PSS), or for self-doped polymers (*i.e.* conducting polymers in which the counterions are covalently bound to the polymer backbone), it is not so strange to imagine that the charge compensation could proceed also by exchange of cations.[61] A general classification of different possibilities of charge compensation mechanisms for different classes of conducting polymers has been listed by Otero *et al.* in a recent review.[62]

Flux of solvent molecules moving in the same direction of the ion flow is also generally observed upon electrochemical doping; consequently, swelling and shrinking processes are generally expected during electrochemical doping of CPs. [61,63,64] Charge compensation and swelling phenomena are strictly correlated with the free-volume inside

the film, which limits the number of solvent molecules which can insert within the latter. It must be also considered that changes in free-volume are strictly correlated to the doping level and is in general explained by the osmotic effect.[52] These processes are also likely to lead to a wide variety of unpredictable mechanical defects such as polymer electrode fatigue , stress concentration and delamination from the electrode. The doping state of the film and molecular reconfigurations during the electrochemical reactions control the free-volume of the polymer film.[65–67] The extent of swelling in CPs will be strongly dependent on the electrolyte composition, including solvent nature, nature of the salt as-well-as on its concentration. For instance, it was observed how the high ionic strength of the solution in the case of high electrolyte concentrations allows for a better shielding of the ionic charges, and that in this situation films show more compact structures in comparison to lower electrolyte concentrations.[52,68] For example, it was observed that in the case of PPy, the electrochemical doping in 1 M electrolyte concentration instead of 0.1 M would result in a reduction of up to 30% of the total volume of the film.[59,69]

In the literature, one possibility to study charge compensation is electrochemical quartz crystal microbalance (EQCM). EQCM measurements provide information about the overall mass change taking place during the electrochemical doping of a polymer film. Further, the analysis of the microbalance frequency (or mass) changes allow to distinguish the direction of ion movement as well as the average weight of the species involved in the charge compensation.[20,70] Different examples of charge compensation studies upon electrochemical doping of CPs can be found for different materials and electrolytes.[20] In particular, a very interesting approach to analyze mass changes and charge compensation of different classes of conducting polymers is the one of Hillman and coworkers.[66,67,70,71] They use current and frequency response to generate time-resolved ion and solvent flux data as function of the potential. The temporal dependency of the fluxes, analyzed by using different scan-rates allows one to identify kinetically controlled processes during the electrochemical doping of CPs.

It is generally observed that during the p-doping of common CPs in organic solvents, the charge compensation involves both anion and solvent contributions.[70,72,73] Skompska *et al.* found that the introduction of anions in an electropolymerized polymer film can take place by expulsion of solvent molecules and that this effect strongly depends on the nature of the solvent, of the film's initial state of swelling as well as by the nature of the polymer. Similar considerations are found for the polymer P3HT.[73,74]

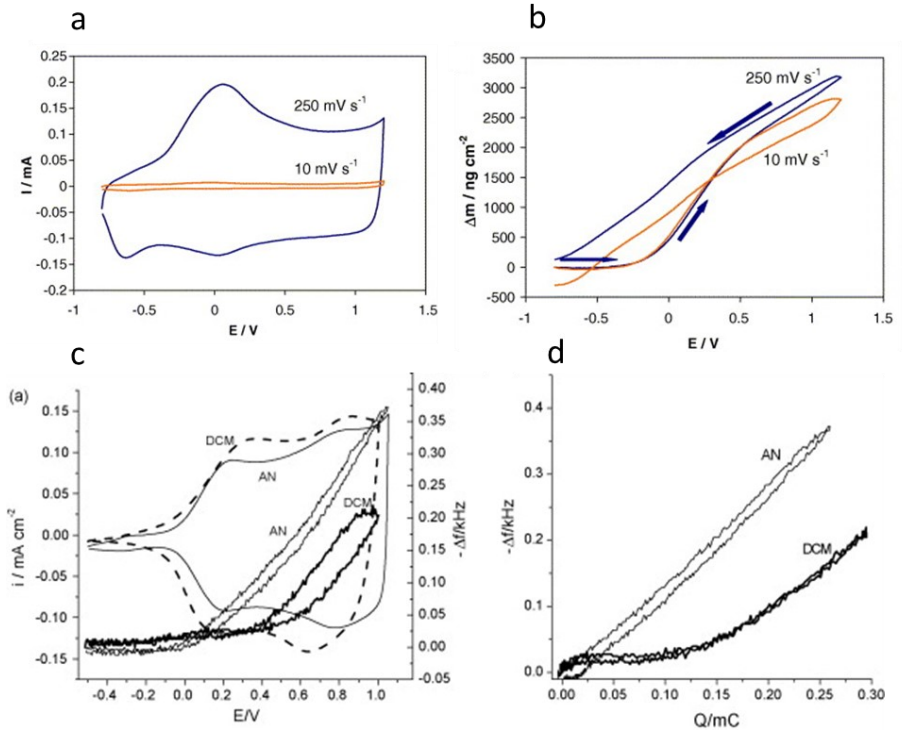

Figure 1.13: (a) CV and (b) Δm obtained from EQCM of PEDOT film in 0.1 M $LiClO_4/CH_3CN$. Adapted from ref. [70] (copyright Elsevier 2007). (c) CV and EQCM data and (d) -Δf vs Q plots for poly(3,6-Bis(2-thienyl)-N-ethylcarbazole) film in 0.1 M NBu_4PF_6/CH_3CN or CH_2Cl_2 at the scan rate 100 mV/s. Adapted from ref. [75]. Copyright Elsevier (2006).

In general, ion dynamics are strongly influencing the charge injection in the polymer.[52] The EQCM response of conducting polymers can also be affected by different experimental parameters including the scan-rate employed for the voltammetric experiment; preconditioning of the film, electrolyte concentration and electrodeposition conditions. A good example for this is the result of the study of Naoi *et al.*, who analyzed the charging and discharging of differently prepared poly(pyrrole) films in the presence of various supporting electrolytes, which differed for the size of the doping anion.[76] On the other hand, the authors observed that in the case of film prepared in presence of smaller anions (ClO_4^-, BF_4^-), upon oxidation only the anion intercalation was observed. On the other hand, in the case of films electrodeposited using bulkier anions such as poly(styrenesulfonate) or poly(vinylsulfonate), due to anion trapping in the polymer film, charge compensation is overtaken by cation motions. Finally, in the case of anions of "intermediate size" (e.g., tosylate), both anions and cations were observed to take part in the charge compensation process. One drawback of this classical EQCM approach is the impossibility of an easy way to discriminate the various contributions.

More advanced techniques, such as *AC*-electrogravimetry, have also in the last decades been developed to analyze charge compensation at the electrode│CP film│electrolyte interface, which also allow to gather the single mass and kinetics contributions of all the species involved in the charge compensation mechanism.[58,77,78] *Ac-*

electrogravimetry has been for instance successfully employed for splitting the contribution of different species in different redox processes, including for example the analysis of charge transport upon redox switching of Prussian Blue ($Fe_4[FeCN_6]$)[79] as well as in poly(pyrrole) (PPy) films[60,80] and for many other electroactive materials.[77,81,82]

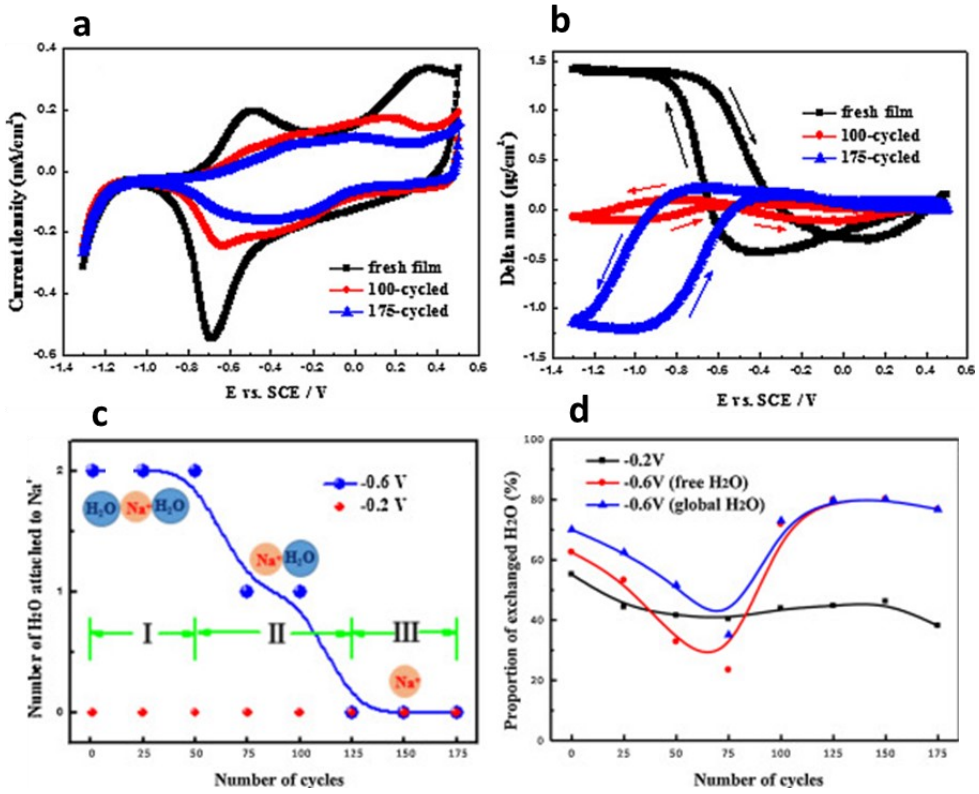

Figure 1.14: (a) CV, (b) mass change (Δm) of PPy-DS (dodecyl sulfate) film in 0.25 M NaCl aqueous solution between -1.3 V and 0.5 V vs. SCE at a scan rate of 50 mV/s, different cycle numbers are presented. (c) Dehydration process for hydrated cations transferred at the film/solution interface at -0.6 V as the film is electrochemically cycled, and (d) proportion of exchanged H_2O participating in charge compensation at both potentials obtained by ac-electrogravimetry. Adapted from ref. [60]*. Copyright Elsevier (2017).*

For example, in one of the first examples with this technique, it was possible to distinguish between the role of hydrated protons and potassium ions involved in the charge compensation of electrodeposited Prussian Blue (PB) films polarized at different potentials. It was found that for the mixed-valence states of PB the charge compensation was undertaken by hydrated protons, while in the case of more cathodic potentials, the contribution of the latter was almost negligible in comparison to potassium ions.[79] The technique was also employed in the case of electrodeposited dodecylsulfate-doped polypyrrole (PPy-DS) films to analyze the contribution of ions in the charge compensation process, analyzing the effect of cycling on the charge compensation in the films.[60] The authors find a transition in the nature of ions in the charge compensation process, passing from cations to anions as the film is progressively cycled (Figure 1.14). In general, *ac*-electrogravimetry allows to disentangle and quantitatively determine the contribution to the global charge compensation process by multiple species. Further, it offers a quantitative

picture of each contributor with their transfer kinetics and identification by their molar masses. *Ac*-electrogravimetry can provide very useful information in complementarity to EQCM; limitations of each of the techniques can be compensated by each other, and together they constitute an extremely powerful tool for the analysis of mass changes at the electrode | film | electrolyte interface.[79,81,83] A detailed description of this technique is provided in section 3.1.1.

1.2.4 *In-situ* Conductance and the Mixed-Valence Conductivity Model

One peculiarity of CPs is their ability to be switched between an insulating to a (semi)conducting state upon doping. Doping of CPs can be achieved by means of chemical oxidizing or reducing agents as well as through electrochemical methods. One advantage in the employment of electrochemical techniques is the possibility of fine-controlling the doping level of a film deposited on a working electrode by polarization of the latter in a three-electrode set-up. In this context, one very useful technique to provide insight of the conductivity behaviors of CPs as function of their doping level, is the microarray-electrode electrochemical transistor, also known with the name "*in-situ* conductance.[9,23,24,49,84] One main advantage of this technique is that it allows a precise correlation of the conductance profile to a specific doping level achieved through electrochemical methods. Most commonly, the technique has been combined with cyclic voltammetry, correlating features of the voltammogram such as faradaic peaks or pseudocapacitive plateaus, with the associated *in-situ* conductance pattern. In the case of a simple redox system, conductivity mechanism can be explained with the mixed-valence conductivity (MVC) model. This model dates back to the description of conductivity observed in stacked radical organic salts, and it interprets conductivity as a result of electron-hopping between the reduced and oxidized sites of a particular redox state.[20,49,85] The conductivity profile encountered for systems characterized by localized redox active sites, present typically narrow windows of electroactivity and of conductivity, with maxima found in correspondence to the half-wave potential of a redox reaction.[9,23,49] Figure 1.15 (a) shows *in-situ* conductance measurements for the redox polymer, poly[$Os(bpy)_2(vpy)_2$]$(ClO_4)_x$ with characteristic conductance maxima in correspondence of the half-wave potential for the different redox reactions of the polymer film.

In the case of π-conjugated polymers, the description of the potential dependent conductivity becomes more complicated. In these systems, maximum conductivity is reached at relatively high doping levels and is generally maintained over a wider window of potential with characteristic plateau-conductivity trends in comparison to the peak behavior of redox-polymers (Figure 1.15 (b)), which is followed by a decrease in conductivity as the polarization potential is further increased (doping level over 0.5 for PT).[22–24] The

experimental results contrast the bipolaron model, which predict the achievement of a metallic behavior upon generation of bipolarons, due to overlapping of the valence and conductance bands.[16,86]

The decrease in conductivity found at high doping levels in CPs, was tried to be explained in different ways, including increase in coulombic repulsion and localized charges at higher doping levels which diminish conductivity (Wrighton *et al.*)[22] or by the hopping of polarons and bipolarons by Zotti et *al.* analogously to the mixed-valence model[87] explaining the decrease in conductivity at high doping levels as the available number of sites for hopping decreases. The oligomeric approach, i.e. the analysis of conjugated oligomers as prototype systems for explaining behaviors of conjugated polymers, has resulted very useful to study and interpret the conductivity behaviors in CPs. Indeed, striking similarities are found in the case of oligothiophenes with a number of units higher than sexithiophene (T6), such as octamers (T8) and decamers (T10), showing a pseudocapacitive region at higher doping levels associated with a conductance plateau, in a similar fashion to PT.[88–90] In the case of T6, only faradic peaks and a characteristic mixed-valence conductivity behavior are encountered. The authors try to explain the phenomena associating a strong spin-dimerization of the polarons in T6 which become conducting only in association with bipolarons, through a mixed-valence conductivity mechanism, to further decay when only bipolarons are present. In the case of T8 and T10 on the other hand, the polarons are associated to a lower Peierls distortion due to the presence of two or four additional units for delocalization, and instead of stabilizing by spin dimerization, they create a lattice of strongly interacting oligothiophene chains with extra electron-filled states available for conduction. As a consequence the two-electron oxidized octamer and decamer display capacitive properties.

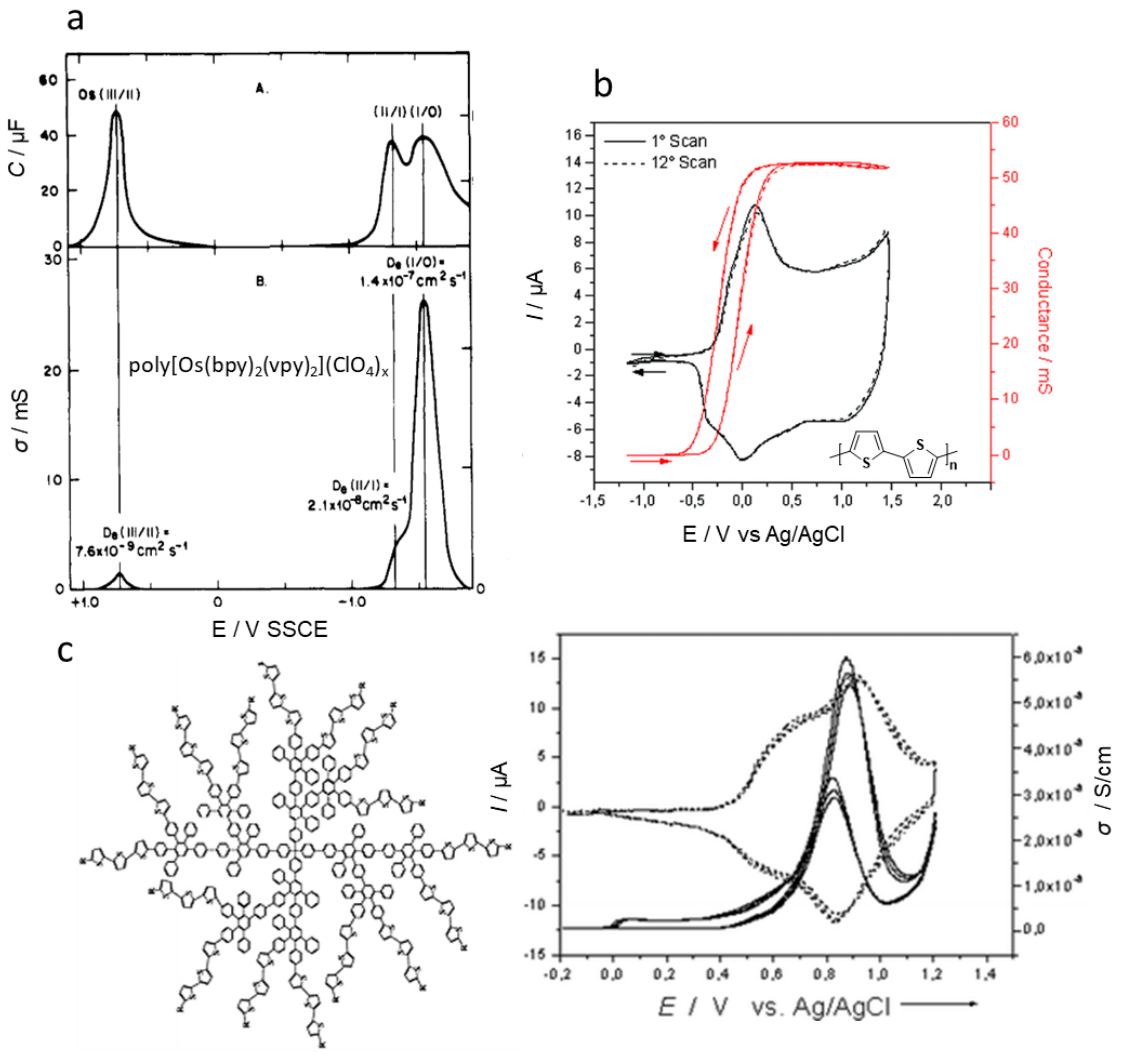

Figure 1.15: in-situ conductance of (a) poly[Os(bpy)$_2$(vpy)$_2$](ClO$_4$)$_x$ redox polymer, adapted from ref. [49] (copyright ACS 1996), (b) of poly(4,4'-bithiophene) characterized by a conductance plateau, adapted from ref. [20] (copyright ACS 2010) and (c) of electropolymerized terthiophene functionalized polyphenylene core dendrimer, as example of mixed-valence behavior in π-conjugated polymers, adapted from ref. [91]*. Copyright Wiley (2005).*

Heinze *et al.* support the hypothesis of mixed-valence conductivity between successive and overlapping redox states in conjugated polymers in a similar fashion as for redox systems. In the case of conjugated systems, the presence of multiple and closely located redox states results from the intrinsic nature of conjugated systems bearing different conjugation lengths, with these segments corresponding to interacting redox states through conjugation and by space-interactions. Through this model, the potential dependent conductivity can be explained as follows: initially the amount of freely hopping electrons between neighboring redox sites, and therefore conductivity increases slowly, due to formation of σ-dimers, which diminish the amount of free moving electrons for hopping.[39] Within the plateau region of conductivity, successive and overlapping redox states are passed one by one. In this way, the system is in a mixed-valence state where electron hopping occurs between occupied and unoccupied sites of one redox state and the number

of charge carriers remains almost constant. Finally, at higher doping levels, as the amount of available redox states for hopping diminishes, the conductivity decreases.[20,91,92] Characteristic potential dependent conductivity plots (*in-situ* conductance) measured for a redox polymer (a), a conjugated polymer (b) and an electropolymerized hexathiophene network (c) are presented in Figure 1.15.

The oligomeric approach was highly employed in the last decades and has resulted very useful to try to explain the behavior of conjugated polymers, despite the amount of information obtained, it remains a simplified model.[32,56,93,94] Other approaches have also been introduced in order to describe the properties of these systems, in particular to identify/ differentiate between the different charge carriers, interacting and non-interacting, directly on polymer chains. This leads for example to the idea of separating the polymer backbone from neighboring chains to analyze intra-chain transport, limiting the influence of inter-chain interactions. Conducting polymer backbones were tried to be isolated from by embedment in zeolites or in mesoporous silica.[95] Another successfully employed approach involves the use of "isolated molecular wires" obtained by synthesis of tailored sterically hindered conjugated oligomers and polymers, for which interaction with neighboring chains are minimized, to this class belong also the series of rotaxanes.[32,96–99] It is generally found that isolation of polymer backbone to avoid inter-chain interactions cause important decrease in conductivity. Decrease in conductivity is for example utilized in the case of polymer chains in zeolites or mesoporous silica to prove successful hosting.[95]

Sterically hindered molecular wires which can undergo electrodeposition were also studied and presented in combination with *in-situ* conductance characterization. Particularly interesting is the work of Swager *et al.* on electropolymerizable molecular wires based on canopied PPy.[97,99] The authors find that the introduction of sterically hindered canopy-shaped substituents on PPy, associated with a decreased dimensionality for hopping, result in a bell-shape conductance profile and lower absolute conductance values, in comparison to the broader plateau region of conductance for the non-substituted PPy (Figure 1.16 (a)).

Another peculiar work on insulated molecular wires and the effect on charge carriers and charge transport of hindered inter-chain processes was described by Shomura et al on electropolymerizable PEDOT and PT systems.[32] In particular, the authors attempt to identify the contribution to conductivity, optical and magnetic properties in these types of CPs, by preventing for example interwire interaction (i.e., π−π stacking) through the use of sterically hindered substituents on electropolymerizable monomers. The authors found that upon electrochemical doping of isolated chains through bulky substituents, the charge carriers form as follows: first at low doping levels ESR active polarons, followed for higher doping levels of doping, as the polaron concentration increases by the formation of polaron pairs. For higher doping levels, the latter merge into bipolarons to minimize the geometric

distortion. A scheme of the charge carriers generated as function of the doping level[9,32] is presented in Figure 1.6. The comparison of the isolated single wire (1-EDOT) to the non-insulated polymer (3-EDOT) films indicates significant differences in the generation of charge carriers and their stability as a consequence of π−π stacking. Interestingly, the *in-situ* conductance profile shows a peculiar change from a plateau like behavior to bell-shaped conductance when hindering intrachain transport, together with a less capacitive voltammogram (Figure 1.16 (a)).

Electroactive films obtained by electrodeposition of highly torsional starting molecules also hint in this direction, showing a bell-shaped conductivity window, as found in a collaboration of our research group and the one of Benincori *et al.* when studying *in-situ* conductance of the electropolymerization product of a bis-EDOT derivative (2'-bis{bi[2,2'-(3,4- ethylenedioxy)thiophen-5-yl]}-3,3'-bithianaphthene) endowed by an atropoisomeric backbone imparting high tridimensionality to the starting molecule and the relative electrodeposition products.[100] In their work, two independent maxima of conductance are observed and described in terms of mixed-valence conductivity behavior between tetrameric EDOT units in their polaron and bipolaron state, respectively.

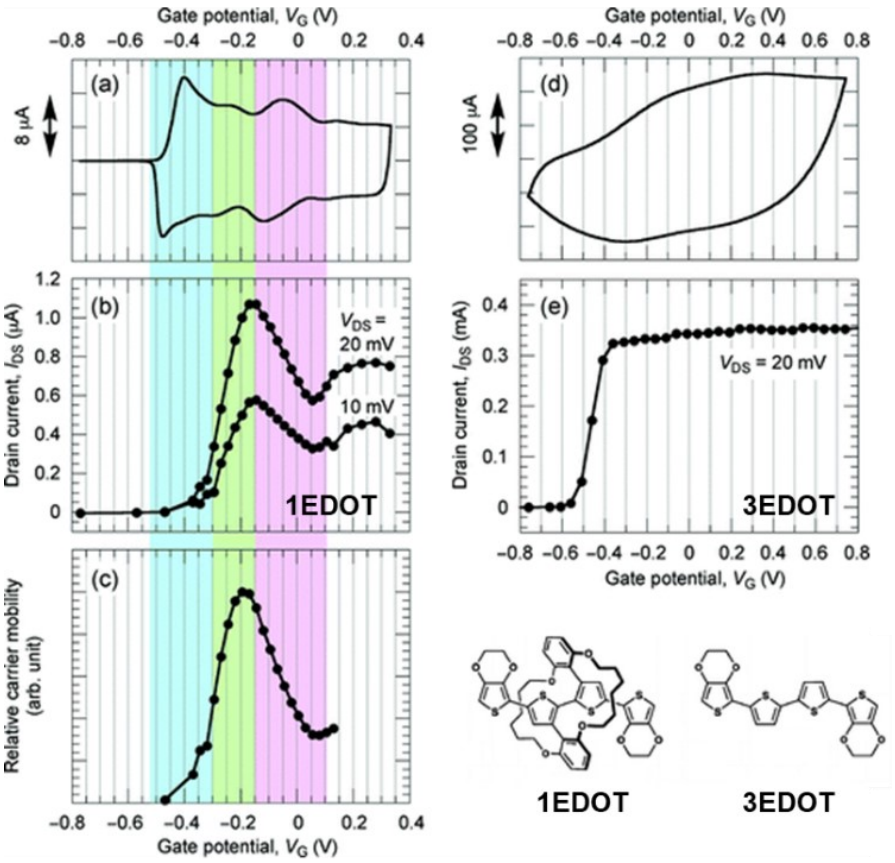

Figure 1.16: Conducting molecular wires, electrochemical and in-situ conductance results of electropolymerization of compounds 1EDOT (sterically hindered, no π-π interactions) and 3EDOT (π-π interactions); adapted from ref. [32]. Copyright ACS (2012).

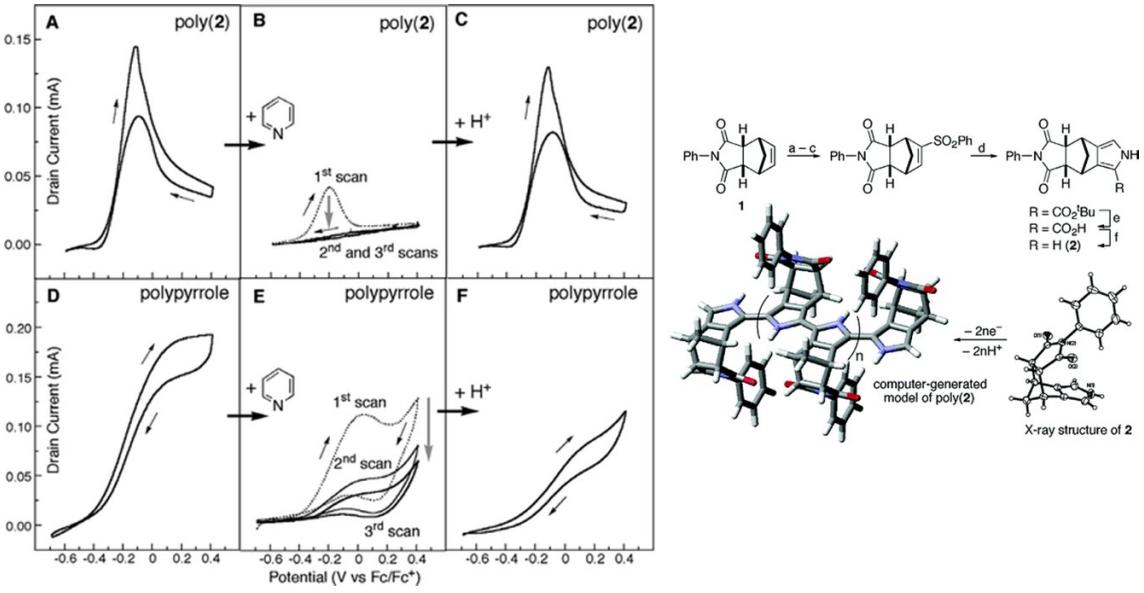

Figure 1.17: In-situ conductance of sterically hindered poly(2) and of PPy adapted from ref. [97] *(copyright Elsevier 2003).*

Similar results have been described in a recent work of our group on electrodeposited Tris(4-(2,3-dihydrothieno[3,4-b][1,4]dioxin-5-yl)phenyl)amine (P(TPA-

EDOT3)) which are also explained on the basis of the distorted nature of the repeating units causing lower effective conjugation of the system and the inter-chain interaction when compared to the linear PEDOT counterpart.[101] In the same study the *in-situ* conductivity of PEDOT:PSS characterized by different ratios of PEDOT to PSS also hints in this direction.[101] A decrease in the conductivity region, with the characteristic bell shape is found and becomes more pronounced as the amount of PSS polymer in the blend is increased (Figure 1.17). The experimental data are explained as the result of decreased interactions and connectivity between PEDOT chains accompanied by a less planar backbone evidenced for these systems.[97]

Finally, dominant interchain processes in determining global conductivity were also found for the electrochemical doping with different electrolytes as evidenced by Aubert et *al.*, finding significant conductivity changes for electrodeposited and cycled PEDOT films with different electrolytes, and showing decrease in the *in-situ* conductivity values with the anion size in the order: ClO_4^- > BF_4^- > $CF_3SO_3^-$ > PF_6^-.[102]

1.3 Electroactive Films Based on Arylamine and Carbazole Derivatives

Among different classes of organic semiconductors, arylamine derivatives have gained increasing attention within the scientific community due to their versatility as redox-active molecules and, most of all, because of their promising hole-transport properties. Triphenylamine (TPA) and more in general arylamine derivatives have indeed found successful application as outstanding building blocks for the preparation of electroactive materials for opto-electronic applications.[103–105] These include various thin layer opto-electronic devices[105,106] comprising organic light emitting diodes (OLEDs),[107,108] dye sensitized solar cells, organic solar cells (OSCs)[109,110] and perovskite solar cells[111] as well as electrochromic devices[112]. Further, the electron-rich character and electroactivity of TPA derivatives has also been exploited for electrochemical storage of energy.[113,114] The wide employment of arylamine derivatives as hole transport materials derives from the peculiar electron-rich character of the arylamine unit allowing for a facile generation of stable positive charges in the form of radical cations either electrochemically or photochemically. Triarylamine derivatives are well-known photoconductors with appreciably high hole transport mobility and therefore are extensively used in xerography.[115] Further, electrochemical reversibility and formation of stable radical cations, as later discussed, can be generated upon protection of otherwise reactive para-positions of the molecule (Figure 1.18).

In addition to exceptional hole transport properties, arylamine derivatives can also present a distinct electrochemical behavior resulting in the molecule dimerization triggered

by their electrochemical oxidation.[29,116,117] Carbazole and its derivatives are also widely employed in molecular electronics, and present similar reactivity to arylamine units. In general, a detailed knowledge of the electrochemical behavior of arylamine as well as carbazole derivatives is of great importance for targeting the synthesis of new stable compounds as well as for implementation of performance in applications. In particular, the dimerization ability of these units, can be exploited to generate highly crosslinked electroactive films for electro-optic applications. [118,119]

1.3.1 Electrochemistry of Arylamines and N-Substituted Carbazoles

The electrochemical reactivity of arylamines and carbazoles has been extensively studied through the years. The reaction mechanism upon oxidation of a triphenylamine unit is presented in Figure 1.18 (a), the oxidation of N-substituted carbazole molecules proceeds also with an analogous mechanism.[29,117,120,121] It has been proved that in the case of this class of molecules the one-electron oxidation generates a radical cation which is unstable because of the high spin density at the para-phenyl position and undergoes a chemical dimerization through radical-radical paring with generation of a dimer. The generation of a dimer takes place through formation of charged σ-dimer intermediates which undergoes proton elimination driven by the increase in aromatization energy.[117,122,123]

Figure 1.19 (a) shows the first two voltammetric cycles measured in thin-layer conditions for a TPA solution in 0.1 M CH_2Cl_2/NBu_4PF_6.[29] A different voltammetric pattern is obtained for the two cycles, evidencing the chemically irreversible oxidation of TPA leading to (N,N,N^0,N^0)-tetraphenylbenzidine units (TPB). In the first oxidation scan only one high peak at 0.69 V versus Fc/Fc^+ is observable. This peak is assigned to the chemically irreversible oxidation of TPA to its radical cation, which undergoes in the time scale of the experiment a follow-up reaction to TPB.[29] In the same potential range in which the radical cation of TPA is formed, the more conjugated dimer is immediately oxidized to its dicationic state. In the reverse voltammetric sweep the so formed TPB dication is reduced through two reversible steps, first to the radical cation (0.41 V) and then, at less positive polarization potential, to the neutral dimer (0.16 V). The reversible redox switching of the dimer is observable in the second voltammetric cycle for both forward and backward scan. In contrast to other conjugated heteroaromatic molecules, the radical-radical coupling of arylamines and N-substituted carbazole units stops at the level of dimerization. Evidence for the dimerization is given by spectroelectrochemical measurements in thin-layer conditions (Figure 1.19 and Figure 1.20), as well as by chemical oxidation experiments.[29,117,121,124]

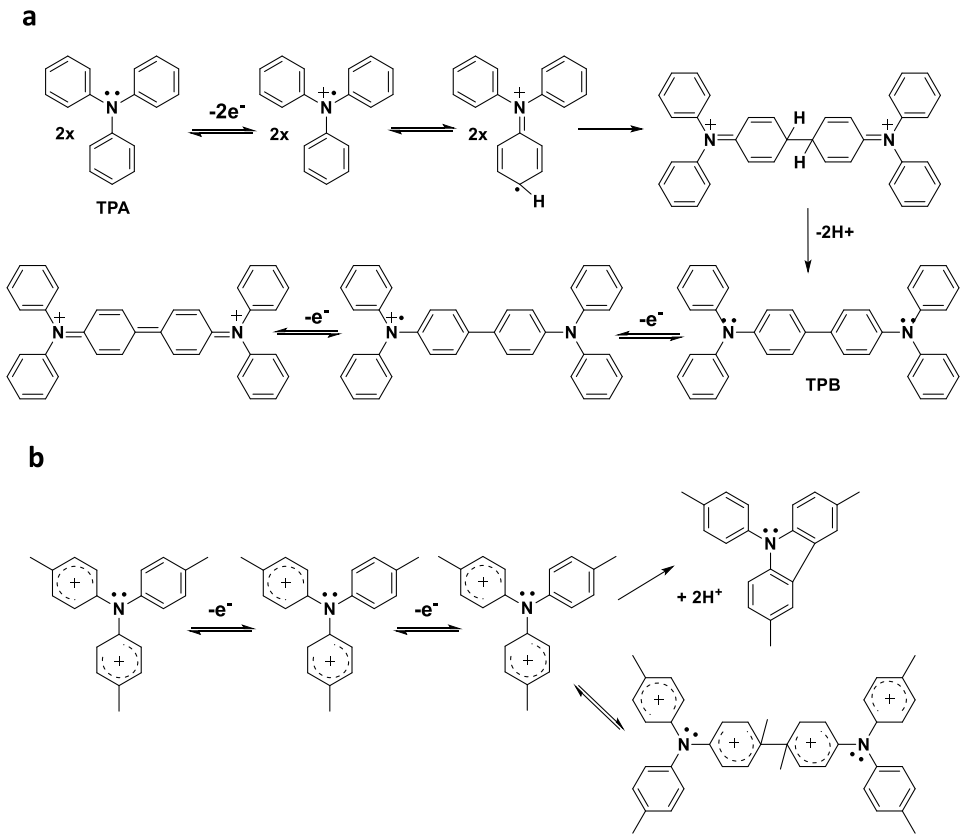

Figure 1.18: (a) Reaction mechanism for the dimerization of TPA upon anodic oxidation, (b) reversible and irreversible coupling of methyl-substituted tri-p-tolylamine pTTA.

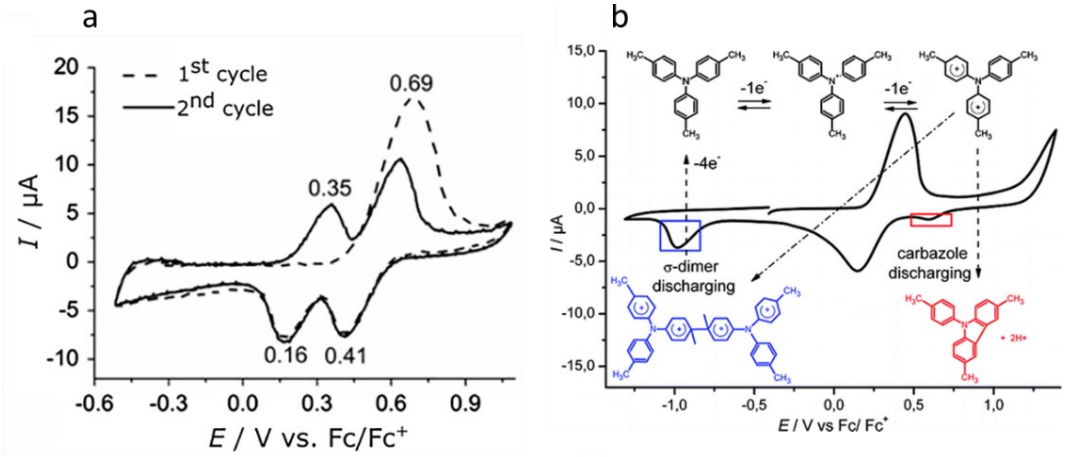

Figure 1.19: CV in thin layer conditions of (a) TPA and (b) pTTA in 0.1 M CH_2Cl_2/NBu_4PF_6 with peak assignment for the products of the reversible and irreversible follow up reactions. Adapted with permission from ref. [29] (copyright ACS 2011).

Similarly to an electropolymerization mechanism, electronic and steric effects as well as substitutions in particular positions of the molecule can lead to a dramatic change in the reactivity of π-conjugated radical cations towards the coupling reaction.[20,29,125] In this context, it was observed that the one-electron oxidation of tri-methyl substituted TPA, in which the reactive para positions are substituted, leads to the formation of stable radical

cation species, evidenced by constant intensity EPR spectra.[29] Although, when the tri-substituted pTTA is oxidised at the dication state, different chemical follow up reactions, through two competing reaction pathways can take place (Figure 1.18 (b) and Figure 1.19 (b)). The first pathway involves an irreversible intramolecular coupling reaction resulting in the formation of a carbazole unit; as already reported by Nelson *et al.*[126], whereas the second reaction pathway corresponds to a reversible intermolecular coupling leading to the formation of a σ-dimer.[29] These species were observed to be stable at the charged state and discharge only at negative potential values. This observation led Heinze *et al.* to explain hysteresis effects between charging and discharging in CPs and π-conjugated oligomers by formation of such intermediates. It is found that temperature and concentration highly favour one of the two reaction pathways, in particular, due to entropic effects intermolecular coupling with σ-dimers formation is favoured at lower temperatures.[29]

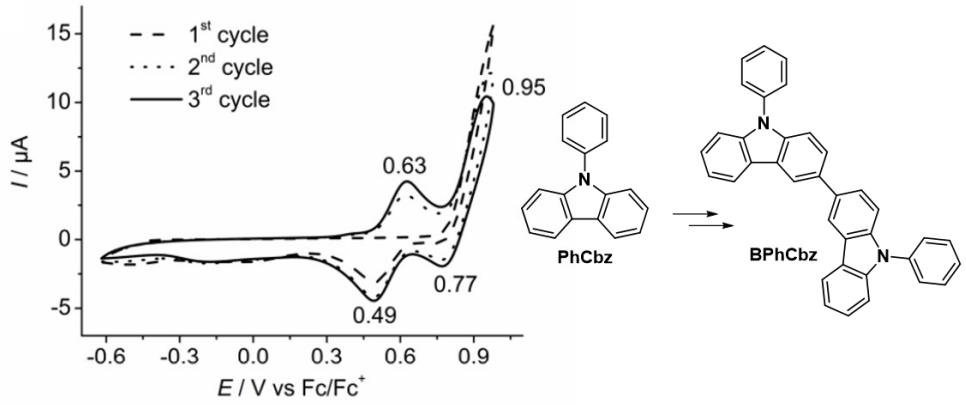

Figure 1.20: CV in thin layer conditions of (9-phenylcarbazole) PhCbz in 0.1 M CH_2Cl_2/NBu_4PF_6. Adapted with permission from ref. [29]. Copyright ACS (2011).

The cyclic voltammetry experiment of the dimerization of phenyl-carbazole molecule, taking place with a similar reaction mechanism as for triphenylamine, is presented in Figure 1.20.

1.3.2 Crosslinking Approaches with Arylamine and Carbazole Units

The electrochemically generated electroactive benzidine based dimers, endowed with a biphenyl bond, are generally soluble and diffuse from the working electrode to the electrolyte solution.[116,120,124] Electrochemical deposition has proved to be a very useful approach to fabricate electroactive films used as emitting layers and interface layers for OLEDs with high device performance properties, as a successful alternative to thermal evaporation and solution-processing, allowing for example for a reduction of the high costs that now characterize OLEDs in comparison to other display materials such as LCDs.[20,127–129] Electrodeposition has indeed the advantage in comparison to the above mentioned approaches of reduced complexity, simple and scalable setups, reduced material wastage, need of low temperatures, as well as of superior stability and insolubility of the deposited

films. Further, it is also characterized by a relatively good control of the film thickness and of the film morphology by choice of electrodeposition conditions.[128] Despite electrodeposition is a very simple and convenient technique for the obtainment of thin layers, when it is performed from a solution containing monomer of small dimensions problems of poor electroactivity and of poor/rough morphologies can be observed, often as a consequence of the high potentials necessary for electro-oxidation leading to overoxidation of the electrodeposited film or irregular growths.[20,127]

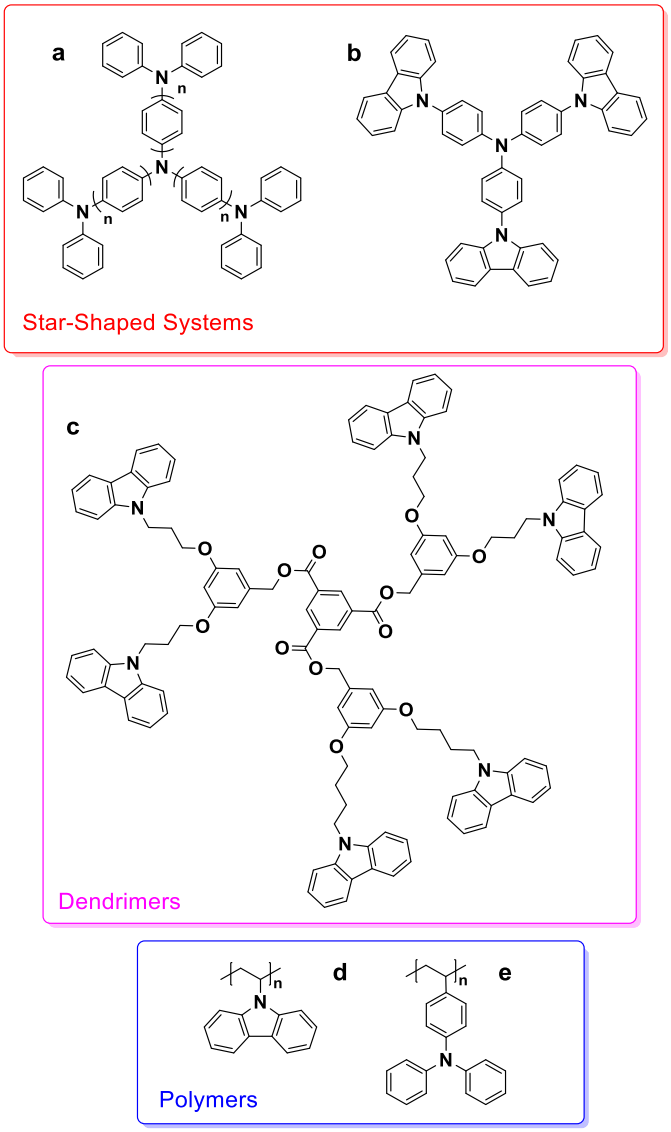

Figure 1.21: Examples of electrochemically crosslinkable precursors: star-shaped arylamine and carbazole (a) from ref. [130], (b) ref. [131], (c) a dendrimeric system from ref. [127] and poly(vinylcarbazole) and poly(vinyltriphenylamine) ref. [132].

In the case of N-substituted carbazole and arylamine films, electrodeposition of a redox active film can be achieved exploiting the dimerization ability of two or more unsubstituted redox-active units in a precursor molecule endowed by multiple dimerization

sites, for example in star-bust or multimeric systems or, as discussed later, using precursor polymers with free arylamine or carbazole units. Figure 1.21 shows examples of electrochemically crosslinkable precursors endowed with multiple dimerization sites through electrochemical activation that can be utilized for the preparation of electroactive films to be employed for opto-electronic applications. In general, the electrodeposition of highly branched starting monomers systems allows for the obtainment of electroactive films with lower aggregation between polymer chains and remarkable electrochemical properties due to the intrinsic 3D network that facilitates counterion movement and electron hopping.[105,131,133–135] Last but not least, the latter are also characterized by superior electrodeposition ability due to the presence of multiple sites for coupling. This approach has indeed been exploited for the electropolymerization of arylamine derivatives to produce modified electrodes for electro-optic applications.[119,130,131,136–143]

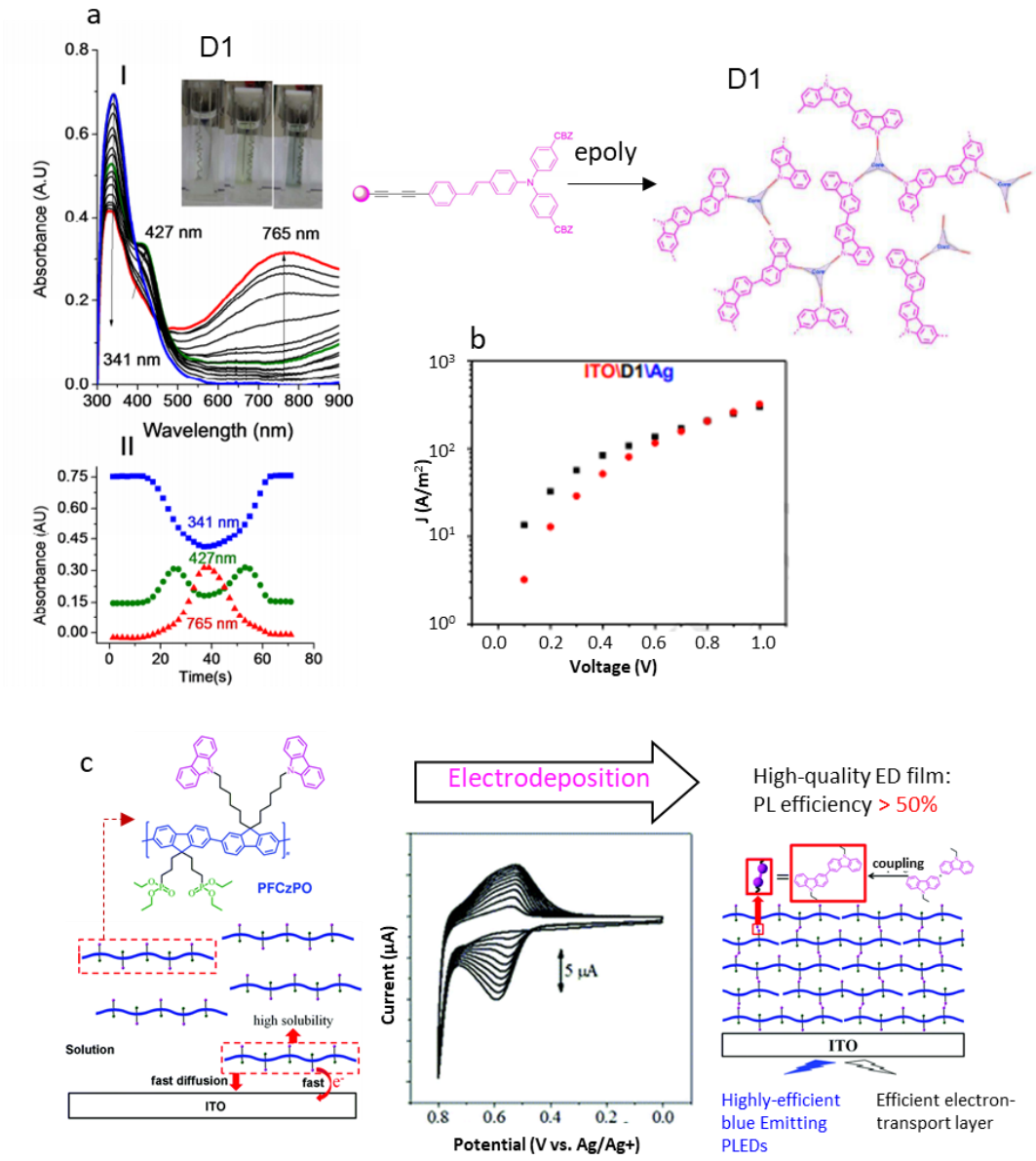

Figure 1.22: (a) Absorption and peak—trend of electrodeposited N-substituted carbazole dendrimer film with proposed schematic illustration of the highly crosslinked structure after electrodeposition. (b) Current density vs. applied potential measured curves at room temperature of ITO/dendrimer films/Ag single layer devices (black points). Calculated J-V values (red points). Adapted with permission from ref. [140] (copyright ACS 2013). (c) Electrodeposition of high-quality ED film for HTLs and polymer-LEDs from reference [119] *(copyright RSC 2020).*

Electrodeposited films of highly crosslinked networks obtained by oxidation of multimeric starting monomers have also found interesting application in the field of electrochromic devices with different advantages over linear systems.[130,131,136,141,143] In particular, the introduction of push-pull segments, in which arylamine and N-substituted carbazole act both as donor units as well as crosslinking sites have raised particular attention thanks to the possibility of extending the palette of colors achievable and to their intrinsic strong absorption, for example by the choice of the donor (D)-π spacer (π)-acceptor (A) terminals allowing for control on the macromolecular properties.[127,144] In this

context, Mangione *et al.*[129,140] report the electrodeposition of different dendron systems endowed with terminal carbazole units acting as dimerization points to obtain homogeneous and stable electroactive films which show reversible electrochemical and electrochromic behavior, enhanced electron transport and good charge injection properties. The authors found that hole mobility of the electrodeposited films was found to be dependent of the dendrimeric structure and film morphologies, with values ($8.98\ 10^{-4}$ $cm^2 \bullet V^{-1}$) in the range of those obtained for the well-known TPA derivative films deposited with classical methods.[103,145] The associated molecule and measurements are reported in Figure 1.22 (a, b).

Another attractive approach for the obtainment of functionalized triarylamine electroactive surface, as an alternative to electrodeposition from monomer solution, exploits the dimerizing ability of arylamine units just in a post deposition step of pre-deposited films. In this case the triarylamine unit is present for example as a redox-active pendant covalently bound to a polymer backbone, acting as a crosslinker unit upon oxidative triggering, and generating polymer films crosslinked with redox-active tetraphenylbenzidine (TPB) or biscarbazole (BCbz) moieties. The pioneer in this research line is Rigoberto Advincula who focused on the generation of HTLs by electropolymerization of carbazole containing polymers.[127,128,132] In particular, Advincula and coworkers made use of precursor polymers constituted of an insulating polymer backbone to which are connected electroactive redox-units corresponding to reactive crosslinking terminals upon electrochemical trigger. The author particularly focused and analyzed the crosslinking behavior upon different starting materials including linear polymers such as polyvinylcarbazole and dendrimeric systems. In general, electropolymerization or chemical oxidation results in a network conjugated polymer having both inter- and intramolecular crosslinking possibilities and a well-defined redox behavior associated to the one of the crosslinking unit. A recent review from Zhao et *al.*[119] also reports different examples of electrodeposition of dendrimeric systems and polymers with crosslinkable carbazole units to obtain stable and highly performing active layers for OLED applications. The authors show how, by optimization of electrodeposition conditions, it is possible to obtain films with high luminescence efficiency and stability, which can overcome the one of films of other deposition techniques. The results emphasize the high commercial potential of electrodeposition due to its reduced costs and scalability associated to good performance in comparison to other techniques (Figure 1.22 (c)).

This approach, was also exploited with some modifications by the Ludwigs group for the preparation of conductive and hole transport films, as an alternative to the more commonly employed deposition of chemically synthesized polymers and the electrochemical polymerization of π-conjugated monomers.[146–148] The said strategy includes in a first step the deposition of chemically synthesized polymers through solution

casting methods and, in a second step, the oxidative crosslinking/dimerization of the redox-active units initiated either chemically or electrochemically (analogous to a solid state electropolymerization) resulting in crosslinked films.

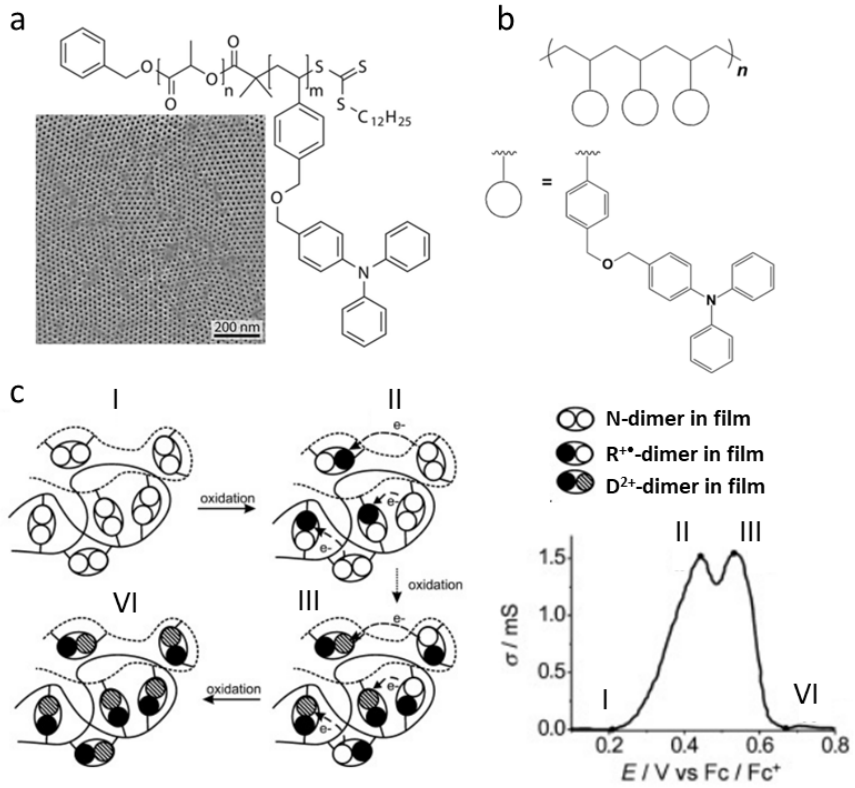

Figure 1.23: (a) Chemical structure of PSTPA-b-PLA and SEM image of the surface of electroactive PSTPA porous structure after PLA removal. Adapted from ref.[146] (copyright Wiley 2010). (b) Structure of PSTPA (ref. [147]) and (c) in-situ conductance of electrochemically crosslinked PSTPA with representation of the mixed-valence conductivity model operating within the film in different charged states, adapted from ref. [147] (copyright ACS 2010).

The approach of post solution-deposition electrochemical crosslinking has been indeed successfully employed with different systems, including a diblock-copolymer, PSTPA-b-PLA (Figure 1.23 (a)), constituted of PSTPA and a poly(D,L-lactide) blocks to achieve a microphase separation followed by functionalization, for employment in bulk heterojunction hybrid photovoltaic devices.[146,149] For the post -casting functionalization of the micro-to-nanostructured films, PLA block is chosen to introduce a cylindrical morphology in the PSTPA electroactive phase, constituting the majority component. The polymer films present perpendicularly oriented cylinders (center-to-center distance is of 21 ± 2 nm and an average diameter of 13 ± 2 nm) at the surface and a winding inner structure spontaneously formed after spin coating. Etching through mild hydrolysis conditions of PLA leads to a mesoporous structure within the PSTPA semiconducting medium. Further functionalization of the pore cavities (electrodeposition of other materials) is performed also exploiting TPA electroactivity.[150]

Post deposition modification exploiting TPA oxidative coupling can be successfully performed by using chemical oxidants as shown for the system PT-TPA (Figure 1.24) characterized by pendant TPA units attached to a polythiophene backbone.[148] In this case, the use of a strong oxidizing agent such as iron(III)chloride ($FeCl_3$) leads to the simultaneous crosslinking and doping of the polymer film. The variations brought by chemically induced oxidative crosslinking allowed for a decrease in the solubility of the film in different organic solvents in which the as-casted film was solubilized, making the approach interesting for applications requiring the use of organic solvents. Further, chemical oxidation of PT-TPA polymer films generated also charge carriers and bulk conductivities were analyzed by means of four-point probe measurements, reaching values of 8 ± 2.1 $S \cdot cm^{-1}$ upon employment of $FeCl_3$.

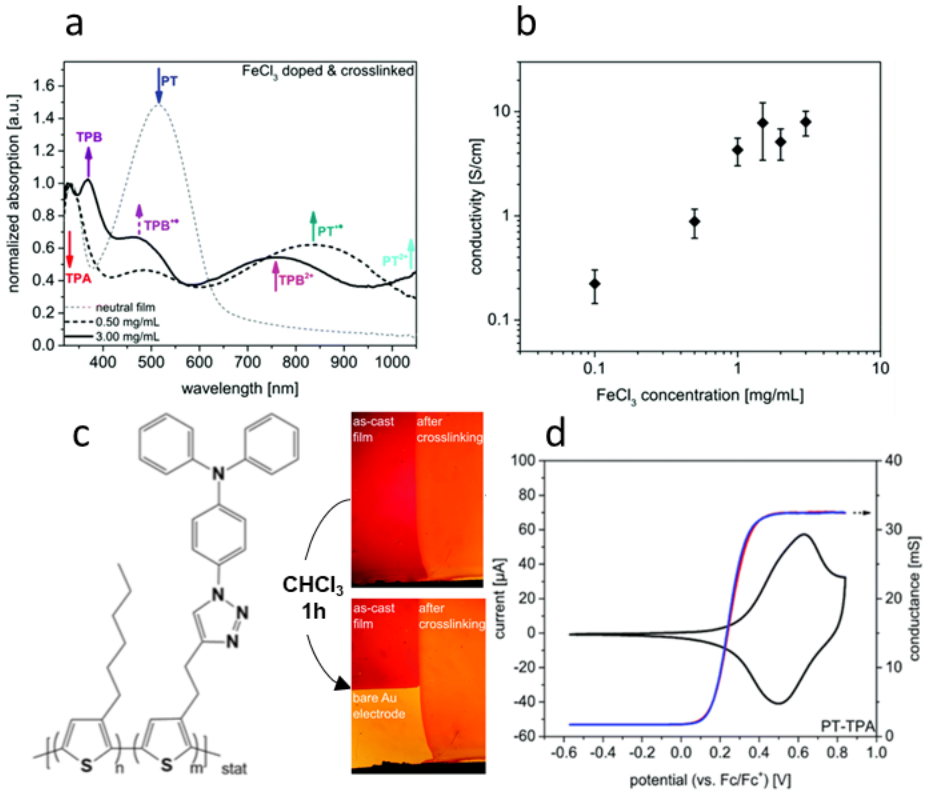

Figure 1.24: PT-TPA thin film (a) absorption spectra and (b) conductivity measurements of crosslinked PT-TPA for different dopant solution ($FeCl_3$/CH_3CN) concentrations. (c) Film before and after immersion in $CHCl_3$ d) CV and in-situ conductance measurement. Adapted from ref. [148] (copyright RSC 2017).

Yurchenko *et al.* analyzed the potential dependent conductivity of electrochemically crosslinked films of PSTPA. The authors find for the electrochemically crosslinked film two independent, partially superimposing conductivity regimes associated with two discrete mixed-valence states for radical cation and dication state of the tetraphenylbenzidine unit. These systems are non-conductive in both the neutral and fully oxidized state and the

charge transport is ascribed to the one-electron interchain hopping process between oxidized and reduced sites of a redox state, with maximum conductivity reached for an equal number of oxidized and reduced sites. Figure 1.23 (c) presents a schematization of the conductivity regimes of intermolecularly and intramolecularly linked TPB units. In analogy to this behavior, Heinze and colleagues observed a conductivity pattern for a three-dimensional hybrid network with sexithiophene oligomers bridging dendrimeric cores, with maximum conductivity reached for half charge level. These above mentioned studies were very relevant leading Heinze to the assumption of a mixed-valence conductivity behavior operating also as charge transport mechanism in doped CPs, considering the presence of multiple mixed-valence states in conjugated systems, between which electron hopping can take place.[23]

1.4 References

[1] H. Letheby, *On the Production of a Blue Substance by the Electrolysis of Sulphate of Aniline*, **1862**.

[2] H. Shirakawa, E. J. Louis, A. G. MacDiarmid, C. K. Chiang, A. J. Heeger, *J. Chem. Soc. Chem. Commun.* **1977**, 578–580.

[3] X. Guo, A. Facchetti, *Nat. Mater.* **2020**, *19*, 922–928.

[4] N. G. Connelly, W. E. Geiger, *Chem. Rev.* **1996**, *96*, 877–910.

[5] A. I. Hofmann, R. Kroon, S. Zokaei, E. Järsvall, C. Malacrida, S. Ludwigs, T. Biskup, C. Müller, *Adv. Electron. Mater.* **2020**, 2000249.

[6] Y. M. Gross, D. Trefz, C. DIngler, D. Bauer, V. Vijayakumar, V. Untilova, L. Biniek, M. Brinkmann, S. Ludwigs, *Chem. Mater.* **2019**, *31*, 3542–3555.

[7] C. Malacrida, Y. Lu, K. Dirnberger, S. Gámez-Valenzuela, M. C. Ruiz Delgado, S. Ludwigs, *J. Mater. Chem. C* **2020**, *8*, 15393–15405.

[8] J. Reynolds, B. C. Thompson, T. A. Skotheim, *Handbook of Conducting Polymers, Fourth Edition*, **2019**.

[9] T. M. Swager, *Macromolecules* **2017**, *50*, 4867–4886.

[10] S. Ludwigs, Ed. , *P3HT Revisited - from Molecular Scale to Solar Cell Devices*, Springer, Heidelberg, **2014**.

[11] D. Neusser, C. Malacrida, M. Kern, Y. M. Gross, J. van Slageren, S. Ludwigs, *Chem. Mater.* **2020**, *32*, 6003–6013.

[12] U. Salzner, J. B. Lagowski, P. G. Pickup, R. A. Poirier, *Synth. Met.* **1998**, *96*, 177–189.

[13] R. E. Peierls, *Quantum Theory of Solids*, Oxford University Press, **1996**.

[14] J. L. Brédas, *J. Chem. Phys.* **1985**, *82*, 3808–3811.

[15] J. Roncali, *Macromol. Rapid Commun.* **2007**, *28*, 1761–1775.

[16] J. L. Brédas, F. Wudl, A. J. Heeger, *Solid State Commun.* **1987**, *63*, 577–580.

[17] J. L. Bredas, G. B. Street, *Acc. Chem. Res.* **1985**, *18*, 309–315.

[18] K. Meerholz, H. Gregorius, K. Müllen, J. Heinze, *Adv. Mater.* **1994**, *6*, 671–674.

[19] M. Nechtschein, F. Devreux, F. Genoud, E. Vieil, J. M. Pernaut, E. Genies, *Synth. Met.* **1986**, *15*, 59–78.

[20] J. Heinze, B. A. Frontana-Uribe, S. Ludwigs, *Chem. Rev.* **2010**, *110*, 4724–4771.

[21] I. Zozoulenko, A. Singh, S. K. Singh, V. Gueskine, X. Crispin, M. Berggren, *ACS Appl. Polym. Mater.* **2019**, *1*, 83–94.

[22] D. Ofer, R. M. Crooks, M. S. Wrighton, *J. Am. Chem. Soc.* **1990**, *112*, 7869–7879.

[23] J. Heinze, B. A. Frontana-Uribe, S. Ludwigs, *Chem. Rev.* **2010**, *110*, 4724–4771.

[24] G. Salinas, B. A. Frontana-Uribe, *ChemElectroChem* **2019**, 1–14.

[25] L. L. Miller, K. R. Mann, *Acc. Chem. Res.* **1996**, *29*, 417–423.

[26] K. M. Knoblock, C. J. Silvestri, D. M. Collard, *J. Am. Chem. Soc.* **2006**, *128*, 13680–13681.

[27] T. Nakano, *π-Stacked Polymers and Molecules*, **2013**.

[28] A. Smie, J. Heinze, *Angew. Chemie - Int. Ed.* **1997**, *36*, 363–367.

[29] O. Yurchenko, D. Freytag, L. Zur Borg, R. Zentel, J. Heinze, S. Ludwigs, *J. Phys. Chem. B* **2012**, *116*, 30–39.

[30] J. Heinze, H. John, M. Dietrich, P. Tschuncky, *Synth. Met.* **2001**, *119*, 49–52.

[31] A. Rasche, J. Heinze, *Electrochim. Acta* **2008**, *53*, 3812–3819.

[32] R. Shomura, K. Sugiyasu, T. Yasuda, A. Sato, M. Takeuchi, *Macromolecules* **2012**, *45*, 3759–3771.

[33] Y. Harima, X. Jiang, Y. Kunugi, K. Yamashita, A. Naka, K. K. Lee, M. Ishikawa, *J. Mater. Chem.* **2003**, *13*, 1298–1305.
[34] R. Takita, C. Song, T. M. Swager, *Org. Lett.* **2008**, *10*, 5003–5005.
[35] J. Heinze, J. Mortensen, K. Müllen, R. Schenk, *J. Chem. Soc. Chem. Commun.* **1987**, 701–703.
[36] X. Jiang, Y. Harima, L. Zhu, Y. Kunugi, K. Yamashita, M. aki Sakamoto, M. aki Sato, *J. Mater. Chem.* **2001**, *11*, 3043–3048.
[37] C. Enengl, S. Enengl, S. Pluczyk, M. Havlicek, M. Lapkowski, H. Neugebauer, E. Ehrenfreund, *ChemPhysChem* **2016**, *17*, 3836–3844.
[38] M. Barth, S. Guilerez, G. Bidan, G. Bras, M. Lapkowski, *Electrochim. Acta* **2000**, *45*, 4409–4417.
[39] M. A. Vorotyntsev, J. Heinze, *Electrochim. Acta* **2001**, *46*, 3309–3324.
[40] M. Zhou, M. Pagels, B. Geschke, J. 1rgen Heinze, **2002**, DOI 10.1021/jp0210778.
[41] K. Meerholz, J. Heinze, *Synth. Met.* **1993**, *57*, 5040–5045.
[42] V. M. Geskin, J. L. Brédas, *ChemPhysChem* **2003**, *4*, 498–505.
[43] J. A. E. H. Van Haare, E. E. Havinga, J. L. J. Van Dongen, R. A. J. Janssen, J. Cornil, J. L. Brédas, *Chem. - A Eur. J.* **1998**, *4*, 1509–1522.
[44] R. Ponce Ortiz, J. Casado, V. Hernández, J. T. López Navarrete, P. M. Viruela, E. Ortí, K. Takimiya, T. Otsubo, *Angew. Chemie - Int. Ed.* **2007**, *46*, 9057–9061.
[45] J. Casado, R. P. Ortiz, J. T. L. Navarrete, *Chem. Soc. Rev.* **2012**, *41*, 5672–5686.
[46] S. R. González, Y. Ie, Y. Aso, J. T. López Navarrete, J. Casado, *J. Am. Chem. Soc.* **2011**, *133*, 16350–16353.
[47] G. Tan, X. Wang, *Acc. Chem. Res.* **2017**, *50*, 1997–2006.
[48] D. Oeter, H. J. Egelhaaf, C. Ziegler, D. Oelkrug, W. Göpel, *J. Chem. Phys.* **1994**, *101*, 6344–6352.
[49] C. E. D. Chidsey, R. W. Murray, *J. Phys. Chem.* **1986**, *90*, 1479–1484.
[50] A. J. Bard, L. R. Faulkner, V. S. Bagotsky, *Electrochemical Methods Fundamentals of Electrochemistry*, **2001**.
[51] O. Hammeric, B. Speiser, *Organic Electrochemistry, Revised and Expanded*, **2016**.
[52] G. Inzelt, *Monographs in Electrochemistry*, **2008**.
[53] P. J. Peerce, A. J. Bard, *J. Electroanal. Chem.* **1980**, *114*, 89–115.
[54] K. Meerholz, J. Heinze, *Electrochim. Acta* **1996**, *41*, 1839–1854.
[55] P. Bäuerle, *Adv. Mater.* **1992**, *4*, 102–107.
[56] K. Meerholz, J. Heinze, *Angew. Chemie Int. Ed. English* **1990**, *29*, 692–695.
[57] J. Wang, A. J. Bard, *J. Am. Chem. Soc.* **2001**, *123*, 498–499.
[58] C. Gabrielli, J. J. Garcia-Jareo, H. Perrot, *Electrochim. Acta* **2001**, *46*, 4095–4103.
[59] S. Maw, E. Smela, K. Yoshida, R. B. Stein, *Synth. Met.* **2005**, *155*, 18–26.
[60] W. Gao, O. Sel, H. Perrot, *Electrochim. Acta* **2017**, *233*, 262–273.
[61] T. F. Otero, J. G. Martínez, in *Electromechanically Act. Polym.*, **2016**, pp. 1–19.
[62] T. F. Otero, *Polym. Rev.* **2013**, *53*, 311–351.
[63] T. F. Otero, M. Alfaro, V. Martinez, M. A. Perez, J. G. Martinez, *Adv. Funct. Mater.* **2013**, *23*, 3929–3940.
[64] W. Plieth, A. Bund, U. Rammelt, S. Neudeck, L. M. Duc, in *Electrochim. Acta*, Pergamon, **2006**, pp. 2366–2372.
[65] J. Agrisuelas, C. Gabrielli, J. J. García-Jareño, H. Perrot, O. Sel, F. Vicente, *Electrochim. Acta* **2015**, *164*, 21–30.
[66] S. Bruckenstein, A. R. Hillman, *J. Phys. Chem.* **1988**, *92*, 4837–4839.
[67] S. Bruckenstein, A. R. Hillman, *J. Phys. Chem.* **1991**, *95*, 10748–10752.

[68] G. Inzelt, J. Bacskai, J. Q. Chambers, R. W. Day, *J. Electroanal. Chem.* **1986**, *201*, 301–314.
[69] G. Xiong, H. Huang, C. Yang, in *Adv. Mater. Res.*, **2010**, pp. 634–637.
[70] A. R. Hillman, S. J. Daisley, S. Bruckenstein, *Electrochem. commun.* **2007**, *9*, 1316–1322.
[71] M. Skompska, A. R. Hillman, *J. Electroanal. Chem.* **1997**, *433*, 127–134.
[72] V. Carlier, M. Skompska, C. Buess-Herman, *J. Electroanal. Chem.* **1998**, *456*, 139–152.
[73] E. Sezer, M. Skompska, J. Heinze, *Electrochim. Acta* **2008**, *53*, 4958–4968.
[74] C. Visy, J. Kankare, *J. Electroanal. Chem.* **1998**, *442*, 175–188.
[75] E. Sezer, J. Heinze, *Electrochim. Acta* **2006**, *51*, 3668–3673.
[76] K. Naoi, M. Lien, W. H. Smyrl, *J. Electrochem. Soc.* **1991**, *138*, 440–445.
[77] F. Escobar-Teran, A. Arnau, J. V. Garcia, Y. Jiménez, H. Perrot, O. Sel, *Electrochem. commun.* **2016**, *70*, 73–77.
[78] C. Gabrielli, H. Perrot, in *Mod. Asp. Electrochem.*, Springer, New York, NY, **2009**, pp. 151–238.
[79] C. Gabrielli, J. J. García-Jareño, M. Keddam, H. Perrot, F. Vicente, *J. Phys. Chem. B* **2002**, *106*, 3182–3191.
[80] H. Goubaa, F. Escobar-Teran, I. Ressam, W. Gao, A. El Kadib, I. T. Lucas, M. Raihane, M. Lahcini, H. Perrot, O. Sel, *J. Phys. Chem. C* **2017**, *121*, 9370–9380.
[81] C. Gabrielli, M. Keddam, H. Perrot, M. C. Pham, R. Torresi, *Electrochim. Acta* **1999**, *44*, 4217–4225.
[82] C. R. Arias, C. Debiemme-Chouvy, C. Gabrielli, C. Laberty-Robert, A. Pailleret, H. Perrot, O. Sel, *J. Phys. Chem. C* **2014**, *118*, 26551–26559.
[83] F. Razzaghi, C. Debiemme-Chouvy, F. Pillier, H. Perrot, O. Sel, *Phys. Chem. Chem. Phys.* **2015**, *17*, 14773–14787.
[84] G. Schiavon, S. Sitran, G. Zotti, *Synth. Met.* **1989**, *32*, 209–217.
[85] E. F. Dalton, N. A. Surridge, J. C. Jernigan, K. O. Wilbourn, J. S. Facci, R. W. Murray, *Chem. Phys.* **1990**, *141*, 143–157.
[86] R. R. Chance, J. L. Brédas, R. Silbey, *Phys. Rev. B* **1984**, *29*, 4491–4495.
[87] B. G. Zotti, G. Schiavon, A. Berlin, G. Pagani, *Adv. Mater.* **1993**, *5*, 551–554.
[88] B. G. Zotti, G. Schiavon, A. Berlin, *Adv. Mater.* **1993**, *5*, 551–554.
[89] G. Zotti, G. Schiavon, A. Berlin, G. Pagani, *Synth. Met.* **1993**, *61*, 81–87.
[90] V. Vijayakumar, Y. Zhong, V. Untilova, M. Bahri, L. Herrmann, L. Biniek, N. Leclerc, M. Brinkmann, *Adv. Energy Mater.* **2019**, *9*, 1–12.
[91] H. John, R. Bauer, P. Espindola, P. Sonar, J. Heinze, K. Müllen, *Angew. Chemie - Int. Ed.* **2005**, *44*, 2447–2451.
[92] S. Link, T. Richter, O. Yurchenko, J. Heinze, S. Ludwigs, *J. Phys. Chem. B* **2010**, *114*, 10703–10708.
[93] S. S. Zade, N. Zamoshchik, M. Bendikov, *Acc. Chem. Res.* **2011**, *44*, 14–24.
[94] A. Smie, A. Synowczyk, J. Heinze, R. Alle, P. Tschuncky, G. Götz, P. Bäuerle, *J. Electroanal. Chem.* **1998**, *452*, 87–95.
[95] M. J. Frampton, H. L. Anderson, *Angew. Chemie - Int. Ed.* **2007**, *46*, 1028–1064.
[96] J. J. Apperloo, R. A. J. Janssen, P. R. L. Malenfant, L. Groenendaal, J. M. J. Fréchet, *J. Am. Chem. Soc.* **2000**, *122*, 7042–7051.
[97] D. Lee, T. M. Swager, *J. Am. Chem. Soc.* **2003**, *125*, 6870–6871.
[98] T. M. Swager, *Macromolecules* **2017**, *50*, 4867–4886.
[99] D. Lee, T. M. Swager, *Chem. Mater.* **2005**, *17*, 4622–4629.

[100] T. Benincori, S. Gámez-Valenzuela, M. Goll, K. Bruchlos, C. Malacrida, S. Arnaboldi, P. R. Mussini, M. Panigati, J. T. López Navarrete, M. C. Ruiz Delgado, et al., *Electrochim. Acta* **2018**, *284*, 513–525.
[101] M. Wieland, C. Malacrida, Q. Yu, C. Schlewitz, L. Scapinello, *Flex. Print. Electron.* **2020**, *5*, 014016.
[102] P. H. Aubert, L. Groenendaal, F. Louwet, L. Lutsen, D. Vanderzande, G. Zotti, *Synth. Met.* **2002**, *126*, 193–198.
[103] P. Blanchard, C. Malacrida, C. Cabanetos, J. Roncali, S. Ludwigs, *Polym. Int.* **2019**, *68*, 589–606.
[104] Y. Shirota, H. Kageyama, *Chem. Rev.* **2007**, *107*, 953–1010.
[105] M. Thelakkat, *Macromol. Mater. Eng.* **2002**, *287*, 442–461.
[106] R. Rybakiewicz, M. Zagorska, A. Pron, *Chem. Pap.* **2017**, *71*, 243–268.
[107] E. Bellmann, S. E. Shaheen, S. Thayumanavan, S. Barlow, R. H. Grubbs, S. R. Marder, B. Kippelen, *Chem. Mater.* **1998**, *10*, 1668–1676.
[108] X. Gu, Y. Li, Y. Mu, M. Zhang, T. Lu, P. Wang, *RSC Adv.* **2018**, *8*, 9409–9413.
[109] J. Roncali, *Chem. Rev.* **1992**, *92*, 711–738.
[110] V. Malytskyi, J.-J. Simon, L. Patrone, J.-M. Raimundo, *RSC Adv.* **2015**, *5*, 354–397.
[111] J. Wang, K. Liu, L. Ma, X. Zhan, *Chem. Rev.* **2016**, *116*, 14675–14725.
[112] L. Y. Lin, Y. H. Chen, Z. Y. Huang, H. W. Lin, S. H. Chou, F. Lin, C. W. Chen, Y. H. Liu, K. T. Wong, *J. Am. Chem. Soc.* **2011**, *133*, 15822–15825.
[113] C. Su, F. Yang, L. Ji, L. Xu, C. Zhang, *J. Mater. Chem. A* **2014**, *2*, 20083–20088.
[114] C. Li, J. Xue, A. Huang, J. Ma, F. Qing, A. Zhou, Z. Wang, Y. Wang, J. Li, *Electrochim. Acta* **2019**, *297*, 850–855.
[115] T. P. Bender, J. F. Graham, J. M. Duff, *Chem. Mater.* **2001**, *13*, 4105–4111.
[116] E. T. Seo, R. F. Nelson, J. M. Fritsch, L. S. Marcoux, D. W. Leedy, R. N. Adams, *J. Am. Chem. Soc.* **1966**, *88*, 3498–3503.
[117] R. F. Nelson, R. N. Adams, *J. Am. Chem. Soc.* **1968**, *90*, 3925–3930.
[118] Y. Wang, S. Zhang, J. Wu, K. Liu, D. Li, Q. Meng, G. Zhu, *ACS Appl. Mater. Interfaces* **2017**, *9*, 43688–43695.
[119] M. Zhao, H. Zhang, C. Gu, Y. Ma, *J. Mater. Chem. C* **2020**, *8*, 5310–5320.
[120] K. Karon, M. Lapkowski, *J. Solid State Electrochem.* **2015**, *19*, 2601–2610.
[121] E. T. Seo, R. F. Nelson, J. M. Fritsch, L. S. Marcoux, D. W. Leedy, R. N. Adams, *J. Am. Chem. Soc.* **1966**, *88*, 3498–3503.
[122] E. T. Seo, Ia F. Robert Nelson, J. M. Fritsch, Ib S. Lynn Marcoux, D. W. Leedy, R. N. Adams, Z. Galus, H. Y. Lee, R. N. Adams, J. Eiectroanal Chem, *J. Eiectroanal. Chem* **1962**, *84*, 151.
[123] S. C. Creason, J. Wheeler, R. F. Nelson, *J. Org. Chem.* **1972**, *37*, 4440–4446.
[124] M. Li, *Chem. - A Eur. J.* **2019**, *25*, 1142–1151.
[125] J. Heinze, C. Willmann, P. Bäuerle, *Angew. Chemie Int. Ed.* **2001**, *40*, 2861–2864.
[126] R. Reynolds, L. L. Line, R. F. Nelson, *J. Am. Chem. Soc.* **1974**, *96*, 1087–1092.
[127] P. Taranekar, T. Fulghum, D. Patton, R. Ponnapati, G. Clyde, R. Advincula, *J. Am. Chem. Soc.* **2007**, *129*, 12537–12548.
[128] G. Jiang, C. Huang, A. Baba, R. Advincula, *Macromol. React. Eng.* **2012**, *6*, 153–159.
[129] M. I. Mangione, R. A. Spanevello, D. Minudri, P. Cavallo, L. Otero, F. Fungo, *Electrochim. Acta* **2018**, *263*, 585–595.
[130] M. Y. Chou, M. K. Leung, Y. O. Su, C. L. Chiang, C. C. Lin, J. H. Liu, C. K. Kuo, C. Y. Mou, *Chem. Mater.* **2004**, *16*, 654–661.

[131] K. Karon, M. Lapkowski, A. Dabuliene, A. Tomkeviciene, N. Kostiv, J. V. Grazulevicius, *Electrochim. Acta* **2015**, *154*, 119–127.
[132] A. Baba, K. Onishi, W. Knoll, R. C. Advincula, **2004**, DOI 10.1021/jp047965f.
[133] C. Xu, J. Zhao, C. Cui, M. Wang, Y. Kong, X. Zhang, *J. Electroanal. Chem.* **2012**, *682*, 29–36.
[134] F. Sannicol, S. Rizzo, T. Benincori, W. Kutner, K. Noworyta, J. W. Sobczak, V. Bonometti, L. Falciola, P. R. Mussini, M. Pierini, in *Electrochim. Acta*, **2010**, pp. 8352–8364.
[135] A. Ruff, M. Scheuble, A. Hoffmann, M. Goll, S. M. Link, T. V. Richter, E. Muks, S. Ludwigs, J. T. Lopez Navarrete, M. C. Ruiz Delgado, *Langmuir* **2013**, *29*, 15463–15473.
[136] T.-G. Sun, Z.-J. Li, J.-Y. Shao, Y.-W. Zhong, *Polymers (Basel).* **2019**, *11*, 73.
[137] C. Liu, H. Luo, G. Shi, J. Yang, Z. Chi, Y. Ma, *J. Mater. Chem. C* **2015**, *3*, 3752–3759.
[138] H. Hao, H. Luo, A. Yi, C. Liu, B. Xu, G. Shi, Z. Chi, *Org. Electron.* **2019**, *69*, 281–288.
[139] J. Li, X. Han, Q. Bai, T. Shan, P. Lu, Y. Ma, *J. Polym. Sci. Part A Polym. Chem.* **2017**, *55*, 707–715.
[140] M. I. Mangione, R. A. Spanevello, A. Rumbero, D. Heredia, G. Marzari, L. Fernandez, L. Otero, F. Fungo, *Macromolecules* **2013**, *46*, 4754–4763.
[141] H. J. Yen, G. S. Liou, *Polym. Chem.* **2018**, *9*, 3001–3018.
[142] N. Cocherel, P. Leriche, E. Ripaud, N. Gallego-Planas, P. Frère, J. Roncali, *New J. Chem.* **2009**, *33*, 801–806.
[143] S. H. Hsiao, J. W. Lin, *Polym. Chem.* **2014**, *5*, 6770–6778.
[144] X. Lv, W. Li, M. Ouyang, Y. Zhang, D. S. Wright, C. Zhang, *J. Mater. Chem. C* **2017**, *5*, 12–28.
[145] Z. Fang, V. Chellappan, R. D. Webster, L. Ke, T. Zhang, B. Liu, Y.-H. Lai, *J. Mater. Chem.* **2012**, *22*, 15397–15404.
[146] E. J. W. Crossland, P. Cunha, S. Scroggins, S. Moratti, O. Yurchenko, U. Steiner, M. A. Hillmyer, S. Ludwigs, *ACS Nano* **2010**, *4*, 962–966.
[147] O. Yurchenko, J. Heinze, S. Ludwigs, *ChemPhysChem* **2010**, *11*, 1637–1640.
[148] P. Reinold, K. Bruchlos, S. Ludwigs, *Polym. Chem.* **2017**, *8*, 7351–7359.
[149] E. J. W. Crossland, M. Nedelcu, C. Ducati, S. Ludwigs, M. A. Hillmyer, U. Steiner, H. J. Snaith, *Nano Lett.* **2009**, *9*, 2813–2819.
[150] G. L. Whiting, H. J. Snaith, S. Khodabakhsh, J. W. Andreasen, D. W. Breiby, M. M. Nielsen, N. C. Greenham, R. H. Friend, W. T. S. Huck, *Nano Lett.* **2006**, *6*, 573–578.

2 Motivation and Approach

Electrodeposition of redox active units has been employed since the discovery of conducting polymers as a straightforward approach for their synthesis on an electrode surface.[1] The possibility to employ simple and scalable setups, to reduce material wastage, the characteristic low temperature of the process as well as the superior stability and insolubility of the deposited films have made electrodeposition a very appealable technique for the preparation of active layers to be employed in optoelectronic applications, as an alternative to very expensive and technically demanding approaches such as thermal evaporation and solution casting techniques.[1–4] Further, electrodeposition generally allows for a relatively good control of the film thickness and variation of the film morphology by choice of the electrodeposition conditions.[3]

The mechanism of electrodeposition generally involves the radical-radical coupling of suitable monomers upon oxidization to radical-cations (or reduction to radical-anions), followed by proton elimination. The active species undergoing this coupling are generally generated by oxidative route (radical cations), and, less frequently by reductive route (radical anions). Depending on the properties of the monomers employed, it is possible to modulate the chemical, physical and electronic properties of the films obtained. Generally, molecules of small size are used as monomers for electrodeposition as they are easier to synthesize and are also characterized by a higher solubility and marked reactivity.[1] The use of the latter however, also presents drawbacks as the employment of high potentials can lead to overoxidation of the electrodeposited film or to irregular growths. In addition, the films obtained by electrodeposition from "traditional" monomers are associated with the formation of highly polydisperse polymer chains characterized by a wide range of oxidation potentials.[1,2]

In light of this, it has been shown how the employment of precursor monomers endowed with multiple oxidation sites and well defined electroactivity can reduce overoxidation problems and allow for the deposition of electroactive films with high control of conjugation, electroactivity, film thickness and, by optimization of the deposition conditions, also of the film roughness and morphology.[2,5,6] In this context, the study of the reactivity and electrodeposition of molecules and systems of optoelectronic interest, focusing on structural correlations, as well as the characterization of the so obtained films, aims to provide additional background for the development and optimization of new systems to be employed in optoelectronic applications.

In this thesis the electrochemical reactivity of different classes of redox molecules of optoelectronics interest, including thiophene, arylamine and carbazole derivatives, is studied and exploited to crosslink precursor systems endowed with multiple dimerization

sites to obtain functional electroactive films. The latter are characterized by a well-defined and controlled π-conjugation and redox behavior, which can be directly related to the one of the dimer of the starting redox unit.[7–9] More precisely, in the first section of the dissertation the reactivity towards oxidative dimerization and crosslinking of small molecules of optoelectronic interest was studied. In the second section, electrochemical crosslinking of well-known redox active polymers was carried out, analyzing structure-properties relationships in electrochemical and physico-chemical behavior of the crosslinked films.

I - Electrochemical Crosslinking of Multimers From Solution

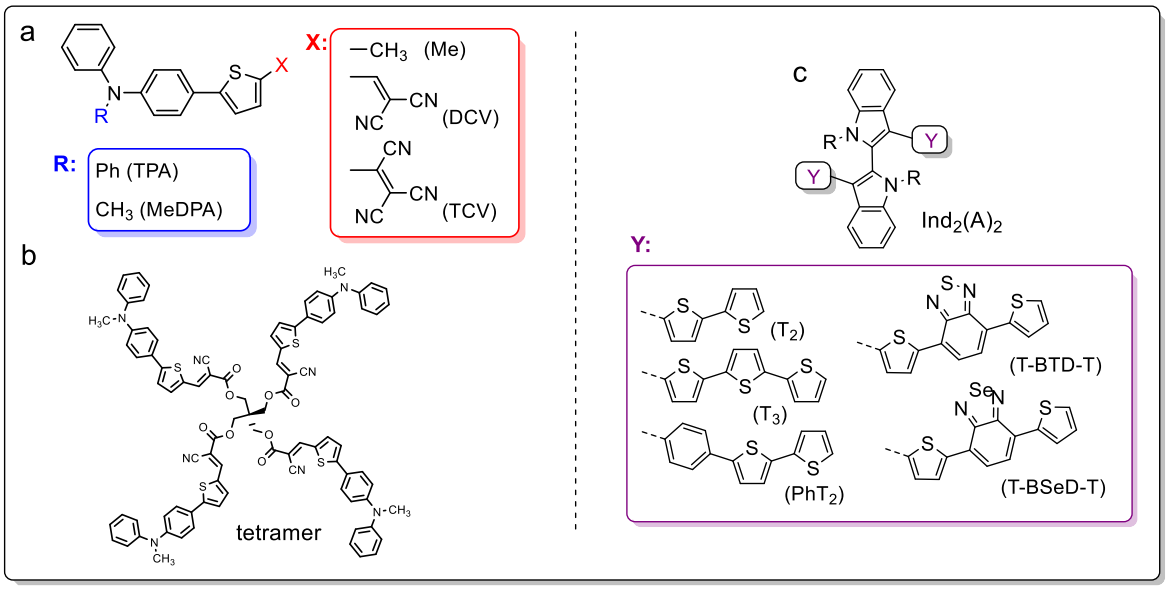

Figure 2.1: Structure of (a) D-π-A push-pull chromophores studied and (b) of tetramer employed for electrodeposition of highly crosslinked push-pull networks. Structure of (c) 2,2'-biindole architecture with oligothiophene terminals.

In the first section of the thesis, the electrochemical crosslinking from solution of different multimeric systems was exploited. In this context, in collaboration with the groups of Prof. P. Blanchard (University of Angers) and of Prof. C. Ruiz-Delgado (University of Malaga), the reactivity towards dimerization of a set of D-π-A push-pull molecules (Figure 2.1 (a)) was studied.[7,8,10] The chromophores analyzed are based on a similar molecular architecture, consisting of a small push-pull system with an arylamine donor block, triphenylamine (TPA) and methyldiphenylamine (MeDPA), respectively, connected to an acceptor group through a thienyl linker. While the redox behavior upon oxidation of simple arylamines is known and well-characterized, their functionalization by π-conjugated blocks, such as in the case of D-π-A push-pull molecules, can result in a change in reactivity towards dimerization. *In-situ* UV-Vis-NIR spectroelectrochemistry is performed to clarify the nature of the species generated upon oxidation, comparing the experimental results with calculated TD-DFT vertical transition energies. DFT calculations of the chromophores are

further performed in order to provide an explanation of the different reactivity behaviors. Defining the electrochemical reactivity of push-pull systems is interesting from a fundamental point of view considering their ubiquitous employment in OPV, as well as to find suitable units to be employed for electrodeposition of functional films for optoelectronics applications. Electro-oxidation of a tetrameric derivative was for this purpose conducted (Figure 2.1 (b)).[8] and the obtained highly crosslinked network was then fully characterized.

As a second example, in collaboration with the group of Prof. T. Benincori (Università dell'Insubria, Como) the electrochemical characterization of a set of chiral molecules endowed with a 2,2'-biindole architecture with oligothiophene terminals modified through different π-spacers (Figure 2.1, c) was conducted.[11] Electrochemical crosslinking of these molecules can be achieved by oxidation at two partially interacting thienyl redox terminals, and leads to generation of films with well-defined π-conjugation. The electrochemical and doping behavior of these materials was studied in detail, and the suitability of an enantiomeric film as chiral selector was further assessed, paving the way towards their employment as chiral electrochromic films.

II - Electrochemical Crosslinking as Post Film-Deposition Functionalization Step

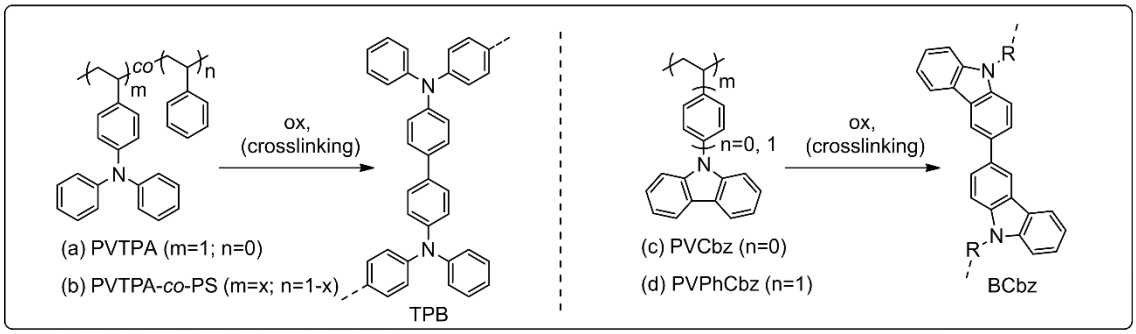

Figure 2.2: PVTPA, PVTPA-co-PS, PVCbz and PVPhCbz (left) and of the dimerization products tetraphenylbenzidine (TPB) and biscarbazole (BCbz) (right).

In the second part of the thesis, insight of oxidative crosslinking as a post-solution deposition step to obtain electroactive films is provided. The dimerizing ability of triarylamine (TPA) and carbazole (Cbz) in the form of redox-active pendant units on a saturated polymer backbone as crosslinkers was studied upon oxidation (Figure 2.2).[9,12] Electrochemical and doping behaviors of the crosslinked polymer films were characterized by *in-situ* electrochemical methods (*in-situ* conductance and *in-situ* UV-Vis spectroelectrochemistry). Additionally, in collaboration with the group of Prof. H. Perrot (Sorbonne University, Paris) electrochemical quartz crystal microbalance (EQCM) and *ac*-electrogravimetry were performed upon electrochemical doping of the films, providing information about the specific contributions and kinetics of the species involved in the charge-compensation process.[13] With the know-how on *in-situ* electrochemical results,

concomitant crosslinking and doping with the strong oxidant $FeCl_3$ was performed and optimized. The increased chemical stability resulting from crosslinking, together with the transparency and “high” conductivity of the resulting doped layers makes them interesting candidates for hole transport layers and transparent electrodes in optoelectronics applications.[9]

2.1 References

[1] J. Heinze, B. A. Frontana-Uribe, S. Ludwigs, *Chem. Rev.* **2010**, *110*, 4724–4771.

[2] P. Taranekar, T. Fulghum, D. Patton, R. Ponnapati, G. Clyde, R. Advincula, *J. Am. Chem. Soc.* **2007**, *129*, 12537–12548.

[3] G. Jiang, C. Huang, A. Baba, R. Advincula, *Macromol. React. Eng.* **2012**, *6*, 153–159.

[4] M. I. Mangione, R. A. Spanevello, D. Minudri, P. Cavallo, L. Otero, F. Fungo, *Electrochim. Acta* **2018**, *263*, 585–595.

[5] M. Zhao, H. Zhang, C. Gu, Y. Ma, *J. Mater. Chem. C* **2020**, *8*, 5310–5320.

[6] S. Orlandi, G. Pozzi, M. Cavazzini, D. Minudri, M. Gervaldo, L. Otero, F. Fungo, **2015**, DOI 10.1021/acs.macromol.5b00845.

[7] P. Blanchard, C. Malacrida, C. Cabanetos, J. Roncali, S. Ludwigs, *Polym. Int.* **2019**, *68*, 589–606.

[8] C. Malacrida, A. H. Habibi, S. Gámez-Valenzuela, I. Lenko, P. S. Marqués, A. Labrunie, J. Grolleau, J. T. López Navarrete, M. C. Ruiz Delgado, C. Cabanetos, et al., *ChemElectroChem* **2019**, *6*, 4215–4228.

[9] C. Malacrida, Y. Lu, K. Dirnberger, S. Gámez-Valenzuela, M. C. Ruiz Delgado, S. Ludwigs, *J. Mater. Chem. C* **2020**, *8*, 15393–15405.

[10] C. Malacrida, S. Gámez-Valenzuela, D. Gepperth, M. C. Ruiz Delgado, P. Blanchard, S. Ludwigs, **2021**.

[11] C. Malacrida, L. Scapinello, R. Cirilli, S. Grecchi, A. Penoni, T. Benincori, S. Ludwigs, *ChemElectroChem* **2021**, *8*, 3250–3261.

[12] D. Neusser, C. Malacrida, M. Kern, Y. M. Gross, J. van Slageren, S. Ludwigs, *Chem. Mater.* **2020**, *32*, 6003–6013.

[13] C. Malacrida, O. Sel, H. El. M., L. Stein, H. Perrot, S. Ludwigs, *(Manuscript in preparation).*

3 Experimental Section

In this section the theoretical basis of the employed techniques, general procedures with regards to data evaluation as well as information about materials and chemicals employed are provided. Detailed experimental conditions are provided at the end of each experimental chapter.

3.1 Methods and Techniques

3.1.1 Electrochemical Methods

3.1.1.1 Cyclic Voltammetry (CV)

The term voltammetry refers to a set of electroanalytical methods that offer a broad spectrum of diagnostic potentialities, that provides qualitative, quantitative, and mechanistic information regarding all the electroactive species present in the bulk solution and on the electrode surface. For the aforementioned reasons, as well as for the characteristic shapes of the voltametric waves, and their specific position on the potential scale which unequivocally fingerprints the electrochemical properties of the different redox systems, voltametric techniques have earned the nickname of “electrochemical spectroscopy”. Signal recording is performed by the measurement of the current that flows between a working electrode (WE) and a counter electrode (CE), and which is proportional to the rate of the electron transfer process, as a function of the potential applied to the WE with respect to a reference electrode (RE), with a regular modulation over time.

Voltammetry includes many techniques which differ in:

• **Mode of potential variation with time**: linear (simple or cyclic), baseline or staircase with overlapping pulses, series of square pulses etc, with the possibility of combining with controlled potential steps for accumulation purposes. The current can be detected either directly or by differential processing.

• **Rate of potential variation with time**: signals can be obtained either by a slow variation of the potential, in "steady conditions" (1-5 $mV \cdot s^{-1}$), or very quickly, under "non-stationary conditions" (20-50000 $mV \cdot s^{-1}$ and above). (Figure 3.2)

• **Type of working electrodes employed**: the most common are microelectrodes with surface areas of a few square millimeters; additionally, ultramicroelectrodes can be employed for particular studies, offering exceptional performances. Generally, working electrodes are solid (metals, graphite, oxides, etc.) with two exceptions: rotating disk electrodes, employed for kinetics studies, and mercury electrodes (stationary or dropping) particularly suitable for reduction studies in aqueous medium. The processes are

associated with very low current values and take place in very short periods of time, therefore the associated current-potential signal is a peak; this particular shape is determined by the fact that cyclic voltammetry never reaches a stationary regime due to the high scanning speed (Figure 3.2). In the case of a voltammetry experiment performed in stationary conditions, i.e. at slow scan-rates, a linear concentration gradient in a "diffusion layer" of constant δ thickness at the electrode surface is obtained at every time of the experiment (Figure 3.2 (a)). In this case, the concentration gradients are subjected to an increase until reaching a maximum in correspondence of zero concentration on the electrode surface. In this case the corresponding current signal progressively increases until reaching a limiting current in correspondence to the maximum concentration gradient. When the experiment is performed in non-stationary conditions, i.e. at high scan rates, convective motions fail to reintegrate the reagent concentration from the bulk (C_{ob}) to a constant distance from the electrode; therefore δ increases and the current, which is proportional to the concentration gradient, after reaching a maximum, decreases (Figure 3.2 (b)).

Cyclic voltammetry (CV) is a type of potentiodynamic electrochemical measurement. In a CV experiment, the working electrode potential (E_w) is ramped linearly versus time and, after a desired potential is reached, the working electrode's potential is ramped in the opposite direction to return to the initial potential (Figure 3.1). Concurrently, the current (I) flowing between the working and counter electrode is measured as the working electrode is polarized. The basic equipment needed for performing a voltammetric study includes: a potentiostat with a function generator, a cell provided with a fitting for vacuum/inert gas (Ar or N_2) and containing working (WE), reference (RE) and counter (CE) electrodes, an electrolyte and a recorder for data acquisition. The potentiostat, according to a program set by the operator, allows to vary the potential of the WE with respect to the RE over time, varying the cell voltage between the WE and CE and by recording the current circulating between the WE and the CE.

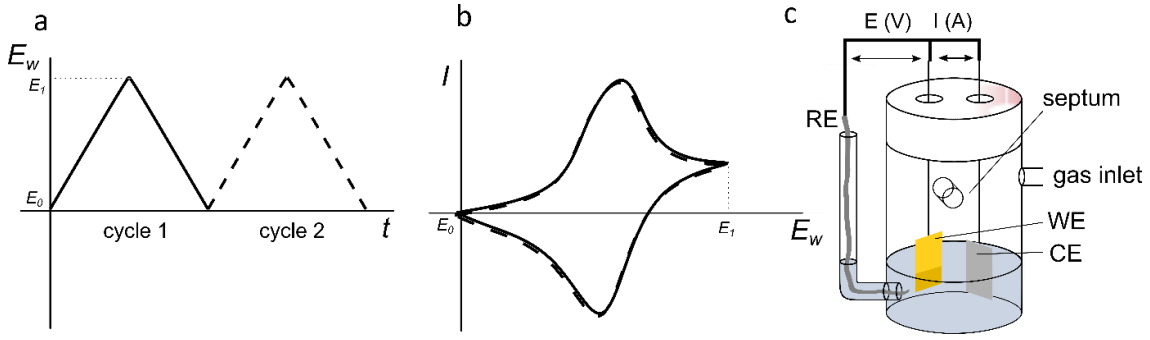

Figure 3.1: (a) Perturbation and (b) response of a typical cyclic voltammetry; with "E_w" being the potential at the working electrode; "I" the current measured between working and counter electrode and "t" the time. (c) Schematization of the electrochemical set-up employed.

Cyclic voltammetry (CV) provides deep insight on all redox systems at the electrode | solution interface and was chosen as one of the principal investigation techniques in this work for several reasons:

- it provides qualitative and quantitative information about both the redox-active species in solution and the electroactive surface;
- cyclic voltammetry can be considered a non-destructive technique on a macroscopic scale.
- it can be easily associated to other *in-situ* techniques allowing a deeper understanding of doping processes and mechanisms.
- It is one of the preferential methods employed for electropolymerization due to the possibility of following the deposition through each cycle; by analyzing the variation of the oxidation potential and current.

Let us consider the reaction: $O + ne^- \leftrightarrow R$, and assume to start scanning to a potential much more positive than the formal potential of the electrode (E°'), initially only small currents, such as capacitive ones which correspond to the charging process of the double layer are detected. For values of potential approaching E°' a faradic current begins to be registered, corresponding to the redox reaction taking place at the electrode surface.

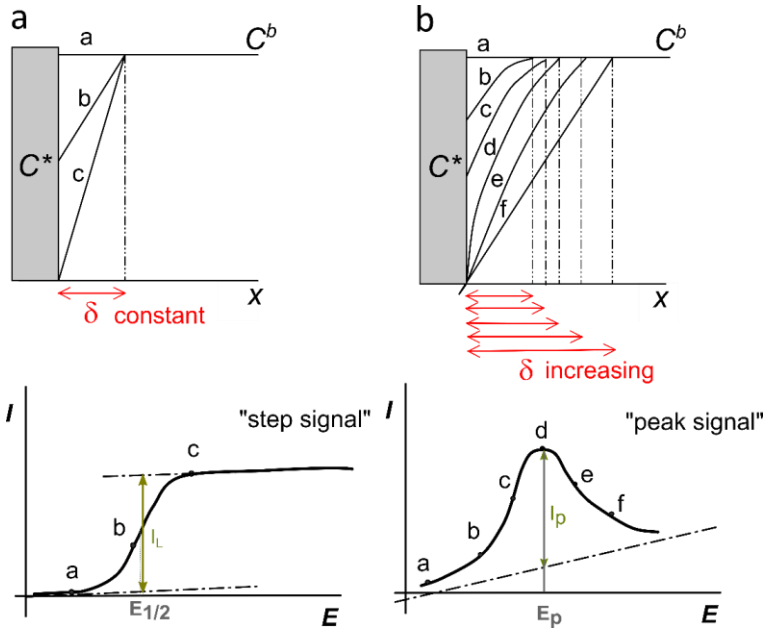

Figure 3.2: Representation of (a) stationary (step) signal and (b) non-stationary (peak) signal with correlated representation of the concentration profile and diffusion layer (δ). An increase in the width of the diffusion layer (boundary moving towards the bulk of the solution) is associated to a peak signal.

Characteristic parameters which can be gathered from a CV experiment are presented in Figure 3.3 (a); these include the anodic and cathodic peak currents ($I_{p,a}$ and $I_{p,c}$

respectively); anodic and cathodic peak potential ($E_{p,a}$ and $E_{p,c}$) and anodic and cathodic half-wave potentials ($E_{p/2,a}$ and $E_{p/2,c}$). Peak currents in a cyclic voltammogram are linearly proportional to the concentration of the redox active species in solution; to the electrode surface (linearly); to the diffusion coefficient of the reactant and to the number of exchanged electrons. From the peak potentials the half-wave potential $E_{1/2}$ for the redox couple, can be determined as follow (3.1):

$$E_{1/2}=\frac{|E_{p,a}+E_{p,c}|}{2} \quad (3.1)$$

$E_{1/2}$ contitutes a good approximation of E^0 of the redox system. $E_{1/2} = E°'$ when the diffusion coefficients of the oxidized and reduced species are similar.

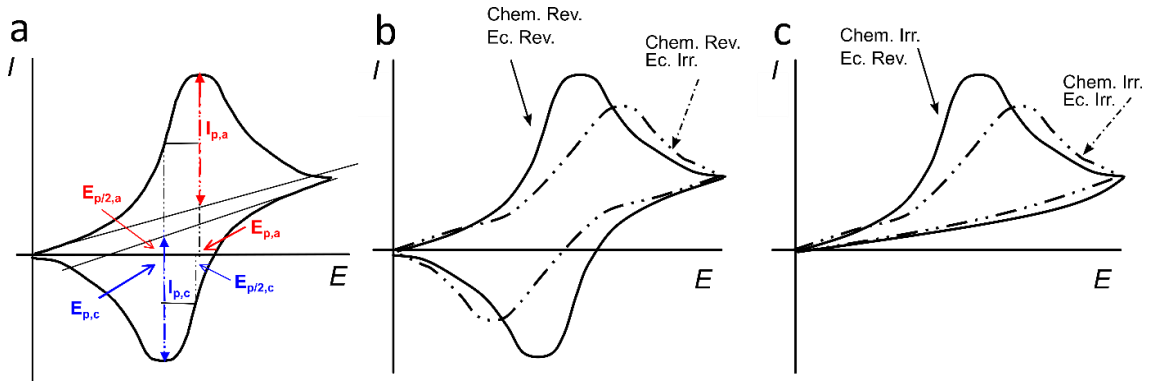

Figure 3.3: (a) Chemically and electrochemically reversible voltammetric signals with key parameters (b) Representation of a chemically reversible and electrochemically irreversible voltammetric signals. Note that electrochemical irreversibility is associated with a broadening of the signal as the scan rate is increased. (c) Representation of chemically irreversible CV signals.

A simple electronic transfer not coupled with chemical reactions can be of two types:

- **Electrochemically reversible:** if its activation barrier is negligible, so, as soon as the reagent reaches the electrode it undergoes charge transfer and it is instantly transformed into the product. In this case, the current, which represents the speed of the process, is controlled only by diffusion within the diffusion layer δ. The form of the signal is that of a reversible wave, in the electrochemical meaning, i.e. only controlled by the mass transfer (Figure 3.3 (a)). In the case of an electrochemically reversible signal, the peak potential E_p and the peak amplitude at half height (E_p- $E_{p/2}$) is 0.057 V at 25°C for a monoelectronic peak. If the case of a chemically reversible process a return peak is observed, too, because electron transfer leads to a chemically stable product; the distance between the direct and return peak is constant for different scan rates, and equal to 0.057 V at 298 K.
- **Electrochemically irreversible:** if the electron transfer activation barrier is not negligible, and the charge transfer becomes kinetically important in the determination of the rate of the whole process. In this case, an additional energy, corresponding to an

"overpotential", is required to obtain the same current with respect to the former case. As consequence, the signals are more stretched and widened, they are increasingly shifted at more extreme potentials with increasing scan rates, and the peak amplitudes at half height (E_p- $Ep_{1/2}$) are > 0.057 V at 298 K for a monoelectronic peak, and increase with the scan rate (v). This broadening also applies to the return peak in the case of a chemically reversible process. In this case, the distance between the direct and return peak is bigger than 0.057 V at 25°C, and increases as the scan rate increases (Figure 3.3 (b), dashed line).

The presence of a backward peak and its relative height with respect to the forward one account for the degree of *chemical reversibility* of the reaction. In particular, the absolute value of the ratio of the *Ip* related to the two peaks ($I_{p,forward}/I_{p,backward}$) should be close to 1 for a diffusion-controlled process in case of complete chemical reversibility. On the other hand, the distance between the forward and backwards peaks provides a further proof of the degree of electrochemical reversibility, along with the above-mentioned E_p *vs* log(v) and (E_p-$E_{p1/2}$) criteria. With (E_p-$E_{p1/2}$) being constant and equal to 0.057 V at 298 K for an electrochemically reversible monoelectronic process, while being higher and increasing with increasing scan rate for an electrochemically irreversible one.

Experimental Set-up and Procedure

The potentiostat used for performing voltammetric measurements was an AUTOLAB PGSTAT204 or a PGSTAT101 (Metrohm), while the software Nova 1.1 was employed for the elaboration of the experimental data. Potential scans were performed by a staircase voltammetry with a step potential variation. An air-tight three-electrode glass cell provided with a Pt plate as counter electrode and an AgCl-coated silver wire as pseudo reference electrode were employed; the WE and CE were positioned in the middle of the ideal triangular configuration with the RE positioned in a lugging fitting. As working electrode for electrochemical experiments different electrode substrates have been employed, including:

- ITO-coated glass slides (≤20 Ω/sq, PGO, Germany);
- Au slides (vacuum deposited on glass slides over 3 nm of adhesion Cr layer; 30 nm Au layer):
- Pt-interdigitated electrodes (DropSens) endowed with either 5 or 10 μm spacing.

The electrochemical cell was connected to a Schlenk-line enabling to perform vacuum/argon cycles to remove traces of water and oxygen; before the measurements, the electrolyte was bubbled through a syringe and saturated with argon. During the measurement, the argon flow was deviated over the solution to avoid introduction of

convection phenomena. All potentials were referenced to the formal potential of the Fc/Fc^+ inter-solvental reference redox couple used as internal standard. Specific experimental conditions or modifications to the setup are indicated in dedicated experimental sections at the end of each chapter.

3.1.1.2 *In-situ* Electrochemical Methods

The electrochemical switching of redox-active polymers is accompanied by changes of several properties including the electronic and vibrational spectra, the spin concentration and structure, as well as conductivity. The combinations of electrochemical methods with non-electrochemical techniques, including spectroelectrochemistry (UV-Vis-NIR, FTIR, EPR), conductance, electrochemical quartz crystal microbalance (EQCM), probe beam deflection, different microscopies, including atomic force microscopy (AFM), scanning electrochemical microscopy (SECM), results very useful in the understanding of structure–property relationships, as well as the mechanisms of chemical transformations taking place during the redox-switching of the polymer (charging-discharging processes). The employment of *in-situ* techniques has the advantage over *ex-situ* techniques of avoiding irreversible changes due to air oxidation or contamination, as well as mechanical damage; further they ensure a precise correlation of the observed properties with a doping level of the desired amount.

The following combined techniques have been utilized as characterization techniques in the thesis:

- *In-situ* UV-Vis-NIR spectroelectrochemistry;
- *In-situ* conductance;
- EQCM;
- *ac*-electrogravimetry.

3.1.1.2.1 *In-Situ* UV-Vis-NIR Spectroelectrochemistry

All molecular spectroscopic techniques compatible with the presence of a liquid electrolyte can be combined with electrochemical experiments allowing for the correlation of the observed spectroscopic features with well-defined electrochemical conditions, e.g. applied potential or doping level. UV-Vis-NIR spectroelectrochemistry is performed using specifically designed three-electrode cells adapted to transmission or reflection geometries (Figure 3.4). Optically transparent electrodes including glass-coated ITO, mini grids and thin metal layers are employed as the working electrodes for spectroelectrochemical measurements performed in transmission mode.

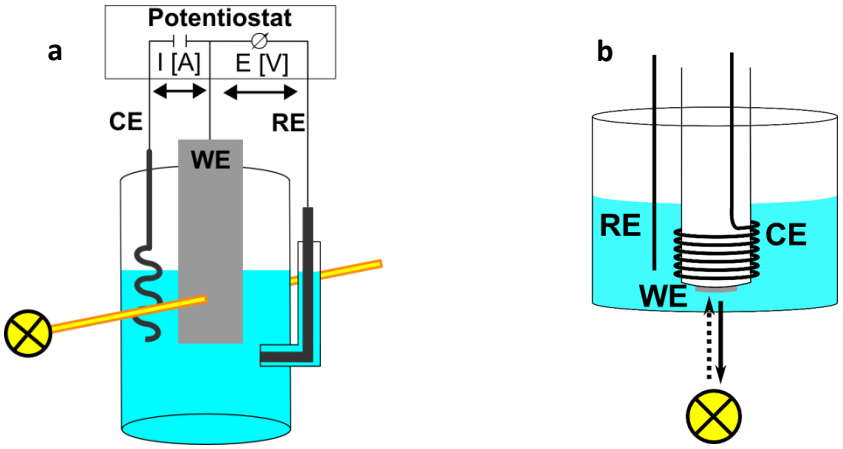

Figure 3.4: Schematic representation of a UV-Vis spectroeletrochemical cell and working principle for measurements in transmission (a) and reflection modes (b) employed.

In the case of spectroelectrochemical measurements performed in reflection mode, the WE is constituted by a reflecting surface, for example a polished platinum disk.[1] The choice of the experimental set-up generally derives from the aggregation state of the material, if the electrochromic species is a thin insoluble film deposited on the electrode, which is also the general case for CPs, or if it is dissolved in a solution, such as in the case of small molecules. In the last case, thin layer conditions (i.e., finite diffusion) are generally employed. It must be noted that in this case, the electroactive species located in the diffusion layer will be completely electrolysed.

In a UV-Vis-NIR spectroelectrochemistry experiment, the transmitted (or reflected) intensity of a light beam is measured as a function of the polarization potential. When employing a diode array spectrophotometer it is possible to acquire a complete spectrum for each wavelength while performing a voltametric measurement. Typical plots and data analysis from spectroelectrochemical measurements are shown in Figure 3.5, for the case of P3HT, and include analysis of the absorption spectra registered as function of the doping level, as well as the peak evolution. A detailed description about characteristic transitions for conducting polymers can be found in paragraph 1.1.1.1.

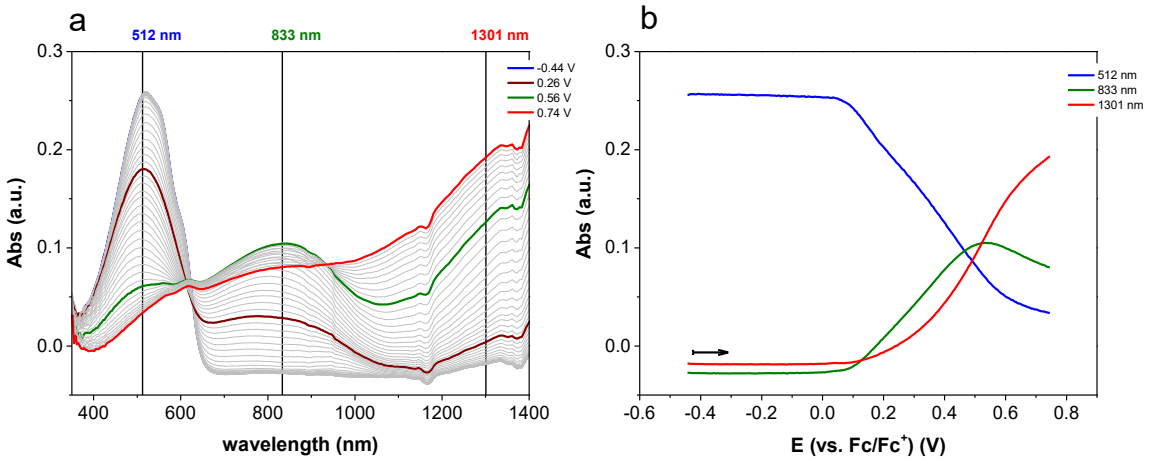

Figure 3.5: (a) UV-Vis-NIR spectra of P3HT measured during the charge cycle; absorption as a function of the wavelength, Abs= f $(\lambda)_E$, at a constant potential. This is the absorption spectrum of the solution or surface film polarized at that potential. (b) Absorption as a function of potential at a constant wavelength, Abs=f$(E)_\lambda$ (Peak-trend of selected wavelength) follow the formation of the different charge carriers in the film as function of the doping level.

Thin-Film UV-Vis-NIR Spectroelectrochemistry

UV-Vis and UV-Vis-NIR thin-film spectroelectrochemistry was performed using an Autolab PGSTAT204 potentiostat (Metrohm) and a Zeiss UV−Vis spectrometer endowed with a MCS621 Vis II spectrometer cassette and a CLH600F lamp or a Zeiss UV−Vis-NIR spectrometer endowed with a MCS621 Vis II and a MCS611 NIR 2.2µ spectrometer cassette and a CLH600F lamp. The measurements were conducted in a custom-made three-electrodes quartz cell employing a Pt wire as counter electrode, an AgCl coated Ag wire as (pseudo)reference electrode and a coated ITO as working electrode. A schematization of the spectroelectrochemical cell is provided in Figure 3.4 (a). The measurements were performed under Ar atmosphere and all the potential values were referenced to the formal potential of the Fc/Fc^+ redox couple. *In-situ* spectroelectrochemical measurements were typically conducted at a scan rate of 20 $mV \cdot s^{-1}$ and potential steps of 10 mV, with simultaneous recording of electrochemical data points and UV-Vis spectra every 0.5 s.

Thin-Layer UV-Vis Spectroelectrochemistry

In-situ thin-layer UV-Vis spectroelectrochemistry was measured in reflection mode in a quartz cell arranged for a three-electrode setup and employing a mirror type working electrode constituted by a polished Pt disk with a nominal diameter of 4 mm (Figure 3.4 (b)). The working electrode was embedded in a glass holder connected to a micrometric screw which was used for adjusting the distance between cell bottom and WE. A platinum wire wrapped around the glass embedment was used as counter electrode; a silver wire was used as (pseudo)reference electrode and calibrated through the redox couple Fc/Fc^+.

Spectroelectrochemical measurements were performed using an Autolab PGSTAT204 potentiostat (Metrohm) and a Zeiss UV−Vis spectrometer endowed with a MCS621 Vis II spectrometer cassette and a CLH600F lamp. The solution absorption upon electrochemical polarization was measured from the difference of the emitted and reflected light from the working electrode surface. All measurements were performed in thin layer conditions, employing ~20 μm distance between the surface of the WE and the bottom of the quartz cell.

3.1.1.2.2 *In-Situ* Conductance

In-situ conductance refers to the combination of conductance measurements with electrochemical methods and represents an extremely insightful technique to follow electrochemical doping processes. The first *in-situ* conductance experiment was developed by Zotti *et al.* and was based on the use of a double-band microelectrode separated by an insulator with a known micrometric spacing, and the concurrent use of two potentiostats.[2] In this technique, a conductive film is deposited onto two closely spaced platinum electrodes bridging the insulating-gap located between them. The double-band microelectrode acts as the working electrode in a three-electrode configuration allowing a precise control of the doping level of the polymer film. Simultaneously, a second potentiostat applies a DC-voltage of small amplitude between the two Pt bands, and the associated drain current is measured and is employed to evaluate the film's conductance. Wrighton *et al.* subsequently improved the experimental setup by replacing the band arrangement with an interdigitated microarray configuration which allows more sensitive determinations of currents.[3]

A schematization of the setup utilized for perform *in-situ* conductance experiments is presented in Figure 3.6. In order to measure the *in-situ* conductance, an electrochemical cell with interdigitated electrodes as WE, a first potentiostat (Autolab), a second potentiostat (Dropsense μSTAT400), a conductivity interface (CIP2 Heka) and a separation amplifier (gain 1: 1) were employed.

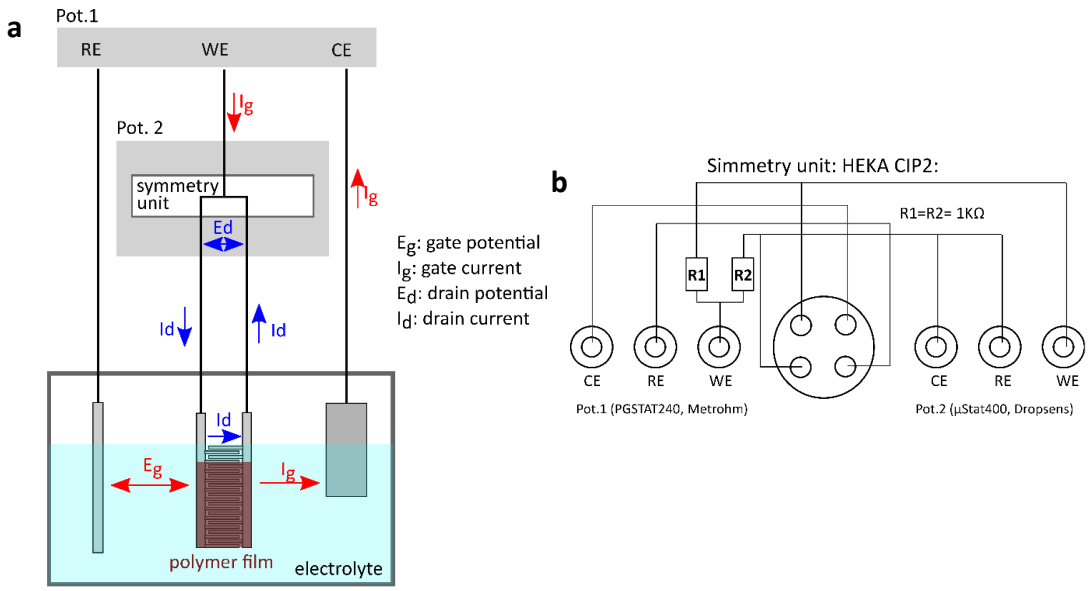

Figure 3.6: (a) Scheme of the experimental setup employed for in situ conductance measurement. (b) Details of the internal connection of the symmetry unit (HEKA CIP2).

Interdigitated electrodes from DropSens (comb distance: 5 or 10 µm) were used as the working electrodes. All CV experiments were performed at room temperature under argon atmosphere using an Autolab PGSTAT204 potentiostat (Metrohm) with a Pt wire as CE and an AgCl-coated Ag wire directly immersed into the electrolyte solution as pseudoreference electrode. A constant bias (E_d) of 10 mV was applied between the combs of the interdigitated electrode using a second potentiostat (µStat400, DropSens) measuring the current (I_d) which was flowing between the two combs of the interdigitated electrodes as a function of the potential in the CV measurement. With the help of two resistors (Heka, conductivity interface CIP2), both current signals are separated to allow to conduct both the CV measurements and to measure the *in-situ* conductance simultaneously. The software packages employed were *Nova 1.1* for running the CV measurement and *DropView* for controlling µStat400. The conductance values G were calculated from the measured current flowing between the combs according to Ohm's law G=1/R=I/V with employment of a multiplicative factor 2 for the current range. Electrolyte solutions were deaerated by argon bubbling before use. Conductance values are given as conductance change (ΔG) with respect to the conductance of the materials in the neutral state.

Whereas *in-situ* conductance measurements allow to precisely correlate different induced states of charge and doping levels with the conductance of the film, realizing a conductivity map of the material as function of the potential, it also presents some drawbacks. These are associated to the difficulty of obtaining precise information about the film thickness of the film, as the latter is subjected to undefined variations during the doping process. Further, the conductivities are measured via the drain current, and their absolute

values are not known and must be determined using an imprecise standard. As consequence, most of the studies using *in-situ* electrochemical-conductance technique report conductance values instead of the specific conductivity. In this way conductance becomes an indirect description of conductivity behavior of the studied films.

3.1.1.2.3 *In-Situ* Electrochemical Quartz Crystal Microbalance (EQCM)

Electrochemical quartz crystal microbalance (EQCM) is the combination of electrochemical methods and quartz crystal microbalance (QCM). The QCM working principle is based on the piezoelectric effect of a quartz crystal which is placed between two metal electrodes. An alternated electric field is applied across the crystal, causing thickness-shear vibrations of the crystal around its resonant frequency.[4,5] Piezoelectricity (from greek "πιέζειν", to press and "ηλεκτρισμός" electricity) of some crystal material, including quartz, Rochelle salt ($NaKC_4O_6 \cdot 4H_2O$) and of some biomolecules was first discovered by Jacques and Pierre Curie in 1880,[6] and consists of a charge separation following the application of a mechanical stress as shown in Figure 3.7. This charge separation generates a difference of potential across the crystal, whose magnitude is proportional to the applied stress and the phenomenon is called *"piezoelectric effect"*. On the opposite, when a difference of potential is applied across a quartz crystal, a related mechanical deformation of the latter takes place; this is indicated as "reverse piezoelectric effect" and serves as the fundamental principle for the QCM.[6] The application of an alternating electrical signal across the quartz crystal will generate an acoustic wave that propagates across the crystal thickness. Around the resonant frequency, the quartz resonator vibrates with minimal energy dissipation which characterizes an ideal oscillation.[6]

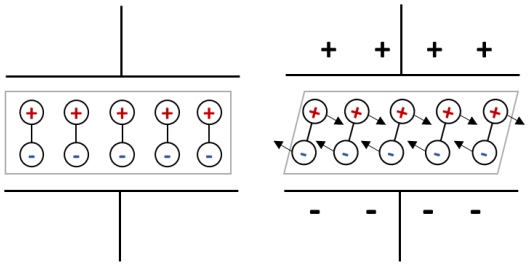

Figure 3.7: Schematic representation of the piezoelectric effect for shear motion. Upon application of a potential difference across the crystal, reorientation of the dipoles takes place resulting in a lattice strain and shear deformation of the material. The direction of the shear motion depends on the applied difference of potential whereas its magnitude of the shear strain depends on the magnitude of the applied potential.[4]

When a material is deposited on the surface of the quartz, it is assumed that the acoustic wave generated will propagate from the quartz center through the deposited film with a continuous displacement (shear stress) across the quartz / film interface. This means that the film can be regarded as an extension of the quartz. The frequency (f) of this movement depends on the crystal thickness, and more precisely, it diminishes with

increasing of the thickness. Upon deposition of a rigid and inelastic film on the crystal surface, the oscillation frequency diminishes. In particular, a relationship between microbalance frequency change (Δf) and variation of the mass (Δm) deposited on the quartz crystal was first reported by Sauerbrey, and is expressed by equation (3.2).[4]

$$\Delta f = \frac{-2f_0^2 \Delta m}{A\sqrt{\mu_q \rho_q}} = -C_f \Delta m \qquad (3.2)$$

In the equation Δf represents the resonance frequency shift, f_0 indicates the quartz resonance frequency before film deposition, A is the piezoelectrically active area of the quartz, μ_q the shear modulus of the quartz and ρ_q the quartz density and C_f is the gravimetric proportionality constant. The analysis of frequency variation allows to study mass variations with high sensibility. For example, in the case of a 9 MHz resonator, with a piezoelectric area of 0.2 cm^2, a change in frequency of 1 Hz corresponds to a change in mass of 1.09 ng.[7]

QCM can be used simultaneously with different electrochemical techniques, including voltammetry, chronoamperometry or chronopotentiometry to monitor correlated changes in the mass of the working electrode. In this case a quartz resonator covered with gold is used as WE. The resonator is mounted on a holder and placed in an electrochemical cell, together with the reference and the counter electrodes, and is connected to a frequency control unit and to a potentiostat. In this case, concurrently to the electrochemical response, the mass variation of the electrode during an electrochemical process is analysed. EQCM has become an extremely powerful tool for the monitoring and interpretation of an electrochemical processes that involve deposition, adsorption, or insertion of ions and species at the working electrode surface. In particular, the latter has been widely employed for the *in-situ* measurement of ionic transport in different electrochemical systems.[5,8–10] By analysis of the current and simultaneous mass change of EQCM measurements, it is possible to determine the mass per mole of electrons (M_i) which are exchanged at the electrode | electrolyte interface according to equation (3.3), which provides a global indication of the molar mass of the species involved in the charge compensation.

$$M_i = F\,\Delta m/\Delta q \qquad (3.3)$$

Due to fact that EQCM measurements are limited to variations of the scan-rates and currents determination in the case of a CV measurement, it does not allow to deconvolution the electrogravimetic response into *gravimetric* and *time dependency*. Similar considerations also hold for combination with other electrochemical methods. Therefore, *ac*-electrogravimetry is introduced as complementary technique to EQCM, allowing for a deeper analysis of the charge compensation, with possibility of deconvolution of the global response into mass and temporal contributes.[11,12]

3.1.1.2.4 *Ac*-electrogravimetry (ACE)

Ac-electrogravimetry was first proposed by C. Gabrielli,[13] this technique is based on a QCM used in dynamic regime, *i.e.* with frequency potential modulation of the WE, and coupled to electrochemical impedance spectroscopy (EIS). Similarly to EQCM, a classical electrochemical configuration is employed and the quartz surface is coated by a thin and uniform layer of film as working electrode. Upon application of a sinusoidal difference of potential (ΔE(ω)) to the coated WE, a variation in the local concentration of the species takes place, due to species transferring to allow charge compensation. The concentration as mass variation of these species can be tracked thanks to the employment of QCM under a dynamic regime. This combination allows for the separation and identification of the contribution of different species taking part to the electrochemical process with different kinetics. Species can be identified with their molar mass.[12,14–17]

During an *ac*-electrogravimetry experiment, the quartz is polarized through a potentiostat to a selected potential E_0. Upon application of a small amplitude difference of potential $\Delta E\sin(\omega t)$ overlayed to E_0, exchange of species at the film| electrolyte interface takes place. This includes anion, cation, solvated ions and free solvent molecules, and can lead to a mass change of the electrode and change in the QCM frequency variation. The latter is further translated in a voltage change ΔV_f by the frequency / voltage converter, which is finally sent to the Frequency Response Analyzer (FRA). To resume, the application of a small $\Delta E\sin(\omega t)$ overlaid to E_0 generates at the WE a current ΔI and a frequency dependent mass response $\Delta V_f(\omega)$. Through a frequency response analyzer (FRA) the transfer functions (ΔE/ΔI) and ($\Delta V_f/\Delta E$) are obtained. These, through a mathematical treatment, are finally converted into impedance (ΔE/ΔI(ω)) and electrogravimetric (Δm/ΔE(ω)) transfer functions (TFs).

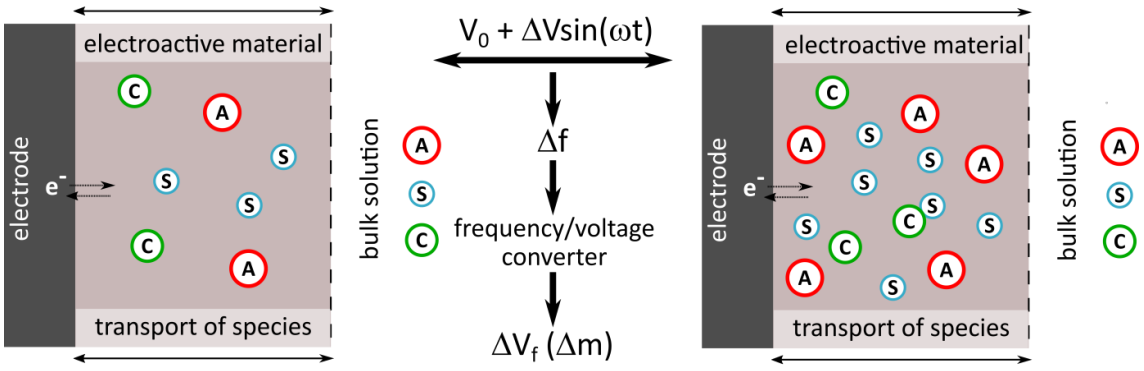

Figure 3.8: Ac-electrogravimetry working principle.

A schematic representation of the *ac*-electrogravimetry experimental set-up is given in Figure 3.9.[14] In the case of *ac*-electrogravimetry measurements, the frequency / voltage

converter plays a fundamental role, allowing for the analogical processing of the signals, by means of a phase-locked loop circuit (generates an output signal, whose phase is related to the phase of an in-put signal). The F/V converter allows indeed to translate the microbalance frequency signal ($f_r - f_w$) in a voltage signal (ΔV_f), which is sent to the Frequency Response Analyzer (FRA, Solartron 1254).[14] The raw transfer functions $\frac{\Delta Vf}{\Delta V}(\omega)$ and $\frac{\Delta V}{\Delta i}(\omega)$ are measured by the FRA simultaneously at a given potential and frequency modulation f (pulsation $\omega = 2\pi f$). In this way, after a mathematical treatment with Mathcad software of the raw transfer functions it is possible to concurrently obtain the electrogravimetric $\frac{\Delta m}{\Delta E}(\omega)$ and the electrochemical impedance $\frac{\Delta E}{\Delta I}(\omega)$ transfer functions.

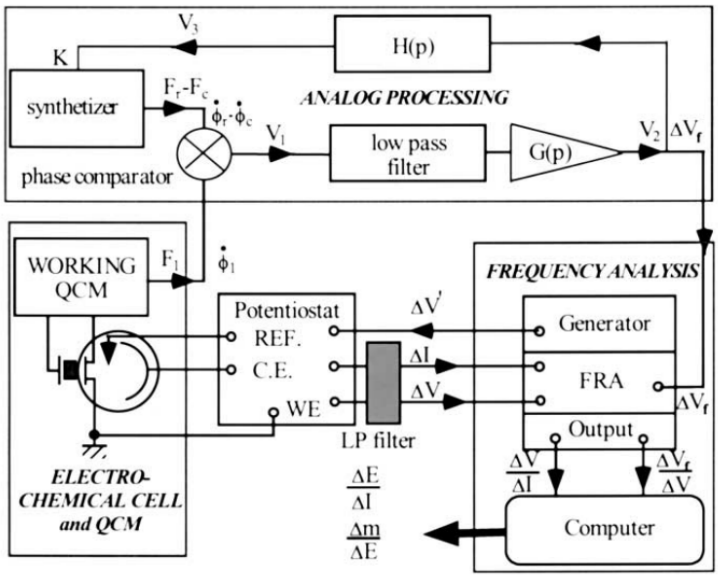

Figure 3.9: Diagram of the experimental set-up. Adapted from ref. [14]. Copyright Elsevier (2001).

Despite electrochemical impedance and the transfer functions are simultaneously measured, the frequency range of measurement for impedance goes from ~65 KHz to ~10 mHz whereas in the case of the electrogravimetric transfer function it is narrower, from ~1 KHz to ~10 mHz. This difference is due to a distortion of working frequency signal (phase shift and modulus attenuation) occurring in the frequency/voltage converter. The F/V converter sensitivity in the linear part is around 29 $mV \cdot Hz^{-1}$. In order to increase the performance at the level of the F/V converter, due to the fact that the microbalance frequency change (Δf_m) is generally in the order of tens of hertz, in contrast to the 9 MHz frequency of the carrier (f_m). The carrier frequency is reduced to some hundreds of Hz (~400 Hz), utilizing a reference frequency synthesizer (Agilent 33250A); in this way ~400 Hz frequency difference between the microbalance quartz frequency f_w and that of the reference synthesizer f_r is hold (Figure 3.9).

The impedance transfer function ($\frac{\Delta E}{\Delta I}(\omega)$) takes into account only the charged species whereas the gravimetric transfer function ($\frac{\Delta m}{\Delta E}(\omega)$) takes into account also non-charged species, for example free solvent molecules. From impedance transfer function, the experimental $\frac{\Delta q}{\Delta E}(\omega)$ can be calculated (3.4). The latter allows to have a clear view of the charged species involved in the electrochemical process.

$$\frac{\Delta q}{\Delta E}(\omega)\Big|_{exp} = \frac{1}{j\omega}\frac{\Delta I}{\Delta E}(\omega)\Big|_{exp} \qquad (3.4)$$

Analogously, from the experimental electrogravimetric transfer function ($\frac{\Delta m}{\Delta E}(\omega)$), multiple partial mass/potential transfer functions can be obtained by removing each contributor in the charge compensation from the global measured value.

Let us consider the case of four species involved in the electrochemical process: the solvent (s), anion (a) endowed with Z_a valence; cation-1 (c_1) with valence Z_{c1} and cation-2 (c_2) with valence Z_{c2}. As the four terms are unknown (the anion, cations 1 and 2 and the solvent response) and only two quantities, $\frac{\Delta E}{\Delta I}(\omega)$ and $\frac{\Delta m}{\Delta E}(\omega)$ are measured, it is not possible to separately calculate the unknown terms. However, it is possible to eliminate the contribution of each term from the mass/ potential transfer function as follows: [20]

$$\frac{\Delta m}{\Delta E}(\omega)\Big|_{exp}^{c1c2s} = \frac{\Delta m}{\Delta E}(\omega)\Big|_{exp} - \frac{M_a}{FZ_a}(\omega)\frac{\Delta q}{\Delta E}(\omega)\Big|_{exp} \qquad (3.5)$$

$$\frac{\Delta m}{\Delta E}(\omega)\Big|_{exp}^{ac2s} = \frac{\Delta m}{\Delta E}(\omega)\Big|_{exp} + \frac{M_{c1}}{FZ_{c1}}(\omega)\frac{\Delta q}{\Delta E}(\omega)\Big|_{exp} \qquad (3.6)$$

$$\frac{\Delta m}{\Delta E}(\omega)\Big|_{exp}^{ac1s} = \frac{\Delta m}{\Delta E}(\omega)\Big|_{exp} + \frac{M_{c2}}{FZ_{c2}}(\omega)\frac{\Delta q}{\Delta E}(\omega)\Big|_{exp} \qquad (3.7)$$

The concentration variation of each component, ΔC_i at the electrode | electrolyte interface upon an alternated potential difference ΔE is expressed by the following relationship:[14,20]

$$\frac{\Delta C_i}{\Delta E}(\omega)\Big|_{th} = \frac{-G_i}{j\omega d_f + K_i} \qquad (3.8)$$

K_i and G_i are the partial derivates of the flux (J_i) with regard to the concentration (3.9) and the potential (3.10), respectively and d_f is the film thickness.

$$K_i = \left(\frac{\partial J_i}{\partial C_i}\right)_E \qquad (3.9)$$

$$G_i = \left(\frac{\partial Ji}{\partial E}\right)_{Ci} \text{ and } \left(Rt_i = \frac{1}{FG_i}\right) \qquad (3.10)$$

K_i represents the transfer kinetics of each species and from which, the characteristic frequency f_i of each species is obtained ($f_i = \frac{K_i}{\pi d_f}$), whereas from G_i the transfer resistance Rt

($Rt_i = \frac{1}{FG_i}$) of each species is obtained. Rt represents the ease with which the related species transfers at the film| electrolyte interface. Faradaic impedance ($Z_F(\omega)$) can be expressed, separating the contribution of the ions (c_1 , c_2, a) and the solvent (s), as follows:

$$Z_F(\omega)|_{th}=\frac{\Delta E}{\Delta I_F}(\omega)\Big|_{th}=\left[j\omega Fd_f\left(-Z_{c_1}\frac{\Delta C_{c_1}}{\Delta E}(\omega)-Z_{c_2}\frac{\Delta C_{c_2}}{\Delta E}(\omega)+Z_a\frac{\Delta C_a}{\Delta E}(\omega)\right)\right]^{-1} \qquad (3.11)$$

with ΔC_i being the variation in concentration for the different species, F is the Faraday constant. The global electrochemical impedance $\frac{\Delta E}{\Delta I}(\omega)$ is defined with equation (3.12), in which C_{dl} stands for the interfacial capacitance and R_{el} for the resistance of the electrolyte.

$$\frac{\Delta E}{\Delta I}(\omega)\Big|_{th}=\left[j\omega C_{dl}+j\omega Fd_f\left(Z_{c_1}\frac{G_{c_1}}{j\omega Fd_f}(\omega)+Z_{c_2}\frac{G_{c_2}}{j\omega Fd_f}(\omega)-Z_a\frac{G_a}{j\omega Fd_f}(\omega)\right)\right]^{-1}+R_{el} \qquad (3.12)$$

The global electrogravimetric transfer function, $\frac{\Delta m}{\Delta E}(\omega)$, can be expressed by (3.13) in which M_i (i = c1, c2, a and s) represents the molar mass of each species contributing to the electrochemical process at the film|electrolyte interface.

$$\frac{\Delta m}{\Delta E}(\omega)\Big|_{th}=-d_f\left(M_{c_1}\frac{G_{c_1}}{j\omega d_f+K_{c_1}}+M_{c_2}\frac{G_{c_2}}{j\omega d_f+K_{c_2}}+M_a\frac{G_a}{j\omega d_f+K_a}+M_s\frac{G_s}{j\omega d_f+K_s}\right) \qquad (3.13)$$

The charge/potential transfer function, $\frac{\Delta q}{\Delta E}(\omega)$, considers exclusively the transfer of the charged species and is defined by equation (3.14):

$$\frac{\Delta q}{\Delta E}(\omega)\Big|_{th}=\frac{1}{j\omega}\frac{\Delta I_F}{\Delta E}(\omega)=Fdf\left(Z_{c_1}\frac{G_{c_1}}{j\omega Fd_f}(\omega)+Z_{c_2}\frac{G_{c_2}}{j\omega Fd_f}(\omega)-Z_a\frac{G_a}{j\omega Fd_f}(\omega)\right) \qquad (3.14)$$

Further, the transfer functions for the single components can be utilized to cross-check and validate the hypothesis involving the transfer of multiple species at the CP film| electrolyte interface. Indeed, the partial transfer functions $\frac{\Delta m}{\Delta E}(\omega)\Big|_{th}^{c1c2s}$ can be obtained by removal of the anion contribution as follows (3.15):

$$\frac{\Delta m}{\Delta E}(\omega)\Big|_{th}^{c1c2s}=\frac{\Delta m}{\Delta E}(\omega)\text{-}M_a\left(-\frac{\Delta C_{c_1}}{\Delta E}(\omega)\text{-}\frac{\Delta C_{c_2}}{\Delta E}(\omega)+\frac{\Delta C_a}{\Delta E}(\omega)\right)=$$

$$=-d_f\left((Mc_1+M_a)\frac{G_{c_1}}{j\omega d_f f+Kc_1}+(Mc_2+M_a)\frac{G_{c_2}}{j\omega d_f f+Kc_2}+M_s\frac{G_s}{j\omega d_f f+K_s}\right) \qquad (3.15)$$

In a similar fashion, by removing the contribution of cations C_1 (or C_2) the partial transfer functions $\frac{\Delta m}{\Delta E}(\omega)\Big|_{th}^{c2as}$ (3.16) and $\frac{\Delta m}{\Delta E}(\omega)\Big|_{th}^{c1as}$ (3.17) are respectively obtained:

$$\left.\frac{\Delta m}{\Delta E}(\omega)\right|_{th}^{c2as} = \frac{\Delta m}{\Delta E}(\omega) + M_{c_1}\left(-\frac{\Delta C_{c_1}}{\Delta E}(\omega) - \frac{\Delta C_{c_2}}{\Delta E}(\omega) + \frac{\Delta C_a}{\Delta E}(\omega)\right) =$$

$$= -d_f\left(\left(M_{c_2} - M_{c_1}\right)\frac{G_{c_2}}{j\omega d_f f + Kc_2} + (Mc_2 + M_a)\frac{G_a}{j\omega d_f f + K_a} + M_s\frac{G_s}{j\omega d_f f + K_s}\right) \qquad (3.16)$$

As well as the last partial transfer function

$$\left.\frac{\Delta m}{\Delta E}(\omega)\right|_{th}^{c1as} = \frac{\Delta m}{\Delta E}(\omega) + M_{c_2}\left(-\frac{\Delta C_{c_1}}{\Delta E}(\omega) - \frac{\Delta C_{c_2}}{\Delta E}(\omega) + \frac{\Delta C_a}{\Delta E}(\omega)\right) =$$

$$= -d_f\left(\left(M_{c_1} - M_{c_2}\right)\frac{G_{c_1}}{j\omega d_f f + Kc_1} + (Mc_1 + M_a)\frac{G_a}{j\omega d_f f + K_a} + M_s\frac{G_s}{j\omega d_f f + K_s}\right) \qquad (3.17)$$

The number of species participating in the charge compensation process and endowed with different time constants can be evaluated.

Let us consider a first simple situation in which a single ion can be inserted (or expulsed) in (or from) the film. The transfer functions $\frac{\Delta E}{\Delta I}(\omega)$, $\frac{\Delta m}{\Delta I}(\omega)$ and $\frac{\Delta q}{\Delta I}(\omega)$ are calculated from (3.12), (3.13) and (3.14), respectively for this situation is given in the first raw of Figure 3.10. In the case of contribution of a single charged species, the $\frac{\Delta E}{\Delta I}(\omega)$ transfer function (Figure 3.10 (a)) shows a high-frequency loop corresponding to charge transfer in parallel to double-layer charging and the straight line in the lower frequency range corresponds to ionic transfer. The $\frac{\Delta q}{\Delta I}(\omega)$ transfer function (Figure 3.10 (b)) is characterized by a low frequency single loop corresponding to the charge compensation independently from the nature of the ion. The electrogravimetric transfer function, $\frac{\Delta m}{\Delta I}(\omega)$ (Figure 3.10 (c)) brings more information, allowing to discriminate between the species involved in the charge compensation. Indeed, a cation would present a characteristic loop in the III quadrant (blue curve), whereas the response of an anion would be characteristically found in the I quadrant (red curve). It is important to stress that $\frac{\Delta m}{\Delta I}(\omega)$ is the only transfer function that can discriminate between the cations or anions and identify them by their molar mass.

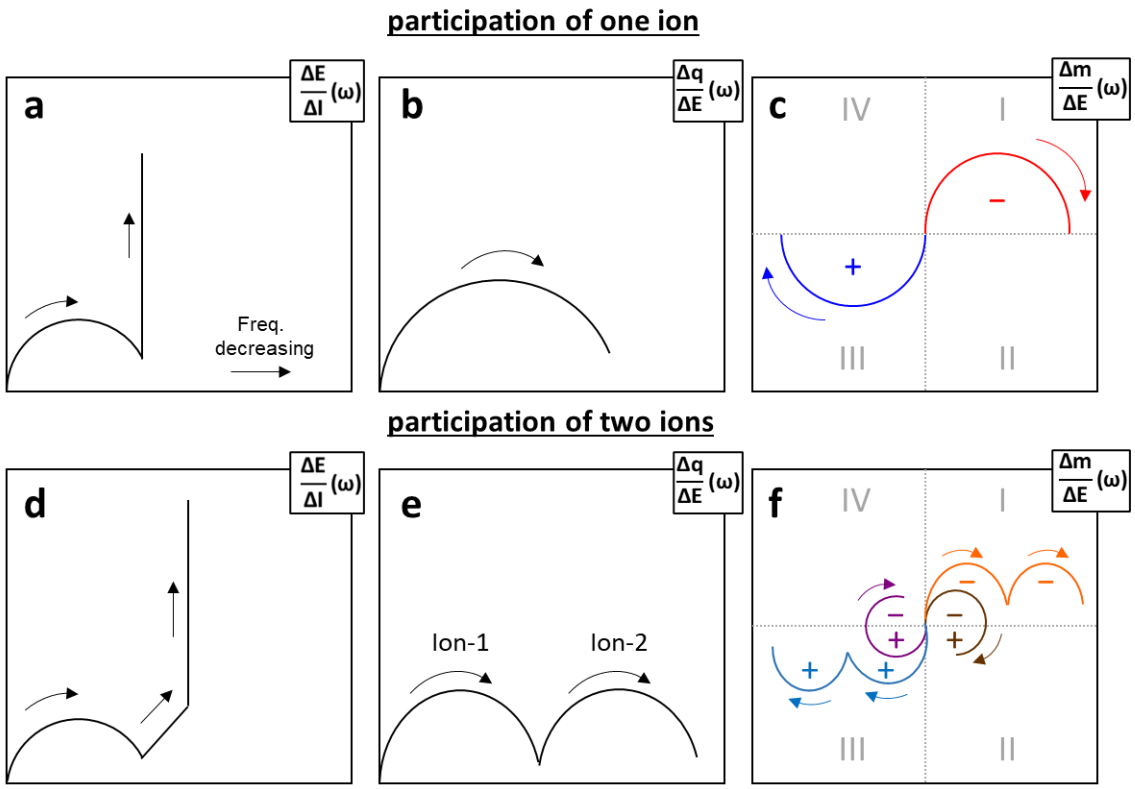

Figure 3.10: Simulation of different transfer functions (TFs) ΔE/ΔI(ω)(a, d), Δq/ΔE(ω)(b, e) and Δm/ΔE(ω)(c, f) in the case of a single (first raw) and two charged species (second raw). In the case of two charged species the time constant is different enough for the couple of ions to see separated contributions.

In the case of charge compensation undertaken by multiple ions simultaneously, the characteristic transfer functions responses are presented in the second raw of transfer function (Figure 3.10). Four different configurations of ionic transfer are considered: two cations (light blue curve), two anions (orange curve), a cation/anion (purple curve) and an anion/cation (brown curve). In the case that the time constant of the different ions is different enough, an additional loop would be found for the $\frac{\Delta E}{\Delta I}(\omega)$ transfer function (Figure 3.10 d). The $\frac{\Delta q}{\Delta I}(\omega)$ transfer function (Figure 3.10 (e)) would present only two subsequent loops found for different frequencies, similarly for the four configurations. The power of $\frac{\Delta m}{\Delta I}(\omega)$ transfer function to separate and define the contributions of the single elements (ions and solvent) can be evinced in Figure 3.10 (f). In this case four different configurations are encountered, for the two cations represented with light blue curve, for the two anions with orange color, a cation / anion with purple and in the case of anion / cation with the brown curve.

3.1.2 Other Methods

3.1.2.1 Conductivity Measurements: Four-Point Probe (4PP)

Conductivity is a bulk property of a material and is defined as the ability to permit electrical current flow; it constitutes a parameter of interest in the field of material characterization. Consequently, a proper approach for conductivity determination is important. In the previous section the *in-situ* conductance method was presented, pointing out its limits correlated to the determination of the specific conductivity, and its preferential use for the study of potential dependent conductance.[21,22]

The specific conductivity ($\Omega^{-1}\cdot cm^{-1}$) of a material characterized by a transversal area ($A\cdot cm^{-2}$) and a known longitude ($L\cdot cm^{-1}$) is determined by equation (3.18).

$$\sigma = \frac{L}{R\cdot A} = \frac{K}{R} \qquad (3.18)$$

Where σ is the specific conductivity and R is the resistance in ohm (Ω) and the term K is the geometrical factor. In the case of uneven samples, the determination of the geometrical factor could result complicated and specific modifications to the term K might be necessary.[21]

The four-point-probe method (4PP) was employed as method for the determination of specific conductivity of chemically doped samples.[23,24] The 4PP method is based on the equidistant linear arrangement of 4 electrodes in the form of metal tips with finite radius, placed in contact with the conducting material. The latter is deposited on the surface of a non-conductive substrate such as glass slides by solution or vapor deposition methods. Specific conductivity measurements are performed by applying to the sample a constant current (I) through the two outside probes (electrodes 1 and 4), and by measuring the voltage (V) between the two inner probes (electrodes 2 and 3). This approach allows to diminish the contact resistance. These measurements can be performed using a proper source-meter, and the specific conductivity can be calculated by equation (2) knowing the specific geometric factor K which depends on the film thickness (d) and a geometry corrector factor (f):[23–25]

$$\sigma = \frac{K}{R} = \frac{\ln(2) f}{R\pi d} \qquad (3.19)$$

In the specific case of a central measurement of quadratic samples, the term f of the geometry-corrector factor equals 1,[25] consequently the specific conductivity results is given.

$$\sigma = \frac{\ln(2)}{R\pi d} \quad (3.20)$$

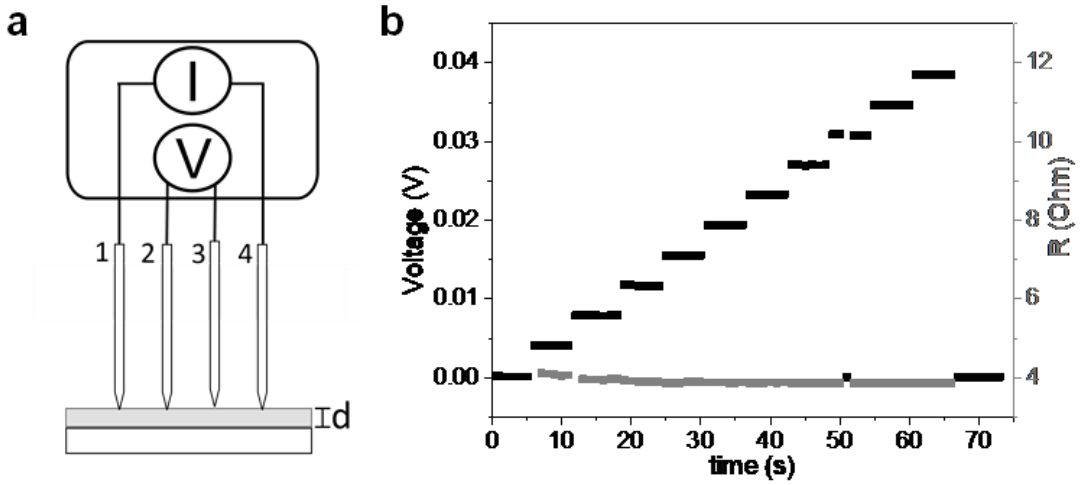

Figure 3.11: (a) Schematic representation of a test circuit for measuring resistivity by the four-point-probes method; I=current, V=voltage and (b) Example of output of a resistance measurement through 4PP technique.

To measure conductivity by 4PP a *SP4 Signatone* probe head (linear tip arrangment, distance 1mm) was employed and the measurements were run through a *Keithley 2636B SourceMeter.* The measurements were performed by applying a series of constant currents in the same order of magnitude to confirm linear ohmic behavior of the sample resistance (Figure 3.11). The polymer films were deposited on square-cut glass substrates and the measurements were conducted with the tips connecting to the film center. Different spots around the center of the samples were tested in order to check reproducibility of conductivity data, final conductivity data are given as average of conductivity values measured on multiple samples. The film thickness (d) of the samples was measured either (depending on the nature and thickness of the sample) through profilometry (Dektak 150, Veeco) or Atomic Force Microscopy (AFM) (Dimension Icon, Bruker) in tapping mode, measuring the height change transversal a scratch on the film's surface. Unless noted all conductivity measurements were performed in a nitrogen-filled glovebox.

3.1.2.2 UV-Vis Absorption Spectroscopy

UV-Vis absorption spectroscopy was also used as a straightforward method for the characterization of the doping level of polymers in the solid state upon chemical doping. In the case of chemically doped polymer films UV-Vis absorption spectra were recorded, unless noticed, in a nitrogen filled glove-box to avoid modification of the doped substrate upon contact with air. A *Zeiss MCS621 Vis II* spectrometer equipped with a *CLH 600 F* halogen lamp and optic fibers from *Ocean Optics.*

3.2 Reagents and Chemicals

The solvents, chemicals and conducting salts employed, including chemical grade and producer are listed in Table 3.1 and Table 3.2.

solvent	grade	producer	abbreviation
acetone	p.a., ≥ 98 %	VWR	-
acetonitrile	anhydrous, electrochemical grade, ≥ 99.8 %	Sigma Aldrich	CH_3CN
chloroform	anhydrous, analytical HPLC grade, ≥ 99.9 %	Sigma Aldrich	$CHCl_3$
dichloromethane	anhydrous, electrochemical grade, ≥ 99.8 %	Sigma Aldrich	CH_2Cl_2
isopropanol	p.a., ≥ 98 %	VWR	-
tetrahydrofuran	analytical HPLC grade, ≥ 99.9 %	Sigma Aldrich	THF
water	demineralized	internal	H_2O

Table 3.1: Overview of employed solvents.

For the preparation of organic electrolytes (CH_3CN and CH_2Cl_2) anhydrous solvents of electrochemical grade were purchased and directly employed without additional treatment. All solutions employed for electrochemical measurements were handled through the Schlenk technique. The conducting salts were stored under vacuum in an desiccator to avoid moisture uptake.

salt	grade	producer	abbreviation
lithium perchlorate	electrochemical grade, ≥ 99.9 %	Sigma Aldrich	$LiClO_4$
tetrabutylammonium hexafluorophosphate	electrochemical grade, ≥ 99.0 %	Sigma Aldrich	NBu_4PF_6
other chemicals	**grade**	**producer**	**abbreviation**
iron(III) chloride	anhydrous , ≥99.99%	Sigma Aldrich	$FeCl_3$
iron(III) *p*-toluensulfonate hexahydrate	technical grade	Sigma Aldrich	$Fe(Tos)_3$

Table 3.2: Overview of employed conducting salts and reactants.

3.3 Substrates

substrate	characteristic	producer	abbreviation
Au coated glass slides	Cr/Au (3/30 nm) prepared by evaporation deposition	internal	Au
Indium doped Tin Oxide coated glass slides	R ≤ 20 Ω sq^{-1}	PGO	ITO

Float glass	-	PGO	Glass
Pt interdigitated electrodes	5 or 10 µm interdigitated spacing	DropSens, Metrohm	Pt-IDE 5 / 10 µm
Au coated 9 MHz Quartz Resonators	9 MHz	AW Sensors	-

Table 3.3: Overview of employed substrates.

The substrates were cut prior to the cleaning process in pieces of 1 cm *x* 1 cm (Glass Substrates), 1 cm *x* 1.5 cm (Au electrodes) and 0.8 cm *x* 1.5 cm (ITO electrodes), respectively. Prior to usage, all substrates were subjected to cleaning steps which involved 10 minutes sonication in isopropanol (p.a.), 10 minutes in water followed by 10 minutes sonication in acetone (p.a.). After being cleaned, the samples were dried by an argon flux. In the case of ITO and float glass substrates a 10 minutes treatment in a plasma chamber was also performed; Au electrodes were subjected to further mechanical cleaning by "*snow jet*" (sample positioned on a heat plate at ca 200°C and bombarded with a stream of dry ice from high pressure CO_2).

3.4 References

[1] A. Scott Hinman A N D, B. J. Pavelich, *Versatile Thin Layer Spectroelectrochemical Cell Employing Specular Reflectance*, **n.d.**

[2] G. Schiavon, S. Sitran, G. Zotti, *Synth. Met.* **1989**, *32*, 209–217.

[3] C. E. D. Chidsey, R. W. Murray, *J. Phys. Chem.* **1986**, *90*, 1479–1484.

[4] D. A. Buttry, M. D. Ward, *Chem. Rev.* **1992**, *92*, 1355–1379.

[5] W. Y. Tsai, P. L. Taberna, P. Simon, *J. Am. Chem. Soc.* **2014**, *136*, 8722–8728.

[6] J. Curie, P. Curie, *Bull. la Société minéralogique Fr.* **1880**, *3*, 90–93.

[7] K. Bizet, C. Gabrielli, H. Perrot, in *Appl. Biochem. Biotechnol. - Part A Enzym. Eng. Biotechnol.*, **2000**, pp. 139–149.

[8] V. Dargel, M. D. Levi, L. Daikhin, D. Aurbach, *Russ. J. Electrochem.* **2017**, *53*, 980–993.

[9] W. Plieth, A. Bund, U. Rammelt, S. Neudeck, L. M. Duc, in *Electrochim. Acta*, Pergamon, **2006**, pp. 2366–2372.

[10] F. Razzaghi, C. Debiemme-Chouvy, F. Pillier, H. Perrot, O. Sel, *Phys. Chem. Chem. Phys.* **2015**, *17*, 14773–14787.

[11] C. Gabrielli, M. Keddam, H. Perrot, M. C. Pham, R. Torresi, *Electrochim. Acta* **1999**, *44*, 4217–4225.

[12] C. Gabrielli, J. J. García-Jareño, M. Keddam, H. Perrot, F. Vicente, *J. Phys. Chem. B* **2002**, *106*, 3182–3191.

[13] S. Bourkane, C. Gabrielli, M. Keddam, *J. Electroanal. Chem.* **1988**, *256*, 471–475.

[14] C. Gabrielli, J. J. Garcia-Jareo, H. Perrot, *Electrochim. Acta* **2001**, *46*, 4095–4103.

[15] W. Gao, O. Sel, H. Perrot, *Electrochim. Acta* **2017**, *233*, 262–273.

[16] H. Perrot, O. Sel, **n.d.**

[17] F. Escobar-Teran, A. Arnau, J. V. Garcia, Y. Jiménez, H. Perrot, O. Sel, *Electrochem. commun.* **2016**, *70*, 73–77.

[18] H. Goubaa, F. Escobar-Teran, I. Ressam, W. Gao, A. El Kadib, I. T. Lucas, M. Raihane, M. Lahcini, H. Perrot, O. Sel, *J. Phys. Chem. C* **2017**, *121*, 9370–9380.

[19] C. R. Arias, C. Debiemme-Chouvy, C. Gabrielli, C. Laberty-Robert, A. Pailleret, H. Perrot, O. Sel, *J. Phys. Chem. C* **2014**, *118*, 26551–26559.

[20] C. Gabrielli, H. Perrot, in *Mod. Asp. Electrochem.*, Springer, New York, NY, **2009**, pp. 151–238.

[21] G. Salinas, B. A. Frontana-Uribe, *ChemElectroChem* **2019**, 1–14.

[22] J. Heinze, B. A. Frontana-Uribe, S. Ludwigs, *Chem. Rev.* **2010**, *110*, 4724–4771.

[23] P. Bøggild, F. Grey, T. Hassenkam, D. R. Greve, T. Bjørnholm, *Adv. Mater.* **2000**, *12*, 947–949.

[24] V. S. Mironov, J. K. Kim, M. Park, S. Lim, W. K. Cho, *Polym. Test.* **2007**, *26*, 547–555.

[25] D. K. Schroder, *Semiconductor Material and Device Characterization*, IEEE Press And Wiley, **2006**.

4 Electrochemical Coupling of Redox Active Molecules and Electrodeposition of Functional Surfaces via Crosslinking of Multimeric Systems

In this section the oxidative coupling of redox active moieties of opto-electronic interest and consisting of substituted arylamines, carbazoles as well as thiophenes is studied, focusing on structure-properties relationships. The systems herein presented are characterized by a peculiar ability to undergo selective dimerization upon oxidation, the latter was exploited in systems bearing multiple oxidative sites to electrodeposit films with a reversible electrochemical behavior which mirrors to the one of the dimeric moieties. The so-obtained electroactive film show a highly reversible electrochemical and electrochromic switching, good charge transport and increased chemical stability, making them good candidates to be tested for example as active layers in BHJ solar cells[1,2] and in electrochromic devices.[3]

The first study presented deals with linear D-π-A push-pull systems widely employed in OSCs and based on modifications of the arylamine donor unit and of the acceptor moiety. In this case the reactivity towards dimerization is studied as function of the modification of the molecular structure, and is exploited in a multimer to deposit highly crosslinked and three-dimensional D-A push-pull films with well-defined π-conjugation and redox behavior, to be employed as active layer in BHJ solar cells. The study is made in cooperation with the groups of Prof. P. Blanchard (MOLTECH Angers, University of Angers) responsible for the molecule synthesis, and of Prof. C. Ruiz-Delgado (University of Malaga) responsible for the DFT and TD-DFT calculations.

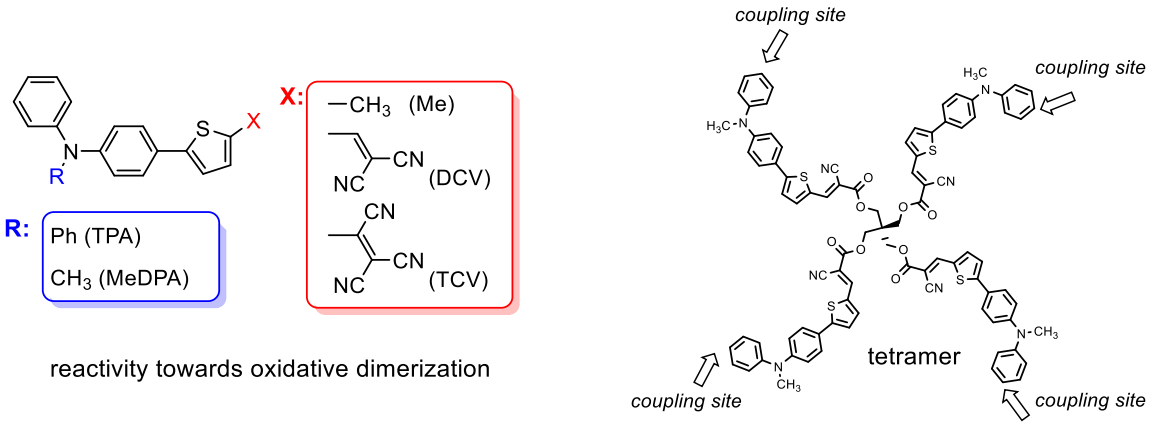

Figure 4.1: Structure of TPA and MeDPA based chromophores and multimer analyzed in chapter 4.1.

The second example includes a class of conjugated oligomers endowed with inherently chiral 2,2'-biindole architectures with two oligothiophene terminals acting as partially interactive redox sites. The molecule electroactivity is analyzed and variations resulting from

different π-spacers or by introduction of an acceptor unit are defined both for the monomer as well as for electrodeposited thin films. Electrochromic switching performance of the so obtained film is tested and paves the way to their employment in a chiral environment as chiral electrochromic films.[3] This second study is done in collaboration with the group of Prof. T. Benincori (University of Como) responsible for the molecules synthesis and of the group of Prof. P. Mussini (University of Milan), who carried out characterization of the chiral properties of the molecules.

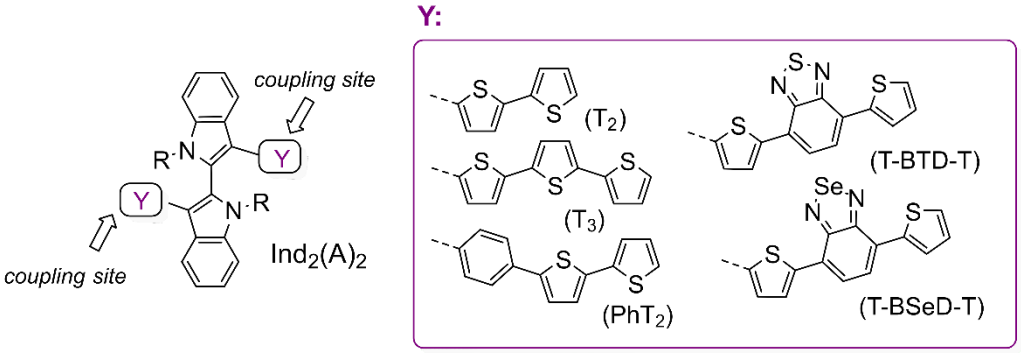

electrochemical oxidation of multimers to obtain redox active thin films

Figure 4.2: Structure of atropoisomeric oligomers endowed with two coupling sites analyzed in chapter 4.2.

4.1 Oxidative Dimerization Study of Arylamine-based Linear Push-Pull Chromophores and Crosslinking of a Tetramer for Optoelectronic Applications.

4.1.1 Introduction and Objectives

Triphenylamine (TPA) and more generally arylamine derivatives, constitute outstanding building blocks for the preparation of electroactive materials for opto-electronic applications.[2,4,5] In particular, D-π-A push-pull molecules, in which the electron-donating group (D) derived from an arylamine is connected to an electron-withdrawing group (A) through a π-conjugated spacer, have been extensively investigated as efficient donor materials for organic photovoltaics (OPV)[6–9] Due to its electron-rich nature, TPA or aryl derivatives have been selected as promising electron-donating blocks (D) in D–π–A push–pull molecules where they are connected via a π -spacer to various electron-withdrawing blocks (A); and have been widely developed as electron-donor materials especially for OPV. Linear TPA-based DA push–pull molecules, characterized by simple and cost-effective synthesis, have led to solution or vacuum-processed single junction OSCs showing power conversion efficiencies as high as 8%.[2]

While the redox behavior of simple arylamines upon oxidation is known and well-characterized, their functionalization by π-conjugated blocks, such as in the case of D-π-A

push-pull molecules, results in an enhanced charge delocalization of the charged species that can result in a different electrochemical behavior. It was already observed in the literature that the elongation of the π-system and substitution of reactive para terminals leads to a stabilization of the radical cation state in comparison to unsubstituted triarylamines.[10] Furthermore, the presence of a dipole moment within the molecule makes the latter very susceptible to solvation effects. Different examples of reactivity modification and solvation effects on the cyclic voltammetry of different molecules can be identified. In particular, the choice of the solvents can dramatically modify electrochemical reactivity of charged species, for example, in the case of aprotic solvents the different dielectric constant of the medium is associated with different extents of stabilization of the charged state including reactivity,[11] π-dimers formation and signal multiplicity for equivalent interacting redox sites.[12]

In this study, the oxidative behavior of a series of arylamine-based D-π-A push-pull molecules (**1**-**6**) (Figure 4.3), which represent promising systems for OSCs applications,[2,6,13] is presented.

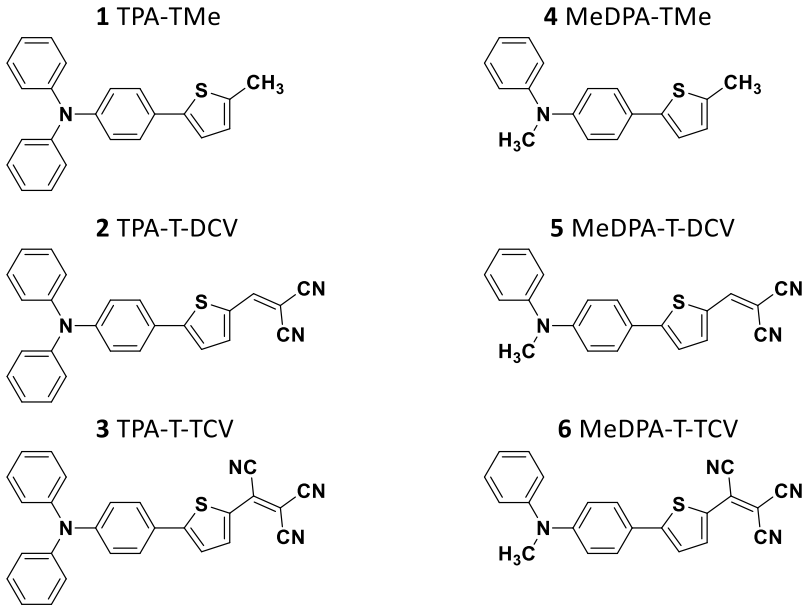

Figure 4.3: List of analyzed molecules based on triphenylamine (TPA) and methyl-diphenylamine (MeDPA).

The electrochemical effects upon structural modification of a parenting D-π-A molecule having an arylamine molecule as donor, a thienyl unit as π-spacer and an acceptor unit are analyzed, the list of molecules analyzed is given in Figure 4.3. The following structure-property relationships are analyzed with regards to radical-cation reactivity:

- the substitution of triphenylamine (TPA) (molecules **1**-**3**) with a methyl diphenylamine (MeDPA) (molecules **4**-**6**) donor unit,

- the nature and electron withdrawing character of the acceptor unit.

Compounds **1** (TPA-TMe) and **4** (MeDPA-TMe) are synthetized to analyze the effect of introduction of an acceptor unit. In all cases a thienyl unit is used as π-linker. The strength of the acceptor unit is increased in the order dicyanovinyl (DCV) (chromophores **2** and **5**) and tricyanovinyl (TCV) (chromophores **3** and **6**) respectively.

The aim of this study is to provide understanding of the dimerization ability of arylamine-based systems, in particular, of linear D-π-A push-pull systems. The analysis of their reactivity and the dependency of the later on molecular structure, is interesting both under a fundamental point of view and considering the ubiquitous employment of this class of D-π-A push-pull systems in OPV.[6] This should provide a detailed knowledge of the electrochemical behavior as well as for targeting the synthesis of new stable compounds. Secondly, it is aimed to identify suitable dimerizing units on the basis of emerging approaches employing crosslinking of two arylamine or carbazole units in multimer-systems to prepare functional films for electro-optic application.[14,15] The electrochemical oxidation leading to the dimerization of electroactive units in multimeric systems results in the generation of insoluble electroactive deposits endowed with a reversible electrochemical behavior and increased chemical stability. The dimerization study and identification of arylamine-based push-pull molecules capable of dimerizing is therefore interesting to electrochemically crosslink redox active films with reduced band-gap, which could find use in different applications as active electro-optic layers as described by recent literature works.[14–17] In particular, multimer systems based on push-pull moieties including arylamine or carbazole donor units have raised particular attention in electrochromic devices thanks to the possibility of extending the palette of colors achievable and to their intrinsically strong absorption. [18–23] The donor units play in this context a very important role as normally these materials are analyzed in oxidation and the HOMO is localized on the donor-unit ends, for example the D-π-A units and allow for the synthesis of highly controlled material systems.[24]

To study structure-properties relationships in relation to the electrochemical behavior of arylamine-based chromophore molecules, electrochemical methods, *in-situ* UV-Vis spectroelectrochemical experiments together with DFT and TD-DFT calculations are performed. The latter were performed by S. Gámez and C. Ruiz Delgado (University of Malaga). Synthesis of the chromophores **2** and **5**, was performed in the group of Philippe Blanchard (MOLTECH Angers, University of Angers). The remaining molecules were synthetized by Dr. D. Gepperth (Chair of Structure and Properties of Polymeric Materials, University of Stuttgart). Details about the chromophores' synthesis can be found in ref. [25].

4.1.2 Characterization of Linear D-π-A Push-Pull Compounds

4.1.2.1 Electrochemical Characterization by Cyclic Voltammetry (CV) & Differential Pulse Voltammetry (DPV).

To study the oxidative behavior of chromophores **1**-**6**, cyclic voltammetry was performed on Au electrodes in 0.1 M CH_2Cl_2/NBu_4PF_6. Dichloromethane was chosen as electrolyte as it allows for enhanced solubility in comparison to other organic solvents. CV measurements at a scan-rate of 50 $mV \cdot s^{-1}$ are reported in Figure 4.4 including the respective half-wave potentials measured from CV data. From a first analysis of the cyclic voltammograms, a similar voltametric pattern corresponding to a chemically reversible single oxidation wave is found for compounds **1** (TPA-TMe); **2** (TPA-T-DCV); **3** (TPA-T-TCV) and **4** (MeDPA-TMe), which can be associated to the one electron oxidation of TPA donor to its radical cation state.[26–29] In the case of chromophores **5** (MeDPA-T-TCV) and **6** (MeDPA-T-TCV) a chemically irreversible oxidation signal is observed, this is due to the formation of reactive radical cations undergoing a follow up process which can be identified with the dimerization at the *para* position of the phenyl ring generating covalent biphenyl bonds.[27–29] The so formed benzidine can then be reversibly oxidized to its radical cation and dication state in two distinct oxidation steps, resulting in two reversible peaks observed for the backward scan and subsequent oxidation cycles.[26] Evidence of the dimerization process is found also by spectroelectrochemical characterization, aid by comparison to TD-DFT calculation, as well as to analysis of the products obtained upon chemical oxidation.

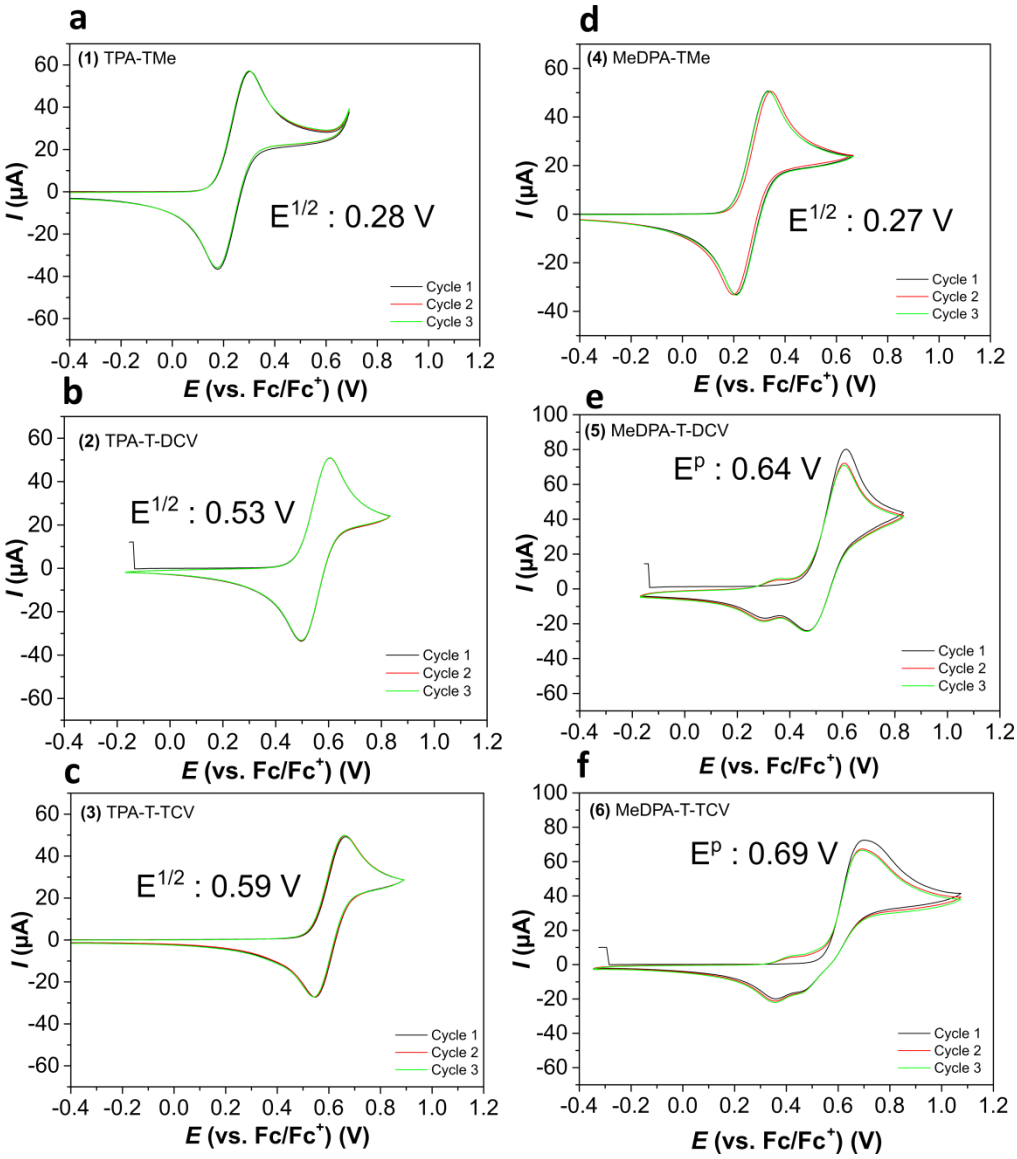

*Figure 4.4: CV measurements for 0.5 mM solution of compounds **1-6** in 0.1 M CH_2Cl_2/NBu_4PF_6; scan-rate 50 mVs^{-1}; Au electrode.*

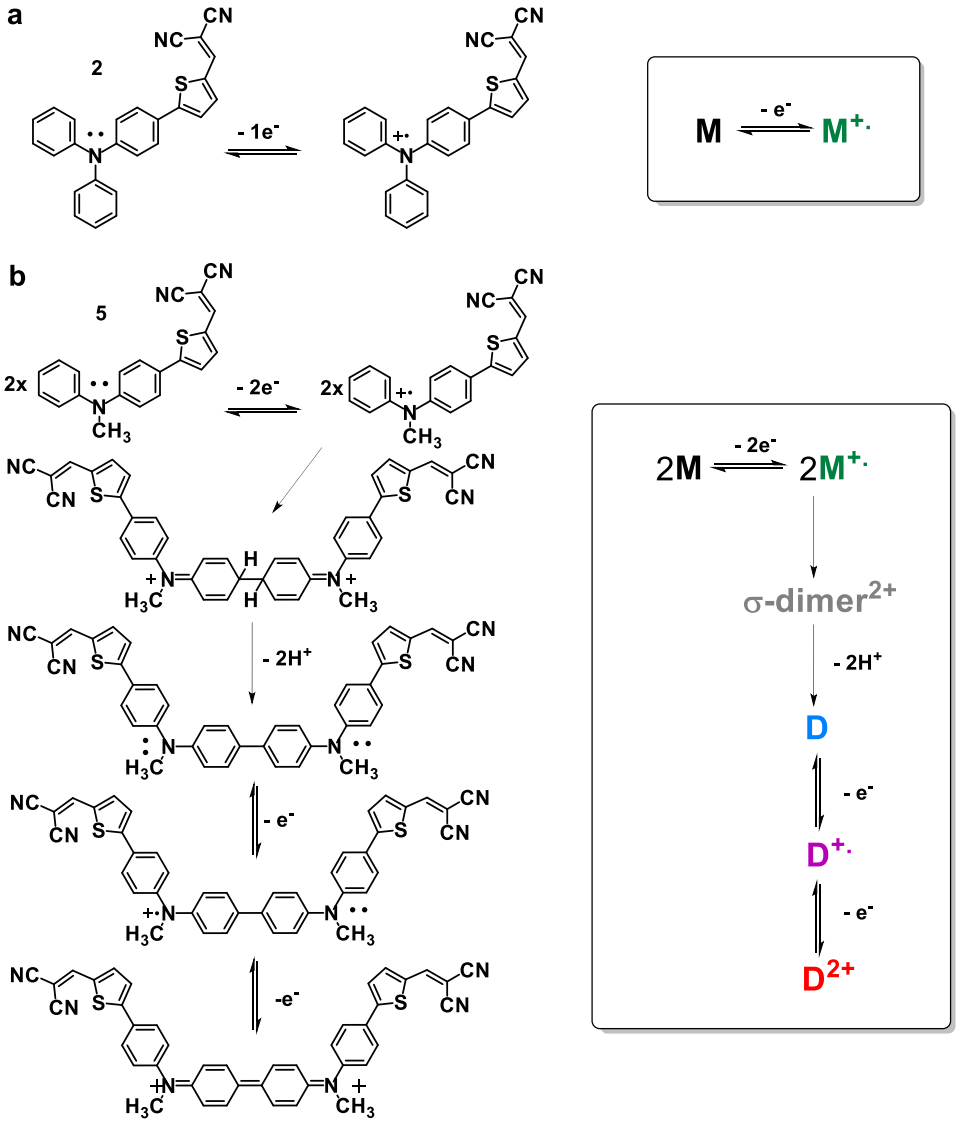

*Figure 4.5: Exemplification of reaction mechanism for chromophores **2** (a) and **5** (b). M: monomer, D: dimer.*

The reaction mechanism upon electrochemical oxidation of triphenylamine leading to generation of electroactive follow-up products, identified as dimers of the starting compounds was reported in paragraph 1.3.1 and is recalled in Figure 4.5 for the specific cases of chromophores **2** and **5**, respectively. Considering the measured $E_{p,ox}$ (chromophores **1**-**6**) and calculated $E_{1/2}$ (chromophores **1**, **2**, **3** and **4**) it is observed that the substitution of a phenyl unit in the triarylamine with a methyl unit results in a small variation of the oxidation potential between couple of molecules characterized by the same acceptor unit. For example, considering the reversible oxidations of compounds 1 and 4, the $E_{1/2}$ lies at very similar values: +0.28 V and +0.27 V, respectively. Note that half wave potentials values obtained from DPV measurements are reported in Table 4.1. The replacement of a Ph with a Me unit in the arylamine-based push-pull molecules affects the reactivity of the compounds, with Me substituted molecules being more reactive. The introduction of an

acceptor unit results in a shift towards more positive oxidation potentials; with the highest oxidation potentials found for TCV containing chromophores, followed by DCV substituted ones.

Peak-separations (E_p-$E_{p/2}$) of the chemically reversible signals for compounds **1**-**4** were also determined. A difference E_p-$E_{p/2}$ of ~57 mV at RT for 50 $mV \cdot s^{-1}$ was found, this value is characteristic for a monoelectronic peak and indicates the oxidation to the radical cation state of the molecules. In the case of the electrochemical signal for the follow-up reaction the difference E_p-$E_{p/2}$ is of 25 mV, smaller than for the one electron oxidation, this result might be explained by the fact that the signal is not completely independent from the one of the main chromophores which lays at closer potentials (no base line separated monoelectronic signals).

To better differentiate between signals of the electroactive species generated, differential-pulse voltammetry (DPV) was employed considering its enhanced sensibility in comparison to linear sweep voltammetry. Pulsed techniques combine indeed higher sensitivity (10^{-7} M) obtained in terms of both potential and current, and better resolution of overlapping redox signals, for example in the case of presence of multiple electroactive species with similar oxidation potentials. Upon these considerations, pulsed techniques have been employed in the field of electroanalysis and for studying homogeneous reaction mechanisms. In the case of a reversible electrochemical system, the peak potential and the formal standard potential are correlated by the equation $E_p = E_a^{\ominus\prime} + \frac{\Delta E_{pulse}}{2}$ where $E_a^{\ominus\prime}$ stands for the formal potential for the oxidation species, ΔE_{pulse} for the pulse potential (or modulation amplitude). In the case of a reduction, this term is preceded by a negative sign.[30,31] Formal potentials for the different redox couples were also determined by DPV measurements, and the data are reported in Figure 4.6. The values well correlate with the ones obtained from CV measurements, with exception for chemically irreversible peaks for which only the forward oxidation peak of the CV measurements was taken into consideration. DPV measurements allow to better analyze the reversibility of the oxidation processes. In addition to compounds **5** and **6** the formation of an electroactive follow-up product is upon DPV characterization also detected for compound **3**. Table 4.1 resumes all half-wave potentials measured through DPV for the $1e^-$ oxidation of the chromophores at their radical cation level ($M/M^{+\bullet}$) and, in the case of irreversible oxidation, also of the two folded $1e^-$ step of the dimers: ($D/D^{+\bullet}$) and ($D^{+\bullet}/D^{2+}$). In the case of compound **6**, three separated peaks are observed from DPV measurements, and are interpreted as the signals of the monomer and the two folded dimer oxidations, respectively. In the case of compounds **3** and **5** on the other hand only two peaks are observed (Figure 4.6 (c, e)).

Upon analysis of the backward scan of oxidation of compounds **3**, **5** and **6**, different relative intensities of the δI peaks are encountered. In the backward scan the electroactive follow-up products (dimers) are detected, considering that the dimers are characterized by similar structures and consequently by comparable diffusion coefficients[31] the fact that different relative intensities are obtained from the DPV measurements hint to a different reactivity of the compounds. With this consideration compound **6** is characterized by the highest relative intensity and therefore concentration of the $D/D^{+\bullet}$ peak. The lower intensity registered for the dimers during the backward scan of compounds **3** and **5** could also result in the lower multiplicity of the DPV signal (two peaks) in comparison to compound **6** (three peaks) as the $E^{II,ox}_{1/2}$ for the dication state of the dimers lies in fact very close to the $E^{I,ox}$ of the starting chromophores and due to the low intensity of the first the associated signal might be overimposed to each other.[32] In order to verify this hypothesis and to compare the reactivity of the different chromophores, DPV measurements were repeated after electrolyzing the solutions for different times and therefore increasing the concentration of the dimers in the surrounding of the electrode.

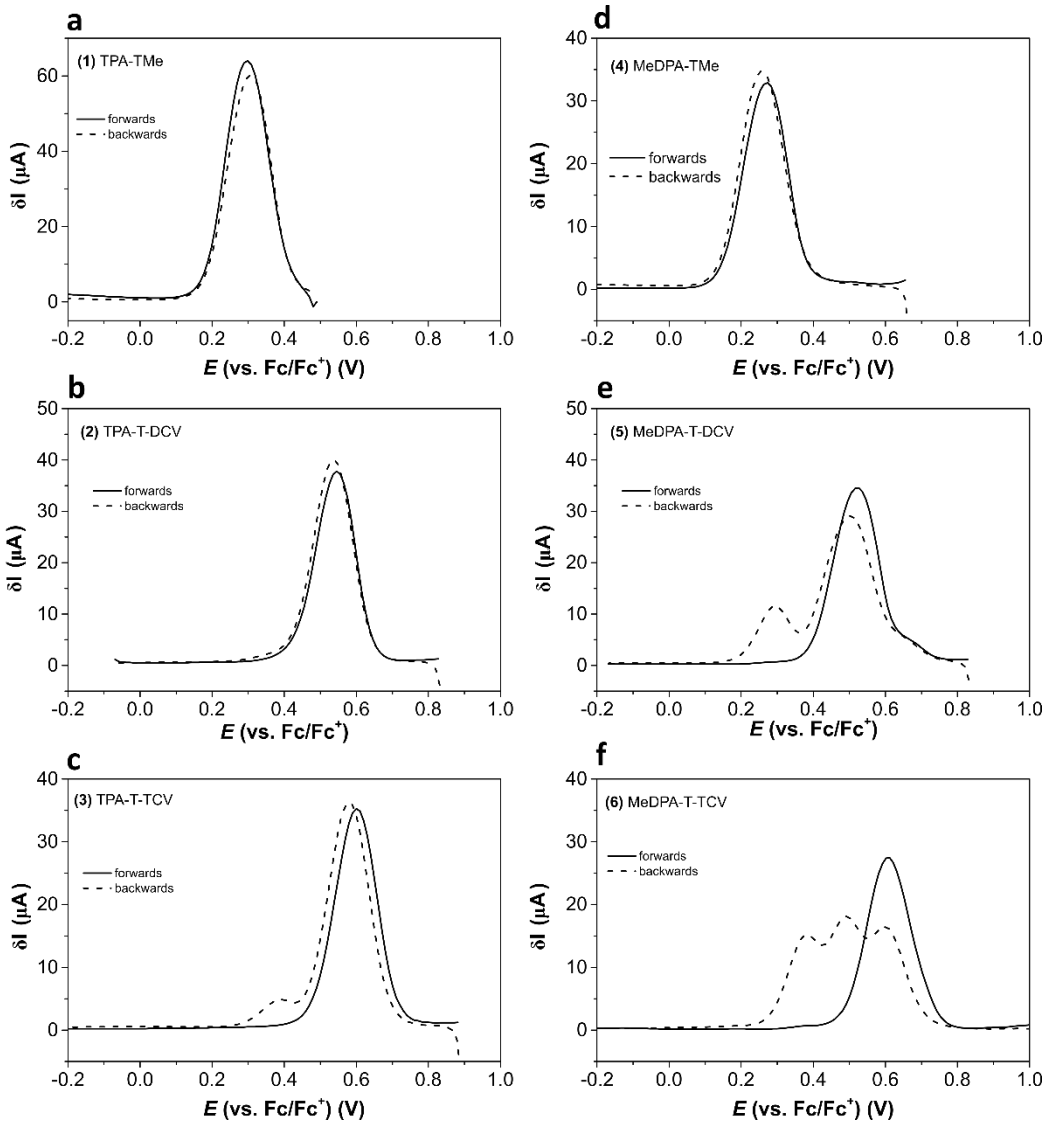

*Figure 4.6: Differential pulse voltammetry of compounds **1**-**6** in 0.1 M CH_2Cl_2/NBu_4PF_6; scan-rate 20 mVs^{-1}; Au electrode. Modulation amplitude employed is 25 mV.*

Chromophore	$E^{M/M+\bullet}_{1/2}$ vs Fc/Fc$^+$ (V)	$E^{D/D+\bullet}_{1/2}$ vs Fc/Fc$^+$ (V)	$E^{D+\bullet/D2+}_{1/2}$ vs Fc/Fc$^+$ (V)
1	0.30 V	-	-
2	0.54 V	-	-
3	0.58 V	0.39V	0.58V (overlapped)
4	0.27 V	-	-
5	0.53 V	0.32	0.53 (overlapped)
6	0.60 V	0.38	0.49

Table 4.1: $E_{1/2}$ determined from DPV measurements for starting chromophores (M) and dimerized systems (D).

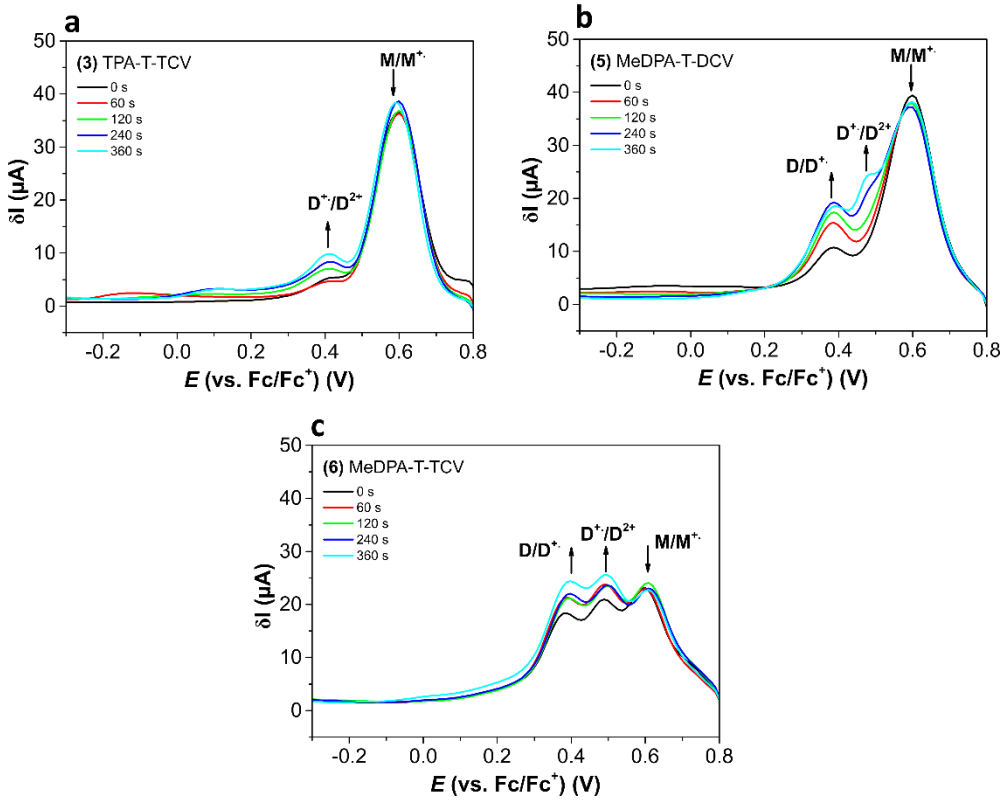

*Figure 4.7: DPV for backward oxidation scan for chromophores **3**, **5** and **6**. The DPV measurements are performed after potentiostatically charging the electrode at 0.8 V for increasing times: 60 s; 120 s; 240 s and 360 s.*

To analyze the reactivity of the different compounds an electrolysis was performed with different reaction times, 0 s, 60 s, 120 s, 240 s and 360 s. The DPV signal registered for the backward scan is analyzed directly after each electrolysis, the results are reported in Figure 4.7. As expected, the peak intensity is observed to increase with increasing the electrolysis time, as the local concentration of the dimeric species increases. In the case of compound **3** TPA-T-TCV the increase of the electrolysis time results in the only increase of the peak at 0.39 V, whereas for compound **5**, longer electrolysis times allow the observation, in addition to the two peaks at +0.32 V ($D/D^{+\bullet}$); and +0.6 V ($M/M^{+\bullet}$) also of a third peak at +0.51 V ($D^{+\bullet}/D^{2+}$). The signal for ($D^{+\bullet}/D^{2+}$) oxidation lies at potential values very close to the chromophore oxidation, therefore only for higher dimer concentrations this peak can be distinguished. In the case of compound **6**, the reaction seems to proceed to a higher extent (hinting towards the higher reactivity of the compounds) also without electrolysis. By applying longer electrolysis times, the peaks associated to the dimer charging +0.38 V and +0.49 V increase, and their intensity becomes higher than the one for the monomer oxidation +0.60 V. These results suggest increasing reactivity towards radical-radical coupling in the order: **6** MeDPA-T-TCV > **5** MeDPA-T-DCV > **3** TPA-T-TCV.

Based on the literature, the oxidation of triarylamine based molecules leads to the formation of stable dimerization products with formation of a new benzidine bond. To prove

that oxidation of an arylamine unit on a chromophore leads to same type of reactivity we performed chemical oxidation trying to mimic the conditions used during the electrochemical experiment, using $FeCl_3$ in $CHCl_3$. Chemical oxidation and characterization were performed at MOLTECH, Angers. The reaction product was separated and analyzed by mass spectroscopy. Unfortunately, due to insolubility of the oxidation product, it was not possible to register satisfying NMR spectra to analyze the nature of the compound.

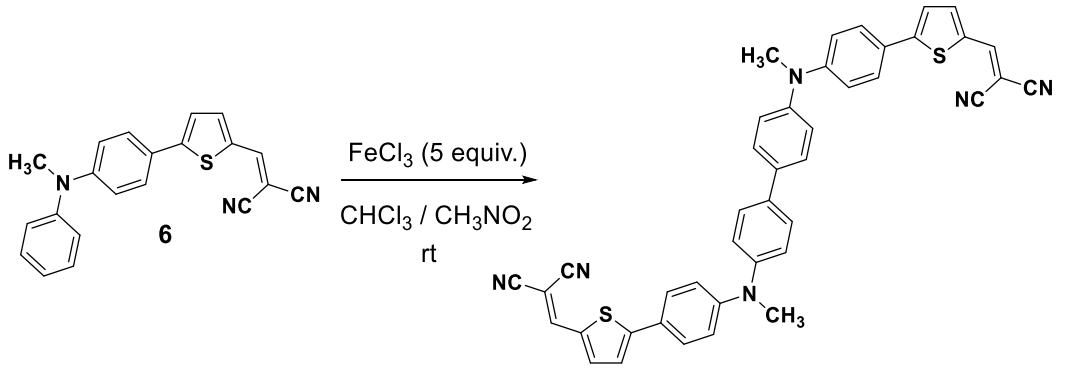

*Figure 4.8: Chemical oxidation of monomer **5.***

The experiment was performed by adding to a solution of monomer **5** (9.2 mg, 0.027 mmol) in a mixture of $CHCl_3$ (2 mL) and nitromethane (0.5 mL), anhydrous $FeCl_3$ (5 equiv.) was added in one portion. After 3 h of stirring at rt, the mixture was diluted with 75 mL of dichloromethane and the mixture was washed with water (3 x 20 mL). After separation, the organic phase was dried over $MgSO_4$ and concentrated. It was possible to separate the small quantity of starting material by column chromatography on silica gel (eluent: CH_2Cl_2). Then, elution with a large quantity of CH_2Cl_2 and with increasing amount of EtOAc up to 3% allowed us to collect **dimer-5** (7 mg) as dark powder. The maxima of absorbance for the dimer are in line with spectroelectrochemical results. Considering the reactivity upon oxidation of TPA and MeDPA reported in the literature and the fact that also in the case of chromophore **5** the oxidation product is a dimer at the arylamine position, we expect an associated behavior for all the chromophores studied. MALDI-TOF (Figure 4.10) measurements performed on the chemical oxidation product well match the molecular weight of the dimer: 680.18 $g \cdot mol^{-1}$.

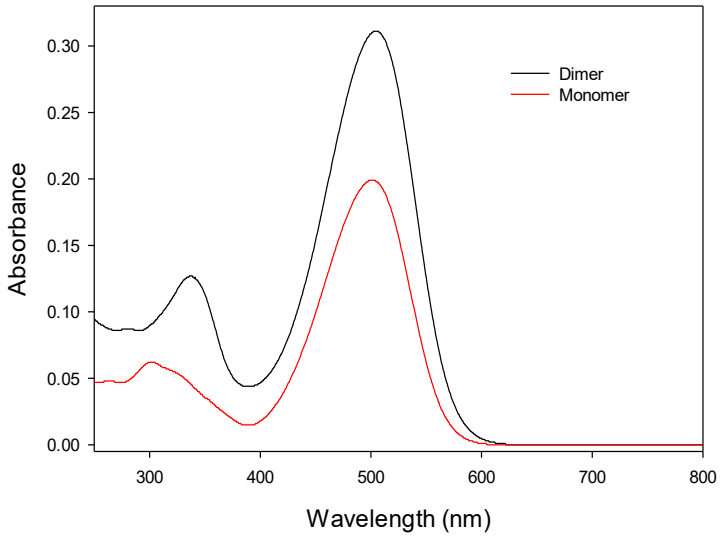

*Figure 4.9: UV-vis spectrum of dimer of **5** (black line) and monomer **5** (red line) in CH_2Cl_2 (in the presence of small amount of 1,1,2,2-tetrachloroethane). Dimer: λ_{max} = 337 nm, 505 nm. Monomer: λ_{max} = 302 nm, 501 nm. (Measurements performed in MOLTECH, Angers).*

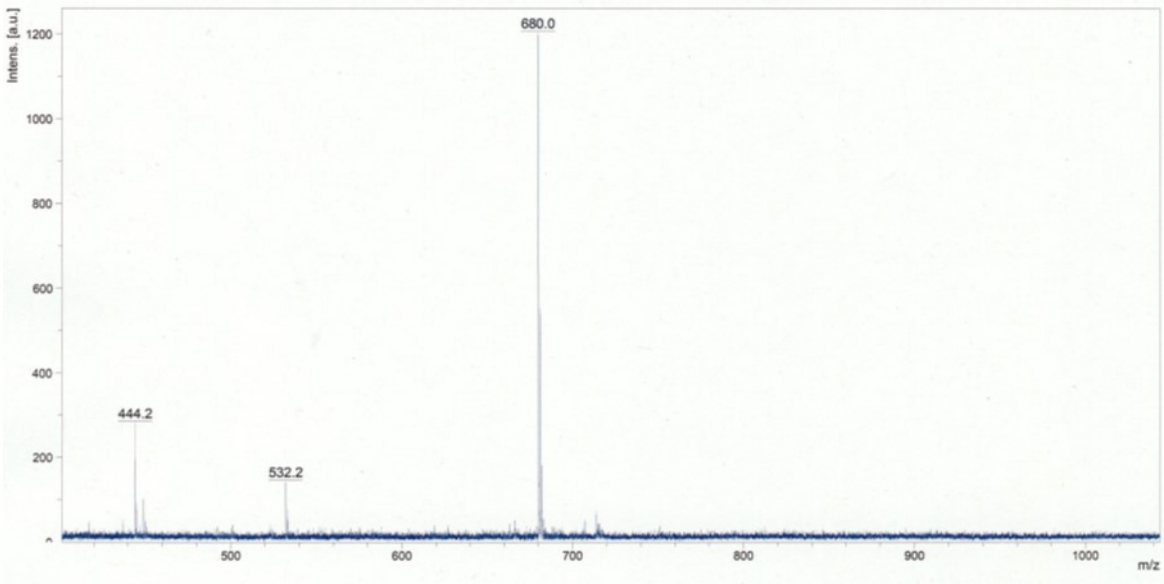

*Figure 4.10: MALDI-TOF mass spectrum of dimer of chromophore **5** obtained by chemical oxidation. (Measurements performed in MOLTECH, Angers). Primary m/z registered from MALDI-TOF corresponding to dimer mass, $C_{42}H_{28}N_6S_2$: 680.18 g·mol^{-1}.*

4.1.2.2 *In-situ UV-Vis Spectroelectrochemistry and Investigation on Charged Species*

In-situ spectroelectrochemical experiments were performed to clarify the nature of the species generated upon oxidation. The absorption profiles of chromophore molecules as a function of the oxidation potential are analysed and correlated the shape of the CV waves with the nature of the species involved in the oxidation process.[30] To follow the variation of the relative abundances of the chemical species involved in the electrochemical oxidation, the progression of the absorbance as function of the potential is monitored. A detailed analysis of the spectroelectrochemical behavior of modified arylamine redox-units bringing different substituents, provides also interesting information for the development of electrochromic applications, due to the ubiquitous employment in this field of arylamine redox-active units.[5,20,33,34] The experimental results are compared with calculated TD-DFT vertical transition energies for a clear assignment of the species.

(1) TPA-T-Me

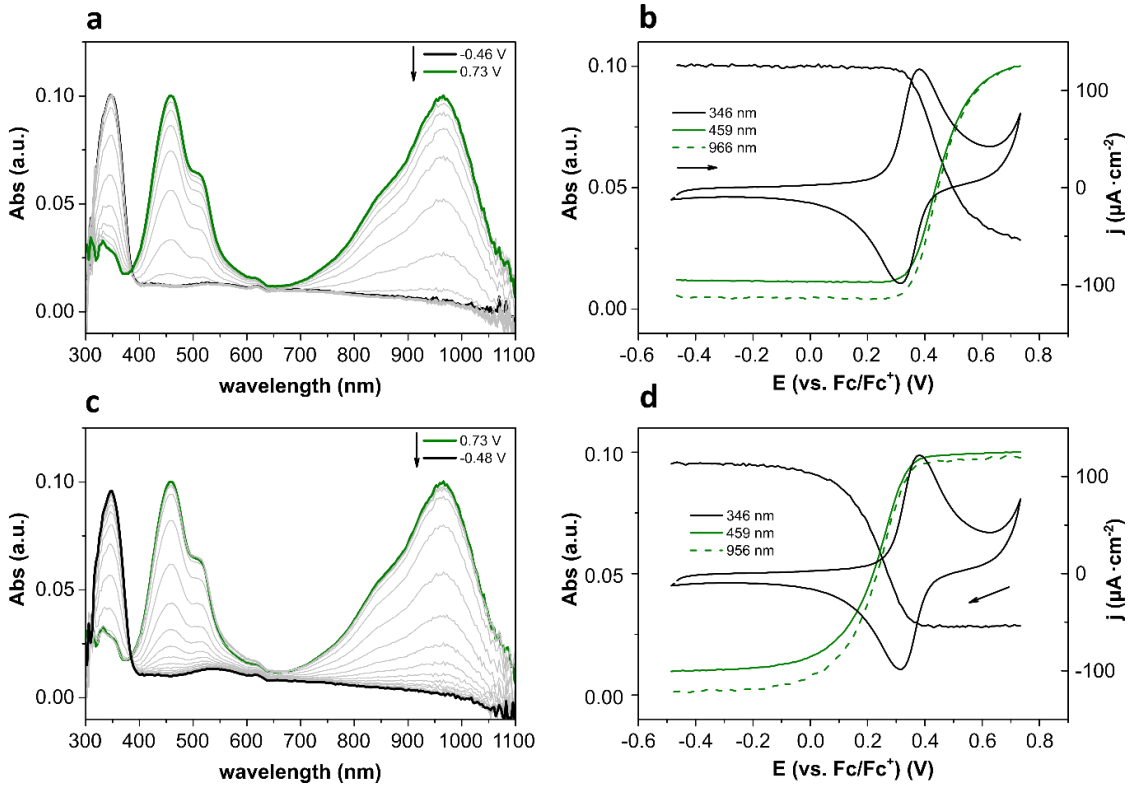

*Figure 4.11: In-situ UV-Vis spectroelectrochemistry of compound **1 (TPA-T-Me)** (black, neutral state; green: radical cation). (a) UV-Vis absorption spectra for 1st forward cycle; (b) peak-trend for 1st forward cycle, (c) UV-Vis absorption spectra for 1st backward cycle; d) peak-trend for 1st backward cycle.*

In-situ spectroelectrochemistry of **1** is reported in Figure 4.11. The neutral state (black line) of compound **1** registered for the first forward oxidation cycle (Figure 4.11 (a)) shows an

absorption maximum at 346 nm (black line; -0.46 V). The molecule oxidation starting from +0.25 V vs Fc/Fc^{+} leads to the bleaching of this band with concomitant formation of two new bands at 459 nm and 966 nm; both bands are characterized with a pronounced vibronic structure. One isosbestic point is found at 382 nm, for the two species in equilibrium $M/M^{+\bullet}$. The presence of only one species resulting from the oxidation of compound **1** is also clear by analysing the absorption variation as a function of the potential (Figure 4.11 (b)) at the main λ_{max} : 346 nm (black line) and 459; 966 nm (radical cation, green). The absorption variations during the forward oxidation scan start concomitantly at +0.25 V with a monotone variation (neutral band increasing and radical cation band decreasing). No evidence for the formation of other species was found. Upon multiple cycles compound **1** presents a reversible spectroelectrochemical behavior and no variations from the pristine solution are found upon subsequent cycling. Further, the experimental evolution of the absorption spectra of compound **1** upon oxidation is well captured by the calculated electronic transitions when going from neutral and radical cation state (Figure 4.12). The time-dependent density functional theory (TD-DFT) predicts for the radical cation state similar absorption pattern as the one experimentally observed with a good correlation also for the absorption maxima (Table 4.3), supporting the assignment done.

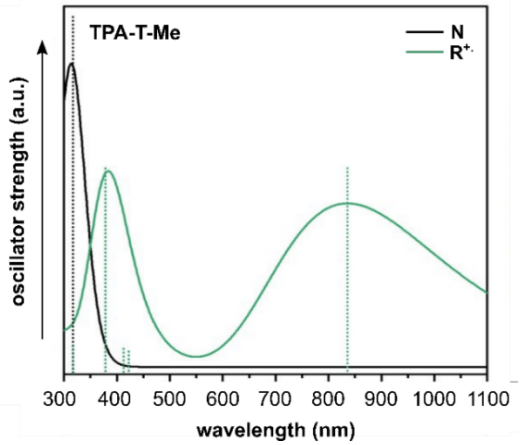

1	Exp.	Calc.
λmax N (nm)	346	312
λmax $R^{+\bullet}$(nm)	459; 966	384, 834

*Figure 4.12: M06-2X/ 6-31G** in CH_2Cl_2 TD-DFT calculated vertical transition energies for **1 (TPA-T-Me)** in different states of oxidation.*

(2) TPA-T-DCV

In-situ spectroelectrochemistry and peak-trend of chromophore 2 is presented in Figure 4.13. Overall, it is found that the spectroelectrochemical behavior is comparable to the one of compound **1** with a few differences: in the neutral state two absorption bands are observed: at 350 nm and 500 nm (Figure 4.13 (a), black line). The introduction of an acceptor unit is associated with presence of an internal charge transfer transition (ICT) (500 nm). Analysing the variation of the UV-Vis absorption pattern for the molecule forwards oxidation CV cycle, (Figure 4.13 (a)) it is observed that a polarization of the WE potential

until +0.80 V vs Fc/Fc^+ leads to the bleaching of the neutral absorption band with concomitant formation of new bands around 378, 614 and 1000 nm, endowed with a pronounced vibronic structure.

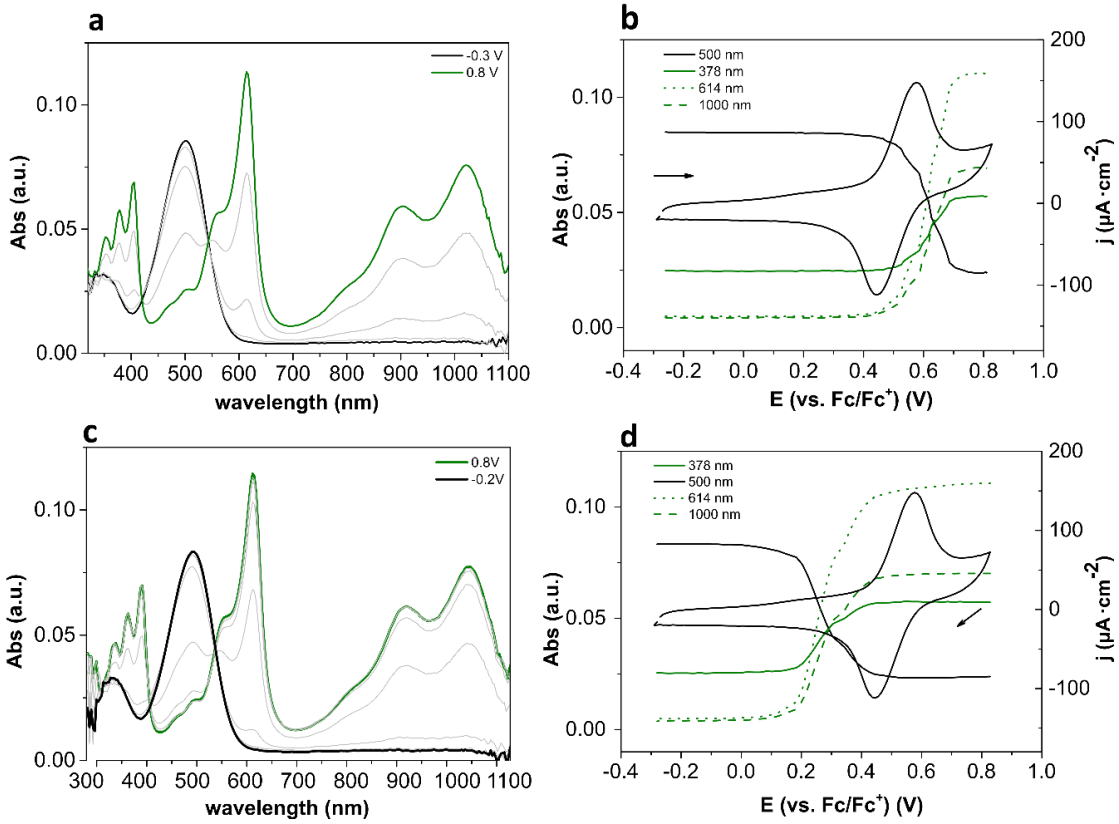

*Figure 4.13: In-situ UV-Vis spectroelectrochemistry of compound **2** **(TPA-T-DCV)**. (a) UV-Vis absorption spectra for 1st forward cycle; (b) peak-trend for 1st forward cycle, (c) UV-Vis absorption spectra for 1st backward cycle; (d) peak-trend for 1st backward cycle.*

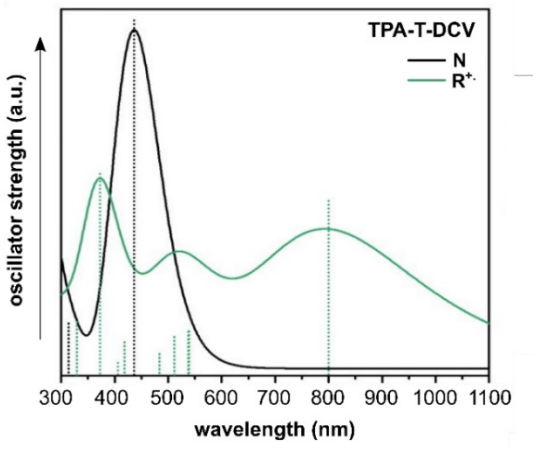

2	Exp.	Calc.
λmax N (nm)	351, 500	436
λmax $R^{+\bullet}$(nm)	384, 834	375, 520, 792

*Figure 4.14: M06-2X/ 6-31G** in CH_2Cl_2 TD-DFT calculated vertical transition energies for **2** in different states of oxidation.*

Also, the presence of isosbestic points at 420 and 540 nm indicate that two species are in equilibrium in solution, which is consistent with the gradual conversion of the neutral species

into the radical cation. The potential dependent peak-trend shows no presence of absorbing intermediates. As for compound **1**, the calculated electronic transitions when going from neutral and radical cation state, support the assignment of the charged states both in multiplicity of the bands and their position. (Figure 4.14).

(3) TPA-T-TCV

The UV-Vis spectroelectrochemical signature and potential dependent peak-trend of chromophore **3** is shown in Figure 4.15. The first forward cycle (a, b) and a forward oxidation cycle after polarization at oxidative potentials to concentrate the dimeric species (c, d) are reported. DPV and CV measurements evidenced for this molecule a chemical follow-up process upon oxidation, giving rise to chromophore **3** dimers. *In-situ* UV-Vis spectroelectrochemistry is a very useful diagnostic tool to evidence formation of UV active follow-up products, such as dimers and their charged states.

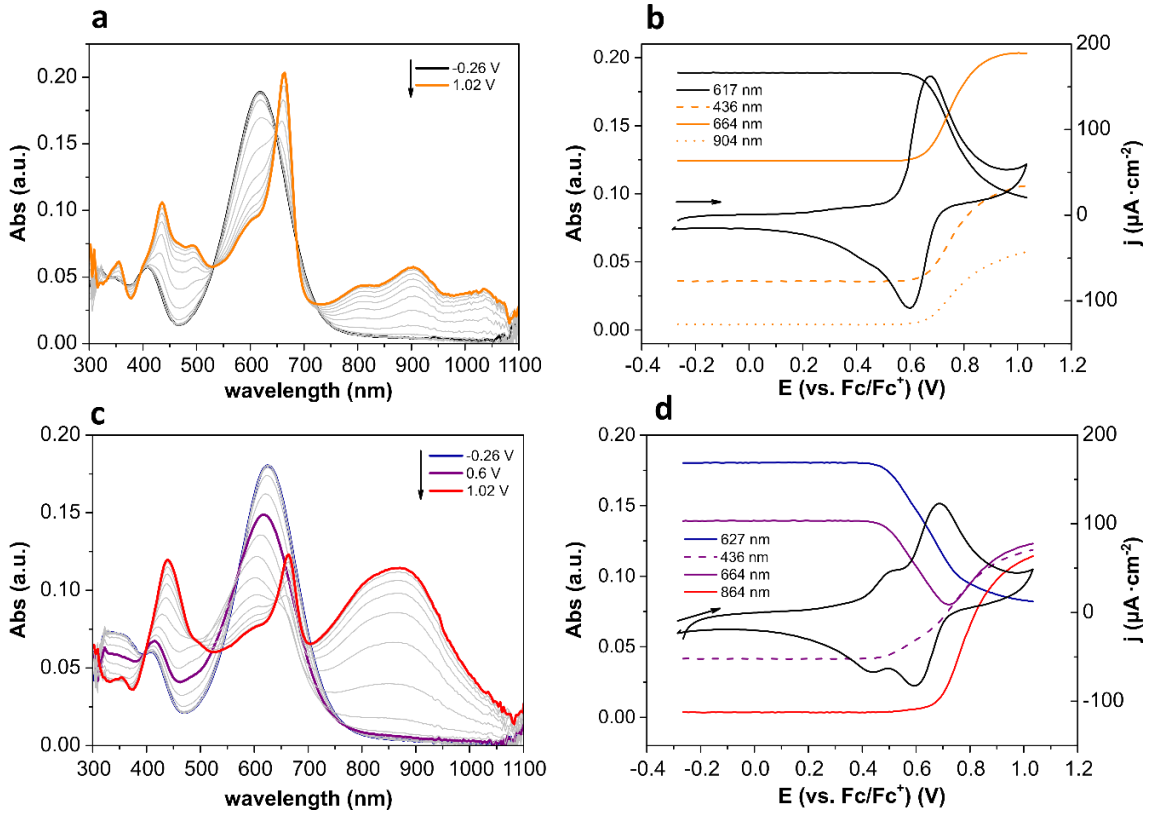

*Figure 4.15: In-situ UV-Vis spectroelectrochemistry spectroelectrochemistry of compound **3 (TPA-T-TCV)**. UV-Vis absorption spectra and peak-trend for 1st forward oxidation cycle (a) and (b) respectively. After potentiostatic oxidation at +1 V for 60 s, forward oxidation cycle (c) and (d).*

In the neutral state, chromophore **3** is characterized by two main maxima of absorption, 418 nm (π-π* transition) and 617 nm (ICT transition) (black line, Figure 4.15 (a)). During the first forward cycle, in correspondence with the CV onset (+0.57 V), the neutral band bleaches with concurrent formation of a spectral-band with maxima 435 and 490 nm, and a broad band located in the range of 750-1100 nm. A pronounced vibronic

structure in the NIR is found. This absorption pattern is not reversibly observed in the reverse scan and in the following oxidation cycles, showing a different absorption signature in the potential window analysed. As the presence of radical cations of chromophore **3** results in follow-up dimerization, the absorption signature at +1.02 V (orange curve) can be attributed to a mixture of chromophore **3** radical cation and dimer **3** in the dication state. After the first oxidation cycle, the CV cycle presents significant changes to the first cycle, such as a peak with $E_{1/2}$ of 0.47 V in addition to the one already observed for the monomer oxidation at $E_{1/2}$ of +0.63 V. The neutral state in a following cycle, performed after pre-polarizing the molecule at +1 V, (blue curve, Figure 4.15 (c)) presents a red shift of 6 nm to the neutral state of the first forward cycle. This (small) variation is the result of the increase in the conjugation length passing from monomer to dimer. Similar change (in terms of direction and entity) is also observed in the case of the other dimerizing chromophores **5** (502 nm → 509 nm) and **6** (620 nm → 627 nm). Furthermore, the neutral state after oxidation presents a different signature with absorption also in the wavelength range of 300 – 400 nm.

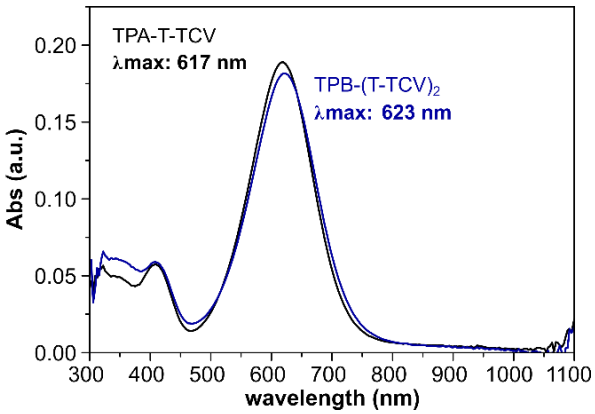

*Figure 4.16: Absorption comparison for **3** (λ_{max} 617 nm) and **dimer-3** (λ_{max} 623 nm) registered at -0.23 V.*

Further oxidation cycles are characterized by a different absorption signature in comparison to the first cycle. In particular, the spectroelectrochemical variation upon oxidation can be distinguished into two main potential intervals of -0.26 - +0.71 V and +0.71V - +1.02 V, which correlate with the two redox events for the two folded oxidation of the dimer into the radical cation ($D/D^{+\bullet}$) and dication ($D^{+\bullet}/D^{2+}$) states, respectively. In concomitance with the oxidation onset of the first oxidation peak at +0.39 V the neutral band starts bleaching with development of bands in the lower wavelengths region of 300-500 nm.

The wavelength 664 nm was sampled for the potential dependent peak trend; the absorption at this wavelength reaches a minimum at +0.71 V, i.e., at the end of the first oxidation event when the neutral dimer is converted to dimer radical cation. For potentials higher than +0.71 V the second monoelectronic oxidation is taking place for dimer radical

cation/dimer dication. (Figure 4.15 d) By analyzing the UV-Vis signature at +1.02, a different UV-Vis signature is also observed in comparison to the first cycle of oxidation. The dimer dication is characterized by a broad absorption band located at 700-1000 nm (max 864 nm) with no absorption for observed for λ>1000 nm (red curve, Figure 4.15 c). Further, the vibronic structure that was characterizing the radical cation of **3** is not observed for the dimer-dication. The spectra registered at + 1.02 V (red curve, Figure 4.15 c) also presents the characteristics absorptions at 436 and 664 nm, which were previously encountered by oxidation of chromophore **3** monomer.

3	**Exp.**	**Calc.**
λmax N (nm)	418, 617	523
λmax $R^{+\bullet}$(nm)	436, 489, 664, 804, 904, 1027	405, 638
Dimer-3	**Exp.**	**Calc.**
λmax N (nm)	627	314, 533
λmax $R^{+\bullet}$(nm)	664	445, 1488
λmax D^{2+}(nm)	(438, 460), 864	394, 786

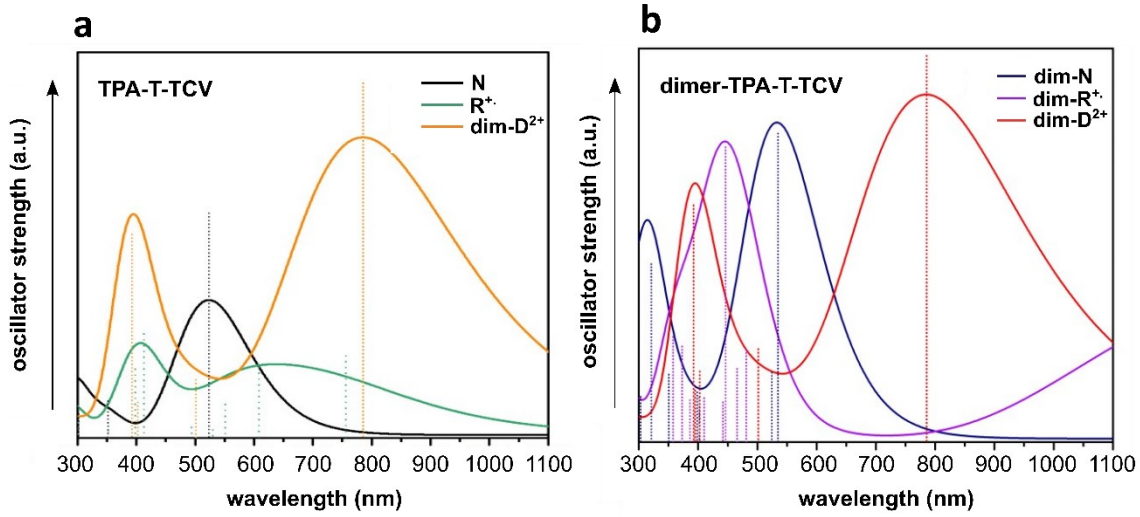

*Figure 4.17: M06-2X/ 6-31G** in CH_2Cl_2 TD-DFT calculated vertical transition energies for (a)* ***3 (TPA-T-TCV)*** *and (b)* ***dimer-3*** *in different redox states. Note that orange curve in (a) also corresponds to red curve in (b), representing the absorption pattern of the TPB-(T-TCV)$_2$ in the dication state.*

Despite measurements were performed in thin-layer conditions, partial diffusion of the chromophore, as well as an incomplete oxidation of chromophore **3** during the first cycle, might result in the presence of radical cation signature of chromophore **3**. Indeed, the absorption at 664 nm was systematically observed also for other chromophores in the radical cation state. This band remains present also after the first oxidation cycle, but its intensity decreases after more cycles are performed (appendix 1.7). A hint to the lower

reactivity of chromophore **3** in comparison to the other compounds is also evidenced by the progressive formation of dimerizing product also after the first oxidation cycle. This can be observed by analyzing variations of the absorption pattern between multiple cycles.[25]

A good correlation with the theoretical results was encountered (Figure 4.17). Namely, one band is predicted at 405 nm which can be good assigned to the one experimentally found at 436 nm. Another single broad band is found from calculations in the region between 500 to 1000 nm, whereas experimentally two bands are assigned to the radical cation state: 664 and 904 nm. It should also be reminded that in the first cycle, overimposition of the absorption of both radical cation of the monomer as well as dimer-dication might be observed. A good correlation is also found in the case of the different states of charge found for the dimers, supporting the interpretation. Indeed, for the neutral dimer two bands are predicted, which is also experimentally observed in the lower wavelength region. For dimer-radical cation however, the NIR band theoretically predicted is not observed, while the two bands predicted at 394 and 786 nm also found correspondence in the experimental spectra.

(4) MeDPA-T-Me

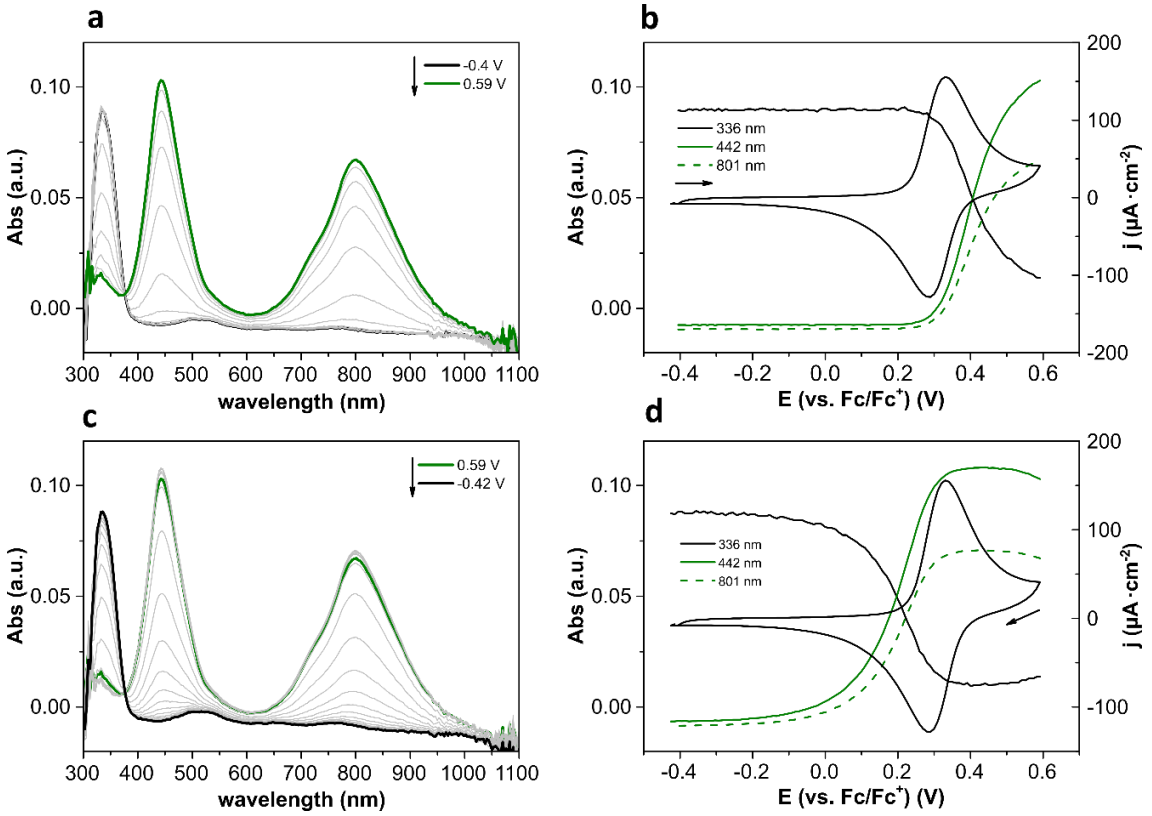

*Figure 4.18: In-situ UV-Vis spectroelectrochemistry of compound **4 (MeDPA-T-Me)**. (a) UV-Vis absorption spectra for 1st forward cycle; (b) peak-trend for 1st forward cycle, (c) UV-Vis absorption spectra for 1st backward cycle; d) peak-trend for 1st backward cycle.*

In-situ spectroelectrochemistry and peak-trend of chromophore **4** are comparable to the one of compound **1**. With only a partial shift at lower wavelengths for the characteristic absorptions of the $R^{+\bullet}$ state. The neutral state (black line, -0.4 V) is characterized by a maximum at 336 nm. The radical cation, generated at potentials more positive than + 0.28 V for the forward cycle, is characterized by absorption maxima at 442 and 801 nm. The stability of this redox species is confirmed by the monotone variation of all absorbances in the peak-trend and the absence of intermediates. In comparison to compound **4**, the radical cation bands are shifted to lower wavelengths and the vibronic structure is less pronounced. Good correlation between experimental and theoretical results are found with regard to band multiplicity and positions found (Figure 4.19).

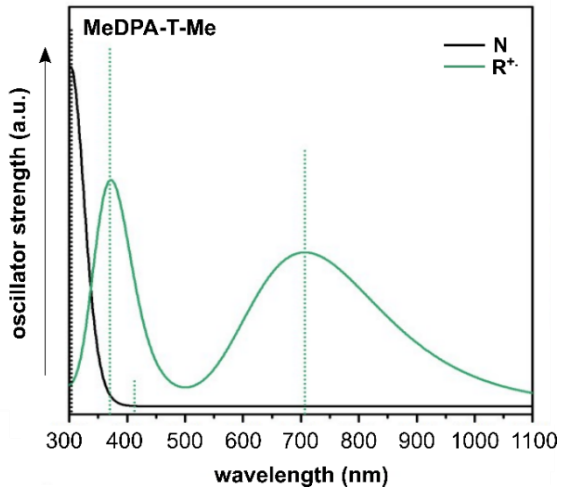

4	Exp.	Calc.
λmax N (nm)	336	302
λmax $R^{+\bullet}$(nm)	442; 801	372, 706

*Figure 4.19: M06-2X/ 6-31G** in CH_2Cl_2 TD-DFT calculated vertical transition energies for **4 (MeDPA-T-Me)** in different states of oxidation.*

(5) MeDPA-T-DCV

Figure 4.20 shows the potential dependent absorption spectra of chromophore **5** in solution. The black absorption spectrum recorded at -0.20 V corresponds to the absorption pattern of the neutral chromophore in solution. Two bands are observed, one at wavelengths below 350 nm and one with a maximum at 503 nm. The former one can be assigned to a π–π* electronic transition whereas the latter is due to an internal charge transfer (ICT).[35,36] This is in good accordance with DFT calculations that predict that the low energy band is associated with a HOMO-LUMO one-electron excitation which implies an electron density transfer from the thienyl spacer including the electron donor group to the electron-withdrawing group.[25] The potential-dependent absorption for the first forward oxidation scan of compound **5** differs from the one observed in the backward scan and the subsequent polarization cycles. This experimental result is consistent with the formation of new species upon electrochemical oxidation of compound **5** leading to dimers.[26,28,37]

The progressive increase of the WE oxidation potential induces a bleaching of the two absorption bands of **5** in its neutral form and the development of different maxima at 392, 550, 594, 840 and 956 nm (green curve at +0.70 V). For higher polarization potentials, two main maxima of absorption are observed at 392 and 498 nm (bands that are also involved in the radical cation state) together with a new broad band centered at 701 nm (red curve at +1.00 V) which can be ascribed to the dication state of the dimeric form of the chromophore.[19]

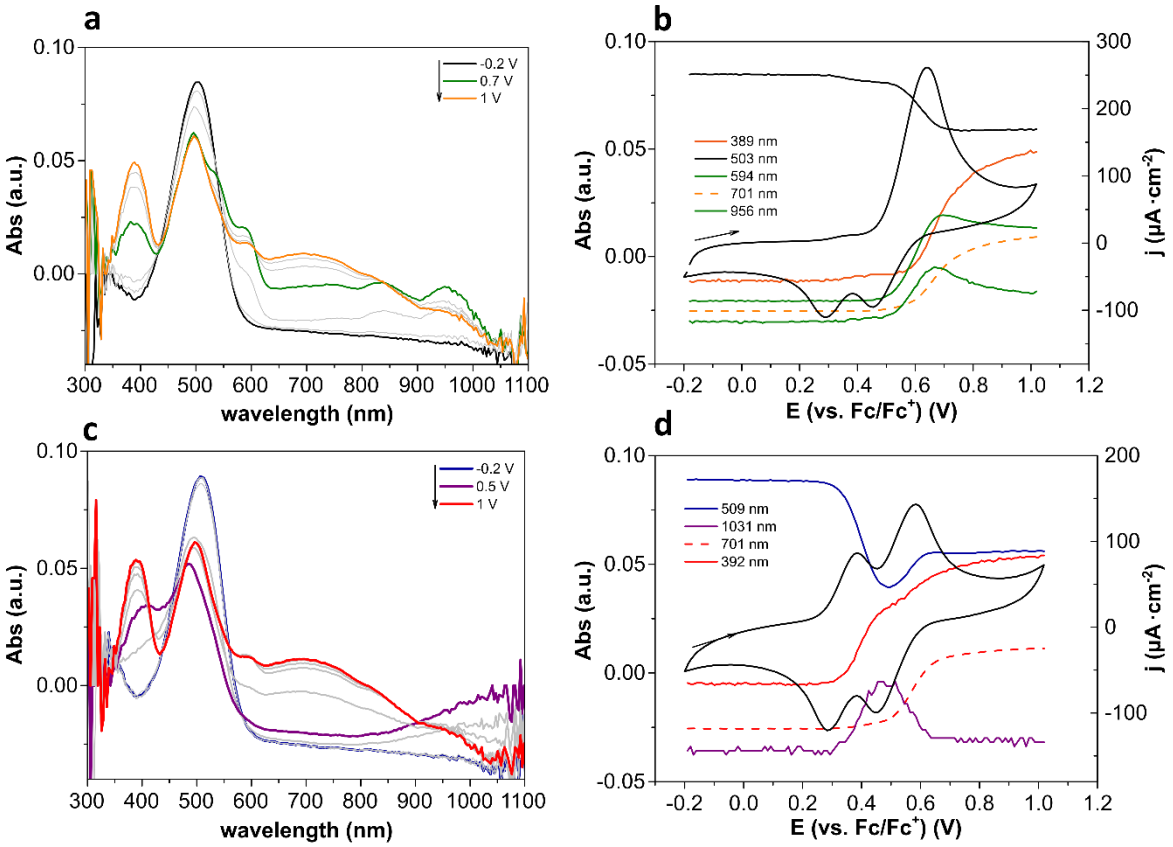

*Figure 4.20: In-situ UV-Vis spectroelectrochemistry of compound **5 (MeDPA-T-DCV)**. 1st forward oxidation cycle (a, b) and 2nd forward oxidation cycles (c, d).*

This statement is confirmed by the same optical signature observed for the dimers of chromophore **5** recorded at +1.00 V (Figure 4.20 c). When comparing the absorption maxima for the neutral dimer with respect to pristine compound **5**, a slight red shift from 503 nm (monomer) to 509 nm (dimer) is observed (spectrum at -0.20 V, Figure 4.20 c) in agreement with the slightly increased conjugation with the extension of the conjugated core. In addition, the examination of the *in-situ* absorption pattern for the following cycles for intermediate oxidation potentials (Figure 4.20 d: purple line at +0.50 V) shows a different behavior with a characteristic single broad band at wavelengths higher than 1050 nm and two maxima of absorption at 398 and 496 nm; this absorption pattern is then maintained for the subsequent charge/discharge cycles.

5	Exp.	TD-DFT
λmax N (nm)	503	435
λmax $R^{+\bullet}$(nm)	550; (594); 840; 956	442, 768
Dimer-5	**Exp.**	**TD-DFT**
λmax N (nm)	509	439
λmax $R^{+\bullet}$(nm)	398; 496; > 1050	370, 1040
λmax D^{2+}(nm)	392; 498; (593); 701	399, 365

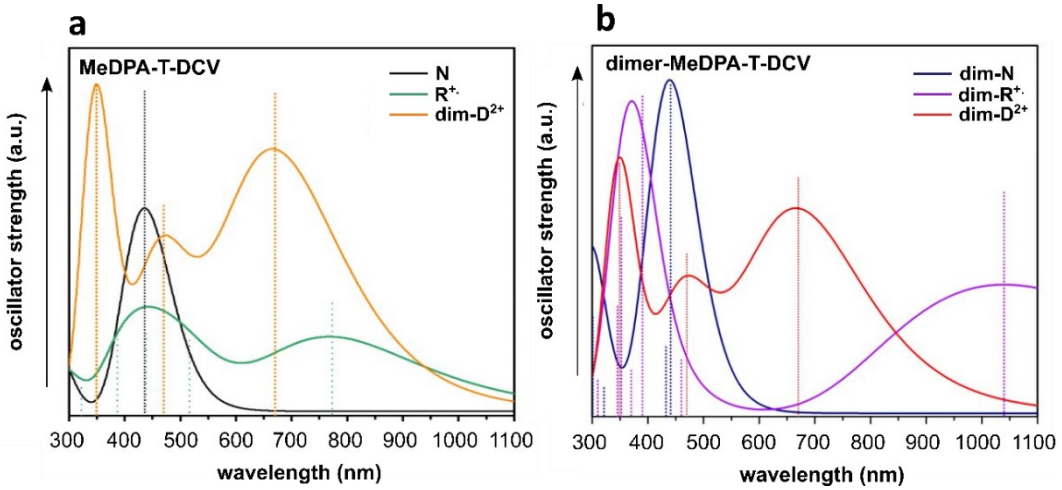

*Figure 4.21: M06-2X/ 6-31G** in CH_2Cl_2 TD-DFT calculated vertical transition energies for a)* ***5*** *and b)* ***dimer-5*** *in different redox states. Note that orange curve in (a) is equal to red curve in (b), representing the absorption pattern of* ***dimer-5*** *in the dication state.*

The measured absorption spectra of chromophore **5** and its redox states as well as for its dimeric form can also be satisfactorily compared with the TD-DFT calculated vertical transition energies (Figure 4.21). Similarly to what observed for the other chromophores, a red-shift in the absorption maxima of the neutral species upon dimerization is predicted from the calculated values (530 nm vs 563 nm for its dimer). Particularly significant in supporting the band assignment is the change in the calculated absorption pattern of the radical cation for pristine **5** (Figure 4.21 (a)) and that of its dimer (Figure 4.21 (b)). While for the radical cation of monomer **5** theory predicts a broad band between 400–600 nm due to different electronic transitions and an intense absorption band at 923 nm, a different behavior is found for the radical cation of its dimer with a very intense electronic transition predicted at 527 nm and another one with low intensity at 934 nm in agreement with experimental data. Note that this trend is captured by the M06-2X functional, which includes mid-range interactions, and a more pronounced red-shifting of the lowest energy transition is predicted when going from the radical cation state of chromophore **5** to that of its dimer, calculated at 774 nm and 1040 nm, respectively. Further, good correlation in absorption shift between

the neutral **5** and neutral **dimer-5** encountered from spectroelectrochemical experiments and the products of chemical oxidation of **5** reported in Figure 4.9.

(6) MeDPA-T-TCV

Figure 4.22 shows *in-situ* UV-Vis spectra and potential dependent peak-trend of selected wavelengths of chromophore **6**. In the neutral state, the chromophore presents two absorption bands, at 329 nm (π-π*) and 620 nm (ICT).[35,36] Also in the case of chromophore **6** the potential-dependent absorption for the first forward oxidation scan differs from the one observed in the backward scan and the subsequent polarization cycles, indicating the formation of new species upon electrochemical oxidation (dimers).[26,28,37]

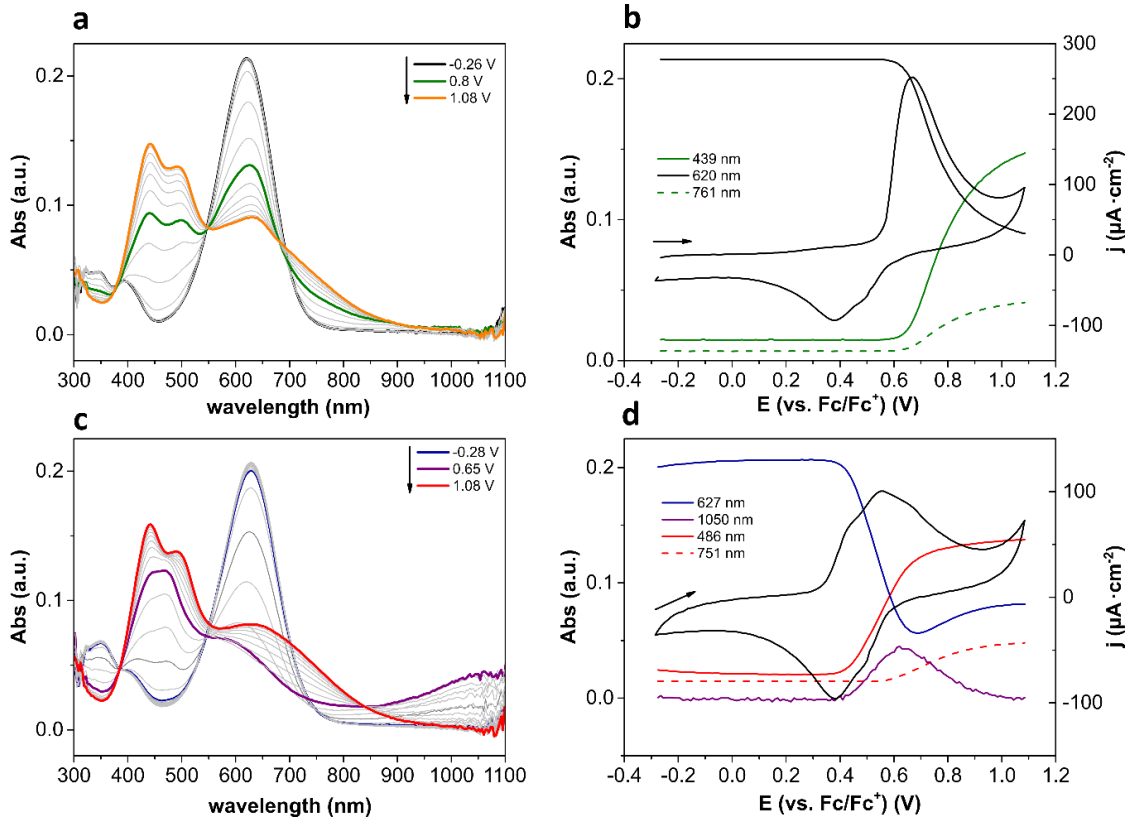

*Figure 4.22: In-situ thin-layer UV-Vis spectroelectrochemistry of compound **6 (MeDPA-T-TCV)**. 1st forward oxidation cycle (a, b) and 2nd forward oxidation cycles (c, d).*

In the first forward cycle, polarization of the WE at potential values more positive than +0.58 V causes the bleaching of the neutral band (black curve, Figure 4.22 (a)) and formation of new bands with maxima at 439, 496, 751 (orange curve, Figure 4.22 (a)). This absorption pattern is very similar to what observed for high polarization potentials during the second and subsequent cycles of oxidation, and is assigned to the dimer-dication.

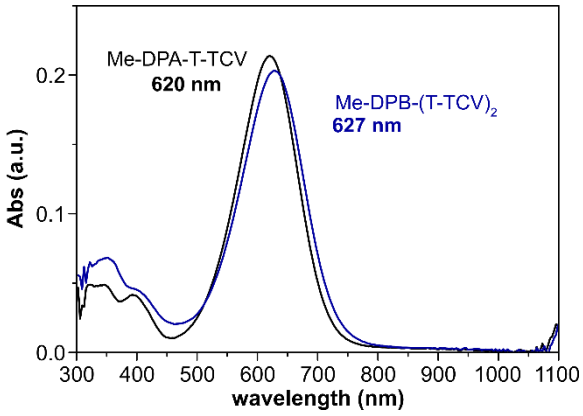

Figure 4.23: Absorption comparison for ***6 (MeDPA-T-TCV)*** *(λ_{max} 617 nm) and the correlated* ***dimer-6*** *(λ_{max} 620 nm) registered at -0.26 V.*

6	**Exp.**	**TD-DFT**
λmax N (nm)	329, 620	521
λmax $R^{+\bullet}$(nm)	(439, 496, 751)	425, 607
Dimer-6	**Exp.**	**TD-DFT**
λmax N (nm)	405, 627	307, 526
λmax $R^{+\bullet}$(nm)	496, > 1050	426, 1030
λmax D^{2+}(nm)	(439, 496, 751)	635, 399

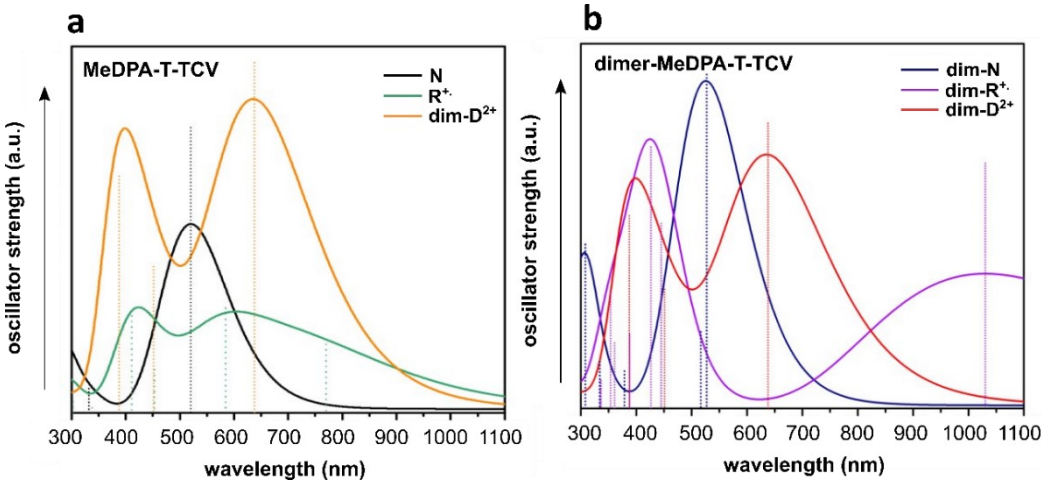

*Figure 4.24: M06-2X/ 6-31G** in CH_2Cl_2 TD-DFT calculated vertical transition energies for (a)* ***6 (MeDPA-T-TCV)*** *and (b)* ***dimer-6*** *in different redox states. Note that orange curve in (a) is equal to red curve in (b), representing the absorption pattern of* ***dimer-6*** *in the dication state.*

A red shift for the absorption maxima from **6** and neutral dimer-**6** is observed passing from 620 nm (monomer) to 627 nm (dimer) (Figure 4.23) at the end of the first oxidation cycle. The examination of the *in-situ* absorption pattern for the following cycles for intermediate oxidation potentials (Figure 4.22 c, purple line at +0.55 V) shows a different behavior than the first forward oxidation cycle with a characteristic single broad band developing in the

NIR (1050 nm sampled for the peak-trend, Figure 4.22 (d)) and a band with maximum 496 nm; this absorption pattern is then maintained for the subsequent charge/discharge cycles. For potential values more positive than +0.62 V, new absorption develops at 750 nm; considering the voltametric signature, this band should be assigned to the dication state of the dimer. The red spectra registered at +0.83 V is very similar to the one registered for the completed first oxidation cycle (orang line). The high reactivity of the radical cations of chromophore **6** leading to the fast formation of dimers causes difficulties to distinguish its characteristic absorption; further, the characteristic vibronic bands found for all chromophores radical cations are not encountered. Comparison with calculated transitions is presented as support for the band assignation. Theoretical calculations show also in this case a good correlation for the different states of charged assigned (Figure 4.24).

4.1.2.3 Theoretical Calculations

DFT and TD-DFT calculations were performed by Sergio Gámez and Carmen Ruiz Delgado from the University of Malaga to provide support in explaining the tendency towards oxidative dimerization of the different chromophores, in particular, charge distribution, planarization, spin density for all compounds in different states of charge was calculated, and correlation with the experimental results was done. All the data showed have been calculated at M06-2X/6-31G** level in CH_2Cl_2. The same trends are also predicted using the B3LYP functional; this was performed to ensure a good reliability of the obtained results. TD-DFT calculations were also performed to support assignment of the different absorption spectra registered during spectroelectrochemical experiments. Theoretical results are reported for chromophores **1** to **6** and their dimers in different states of charge.

4.1.2.3.1 Theoretical Calculations on Chromophores 1-6

Optical Properties

In push-pull systems, generally, most of the optical properties (linear and non-linear) emerge from the lowest allowed electronic transition, which according with TD-DFT calculations is associated with an $S_0 \rightarrow S_1$ transition with an electron promotion from the HOMO to the LUMO. In view of the calculated HOMO and LUMO topologies, the nature of the lowest energy transition can be satisfactorily considered as an intramolecular charge transfer (ICT). However, it is important to mention that in chromophores **1** and **4**, which are not pure push-pull systems due to the absence of acceptor groups, other electronic transitions contribute to the lowest energy bands.

molecule	λmax N (nm)	λmax $R^{+\bullet}$(nm)	λmax D^{2+}(nm)
1	346	459; 966	-
2	351; 500	378; 614; 1000	-
3	418, 617	436, 489, 664, 804, 904, 1027	-
Dimer-3	627	664	(438, 460), 864
4	336	442; 801	-
5	503	550; (594); 840; 956	-
Dimer-5	509	398; 496; > 1050	392; 498; (593); 701
6	329, 620	(439, 496, 751)	-
Dimer-6	405, 627	496, > 1050	(439, 496, 751)

Table 4.2: Experimental maxima of absorption of chromophores in their neutral (N) and radical cation ($R^{+\bullet}$) state and dication state (D^{2+}) in the case of the dimerization products.

A strong bathochromic shift is observed upon the insertion of the acceptor groups, being this effect more important for the molecules bringing the TCV acceptor, in total agreement with the HOMO-LUMO gap decreased. Further, the probability that the $S_0 \rightarrow S_1$ electronic transition takes place (reflected by the oscillator strength "*f*") is higher in the case of TCV acceptor containing chromophores. Simulated absorption spectra (M06-2X/6-31G**) reproduce quite well the experimental results. The absorption maxima registered in CH_2Cl_2 for the different chromophores in their neutral and charged state are reported in Table 4.2. In the neutral state, all molecules with exclusion of compounds **1** and **4**, which do not have an acceptor unit, are characterized by the presence of an ICT transition. TCV containing chromophores show the smallest E_g, which is also expected from theoretical calculations, followed by DCV containing chromophores.

molecule	λmax N (nm)	λmax $R^{+\bullet}$(nm)	λmax D^{2+}(nm)
1	312	384, 834	-
2	436	375, 520, 792	-
3	523	405, 638	-
Dimer-3	314, 533	445, 1488	394, 786
4	302	372, 706	-
5	435	442, 768	-
Dimer-5	439	370, 1040	349, 472, 666
6	521	425, 607	-
Dimer-6	307, 526	426, 1030	635, 399

*Table 4.3: Theoretical maxima of absorption for the analyzed chromophores using the functional M06-2X/ 6-31G** in CH_2Cl_2 in their neutral (N) and radical cation ($R^{+\bullet}$) state and dication state (D^{2+}) in the case of the dimerization products.*

In the radical cation state all molecules present a vibronic structure in the different bands, the vibronic progressions, indicating the coupling with the vibrational modes, are particularly pronounced in the case of TPA containing chromophores in comparison to the MeDPA ones. In general, the radical-cation bands (UV-Vis preceding the ICT transition of the neutral state and broader band in the NIR) undergo a bathochromic shift in the case of introduction of the acceptor unit. Further, a slight red-shift is observed for the NIR band passing from MeDPA to TPA donor unit. Overall, a good correlation between experimental and theoretical results is encountered with regards to the bands multiplicity and positions. Calculated absorption spectra predict indeed very well the variation in the band shift for the single chromophores as well as for the dimeric compounds in different states of charge. For example, a change of 10 nm is found between chromophores **1** (Exp. 346 nm *vs.* Theo. 312 nm) and **4** (Exp. 336 nm *vs.* Theo. 302 nm) both from calculations and theoretical spectra. It must be noted that the functional M06-2X/ 6-31G**tends to underestimate the conjugation, for this reason the value of band maxima from the theoretical data is blue-shifted in comparison to the experimental ones. Although, discarding the absolute values, very good correlations are found in the series analyzed.

Molecular Structure

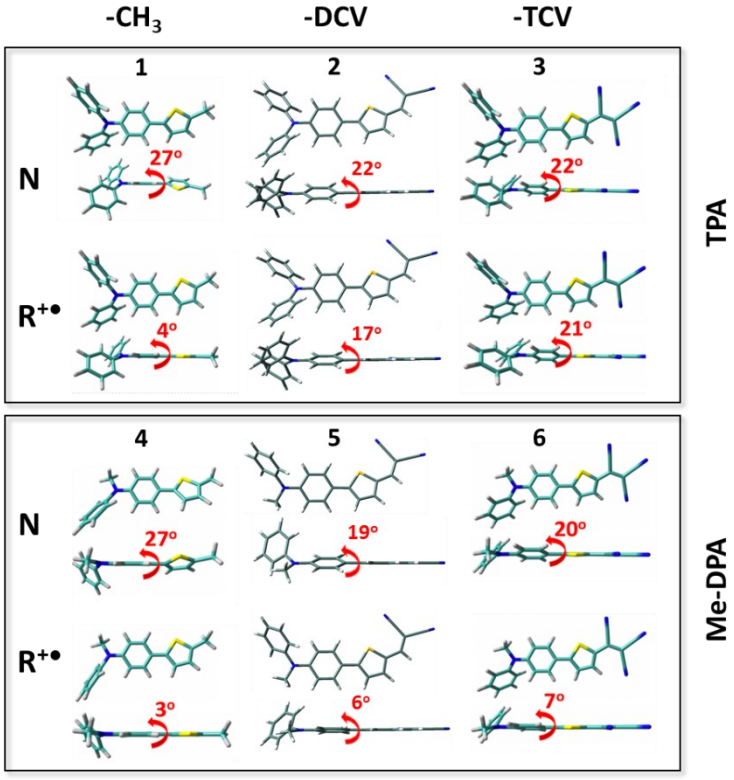

*Figure 4.25: Top and lateral views of the DFT-optimized structures (PCM-M06-2X/6-31G** level using CH_2Cl_2 as solvent) for **1**-**6** chromophores in their neutral (N) and radical cation state ($R^{+\bullet}$). The dihedral angles between the donor moiety and the π-bridge (in absolute values) are also shown.*

From a geometrical point of view (Figure 4.25), all six chromophores present an almost planar structure where the phenyl ring of the donor unit adjacent to the thiophene ring is distorted by around 20°. Interestingly, a slight decrease of the dihedral angle between the phenyl ring of the donor and its adjacent thiophene unit is found upon the substitution of the methyl group by DCV or TCV acceptor groups. Upon oxidation ($R^{+\bullet}$), a planarization of the π-conjugated framework is predicted for the radical cation state, except for chromophore **2** and **3** which interestingly retains their distortion between the thiophene spacer ring and adjacent phenyl unit.

Mülliken atomic charges

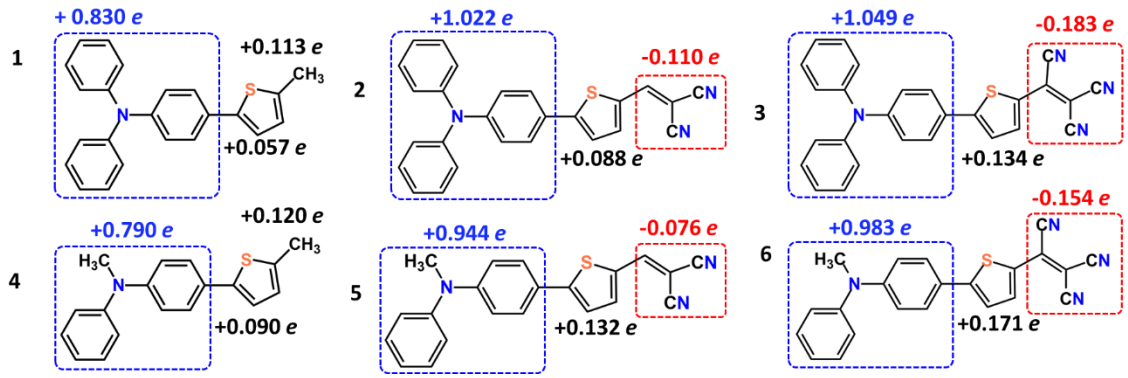

*Figure 4.26: Mülliken atomic charges for **1**-**6** systems in the radical cation state, calculated at the PCM-M06-2X/6-31G** level using CH_2Cl_2 as solvent.*

To better understand the polarization degree of these chromophores in the ground state, the Mülliken atomic charges for the radical cation state have been calculated. The resulting atomic charge distribution suggests a more polarized structure, meaning a large variation on the atomic charges at the different molecular domains, for the molecules containing an acceptor unit. The results go hand in hand with the results previously reported for molecular geometry, showing a higher degree of planarity. On considering the nature of the donor moiety, TPA-based chromophores display a more polarized (more zwitterionic) structure than the analogous Me-DPA chromophores. Further, increase in the charge separation is observed upon introduction of an acceptor unit in the molecular structure and, in correlation with the electron withdrawing character of the acceptor unit, with TCV substituted chromophores showing the highest charge separation in their ground state.

Spin-Densities

As a first approach to assess the reactivity of the different chromophores, spin density values at different molecular position were calculated and compared, with particular focus on values at the phenyl para position.[38,39] The highest spin densities in para position of the nitrogen atoms are expected for chromophores **2, 3** and **5, 6** respectively. On considering

the nature of the donor moiety, MeDPA-based chromophores display a more delocalized spin density over the π-spacer group than the analogous TPA chromophores, due to the presence of only one external phenyl ring stabilizing the charge in Me-DPA based chromophores and their higher planarity. Similar trends are found when comparing NPA (natural population analysis) and Mülliken spin densities.

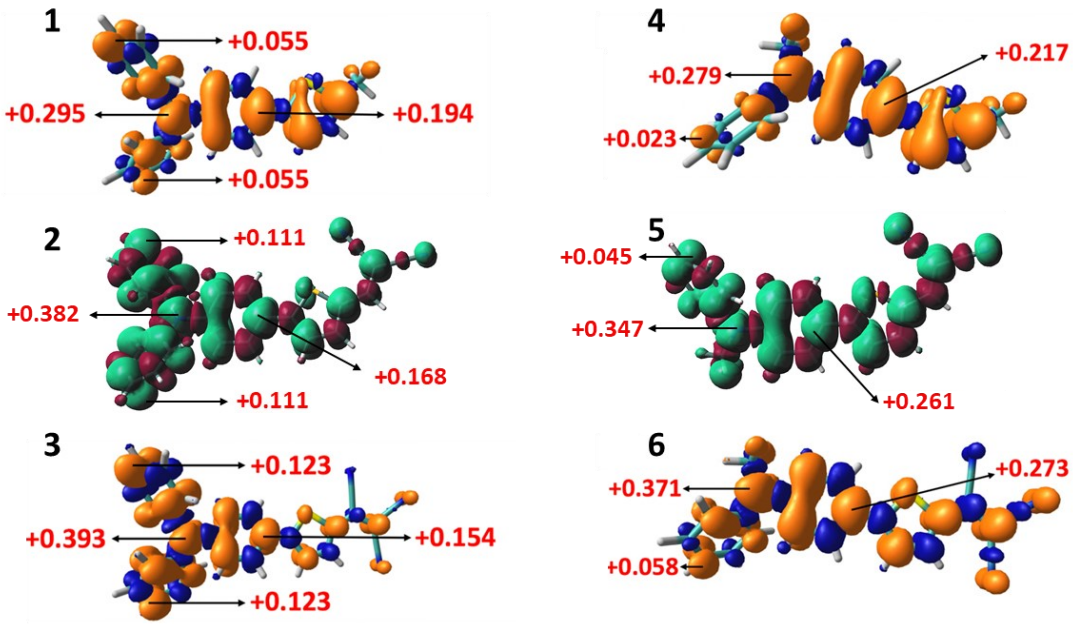

*Figure 4.27: DFT-calculated Mülliken spin density distributions (PCM-M06-2X/6-31G** level using CH_2Cl_2 as solvent) of the chromophores in their radical cation state. The spin density values of the Nitrogen atoms and the carbon atoms localized in para position with respect to the N atoms are also shown.*

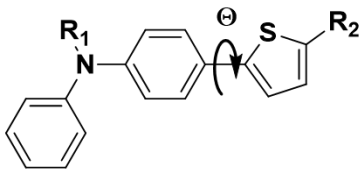

	1	2	3	4	5	6
R_1	Ph	Ph	Ph	Me	Me	Me
R_2	Me	DCV	TCV	Me	DCV	TCV

Mol.	Dihedral Angle Θ (°)	Mülliken Atomic Charges (e)			Spin-Density		
		Donor	Thiophene	Acceptor	ext-Ph	N	Int-Ph
1	27	+0.080	-0.144	-			
$1^{+\cdot}$	4	+0.830	+0.057	-	+0.055	+0.295	+0.194
2	22	+0.180	+0.197	-0.377			
$2^{+\cdot}$	17	+1.022	+0.290	-0.312	+0.111	+0.382	+0.168
3	22	+0.215	+0.061	-0.276			
$3^{+\cdot}$	21	+1.049	+0.134	-0.183	+0.123	+0.393	+0.154
4	27	+0.096	-0.157	-			

4$^{+\cdot}$	3	+0.790	+0.090	-	+0.023	+0.279	+0.217
5	19	+0.203	+0.182	-0.385			
5$^{+\cdot}$	6	+0.943	+0.132	-0.076	+0.045	+0.347	+0.261
6	20	+0.248	+0.048	-0.296			
6$^{+\cdot}$	7	+0.983	+0.171	-0.154	+0.058	+0.371	+0.273

*Table 4.4: DFT-calculated structural parameters for both neutral (black) and radical cation (blue) states at PCM-M06-2X/6-31G** level using CH_2Cl_2 as solvent.*

Direct correlation between calculated spin density values and the observed molecular reactivities are not found. In summary, all the above discussed structural parameters for both neutral (black) and radical cation (blue) states, which were calculated to provide support in explaining the dimerization reactivity of compounds **1**-**6**, are collected in the Table 4.4.

4.1.2.3.2 Theoretical Calculations on Charged Dimers

To elucidate the nature of charging products, theoretical calculations on dimers of compounds **1**-**6** in different states of charge were also performed, focusing in particular on following aspects:

- energy differences between the open (OS) and closed-shell (CS) states of the different dimer dications,
- geometrical analysis,
- charge distribution analysis,
- energy levels.

For the dimer radical cation state two characteristic resonance structures namely, closed-shell (CS) quinoidal form and open-shell (OS) singlet diradicals are possible.

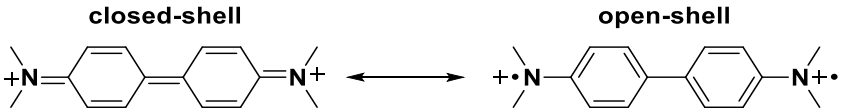

Figure 4.28: Open and closed shell resonance structures of dimeric benzidine compounds in the dication state.

The energy difference between the two resonance structures is reported in Figure 4.29. A trend correlating the closed-shell character in the dimeric dication state with the dimerizability of the compounds was found. In particular, systems characterized by a stronger closed-shell character seem to present a stronger tendency to dimerization. For instance, the dication state of compound dimer-**6** presents the highest closed-shell character in the set of compounds analysed. The values obtained for interconversion between closed shell and singlet open shell for the dimer dications (Energy difference

closed-sheall and singlet-open shell state (CS-SOS)) are in the order of 0 – 4 kcal/mol in the case of the B3LYP/6-31G** functional, whereas a in the order 0 – 9 kcal/mol for the functional M06-2X/6-31G**.

To gain further information about the characteristic OS or CS nature of the dimer dications analysed, the bond length alternations (BLA) were also calculated for the different species. For the CS state, BLAs are close to the values of Thiele's hydrocarbon (value: 0.103), suggesting they feature quasi-quinoidal structures. In contrast, the BLA value for the OS state is greatly reduced in comparison to those of CS state, indicating a diradical nature.[40] Also geometrical analysis hints to a more pronounced closed shell character for the dimerizing compounds. The comparison of the experimental and calculated structural parameters clearly reveals that the dication state of tetraphenylbenzidine (TPB^{2+}) has a closed-shell structure. The ground-state electronic structures of these systems are tunable with different substituents or bridging units. Experimentally, the EPR and SQUID measurements for tetraphenylbenzidine in the dication state (TPB^{2+}) confirm their closed-shell structure.[41,42]

Coupling products	Energy (HF) B3LYP/6-31G** in CH_2Cl_2			Energy difference CS-SOS (Kcal/mol)	Energy difference TOS-SOS (Kcal/mol)
	Closed Shell (CS)	Singlet Open Shell (SOS)	Triplet Open Shell (TOS)		
1^{2+}	-2680.16851176	-2680.17612443	-2680.17531074	4.78	0.51
2^{2+}	-3125.29639521	-3125.30038019	-3125.29843606	2.50	1.22
3^{2+}	-3309.74400210	-3309.74731796	-3309.74494040	*2.08*	*1.49*
4^{2+}	-2296.67646531	-2296.68627306	-2296.68610353	6.15	0.11
5^{2+}	-2741.80540763	-2741.80726098	-2741.80676436	1.16	0.31
6^{2+}	-2926.25237292	-2926.25208526	-2926.25126261	CS *-0.18*	*0.52*

Coupling products	Energy (HF) M06-2X/6-31G** in CH_2Cl_2			Energy difference CS-SOS (Kcal/mol)	Energy difference TOS-SOS (Kcal/mol)
	Closed Shell (CS)	Singlet Open Shell (SOS)	Triplet Open Shell (TOS)		
1^{2+}	-2679.27092460	-2679.28628066	-2679.28596980	9.64	0.20
2^{2+}	-3124.26040192	-3124.26782541	-3124.26652439	4.66	0.82
3^{2+}	-3308.65504044	-3308.66151204	-3308.65992490	*4.06*	*1.00*
4^{2+}	-2295.93117571	-2295.94610772	-2295.94606098	9.37	0.03
5^{2+}	-2740.92219052	-2740.92364252	-2740.92348504	0.91	0.10
6^{2+}	-2925.31642866	-2925.31484582	-2925.31444259	CS *-0.99*	*0.25*

*Figure 4.29: Characterization of resonance structures for the dimeric dication state of the analysed chromophores, the same trend is predicted with the two levels of theory utilized: B3LYP/6-31G** (top) and M06-2X/6-31G** (bottom) level using CH_2Cl_2 as solvent.*

Mülliken charges and the dihedral angles of **dimers-1-6** in the dication state are also calculated, confirming the higher quinoidal character (dihedral angles closer to zero) of the biphenyl bond (Θ_1, purple) and the N-Ph bond (Θ_3, green) in the case of compounds **dimer-6^{2+}**, **dimer-5^{2+}** and **dimer-3^{2+}** in the order for the CS state, as well as more positive charge localized in the internal rings and the biphenyl bond. In the case of compounds **dimer-1^{2+}**,

dimer-2^{2+} and **dimer-4**$^{2+}$ instead, the positive charge is more localized on the external phenyl rings. These theoretical results hint for a higher CS character of the dimer dication of compounds undergoing dimerization

	State	Avg. N-C_i	Avg. C_{p1}-C_{p2}	BLA
1^{2+}	CS	1.341	1.403	0.085
	OS	**1.423**	**1.479**	**0.014**
	T	1.425	1.481	0.013
2^{2+}	CS	1.338	1.399	0.089
	OS	**1.405**	**1.473**	**0.025**
	T	1.415	1.479	0.018
- 3^{2+}	**CS**	**1.337**	**1.398**	**0.090**
	OS	1.400	1.470	0.028
	T	1.413	1.479	0.019
4^{2+}	CS	1.324	1.393	0.096
	OS	**1.431**	**1.482**	**0.010**
	T	1.431	1.482	0.010
5^{2+}	**CS**	**1.322**	**1.391**	**0.099**
	OS	1.427	1.481	0.012
	T	1.428	1.482	0.012
+ 6^{2+}	**CS**	**1.322**	**1.391**	**0.099**
	OS	1.423	1.479	0.014
	T	1.426	1.481	0.012
$2TPA^{2+}$	**X-Ray**	**1.339**	**1.414**	**0.074**
	CS	**1.333**	**1.396**	**0.092**
	OS	1.394	1.468	0.032
	T	1.409	1.479	0.021

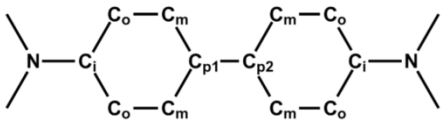

*Figure 4.30: Bond-length-alternation (BLA) values calculated at the (U)M062X/6-31G**level of theory for the different dimer-dications of chromophores **1-6**. Comparison of dimer dication of TPA with references.* [41,42]

Finally, the analysis of the frontier molecular orbitals (Figure 4.32) indicates more stabilized HOMO levels and more electron deficient central biphenyl rings going from molecules **6** > **5** > **3** hint to a higher stability of dication of dimer **6** when compared to that of dimer **5** and finally the dimer **3**.

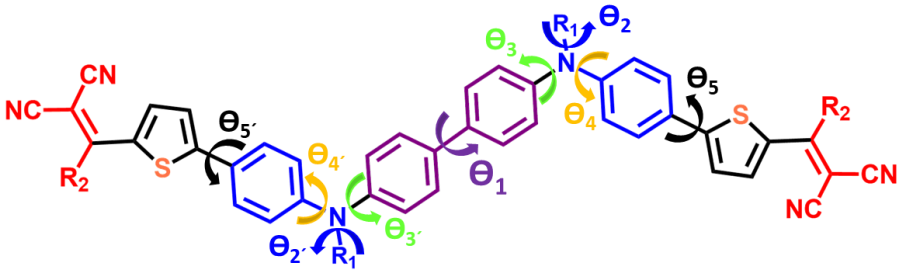

		Mülliken charges (*e*)				Inter-ring Dihedral Angles (°)				
	State	Internal Rings	External Rings	Thiophene	Acceptor	Θ_1	Avg. $\Theta_2\Theta_{2'}$	Avg. $\Theta_3\Theta_{3'}$	Avg. $\Theta_4\Theta_{4'}$	Avg. $\Theta_5\Theta_{5'}$
1^{2+}	**CS**	**1.352**	**0.303**	**-0.065**	--	**11**	**51**	**20**	**46**	**18**
	OS	**0.780**	**0.432**	**0.067**		**35**	**48**	**44**	**25**	**5**
2^{2+}	**CS**	**1.432**	**0.350**	**0.062**	**-0.128**	**12**	**51**	**19**	**49**	**23**
	OS	**0.984**	**0.523**	**0.089**	**-0.104**	**32**	**42**	**37**	**33**	**17**
3^{2+}	**CS**	**1.448**	**0.360**	**0.113**	**-0.197**	**11**	**50**	**19**	**50**	**25**
	OS	1.032	0.533	0.131	-0.180	32	41	35	36	20
4^{2+}	**CS**	**1.498**	**0.246**	**-0.077**	--	**9**	--	**12**	**55**	**21**
	OS	0.714	0.422	0.102		36		57	13	1
5^{2+}	**CS**	**1.558**	**0.294**	**0.059**	**-0.132**	**8**	--	**11**	**57**	**27**
	OS	0.814	0.520	0.140	-0.068	36		54	15	3
6^{2+}	**CS**	**1.564**	**0.308**	**0.109**	**-0.199**	**8**	--	**10**	**58**	**26**
	OS	0.865	0.540	0.176	-0.148	36		52	18	10

*Figure 4.31: Mülliken charges and dihedral angles calculated for **dimers-1-6** in the dication states at the (U)M062X/6-31G**level of theory.*

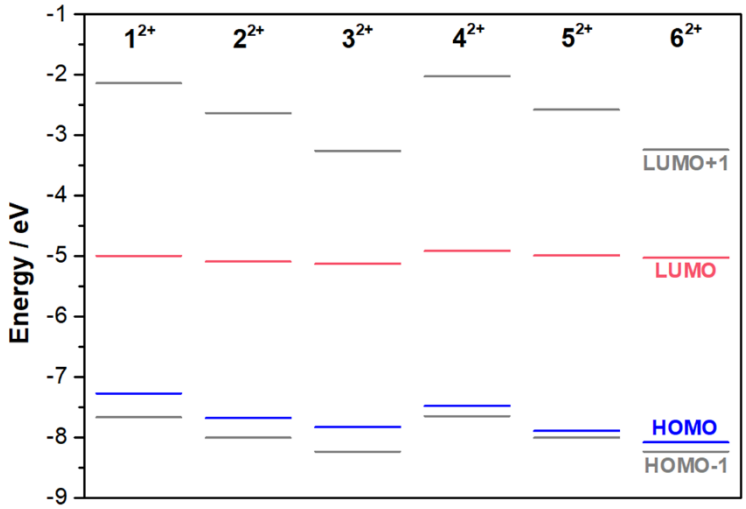

*Figure 4.32: HOMO-LUMO energy levels for dimers-**1-6** dications at M06-2X/6-31G** level of theory in CH_2Cl_2.*

4.1.2.3.3 Comparison

DFT calculations were performed to provide an explanation of the different reactivity observed for the chromophores upon electrochemical oxidation. In literature several works can be found describing the electrochemical behavior of aromatic amines upon oxidation.[27–29] The oxidative pathway of tri-substituted aromatic amines is described as an EC mechanism (namely electrochemical-chemical mechanism), resulting in the dimerization at the para position of the phenyl ring. The reaction pathway includes the radical formation upon electrochemical oxidation followed by the coupling of the radicals followed by deprotonation. When analyzing the reactivity towards dimerization of different classes of tri-substituted aromatic amines, the spin density at the phenyl para-position and the blocking of the latter are two determining factors defining the reactivity of the amine radical cations.[27,43,44]

It is important to consider that, by analogy with redox active π-conjugated systems, the nature of substituents at the arylamine para-position can influence the radical stability towards the coupling reaction both from a thermodynamic and a kinetic point of view. Radical cations can indeed be thermodynamically stabilized by an increase or more efficient conjugation of the system as well as by introducing electron-donor groups.[45] Sterically hindered substituents or the blocking of the reactive sites (end-capping) can also diminish the reactivity of the radical-cation state towards the coupling reaction.[34,35] For instance, Bäuerle *et al*. reported the electrochemical behavior upon oxidation of a series of end capped oligothiophenes leading to the formation of stable radical cations when compared to highly reactive thiophenes. Similar facts are also found by Roncali *et al*. regarding the influence of steric effects on the electropolymerization of 3-alkyl thiophenes.[48]

As a first approach to assess the reactivity of the different compounds, calculated spin densities at the phenyl para position[38,39] for the six chromophores were compared (Table 4.4). Contrary to what was initially expected, the dimerization tendency cannot be explained by the spin-density at the reactive site alone. Increasing the Mülliken spin-density at the Ph para position in a chromophore series, bearing the same donor moiety (MeDPA or TPA), which is realized by increasing the strength of the acceptor unit, results in an increase in the molecular reactivity (Figure 4.27). Whereas this statement holds for a molecular series characterized by the same donor molecule, in the case of different donor units, considering only the spin density would not explain the experimental results.

The oxidation of a molecule to its radical cation state reverses its reactivity, turning a relatively electron-rich and therefore nucleophilic moiety into an electron-poor and highly electrophilic unit. Therefore, the removal of electron-density from the donor unit (TPA or Me-DPA) by tailoring the chromophore molecules with more electron-withdrawing units, in the order TCV > DCV, results in an increased instability of the radical cation state and in its

tendency towards a radical cation – radical cation coupling (Figure 4.26). In the case of TPA based chromophores the only molecule capable of oxidative dimerization is compound **3,** endowed with TCV acceptor unit, which is also the molecule associated with the highest spin-density among all analyzed compounds (+0.123, see Figure 4.27). Despite the higher spin-density, the dimerization tendency of molecule **3** is lower in comparison to other MeDPA based chromophores, compounds **5** (DCV) (+0.045) and **6** (TCV) (+0.058).

To account for the different observed reactivity, the molecular geometries need to be also considered (Figure 4.25). DFT calculated geometries indicate that in the case of TPA compounds bearing DCV and TCV acceptor units, the oxidation to the radical cation state leads to smaller changes in the dihedral angle between the arylamine and the thienyl π-linker, in comparison to the respective MeDPA chromophores. The dimerization products of TPA based chromophores were also calculated to be less planar and characterized by deeper HOMO value.

A good correlation between a less quinoidal nature in the radical-cation state, with the charge distribution over the whole molecule in the case of non-dimerizing **1** and **2** molecules with their MeDPA counterparts was also found. The spin-density at the phenyl para-position does not seem to be the key factor in determining reactivity of the arylamine compounds when comparing the two series of molecules, although within a single series the radical-radical coupling of compounds appears to increase as the spin density increases.

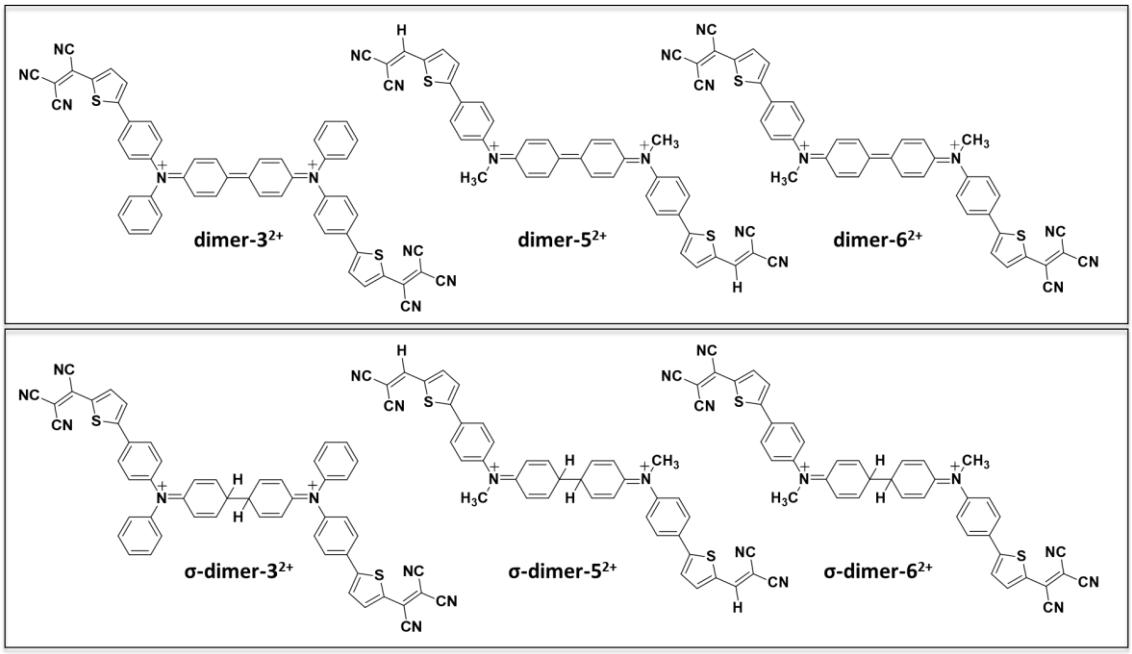

*Figure 4.33: Structure of σ-dimer-dications representing the intermediate species in the dimerization reaction mechanism***.**

Considering the mechanism for radical-radical-coupling, it has been reported that the formation of σ-dime, whose proton elimination is driven by aromatization energy, is found to be the rate determining step in the electrodeposition mechanism. [49–51] In particular, in the case of electrodeposition, it is found that the rates of proton elimination from "dimeric" coupling intermediates may diminish significantly when the conjugation of the starting coupling monomer increases, that charged σ-dimers with more than four units in a conjugated chain segment could be stable enough to not lead to oligomerization. A similar situation could be pictured in the systems here analyzed, considering that the reactivity might be limited by the extended conjugated backbone found in the push-pull systems. Proton elimination from such species might take place only when σ-intermediates are oxidized to a higher charging level, which increases the reactivity of the system. [49–51] The stability of the positive charges in a σ-dimer is dependent on electronic factors and the extent of the conjugated system. The chain length criterion proves greater stability, meaning a lower tendency for proton releases of such intermediates for an increasing chain length. Therefore, formation of the radical cations is followed by a reversible dimerization of the species producing a dimeric-dication.

As previously mentioned, in the case of the molecules here reported an interesting correlation between increasing closed-shell character of the dimer-dication state with the dimerization tendency is observed. This aspect is therefore taken into consideration due to the structural similarity of dimer-dications with σ-dimer-dications, as the latter are intermediate species in the electrodeposition and dimerization process (Figure 4.33). Two different resonance structures i.e. open shell with quinoid nature (OS) and closed-shell with benzoid nature (CS) are present for the dimer-dications of bis-triarylamine systems.[41,42] The open-shell structure delocalizes the charge on the external phenyl-rings, whereas in the case of the closed shell, the charge is delocalized more on the internal phenyl-rings with a higher electron density over the internal biphenyl-bond and a more pronounced double-bond character. A trend regarding these two resonance forms, and in particular with a more pronounced closed-shell (CS) structure, is found to correlate with the observed reactivity. By further comparing dimerization ability of para-substituted triarylamines reported in the literature,[27,38] and their dimer-dication open or closed shell nature, similar tendences are found with trends similar to those observed here [52]. Indeed, *p*-methoxy tetraphenylbenzidine is characterized by an open-shell structure and has low yields of electrochemical dimerization in CH_2Cl_2, and on the contrary tetraphenylbenzidine which has a higher reactivity towards dimerization than the latter, is characterized in the dication-state by a stable closed-shell structure. In the literature this aspect, i.e., OS or CS character of the dimer dication, has not yet been considered with regards to coupling reactivity of the respective monomers.

Based on the reported results, we think that the nature of the dimeric-dication states also of different arylamine systems as well as with other systems from the literature, should be further analyzed considering preliminary results herein obtained. Finally, the trend in the HOMO levels of the analysed species is found, lower energies are in fact encountered with the dimer-dications of the dimerizing compounds. The more planarized conjugated backbones, more stabilized HOMO levels and more electron deficient central biphenyl rings going from dimer-**6** > dimer-**5** > dimer**-3** might also sustain the coupling behavior observed for the different chromophores. It must also be considered that the energy calculated for all compounds lay in a very close range of energy, in the order of 0-4 kcal/mol. Similar results are expected introducing two additional hydrogen units for the intermediates, therefore for the main σ-dimer-dications of the chromophores (Figure 4.33). This implies that we might be very close to the limit of dimerizability, with trends supporting the experimental results. Further, steric hindrance could also play a determining role in the reactivity of the analyzed systems.

4.1.3 Towards Arylamine-Based Multimers

The study of the tendency towards dimerization of linear push-pull molecules **1**-**6** endowed with TPA or Me-DPA donor units, has also the aim of identifying suitable reactive units to be employed in multimeric systems as crosslinking sites to electrodeposit push-pull films with well-defined redox behavior. In collaboration with the group of Philippe Blanchard (MOLTECH Angers), electrodeposition and characterization of the tetrameric counterpart of compound **5,** tetra-**5** ((2E,2'E)-2,2-bis((((E)-2-cyano-3-(5-(4-(methyl(phenyl)amino)phenyl)thiophen-2- yl)acryloyl)oxy)methyl)propane-1,3-diyl-bis(2-cyano-3-(5-(4- (methyl(phenyl)amino)phenyl)thiophen-2-yl)acrylate) T), and of the so deposited electroactive films was performed. The choice of synthesizing and characterizing compound tetra-**5** is based on previous studies of simple and synthetically accessible linear push-pull molecule based on arylamine donor units as previously described. Indeed, the molecule TPA-T-DCV was observed to exhibit good absorption properties in the visible spectrum and interesting photovoltaic properties as donor material combined with C_{60} [35,37,53] or its soluble analogue [6,6]-phenyl-C_{61}-butyric acid methyl ester ($PC_{61}BM$) as acceptors.[54] Following a “multimer” approach, the related pentaerythritol based push–pull tetramer **Tetra-2** was also synthetized (Angers MOLTECH) and showed to give promising and higher power conversion efficiencies (*PCE*s) when blended with $PC_{71}BM$ in bulk heterojunction solar cells.[55] The substitution of one terminal phenyl ring of the TPA unit of molecule **2** by a methyl group affording **5**, induced a 50-fold increase of hole mobility hence resulting in better photovoltaic properties.[26] Based on these results, the analogue of **Tetra-5** bearing methyldiphenylamine (MeDPA) units instead of TPA, namely **Tetra-5**, was also

synthesized (Angers MOLTECH). In the following paragraphs, the electrodeposition and characterization of this tetramer, showing promising optoelectronic properties is performed and described to show the versatility of the dimerization approach of arylamine-based compounds. The so synthetized electroactive 3D-push-pull network of **Tetra-5** have been crosslinked and the deposit has been characterized by means of cyclic voltammetry and *in-situ* UV-Vis spectroelectrochemistry. The reactivity of the molecule is compared with the one of the paternal compound, chromophore **5**.

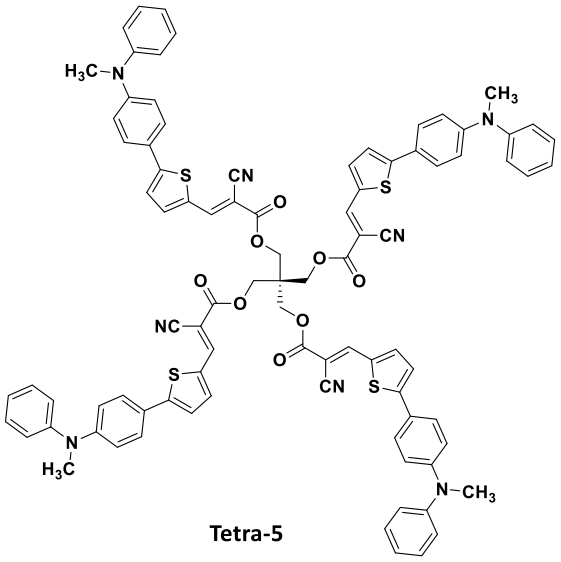

*Figure 4.34: Structure of compound **Tetra-5**, push-pull tetramer bearing four MeDPA-T-DCV push pull units.*

4.1.3.1 Electrochemical Crosslinking of Tetra-5 (ec-Tetra-5)

To show the versatility of the dimerization approach of arylamine-based compounds, the specific electrochemical coupling of **5** is utilized to generate 3D-push-pull networks on electrode surfaces through oxidative electrodeposition.

The oxidative voltammetric pattern and subsequent potentiodynamic cycles recorded during the electrodeposition of **Tetra-5** on ITO are presented in Figure 4.35. The CV pattern for the monomer oxidation (Figure 4.35 (a)) consists of a single irreversible oxidation peak at +0.51 V. This peak can be assigned to the oxidation of the four-independent push-pull units linked to the non-conjugated central pentaerythritol σ-linker generating a tetra- radical cation species (non-interacting redox centers on the same molecule). The oxidative peak for the one-electron oxidation of **Tetra-5** monomer falls at +0.51 V slightly shifted towards less positive oxidation potential with respect to the first oxidation of chromophore **5** (+0.64 V; see Figure 4.4 e). **Tetra-5**, in analogy with what was observed for chromophore **5**, readily undergoes an oxidative electrodeposition process involving the coupling of the arylamine radical cation at the free phenyl para position, with

formation of biphenyl bonds. From the CV pattern recorded during electrodeposition a steady and regular film growth within consecutive cycles can be observed (Figure 4.35 (b)).

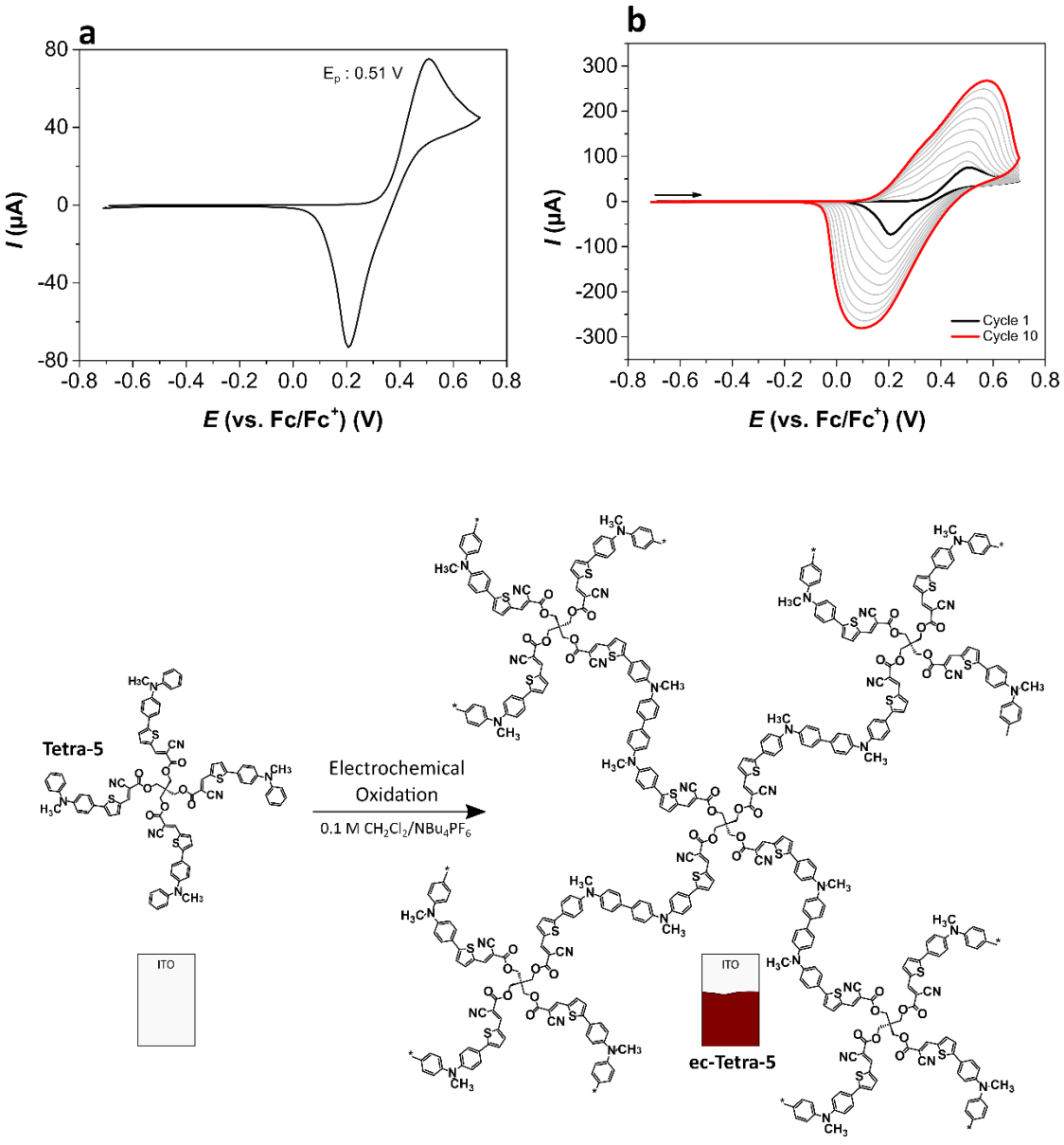

*Figure 4.35: (a) I cycle of electrodeposition of **Tetra-5** and (b) complete electrodeposition pattern in CH_2Cl_2/NBu_4PF_6 0.1 M, ITO electrode; scan-rate 50 mV·s^{-1}. Adapted with permission from ref. [1] (Wiley 2019).*

The progressive deposition of electroactive material on the electrode surface is indeed associated with increasing current registered for each subsequent cycle. Due to the branched nature of the starting monomer we expect a highly crosslinked material, generated upon dimerization into dimethyl-diphenyl-benzidine units. The latter, modulated by the interactions between neighboring units on the electrode surface, dominate the redox behavior of electrodeposited **Tetra-5** film (**ec-Tetra-5**).

4.1.3.2 Characterization of ec-Tetra-5

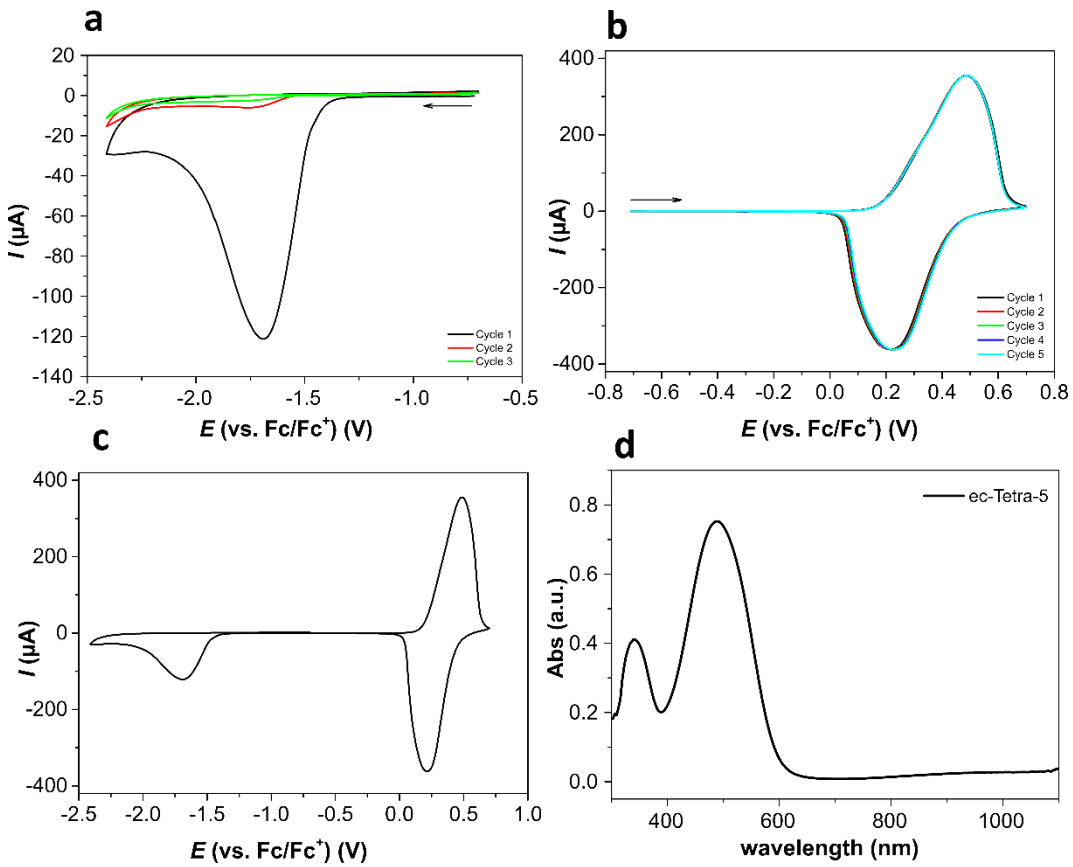

*Figure 4.36: CV cycles in monomer-free solution. Oxidation cycles performed before reduction cycles in 0.1 M CH_2Cl_2/NBu_4PF_6, ITO; scan-rate 50 $mV \cdot s^{-1}$. (a) CV, multiple reduction cycles for **ec-Tetra-5**; (b) multiple oxidation cycles for **ec-Tetra-5**,(c) CV plot including both **ec-Tetra-5** oxidation and reduction; (d) UV-Vis absorption spectra of **ec-Tetra-5** in the neutral state. Adapted with permission from ref. [1] (Wiley 2019).*

The oxidative voltammetric pattern of **ec-Tetra-5** in a monomer free electrolyte indicates a stable behavior upon subsequent cycling in the potential region -0.7 and +0.7 V, exhibiting a broad oxidation wave peaking at 0.36 V with a shoulder at 0.44 V (Figure 4.36 b), electroactivity is lost by n-doping the redox film (Figure 4.36 a). The onset of oxidation of **ec-Tetra-5** obtained through the tangents method gives a value of +0.2 V, corresponding to a HOMO level at -5.3 eV while the optical bandgap calculated from the ICT band onset (λ_{onset}=625 nm) for **ec-Tetra-5** film is estimated at 1.98 eV. The potentiodynamic deposition of **Tetra-5** was also performed on a Pt working electrode, showing a similar CV pattern. Analogously as for chromophore **5**, the electrochemical oxidation of **Tetra-5** in 0.1 M CH_2Cl_2/NBu_4PF_6/is characterized with a single chemically reversible oxidation peak, assigned to the concomitant oxidation of the four independent push-pull units to the radical cation state, without involving irreversible follow-up reactions.

Uv-Vis spectroelectrochemistry shows the changes in the absorption spectra of an electrochemically crosslinked **ec-Tetra-5** film recorded during UV-Vis *in-situ*

spectroelectrochemical experiments for the forward oxidation scan. The UV-Vis absorption pattern of the electrodeposited tetramer in its neutral state (-0.26 V blue absorption spectrum) shows two maxima of absorption at wavelength 339 nm and 489 nm, respectively. The particularly intense band observed for the polymer film in its neutral state at 489 nm can be assigned to an ICT band, while the one at shorter wavelengths to a π–π* electronic transition, in agreement with TD-DFT calculations.

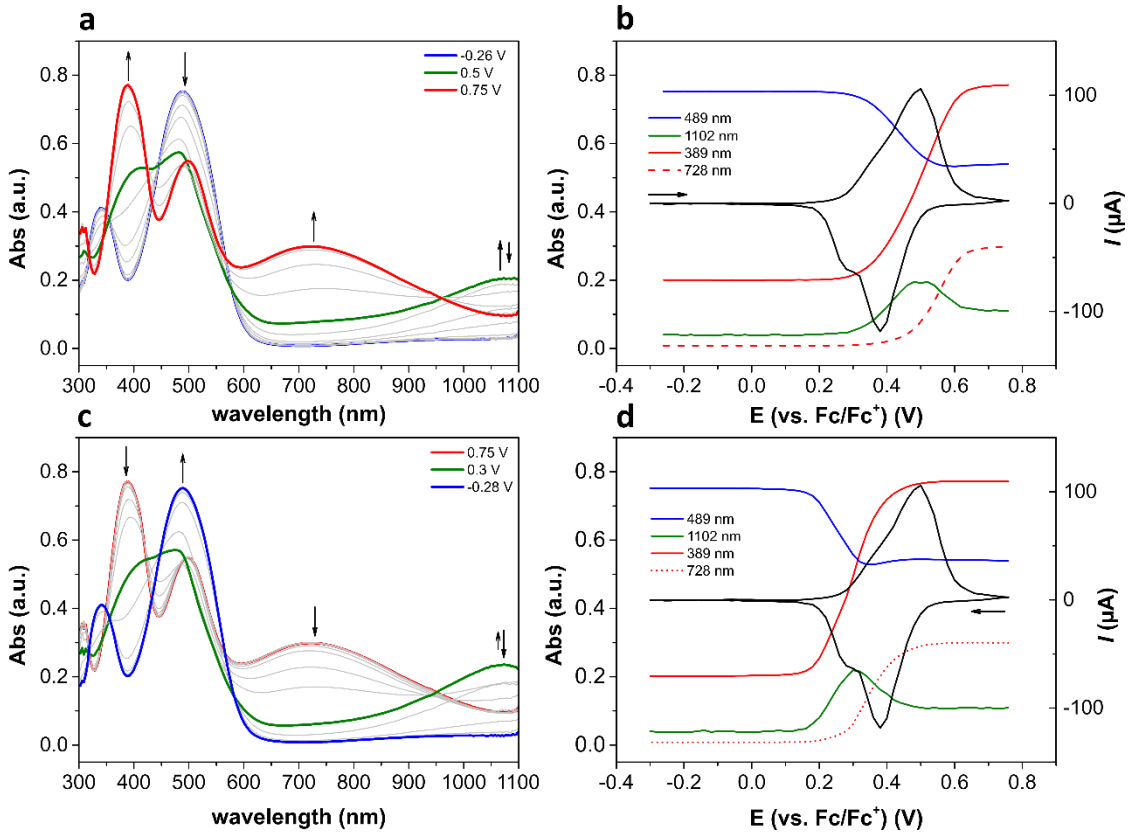

Figure 4.37: Thin-Film in-situ UV-Vis spectroelectrochemistry of ***ec-Tetra-5*** *in 0.1 M CH_2Cl_2/NBu_4PF_6, ITO; scan-rate 20 mV·s^{-1}. (a) UV-Vis absorption spectra as function of the potential for forward oxidation cycle; (b) Peak trend of elected wavelengths as function of the potential for forward oxidation cycle, overlap to CV plot. (c) UV-Vis absorption spectra as function of the potential for backward oxidation cycle; (d) Peak trend of elected wavelengths as function of the potential for backward oxidation cycle, overlap to CV plot. Adapted with permission from ref. [1] (Wiley 2019).*

The anodic polarization for values of potential between -0.26 and +0.5 V leads to the formation of a new absorption band, with maxima at wavelengths higher than 1050 nm together with the development of two new bands at 392 and 482 nm, respectively, and concomitant bleaching of the neutral bands at λ_{max} <350 nm and at 489 nm. The broad band with absorption maxima at 1102 nm in the NIR region generated for polarization potentials for values in between +0.3 and +0.56 V should be reasonably attributed to the radical cation state of the polymer. The progressive conversion of the neutral species into its radical cation state also results in an isosbestic point around 580–600 nm. By further increasing the oxidation potential of the polymer film to +0.75 V new absorption bands with maxima at 389,

500 and 728 nm are observed, with concurrent vanishing of the polaron band in the NIR. This new band generated at 728 nm should be reasonably attributed to the dication state of the polymer.

Comparing the spectroelectrochemical behavior of the electrodeposited **ec-Tetra-5** with the one of the dimer of chromophore **5** (Figure 4.37 c) strong similarities are observed in the variation of the absorption spectra upon oxidative polarization. These encountered similarities are consistent with the molecular structure and the similar electrochemical behavior observed upon oxidation. Both systems present a similar absorption pattern upon electrochemical oxidation. In particular, the absorption band at λ_{max} >1050 nm observed for the electrodeposited tetramer film and assigned to the radical cation state is also observed for the first oxidation peak, i.e oxidation to the radical cation of the dimer of chromophore **5**. Analogously, both systems present for higher values of oxidation potential a band around 700 nm, assigned to the dication state. These experimental observations are consistent with the fact that, independently from the number of monomer units constituting the electrochemically crosslinked tetramer film, the same dimethyl-diphenyl-benzidine redox unit is responsible for the electrochemical properties of the dimer of compound **5** and of **ec-Tetra-5**, although partially modulated by the degree of planarity and possible reciprocal chain interactions in the electrodeposited film of the latter.

4.1.4 Conclusions

In this chapter, the electrochemical behavior towards dimerization of different linear push-pull chromophores based on an arylamine redox-active unit is compared by cyclic voltammetry, DPV, thin-layer and thin-film spectroelectrochemistry. We found that the increase in the acceptor strength in a series of chromophores increases the reactivity towards dimerization and that the substitution of a Ph unit with a Me unit in the arylamine donor has a major impact on the reactivity. TD-DFT calculations were performed on the molecules in their neutral and charged state to try explaining the observed reactivity. We found that spin-density alone (Mülliken) does not completely explain the observed reactivity, but rather steric hindrance and geometrical factors must be taken in consideration. For the first time we also report correlations between the closed-shell nature of the dimeric-dication state, with the dimerization ability of arylamine based compounds. Correlations are also found by other benzidine molecules from the literature with regards to dimerization reactivity.[41,56] We think that further studies in this direction should be performed to further asset the correlation between OS and CS character of dimeric dications and dimerization ability of electrochemically generated radical cations. The study could be in this context expanded towards different monomer species, analyzing substitution effects. A detailed spectroelectrochemical characterization, also supported by theoretical calculations, is also

provided. This could be useful for the interpretation and development of electrochromic devices utilizing arylamine units as active material. Finally, the dimerization ability of arylamine-based chromophores is exploited to electrodeposit electroactive films of **Tetra-5**, which will be tested as in BHJ solar cells.

4.1.5 Experimental

4.1.5.1 *Electrochemical Measurements*

Electrochemical characterization of the chromophores was performed in a 0.1 M CH_2Cl_2 with NBu_4PF_6 as supporting electrolyte employing the electrochemical set-up described in section 3.1.1.1, at RT and under Argon atmosphere. A three-electrode glass cell provided with a Pt plate as counter electrode (CE) and an AgCl-coated silver wire as pseudo reference electrode (RE) were employed. As working electrode (WE) Au slide was employed. The surface area of the electrode was ~0.5 cm^2. Chromophore molecules were dissolved in 0.1 M CH_2Cl_2/NBu_4PF_6 to obtain 0.5 mM solutions; the molecule reactivity was characterized through cyclic voltammetry and differential pulse voltammetry (DPV). DPV measurements were performed with a scan-rate of 20 $mV \cdot s^{-1}$; and a modulation amplitude of 25 mV. All potential values are referred to the internal standard Fc/Fc^+ employed for calibration of Ag/AgCl pseudoreference.

4.1.5.1.1 Electrodeposition of Tetra-5 (ec-Tetra-5)

Electrodeposition was performed under potentiodynamic conditions in the potential window -0.69–0.69 V vs Fc/Fc^+ with 10 subsequent voltammetric cycles at a scan rate of 50 $mV \cdot s^{-1}$. For the oxidative electrodeposition of **Tetra-5** films on ITO a 0.2 mM monomer solution 0.1 M CH_2Cl_2/NBu_4PF_6 was employed. After the deposition, the films were rinsed with dichloromethane to remove the excess of monomer and electrolyte. For the determination of HOMO and LUMO values, the electrodeposited films were repeatedly cycled in a monomer free solution (0.1 M CH_2Cl_2/NBu_4PF_6; scan-rate 50 $mV \cdot s^{-1}$); with reduction (-0.71–0.70 V vs Fc/Fc^+) and oxidation (-0.71 – -2.4 V vs Fc/Fc^+) cycles performed separately. Electrodeposition and characterization of the film were performed under argon Atmosphere, all potential values are reported with respect to the internal standard Fc/Fc^+.

4.1.5.1.2 *In-Situ* Spectroelectrochemistry

In-situ spectroelectrochemistry of D-A push-pull molecules (**1**-**6**) was measured in thin layer conditions employing 0.5 mM chromophore solutions in 0.1 M CH_2Cl_2/NBu_4PF_6 at a scan-rate of 20 $mV \cdot s^{-1}$ with the experimental set-up described in section 3.1.1.2.1, employing a polished Pt disk as WE, a Pt wire as CE, and an Ag/AgCl coated wire as pseudoreference electrode. The measurements were performed under Argon atmosphere and all the potential values were referenced to the formal potential of the Fc/Fc^+ redox couple.

Thin-film *in-situ* spectroelectrochemical measurements of **ec-Tetra-5** were conducted in 0.1 M CH_2Cl_2/NBu_4PF_6 at a scan-rate of 20 $mV \cdot s^{-1}$ with the experimental set-up described in section 3.1.1.2.1 employing a ITO slide coated with the electrodeposited film as WE, a Pt wire as CE, and an Ag/AgCl coated wire as pseudoreference electrode. The measurements were performed under Argon atmosphere and all the potential values were referenced to the formal potential of the Fc/Fc^+ redox couple.

4.1.5.2 *Computational Methods*

Theoretical calculations here presented were performed by Prof. Carmen Ruiz Delgado and Sergio Gámez (University of Malaga). The optimum structures of the neutral and charged species of compounds **1**-**6** and their dimers were determined in CH_2Cl_2 using the PCM method. [57] All calculations were performed in the framework of the density functional theory (DFT) using the hybrid, generalized gradient approximation (GGA) functional B3LY[58,59] and the hybrid meta-GGA functional M06-2X[60] together with the 6-31G** basis set[61,62]. All geometrical parameters were allowed to vary independently apart from planarity of the rings. Harmonic frequencies calculations were performed on the resulting ground-state optimized geometries to ensure the finding of the global minimum.

4.1.6 Appendix to section 4.1

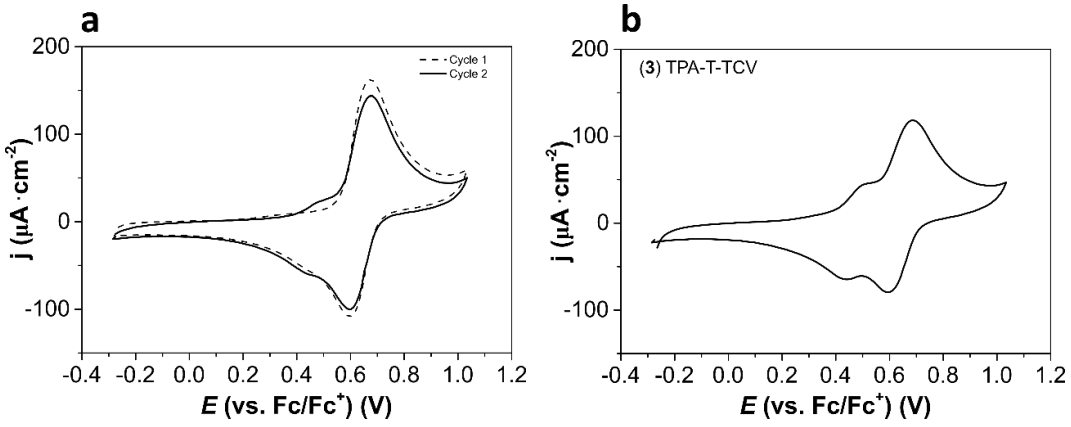

Figure 4.38: Chromophore 3, a) I and II voltammetric cycles, b) CV cycle after 60s potentiostatic holding at 0.8 V.

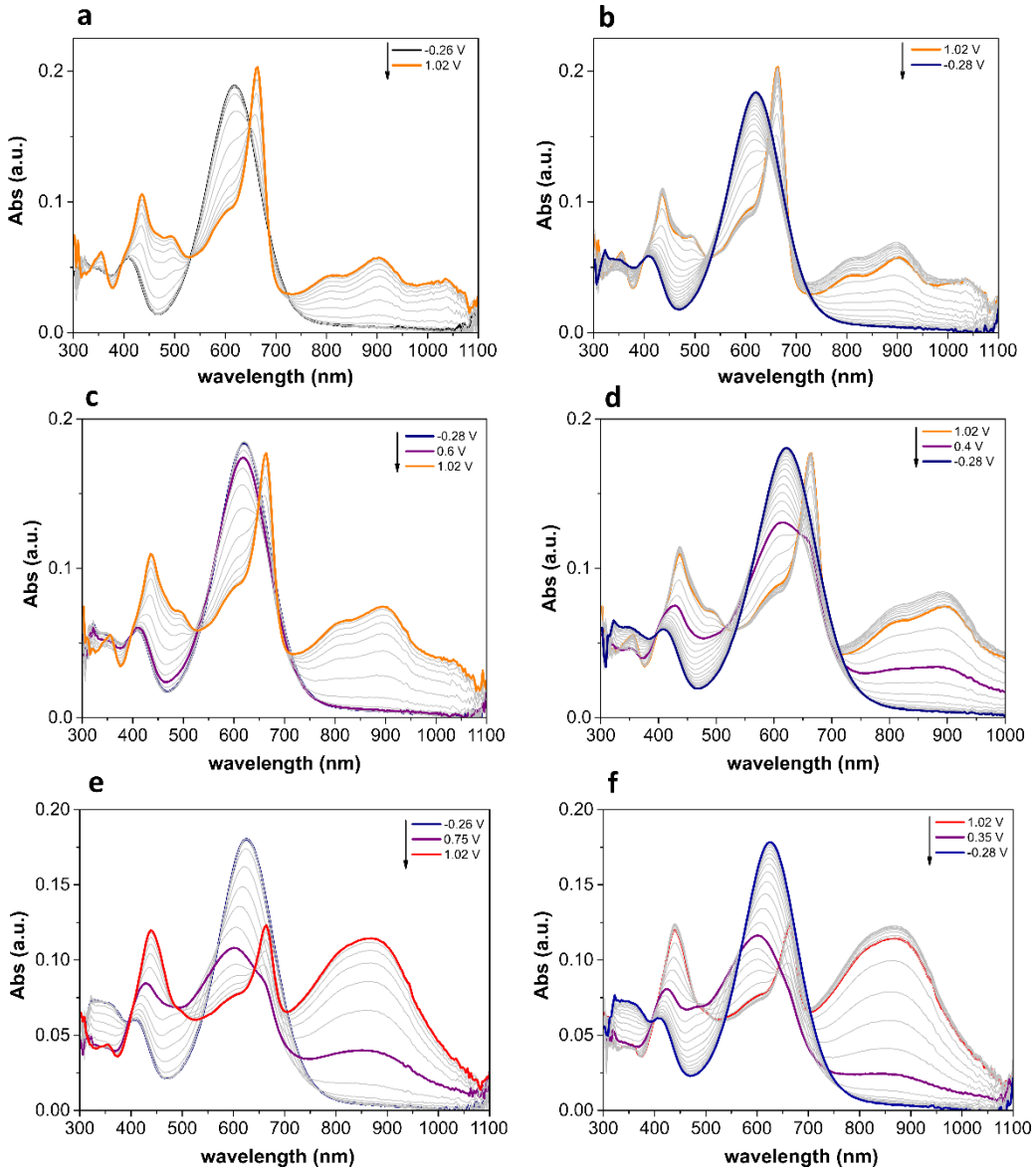

*Figure 4.39: Chromophore **3**, (a, b) in-situ spectroelectrochemistry of I cycle (c, d) II cycle and (e, f) cycle after holding the potential at 0.8 V for 60 s.*

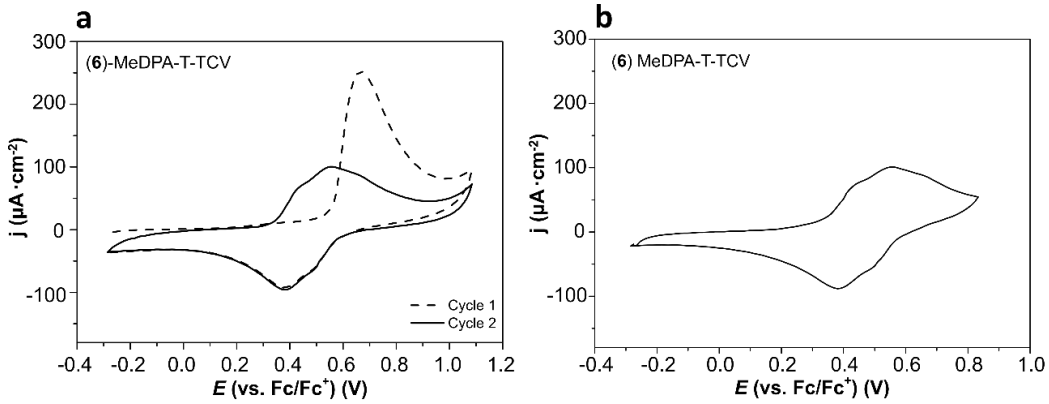

Figure 4.40: *Chromophore **6**, a) I and II voltammetric cycles, b) CV cycle after 60s potentiostatic holding at 0.8 V.*

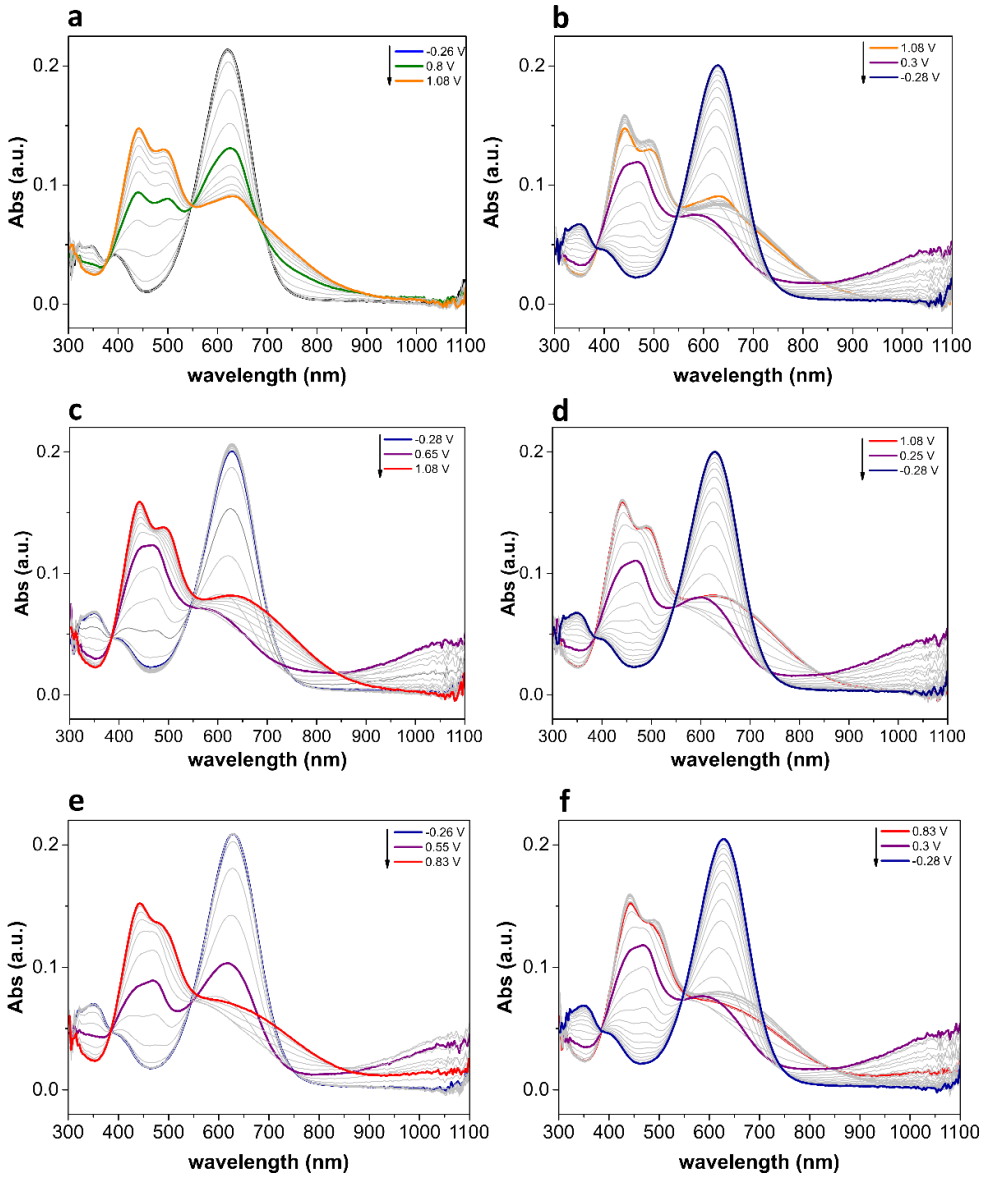

*Figure 4.41: Chromophore **6**, a) I and II voltammetric cycles, b) CV cycle after 60s potentiostatic holding at 0.8 V.*

4.2 Electrochemical Characterization of Atropoisomeric Compounds Based on Inherently Chiral 2,2'-Biindole Architectures with Oligothiophene Terminals

4.2.1 Introduction and Objectives

In this chapter a particular class of conjugated oligomers based on 2,2'-biindole architectures, and bearing oligothiophene terminals (Figure 4.42), is studied.[3] The molecules analysed are a new class of polyheterocycles presenting a biheteroaromatic atropoisomeric core with a C_2 stereogenic axis as dissymmetric stereogenic element. Due to the presence of an internal element of chirality, this class of molecules has been referred with the name "inherently chiral molecules".

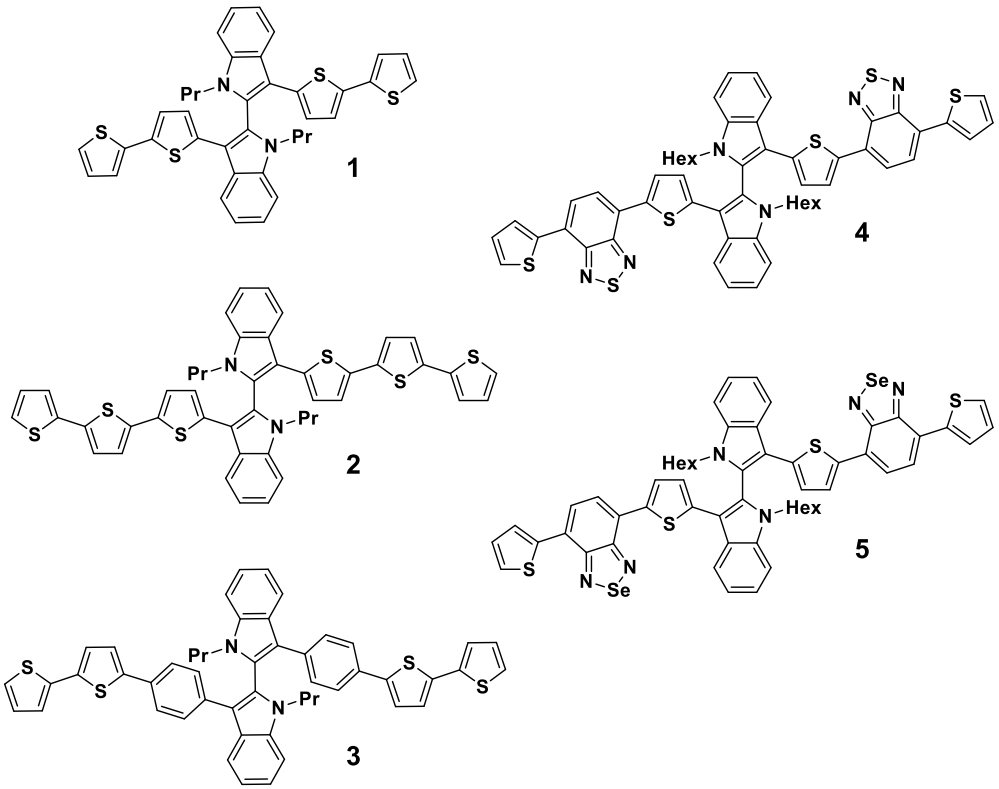

Figure 4.42: Atropoisomeric 2,2´-biindoles-3,3´diheteroaryls molecules studied in this chapter. ***1*** *(Ind$_2$T$_4$),* ***2*** *(Ind$_2$T$_6$),* ***3*** *(Ind$_2$Ph$_2$T$_4$),* ***4*** *(Ind$_2$T$_2$BTD$_2$T$_4$),* ***5*** *(Ind$_2$T$_2$BSeD$_2$T$_4$).*

Upon electrooxidation thin films of electroactive oligomers with interesting electronic properties can be obtained. Electrodeposition of these molecules can be achieved by oxidation of the two thienyl redox terminals, and leads to generation of films with well-defined π-conjugation and showing mixed-valence conductivity behavior.

The first example of inherently chiral molecules of this type was reported by F. Sannicolò *et al.* for the molecule 2,2'-bis(2,2'-bitiofene-5-il)-3,3'-bi-1-benzotiophene (BT_2T_4), which was designed to develop artificial chiral electrodes and sensors.[63,64] The employment of electroactive selectors and electrochemical methods for chiral analysis is

highly attractive because of the high sensitivity, selectivity and simplicity and ease of transduction of electrochemical methods, as well as of the possibility of *in-situ* analysis without previous separation steps. Starting from 3,3′-bithianaphthene based atropoisomeric oligomers, several classes of molecules have been designed utilizing different biheteroaromatic cores with the same concept of inherent chirality.[65,66] Examples include 3,3'-bithiophene; 2,2'-bisindoles; 3,3'-bipyridine and 1,1'-dibenzimidazole cores (Figure 4.43). These mojeties can be connected to side chains composed of oligo-thienyl units of different lengths and / or bearing substituents, allowing modulation of the solubility, as well as other properties.

A peculiarity of these atropoisomeric molecules, is that the presence of a C_2 symmetry axis makes the thiophene α-positions a homotopic site. In this way, upon oxidative coupling at this position, a complete regioregularity in the products is ensured, with each propagation step, resulting in fact in C_2 symmetric products. The molecules are designed in such a way that the biheteroaromatic core allows the conjugative interconnection of the oligothienyl moieties from one terminal to the other. Furthermore, the energy barrier associated with the interannular torsion is high enough to not be overcome at room temperature, to not have interconversion between the two chiral antipodes.[63,67]

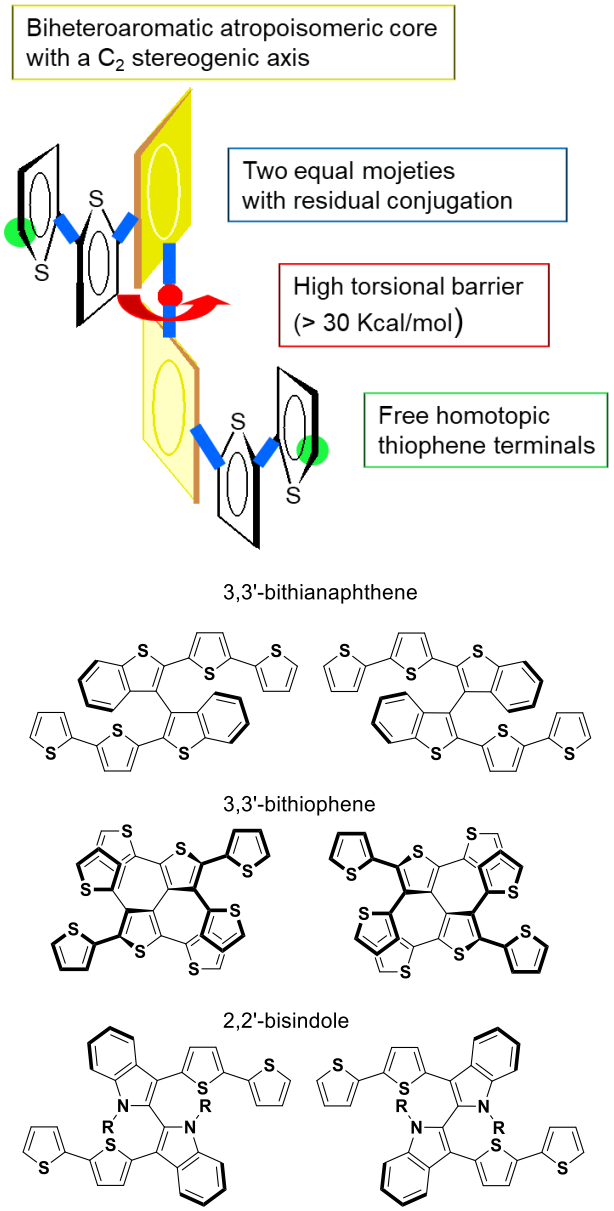

Figure 4.43: Different classes of chiral molecules based on an heteroaromatic atropoisomeric core: 3,3´-bithianaphthene, 2,2´-biindole and 3,3´-bithiophene each with optical antipodes.

A summary of the main properties of atropoisomeric molecules is listed below.

- High torsional angle barrier: they can be obtained as stable enantiopure antipodes and are endowed with a good three-dimensional oligomerization ability.
- Presence of two equal moieties with residual conjugation: the systems represent a case of a couple of equivalent redox centres, partially interacting through the central barrier and/or in the space. This results in twin peaks in the CV pattern, which distance is strictly related to the employed solvent and the moiety connectivity,
- Free homotopic thiophene terminals: which allows a high regioregularity in the electrodeposition.

As mentioned above, oligothiophenes based on a biheteroaromatic scaffold can be oxidized with activation of the two symmetric thienyl terminals generating higher order oligomers. Oxidation can be performed with chemical oxidants such as $FeCl_3$ generating oligomers of different lengths, including opened and closed structures, that can be utilized as mixture or as single components after column chromatography separation.[63,64,68] Via electrochemical oxidation the oligomerization products can be deposited directly on an electrode surface which can further be used as an electroactive layer, or in the form of self-standing membranes from, which has recently found application for analytical purposes.[69] This means that the oxidation products obtained from an enantiopure mixture will be enantiopure, bearing the same chirality sense of the starting monomer, and in the case of a starting racemate monomer solution the products will also be raceme.[67] In the racemate form the molecules can be treated as regular electrodeposited films sharing characteristics of oligo-thiophene systems, including facile and reversible charge-transfer ability, good charge transport, electrochromic and photoactive properties and a tunable redox-activity modulable by structure design.[63,64] Electroactive films obtained from enantiopure monomers, in addition to a reversible redox behavior also show significant chiral manifestation when exposed to a chiral environment, including circularly polarized light, chiral molecules etc., and particularly, electrochemical enantioselective abilities. [63,65] As example, Figure 4.44 (a) reports the HPLC resolution of the two enantiomers of (N-Me-Ind)$_2$-T_4 Figure 4.44 (b) the experimental Electronic Circular Dichroism (ECD) spectra of both enantiomers of (N-Me-Ind)$_2$-T_4 and Figure 4.3 (c). experimental Circularly Polarized Luminescence (CPL) spectra, showing for the two enantiomeric films two specular signals. Finally, an example of enantioseparation on the enantiopure film oligo-(S)-(N-Me-IND)$_2T_4$ towards (S)- and (R)-N,N-dimethyl-1-ferrocenylethylamine (Fc S and Fc R, dashed and solid lines, respectively) is showed in Figure 4.44 (d). In this case, two well defined and separated signals are reproducibly found for the reported electrodeposition conditions, with a shift of several hundreds of mV for the oxidation peak of the two enantiomers of the ferrocenyl probe.

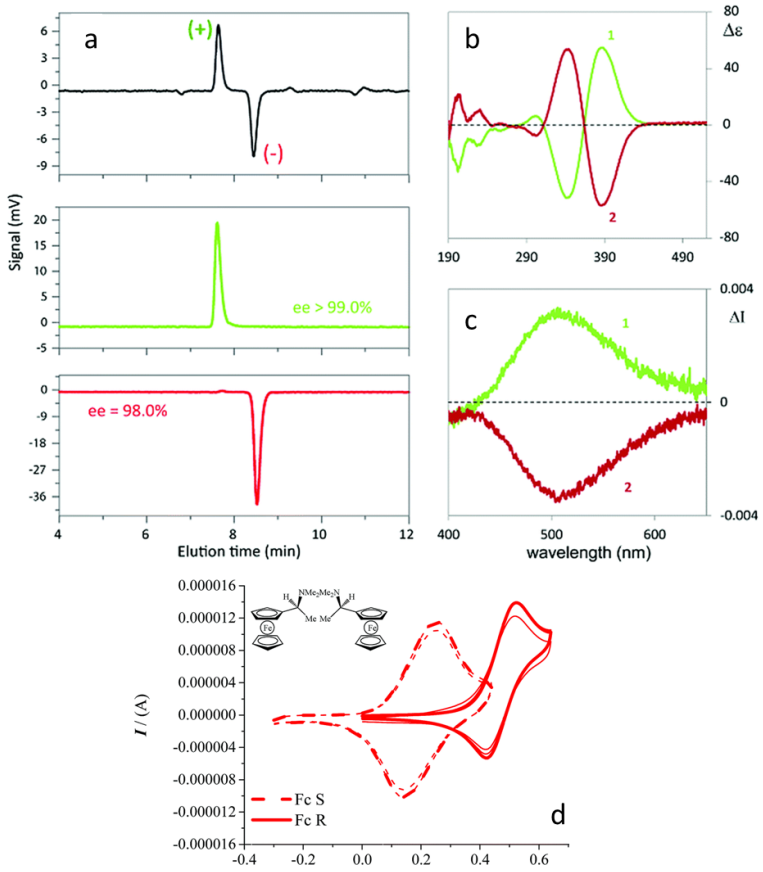

Figure 4.44: (a) Analytical HPLC resolution of (N-Me-Ind)$_2$-T$_4$. (b) Experimental Electronic Circular Dichroism (ECD) spectra of both enantiomers of (N-Me-IND)$_2$-T$_4$; I and II designate the elution order. (c) Experimental Circularly Polarized Luminescence (CPL) spectra. (d) Enantioselection on the enantiopure film oligo-(S)-(N-Me-IND)$_2$T$_4$ towards (S)- and (R)-N,N-dimethyl-1-ferrocenylethylamine (Fc S and Fc R, dashed and solid lines, respectively. Adapted with permission from ref. [67] (Copyright RCS 2019).

Due to the presence of only residual conjugation between the oligthienyl-units, the atropoisomeric core makes all oxidation products a collection of redox active oligomers of similar effective conjugation lengths, characterized by slightly different oxidation energies. As consequence of this partial conjugation between the interannular bond, electroactive films obtained from oxidation of biheteroaromatic atropisomeric molecules behave as mixed valence-film with limited potential-dependent conductivity windows.[70]

Whereas this class of atropoisomeric molecules and the correlated oligomerization products have been at this point deeply characterized in terms of chiroptical and enantioselective ability, their characterization as redox films, electrochromism and conductance is limited and only devoted to the 3,3'-bithianaphtene based system, presented on a preliminary work by T. Benincori *et al.*[12] in which the electrochemical and spectroelectrochemical behavior of bithianaphthene based oligothiophenes, BT$_2$T$_4$, and of a structural analogue based on EDOT-substituted bithianaphthene, BT$_2$E$_4$, are presented.

Recent studies on inherently chiral compounds have focused on oligothiophenes based on a 2,2'-biindole atropoisomeric scaffold. It has been observed that the performances as

chiral selector of enantiopure (*N*-Me-Ind)$_2$T$_4$ films are superior to the ones of BT$_2$T$_4$ analogues.[71] Additionally, they allow easier tunability of reactivity and solubility by direct substitution at the N atom. On these bases, development and study of new inherently chiral 2,2'-biindole-based materials is highly attractive.[72] 2,2'-biindoles molecules based on structural modification of the prototype molecule **1** have been synthetized (Dr. Scapinello, Università dell'Insubria) (Appendix). Analysis of the redox, spectrolectrochemical and conductivity behavior of this class of molecules was performed, focusing on the following structural modifications:

- addition of a π spacer between 2,2'-biindole backbone and the bi-thienyl substituent (T$_2$); compounds **2** (Ind$_2$T$_6$) and **3** (Ind$_2$Ph$_2$T$_4$).
- introduction of an acceptor unit within the thienyl terminals to yield donor-acceptor (D-A) oligomers; compounds **4** (Ind$_2$T$_2$BTD$_2$T$_2$) and **5** (Ind$_2$T$_2$BSeD$_2$T$_2$).

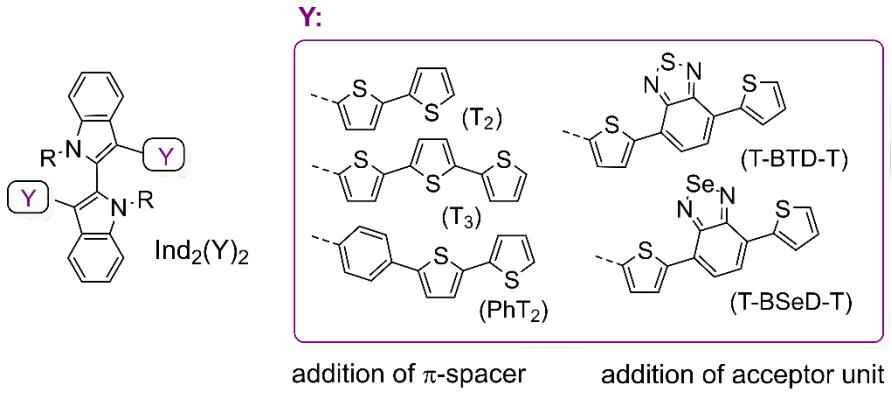

Figure 4.45: Schematization of molecules analyzed in chapter 4.

A systematic electrochemical analysis of monomers **1** to **5** and of the corresponding electrodeposited films (**oligo-1** to **oligo-5**) was performed. In particular, combined electrochemical methods are carried out to study the doping process of electrodeposited films obtained from racemic mixtures of the monomers. Further, characterization of electrochromic properties of racemate electrodeposited films was performed via charging and discharging cycles. Finally by cooperation with the group of Prof. Mussini of the University of Milan, the enantiodiscrimination ability of an enantiopure **oligo-2** films towards a benchmark chiral ferrocenyl-probe was also assessed. The results reported in this section can also be found in the publication *ChemElectroChem* **2021**, *8*, 3250–3261.

4.2.2 2,2´-Biindoles-3,3´-Diheteroaryls with Different π-Spacers (1-3)

Structure-property relationships upon structural modification of the prototype molecule **1** by addition of a π spacer between 2,2'-biindole backbone and the bithienyl substituent (T_2) are analysed at first in molecules **2** and **3**.

4.2.2.1 *Characterization of (1) Ind_2T_4, (2) Ind_2T_6 and (3) $Ind_2Ph_2T_4$*

4.2.2.1.1 UV-Vis Spectroscopy

The absorption spectra of compounds **1**, **2** and **3** are reported in Figure 4.46. The characteristic maximum wavelengths λ_{max} and extinction coefficients ε_{max} are reported in Table 4.5. All compounds show a maximum around 220 nm and another band at ~400 nm, both can be attributed to the π - π* transitions.[73] More precisely, the observed transitions seem to result from intra-molecular charge transfer transitions (ICT) from the π system of the pyrrole ring of the core to the π* of the oligothiophene wings as evidenced by DFT calculations.[72] The absorption spectra of compounds **1** and **3** appear very similar in shape with only small variations of the absorption maximum λ_{max} at ~400 nm. In general, the λ_{max} are comparable with tabulated literature values for π - π* transitions of bithiophene and terthiophene units.[74]

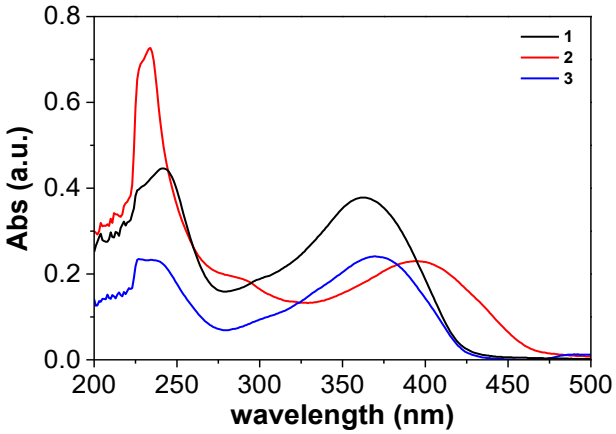

*Figure 4.46: Absorption spectra of 1.5 mM solutions of (**1**) Ind_2T_4 (black curve); (**2**) Ind_2T_6 (red curve) and (**3**) $Ind_2Ph_2T_4$ (blue curve) in CH_2Cl_2. Adapted with permission from ref. [3] (Wiley 2021).*

Considering the increase in the number of the thienyl arms from two to three, a red shift of 31 nm with increase of the conjugation is observed for compounds **1** to **2**, respectively. The introduction of the phenyl spacer induces a small increase of the absorption maximum of only 9 nm in comparison to the addition of a terthiophene unit. This is regarded as consequence of a less efficient conjugation of the phenyl unit.[75]

4.2.2.1.2 Electrochemical Characterization and Electrodeposition

The electrochemical characterization of compounds **1**, **2** and **3** was performed in 0.1 M NBu_4PF_6/CH_2Cl_2 with a monomer concentration of 0.5 mM. The CVs of the biindole

molecules, obtained by cycling around the different oxidation peaks and their over-imposition are presented in Figure 4.47 (**1**); Figure 4.48 (**2**) and Figure 4.49 (**3**). For a direct comparison and a better resolution of the oxidation peaks, differential pulse voltammetry (DPV) was also carried out during the forward oxidation sweep. All the electrochemical analysis presented in the following is performed on the molecules and oligomers in their racemate form.

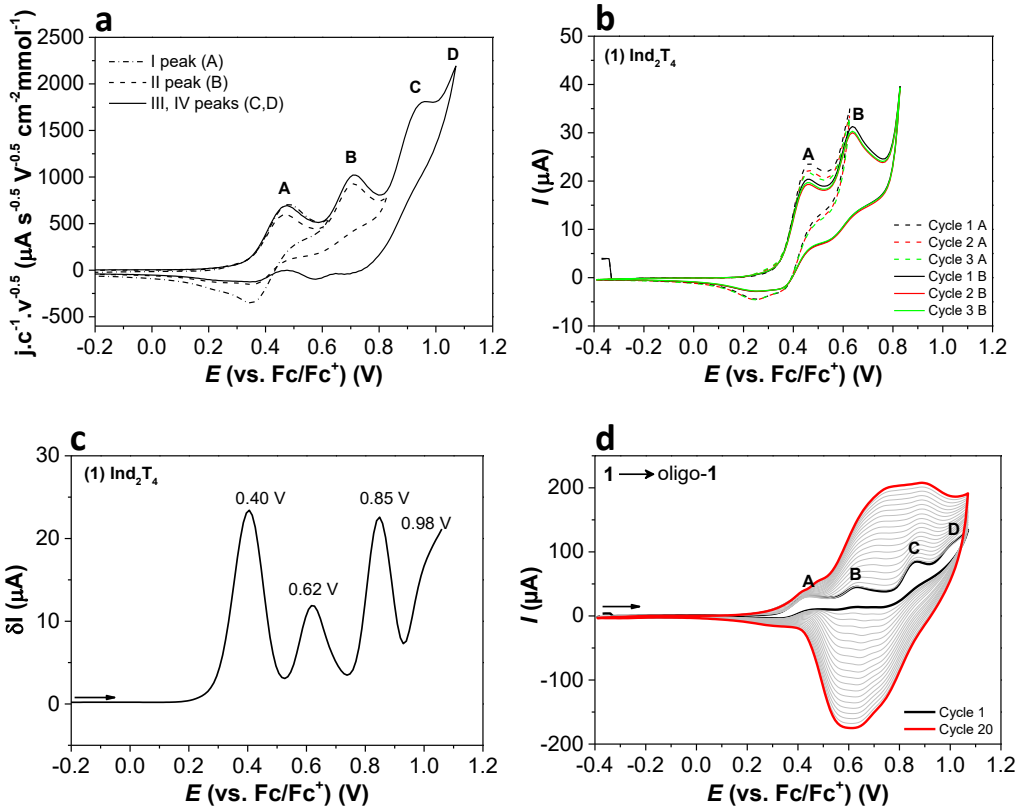

*Figure 4.47: Molecule **1** - Ind_2T_4 : (a) CV signals registered at 20 mV/s including oxidation peaks A-D, first cycle is reported. Current values are normalized by the square-root of the scan-rate, surface area and analyte concentration. (b) Multiple CV cycles obtained by cycling around the first and second chemically reversible oxidation peaks at 20 mV/s. (c) Differential pulse voltammetry (DPV) of molecule **1** registered for the oxidation, forward direction, with a scan-rate of 20 mV/s and a modulation amplitude of 25 mV. (d) Electrodeposition of **1** to yield **oligo-1**. All measurements are performed on ITO electrode in CH_2Cl_2/NBu_4PF_6 0.1 M, with a molecule concentration of 0.5 mM. Adapted with permission from ref. [3] (Wiley 2021).*

For all three molecules the oxidative CV patterns are characterized by multiple peaks. The featured voltammetric shape is a consequence of the molecular structure and particularly of the molecular symmetry, which results in the presence of two equivalent partially interacting pyrrole and oligo-thiophene redox sites. Considering the structural differences between the compounds, a first couple of peaks, A and B respectively, results in reversible oxidation and no electrodeposition. Supported by previous calculations,[67] and the fact that no oligomerization is possible by oxidation around this first set of peaks (Figure 4.47, Figure 4.48 and Figure 4.49 b), the oxidations associated with these two signals A and B should be localized on the more electron-rich indole moieties with only partial

delocalization on the oligo-thiophene system. That suggests that the two peaks belong to the two interacting radical cations which are localized on both indole centers, i.e. two $IndT_2$, $IndPhT_2$ and $IndT_3$ partially interacting redox sites. Scheme 4.1 exemplarily shows the scheme for the oxidation steps of compound **2**.

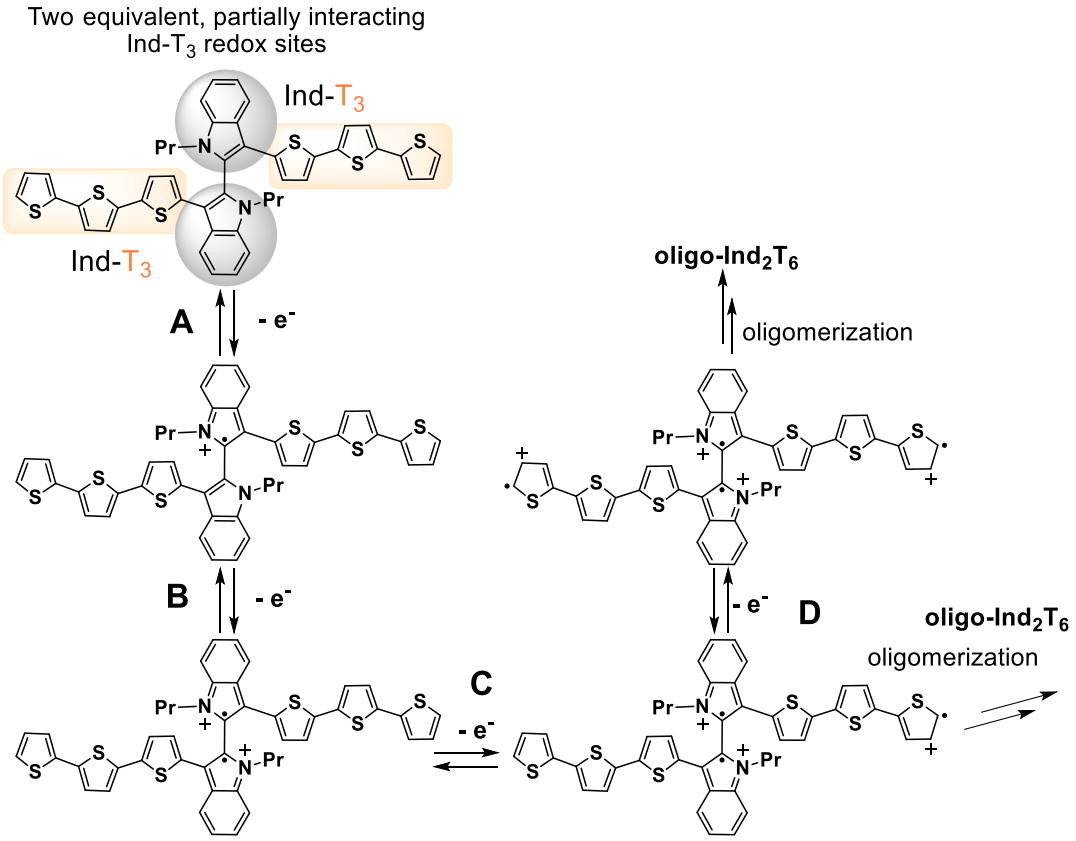

*Scheme 4.1: Oxidation mechanism for (**2**) Ind_2T_6 with reference to CV peaks, evidencing oxidation on the two partially interacting redox sites Ind_2T_3. Adapted with permission from ref. [3] (Wiley 2021).*

The electrochemical behavior of this class of molecules is extremely dependent on the nature of the solvent.[64,67] In a previous work, it was found that the observed peak-splitting is strongly dependent on solvent polarity; indeed, the use of a solvent such as CH_3CN having a higher dipolar moment, and consequently, a higher charge screening ability than CH_2Cl_2 results in the "twin peak merging". Charge generation on the two symmetrical units of the molecule is affected by greater shielding and stabilization, reducing the effects of space interactions and partial conjugation. In this case, only two oxidation peaks are observed upon complete molecule oxidation, the first one associated with concurrent activation of the two pyrrole units on the biindole core and the second of concurrent activation of the thiophene oligomers. This fact, together with the solvatochromism observed in UV-Vis experiments, hint to a charge transfer character of the transitions between the electron-rich biindole core and the thiophene wings.[72] The second

set of peaks, C and D, obtained by polarizing the WE at more positive potentials corresponds to the activation of the thiophenes terminals. This oxidation leads in CH_2Cl_2 to the deposition of an electroactive film by the coupling of the so generated radical cations, generating oligomers of higher order which nucleate on the electrode surface.[51,72] Also in this case, the choice of a more polar solvent such as CH_3CN stabilizes the formed charged species and no oligomerization process is observed. Examples of solvent influence on the radical-cation reactivity towards dimerization can be found in the literature.[25,72]

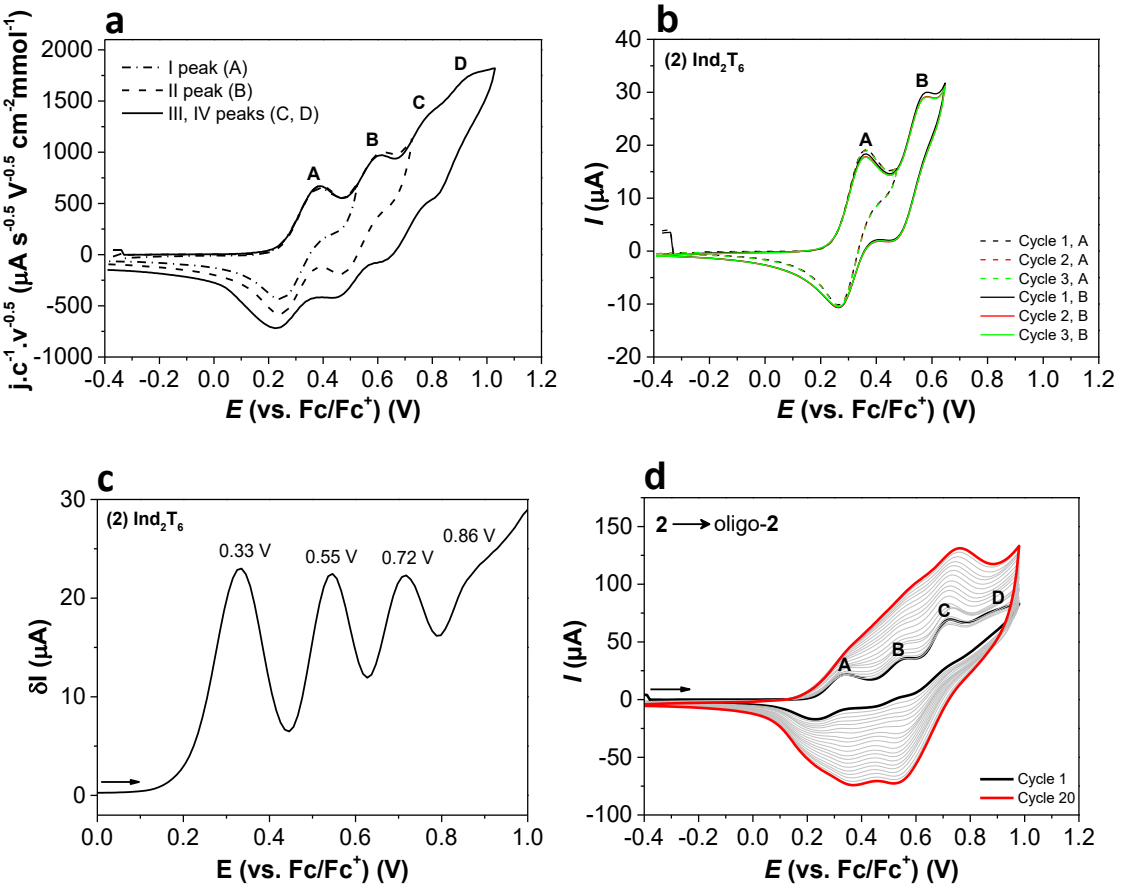

*Figure 4.48: Molecule **2** - Ind_2T_6 : (a) CV signals registered at 20 mV/s including oxidation peaks A-D, first cycle is reported. Current values are normalized by the square-root of the scan-rate, surface area and analyte concentration. (b) Multiple CV cycles obtained by cycling around the first and second chemically reversible oxidation peaks at 20 mV/s. (c) DPV signal, forward scan, for the oxidation of **2** at 20 mV/s and a modulation amplitude of 25 mV. (d) Electrodeposition of **2** to yield **oligo-2**. All measurements are performed on ITO electrode, CH_2Cl_2/NBu_4PF_6 0.1M with a monomer concentration of 0.5 mM. Adapted with permission from ref. [3] (Wiley 2021).*

For both molecules **1** and **3** the chemical reversibility of peak B is lower than for peak A, this might be explained by the higher density of charge that needs to be partially delocalized on the reactive thienyl side-groups. In the case of molecule **2**, having a higher number of conjugated units the chemical reversibility is increased for both peaks, A and B, of the indole-localized oxidation. This fact might be explained by the higher stability of T_3 units in comparison to T_2 and Ph-T_2 units.[51]

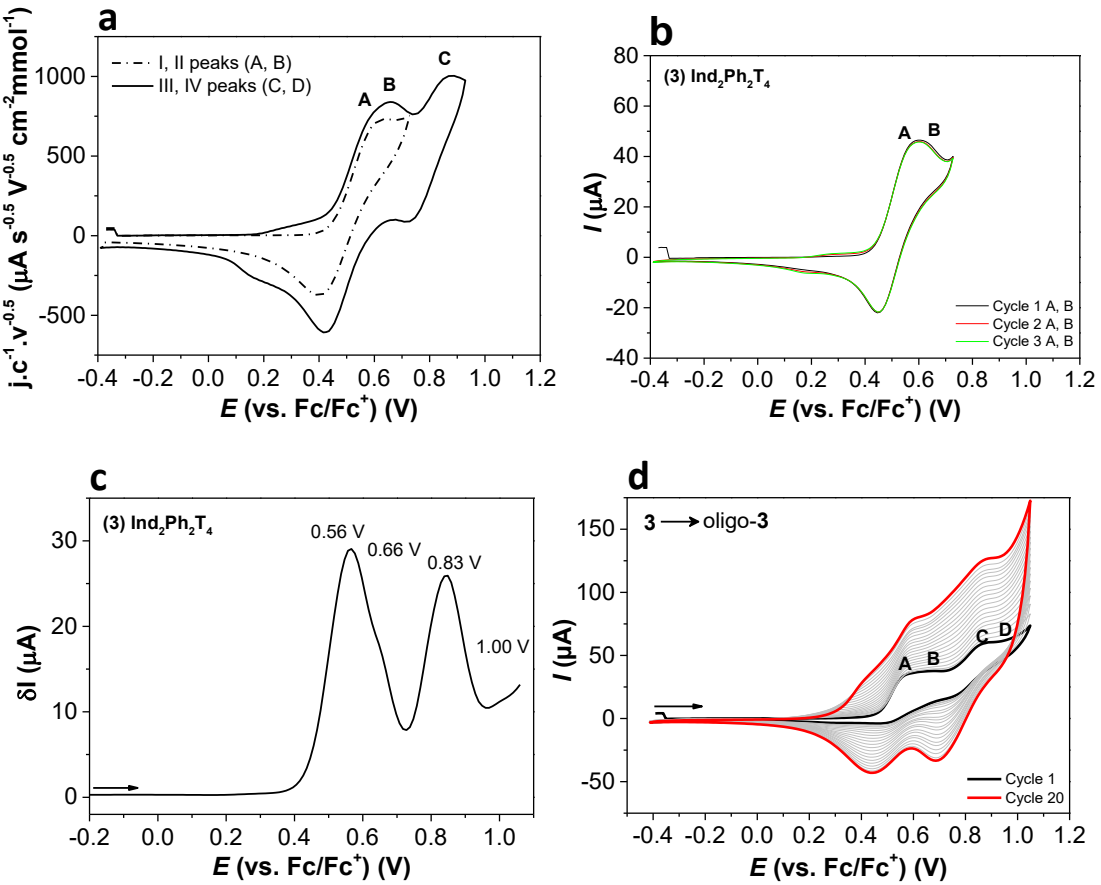

*Figure 4.49: Molecule **3** - $Ind_2Ph_2T_4$: (a) CV signals registered at 20 mV/s including oxidation peaks A-C, first cycle is reported. Current values are normalized by the square-root of the scan-rate, surface area and analyte concentration. (b) Multiple CV cycles obtained by cycling around the first and second chemically reversible oxidation peaks at 20 mV/s. (c) DPV signal, forward scan, for the oxidation of **3** at 20 mV/s and a modulation amplitude of 25 mV. (d) Electrodeposition of **3** to yield **oligo-3**. All measurements are performed on ITO electrode, in CH_2Cl_2/NBu_4PF_6 0.1M with a monomer concentration of 0.5 mM. Adapted with permission from ref. [3] (Wiley 2021).*

Table 4.5 collects the peak potentials (E_p) from the DPV experiments of all analyzed compounds. The CV and DPV measurements registered for compounds **1** and **2** present strong similarities with each other. The first couple of peaks A and B shows for both molecules a similar peak-to-peak potential separation $\Delta E_{pB\text{-}pA}$ of 22 mV. For molecule **1** E_{pA}(**1**) = 0.44 V and E_{pB}(**1**) = 0.62 V and for **2** E_{pA}(**2**) = 0.33 V and E_{pB}(**2**) = 0.55V are measured. In the case of the phenyl substituted molecule **3**, this separation is significantly lower with $\Delta E_{pB\text{-}pA}$ around 10 mV, with E_{pA}(3) = 0.56 V and E_{pB}(3) = 0.65 V, and shifted towards more positive potentials, compared to the second oxidation peak of **1**. Further, in the case of compound **3** the fourth oxidation peak (D) is not observed from the CV experiments as for compounds **1** and **2**.

For a higher conjugation efficiency between equivalent redox centers, a higher peak potential separation is expected. An explanation to the smaller separation of peaks A and B of compound **3** could be attributed to a slightly higher torsion between the two moieties

resulting from the presence of a phenyl group, more sterically hindered in comparison to the thiophene units. In these atropoisomeric systems indeed, the conjugation efficiency is inversely proportional to the torsional angle.[63,72] Further, In the case of molecule **3** a decrease in the molecular planarity and communication is expected from introduction of the less efficient π-linker. The phenyl linker is indeed associated with a higher degree of aromaticity, which makes the latter a less efficient π-spacer in comparison to the thiophene unit.[75]. The structural similarity of **1** and **2** and the good correlation in their peak-to-peak separation suggests overall a similar degree of interaction between the two symmetric moieties, in accordance with their similar structures. The lower oxidation potential for all oxidation peaks of compound **2** with respect to **1** and **3** correlates well with the higher conjugation of the T_3 in comparison to the T_2 and PhT_2 units. The peak-to-peak separation encountered for the second couple of peaks of oxidation, C and D, respectively, is overall lower than in the case of the oxidation at the biindole core, peaks A and B. No reduction signal is observed for all the three molecules upon reduction in CH_2Cl_2.

As previously mentioned, potentiodynamic cycling around the peaks associated with activation of the thienyl alpha terminals of the molecules, *i.e.* peaks C and D, results in electrodeposition of oligomers on the electrode surface. Examples of electrodeposition of compounds **1**, **2** and **3** performed in racemate monomer solutions by subsequent potentiodynamic cycles are presented in Figure 4.47 (d), Figure 4.48 (d) and Figure 4.49 (d). The film growth appears for all the species rather regular with a reversible CV pattern also for a higher number of cycles. In all cases, upon potentiodynamic oxidation some of the oxidized monomers were observed to diffuse away from the electrode surface. After electrodeposition, the samples were carefully rinsed with dichloromethane to remove excess of monomer and electrolyte, they were then dried and stored in inert atmosphere. Scanning electron microscopy (SEM) on electrodeposited shows rather homogeneous surface deposits, with film thickness determined by atomic force microscopy between 200-300 nm in the case of samples deposited at 20 mV/s, the associated data can be found in Figure 4.50, Figure 4.51 and Figure 4.52.

Due to the presence of the atropoisomeric scaffold, the effective conjugation length between the two symmetric units of the molecule is limited. The electroactive film can be therefore regarded as a collection of “localized” redox units.[76] A direct determination of the film composition by MALDI was not possible as the electrodeposited films were obtained in a partially charged state. Considering the structural similarities with (*N*-Me)Ind_2T_4 [72], we expect that the herein electrodeposited film are constituted by a series of oligomers with the same conjugation length, namely **oligo-1**, **oligo-2** and **oligo-3**, in the form of open and closed oligomers.[64,72,76] In particular, a similar outcome was obtained after chemical oxidation with $FeCl_3$ in $CHCl_3$ of (*N*-Me-Ind)$_2T_4$, from which it was possible to purify the

closed dimer.[72] The specific composition of each film might depend on the deposition conditions including scan-rate, monomer concentration or substrate nature.

Molecule	λ_{max} (nm)	ε_{max} ($L \cdot mol^{-1} \cdot cm^{-1}$)	E_p from DPV (V *vs* $Fc|Fc^+$)			
			A	B	C	D
1	364	44286	0.40	0.61	0.84	0.99
2	395	17958	0.33	0.53	0.70	0.85
3	373	36400	0.56	0.65	0.85	1.0

Table 4.5 Summary of absorption measurements and oxidation E_p from DPV experiments; analyte concentration 0.5 mM in CH_2Cl_2/NBu_4PF_6 0.1 M on ITO electrode; scan-rate 20 mV/s, voltage amplitude (ΔE) of 25 mV. $E^{\ominus} = E_p - \frac{\Delta E}{2}$ for reversible peaks.

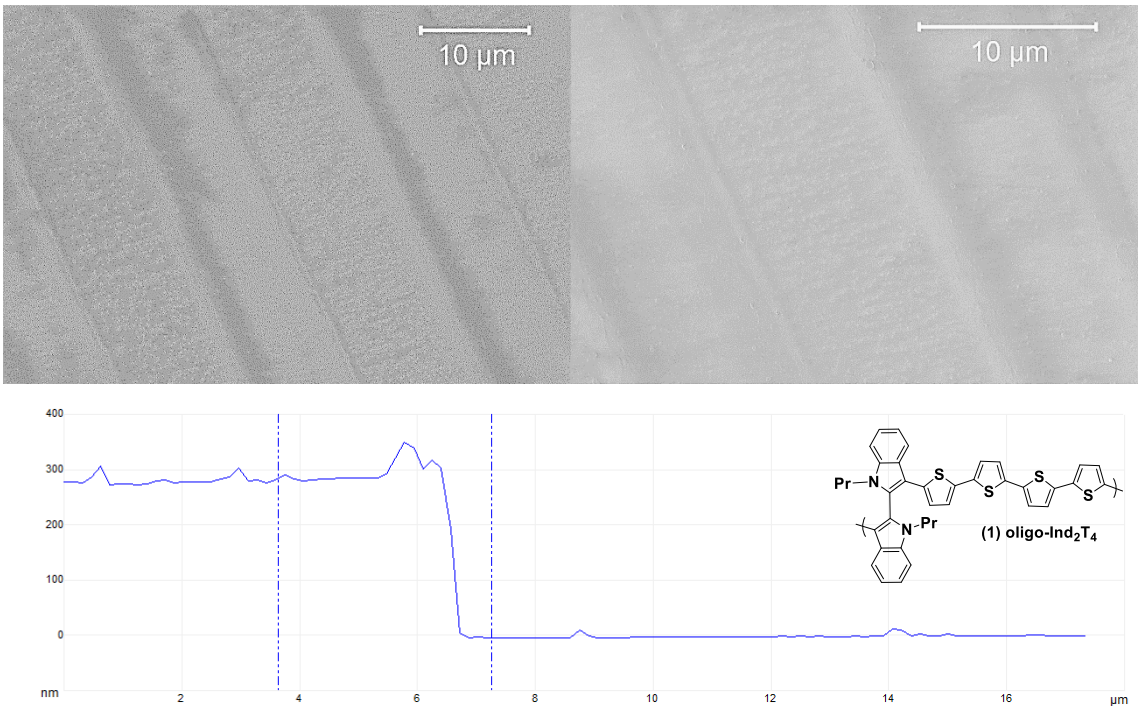

*Figure 4.50: SEM picture of **oligo-1** electrodeposited with a scan-rate of 20 mV/s on Pt-IDE electrode with 10 µm spacing (EHT 0.900 kV, In-Lens signal) (top). Film thickness measured by AFM in tapping mode on coated ITO substrate for **oligo-1** (bottom). Adapted with permission from ref. [3] (Wiley 2021).*

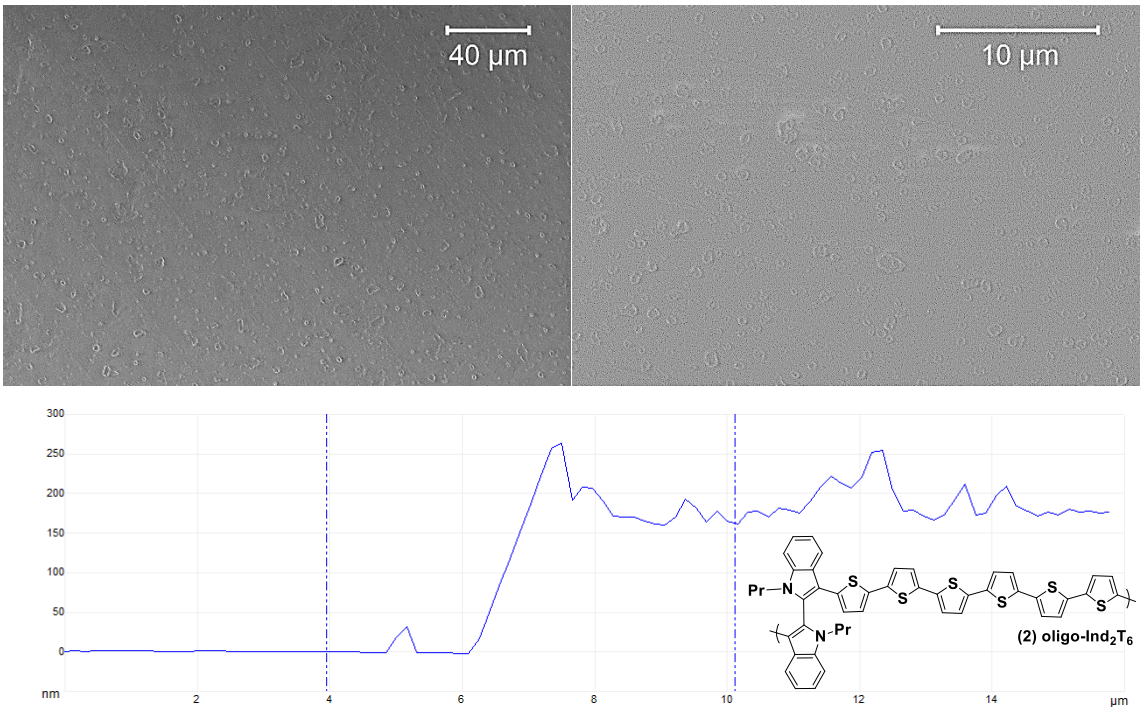

*Figure 4.51: SEM picture of **oligo-2** electrodeposited with a scan-rate of 20 mV/s on Pt-IDE electrode with 10 µm spacing (EHT 0.500 kV, In-Lens signal) (top). Film thickness measured by AFM in tapping mode on coated ITO substrate for **oligo-2** (bottom). Adapted with permission from ref. [3] (Wiley 2021).*

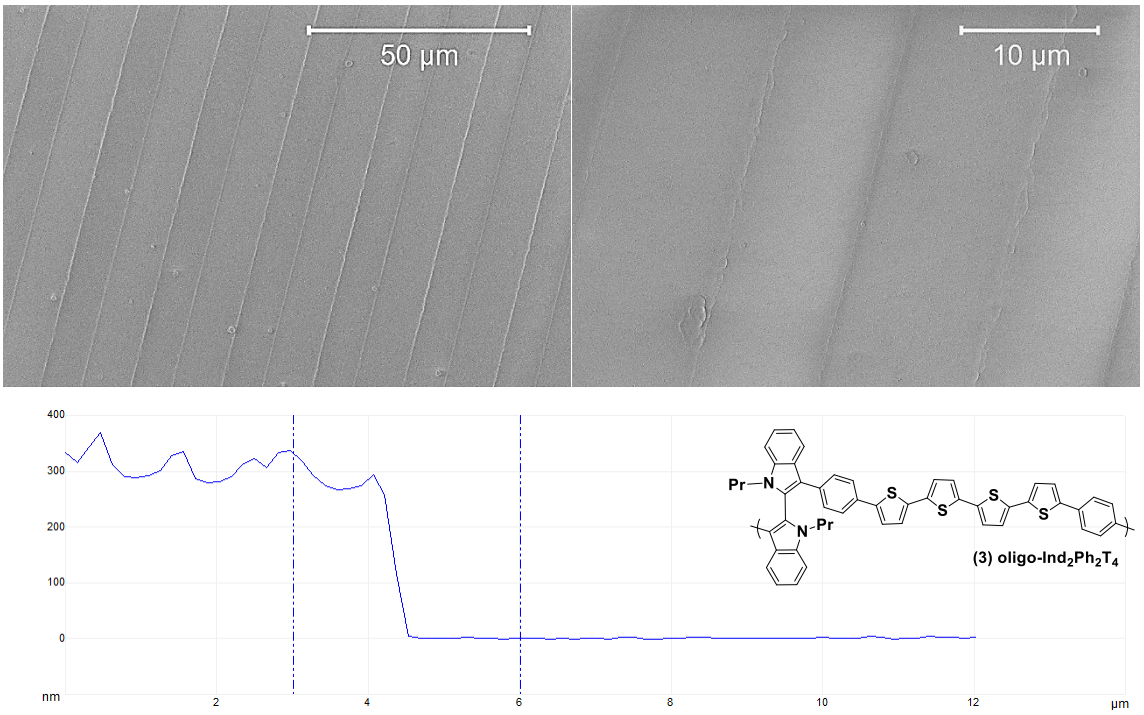

*Figure 4.52: SEM picture of **oligo-3** electrodeposited with a scan-rate of 20 mV/s on Pt-IDE electrode with 10 µm spacing (EHT 0.800 kV, In-Lens signal) (top). Film thickness measured by AFM in tapping mode on coated ITO substrate for **oligo-3** (bottom). Adapted with permission from ref. [3] (Wiley 2021).*

4.2.2.2 *Characterization of Oligo-(1-3)*

Due to the presence of the atropoisomeric scaffold, the efficient conjugation length between the two symmetric units of the molecule is limited and the electroactive film should be regarded as an oligomeric film. If no oxidation at the thiophene β-position is taking place, the electrodeposited film should be constituted by a series of oligomers with the same conjugation length: Ind-T_4-Ind; Ind-Ph-T_4-Ph-Ind and Ind-T_6-Ind, respectively.

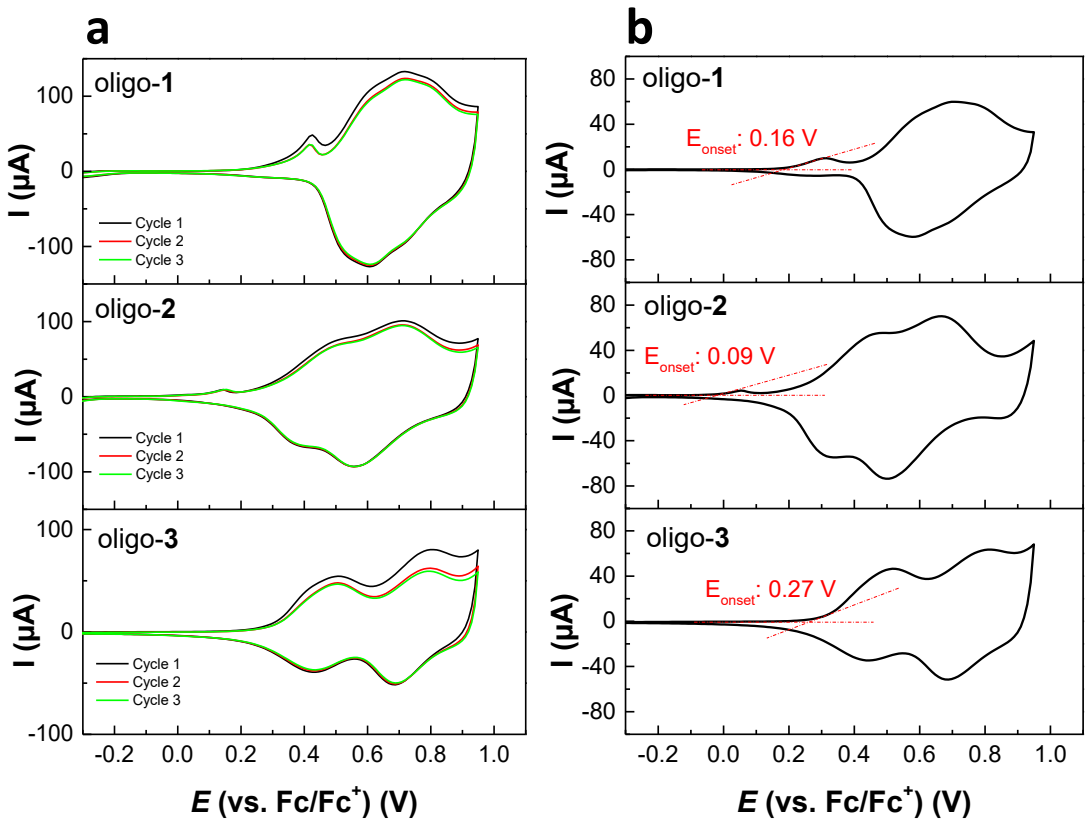

*Figure 4.53: (a) three subsequent CV oxidation cycles of **oligo-1**; **oligo-2** and **oligo-3**; 20 mV/s in 0.1 M CH_2Cl_2/NBu_4PF_6, Au electrode. (b) II oxidation cycle; 20 mV/s in 0.1 M CH_2Cl_2/NBu_4PF_6, ITO electrode. Adapted with permission from ref. [3] (Wiley 2021).*

The electrochemical behavior of the deposited films upon cyclic voltammetry was studied in the same medium of electrodeposition 0.1 M CH_2Cl_2/ Bu_4NPF_6. The associated data are presented in Figure 4.53. The CV of **oligo-2** on ITO substrate shows two main oxidation waves with half-wave potentials of 0.39 V and 0.58 V. The analysis of the CV signal registered on other electrode substrates (Au and ITO, Figure 4.53) also presents a reversible signal at 0.22 V. In the case of **oligo-1** three well distinguished oxidation waves with half-wave potentials 0.30 V, 0.54 V and 0.75 V are measured. In the case of **oligo-3**, the CV shows two reversible oxidation waves with half-wave potentials of 0.47 V and 0.74 V. The oxidation of the oligo-thiophene of the electrodeposition products takes place with completely or partial superimposition to the biindole core oxidation as consequence of the

increase in conjugation length after oligomerization. Analogously, the oxidation localized on the indole core shifts towards less positive potentials.

The electrochemical onset for oxidation obtained via tangent methods (Figure 4.53 b), corresponds for **oligo-1** to a potential value of 0.16 V; for **oligo-2** to a potential value of 0.09 V and for molecule **3** to a potential value of 0.27 V. The onset of oxidation in the case of **oligo-1** and **oligo-2** is defined by the redox-activity of the biindolic core. In the case of **oligo-1**, an almost baseline separated peak is measured at 0.30 V, which is 10 mV shifted at lower potential values in comparison to the biindole oxidation in the corresponding monomer **1**, see *Table 4.5*.

The hexathiophene oxidation (radical cation) of **oligo-2** is almost completely superimposed to the oxidation centered on the biindole, for which only a shoulder at 0.20 V is measured. In the case of **oligo-3** the oxidation at the level of radical cation for the terthiophene is completely superimposed to the biindole centered oxidation. Figure 4.58 schematizes the different states of charge obtained with increasing potential. All electrodeposited films present upon cycling a good charge reversibility, with $Q_{discharge}/Q_{charge}$ > 90 %. The electroactive films were subjected to multiple oxidative cycles (100 cycles at a scan-rate of 200 mV/s) showing good stability with only partial loss of electro-activity after several charge/discharge processes (Figure 4.54). All polymers show a first cycle effect, evidenced by the black line in Figure 4.54.

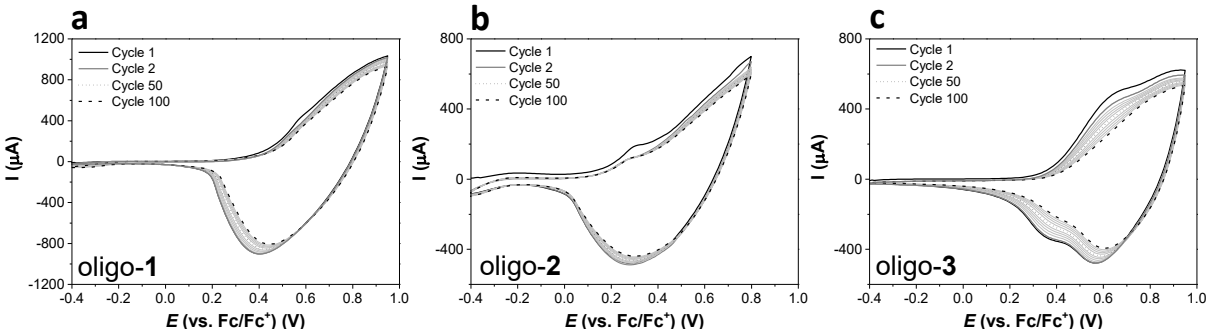

*Figure 4.54: 100 subsequent cycles of (a) **oligo-1**; (b) **oligo-2** and (c) **oligo-3** in 0.1 M CH_2Cl_2/$NBu4PF_6$ on Au electrode. Adapted with permission from ref. [3] (Wiley 2021).*

4.2.2.2.1 Scan-Rate Dependency

The scan rate analysis of **oligo-1** - **3** electrodeposited on Au electrodes showed that the anodic and cathodic peak current (Ip) follow a linear trend up to scan rate values of 500 mV/s. A linear tendency observed, even at high scan rate values, can be explained if a very fast ion diffusion into the electrodeposited film is taking place. To obtain a better understanding about the diffusion limitations of the counterions inside the electrodeposited film, the double logarithmic plot of the peak current with respect to the scan rate was evaluated.

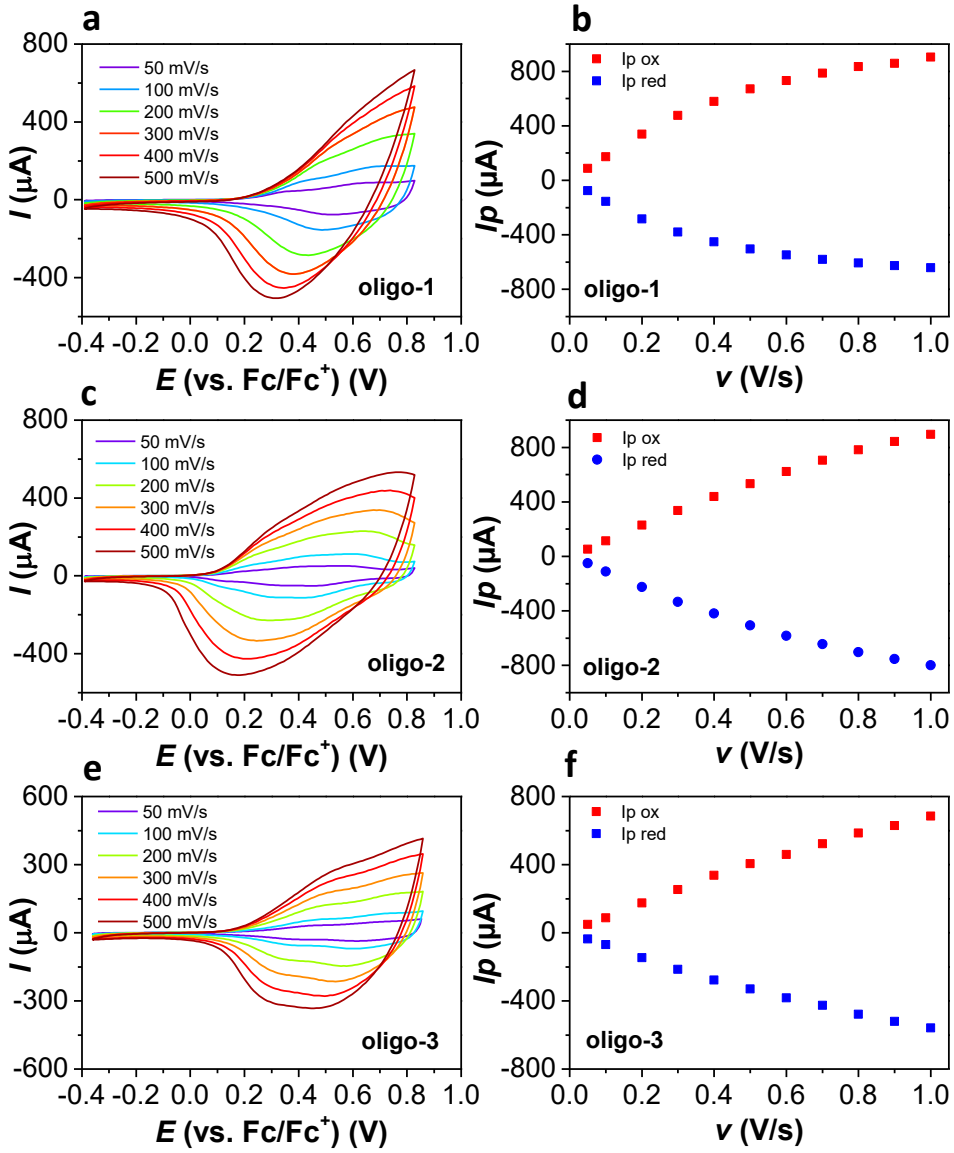

Figure 4.55: CV for scan-rates 50 to 500 mV/s in 0.1 M CH_2Cl_2/NBu_4PF_6 of (a) ***oligo-1****, (c)* ***oligo-2*** *and (e)* ***oligo-3*** *electrodeposited on Au electrode substrate. Current vs. scan-rate dependency for electrodeposited films (b)* ***oligo-1****, (d)* ***oligo-2*** *and (f)* ***oligo-3****. Adapted with permission from ref. [3] (Wiley 2021).*

Film	*ox*		*red*	
	Slope	**R^2**	**Slope**	**R^2**
Oligo-1	0.95	0.999	0.90	0.994
Oligo-2	1.00	0.998	1.00	0.996
Oligo-3	0.98	0.998	0.93	0.999

Table 4.6: Slope and R^2 values upon fitting Log(I_p) vs Log(v) from Figure 4.55 up to scan-rate values of 500 mV/s.

Oligo-2 (slope: 1.00) and **oligo-3** (slope: 0.98) electrodeposited films present higher slope values in the double logarithmic plot, showing linear dependency for scan-rates up to 500 mV/s whereas for higher scan rates diffusion limitations start to dominate the ion-transport behavior of the film. Interestingly **oligo-1** seems to present a more sluggish charging/discharging behavior with diffusion limitations, indicated by the loss of linearity in the I_p *vs.* v relationship, reached at lower scan-rates in comparison to the other compounds. A smaller size of the cavity of the closed macrocycle (closed dimers and trimers) generated by electrodeposition of **1** in comparison to **2** and **3**, and a lower film conductivity, might explain the non-linearity in the scan-rate dependency (slope: 0.95 up to 500 m V/s).

4.2.2.2.2 *In-Situ* UV-Vis-NIR Spectroelectrochemistry

In-situ UV-Vis NIR spectroelectrochemical characterization of the electrodeposited film was performed with the aim of elucidating the nature of the charged species. In Figure 4.56 (b, d and f), characteristic spectra taken during oxidation of the electrodeposited films are highlighted. To monitor the relative distribution of the different states of charge, neutral (N), radical cation ($R^{+\bullet}$) and dication (D^{2+}), the absorption at selected wavelengths was plotted as function of the electrode potential in Figure 4.56 (a, c and e) in superposition with the CV. Absorbances at specific wavelengths correlate with the change in population of the different states of charge.[77] These results are further combined with *in-situ* conductance measurements allowing for a more detailed assignment of the states of charge, and to analyze the conductive properties of these materials.

Oligo-1

The electrodeposited film, **oligo-1** presents in the neutral state a band with a maximum at 425 nm. Furthermore, two less pronounced bands at 673 nm and 1151 nm are visible. Upon increasing the oxidation potential, the intensity of the neutral band at 425 nm decreases with concurrent increase of the bands at 673 nm and 1151 nm. The band at 1151 nm evolves in two maxima (orange to green curve in Figure 4.56 (b)) at 1295 nm and 999 nm upon progressive increase of the oxidation potential. For potential values more positive than 0.61 V a peak at 552 nm is formed gaining in intensity with increasing oxidation potential. The initial absorption is reversibly recovered upon the discharging cycle.

The peak-trend as function of the potential for the charging of **oligo-1** is presented in Figure 4.56 (a). The blue curve represents the peak absorption variation for the neutral state (425 nm), the green curve for the first oxidized radical cation state (673 nm), and the red curves for the dication states (552, 999 and 1295 nm). The potential dependent peak-absorption is characterized by a step-like variation of the absorbances for the neutral (blue line) and oxidized states, red and green lines, respectively, which correlate well with the redox peaks in the CV experiment. A first (small) change of absorption is observed

concurrently with the first absorption peak with an onset for the absorption variation at 0.15 V, coinciding with the electrochemical onset. For potentials more positive than 0.4 V the neutral band starts significantly to decrease in intensity. This is followed by the band at 673 nm reaching an intensity maximum at 0.49 V, the value corresponding to the second redox peak observed in the voltammogram. For potential values more positive than 0.4 V also the bands in the NIR at 999 and 1295 nm are characterized by a marked intensity variation.

The presence in the pristine films of absorption bands at 673 nm and 1151 nm, which are characteristic of the oxidized state, indicates that the latter are obtained in a partially oxidized state directly after electrodeposition.

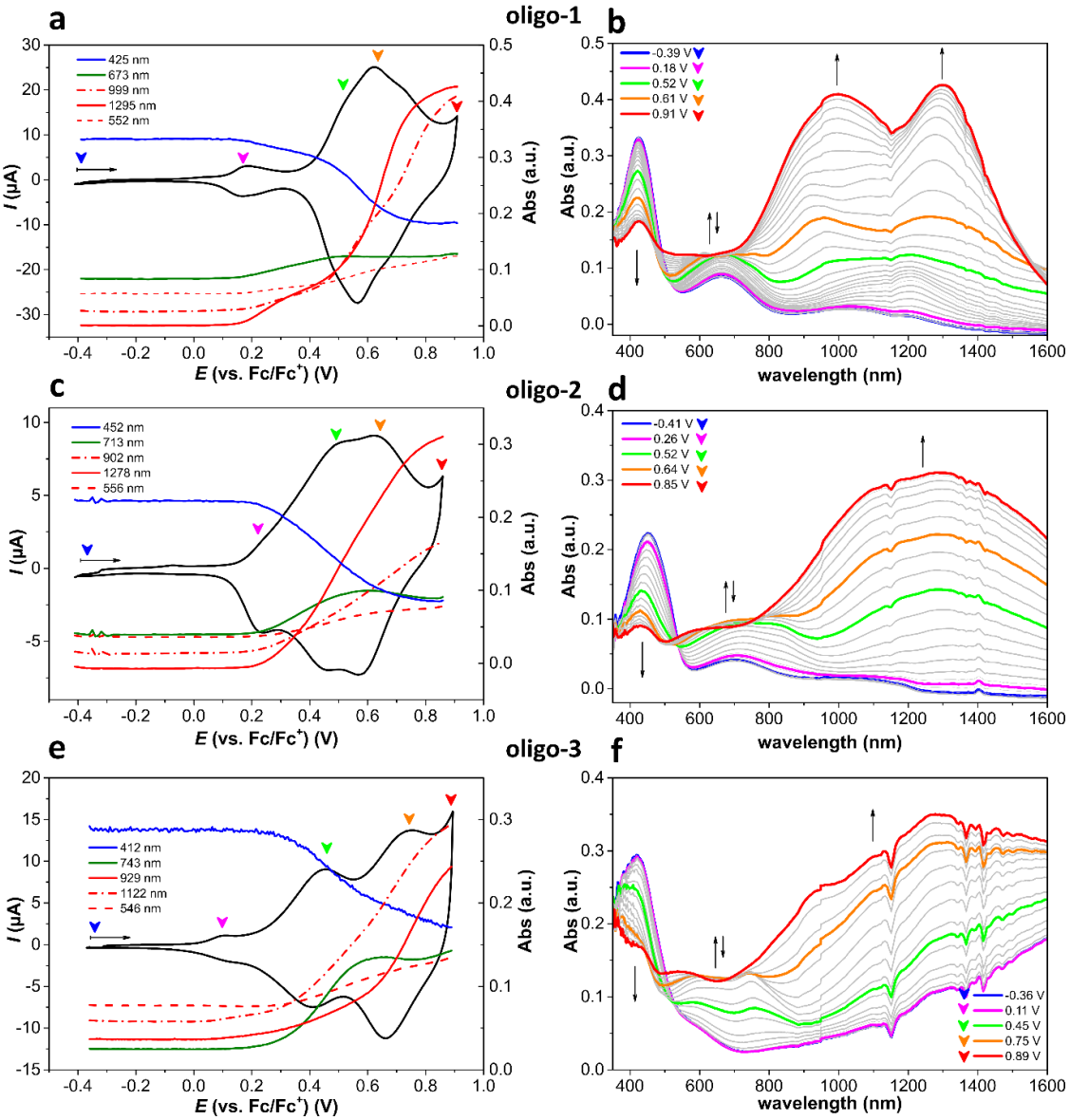

*Figure 4.56: UV-Vis-NIR spectroelectrochemical measurements registered during the forward oxidation cycle at a scan-rate of 20 mV/s in 0.1 M CH_2Cl_2/NBu_4PF_6. Left side CVs and peak-trends of characteristic absorption wavelengths; right side corresponding UV-Vis-NIR spectra registered for **oligo-1** (a, b); **oligo-2** (c, d) and **oligo-3** (e, f). Adapted with permission from ref. [3] (Wiley 2021).*

In the case of **oligo-1** the intensity of the band for the π–π* transition in the neutral state (425 nm) is associated with significant changes in absorption at a potential value more positive than 0.4 V *vs* $Fc^+|Fc$, some hundreds of mV after the oxidation onset and the first redox peak (0.23 V). A possible explanation could be that the first oxidation is localized on a moiety of the biindole core, causing only a limited planarization of the structure, for instance, significant variations of the absorption properties are obtained only by further charging, as the oxidation of the thiophene chains is addressed and the structure passing from aromatic to quinoid.[64] Moreover, it should also be considered that indole absorption is located at higher energies with respect to a tetratiophene system.[37,78,79] The spectrum seems to change only when the second, interacting indole moiety and the thiophene chain are oxidized.

Oligo-2

In-situ UV-Vis spectroelectrochemistry of electrodeposited **oligo-2** film (Figure 4.56) is characterized by an absorption maximum in the neutral state (blue curve) of 452 nm. Upon polarization to values more positive than 0.14 V, which coincides with the electrochemical oxidation onset, the neutral band (452 nm) progressively bleaches with concurrent formation and increase in intensity of two bands at 713 nm (green-line) and 1278 nm (red-line). These bands are assigned to the radical-cation and dication state localized on the T_6 moieties of **oligo-2**, respectively. The middle-energy band with a maximum at 713 nm reaches an absorption maximum during the forward oxidation scan at ca. 0.6 V, between the second and third couple of redox waves found in the CV signal. Upon potential values superior to 0.52 V (second redox wave, orange band in the spectra) the band with a maximum at 1278 nm broadens, showing absorption also in the spectral region of 750-1000 nm (λ 902 nm was sampled, red dashed line) and at 556 nm. **Oligo-2** can be reversibly oxidized over several cycles, without loss of absorption properties.

Oligo-3

Figure 4.56 (e) and (f) show the analysis of **oligo-3** (complete data-sets are found in the appendix section to this chapter). In the neutral state, the film is characterized by an absorption maximum at 412 nm. Upon increase of the oxidation potential the neutral band (412 nm) bleaches with concurrent formation of two bands at 743 nm and 1122 nm, which are assigned to the radical cation state localized on the Ph-T_4-Ph units. Upon further increase of the oxidation potential during the forward scan, the band at 743 nm reaches its maximum of absorption at a potential value of 0.62 V. In correspondence with the third redox wave, the film absorption further changes, showing a broadening of the low-energy band also in the spectral region of 800-1000 nm (a wavelength of 929 nm is sampled for peak-trend). The potential dependent peak-absorption is analyzed. The first redox signal

observed for **oligo-3** consists of a small reversible couple of peaks at $E^{1/2}$ 0.14 V. Interestingly, no absorption variations were observed in the range of potentials of this peak. Significant variations in the absorption pattern are observed only at potentials more positive than 0.23 V. This potential value should be assigned, during the forward scan, to the concomitant oxidation localized on the biindole core, and the oxidation on the Ph-T_4-Ph moieties at the radical cation level. The absorption at 743 nm, green line, increases up to 0.62 V during the forward scan of oxidation, this value well matches the simultaneous oxidation of the indole centers and the Ph-T_4-Ph units to their radical cation state at $E^{1/2}$ 0.47 V. In the experiment, the potential value of 0.62 V also coincides for the forward scan of oxidation with the abrupt increase in absorption of the band at 929 nm during the redox event and is associated with the oxidation of Ph-T_4-Ph units to the dication level. **Oligo-3** can be charged and discharged repeated times reversibly with complete recovery of the absorption of the neutral state.

Comparison

All electrodeposited films are characterized at the neutral state after deposition by similar patterns of absorption. The λ_{max} in the case of **oligo- 2**, which is characterized by the highest conjugation length, is found at 452 nm; in the case of **oligo-1** at 425 nm and of **oligo-3** at 412 nm. Generally, a red shift from the monomer absorption is found upon electrodeposition due to the increased conjugation. The absorption maxima in the neutral state of **oligo-1** and **oligo-3** find good correlation with the one measured in CH_2Cl_2 for the π- π * transition of T_4 oligomers (408 nm), and of **oligo-2** with the maxima of T_6 (449 nm).[46] In general this correlation is also observed for the different states of charge, indicating that the biindole central core has a limited effect on the spectroscopic properties of the molecules. Interestingly, the introduction of the phenyl spacers presents an absorption maximum at lower wavelengths in **oligo-3** with respect to **oligo-1** despite the higher amounts of conjugated units. This experimental observation could result from the higher steric hindrance introduced by the phenyl units limiting planarity and causing a loss in the conjugation efficiency.

Table 4.7: $E^{1/2}$ from electrochemical doping of the redox films and characteristic wavelengths for different states of charge from spectroelectrochemical experiments.

	$E^{1/2}$ *vs* Fc|Fc$^+$ (V)				**λ_{max} (nm)**	
	I ox	**II ox**	**III ox**	**N**	**$R^{+\bullet}$**	**D^{2+}**
Oligo-1	0.23	0.53	0.73	425	673, 1151	552, 999 1295
Oligo-2	0.20	0.39	0.58	452	713; (826)	556; (902); 1278
Oligo-3	-	0.46	0.75	412	606; 743	546; (929); 1227

As already observed from the monomer analysis, the introduction of the phenyl unit as spacer reduces the conjugation efficiency both at the level of the atropoisomeric core, and at the level of the oligothienyl units (increasing the distortion of the conjugated backbone) resulting in an increase of the ionization potential (Table 4.7).[80] As a consequence of the increase in conjugation length after oligomerization, the oxidation of the oligo-thiophene units of the electrodeposition products takes place with complete or partial superimposition to the biindole core oxidation. Analogously, the oxidation localized on the indole core shifts towards less positive potentials than for the monomers. A scheme of the charging steps is proposed in Figure 4.58. The onset of oxidation in the case of **oligo-1** and **oligo-2** is defined by the redox-activity of the biindolic core. In the case of **oligo-1**, an almost baseline separated peak is measured at 0.23 V, which is 17 mV shifted to lower potentials in comparison to the biindole oxidation in the associated monomer. The hexathiophene oxidation at the radical cation level of **oligo-2** is almost completely superimposed to the oxidation centered on the biindole, for which only a shoulder at 0.20 V is measured.

In the case of **oligo-3** the radical cation oxidation of the tetrathiophenes is almost completely superimposed to the biindole centered oxidation, evidenced by spectroelectrochemistry data.[80,81] It has to be mentioned that all the samples as obtained after electrodeposition are already characterized by two shoulders at ca 700 and 1100 nm, a wavelength region which is characteristic for the radical cation state. This result hints to a partial oxidation of the films after electrodeposition. The same shoulder remains present, without change in intensity, also upon pre-polarization at negative potentials. Studies on electropolymerization of indole by Inzelt *et al.*[82] have revealed that during the electrodeposition a fraction of the polymer and of the monomers are overoxidized leading to non-uniform film deposition. A similar situation was found with the materials herein analyzed.

4.2.2.2.3 *In-Situ* Conductance

In-situ conductance measurements are performed to analyze conductivity changes as function of the redox state of the film with reference to the nature of the π-spacer. The measurements are performed using interdigitated electrodes on which the indole-films were electrodeposited. An electrochemically gated transistor configuration is used to measure changes in conductance as function of the doping level of the films. Upon doping, charge carriers are generated within the electroactive film; the application of a small difference of potential between the platinum combs (10 mV), acting as gate potential, allows for the flow and measurement of a current between the platinum combs.

The successful coverage of the interdigitated area after electropolymerization was assured by scanning electron microscopy (SEM) as reported in Figure 4.50, Figure 4.51 and Figure 4.52. In the case of **oligo-1** and **oligo-3** the drain currents from which *in-situ* conductance is measured were too low to be distinguished from the background current.

In-situ conductance of electrodeposited **oligo-2** is presented in Figure 4.57. The conductance onset is found in correspondence with the electrochemical onset. The main conductance maximum is localized at 0.55 V for the forward scan and 0.50 V in the backward scan of the CV cycle, in proximity of the half-wave potential for the $R^{+\bullet}$ / D^{2+} oxidation of the hexathiophene units. Further, a small conductance peak can be distinguished for the backward scan at ca. 0.20 V, in correspondence to the oxidation of biindolic cores. Upon these observations, the *in-situ* conductance behavior of **oligo-2** can also be described in terms of mixed valence conductivity. In the neutral state, as well as for the dication state, the films are characterized by a low conductance, whereas for potential values corresponding to the concurrent presence of radical cation and dication species localized on the T_6 units ($Ind^{+\bullet}T_6^{+\bullet}Ind^{+\bullet}$/ $Ind^{+\bullet}T_6^{2+}Ind^{+\bullet}$), the highest conductance is registered.

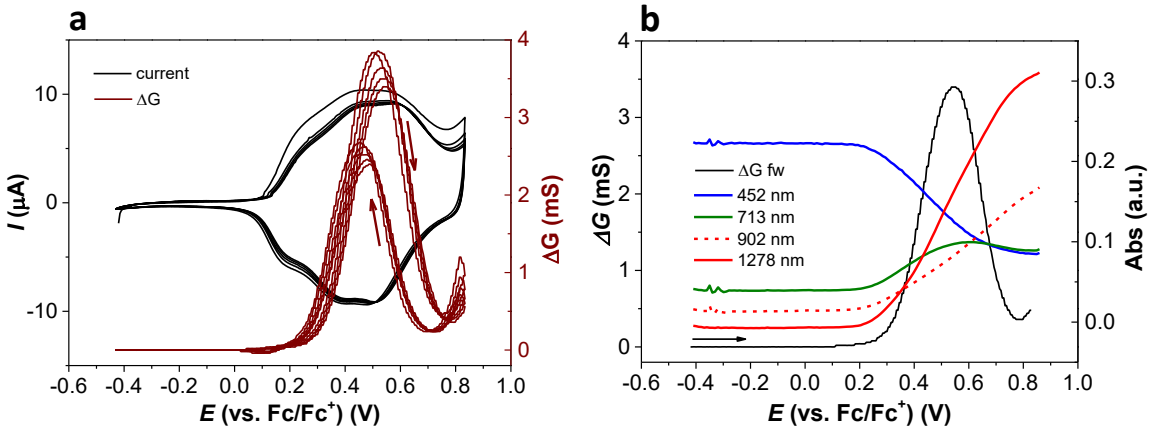

*Figure 4.57: **Oligo-2** (a) In-situ conductance multiple oxidation cycles. (b) In-situ conductance (5th cycle) over-imposed to peak-trend registered for the forward oxidation; measurements registered with a scan-rate of 20 mV/s in 0.1 M CH_2Cl_2/NBu_4PF_6, Pt -10 μm IDE.*

In-situ conductance analysis of **oligo-2** evidenced a mixed valence conductivity behavior, with the highest conductance change observed for the redox couple $R^{+\bullet}/D^{2+}$ involving higher delocalization over the T_6 units ($Ind^{+\bullet}T_6^{+\bullet}Ind^{+\bullet}$/ $Ind^{+\bullet}T_6^{2+}Ind^{+\bullet}$). Several overlapping redox states have to be considered: open and closed oligomers with slightly different $E^{1/2}$ causing a broadening of the conductance window in comparison to pure redox systems. The conductance change is associated with the oxidation involving the oligo-thienyl units as the redox change $N/R^{+\cdot}$ on the biindolic center ($Ind^{+\bullet}T_6Ind$/ $Ind^{+\bullet}T_6^{2+}Ind^{+\bullet}$) at the first peak; is characterized only by a small change in conductance in comparison to T_6, observable during the discharge cycle. This might be explained by the fact that the indole-centers are highly spatially separated resulting in an inefficient center distribution for

electron hopping. A similar experimental observation was found studying *in-situ* conductance of the electropolymerization product of an inherently chiral bis-EDOT derivative (2'-bis{bi[2,2'-(3,4- ethylenedioxy)thiophen-5-yl]}-3,3'-bithianaphthene).[76] In this work two independent maxima of conductance are observed and described in terms of mixed valence conductivity behavior between tetrameric EDOT units in their polaron and bipolaron state respectively. The encountered similarity were explained by the limited conjugation in the molecules determined by the atropoisomeric core, imparting a helicoidal geometry to the system and limiting the conjugation in the electropolymerization products only to tetrameric EDOT units.

Overall, the conductance behavior observed seems to correlate with the results of Zotti *et al* on the analysis of conductivity of some oligothiophenes.[83,84] The results also well correlate the peak-trend variation from UV-Vis NIR spectroelectrochemistry for the different redox states of the film. Overall, the substitution of the dibenzothiophene with biindolic moieties does not induce significant variations in the absorption properties of the electrodeposited film concerning the position and topology of the bands, similarly, the conductivity properties of this class of molecules remain dominated by the ones of the oligothienyl moieties. These observations seem to confirm the charge assignment for the CV experiments and the proposed oxidation steps presented in Figure 4.58.

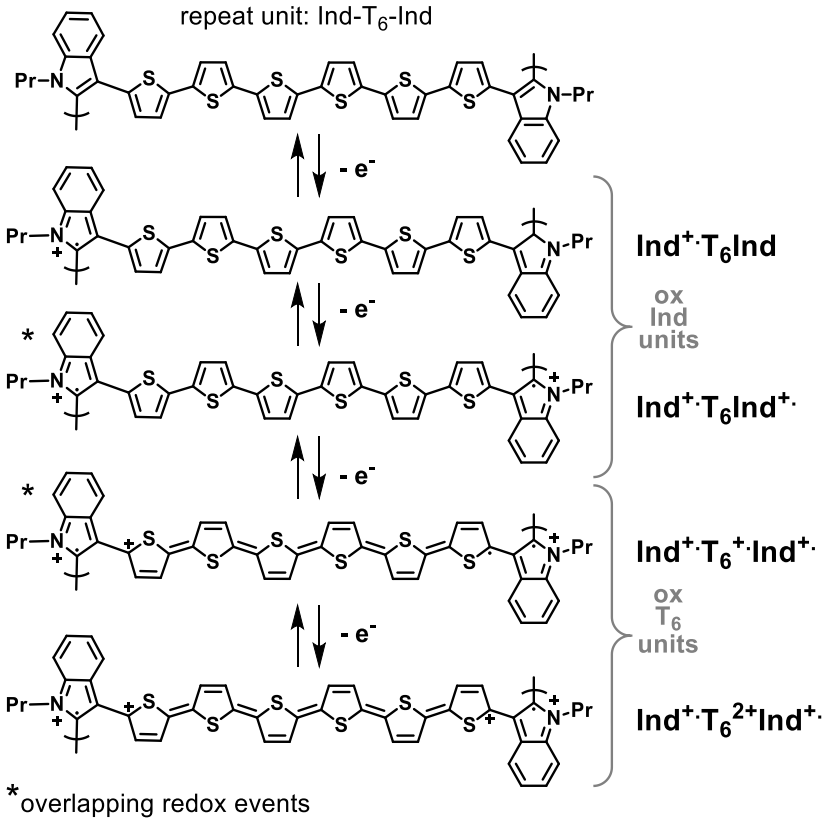

*Figure 4.58: General representation of the different states of charge of **oligo-2**. In the case of the oligomerization products every repeat unit will be oxidized simultaneously. The first oxidation is localized on the more electron-rich biindolic core, in two oxidation steps. Further oxidation involves*

radical cation and dication formation localized on oligothienyl terminals. Picture adapted from ref [1]. Copyright Wiley 2021.

4.2.2.3 *Enantiodiscrimination Tests*

In order to verify the suitability of enantiopure **oligo-2** films as selectors, enantioseparation tests with a benchmark ferrocene probe are demonstrated, showing the potential of the electrochemically generated films for analytics and sensing applications. Enantiodiscrimination measurement were performed by S. Grecchi from the University of Milan. For this purpose, the racemate of monomer **2** was resolved into antipodes by enantioselective HPLC on a polysaccharide based chiral stationary phase under normal phase mode. Absolute configuration was not assigned, and the two enantiomers are generically indicated as **(*EN1*)-2** as the first and **(*EN2*)-2** as the second eluted enantiomers respectively. **Oligo-(*EN1*)-2** and **oligo-(*EN2*)-2** films were prepared by the electrooligomerization of the corresponding enantiopure monomers (***EN1*)-2** and **(*EN2*)-2**, respectively. Enantio-discrimination experiments were performed by Differential Pulse Voltammetry (DPV, 5 mV step, 50 mV amplitude) using 0.002 M solutions of the chiral probes ((*S*)-(-)- or (*R*)-(+)-*N,N'*-dimethyl-1-ferrocenylethylamine) named (*R*)-Fc and (*S*)-Fc in 0.1 M CH_2Cl_2/NBu_4PF_6 as supporting electrolyte (Figure 4.59 (a, b)).

These chiral probes are generally nice model compounds when testing new advanced chiral selectors, on account of ferrocene's facile and reversible electron transfer at a mild oxidation potential (in a region where the film is generally uncharged, *i.e.* in a potential range close to 0 V *vs* $Fc^+|Fc$).[65] In the case of a bare GC electrode, upon oxidation of both enantiomers of the chiral ferrocenyl-probes, no variations in peak potential were observed (E_p: -0.09 V, grey curves).

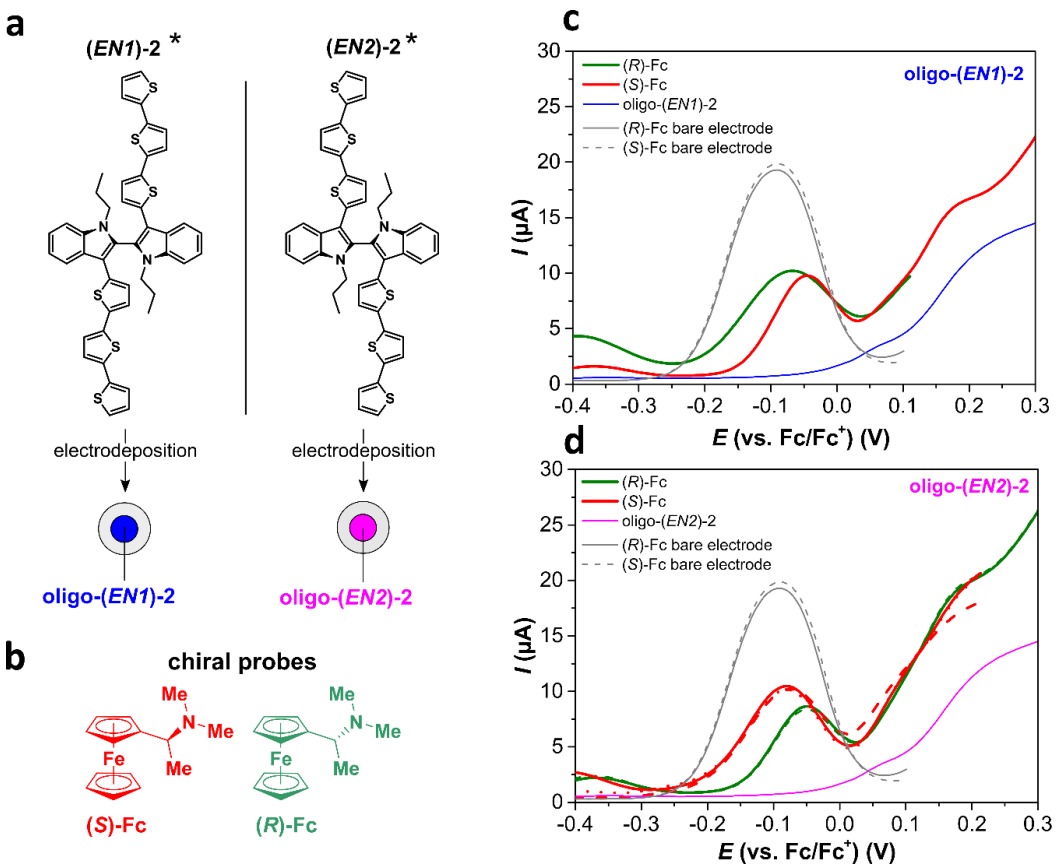

*Figure 4.59: (a) Sketch of enantiopure **oligo-(EN1)-2** and **oligo-(EN2)-2** (d) deposited on GC electrode. (b) Electroactive ferrocenyl-probes employed: (S)-(-)- and (R)-(+)-N, N'-dimethyl-1-ferrocenylethylamine, named (S)-Fc (red) and (R)-Fc (green). c) and d) DPV measurements showing performances of enantiopure **oligo-(EN1)-2** and of (c) **oligo-(EN2)-2** (d) electrode surfaces towards chiral electroactive ferrocenyl-probes. In grey are also reported the signals of (R)-Fc and (S)-Fc recorded on bare GC electrodes. The blue line in c) corresponds to the DPV pattern of **oligo-(EN1)-2** and the pink line in (c) of **oligo-(EN2)-2**. Reproducibility tests on the two ferrocenyl-probes are also reported with dashed or dotted lines and the associated colour. *Note that enantiomers were resolved by chiral HPLC but no configuration was assigned: represented configurations might not correlate to the real ones. Picture adapted from ref [1]. Copyright Wiley 2021.*

However, when changing to electrodes coated with enantiopure films of **oligo-2**, two splitted and quite different DPV signals, both well defined, are observed for the oxidation of (*R*)-Fc (green curves) and (*S*)-Fc (red curves). A good enantiodiscrimination in terms of peak potential values is obtained, specularly for the two enantiopure films, with a separation of ~40 mV between the two antipodes (for **oligo-(*EN2*)-2** E_p of (*R*)-Fc: -0.040 V and (*S*)-Fc: -0.080 V) (Figure 4.59 c, d). Reproducibility tests were performed by repeatedly recording the DPV patterns of model probes on freshly deposited chiral surfaces (dotted and dashed lines of (*R*)- Fc (green) and (*S*)-Fc DPV curves respectively).

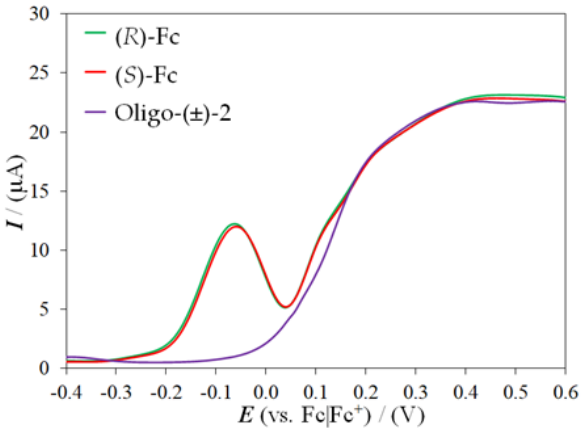

*Figure 4.60: DPV measurements with **oligo-(±)-2** towards chiral electroactive ferrocenyl-probes (R)-Fc (in green) and (S)-Fc (in red). In purple is also reported the DPV pattern of **oligo-(±)-2**. Picture adapted from ref [3]. Copyright Wiley 2021.*

The electron-transfer process should take place at the interface between the metal electrode and the probe molecule within the chiral oligomeric film. The oxidation of chiral probes takes place at potential values at which the films are not yet oxidized. A possible explanation of the potential split could be that the interactions of the enantiopure probes with the enantiopure environment are of diastereomeric nature, and are therefore significantly affected by the energetics of the electron-transfer process in both thermodynamic and kinetic terms. For sake of comparison, Racemic-**2** (namely **(±)-2**) was also electrodeposited at constant working protocol, testing the enantiomers (R)-Fc and (S)-Fc. The results reported in Figure 4.60 confirmed that the potential shift is determined by the combination of the enantiopure chiral electrode surface with the chiral probe.

4.2.3 2,2´-Biindoles-3,3´-Diheteroaryls with Donor-Acceptor Units (4-5)

The possibility to fine tune the band gap by structural modifications makes conducting polymers unique materials to be employed in different applications including electrochromic devices and bulk-heterojunction (BHJ) solar cells. The most common approach to tune the band-gap of conducting polymers is represented by the introduction of donor (D)-acceptor (A) units in the polymer chain. The donor groups raise the energy of the valence band (VB), and the acceptor groups have the effect to lower the energy of the conduction band (CB). By the appropriate selection of repeat units, conducting polymers can be made electron-rich or electron-deficient for the stabilization of holes or electrons; and their band gap can be finely controlled to adjust the wavelengths of absorption and emission.[35,85] The modulation of Eg by creating alternating donor and acceptor units also results in the organization between polymer chains by preferential π-stacking of the charge complementary units (i.e., −D−A−D−) enhancing their charge transport properties.[86,87]

Oligothiophene macrocycles derived from the atropisomeric monomer BT_2T_4 have been successfully used as donor materials in bulk-heterojunction (BHJ) solar cells in combination

with fullerene derivatives, giving rise to PCE% of ~ 1.1 in the case of cyclic trimers and open dimers.[68] In order to further explore different donor-acceptor (D)-(A) combinations have been also synthetized. One of the most common electron deficient chromophores is benzothiadiazole (BTD) [88,89], as by conjugation with electron rich substituents (usually thiophenes) affords low band gap polymers[90]. Moreover, BTD well-known chemistry[91] allows fine tuning of photophysical properties by decoration of the benzenoid ring[92–94] or by switch of sulfur with heavy atom[95–97]. In particular, benzoselendiazole (BSeD) containing donor-acceptor-donor (D-A-D) oligomers are reported to lead to higher power conversion efficiencies[98] coming from LUMO lowering effects by Se atom[99]. The introduction of D-A is also expected to provide peculiar electrochromic properties and chiral electrochromism in the enantiopure form. Synthesis of compounds **4** and **5** was performed by Dr. L. Scapinello from the University of Como.

4.2.3.1 *Characterization of Monomers (4) $Ind_2T_2BTD_2T_2$ and (5) $Ind_2T_2BSeD_2T_2$*

4.2.3.1.1 UV-Vis Spectroscopy of Monomers

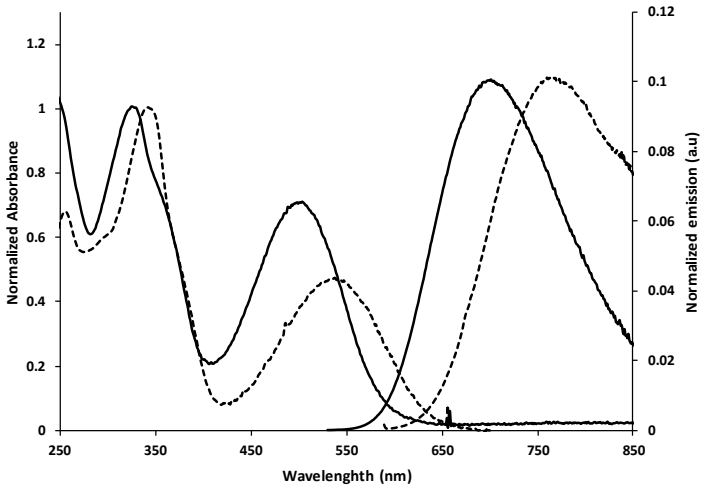

Molecule	4	5
λ_{max} Abs. (nm)	503	538
λ_{max} Fluor. (nm)	701	709
Quantum yeld	13%	6,5%

Figure 4.61: UV-Vis absorption and emission spectra in CH_2Cl_2 for molecules 4 (solid line) and 5 (dashed line). Absorption and emission spectra from Dr. L. Scapinello, University of Como.

Compounds **4** and **5** were characterized by UV-Vis spectroscopy. The introduction of the Se resulted in a clear red shift in absorption λ_{max} (503 nm for **4** vs 538 nm for **5**). Red shifted emission was observed too (701 vs 770 nm), associated with a lower quantum yield (13% for compound **4**, 6.5% for **5**).

4.2.3.2 Electrochemical Characterization and Electrodeposition

The electrochemical characterization of the molecules **4** and **5** was performed in 0.1 M CH_2Cl_2/NBu_4PF_6 with a 0.5 mM of analyte on ITO electrodes. The CV of molecules **4** and **5**

is characterized for the oxidation by multiple peaks, as presented in Figure 4.62 (a) and Figure 4.63 (a), red curves. Similarly to molecules **1**-**3**, two chemically reversible peaks are found at lower potentials, which are associated with the oxidation localized on the more electron rich biindole core. In the case of compound **4** peaks potentials are found at values of 0.43 V for $E_{P,A}$ and of 0.70 V for $E_{P,B}$, whereas in the case of compound **5** at potential values of 0.39 V for $E_{P,A}$ and of 0.61 V for $E_{P,B}$. As previously discussed, oxidation of the molecules results in two sets of interacting redox peaks, A and B which are assigned to the oxidation of one of each interacting indole unit in the biindole center. It can be observed how peak A presents a higher degree of chemical reversibility in comparison to the peak B as presented in Figure 4.62 (b).

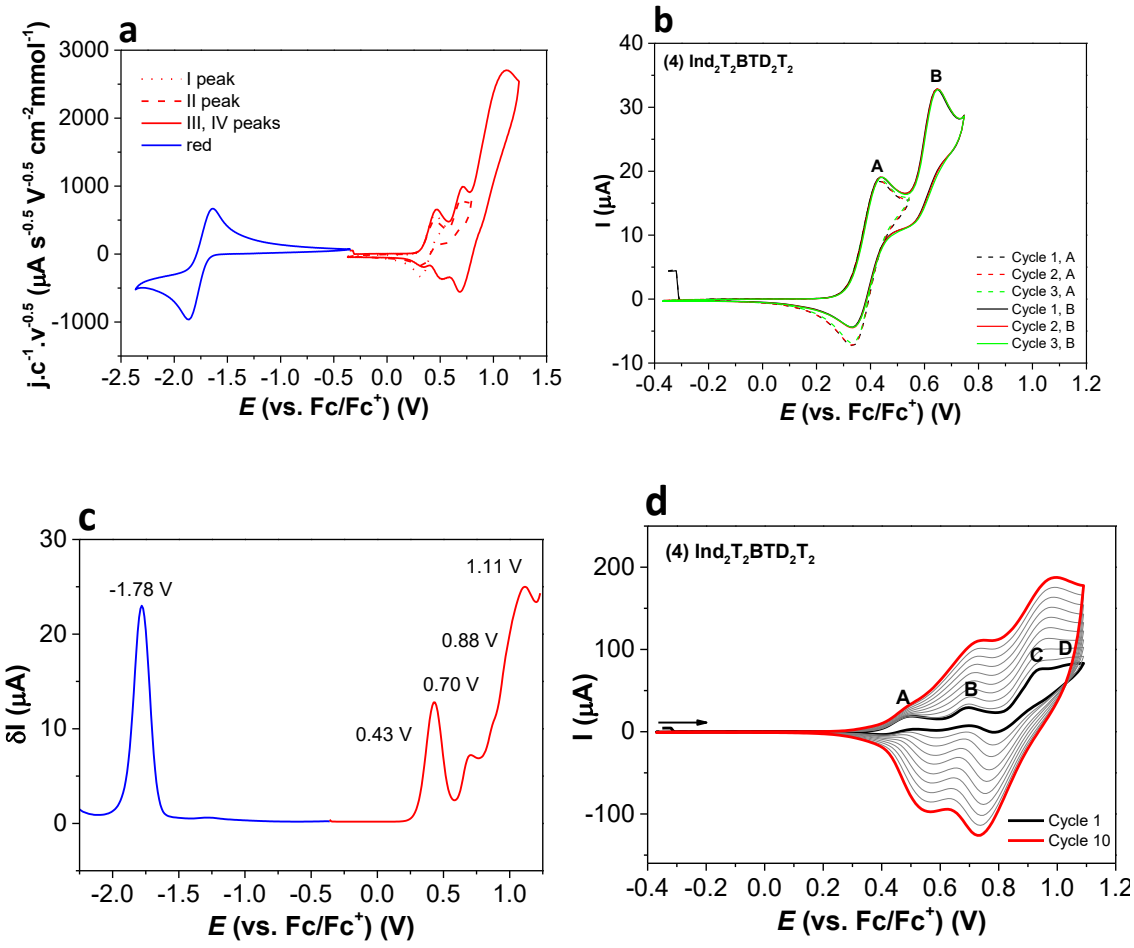

*Figure 4.62: Molecule **4** - $Ind_2T_2BTD_2T_2$: (a) CV signals for oxidation (red curve) and reduction (blue curve), first cycle is reported. CV experiments are performed at a scan-rate of 20 mV/s in 0.1 M CH_2Cl_2/NBu_4PF_6 on ITO electrodes. (b) Multiple CV cycles obtained by cycling around the first (A) and second (B) chemically reversible oxidation peaks at 20 mV/s. (c) DPV signal, forward scan, for the oxidation of **4** at 20 mV/s and a modulation amplitude of 25 mV, oxidation indicated with a red curve and reduction with a blue curve. (d) Electrodeposition of **4** to yield **oligo-4**.*

This might be explained by a higher degree of charge delocalization also on the neighboring thienyl arms, in general multiple cycling of the WE at potential values corresponding to these

two peaks is not associated with deposition of an electroactive layer. The oxidation of the second set of peaks, C and D leads to electrodeposition, and are assigned to the generation of reactive radical cations on the T-BTD-T and T-BSeD-T terminals. The electrodeposition plots are presented in Figure 4.62 (d) and Figure 4.63 (d), for compounds **4** and **5** respectively. These peaks are found at more positive potential values, more specifically in the case of **4** at 0.88 V in the case of $E_{P,C}$; at 1.11 V for $E_{P,D}$, whereas for molecule **5** at 0.79 V for $E_{P,C}$ and at 1.01 V for $E_{P,D}$.

The introduction of the acceptor units BTD and BSeD within the polymer have the effect to significantly decrease the LUMO energy, this results in a reversible reduction peak at -1.78 V (Ep from DPV) for **4** and -1.65 V for **5**.

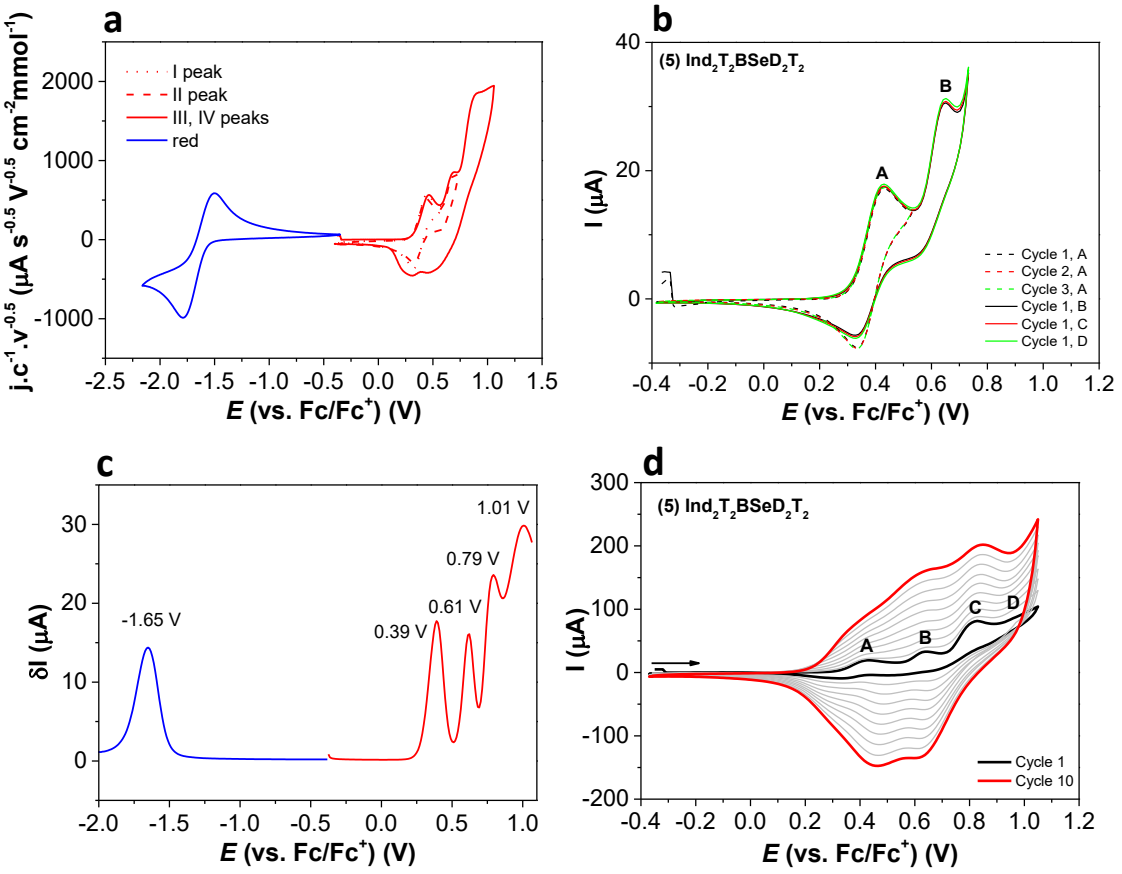

*Figure 4.63: Molecule **5**: (a) CV signals for oxidation (red curve) and reduction (blue curve), first cycle is reported. CV experiments are performed at a scan-rate of 20 mV/s in 0.1 M CH_2Cl_2/NBu_4PF_6 on ITO electrodes. (b) Multiple CV cycles obtained by cycling around the first (A) and second (B) chemically reversible oxidation peaks at 20 mV/s. (c) DPV signal, forward scan, for the oxidation of **5** at 20 mV/s and a modulation amplitude of 25 mV, oxidation indicated with a red curve and reduction with a blue curve. (d) Electrodeposition of **5** to yield **oligo-5**.*

E_p (V) vs Fc/Fc^+ from DPV					
Molecule	**A**	**B**	**C**	**D**	**red**
4	0.43	0.70	0.88	1.11	-1.78
5	0.39	0.61	0.79	1.01	-1.65

Table 4.8: E_p (V) vs Fc/Fc^+ from forward oxidation scan of DPV measurement for compounds 4 and 5.

In general, the signal position in a CV experiment is strongly influenced by the presence of substituents. Inductive effects, making the system more electron-poor or electron-rich, induce translations of oxidation and reduction signals in the same direction: I+ (less favored oxidation, favored reduction) if the substituent is electron-poor; I- (favored oxidation, less favored reduction) if the substituent is electron-rich. Increasing resonance effects instead generally induce a narrowing of the interval between anodic and cathodic peak and therefore a narrowing of Eg. The introduction of the acceptor units has also the effect of shifting the monomer oxidation to more positive values, in particular the benzothiadazole substituted molecule shows among all compounds analyzed in the series the most positive potentials for the different oxidations. The overall result is a narrowing of the bandgap of the molecules with 2.21 eV and 2.04 eV (calculated from E_p) for **4** and **5**, respectively.

4.2.3.2.1 Electrochemical Characterization of Oligo-(4-5)

Electrodeposited films were characterized in a monomer free solution (0.1M CH_2Cl_2/NBu_4PF_6). Both electroactive films present first cycle effect and upon subsequent cycling CV traces show good redox stability. In the case of **oligo-4,** directly after oxidation, two main peaks are observed at 0.50 V and 0.59 V. The experimental data are reported in Figure 4.64 (a). In the case of **oligo-5** three peaks are found at 0.21 V; 0.42 V and 0.56 V. The precise charge localization upon oxidation of the electroactive films could involve the concurrent biindole and oligothiophene oxidation, as reported in the oxidation scheme in Figure 4.58.

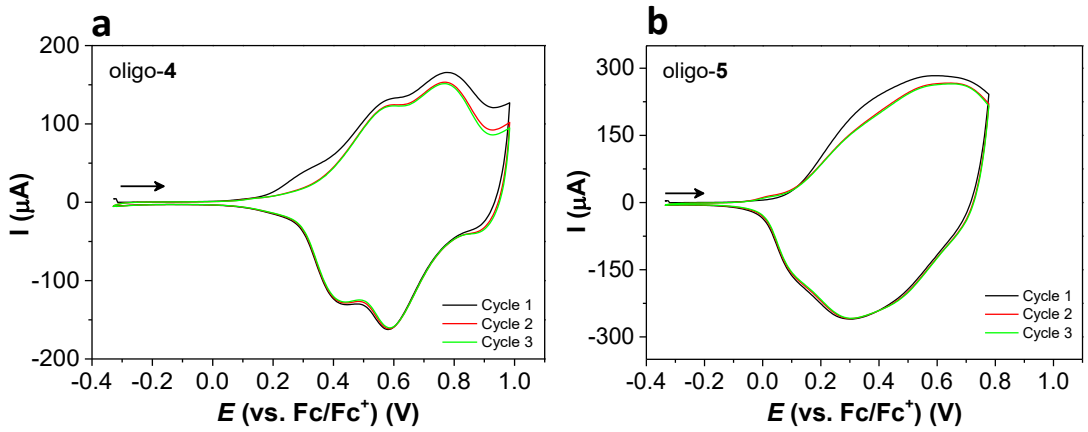

*Figure 4.64. Multiple oxidation cycles of **oligo-4** (a) and **oligo-5** (b) performed at a scan-rate of 50 mV/s; Au; CH_2Cl_2/NBu_4PF_6 0.1 M.*

Oligo-4 and **oligo-5** present a reversible reduction with one single reduction peak encountered at half-wave potentials of -1.80 V and of -1.68 V, respectively. The first reduction cycle shows for both polymer a significant charge irreversibility between the forward and the backward scan with strong similarities between the two polymers. This behavior is reproducibly found for different samples and electrode substrates (Au; ITO). The ratio of Q+ vs Q- charges from the first reduction cycles were evaluated; 30% (forward cycle -2827 μC; backward cycle 815 μC) of reversibility in the case of **oligo-4** and of 38% in the case of **oligo-5** (forward cycle -4360 μC; backward cycle 1665 μC). Upon subsequent cycling the reduction signal remains unchanged with almost complete charging reversibility between forward and backward scan, no charge trapping is found upon reduction after oxidative cycling.

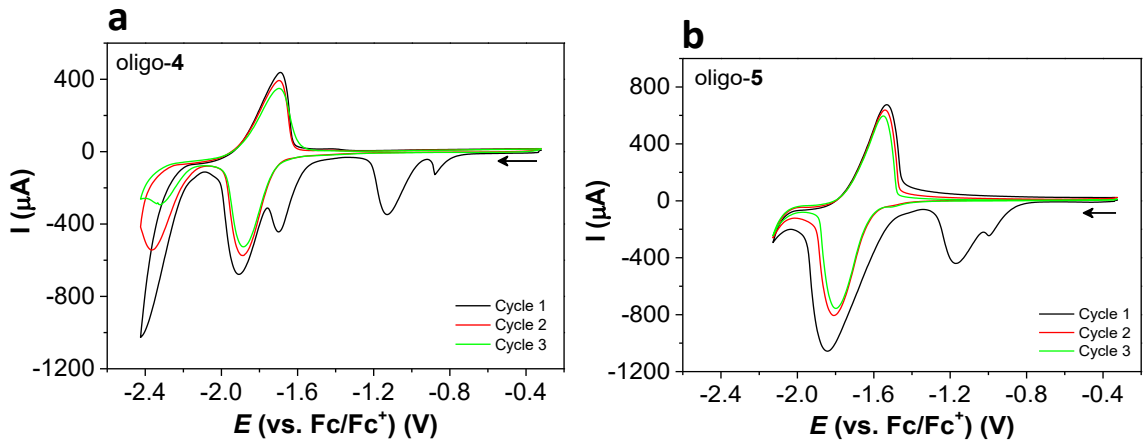

*Figure 4.65: Multiple reduction cycles of **oligo-4** (a) and **oligo-5** (b) performed at a scan-rate of 50 mV/s; Au; CH_2Cl_2/NBu_4PF_6 0.1 M.*

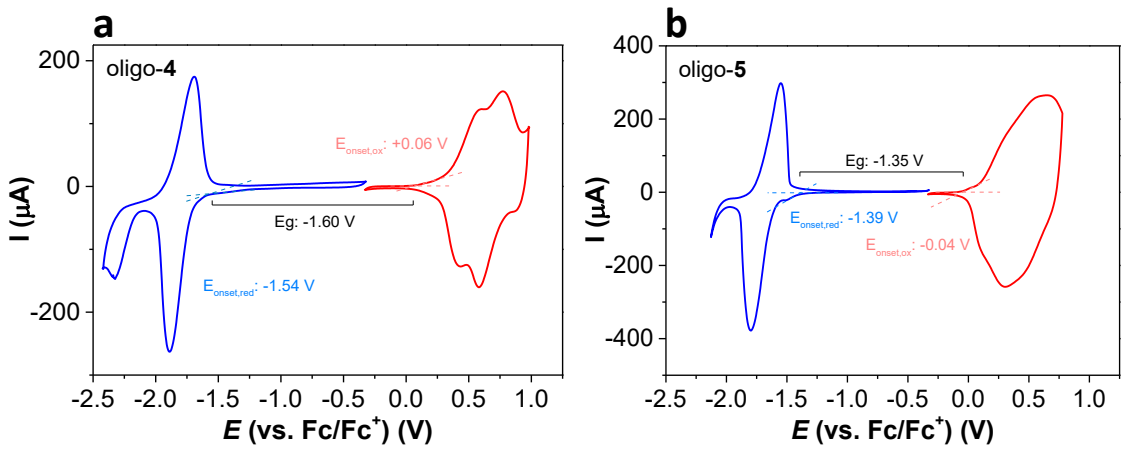

Figure 4.66: Third oxidation (red) and reduction (blue) cycles of (a) ***oligo-4*** *and (b)* ***oligo-5****. Measurements were performed at a scan-rate of 50 mV/s; Au; CH_2Cl_2/NBu_4PF_6 0.1 M.*

Multiple reduction cycles cause significant variations in their electroactivity and stability of the electroactive films. In both cases a decrease in the currents registered upon p-doping performed on previously reduced films with respect to p-doped films (directly after electrodeposition) hints to a decrease in the amount of available redox active sites. A flux of charged (colored) material from the electrode indicating substantial material loss from the electrode surface, was also evidenced by the decreased CV current in the following oxidation cycle in comparison to the pristine film (film directly after electrodeposition) (Figure 4.67). Whereas in the case of **oligo-5** good correlation between onset of oxidation and peaks, the reduction of **oligo-4** results in a variation of the material oxidative CV pattern, new multiple peaks and a shift of the onset potential is observed. Potential values for comparison are reported in Figure 4.67. A consistent portion of the electrochemical window gains in electroactivity after reduction of the polymer. One possible explanation could be that the extremely positive potential values reached during electropolymerization, could result in a highly charge-trapped electroactive film, and the positive charge trapped within the polymer film can only be released upon application of negative potential values, preceding the reduction potential of the polymer. This effect is further analyzed by UV-Vis NIR spectroelectrochemistry. Variation in film absorption are also observed after reduction and discussed in the further section.

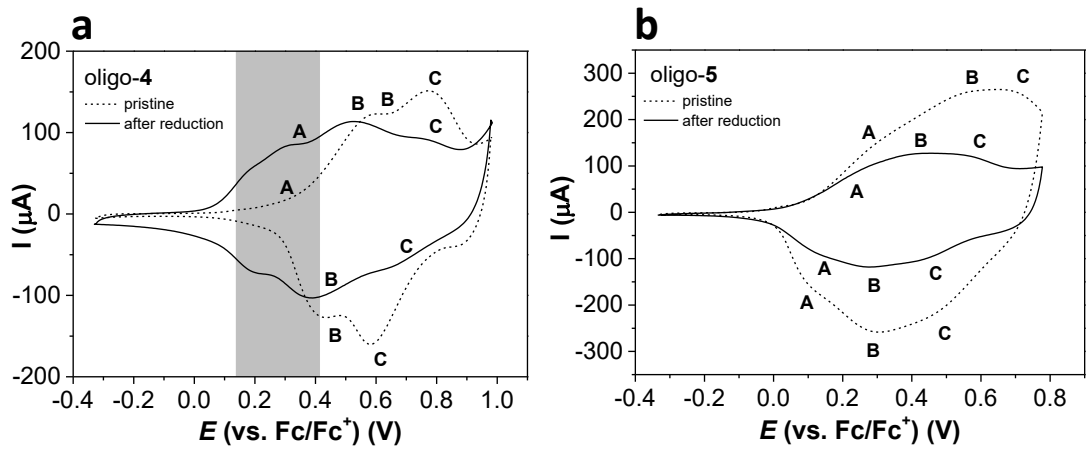

*Figure 4.67: Comparison of the third p-doping cycle in CH_2Cl_2/Bu_4NPF_6 0.1 M; 50 mV/s; Au electrode; of (a) **oligo-4** and (b) **oligo-5**, as pristine film, represented with dashed-line, and after reduction (Figure 4.65), represented with continuous line.*

The electrochemical behavior resulting from reduction and oxidation of benzothiadiazole-thiophene based polymers and oligomers was analyzed by P. Ledwon *et al.*[100]. The author found that in the case of (T-BTD-T) copolymers obtained by electrodeposition; the nature of the reduction products results is different from the oxidation one. While oxidation leads to simultaneous formation of different positive charge carriers (EPR-active polarons and EPR-silent bipolarons), reduction leads to discrete formation of only one type of charger carriers, polarons, within the range of potentials accessible in the study (i.e.: for the dianion generation, polarization at more negative potentials is needed). The authors find also that the EPR signal of the radical-anion is very localized on the BTD moiety, and attribute charge trapping effects during subsequent oxidation/reduction cycles to the localized nature of the charge carriers. The effect is also found to become more pronounced by increasing the film thickness.

4.2.3.2.2 In-situ UV-Vis-NIR Spectroelectrochemistry

UV-Vis-NIR spectrolectrochemistry combined with CV measurements was performed to analyze the p- and n- doping processes and to identify structural variations to the electroactive film, the spectroelectrochemical results obtained during p-doping (pristine), n-doping, as well as further p-doping performed after reduction are reported in sequence.

Oligo-4

In-situ UV-Vis-NIR spectroelectrochemistry upon oxidation of electrodeposited **oligo-4** is reported in Figure 4.68. In the neutral state (-0.41 V) the film is characterized by three maxima of absorption: 452 nm; 556 nm and a shoulder at 676 nm. Within the potential window 0.2 V - 0.6 V two clear transitions at 786 nm and 1515 nm are encountered. In particular, the variation in the intensity of these bands is only limited for potential values

corresponding to the polymer oxidation onset 0.2 V and 0.4 V, at which oxidation of the biindole cores takes place. Absorption at these wavelengths become more intense with progressive increasing of the polarization level as the oxidation includes also the (T-BTD-T)$_2$ units, for potential values between 0.4 V and 0.6 V.

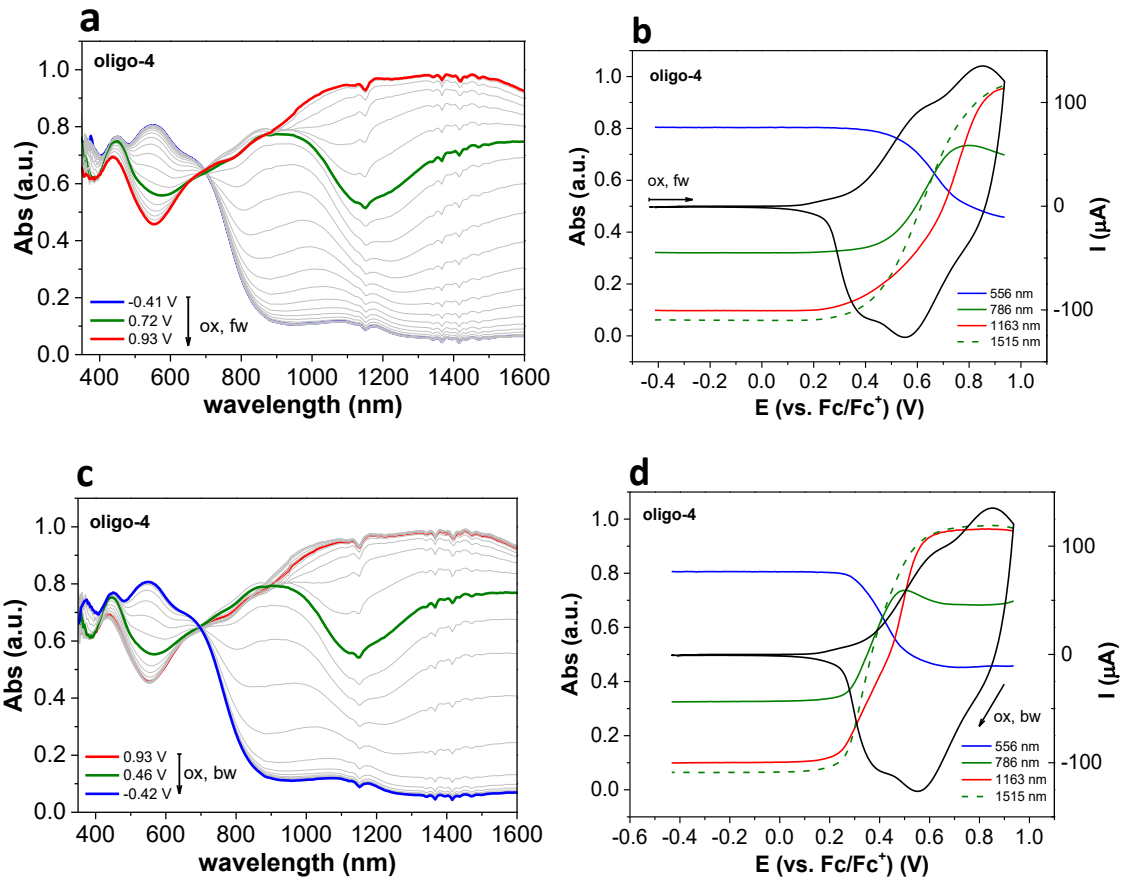

*Figure 4.68: **Oligo-4**: UV-Vis-NIR spectroelectrochemistry on films tested directly after electrodeposition, II oxidation cycle, on ITO electrode, CH_2Cl_2/Bu_4NPF_6 0.1 M; 20 mV/s. First raw, charge (a) UV-Vis (b) CV with peak trend of selected wavelengths, and second raw, discharge (c) UV-Vis (d) CV with peak trend of selected wavelengths.*

For more positive oxidation potential, a complete bleaching of the neutral band (556 nm) indicates a full conversion of the system in the radical cation-dication state localized on the (T-BTD-T)$_2$ units; as well as a decrease in intensity of the transient 786 nm for the radical cation state is observed. The dominant transition includes for higher oxidation potentials a broad band in the Vis-NIR region 900-> 1600 nm. The wavelength 1163 nm was sampled as reference in the peak-trend for this state as it is not absorbing for less positive doping levels.

Isosbestic points are found at wavelengths of 683 nm for the N/I ox and at 412 nm, 879 nm in the case of I ox/II ox. This hints to the presence of different state of oxidation in equilibrium, in accordance with the multiple CV peaks, which are characterized by specific absorptions bands. In comparison to polymer films obtained upon electropolymerization of the monomer T-BTD-T reported in the literature,[101] which are characterized by a single

absorption maximum at ca 600 nm in the neutral state, electrodeposited films of **oligo-4** show multiple absorption maxima in the range 400 nm – 700 nm (Figure 4.68 (a), blue line), including a shoulder at around 700 nm. By comparison to the onset of absorption for electropolymerized T-BTD-T reported in the literature, which is ca. 590 nm and an optical onset of characterized by a single maximum of absorption at around 780 nm, it is striking that **oligo-4** is characterized by a lower bandgap respect to electrodeposited poly-T-BTD-T of the latter. The latter (poly-T-BTD-T) should give in fact rise to multiple and larger conjugation lengths, as well as to better stacking possibilities, due to the absence of the bulky biindole center with long alkyl-units as in the case of **oligo-4**. This first consideration suggests that **oligo-4** could be obtained in a partially oxidized state. This possibility is further analyzed considering the n-doping process as well as of the observations made on electrodeposited **oligo-1, oligo-2** and **oligo-3** films.

The peak trend analysis allows to better follow the variation of absorption for different charge carriers. For the p-doping of **oligo-4** we found that the neutral band (556 nm) starts decreasing only at potential values more positive than +0.4 V. Between potential values of + 0.2 and + 0.4 V, potential values coinciding with polymer onset and to low doping levels, it is already possible to observe increase of intensity of the band with maximum at 1515 nm. This fact could imply, as discussed above, that the polymer is obtained in a partially oxidized state directly after electropolymerization, as the polaron band is not fully bleached. In the case of **oligo-4** such discrepancy between polymer oxidation onset and changes in the absorption spectra are not encountered. The band at 786 nm, is assigned to the radical cation state localized on the $(T\text{-}BTD\text{-}T)_2$ moieties, the maximum of absorption is indeed found between the two main oxidation peaks at higher potential values. Backward cycle shows hysteresis for the absorption, but this seems to be in accordance with the peak maxima in the backward scan (~ 200 mV).

Oligo-5

The UV Vis-NIR spectroelectrochemical behavior of **oligo-5** upon oxidation is reported in Figure 4.69; showing reversible electrochromism. The narrowing of the band-gap, in comparison to the other analyzed systems, results in an almost complete superimposition of the bands of the radical cation and dication states on the $(T\text{-}BSeD\text{-}T)_2$ conjugated units. The charge speciation is analyzed through the peak-evolution: different slopes are found for peak trend of the different species neutral, radical cation and dication, correlating with peak potentials for the different oxidations (peak-trends from Figure 4.69 (b, d)). A red-shift of the neutral state, due to the bathochromic effect upon introduction of Se atom, is found in comparison to **oligo-4** and all compounds analyzed in paragraph 4.2.2. In the neutral

state maximum absorption is found at 385 nm and 613 nm respectively; the first band is assigned to the π- π* transition whereas the second to the push-pull ICT transition.[100,102]

In the potential region 0 V - 0.2 V, during the forward cycle, a broad band covering the whole Vis-NIR region (1187 nm) is formed, starting in concurrence with the electrochemical onset. At around + 0.2 V, the neutral bands 385 and 613 nm start bleaching. Similar to all other compounds, an intermediate state of oxidation is also evidenced by spectroelectrochemical analysis, and is assigned to the radical cation, the absorption data can be correlated to the voltametric ones, as the band with maximum 727 nm reaches its highest intensity at 0.6 V, which coincides with to two close peaks at higher potentials in the CV. The band with maximum 1187 nm upon this potential value continues rising but with a different grow-rate (lower slope); this lower energy transition is assigned to the dication state localized on the $(T\text{-}BSeD\text{-}T)_2$ conjugated moieties.[102]

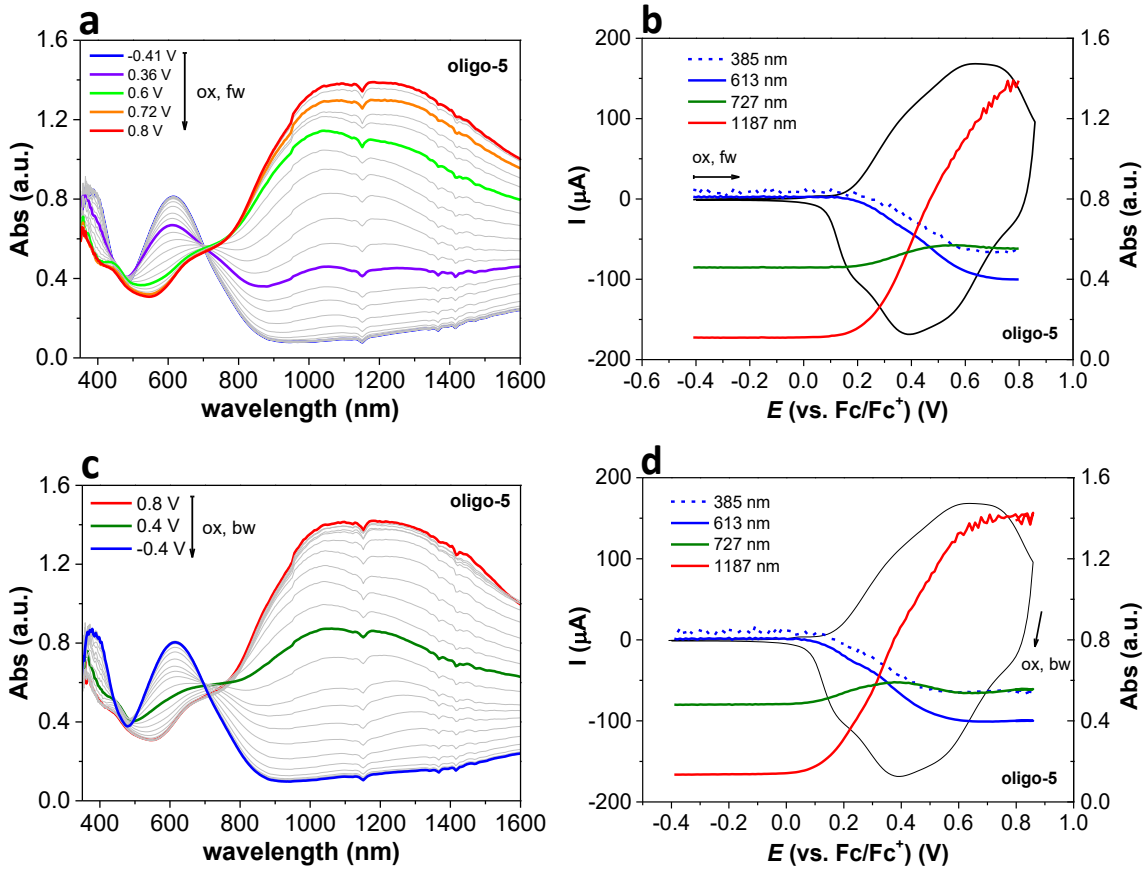

*Figure 4.69: **Oligo-5**: UV-Vis-NIR spectroelectrochemistry on films tested directly after electrodeposition, II oxidation cycle. ITO electrode, CH_2Cl_2/Bu_4NPF_6 0.1 M; 20 mV/s. First raw, charge (a) UV-Vis (b) CV with peak trend of selected wavelengths, and second raw, discharge (c) UV-Vis (d) CV with peak trend of selected wavelengths.*

4.2.3.3 In-Situ Conductance

To characterize the potential dependent conductivity behavior of electrodeposited films of oligo-4 and oligo-5, in-situ conductance experiments on Pt IDE with an interdigitated spacing of 10 μm, covered with the electrodeposited film were carried out. The complete

and homogeneous coverage of the interdigitated active area after electrodeposition was checked via optical microscopy (Figure 4.70 (top)) and scanning electron microscopy (Figure 4.70 (bottom)), indicating complete coverage of the interdigitated layer.

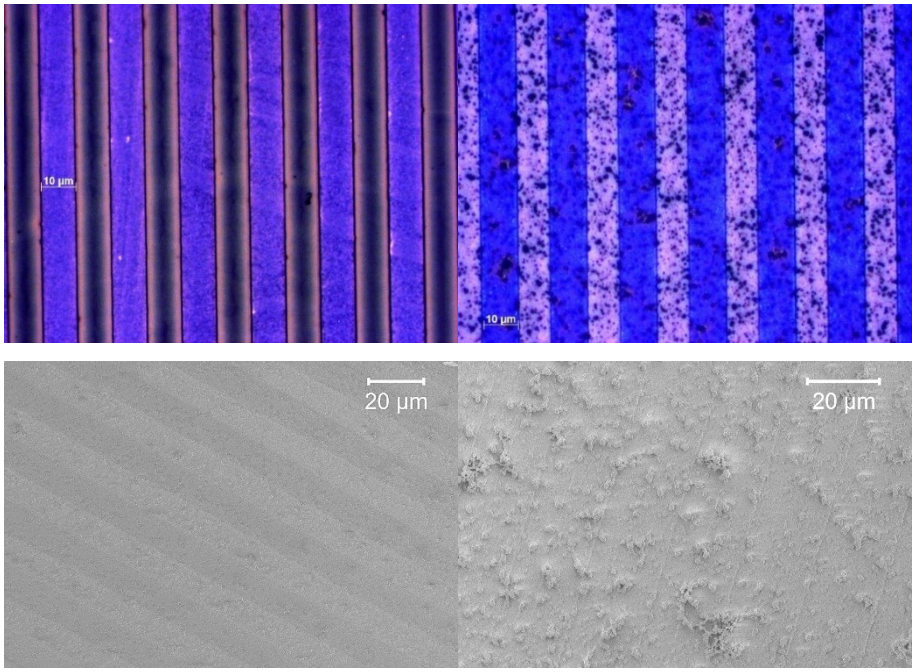

*Figure 4.70: Optical-microscopy pictures (top) and SEM pictures (InLenses, 0.9 and 0.7 kV respectively) (bottom) of **oligo-4** (left) and **oligo-5** (right) electrodeposited on 10 µm band coated interdigitated electrodes.*

In-situ conductance analysis of **oligo-4** (Figure 4.71 a) and **oligo-5** by, shows analogously to **oligo-2** a bell-shape conductance behavior characteristic of the mixed valence conductivity model. In the case of **oligo-4,** two conductance regimes are found at (+0.53 V) and (+0.73 V), and are associated with the two main redox-peaks. Also in the case of this material, the absolute conductance maximum at ca. +0.73 V corresponds to the $R^{+\cdot}$ /D^{2+} redox event on the $(T\text{-}BTD\text{-}T)_2$ moieties. The conductance change reproducibly presents lower values during the backward scan with respect to the forward scan, as already observed in the literature.[25,103,104]

Oligo-5 (Figure 4.71 (c)) is characterized by a wider window of conductivity for p-doping in comparison to the BTD counterpart. The electroactive film presents a bell-shape conductance in the potential window between +0.1 V and +0.8 V, showing a maximum at +0.6 V, in the case of the forward oxidation scan. In the potential window between + 0.1 V and 0.35 V, which includes the first oxidation peak in the voltammogram, with electrochemical oxidation of the biindole cores, only a small change in the *in-situ* conductance is observed. Upon further polarization, as the $(T\text{-}BSeD\text{-}T)_2$ units are oxidized, conductance starts increasing abruptly reaching a maximum at + 0.58 V. This value seems

to be localized on the third set of observable peaks which should be associated with the $R^{+\bullet}$ /D^{2+} redox transformation on the (T-BSeD-T)$_2$ conjugated moieties.

The *in-situ* conductance plot show good reversibility within different cycles; the conductance values are lower during the reverse scan in comparison to the forward scan and hysteresis phenomena are also observed. One possible explanation for the lower conductance values measured during the backward scan in comparison to the forward oxidations sweep could be, as proposed by Ofer *et al.*, [105] the overcoming of a kinetic barrier during the oxidation process. The authors claim that as the polymer becomes highly oxidized, coulombic repulsions might lead to changes in chain conformations, in order to stabilize the progressively more localized charges. The conformation adopted to diminish coulombic repulsions, is non-optimal for conductivity, consequently the conductivity curve during the backward scan could present lower conductance values. This asymmetry between conductivity in the forward and backward scan can be observed in different systems in the literature.[51,103,106] Observation of hysteresis during *in-situ* measurements in conducting polymers is a very common phenomenon. Several explanation have been proposed including: incomplete reversibility of the redox process, stabilization of the charged state or structural change in the charged state with formation of σ-dimers.[107,108] Further film thickness and diffusion of ions during the charge/discharge process also cover a significant role in determining the extent of hysteresis.[107,109]

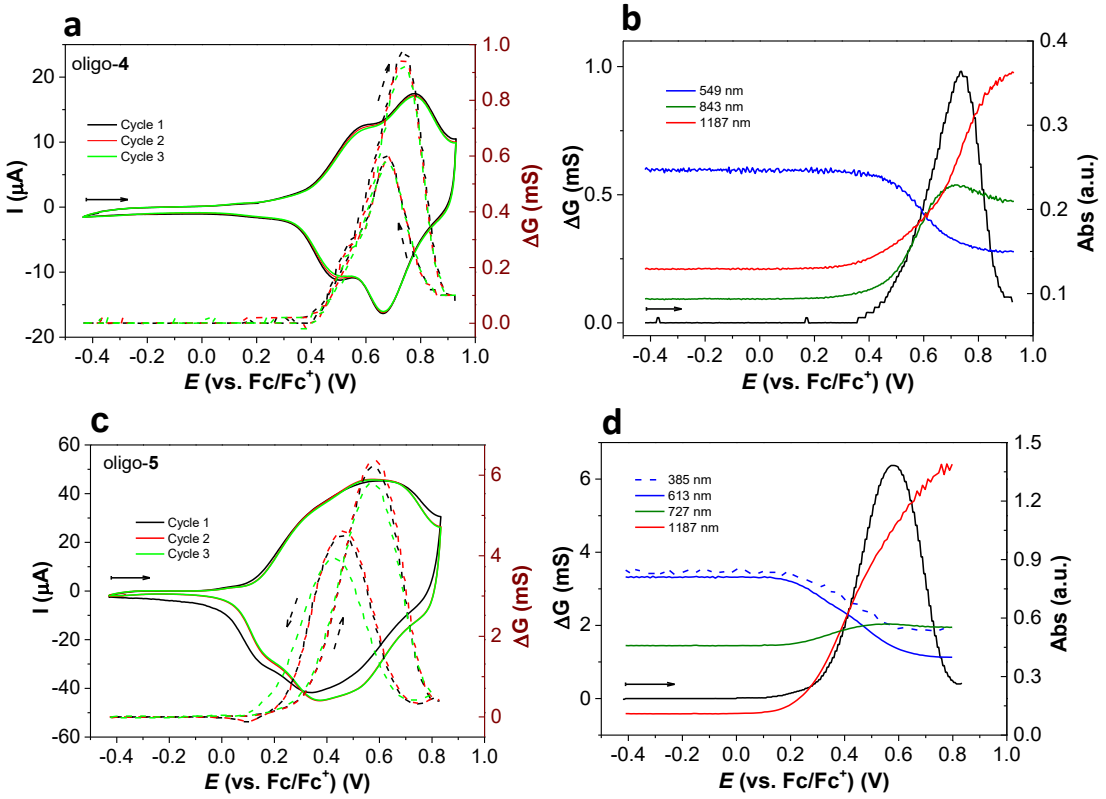

Figure 4.71: In-situ conductance plot of (a) ***oligo-4*** *and (c)* ***oligo-5****, 10 μm Pt interdigitated electrodes, scan-rate 20 mV/s in 0.1 M CH_2Cl_2/NBu_4PF_6. Superimposition of peak-trend and conductance change for selected wavelengths during the forward cycle of oxidation (b)* ***oligo-4*** *and (d)* ***oligo-5****.*

4.2.4 Electrochromism Oligo-(1-5)

The charging / discharging behavior of **oligo-1** to **oligo-5** were analyzed in order to asset the suitability of these systems as substrates for electrochromic applications to be developed with chiral compounds, paving the way towards their use as chiral electrochromic devices. From the spectroelectrochemical measurements performed, it is observed that **oligo-1**, **oligo-2** and **oligo-3,** present a similar signature for absorption in the different states of charge. In particular a maximum in the neutral state between 400 – 450 nm due to the π- π* transition. In the fully oxidized state (red curve) all three systems show a characteristic peak at ~550 nm and around 1200 nm in the NIR region. In the case of **oligo-4** and **oligo-5**.

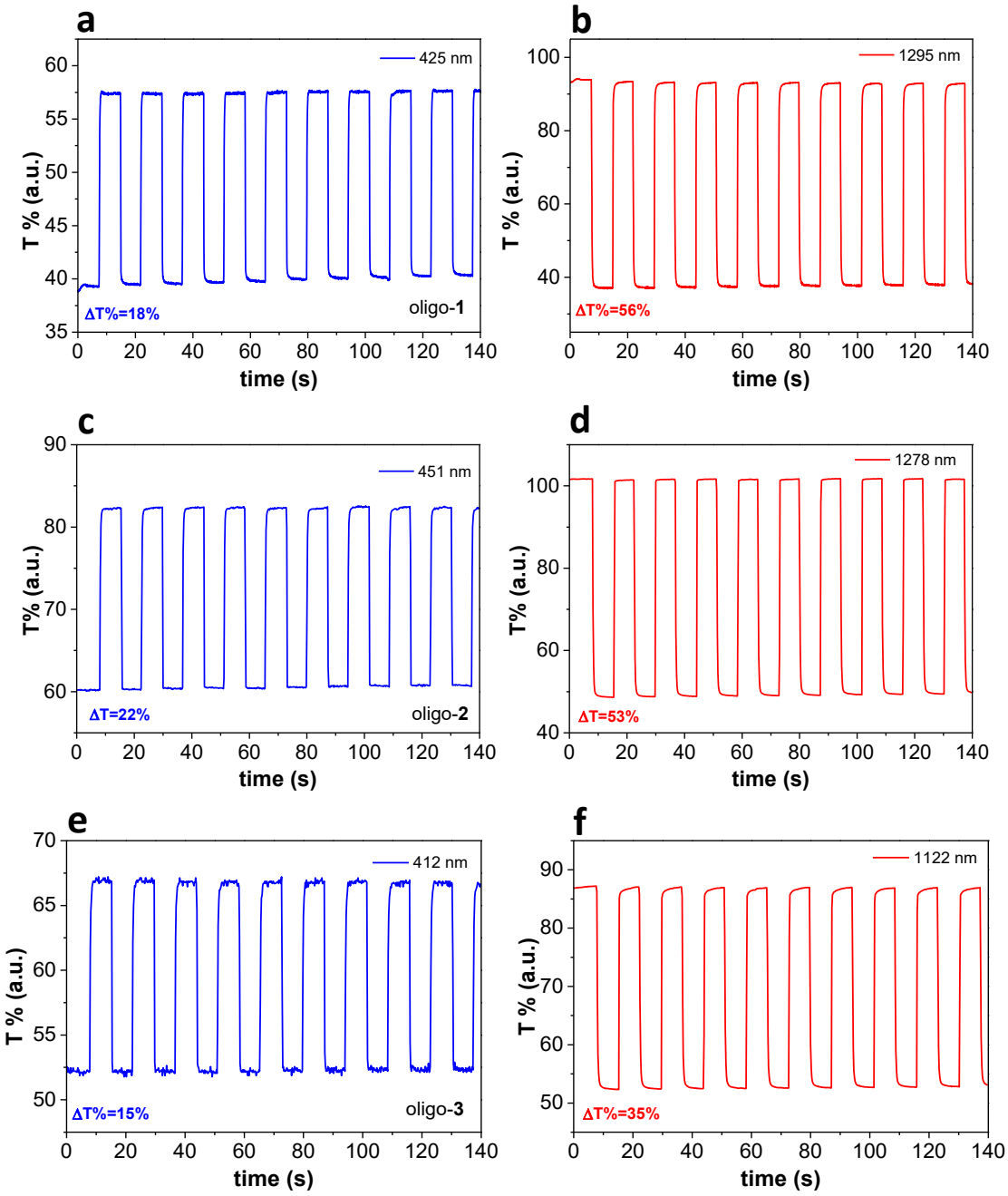

Figure 4.72: (a, b) ***Oligo-1****: percentage transmission (T%) change upon repeated charging / discharging cycles through chronoamperometry by applying a square-wave between 0 and 1.2 V vs Ag/AgCl; (-0.4 V and +0.8 V vs Fc/Fc⁺) (c, d)* ***Oligo-2****, square-wave between 0 and 1.2 V vs Ag/AgCl; (-0.4 V and +0.8 V vs Fc/Fc⁺). (d, e)* ***Oligo-3****, square-wave between 0 and 1.3 V vs Ag/AgCl; (-0.4 V and +0.9 V vs Fc/Fc⁺). All samples were cycled with 10 repetitions for 7 s each.*

The introduction of an acceptor unit causes a decrease in the optical and electrochemical band-gap, with shifting toward lower energies of the transitions for different states of oxidation. The characteristic mid-energy transition for the radical cation state, is found in this case at similar energies as for the internal charge transfer transition.

The electrochromic behavior, with regard to switching abilities of the films was also analysed and compared as function of the oligo-thienyl units. All films generally show good

electrochromic properties with a fast and reversible switch between neutral and oxidized state as evidenced by the chrono-charge-discharge experiments presented in Figure 4.72 - Figure 4.75.

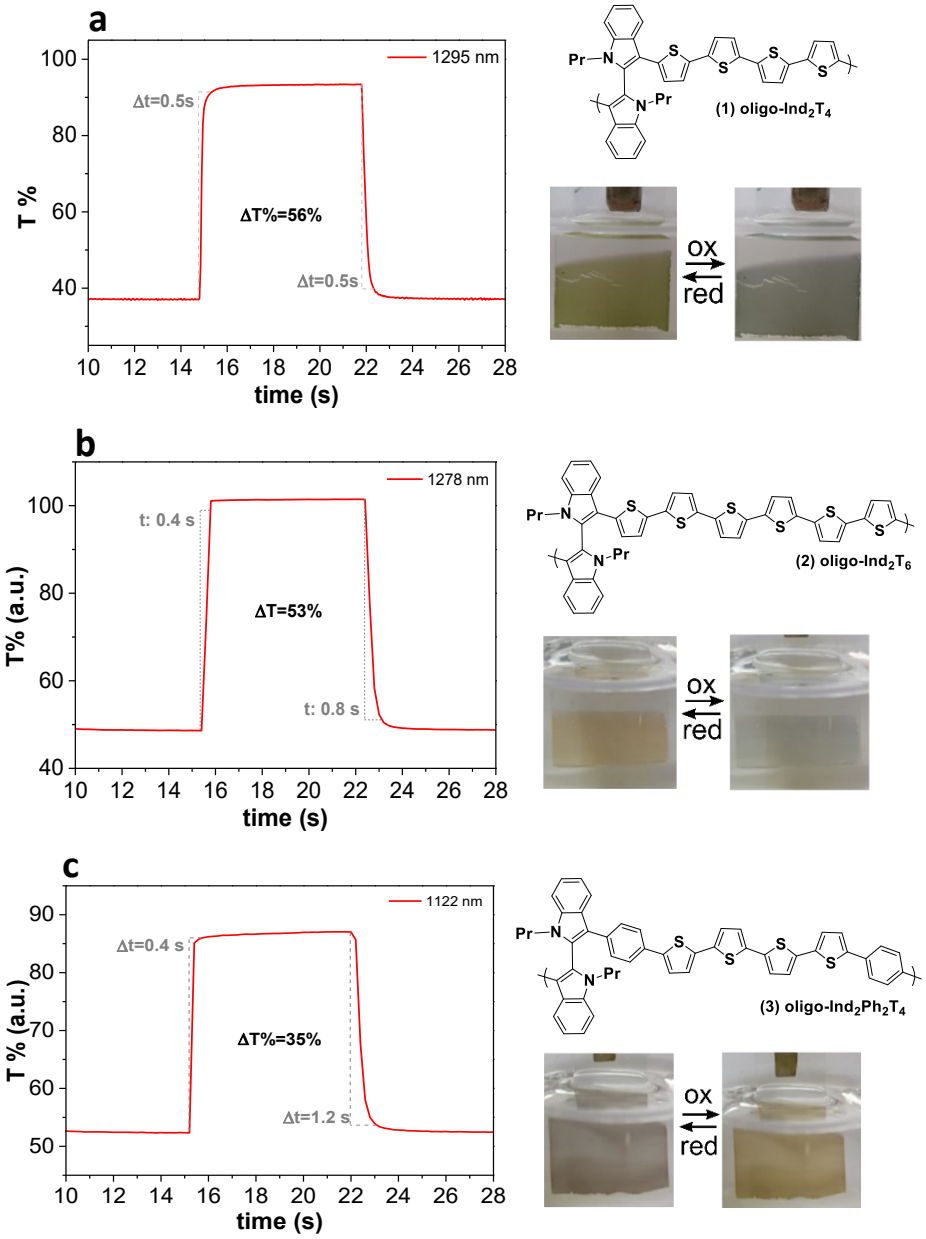

*Figure 4.73: Switch time for NIR maximum for (a) **oligo-1**, (b) **oligo-2** and (c) **oligo-3** (left). Pictures of films in neutral and fully charged states (right).*

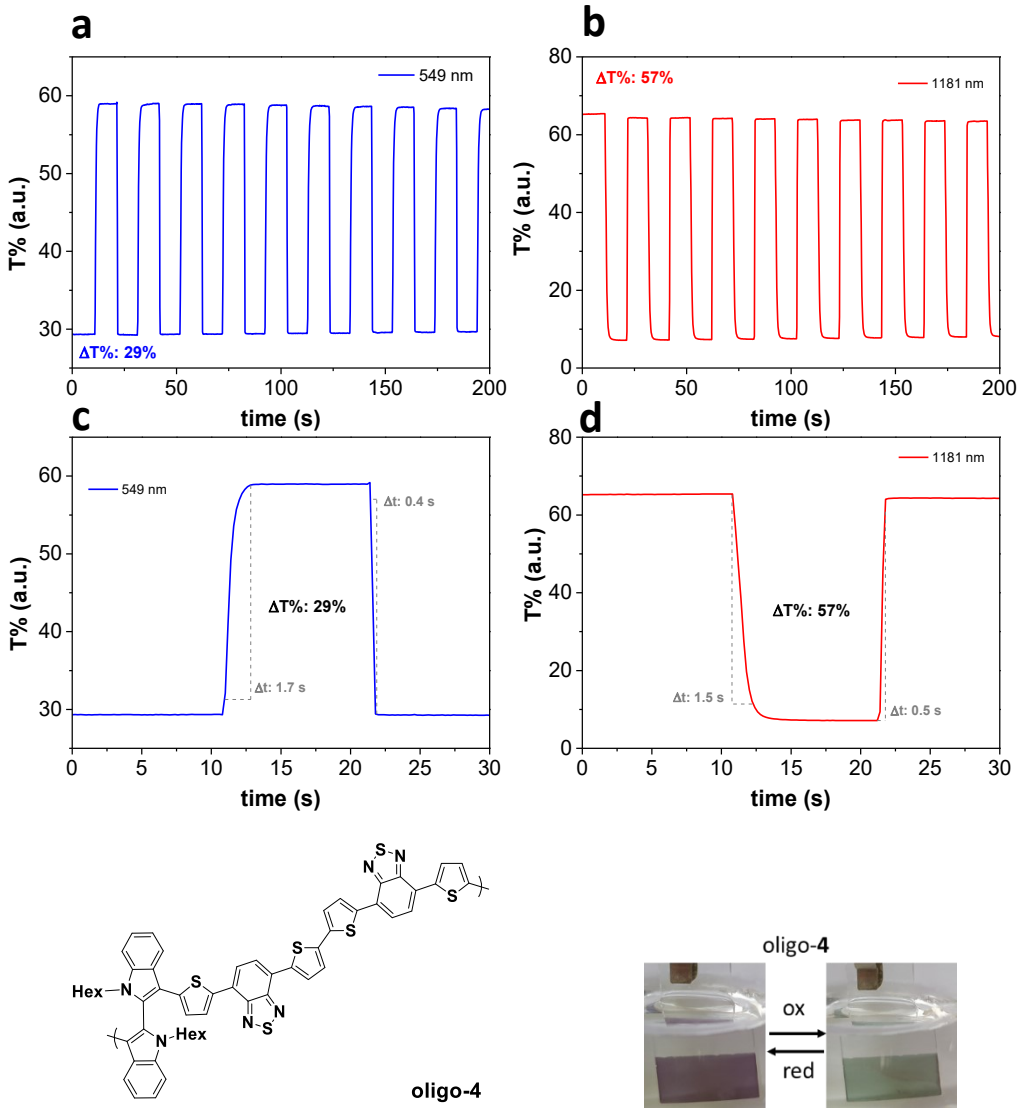

Figure 4.74: ***Oligo-4****: (a, b) percentage transmission (T%) change at 549 nm and 1181 nm upon repeated charging/discharging cycles through chronoamperometry by applying a square-wave between 0 and 1.2 V vs Ag/AgCl; (-0.4 V and +0.8 V vs Fc/Fc⁺). (c, d) Switch time for 95% of change of ΔT% at 549 nm and 1181 nm.*

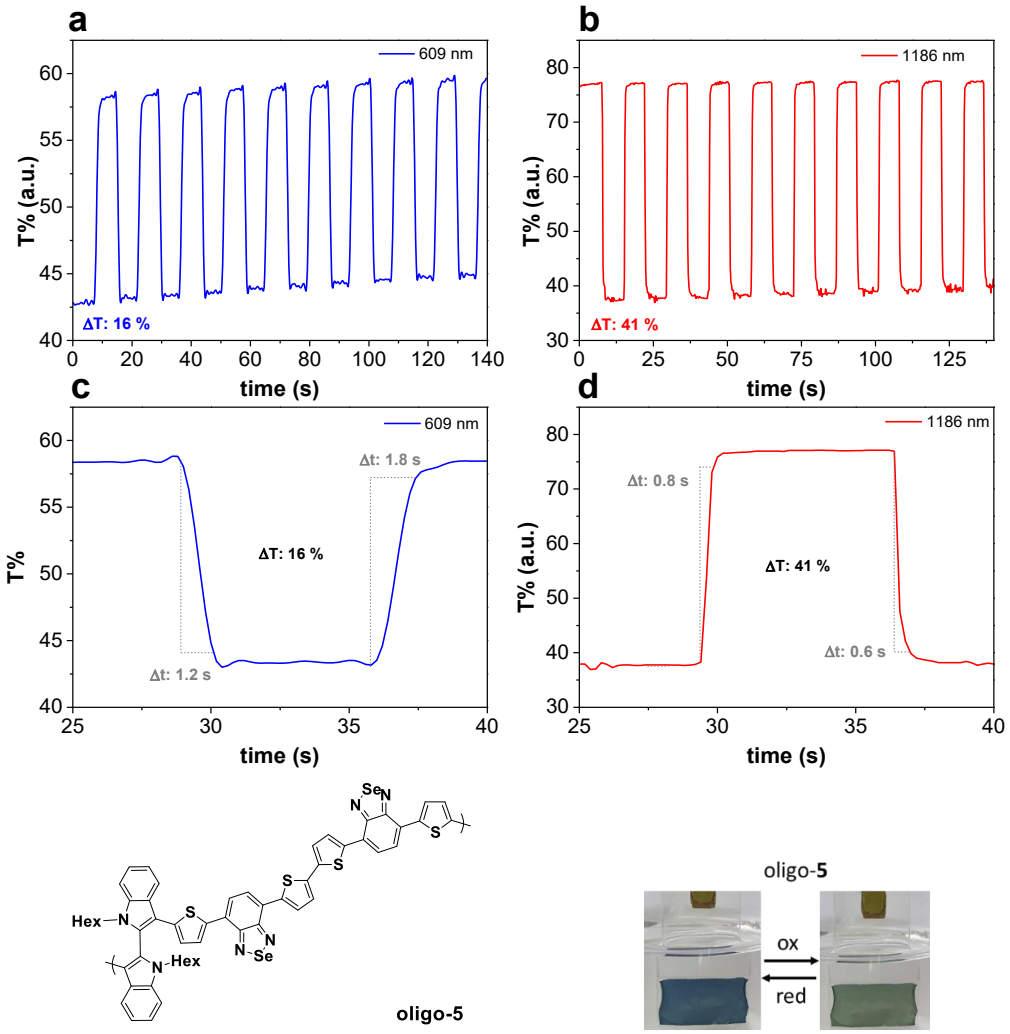

*Figure 4.75: **Oligo-5**: (a, b) percentage transmission (T%) change at 609 nm and 1186 nm upon repeated charging/discharging cycles through chronoamperometry by applying a square-wave between 0 and 1.2 V vs Ag/AgCl; (-0.4 V and +0.8 V vs Fc/Fc⁺). (c, d) Switch time for 95% of change of ΔT% at 609 nm and 1186 nm.*

A very good correlation with similar ΔT% and switching times is found between **oligo-1** and **oligo-3** which might also correlate to their structural similarities. Upon switching between neutral and fully oxidised state, a ΔT% of 18% and 22% is measured for the absorption maxima in the neutral states, and a ΔT% of 56% and 53% for the NIR absorption maximum, is measured for **oligo-1** and **oligo-3**, respectively. In the case of **oligo-2** ΔT% of 15% for the neutral maximum and a ΔT% of 35% for the NIR maximum are measured. All the films present a fast charging/discharging with switching times t <1 s measured for a 95% of ΔT% in the case of the NIR maximum. The obtained results are comparable in values with the ones reported in the literature for oligothiophene derivatives.[21,110,111] In the case of oligo-**4** and of oligo-**5**, a ΔT% of 29% and of 16% for the neutral maximum and a ΔT% of 57% and of 41% for the NIR maximum are respectively measured. **Oligo-4** displays similar

variations as for **oligo-1** and -**2**. In the case of **oligo-5** the lower ΔT% as well as the longer switching times are found. Overall, the most performant film is **oligo-4**.

Compound	E_{red} (V)	E_{ox} (V)	ΔT% (N_{max})	ΔT% (D^{2+}_{max})	t_{red} (D^{2+}_{max}) (s)	t_{ox} (D^{2+}_{max}) (s)
Oligo-1	-0.4 V	+0.8 V	18	56	0.5	0.5
Oligo-2	-0.4 V	+0.8 V	22	53	0.4	0.8
Oligo-3	-0.4 V	+0.9 V	15	35	0.4	1.2
Oligo-4	-0.4 V	+0.95 V	29	57	0.5	1.5
Oligo-5	-0.4 V	+0.8 V	16	41	0.6	0.8

*Table 4.9: Overview of electrochromic parameters for **oligo-1** to **oligo-5**.*

4.2.5 Conclusions

The redox behavior and electrodeposition of molecules **1**-**5** was studied and the doping behavior of the electrodeposited film was analyzed by *in-situ* electrochemical methods. The variations in the redox behavior are analyzed considering the effects of introduction of a π-spacer (**1**-**3**) and of an acceptor unit yielding push-pull systems (**4**-**5**). Compounds **1**-**5** behave as two independent but partially interacting redox systems, due to the presence of symmetric oligothienyl terminals, linked through an internal indole core allowing for residual interactions. By comparison of compounds **1** and **2**, it was found that the introduction of an additional thienyl unit in **2** induces a shift to less positive oxidation potentials in comparison to **1,** but identical peak-to-peak separations (~20 mV). The experimental results hint to the fact that the two molecules have similar residual interactions. Indeed, in the case of monomer **3**, which is characterized by a phenyl spacer, this separation is significantly lower (~10 mV). The results are explained by the less efficient conjugation of a phenyl unit in comparison to a thienyl unit, as also described in the literature. The introduction of an acceptor unit **4** and **5** allows the presence of a reversible reduction signal, thanks to stabilization through inductive effects from BTD and BSeD units, which also cause a shift of the oxidation signal towards more positive potentials and a narrower band-gap. The peak-to-peak separation is for the two compounds also similar (~22 mV) for both sets of peaks. Direct comparison with compounds **1** and **2** is not possible due to the presence of a different N-alkyl chain which also affects torsional angle and the residual interactions through the inter-annular backbone. All molecules can be successfully electrodeposited in a low polar solvent such as CH_2Cl_2; the resulting films present good redox-reversibility and only partial loss of electroactivity upon multiple cycling. The electrochromic properties of the films are also analyzed, showing that all electroactive films can be repeatedly charged and discharged between their neutral and oxidized states in a highly reversible fashion. Further,

all electroactive film present a good electrochromic properties with highest change in transmittance ΔT found for **oligo-4**.

Compared to previous works on systems bearing an atropoisomeric 3,3'-bithianaphthene core,[76] we found that the substitution of the latter with a 2,2'-biindole scaffold does not induce significant variations in the absorption properties of the electrodeposited film, with regards to the position and topology of the bands at different states of charge. It was also found that absorption maxima correlate satisfactorily with the one of the respective oligothienyl moieties. Similar UV-Vis-NIR spectroelectrochemical signatures are found for all compounds, which are dominated by the ones of the oligothienyl moiety. The introduction of acceptor units leads to a bathochromic shift of all absorption bands in the different states of charge; this effect is maximized in the neutral state. It was also found that all electrodeposited films are obtained in a partially oxidized state after electrodeposition as evidenced by residual absorption at typical wavelengths of the radical cation.

Charge trapping phenomena are identified for all compounds analyzing the absorption of the pristine films after electrodeposition. Reduction of **oligo-4** and **oligo-5**, despite chemically reversible, leads to a significant loss of electroactive material from the electrode and hints to significant charge trapping after electrodeposition process. Optimization of electrodeposition conditions and their effects on charging-discharging behavior of the films as well as charge trapping should be further investigated. In all atropoisomeric systems analyzed upon oxidation conductivity is ruled by a mixed-valence behavior, in which the majority of contribution to *in-situ* conductivity is given by the couple $R^{+\bullet}/D^{2+}$ generated on the conjugated oligothienyl units. The measurements also hint towards the marginal role played by the biindole scaffold in determining charge transport within the system, similarly as for absorption properties. For lower oxidation potentials the activation of the biindole centers, more spatially separated between each other and characterized by intrinsic 3D character of the atropoisomeric unit, is generally associated with a negligible conductance increase.

The enantiodiscrimination ability of enantiopure **oligo-2** films was also demonstrated with the benchmark (*S*)-(-)- and (*R*)-(+)-*N,N'*-dimethyl-1-ferrocenylethylamine chiral redox probes. A peak potential separation of ~40 mV between the two antipodes was reproducibly measured, specularly for the two enantiomeric films. As outlook, the enantioselective performance of biindole films for analyzing more advanced and performant chiral probes for applications in analytic and sensing applications will be approved. Further, the reversible electrochromic behavior of these systems might trigger research on chiral electrochromic devices.

4.2.6 Experimental

4.2.6.1 *Electrochemical Measurements*

All the electrochemical measurements were performed in a 0.1 M CH_2Cl_2 with Bu_4NPF_6 as supporting electrolyte with the electrochemical set-up described in section 3.1.1.1. Differential-Pulse-Voltammetry (DPV) experiments were performed at a scan-rate of 20 mV/s and with a modulation amplitude of 25 mV.

4.2.6.1.1 Electrodeposition

Sample preparation was performed through electrodeposition of racemate solution under potentiodynamic conditions on different electrode substrates: (a) ITO-coated glass slides or (b) Au slides and (c) Pt interdigitated electrodes with a 10 µm band width were used. Electrochemical measurements were performed with an Autolab PGSTAT204 potentiostat (Metrohm Autolab, Utrecht, The Netherlands) at room temperature and under Argon atmosphere. A three-electrode glass cell provided with a Pt plate as counter electrode (CE) and an AgCl-coated silver wire as pseudo reference electrode (RE) were employed. For the electrodeposition as well as all the electrochemical measurements a 0.1 M CH_2Cl_2 solution with Bu_4NPF_6 as supporting electrolyte was employed as received, a 0.5 mM molecule concentration was employed for molecules characterization and electrodeposition. The electrolyte solution was degassed through Argon bubbling before the measurements. All potentials were referenced to the formal potential of the Fc/Fc^+ reference redox couple, measured in the same conditions of the analytes. Further details about substrate cleaning, reagents and the electrochemical set-up employed are discussed in section 3.1.1. After electrodeposition, the films were rinsed with CH_2Cl_2 to remove residual NBu_4PF_6 and monomer. When not directly employed, the samples were stored under inert atmosphere.

Molecule	Electrodeposition Window (*vs.* Ag/AgCl V)	Scan-Rate (mV/s)	Cycles Number	Concentration (mM)
1	0 – 1.45	20	20	0.5
2	0 – 1.40	20	20	0.5
3	0 – 1.45	20	20	0.5
4	0 – 1.45	20	10	0.5
5	0 – 1.40	20	10	0.5

*Table 4.10: Overview of electrodeposition parameters for compounds **1**-**5**.*

The potential window of electrodeposition was adapted for each species based on the monomer characterization. In the case of compounds **4** and **5** to achieve similar currents as for compounds **1**-**3,** the number of electrodeposition cycles was limited to 10 cycles

instead of 20 due to their higher tendency towards electrodeposition. Samples deposited at a scan-rate of 50 mV/s were in addition tested for spectroelectrochemical measurements.

4.2.6.1.2 In-situ Conductance

In-situ conductance experiments were performed using a three-electrode set-up electrochemical cell endowed with 10-µm Pt IDE electrodes (DropSens), an Autolab PGSTAT204 potentiostat (Metrohm), a µSTAT400 (DropSens) and a conductivity interface CIP2 (*Heka*). Detailed description of the experimental set-up for *in-situ* conductance are reported in section 3.1.1.2.2. All measurements were performed, unless specified, under Argon atmosphere in 0.1 M CH_2Cl_2/NBu_4NPF_6 with a scan-rate of either 20 mV/s , and by applying a drain potential of 20 mV between the combs. All potential values are referenced to the Fc/Fc^+ internal standard.

4.2.6.1.3 In-situ UV-Vis-NIR Spectroelectrochemistry

In-situ UV-Vis spectroelectrochemistry were performed using an Autolab PGSTAT204 potentiostat (Metrohm) and a Zeiss UV−vis spectrometer endowed with a MCS621 Vis II spectrometer cassette and a CLH600F lamp. The measurements were conducted in a custom-made three-electrodes quartz cell employing a Pt wire as counter electrode (CE), an AgCl coated Ag wire as (pseudo)reference electrode (RE) and polymer-coated 10 µm interdigitated (IDE) Pt electrodes (Dropsens) as working electrode (WE). The measurements were performed in CH_2Cl_2/NBu_4NPF_6 at a scan rate of 20 mV s^{-1} under Ar atmosphere and all the potential values were referenced to the formal potential of the Fc/Fc^+ redox couple. Further Information about the experimental set-up and procedure are found in section 3.1.1.2.1.

4.2.6.1.4 Electrochromism

The electrochromic behavior of **oligo-1** - **oligo-5** was performed by chronoamperometric experiment, applying square-waves between two selected potential and by simultaneous determination of the transmittance every 0.2 s. The electrode was kept for 7 s at each potential performing 10 repetitions for each polarization potential.

4.2.6.2 *Enantioseparation Measurements*

4.2.6.2.1 Semi-preparative Enantioseparations

Semipreparative enantioseparations were performed by Dr. Roberto Cirilli (Istituto superiore di Sanità, Roma) with a HPLC system equipped with a PerkinElmer (Norwalk, CT, USA) 200 LC pump, a Rheodyne (Cotati, CA, USA) injector, a 5 mL sample loop, a PerkinElmer LC 101 oven and Waters (Waters Corporation, Milford, USA) 484 detector. The signal was acquired and processed by the Clarity software (DataApex, Prague, the Czech Republic).

Elutions were performed at 15°C with a Chiralpak IB (250 mm x 4.6 mm, 5 mm) column, using n-hexane-acetone-isopropanol 100:5:1 (v/v/v); flow rate, 1 mL min-1 as mobile phase (*Figure 4.79*). Detection was obtained by circular dicroism (CD) at 380 nm.

4.2.6.2.2 Electrodeposited Inherently Chiral Electroactive Films for Enantiodiscrimination Tests

Enantioseparation tests were performed by S. Grecchi (University of Milan). The conducting oligomer films were electrodeposited from the corresponding enantiopure **2** (*EN1*) or (*EN2*) monomer solutions (0.75 mM), in dichloromethane (CH_2Cl_2, Aldrich, HPLC grade) with 0.1 M Bu_4NPF_6 (Fluka, electrochemical grade) as supporting electrolyte. Electrodepositions were performed by repeated potential cycling (20 CV cycles, at 0.2 V s^{-1} scan rate on the GC disk electrode). CV and Differential Pulse Voltammetry (DPV) experiments were performed using an Autolab PGSTAT potentiostat (Eco-Chemie, Utrecht, The Netherlands), controlled by a PC with the GPES software provided by the same manufacturer. The three-electrode V-shaped minicell (with 3 cm^3 of substrate solution) was equipped with a glassy carbon disk embedded in glass (GC, Metrohm, S = 0.031 cm^2) as working electrode, a Pt disk as counter electrode, and an aqueous saturated calomel (SCE) as reference electrode, inserted in a compartment filled with the working medium and ending with a porous frit, to avoid water and KCl leakage into the working solution. The optimized preliminary polishing procedure for the GC disk electrode consisted in treatment with a diamond powder of 1 μm diameter (Aldrich) on a wet DP-Nap cloth (Struers®). The potential values were referred to the $Fc^+|Fc$ redox measured in the same working conditions (+0.49 V *vs* SCE in CH_2Cl_2).

4.2.7 Appendix to 4.2

4.2.7.1 *Synthesis*

The synthesis and correlated characterization of all molecules employed in this chapter was performed by the PhD student L. Scapinello at University of Como. The synthetic approach to 3,3'-diheteroaryl-2,2'-biindoles was inspired from work published by Abbiati *et al*.[112] in 2006. The reaction protocol exploits Pd catalysed double indole ring closure with 3,3' functionalization in single step starting from dialkyne 2,2,2-trifuoro-*N*-(2-(4-[2,2,2-trifuoro-acetylamino-phenyl]-buta-1,3-diynyl)-phenyl)-acetamide (trifluoroacetamide) **1** and appropriate heteroaryl halide in refluxing MeCN. Heteroannulation was reported by Abbiati to be more performant when iodides were employed [67] (compounds **2** and **3**). The solvent was switched to refluxing DMF to afford biindoles **8** and **9** in discrete yield due to low solubility of starting halides **3** and **4**. A subsequent propylation step was necessary to afford soluble and processable compounds **12-14.**

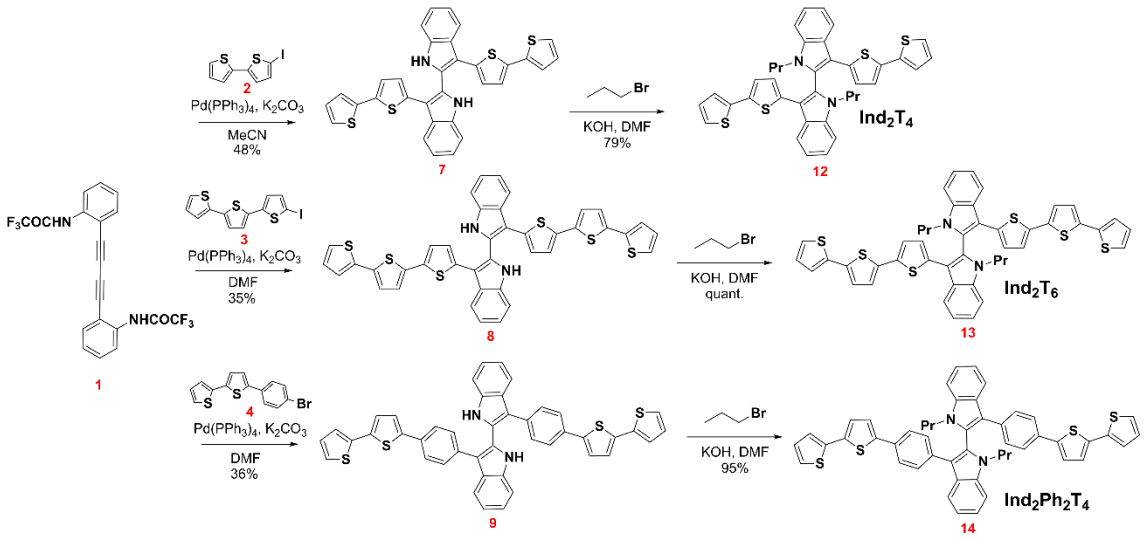

Scheme 4.2 Synthetic route of 3,3'-diheteroaryl-2,2'-biindoles yelding Ind_2T_4; Ind_2T_6 and $Ind_2Ph_2T_4$.

Similarly, also for the synthesis of 2,2'-biindole products bearing thienyl donor-acceptor units, the same Pd catalysed method published by Abbiati *et al*. was employed. Despite bromides were noticed as less reactive than iodide ones; the brominated compounds **5** and **6** were chosen as coupling partners as iodinated analogues were much less soluble and obtained in much lower yield. Best hetero-annulation conditions were found in refluxing reactants in DMF as solvent in presence of palladium(Tetrakis) as catalyst (Scheme 4.3). Corresponding 3,3'-diheteroaryl-2,2'-biindoles **10-11** were isolated as very low soluble solids. Only 2,2'-biindole obtained from halide **1** was soluble enough to be purified by chromatography and it was afforded in 35%. The intermediate compounds (**7-9**) were directly used for subsequent alkylation reaction without any further purification. Hexyl chains were introduced on biindoles **10** and **11** by KOH biindole deprotonation and subsequent alkyl bromide addition.

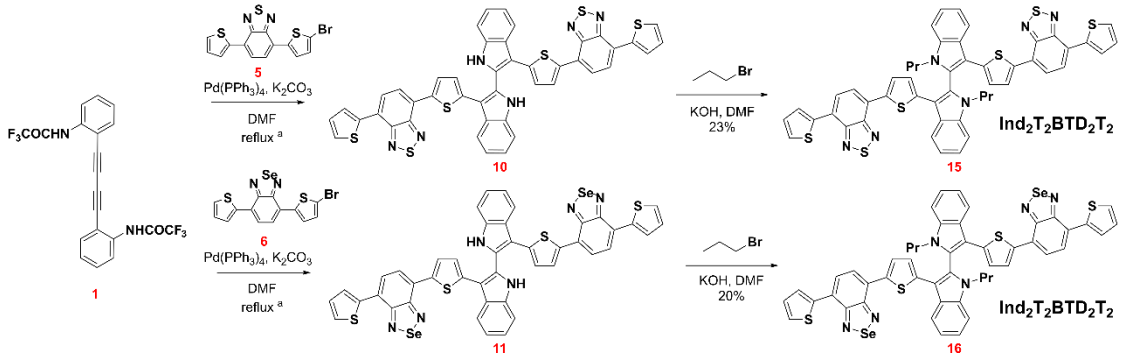

*Scheme 4.3: Synthetic route of 3,3'-diheteroaryl-2,2'-biindoles: $Ind_2T_2BTD_2T_2$; $Ind_2T_2BSeD_2T_2$. Yield of **10** and **11** was not calculated as the raw product was directly used for next step.*

4.2.7.2 *Additional Data*

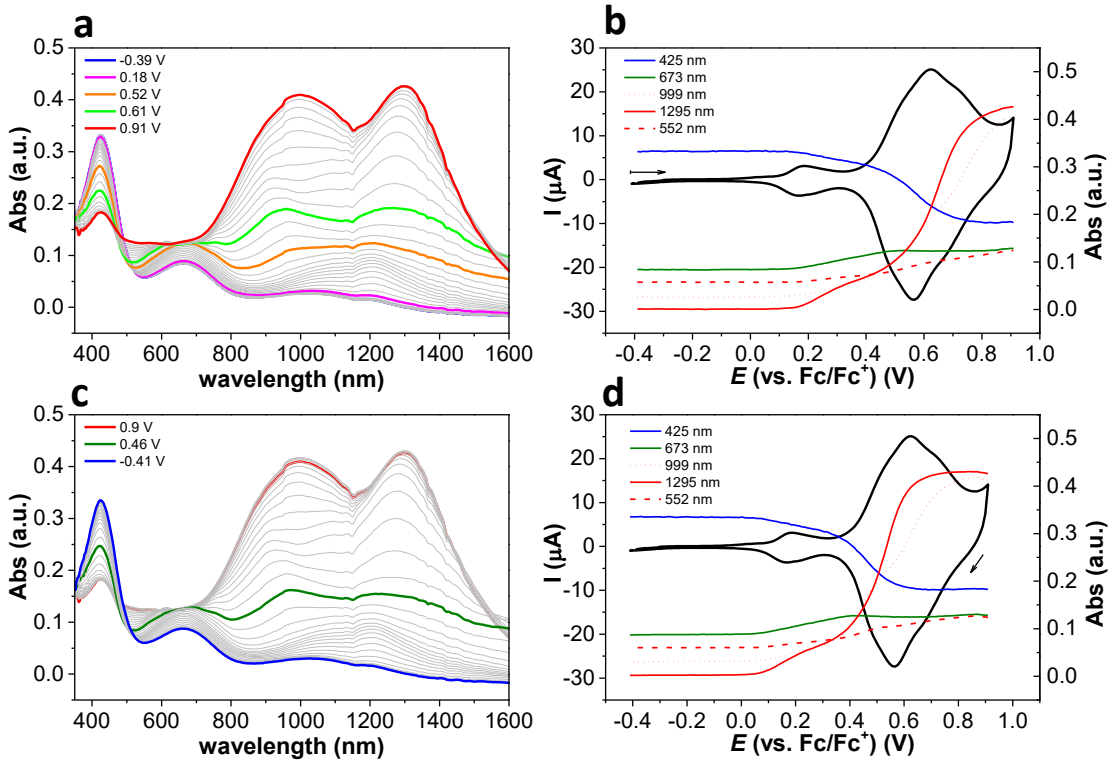

Figure 4.76: UV-Vis-NIR spectroelectrochemistry forward (first raw) and backward cycle (second raw) for ***oligo-1***.

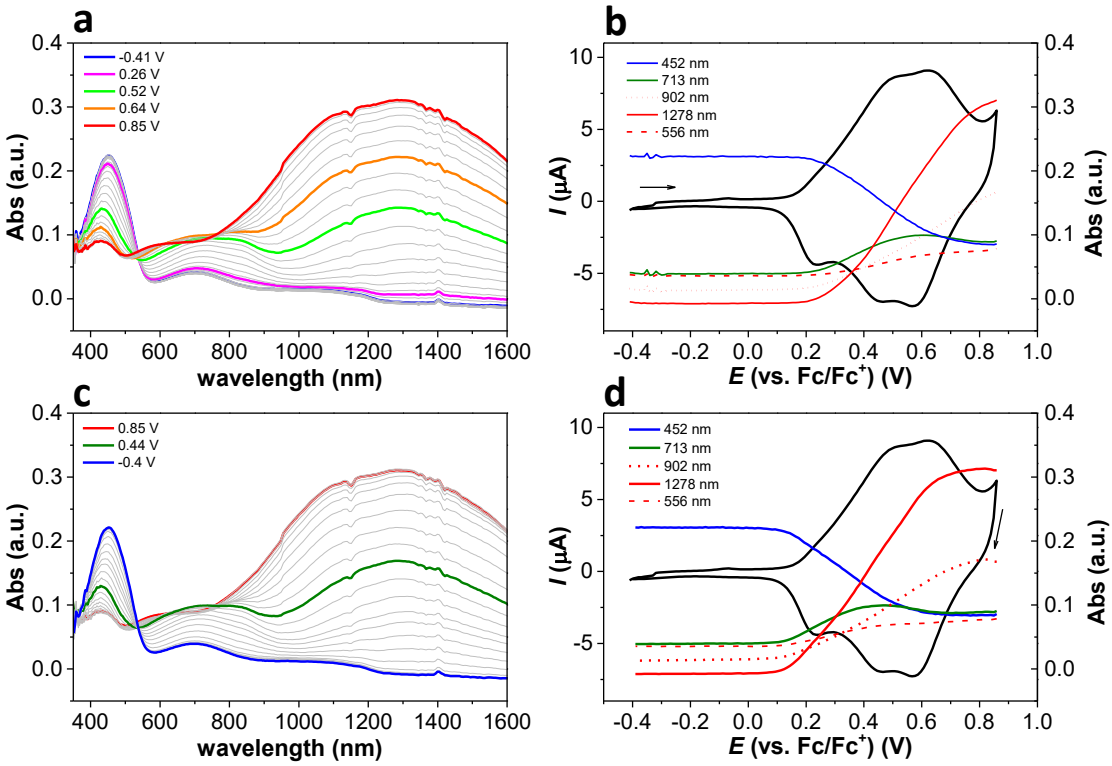

Figure 4.77: UV-Vis-NIR spectroelectrochemistry forward (first raw) and backward cycle (second raw) for ***oligo-2***.

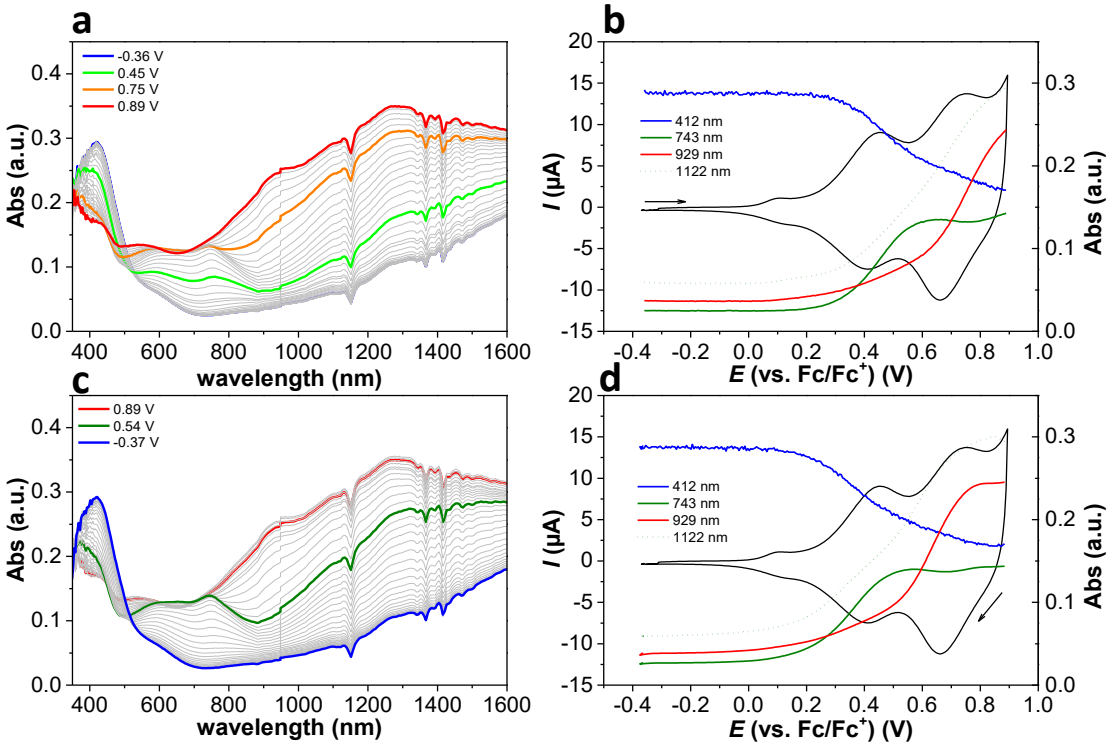

*Figure 4.78: UV-Vis-NIR spectroelectrochemistry forward (first raw) and backward cycle (second raw) for **oligo-3**.*

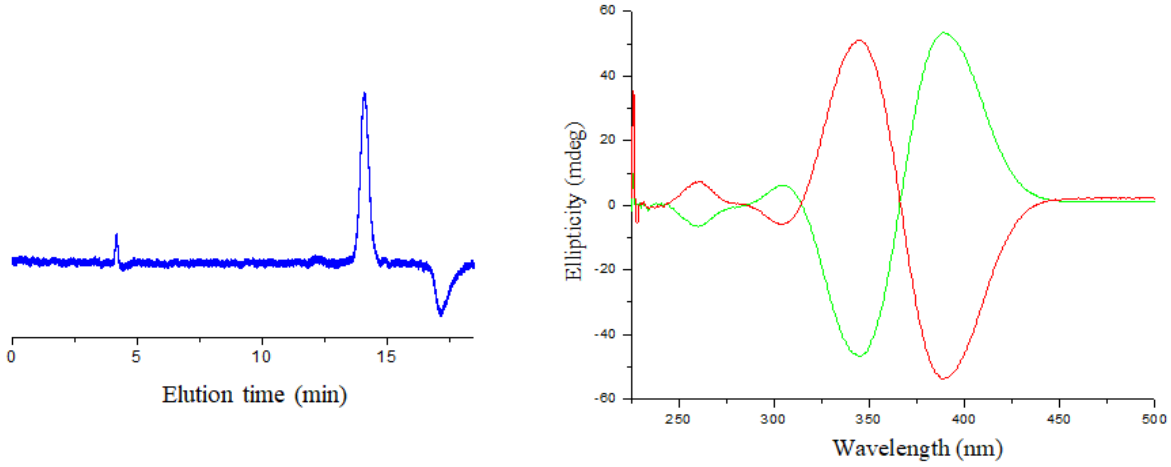

*Figure 4.79: Left side: HPLC enantioseparation of **2**. Right side: CD curves of **2** (EN1) (green) and (EN2) (red).*

4.3 References

[1] C. Malacrida, A. H. Habibi, S. Gámez-Valenzuela, I. Lenko, P. S. Marqués, A. Labrunie, J. Grolleau, J. T. López Navarrete, M. C. Ruiz Delgado, C. Cabanetos, et al., *ChemElectroChem* **2019**, *6*, DOI 10.1002/celc.201900565.

[2] P. Blanchard, C. Malacrida, C. Cabanetos, J. Roncali, S. Ludwigs, *Polym. Int.* **2019**, *68*, 589–606.

[3] C. Malacrida, L. Scapinello, R. Cirilli, S. Grecchi, A. Penoni, T. Benincori, S. Ludwigs, *ChemElectroChem* **2021**, *8*, 3250–3261.

[4] Y. Shirota, H. Kageyama, *Chem. Rev.* **2007**, *107*, 953–1010.

[5] M. Thelakkat, *Macromol. Mater. Eng.* **2002**, *287*, 442–461.

[6] J. Roncali, P. Leriche, P. Blanchard, *Adv. Mater.* **2014**, *26*, 3821–3838.

[7] V. Malytskyi, J.-J. Simon, L. Patrone, J.-M. Raimundo, *RSC Adv.* **2015**, *5*, 354–397.

[8] X. Che, X. Xiao, J. D. Zimmerman, D. Fan, S. R. Forrest, *Adv. Energy Mater.* **2014**, *4*, 1400568–1400574.

[9] X. Che, Y. Li, Y. Qu, S. R. Forrest, *Nat. Energy* **2018**, *3*, 422–427.

[10] R. F. Nelson, R. H. Philp, *J. Phys. Chem.* **1979**, *83*, 713–716.

[11] M. Schmittel, A. Burghart, *Angew. Chemie (International Ed. English)* **1997**, *36*, 2550–2589.

[12] T. Benincori, S. Gámez-Valenzuela, M. Goll, K. Bruchlos, C. Malacrida, S. Arnaboldi, P. R. Mussini, M. Panigati, J. T. López Navarrete, M. C. Ruiz Delgado, et al., *Electrochim. Acta* **2018**, *284*, 513–525.

[13] J. Roncali, *Adv. Energy Mater.* **2011**, *1*, 147–160.

[14] M. Zhao, H. Zhang, C. Gu, Y. Ma, *J. Mater. Chem. C* **2020**, *8*, 5310–5320.

[15] M. I. Mangione, R. A. Spanevello, D. Minudri, P. Cavallo, L. Otero, F. Fungo, *Electrochim. Acta* **2018**, *263*, 585–595.

[16] Y. Wang, S. Zhang, J. Wu, K. Liu, D. Li, Q. Meng, G. Zhu, *ACS Appl. Mater. Interfaces* **2017**, *9*, 43688–43695.

[17] X. Ji, T. Zhou, X. Ke, W. Wang, S. Wu, M. Zhang, D. Lu, X. Zhang, Y. Liu, *J. Mater. Chem. A* **2020**, *8*, 5163–5170.

[18] M. Y. Chou, M. K. Leung, Y. O. Su, C. L. Chiang, C. C. Lin, J. H. Liu, C. K. Kuo, C. Y. Mou, *Chem. Mater.* **2004**, *16*, 654–661.

[19] K. Karon, M. Lapkowski, A. Dabuliene, A. Tomkeviciene, N. Kostiv, J. V. Grazulevicius, *Electrochim. Acta* **2015**, *154*, 119–127.

[20] H. J. Yen, G. S. Liou, *Polym. Chem.* **2018**, *9*, 3001–3018.

[21] T.-G. Sun, Z.-J. Li, J.-Y. Shao, Y.-W. Zhong, *Polymers (Basel).* **2019**, *11*, 73.

[22] S. H. Hsiao, J. W. Lin, *Polym. Chem.* **2014**, *5*, 6770–6778.

[23] X. Lv, W. Li, M. Ouyang, Y. Zhang, D. S. Wright, C. Zhang, *J. Mater. Chem. C* **2017**, *5*, 12–28.

[24] P. Taranekar, T. Fulghum, D. Patton, R. Ponnapati, G. Clyde, R. Advincula, *J. Am. Chem. Soc.* **2007**, *129*, 12537–12548.

[25] C. Malacrida, A. Hossein, S. Gámez-Valenzuela, I. Lenk, P. Simon, A. Labrunie, J. Grolleau, J. T. López Navarrete, M. C. Ruiz Delgado, C. Cabanetos, et al., *ChemElectroChem* **2019**, 1–15.

[26] Y. Jiang, C. Cabanetos, M. Allain, P. Liu, J. Roncali, *J. Mater. Chem. C* **2015**, *3*, 5145–5151.

[27] R. F. Nelson, R. N. Adams, *J. Am. Chem. Soc.* **1968**, *90*, 3925–3930.

[28] O. Yurchenko, D. Freytag, L. Zur Borg, R. Zentel, J. Heinze, S. Ludwigs, *J. Phys. Chem. B* **2012**, *116*, 30–39.
[29] E. T. Seo, R. F. Nelson, J. M. Fritsch, L. S. Marcoux, D. W. Leedy, R. N. Adams, *J. Am. Chem. Soc.* **1966**, *88*, 3498–3503.
[30] C. Sandford, M. A. Edwards, K. J. Klunder, D. P. Hickey, M. Li, K. Barman, M. S. Sigman, H. S. White, S. D. Minteer, *Chem. Sci.* **2019**, *10*, 6404–6422.
[31] A. J. Bard, L. R. Faulkner, V. S. Bagotsky, *Electrochemical Methods Fundamentals of Electrochemistry*, **2001**.
[32] G. Macfie, J. H. Atherton, R. G. Compton, *Electroanalysis* **2002**, *14*, 479–485.
[33] Y. Shirota, *J. Mater. Chem.* **2000**, *10*, 1–25.
[34] L. Jin, B. Hu, Z. Liu, X. Zhang, M. Mo, C. Li, *J. Electrochem. Soc.* **2018**, *165*, 155–162.
[35] A. Leliège, C.-H. Le Régent, M. Allain, P. Blanchard, J. Roncali, *Chem. Commun.* **2012**, *48*, 8907–8909.
[36] E. V. Shklyaeva, O. A. Maiorova, I. V. Lunegov, A. N. Bakiev, D. G. Selivanova, G. G. Abashev, A. N. Vasyanin, A. A. Gorbunov, *Chem. Heterocycl. Compd.* **2016**, *52*, 379–387.
[37] A. Leliège, J. Grolleau, M. Allain, P. Blanchard, D. Demeter, T. Rousseau, J. Roncali, *Chem Eur J* **2013**, *19*, 9948–9960.
[38] S. C. Creason, J. Wheeler, R. F. Nelson, *J. Org. Chem.* **1972**, *37*, 4440–4446.
[39] R. J. Waltman, J. Bargon, *Tetrahedron* **1984**, *40*, 3963–3970.
[40] Y. Su, X. Wang, Y. Li, Y. Song, Y. Sui, X. Wang, *Angew. Chemie - Int. Ed.* **2015**, *54*, 1634–1637.
[41] G. Tan, X. Wang, *Acc. Chem. Res.* **2017**, *50*, 1997–2006.
[42] X. Wang, Z. Zhang, Y. Song, Y. Su, X. Wang, *Chem. Commun.* **2015**, *51*, 11822–11825.
[43] J. Hioe, D. Šakić, V. Vrček, H. Zipse, *Org. Biomol. Chem.* **2015**, *13*, 157–169.
[44] M. Moreno, C. P. Andrieux, J. Bertrán, I. Gallardo, D. Larumbe, *J. Chem. Soc., Perkin Trans. 2* **2004**, *0*, 1437–1443.
[45] A. Smie, A. Synowczyk, J. Heinze, R. Alle, P. Tschuncky, G. Götz, P. Bäuerle, *J. Electroanal. Chem.* **1998**, *452*, 87–95.
[46] P. Bäuerle, *Adv. Mater.* **1992**, *4*, 102–107.
[47] G. Engelmann, G. Kossmehl, J. Heinze, P. Tschuncky, W. Jugelt, H.-P. Welzel, *J. Chem. Soc., Perkin Trans. 2* **1998**, *0*, 169–176.
[48] J. Roncali, R. Garreau, A. Yassar, P. Marque, F. Garnier, M. Lemaire, *J. Phys. Chem.* **1987**, *91*, 6706–6714.
[49] A. Smie, J. Heinze, *Angew. Chemie - Int. Ed.* **1997**, *36*, 363–367.
[50] P. Audebert, J. M. Catel, G. Le Coustumer, V. Duchenet, P. Hapiot, *J. Phys. Chem. B* **1998**, *102*, 8661–8669.
[51] J. Heinze, B. A. Frontana-Uribe, S. Ludwigs, *Chem. Rev.* **2010**, *110*, 4724–4771.
[52] G. Tan, X. Wang, *Acc. Chem. Res.* **2017**, *50*, 1997–2006.
[53] J. W. Choi, C.-H. Kim, J. Pison, A. Oyedele, D. Tondelier, A. Leliège, E. Kirchner, P. Blanchard, J. Roncali, B. Geffroy, *RSC Adv.* **2014**, *4*, 5236–5242.
[54] A. Labrunie, Y. Jiang, F. Baert, A. Leliège, J. Roncali, C. Cabanetos, P. Blanchard, *RSC Adv.* **2015**, *5*, 102550–102554.
[55] A. Labrunie, P. Josse, S. Dabos-Seignon, P. Blanchard, C. Cabanetos, *Sustain. Energy Fuels* **2017**, *1*, 1921–1927.
[56] Y. Huang, E. Egap, *Polym. J.* **2018**, *50*, 603–614.

[57] J. Tomasi, M. Persico, *Chem. Rev.* **1994**, *94*, 2027–2094.
[58] C. Lee, W. Yang, R. G. Parr, *Phys. Rev. B* **1988**, *37*, 785–789.
[59] A. D. Becke, *J. Chem. Phys.* **1993**, *98*, 1372–1377.
[60] Y. Zhao, D. G. Truhlar, *Acc. Chem. Res.* **2008**, *41*, 157–167.
[61] W. J. Hehre, K. Ditchfield, J. A. Pople, *J. Chem. Phys.* **1972**, *56*, 2257–2261.
[62] M. M. Francl, W. J. Pietro, W. J. Hehre, J. S. Binkley, M. S. Gordon, D. J. DeFrees, J. A. Pople, *J. Chem. Phys.* **1982**, *77*, 3654–3665.
[63] F. Sannicolò, S. Arnaboldi, T. Benincori, V. Bonometti, R. Cirilli, L. Dunsch, W. Kutner, G. Longhi, P. R. Mussini, M. Panigati, et al., *Angew. Chemie - Int. Ed.* **2014**, *53*, 2623–2627.
[64] F. Sannicolò, P. R. Mussini, T. Benincori, R. Cirilli, S. Abbate, S. Arnaboldi, S. Casolo, E. Castiglioni, G. Longhi, R. Martinazzo, et al., *Chem. - A Eur. J.* **2014**, *20*, 15298–15302.
[65] S. Arnaboldi, M. Magni, P. R. Mussini, *Curr. Opin. Electrochem.* **2018**, *8*, 60–72.
[66] S. Arnaboldi, T. Benincori, R. Cirilli, W. Kutner, M. Magni, P. R. Mussini, K. Noworyta, F. Sannicolò, *Chem. Sci.* **2015**, *6*, 1706–1711.
[67] S. Arnaboldi, T. Benincori, A. Penoni, L. Vaghi, R. Cirilli, S. Abbate, G. Longhi, G. Mazzeo, S. Grecchi, M. Panigati, et al., *Chem. Sci.* **2019**, *10*, 2708–2717.
[68] E. Quartapelle Procopio, T. Benincori, G. Appoloni, P. R. Mussini, S. Arnaboldi, C. Carbonera, R. Cirilli, A. Cominetti, L. Longo, R. Martinazzo, et al., *New J. Chem.* **2017**, *41*, 10009–10019.
[69] S. Arnaboldi, D. Vigo, M. Longhi, F. Orsini, S. Riva, S. Grecchi, E. Giacovelli, V. Guglielmi, R. Cirilli, G. Longhi, et al., *ChemElectroChem* **2019**, *6*, 4204–4214.
[70] R. Shomura, K. Sugiyasu, T. Yasuda, A. Sato, M. Takeuchi, *Macromolecules* **2012**, *45*, 3759–3771.
[71] S. Arnaboldi, T. Benincori, R. Cirilli, S. Grecchi, L. Santagostini, F. Sannicolò, P. R. Mussini, *Anal. Bioanal. Chem.* **2016**, *408*, 7243–7254.
[72] S. Arnaboldi, M. Magni, S. Grecchi, R. Cirilli, C. Fontanesi, P. R. Mussini, *Chem. Sci.* **2019**, *10*, 2750–2757.
[73] D. Oeter, H. J. Egelhaaf, C. Ziegler, D. Oelkrug, W. Göpel, *J. Chem. Phys.* **1994**, *101*, 6344–6352.
[74] J. Hu, B. Xia, D. Bao, A. Ferreira, J. Wan, I. I. G. Jones, V. I. Vullev, *J. Phys. Chem. A* **2009**, *113*, 3096–3107.
[75] M. I. Nan, E. Lakatos, G. I. Giurgi, L. Szolga, R. Po, A. Terec, S. Jungsuttiwong, I. Grosu, J. Roncali, *Dye. Pigment.* **2020**, *181*, 108527.
[76] T. Benincori, S. Gámez-Valenzuela, M. Goll, K. Bruchlos, C. Malacrida, S. Arnaboldi, P. R. Mussini, M. Panigati, J. T. López Navarrete, M. C. Ruiz Delgado, et al., *Electrochim. Acta* **2018**, *284*, 513–525.
[77] T. Amemiya, K. Hashimoto, A. Fujishima, K. Itoh, *J. Electrochem. Soc.* **1991**, *138*, 2845–2850.
[78] B. Dong, B. Li, Y. Cao, X. Meng, H. Yan, S. Ge, Y. Lu, *Tetrahedron Lett.* **2017**, *58*, 35–42.
[79] Oboru, Ataga, Y. Kazu, K. Ezumi, *Electronic Structures of Carbazole and Indole and the Solvent Effects on the Electronic Spectra*, **1964**.
[80] L. Zhang, N. S. Colella, B. P. Cherniawski, S. C. B. Mannsfeld, A. L. Briseno, *ACS Appl. Mater. Interfaces* **2014**, *6*, 5327–5343.
[81] R. Takita, C. Song, T. M. Swager, *Org. Lett.* **2008**, *10*, 5003–5005.
[82] B. B. Berkes, A. S. Bandarenka, G. Inzelt, *J. Phys. Chem. C* **2015**, *119*, 1996–

2003.
[83] G. Zotti, G. Schiavon, A. Berlin, G. Pagani, *Synth. Met.* **1993**, *61*, 81–87.
[84] B. G. Zotti, G. Schiavon, A. Berlin, *Adv. Mater.* **1993**, *5*, 551–554.
[85] S. S. Zade, N. Zamoshchik, M. Bendikov, *Acc. Chem. Res.* **2011**, *44*, 14–24.
[86] T. M. Swager, *Macromolecules* **2017**, *50*, 4867–4886.
[87] K. Müllen, W. Pisula, *J. Am. Chem. Soc.* **2015**, *137*, 9503–9505.
[88] A. Nowakowska-Oleksy, J. Cabaj, K. Olech, J. Sołoducho, S. Roszak, *J. Fluoresc.* **2011**, *21*, 1625–1633.
[89] J. C. Li, S. J. Kim, S. H. Lee, Y. S. Lee, K. Zong, S. C. Yu, *Macromol. Res.* **2009**, *17*, 356–360.
[90] H. A. M. Van Mullekom, J. A. J. M. Vekemans, E. W. Meijer, *Chem. - A Eur. J.* **1998**, *4*, 1235–1243.
[91] B. A. D. Neto, A. A. M. Lapis, E. N. Da Silva Júnior, J. Dupont, *European J. Org. Chem.* **2013**, 228–255.
[92] N. Jian, H. Gu, S. Zhang, H. Liu, K. Qu, S. Chen, X. Liu, Y. He, G. Niu, S. Tai, et al., *Electrochim. Acta* **2018**, *266*, 263–275.
[93] S. Ming, S. Zhen, K. Lin, L. Zhao, J. Xu, B. Lu, *ACS Appl. Mater. Interfaces* **2015**, *7*, 11089–11098.
[94] S. Shome, S. P. Singh, *Chem. Commun.* **2018**, *54*, 7322–7325.
[95] S. Ghosh, P. B. Pati, S. S. Zade, *J. Lumin.* **2018**, *194*, 164–169.
[96] G. L. Gibson, T. M. McCormick, D. S. Seferos, *J. Phys. Chem. C* **2013**, *117*, 16606–16615.
[97] P. B. Pati, *Org. Electron.* **2016**, *38*, 97–106.
[98] X. He, B. Cao, T. C. Hauger, M. Kang, S. Gusarov, E. J. Luber, J. M. Buriak, *ACS Appl. Mater. Interfaces* **2015**, *7*, 8188–8199.
[99] R. Acharya, S. Cekli, C. J. Zeman, R. M. Altamimi, K. S. Schanze, *J. Phys. Chem. Lett.* **2016**, *7*, 693–697.
[100] P. Ledwon, N. Thomson, E. Angioni, N. J. Findlay, P. J. Skabara, W. Domagala, *RSC Adv.* **2015**, *5*, 77303.
[101] P. Ledwon, R. Turczyn, K. R. Idzik, R. Beckert, J. Frydel, M. Lapkowski, W. Domagala, *Mater. Chem. Phys.* **2014**, *147*, 254–260.
[102] S. Kutkan, S. Goker, S. O. Hacioglu, L. Toppare, **2016**, DOI 10.1080/10601325.2016.1189280.
[103] H. John, R. Bauer, P. Espindola, P. Sonar, J. Heinze, K. Müllen, *Angew. Chemie - Int. Ed.* **2005**, *44*, 2447–2451.
[104] G. Zotti, G. Schiavon, *Synth. Met.* **1989**, *31*, 347–357.
[105] D. Ofer, R. M. Crooks, M. S. Wrighton, *J. Am. Chem. Soc.* **1990**, *112*, 7869–7879.
[106] D. Lee, T. M. Swager, *Chem. Mater.* **2005**, *17*, 4622–4629.
[107] G. Salinas, B. A. Frontana-Uribe, *ChemElectroChem* **2019**, 1–14.
[108] J. Heinze, H. John, M. Dietrich, P. Tschuncky, *Synth. Met.* **2001**, *119*, 49–52.
[109] G. Salinas, J. A. Del-Oso, P. J. Espinoza-Montero, J. Heinze, B. A. Frontana-Uribe, *Synth. Met.* **2018**, *245*, 135–143.
[110] B. B. Carbas, A. Kivrak, E. Kavak, *Mater. Chem. Phys.* **2017**, *188*, 68–74.
[111] W. T. Neo, Q. Ye, S. J. Chua, J. Xu, *J. Mater. Chem. C* **2016**, *4*, 7364–7376.
[112] G. Abbiati, A. Arcadi, E. Beccalli, G. Bianchi, F. Marinelli, E. Rossi, *Tetrahedron* **2006**, *62*, 3033–3039.

5 Electrochemical Crosslinking Approach in Precursor Polymers with Triphenylamine and Carbazole Pendant Redox Units

In the previous chapters crosslinking strategies to obtain functional electroactive films from precursors units provided with multiple sites of dimerization (crosslinking) was discussed. The electrodeposition was performed from solution containing the precursor molecules, and the generated films were characterized by a well-known conjugation and redox behavior dominated by the electroactivity of the dimers created by crosslinking. These functional films based on crosslinkable units in the form of arylamine, carbazole or thiophene derivatives can find employment as electroactive layers in electro-optic applications, and they show outstanding properties in terms of thermal and electrochemical stability.[1–4] We herein discuss another electrochemical crosslinking approach to generate crosslinked electroactive surfaces. In this approach, the triarylamine unit is present in the form of a redox-active pendant unit covalently bonded to a polymer backbone, acting as a crosslinker unit upon oxidative triggering in a post deposition step which implies the solid-state oxidation of a spin-coated polymer film. Following an oxidative dimerization approach of the triarylamine and carbazole redox units, crosslinked polymer thin films can be generated through creation of dimeric redox-active units *N,N,N',N'*-tetraphenylbenzidine (TPB), *9,9'-diphenyl- 9H,9'H-3,3'*-bicarbazole (BPhCbz) and *9,9'-diethyl-9H,9'H-3,3'*-bicarbazole. This approach has already been exploited in our group in different situations,[5–7] and resulted to be particularly suitable when specific self-assembling of microstructures or decrease of the film roughness is needed.

Within these two chapters we aim to gather additional insight on the electrochemical, conductivity and spectroscopic behavior of electrochemically crosslinked films bearing triphenylamine and carbazole redox active units. Also in this case, structure-property relationships of different crosslinkable polymers were analyzed to provide insight about the charge compensation mechanism upon electrochemical doping. Electrochemical and conductivity interpretation in the following section is based on previous interpretations reported by Yurchenko *et al.*[5]

Crosslinkable arylamine and carbazole systems here reported constitute particularly interesting structures to analyze the effects of interactions on the potential dependent conductivity profile, considering their two-folded oxidation into radical cation and dication states also as dimers, in analogy to the oxidation generating polarons and bipolarons in CPs. The experimental results obtained constitute fundamental information of these crosslinked materials considering their widespread use in optoelectronic applications and in applications where they are electrochemically doped.[8–13]

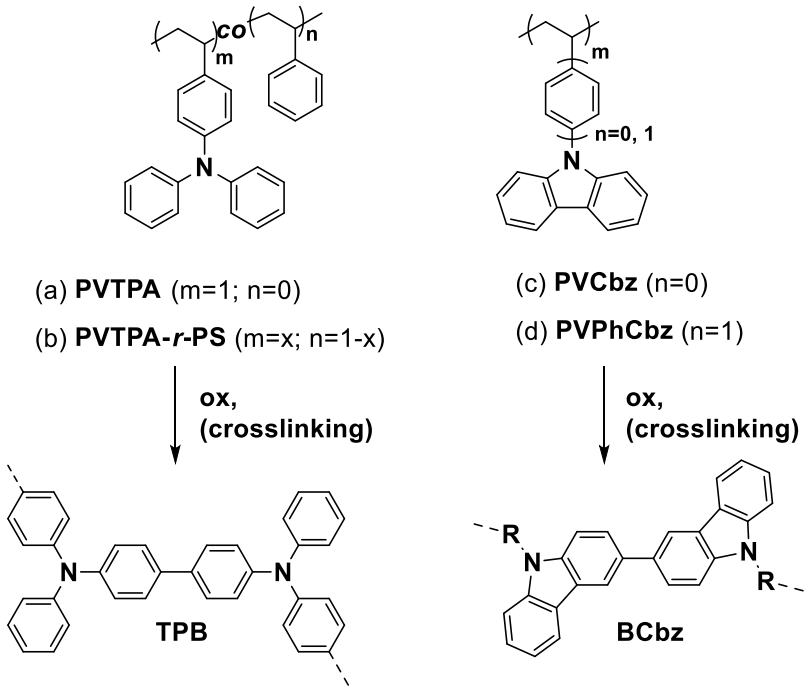

Figure 5.1: Structure of crosslinkable polymers analyzed: PVTPA, PVTPA-co-PS, PVCbz and PVPhCbz (top). Bottom structure of dimerization products: tetraphenylbenzidine (TPB) and biscarbazole (BCbz).

In this context, we also stress the importance of reporting to *in-situ* electrochemical results to optimize chemical doping in order to achieve high conductivities. In the following chapters different starting polymers have been employed and exposed to oxidative crosslinking (Figure 5.1). The polymers are namely polyvinyltriphenylamine (PVTPA), polyvinyltriphenylamine-*co*-polystyrene (PVTPA-*co*-PS) with different ratios of the repeat units, polyvinylphenylcarbazole (PVPhCBz) and polyvinylcarbazole (PVCbz). The structure of dimer units generated upon crosslinking of the films, namely tetraphenylbenzidine (TPB) or biscarbazole (BCbz or BPhCbz) are also reported in Figure 5.1.

At first, the “dilution” of the crosslinkable redox unit in PVTPA-*co*-PS, resulting in films with different composition and crosslinking degree, were analyzed with regards to the effects on the electrochemical behavior, conductivity and charge compensation. Secondly, an analysis of crosslinking and doping behavior of PVTPA and *N*-substituted carbazole redox polymers PVPhCbz and PVCbz was carried out. Simultaneous crosslinking and doping of spin-coated thin polymer films is performed to obtain conducting transparent polymer films endowed with increased chemical and thermal stability to be employed as HTLs and transparent electrodes in optoelectronic applications.

5.1 Electrochemical and Ion Transport Analysis in Electrochemically Crosslinked Redox Homopolymer and Copolymers based on Triphenylamine Pendant Units

5.1.1 Introduction and Objectives

In this chapter electrochemical oxidation of solution deposited PVTPA and PVTPA-*co*-PS thin films endowed with different PVTPA/PS ration was performed to achieve crosslinked electroactive films, namely ec-PVTPA and ec-PVTPA-*co*-PS. A full electrochemical characterization of the crosslinked films was performed, in particular, the voltammetric and potential-dependent conductivity response of these materials, as function of the film composition, which results in different extents of crosslinking and of neighboring redox interactions, was analyzed. Further, charge compensation upon electrochemical oxidation in 0.1 M CH_3CN/NBu_4PF_6 was studied by electro-gravimetric techniques.

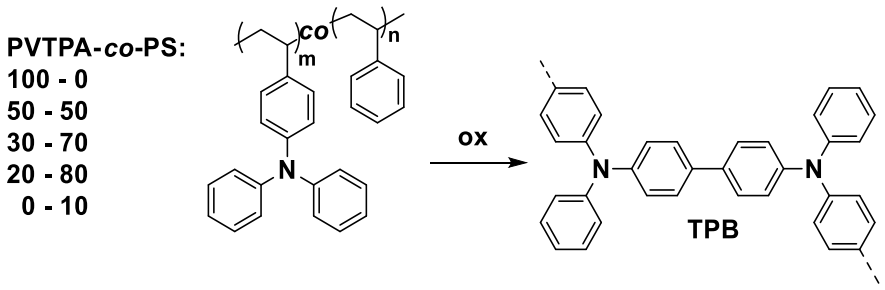

Figure 5.2: Structure of polymers analyzed: PVTPA and PVTPA-co-PS with different PVTPA-PS ratios.

The effects on the dynamic of charge compensation upon variation of the polymer composition by introduction of non-polar polystyrene (PS), leading to different extents of crosslinking and swelling, is analyzed in comparison to the homopolymer. Providing detailed information on the transport phenomena of these systems at the electrode| polymer film| solution interface in organic solvents is interesting from a fundamental point of view to better understand charging mechanism and electrochemical behavior in this class of materials, and for implementation in devices in which similar active layers and doping conditions are employed.[3,14–17] Indeed, in the case of electrochromic devices, arylamine systems constitute a bench-mark material, and device performance is often limited by charge compensation upon electrochemical doping.[15,18] In order to gain insight about the mechanism of charge compensation, electrochemical quartz crystal microbalance (EQCM) as well as by *ac*-electrogravimetry measurements were performed. The two techniques are utilized in a complementary fashion. In this way electrochemical quartz crystal microbalance provides the global electrogravimetric behavior of the films, whereas *ac*-electrogravimetry is performed to disentangle the contribution of single species having a role to the charge compensation and providing kinetics information. As extensively discussed in section

3.1.1.2.4*, the ac*-electrogravimetry technique has already been successfully applied to analyze different conducting polymers films such as electrodeposited PEDOT and PPy.[19,20] Insight on the charge compensation are for the first time provided for crosslinkable triphenylamine redox polymers; in the literature only the mere EQCM analysis of electrochemically polymerized polyvinylcarbazole (PVCbz) was reported by Skompska *et al.*.[21,22] In that case the authors report effects of anion trapping depending on the anion size, which also result in small variations with regards to absorption properties of the films; however, in their study detailed description of ionic contributions and kinetics upon doping are not reported.

5.1.2 PVTPA-*co*-PS: Synthesis and Characterization

The synthesis of the polymers studied was performed by Dr. L. Scapinello and C. Rost-Schmidt, chemical characterization by elemental analysis and differential scanning calorimetry (DSC) was performed by Dr. K. Bruchlos.[23]

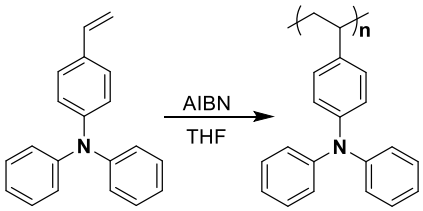

Scheme 5.1: Synthetic route yielding PVTPA.

PVTPA synthesis was performed adding azobisisobutyronitrile (AIBN) (57.24 mg, 0.3486 mmol, 0.02 eq.) to a stirred solution of N,N-diphenyl-4-vinylaniline (4.73 g, 14.43 mmol, 1 eq.) in freshly distilled THF. The reaction mixture was then heated to 50°C for 15 hours. The polymer was precipitated from cold acetone and reprecipitated from THF/acetone to obtain 1.8 g of white powder. The molecular weights and polydispersity indices (PDI) of the polymers were determined by size exclusion chromatography measured in THF at 30° C and calibrated with respect to PS standard. Synthesis was adapted from.[24]

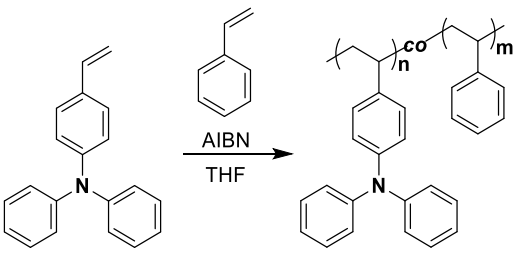

Scheme 5.2: Synthetic route yielding PVTPA-co-PS.

PVTPA-*co*-PS copolymers have been synthesized with a similar procedure as the one above reported.[23] The molecular weights and polydispersity indices (PDI) of the polymers were determined by size exclusion chromatography measured in THF at 30° C and calibrated with respect to PS standard.

Elemental analysis of the copolymers was performed to determine their composition. The repeating unit ratios were calculated from the percentage portion of nitrogen to carbon, neglecting the respective end groups. The data obtained are shown in Table 5.1.

Polymer	TPA:Styrene Elem. Anal.	$\bar{M}n$ [g/mol]	$\bar{M}w$ [g/mol]	PDI
PVTPA	100:0	29 000	48 000	1.6
PVTPA-*co*-PS 50:50	50:50	24 500	37 800	1.54
PVTPA-*co*-PS 30:70	30:70	19 800	31 000	1.57
PVTPA-*co*-PS 20:80	20:80	15 400	24 400	1.59
PVTPA-*co*-PS 10:90	10:90	14 800	24 000	1.62

Table 5.1: Chemical properties of PVTPA-co-PS copolymers including TPA : Styrene ratio determined by elemental analysis. Number and weight average molecular weights determined by SEC experiments in THF. [23]

The glass transition temperature (Tg) of the different PVTPA-*co*-PS copolymers was determined through differential scanning calorimetry (DSC).[23] The experimental glass transition temperatures (Tg) of the copolymers are reported together with calculated Tg values from the Fox Equation for the different weight ratios of the analyzed PVTPA-*co*-PS systems. The DSC experiments present one single Tg measured for each copolymer, indicating that the obtained copolymers do not represent a blend or a blockcopolymer, for which otherwise two separate glass transition temperatures would be present. The glass transition temperatures of the copolymers vary with the repeating unit ratio between 134 °C and 105 °C; decreasing progressively with the decreasing amount of PVTPA. The Tg of the copolymers is observed to follow satisfactorily the progression of the Fox equation.[25,26]

$$\frac{1}{T_g} = \sum_i \frac{\omega_i}{T_{g\,i}} \qquad (5.1)$$

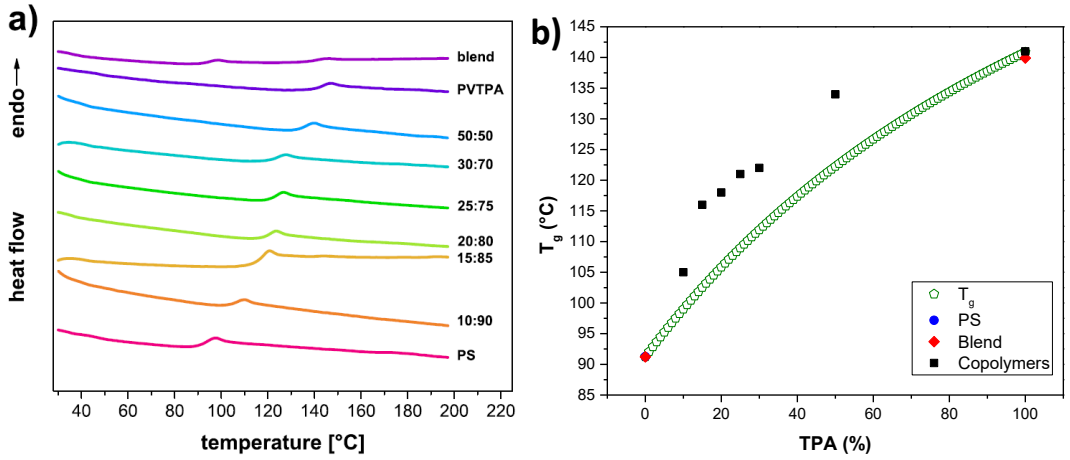

TPA%	10	15	20	25	30	50	100	PS	PS:PVTPA (1:1 w/w) blend:
Tg [°C]	105	116	118	121	122	134	141	91	91, 140°C

Figure 5.3: (a) DSC curves of the heating cycles measured with heating rates of 10 K•min^{-1}; b) Experimentally measured Tg values (black dataset), Tg values from Fox-equation (green dataset) as function of TPA%. Table: Tg values for the different PVTPA-co-PS copolymers, PVTPA and PS: PVTPA blends. Adapted from ref. [23].

From these experimental observations, *i.e.*, considering that only a single glass transition temperature (Tg) was observed, and that the latter satisfies Fox's equation, it can be assumed that the copolymerization of styrene and vinyltriphenylamine into random PVTPA-*co*-PS copolymers was successful. However, to fully describe and prove the nature of the obtained copolymers as a statistical copolymer, the Mayo-Lewis equation should be employed.[25,27]

5.1.3 Electrochemical Crosslinking and Characterization of PVTPA and PVTPA-*co*-PS Thin Polymer Films

5.1.3.1 Electrochemical Crosslinking

Electrochemical crosslinking of PVTPA-*co*-PS thin films deposited by spin coating on Au electrode substrates, was performed by cyclic voltammetry. The electrochemical crosslinking of the three copolymers endowed with decreasing PVTPA-PS ratio, 50-50, 30-70 and 20-80, respectively, is presented in Figure 5.4. All polymers show in the first cycle (dashed lines), a characteristic chemically irreversible peak related to the solid-state dimerization, *i.e.* crosslinking, of the triphenylamine unites within the polymer backbone leading to the formation of charged TPB units.

The first forward voltammetric cycle is characterized by an onset potential of ~0.52 V and a peak potential E^{p}_{cl} of 0.63 V for all copolymers analyzed. The PVTPA-PS unit ratio in the polymer does not seem to affect the dimerization process of the polymer molecules from an energetic point of view, i.e., no change is observed in the crosslinking peak

potential. It is on the other hand observed that the peak-current of the crosslinking peak decreases as the amount of triphenylamine within the film decreases, in agreement with the decrease in the number of oxidizable redox units. From an electrochemical point of view, discrimination of *intra*- and *inter*-molecular crosslinking is not possible, indeed for both situations the amount of electrons exchanged and the conjugation of the product formed (TPB) are similar and indistinguishable. It should also be mentioned that the statistical distribution of TPA units, which differs from polymer to polymer, could lead to different extensions and types of cross-linking, considering different possibilities of *intra*- and *inter*-chain dimerization.[4,11,17]

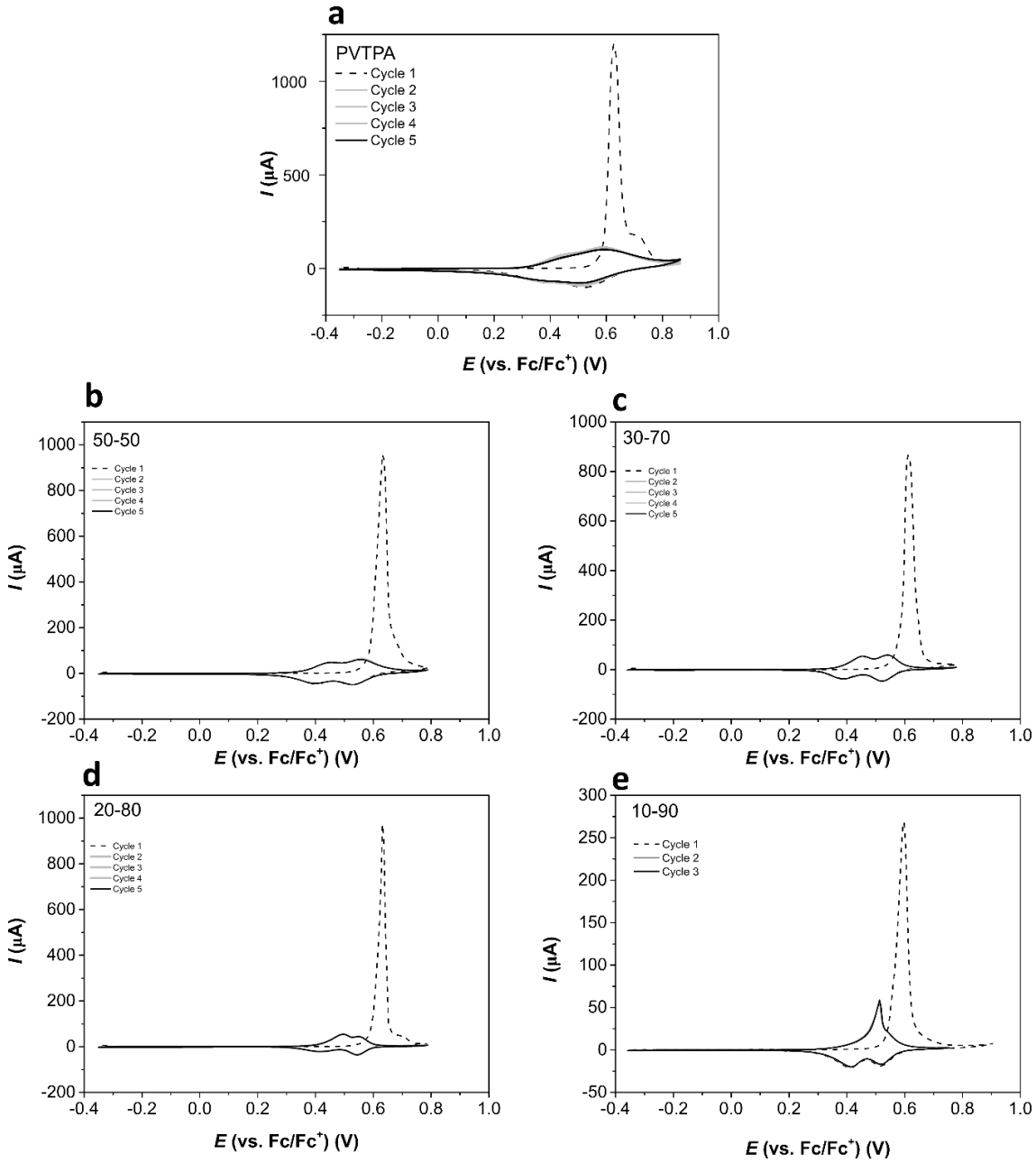

Figure 5.4: Electrochemical crosslinking of PVTPA and PVTPA-co-PS polymer films with different TPA-styrene ratios, on Au electrode, scan-rate 20 mV/s, CH_3CN/NBu_4PF_6.

5.1.4 Electrochemical Characterization of Crosslinked Thin Polymer Films

While strong similarities are found for the first irreversible cycle of oxidation corresponding to the electrochemically crosslinking of the spin-coated films (Figure 5.4, dashed line), the voltammograms of the different electrochemically crosslinked polymer films show marked differences from each other (Figure 5.5 (a)). The current, and more precisely, the charge (chronoamperometry example for ec-PVTPA reported in Figure 5.10 (d)) which is necessary to oxidize the redox units, decreases within the copolymers, in good correlation with the ratio PVTPA-PS (Figure 5.10 (c)).

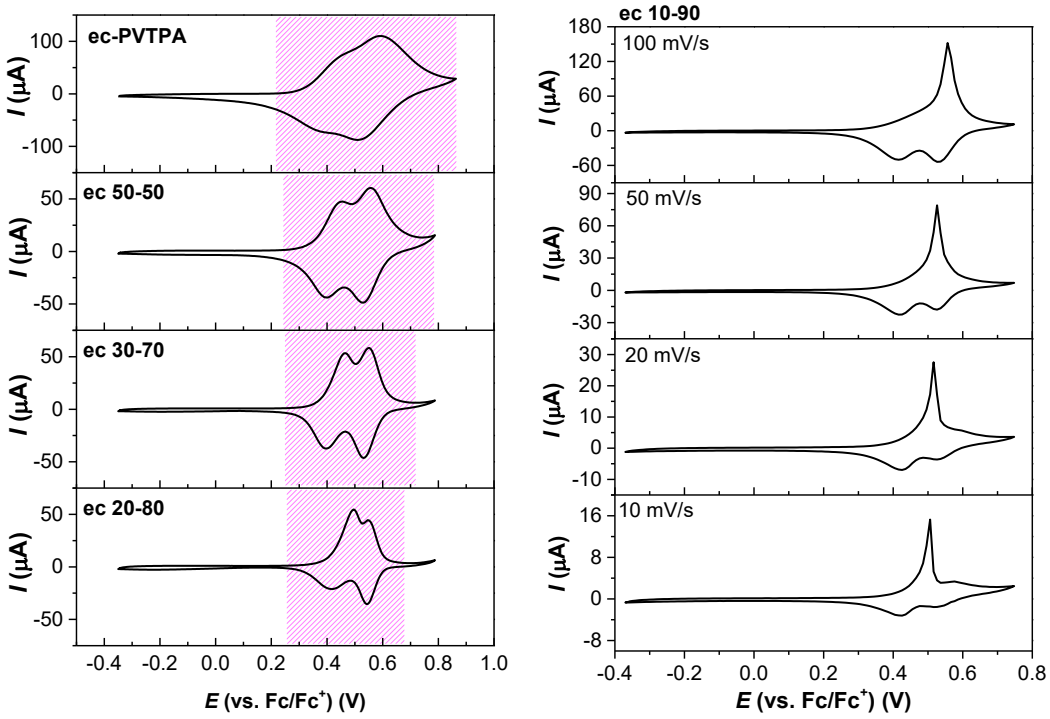

Figure 5.5: (Left) CV of ec-PVTPA and ec-PVTPA-co-PS copolymer films with different PVTPA-PS ratios, Au electrode, scan-rate 20 mV/s, CH_3CN/NBu_4PF_6. (Right) Ec-PVTPA-co-PS 10-90 copolymer film, Au electrode, CH_3CN/NBu_4PF_6.

Furthermore, we observed a progressive decrease in the electroactivity window as the TPA content in the copolymers decreases, from a value of ~0.7 V in the case of the ec-PVTPA homopolymer and of ~0.4 V in the case of the 20-80 copolymer. More specifically, the onset of oxidation does not change, but the current values recorded during CV measurements for polymers with higher PVTPA content, asymptotically decay to zero at more positive potential values, showing also more capacitive characteristics (broader CV signals and window of electroactivity) and indicating a conclusion of the oxidation process at higher oxidation potentials. In fact, in the case of the 10-90, 20-80, and 30-70 copolymers, the current asymptotically decays to zero at potential values of ~0.65 V, whereas the crosslinked polymer films of the 50-50 and ec-PVTPA copolymers still undergo charging processes up to a potential value of ~0.80 V.

The measured peak potentials and the half-wave potentials differ between the copolymers. Interestingly, the half-wave potential in the case of $TPB^{+\bullet}/TPB^{2+}$ oxidation ($E_{1/2, ox2}$) is identical within all polymers, on the contrary, in the case of the of $TPB/TPB^{+\bullet}$ oxidation the half-wave potential ($E_{1/2, ox1}$) is shifted to more positive potential values in the lower TPA content polymers (Table 5.2). Variations of the potential window and capacitive behavior of the CV upon oxidation as function of amount of redox units and their interactions have also been found by Advincula *et al.*[4] in electrochemically deposited carbazole electroactive films. Further, the CV signals in the case of electrochemically crosslinked copolymer films with PVTPA content show upon CV cycling characteristic features of solid-state voltammograms with almost no peak-to-peak separation within the forward and backward scan as well as identical oxidative, and reductive peak-currents in the case of the second peak of oxidation.[28,29] The CV profile of the low redox content polymer ec-PVTPA-*co*-PS 20-80 and, even more pronounced in the case of ec-PVTPA-co-PS 10-90, are characterized by rather asymmetric forward and backward peaks for the $TPB/TPB^{+\bullet}$ oxidation and a higher peak-to-peak separation in comparison to ec-PVTPA and the 50-50 copolymer (Figure 5.5). In the case of ec-PVTPA-*co*-PS 10-90, a peculiar sharp peak with peak-current proportional to the scan-rate is observed at ~0.5 V and is accounted for the first oxidation peak overlapping with the second oxidation peak. This peak shifts towards more positive potentials as the scan-rate is increased, indeed, a potential shift of ~60 mV upon increasing the scan-rate from 10 to 100 mV/s is found.

E vs. Fc/Fc^+ (V)	**ec-PVTPA**	**ec-PVTPA-*co*-PS 50-50**	**ec-PVTPA-*co*-PS 30-70**	**ec-PVTPA-*co*-PS 20-80**	**ec-PVTPA-*co*-PS 10-90**
$Ep_{1,fw}$	0.44	0.44	0.47	0.50	0.52
$Ep_{1,bw}$	0.38	0.39	0.40	0.42	0.42
$E_{1/2, ox1}$	**0.41**	**0.42**	**0.43**	**0.46**	**0.47**
$Ep_{2, fw}$	0.59	0.56	0.55	0.55	0.60
$Ep_{2, bw}$	0.51	0.53	0.53	0.55	0.53
$E_{1/2, ox2}$	**0.55**	**0.55**	**0.54**	**0.55**	**0.57**

Table 5.2: Peak and half-wave potentials for ec-PVTPA-co-PS in CH_3CN/NBu_4PF_6 at 20 mV/s; Au electrode.

In the literature, sharp voltametric peaks as the ones found for ec-PVTPA-*co*-PS 10-90 can be found for different situations. These include for example adsorption processes on the electrode surface in which strong lateral interactions between the adsorbed units take place.[30,31] Further, anodically shifted sharp voltametric signals could also be found in relation to the so called “memory effect” during the first cycle of oxidation of a polymer film. In this case, the charging / discharging process of the conducting polymer is generally associated with a first charging cycle characterized by a sharp peak localized at more

positive potentials than in the following voltammetric cycles. In the literature, different possibilities for explaining the memory effect phenomenon have been proposed, including a rearrangement of chain-configurations or the solvent-expulsion leading to a shrinkage of the polymeric matrix[28,32,33] In this last case, it is expected that during the first forward oxidation the polymer matrix might not yet have incorporated enough electrolyte to allow for a fast oxidation. In order to analyze the effects of experimental conditions on voltammogram shapes for conducting polymer films, Zotti et al.[32] reported the effect of solvents, temperature, and scan-rate on the voltametric shape of P3HT, finding that for high scan-rates and for polar solvents a single narrower peak of higher intensity at more positive potentials, whereas in the case of lower temperature and scan-rates or in solvents with a lower dielectric constant, two peaks could be observed. The authors believe that the rate of counterion transport is responsible for the observed multiplicity of signal, and claim that only one peak can be observed in the case of slow counterion transport.[32]

In the specific case of crosslinked copolymers with PTVPA-PS ratios 20-80 and 10-90, a possible explanation for the sharp voltametric peak and shift in peak potentials might be associated to the different composition of the polymers. In particular, it might be expected that a higher quantity of non-polar PS units might lead to increased resistance of the polymer films and hinder the radical cation formation, which is consequently observed only at more positive potential values in comparison to the crosslinked homopolymer and the higher PVTPA content copolymers.[34]

5.1.4.1 Scan-Rate Dependency

The scan-rate dependency of *ec*-PVTPA-*co*-PS copolymers was analyzed, CV plots and the peak-current (*Ip*) *vs* scan-rate (*v*) relationships are presented in Figure 5.6 and Figure 5.7, respectively. For this purpose, the peak-current relative to the second oxidation peak ($TPB^{+\bullet}/TPB^{2+}$) was sampled for each scan-rate analysis. With exception of ec-PVTPA films, all copolymers show in the range of employed scan-rates a thin-film behavior with linear Ip vs v dependency. In the case of ec-PVTPA a diffusion-controlled behavior showing a linear $Ip\ vs\ v^{0.5}$ relationship is found. The experimental result might indicate a more sluggish ion-transport, possibly due to the higher crosslinking degree as well as of charged species within the film, due to the higher amount of redox units, and therefore also of the ionic species moving into and outside the film in order to allow for electroneutrality of the polymer chains.[35] The double logarithmic plots of *Ip* and *v* were analyzed to better identify the presence of diffusion limitations for the studied experimental conditions (Table 5.3).[28,31] Exact values of of 0.5 or 1 for this slope are found for ideal situations of semi-infinite or thin-film diffusion, respectively. This diagnostic information is determined by simple mathematical logarithmic transformation of the current to scan-rate relationship in the case

of thin-film behavior and of semi-infinite diffusion, respectively, as derivation of the Randles-Sevcik equation.

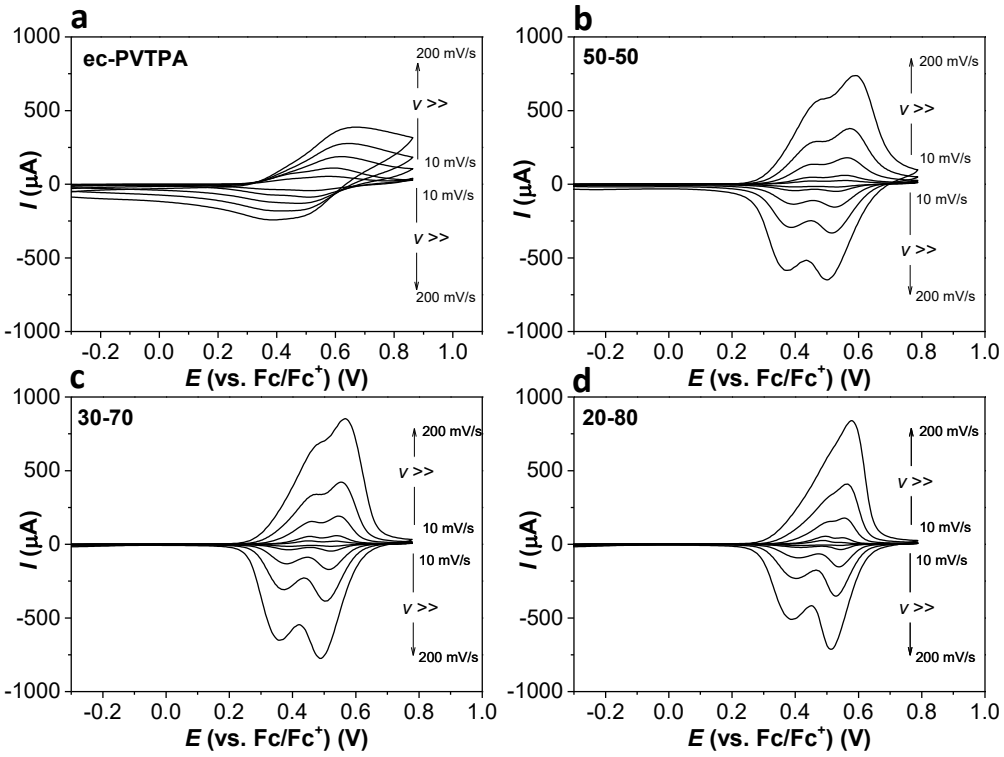

Figure 5.6: Scan-rate dependency plot of ec-PVTPA and copolymers with different PVTPA-PS ratios. Scan rates 10; 20; 50; 100 and 200 mV/s, Au electrode, CH_3CN/NBu_4PF_6 0.1 M.

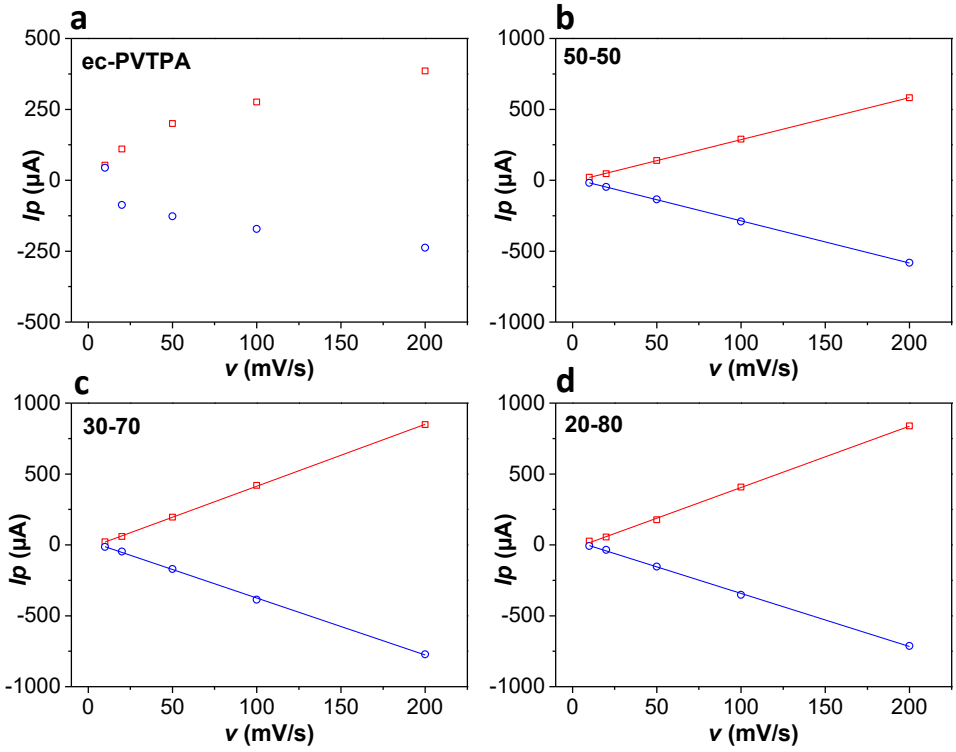

Figure 5.7: Peak-current (Ip) vs scan-rate (v) plots, data from Figure 5.6. The peak-current relative to the second oxidation peak ($TPB^{+\bullet}/TPB^{2+}$) is sampled.

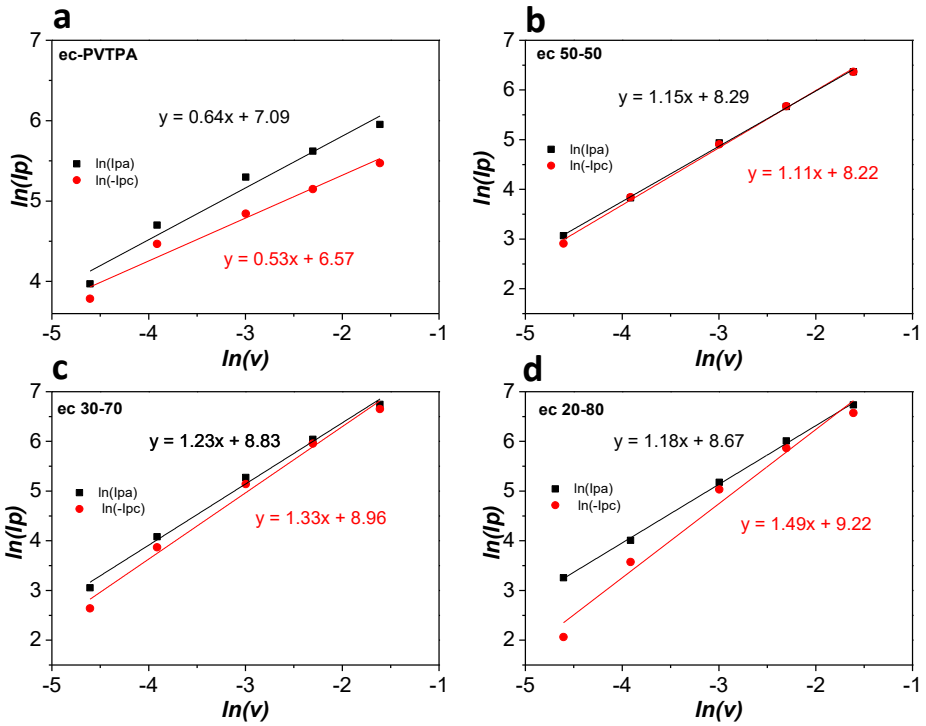

Figure 5.8: Double logarithmic plot ln(Ip) vs. ln(v) and corresponding linear fitting.

Polymer	Behavior	Slope Ox	Slope Red
ec-PVTPA	Finite Diffusion	0.64	0.53
ec-PVTPA-*co*-PS 50-50	Thin-Film	1.15	1.11
ec-PVTPA-*co*-PS 30-70	Thin-Film	1.23	1.33
ec-PVTPA-*co*-PS 20-80	Thin-Film	1.18	1.49

Table 5.3: Slopes for the linear interpolation of ln(Ip) vs. ln(v) .

The slopes of the interpolation lines of the double logarithmic graphs of peak currents versus scan rate should present for an ideal semi-infinite or thin film diffusion situation, values of 0.5 and 1, respectively (see section 3.1.1.1). In the case of ec-PVTPA, the slope of the double logarithmic graph tends to the value of 0.5, indicating for the investigated scan rates a finite diffusion behavior (Figure 5.8 (a)). In the case of copolymers, the slopes of the interpolation lines tend instead to the value of 1 (Figure 5.8 (b,c,d)) characteristic for thin layer behavior. As previously mentioned (section 1.2.2), in the case of polymer films we expect values between 1 and 0.5 depending on the film thickness and the scan-rate used; as the scan rate increases, the thickness of the diffusion layer widens, resembling and finally exceeding the thickness of the polymer film, causing the transition from a thin-layer behavior to finite diffusion.[31] The increase of the slope for the double-logarithmic plot of Ip *vs.* v which is observed by decreasing the PVTPA/PS ratio in the copolymer (see Table 5.3) could be explained by the shift of the TPB/TPB$^{+\bullet}$ peak to more positive potential values as the scan-rate is increased (Figure 5.6). This shift causes the progressive overlapping of the

TPB/TPB$^{+\bullet}$ peak with the TPB$^{+\bullet}$/TPB^{2+} peak. This might eventually result in higher sampled Ip values for TPB$^{+\bullet}$/TPB^{2+} oxidation with the scan-rate. The Ip *vs* v relationship as well as the double-logarithmic analysis are not reported in the case of ec-PVTPA-*co*-PS 10-90 because of the peculiar voltametric profile and the significant change of the peak positions by increasing the scan-rate (Figure 5.5, right).

5.1.4.1.1 Chronoamperometric Analysis

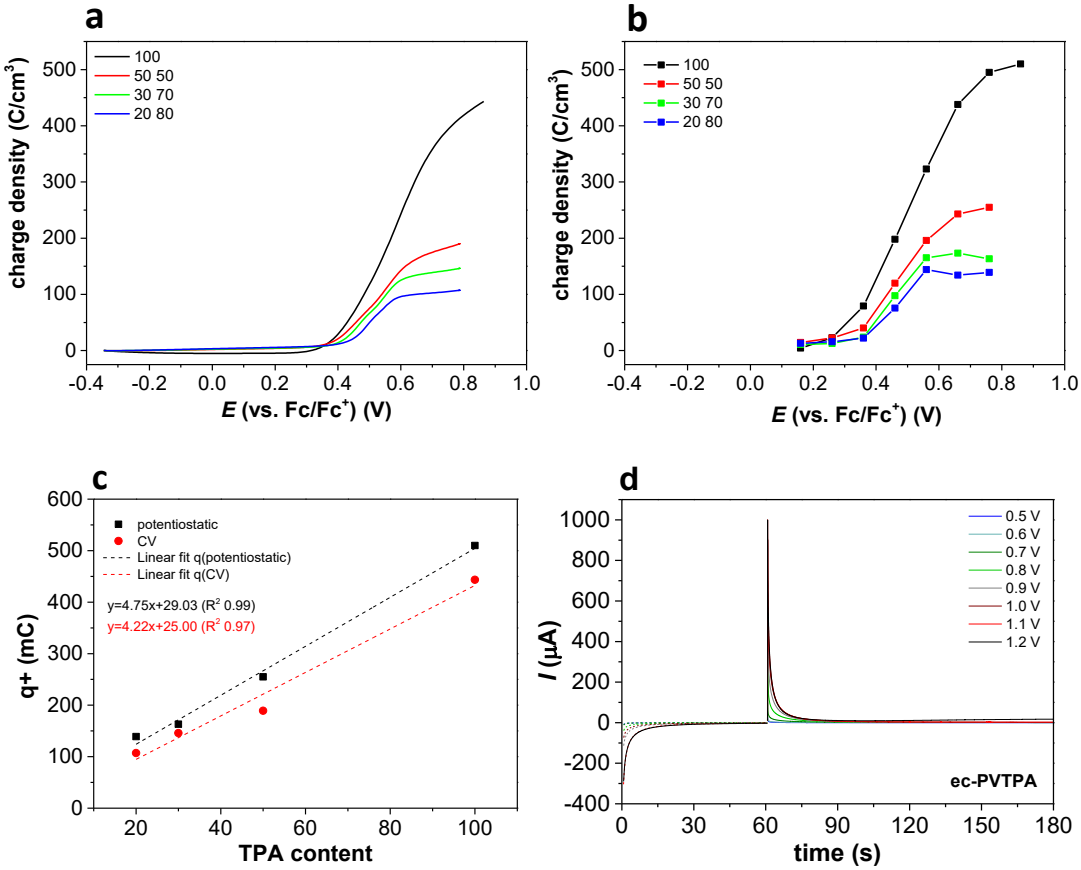

Figure 5.9: Charge density calculated for ec-PVTPA and ec-PVTPA-co-PS with different PVTPA-PS ratios from (a) CV measurements and (b) Chronoamperometry. (c) Full oxidation charge (q+) from potentiostatic (black) and CV (red) measurements reported as function of the TPA content in the polymers. (d) Chronoamperometry at different potential values for ec-PVTPA used for calculation of the complete charge.

The total amount of charge necessary for the two folded oxidations of the different polymers was determined both by chronoamperometry and by cyclic voltammetry. The calculated charge densities show a good linear correlation with the TPA ratio in the polymers (Figure 5.9). Indeed 510 C/cm^3 are necessary for the complete oxidation of the homopolymer *ec*-PVTPA, 255 C/cm^3 (50%) for the oxidation of *ec*-PVTPA-*co*-PS 50-50 copolymer, 163 C/cm^3 (32%) for *ec*-PVTPA-*co*-PS 30-70 and 134 C/cm^3 (26%) for the case of *ec*-PVTPA-*co*-PS. The good correlation of the relative charges found for the different copolymers also suggests that the amount of redox active sites after crosslinking (TPB units), well correlates

with the results from elemental analysis of the synthesized copolymers. The discrepancies in the charge values obtained between the cyclovoltammetry measurements and from the chronoamperometric experiments can be attributed to the different conditions of the experiments performed, i.e., potentiostatically and potentiodynamically, respectively.

5.1.4.2 In-Situ Conductance

The employment of arylamine derivatives as crosslinkable units allows for generation of units of similar conjugation lengths at the level of the dimer tetraphenylbenzidine (TPB). These systems can be regarded as interesting model for the analysis of the conductance behaviors, as their two-folded oxidation into radical cation and dication states can be regarded as the formation of polaron and bipolaron in CPs, in partially overlapping redox events and two distinguished conductance regimes as reported by Yurchenko *et al*.[36] In this context it was thought that one possible way to analyze the effect of interaction induced by the spatial proximity between neighboring redox units is the distribution or dilution of the latter in a statistical copolymer. The dilution of triphenylamine pendant redox units (precisely the TPB units) should correspond under a statistical point of view, in a decrease of the neighboring interactions. The correlated effects on the conductance-trend are further analyzed.

In-situ conductance plots of the crosslinked homopolymer, ec-PVTPA, and of the copolymers ec-PVTPA-*co*-PS 50-50, 30-70 and 20-80 are reported in Figure 5.10; the forward scan is indicated by a continuous purple line while the backward scan by a dashed purple-line. In the case of the electrochemically crosslinked copolymer with 10-90 PVTPA/PS ratio; drain-current values from which *in-situ* conductance is measured could not be distinguished from the background noise. In analogy to the homopolymer, *in-situ* conductance measurements of ec-PVTPA-*co*-PS copolymers present two partially overlapping conductance regimes with maxima in correspondence to the half-wave potentials for the two folded oxidations, $TPB/TPB^{+\bullet}$ and $TPB^{+\bullet}/TPB^{2+}$. The decreasing content of redox-active pendants within the polymer results in a narrowing of the conductance window from a value of 0.68 V in the case of the homopolymer, 0.47 V for the 50-50 copolymer; 0.42 V for the 30-70 copolymer and 0.37 V for the 20-80 copolymer. Interestingly, by plotting the window of conductance as function of the PVTPA content in the polymers, a linear relationship is found (Figure 5.11).

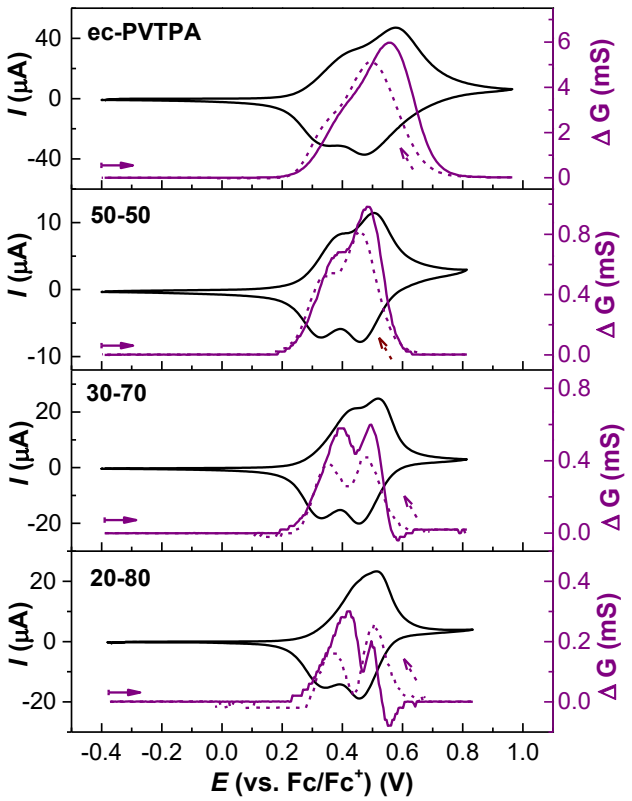

Figure 5.10: In-situ conductance of ec-PVTPA and ec-PVTPA-co-PS with different PVTPA-PS ratios. Measurements performed in CH_3CN/NBu_4PF_6 0.1 M; scan-rate 10 mV/s; Pt 5 μm-IDE; II cycle.

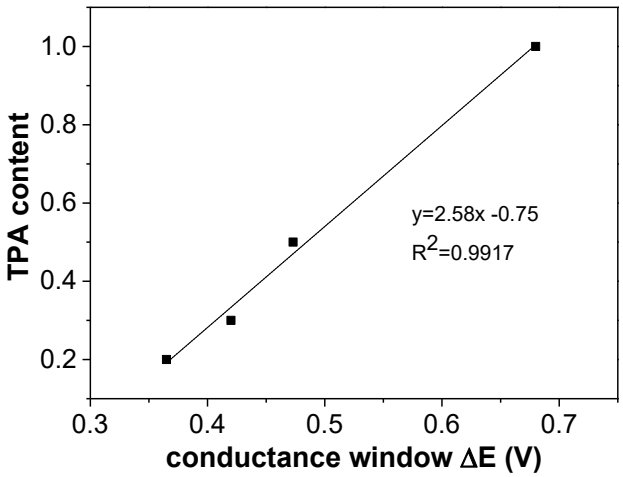

TPA	conductance window		
	ΔE_{fw}	ΔE_{bw}	$\Delta E_{avarage}$
100	0.68	0.68	0.68
50-50	0.46	0.49	0.47
30-70	0.42	0.42	0.42
20-80	0.34	0.39	0.37

Figure 5.11: Average conductance window from forward and backward scan reported as function of TPA content in the polymers from Figure 5.10.

The decreasing amount of redox active pendants is associated with a lower peak overlap of the two conductance regimes, with conductance values also presenting more similar intensities. Indeed, in the case of the 20-80 copolymer, the conductance profile in the

backward scan is characterized by the almost complete separation of the two conductance regimes.

Differences between experimental *in-situ* conductance plots can also be observed on data registered for ec-PVTPA and for ec-PSTPA, a polystyrene backbone bearing TPA electroactive units attached via dimethyl ether spacers employed by Yurchenko *et al.*[36] We claim that also between these two polymers, differences in the *in-situ* conductance profile can be correlated to a different extent of interactions between the redox units in the polymers. Whereas in the case here reported ec-PVTPA, triphenylamine redox units are directly connected to a polyvinyl backbone, the polymer employed by Yurchenko *et al.* is characterized by pendant electroactive triphenylamine units attached via dimethyl ether spacers to a polystyrene backbone. The structural differences between the two polymers should result in variations of the local environments of the redox centers, giving rise to a different range of redox potentials.[36] The larger conductivity potential window encountered in our system could be the result of a greater extent of interactions between neighboring redox centers determined by the different structure with which a greater density of repetitive units in the structure and their mutual distance are possibly associated.

5.1.5 Electrogravimetric Characterization of Electrochemically Crosslinked PVTPA and PVTPA-*co*-PS Thin Polymer Films

Electrochemical quartz crystal microbalance (EQCM) and *ac*-electrogravimetry measurements were performed to study the charge compensation processes of crosslinked polymer films subjected to doping in an electrolyte solution. These two techniques have been used in a complementary way: EQCM measurements have been performed to study the global electrogravimetric behavior of the films, furthermore ac-electrogravimetry measurements have been carried out with the aim of distinguishing the contribution of the individual species involved in charge compensation, also disentangling the flux of uncharged species and providing kinetic information regarding the transport of species within the polymer film.[20,37,38] These studies were carried out at the LISE laboratories of the Sorbonne University in Paris under the supervision of Prof. H. Perrot and Dr O. Sel.

5.1.5.1 Global Electrogravimetric Behavior by EQCM Measurements

The overall electrogravimetric behavior of *ec*-PVTPA and *ec*-PVTPA-*co*-PS 50-50 copolymer films was analyzed using EQCM. We report in Figure 5.12 (a, b) the fifth oxidation cycle of the crosslinked film with the corresponding change in frequency registered by the quartz crystal microbalance. Electrogravimetric measurements of the PVTPA-*co*-PS films with 30-70; 20-80 and 10-90 ratios were also performed in order to provide additional information regarding the changes observed in voltammograms and scan-rate measurements carried out on the TPA-PS ratio. The limited electroactivity window

and the higher resistivity of the copolymer film did not allow to record reliable experimental data for electrogravimetric analysis. Therefore, the discussion reported here is limited to measurements carried out on the *ec*-PVTPA homopolymer and the 50-50 *ec*-PVTPA-co-PS copolymer.

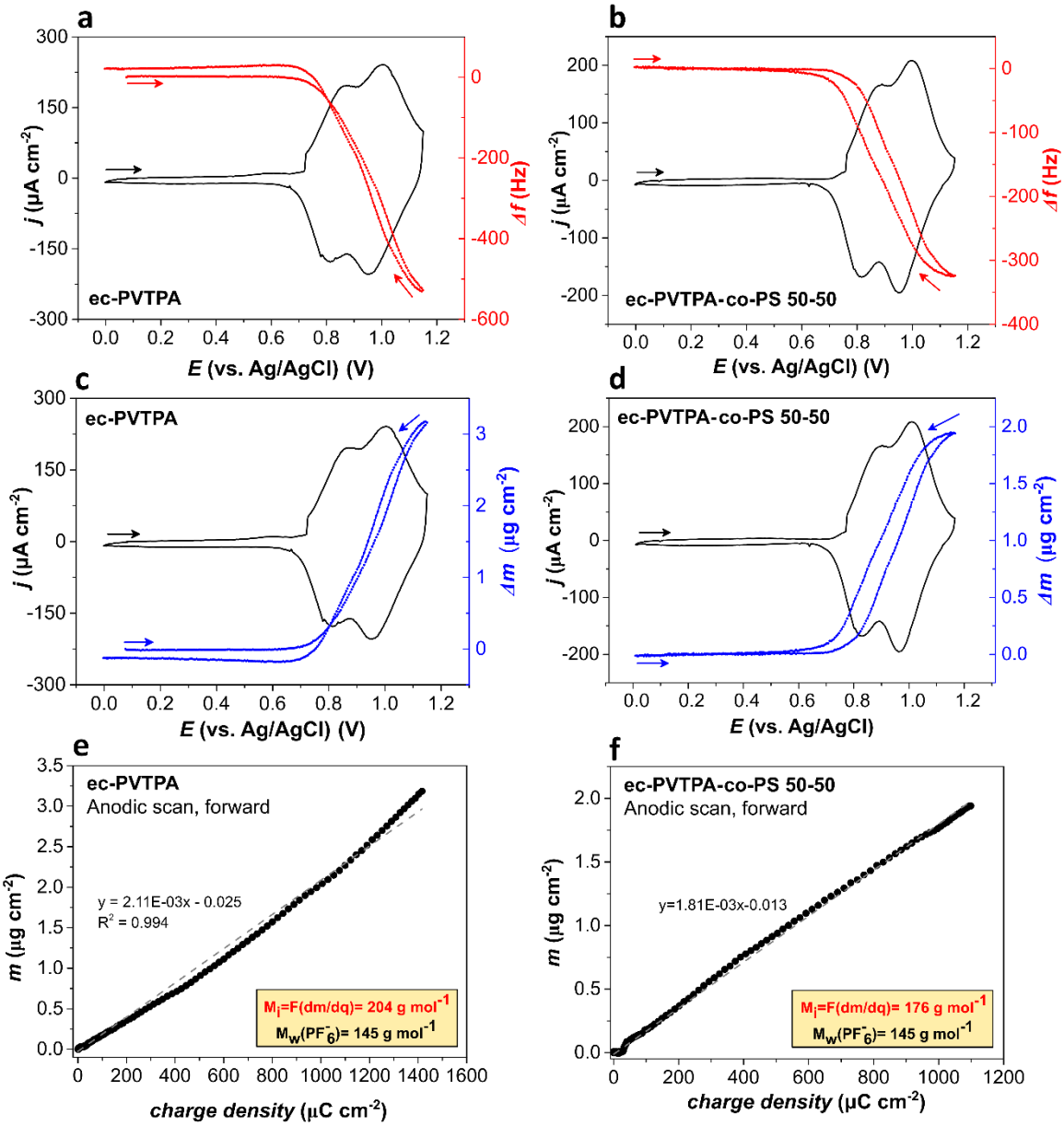

Figure 5.12: Cyclic Voltammetry of (left side) ec-PVTPA and (right side) ec-PVTPA-co-PS combined with QCM Δf_m (a , b red curves); global mass changed from EQCM (c, d blue curves). F(dm/dq) obtained as the slope of the mass change vs. charge density (e, f) plot. Scan-rate 50 mVs^{-1} in CH_3CN/NBu_4PF_6 0.1 M; 5th cycle.

Figure 5.12 (a) and (b) present the fifth cycle of EQCM measurements carried out on the electrochemically crosslinked *ec*-PVTPA and *ec*-PVTPA-co-PS 50-50 films, respectively. In the graph, the CV signal is reported in black while the frequency change recorded by the quartz resonator is shown in red. From the latter, the total mass change of

the film was determined using the Sauerbrey equation (section 3.1.1.2.3). Upon electrochemical oxidation the QCM response of both films is characterized by a decrease in the resonance frequency; It can be observed that ec-PVTPA homopolymer films are characterized by a more pronounced decrease in oscillation frequency (Δf: -450 Hz) and a corresponding increase in mass (Δm: 3.2 μg/cm^3) than ec-PVTPA-co-PS 50-50 (Δf: -325 Hz and Δm: 2.1 μg/cm^3). The data are in agreement with the fact that the homopolymer is characterized by a higher density of redox units and consequently to a higher amount of charge per unit volume to be compensated during electrochemical doping by counterions. For both polymer films, it can be observed that the frequency and mass variation are associated with two well-distinguishable regimes that can be associated with the two folded oxidations of the redox units, TPB/TPB$^{+\bullet}$ and TPB$^{+\bullet}$/TPB^{2+}, respectively. In the case of the electrolyte solution used, 0.1 M CH_3CN/NBu_4PF_6, the possible contributions to the charge balance can come from the anion PF_6^- (145 g·mol^{-1}), and the cation NBu_4^+ (242 g·mol^{-1}). In addition, the possibility that the free solvent and solvated cations may contribute to the overall mass balance must also be considered.

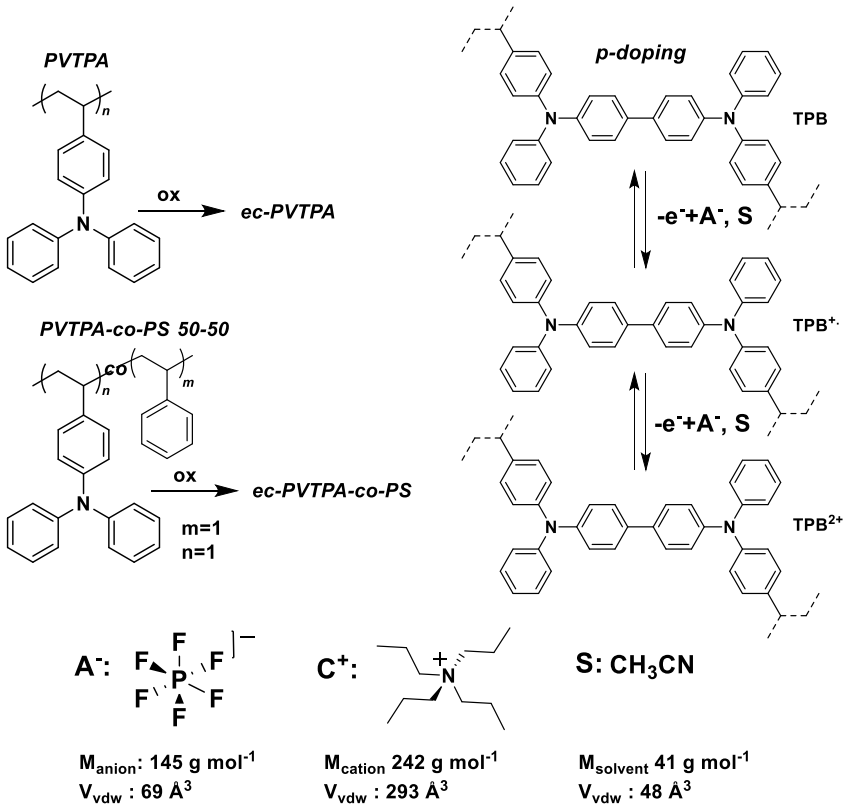

Figure 5.13: structure of PVTPA and PVTPA-co-PS 50-50. Mechanism od oxidation of ec-PVTPA and ec-PVTPA-co-PS 50-50 (TPB units indicated). Structure of ions and solvent employed, molecular weight and Van der Waals volumes are also indicated. [44,45]

We referred for the data interpretation to the literature, where several papers discuss the contribution of solvents in redox processes.[19,39–42] In the case where aqueous solvents are used, it has been observed that ions can contribute to charge compensation both in a

solvated and non-solvated form.[20][43] In organic solvents, on the other hand bare ions normally contribute to the charge balance, and can be associated by solvent fluxes drove by osmotic pressure. The results and interpretations from the literature are generally limited to EQCM measurements. [40–42]

To gather further insight in the nature of the contributors to the charge compensation, also including the contribution of solvent molecules, the mass variation obtained by EQCM measurements is plotted against the charge density in Figure 5.12 (e, f). From the positive slope of the two mass-potential curves, one can deduce that the main contribution to charge compensation is due to anion transfer. From the slope of interpolated line ($\Delta m/\Delta q$), by multiplication by the faraday constant (Figure 5.12 (e,f)), the apparent exchanged molar mass for the oxidation process is calculated.[46] This calculation allows for a global estimation of the molar mass of the species (M_i) participating in the charge compensation process, as indicated in the following, where M_a represents the molar mass of the anion, M_s the molar mass of the solvent and M_c the molar mass of the cation:

$$M_i = F\left(\frac{\Delta m}{\Delta q}\right) = M_a + \alpha M_s + \beta M_c$$

It is found that the value M_i ($g \cdot mol^{-1}$) calculated for the forward step of oxidation of both films is higher than the one of the single PF_6^- contribution (145 $g \cdot mol^{-1}$). Since the molar mass (M_i) calculated from the slope of the interpolation line of the EQCM mass variation *vs* charge density (Figure 5.12 (e, f)) is greater than that of the anion alone (M_a), we can assume that the solvent flux within the film may play a significant role in determining the mass change of the film. Further, the calculated values of global M_i are higher in the case of the homopolymer (ec-PVTPA) than for the copolymer (ec-PVTPA-*co*-PS 50-50). Separation of the contribution of species and their concomitant effect cannot be merely obtained from classical EQCM experiments which, as already remarked, can offer only global information of the charge compensation process by reporting the overall frequency variation upon film charging and discharging. For this purpose, *ac*-electrogravimetric experiments, which correspond to a combination of EQCM and electrochemical impedance spectroscopy experiments, were performed in order to distinguish the contributions of each species being involved in the electrochemical charge compensation process.[20,37,38]

5.1.5.2 Ac-electrogravimetry

The dynamics of species transfer at the film-electrolyte interface for ec-PVTPA and ec-PVTPA-co-PS 50-50 thin films was studied by ac-electrogravimetry, we aimed to identify correlations between the data obtained and the film composition. *Ac*-electrogravimetric experiments were performed at different polarization potentials, in the electroactive window +0.8 to +1.1 V *vs.* Ag/AgCl in 3M KCl, with intervals of +0.1 V. The experimental and

theoretical charge transfer ($\frac{\Delta q}{\Delta E}(\omega)$) and mass transfer ($\frac{\Delta m}{\Delta E}(\omega)$) functions for selected potentials, +0.9 and +1.0 V, respectively, are presented in Figure 5.14 in the case of ec-PVTPA and in Figure 5.15 in the case of ec-PVTPA-*co*-PS 50-50. The charge transfer function of ec-PVTPA, reported in Figure 5.14 (a, c) shows upon oxidation a single loop, which diameter increases with the oxidation potential. The presence of a single loop in the charge transfer function plot theoretically indicates the contribution of one single ion in the charge compensation process.[47,48] In principle, it is also possible that more than one charged species could be involved in the charge compensation with similar kinetic constants. However, considering the bulkier nature of the cation and the fact that the experimental data could be satisfactorily fit using equation (5.5) by considering only a single ionic species in the latter, we do not expect cationic species to also contribute to the charge balance. Analysis of charge compensation of PEDOT and P3HT in organic solvents also indicate no cation participation in *p*-doping process.[49,50] In addition to the charge transfer function, the mass transfer function ($\frac{\Delta m}{\Delta E}(\omega)$) was also simultaneously evaluated

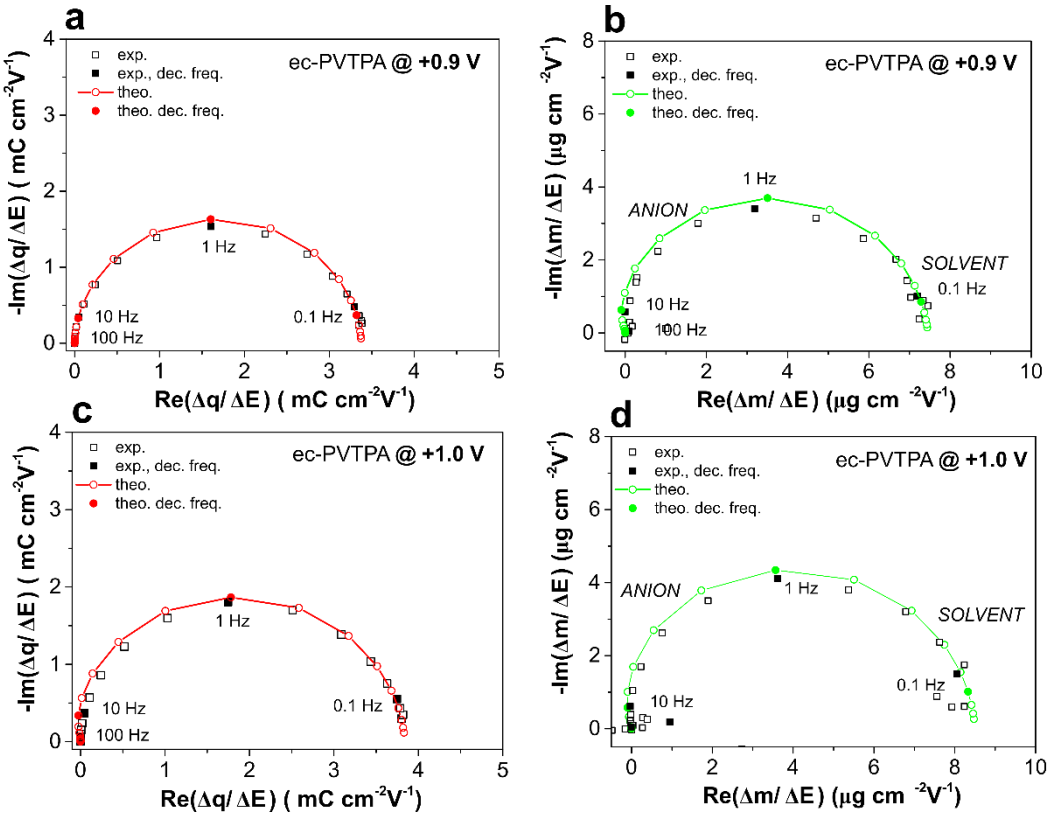

Figure 5.14: Experimental (squares) and theoretical (circles) Δq/ΔE(ω) (red line) and Δm/ΔE(ω) (green line) transfer functions of ec-PVTPA in CH_3CN/NBu_4PF_6 0.1 M, data reported for potential values of +0.9 V and +1.0 V vs. Ag/AgCl in KCl 3M, respectively.

.As described in section 3.1.1.2.4, this transfer function can provide more information about the nature of the charged species as well as of non-ionic species. Indeed, the presence of

one single loop in the first quadrant indicates the main contribution of anion also including contribution of free solvent in the same flux direction of the anion.

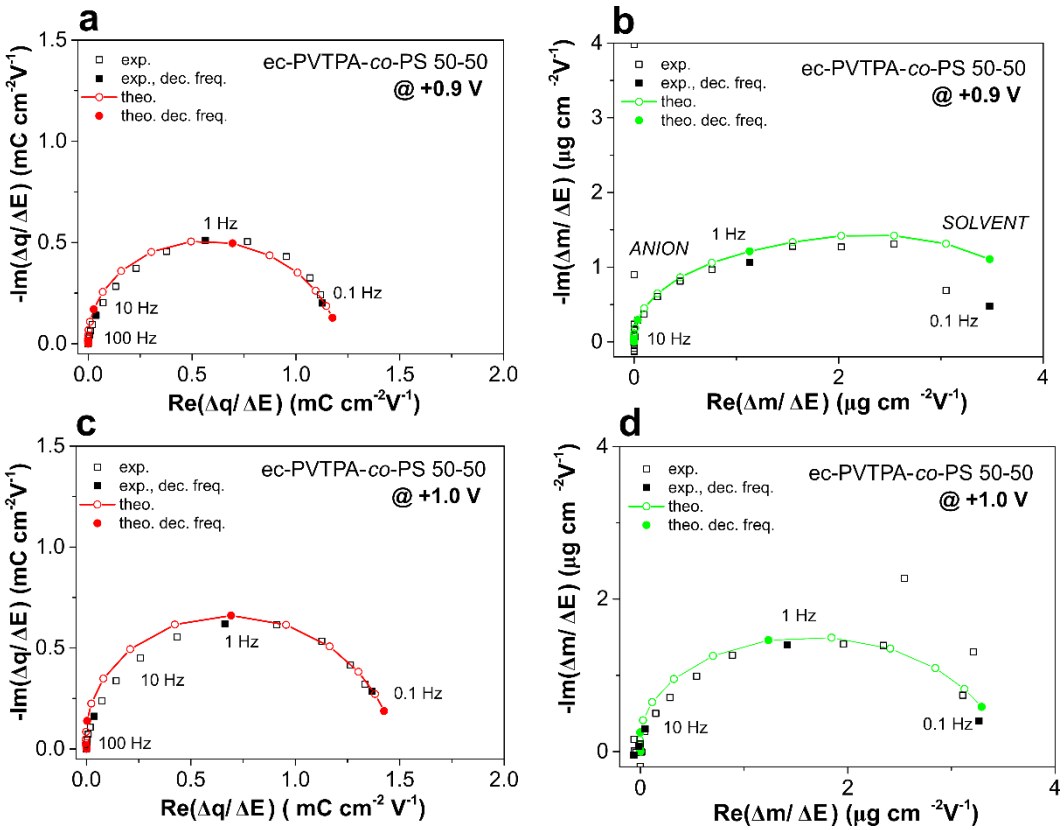

Figure 5.15: Experimental (squares) and theoretical (circles) Δq/ΔE(ω) (red line) and Δm/ΔE(ω) (green line) transfer functions of ec-PVTPA-co-PS 50-50 in CH_3CN/NBu_4PF_6 0.1 M, data reported for potential values of +0.9 V and +1.0 V vs. Ag/AgCl in KCl 3M, respectively.

Similar results are found for the copolymer ec-PVTPA-*co*-PS 50-50. (Figure 5.15 (a-c)) In this case, a lower diameter for both charge and mass transfer functions is found, indicating a lower contribution of ions and solvent to the charge compensation. As in the case of ec-PVTPA, the experimental data for the copolymer were satisfactorily fitted considering the contribution of only the anion and the solvent and, overall, the results are coherent with the lower current values found for the CV measurement due to the lower content of redox-active units in comparison to the homopolymer.

It must be underlined that a good fitting is obtained here considering only anion and free solvent contribution. The anion intervenes at high frequencies as the solvent appears at lower frequencies, even if the discrimination between the two contributions is not an easy task. The quality of the fitting can be examined regarding the shape and the frequencies between the experimental and theoretical curves. A good agreement is observed here which indicates that the assumption is fair. Characteristic parameters including the transfer resistance (Rt_i), the frequencies, (f_i) and the instantaneous capacitance (C_i) obtained by fitting of the *ac*-electrogravimetric data are presented in Figure 5.16. It can be observed that

both the anion and solvent show much lower transfer resistance (Rt_i) and higher frequencies (f_i) in the homopolymer in comparison to the copolymer Figure 5.16 (a, b). As the frequency, f_i, is related with the transfer kinetics of the species whereas the transfer resistance, Rt_i, is related to the ease/difficulty of their transfer, a more facile anion and solvent transfer at the electrode|electrolyte interface can be assumed for the homopolymer.

Polymer	E	G_s ($\times10^{-8}$)	K_s ($\times10^{-6}$)	G_A ($\times10^{-8}$)	K_A ($\times10^{-6}$)
ec-PVTPA	+ 0.9 V	-91.3	110	-110	220
	+ 1.0 V	-105	110	-110	220
ec-50-50	+ 0.9 V	-7.48	8.80	-15.8	88.0
	+ 1.0 V	-9.90	22.0	-14.5	66.0

Table 5.4: Fitting parameters, Ki and Gi, obtained from ac-electrogravimetry where in the subscript "s" stands for solvent and "a" for anion, where Ki and Gi are the partial derivatives of the flux (Ji) with respect to the concentration and the potential, respectively. Note that $cm \cdot s^{-1}$ and $mol \cdot s^{-1} \cdot cm^{-2} \cdot V^{-1}$ are the units of Ki and Gi parameters, respectively. Ki represents the transfer kinetics of each species related to the characteristic frequency of one species (f_i) while G_i is the reciprocal of the transfer resistance ($1/Rt_i$).

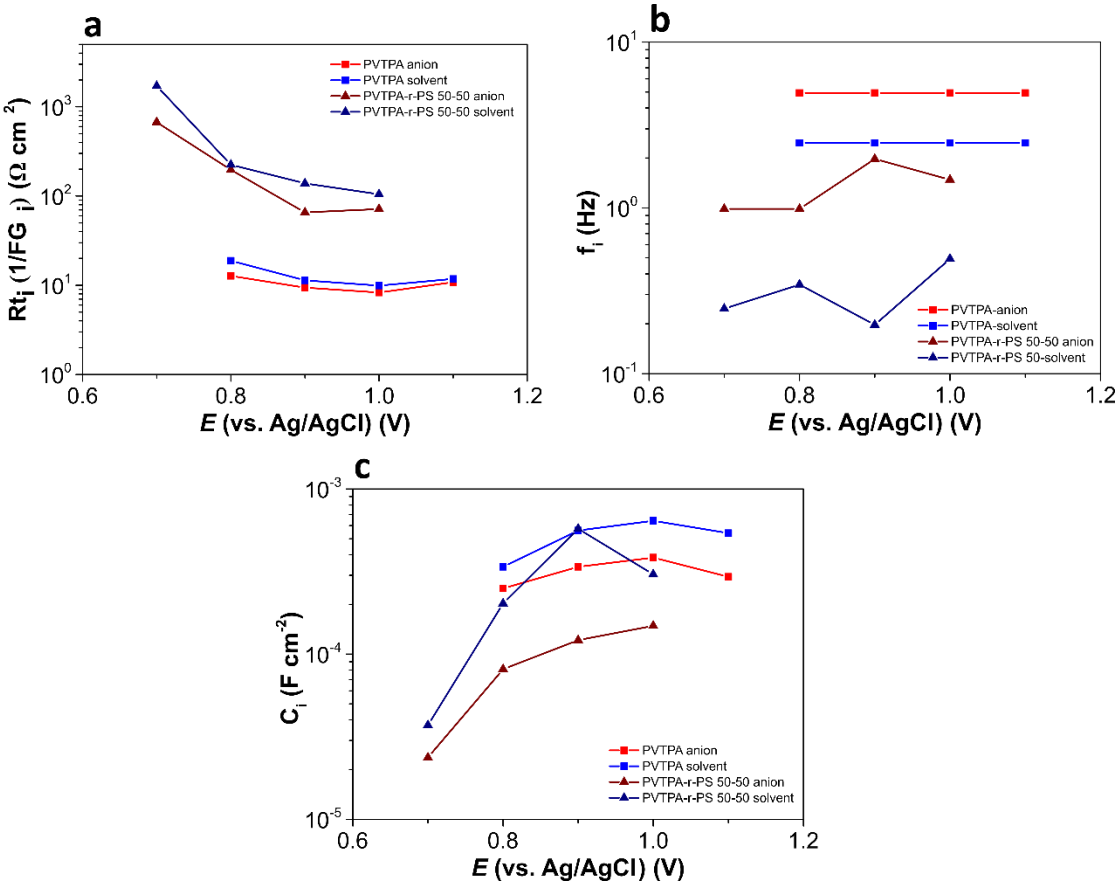

Figure 5.16: (a), Evolution of (a) transfer resistance (Rti), (b) frequency (c) instantaneous capacitance (Ci) for the anion (red) and the solvent (blue) as function of the analyzed potentials are presented for ec-PVTPA (squares) and ec-PVTPA-co-PS 50-50 (triangles).

The experimental results could be correlated with the less polar nature of the polymer due to the presence of PS units. The anion and the solvent present similar transfer resistance values (Rt_i) when considering the same film of ec-PVTPA and of ec-PVTPA-co-PS 50-50. When analyzing the Rt_i values of the anion (or solvent) for the two films, lower values are found in the case of ec-PVTPA with respect to ec-PVTPA-*co*-PS 50-50. As the polarization potential increases, we observe for both analyzed materials a decrease in the transfer resistance Rt_i and an increase in the instantaneous capacitance Ci. In general, the transfer resistance shows a less pronounced dependence on the polarization potential than the other analyzed parameters. The order of magnitude of the ion frequency and transfer resistance found in the anion and solvent for ec-PVTPA upon oxidation is comparable to those observed for cations and water in a PPy conducting polymer film (10-100 Ω cm^2) by reduction in 1M NaCl aqueous solution.[20]

5.1.5.3 Comparison of EQCM and ac-electrogravimetry data

To verify the quality of the fitting, the global mass reconstructed from *ac*-electrogravimetry is compared to the one obtained by Sauerbrey relationship from EQCM data. the results for ec-PVTPA and ec-PVTPA-*co*-PS 50-50 are presented in Figure 5.17 and Figure 5.18, respectively. The reconstruction of the partial concentration change is performed by integration of equation (5.4) with G_i and K_i terms obtained by Mathcad data treatment. K_i represents the transfer kinetics of each species related to the characteristic frequency of one species (f_i) while G_i is the reciprocal of the transfer resistance (1/Rti). In Table 5.4 we report the set of data for K_i and G_i in the case of the anion and the solvent for potential values of +0.9 V and +1.0V.

The partial mass contribution Δm_i is obtained through multiplication of ΔC_i by the film thickness and the molecular weight of the species *i*. By summation of the different Δm_i of the species involved in the charge compensation, the global mass change reconstructed from ac-electrogravimetry is obtained and compared to the mass change from EQCM, the data comparison is reported in Figure 5.17 and Figure 5.18, for ec-PVTPA and ec-PVTPA-*co*-PS, respectively. In the case of both redox polymer films a good correlation between the global mass change obtained by reconstruction from *ac*-electrogravimetry and EQCM is found. The variations encountered between the data might be explained on the basis of the different nature of the two experiments, i.e in EQCM the potential is changed potentiodynamically and in *ac*-electrogravimetry potentiostatically.

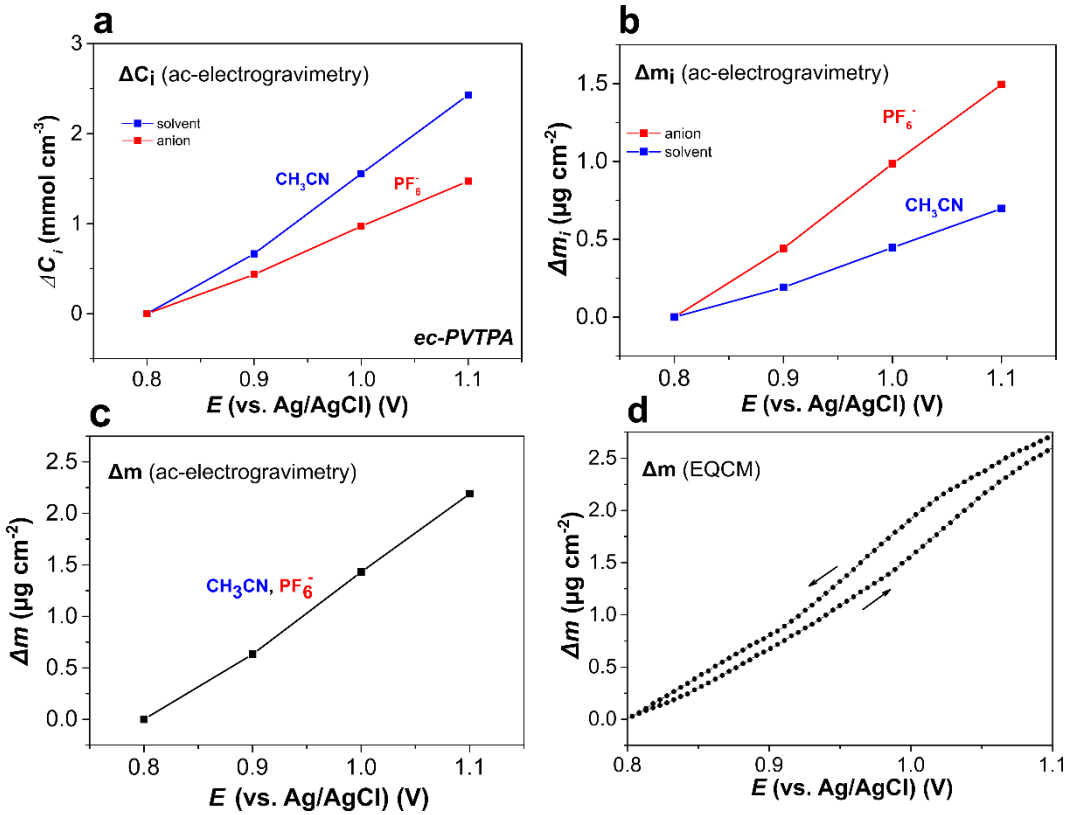

Figure 5.17: Change of concentration ΔC_i (a) and mass Δm_i (b) for the single species involved in the charge compensation, and (c) global mass change Δm for ec-PVTPA reconstructed from ac-electrogravimetry upon oxidation. Global mass change from EQCM (d) for comparison.

As already mentioned, the fitting of *ac*-electrogravimetric data for the charge compensation at the electrode | electrolyte interface was performed considering the only contribution of the anion and of the solvent for all the oxidation potentials analyzed. It can be observed how similarly for both electroactive films, the change of concentration within the polymer film ΔC_i of PF_6^- as well as of the solvent CH_3CN increases with increasing the potential (Figure 5.17 (a) and Figure 5.18 (a)). In the case of ec-PVTPA (Figure 5.17 (a)) a total ΔC_i of 1.5 mmol·cm^{-3} and of 2.5 mmol·cm^{-3} for the anion and the solvent, respectively, is observed, whereas for ec-PVTPA-*co*-PS (Figure 5.18 (a)) the reconstructed ΔC_i for the anion and the solvent is of 0.25 mmol·cm^{-3} and of 1.4 mmol·cm^{-3} , respectively. Further, a flux of solvent in the same direction of the anion flux is also observed (Figure 5.15 (a) and Figure 5.16 (a), blue line). An almost linear trend with the potential is found for the concentration change in both species, with solvent contribution being more pronounced (higher slope) as the potential is increased. Once the molecular weight of the two species is considered (Figure 5.15 (b) and Figure 5.16 (b)), the PF_6^- contribution to the global mass change is more significant than the one of CH_3CN. Overall, a good correlation of the mass change by ac-electrogravimetry reconstruction and by EQCM is found. In the case of ec-PVTPA the reconstructed total mass change Δm from ac-electrogravimetry is 2.2 μg cm^{-2}

in comparison to 2.45 μg cm^{-2} obtained from EQCM. Whereas in the case of ec-PVTPA-*co*-PS 50-50 the reconstructed total mass change Δm from ac-electrogravimetry is 0.84 μg cm^{-2} in comparison to 1.15 μg cm^{-2} (average of forward and backward scan) from EQCM.

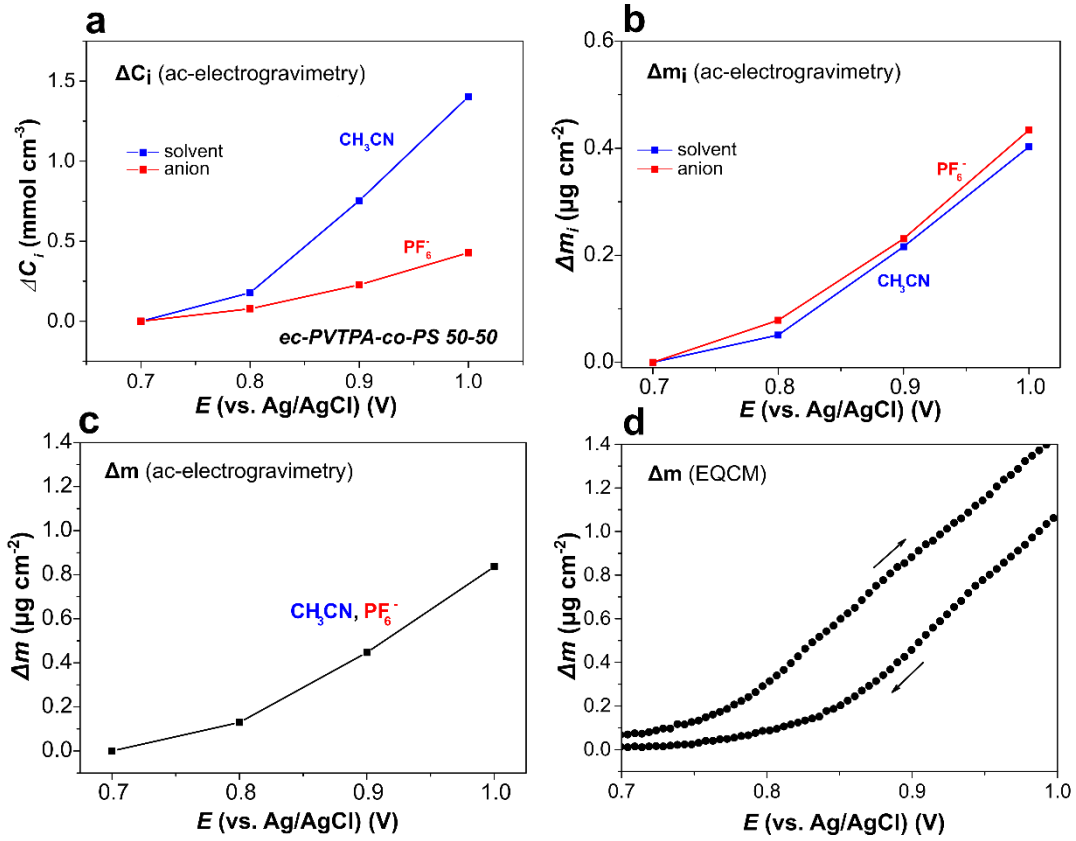

Figure 5.18: Change of concentration ΔC_i (a) and mass Δm_i (b) for the single species involved in the charge compensation, and (c) global mass change Δm for ec-PVTPA-co-PS 50-50 reconstructed from ac-electrogravimetry upon oxidation. Global mass change from EQCM (d) for comparison.

5.1.6 Conclusions

In this chapter electrochemical oxidation of solution deposited PVTPA and PVTPA-*co*-PS thin films endowed with different PVTPA/PS ratios was performed to achieve crosslinked electroactive films, namely *ec*-PVTPA and *ec*-PVTPA-*co*-PS. Variations in the CV profiles of electrochemically crosslinked films were observed modifying the redox active content in the polymer films. These included a variation of the total oxidative charge, of the peak positions and of the window of electroactivity. Interestingly, it is found that in the case of electrochemically crosslinked copolymers bearing a low PVTPA content (20-80 and 10-90), a shift in the peak position and shape is observed by varying the scan-rate. The sharp voltametric peak and shift in peak potentials might be associated to the different composition of the polymers. In particular, it might be expected that a higher quantity of non-polar PS units might lead to increased resistance of the polymer films and hinder the

radical cation formation, experimentally observed at more positive potential values in comparison to ec-PVTPA and higher PVTPA content copolymers.[34]

Similarly to the voltammetric behavior, differences in the conductivity profile are also found by variation of the redox unit content. A decrease in the potential region where the polymer is electroactive is found, together with a decrease in the capacitive characteristics of the voltammogram. The conductivity region follows a linear trend with the amount of redox units' content of the polymers. In addition to changes involving the conductivity region, a narrowing of the peaks-width associated with the two conductance regimes is observed. In the case of polymers with reduced PVTPA content, two separate conductance regimes are observed. In the case of the homopolymer, significant overlap between the two conductance regimes is found, and the second conductance regime is characterized by relative higher conductance values in comparison to the first regime, which might be a consequence of the convolution of the two peaks.

The charge compensation properties upon oxidation of electrochemically crosslinked arylamine-based polymers, ec-PVTPA and ec-PVTPA-*co*-PS 50-50 in 0.1M CH_3CN/NBu_4PF_6 were studied through classical and advanced EQCM. The effect of film composition on the transfer of ions and solvents upon oxidation was analyzed. EQCM measurements coupled with CV, indicate a mass uptake upon oxidation, also showing two regimes in the mass change, with good correlation with the oxidation steps $TPB/TPB^{+\bullet}$ and $TPB^{+\bullet}/ TPB^{2+}$. The calculation of $f(\Delta m/\Delta q)$ (g mol^{-1}) from EQCM data, gives in both cases molar mass values for the species higher than the one of the sole anion PF_6^-. The participation of other species in addition to the single anion was further investigated by *ac*-electrogravimetry. This latter indicates that the species transfer at electrode│electrolyte interface is dominated by anions and solvent moving in the same flux direction. Good correlation of the mass change by *ac*-electrogravimetry reconstruction and by EQCM is found. Characteristic parameters from ac-electrogravimetric measurements including the transfer resistance Rt_i, the frequency f_i and the instantaneous capacitance Ct_i were determined for solvent and anion for both homopolymer and copolymer. The frequency f_i is related to the transfer kinetics of the species, whereas the transfer resistance, Rt_i is related to the ease / difficulty of their transfer. We found a more facile anion and solvent transfer at the electrode│electrolyte interface for the homopolymer ec-PVTPA in comparison to the copolymer ec-PVTPA-*co*-PS 50-50. The observed results could be attributed to the less polar nature of the polymer due to the presence of PS units. The modification of the polymer structure with PS units shows an effect on the transport characteristics of the species involved at the film| electrolyte interface but not on their nature. In general, the homopolymer ec-PVTPA shows for both electronic conductivity and ion transfer superior performance in comparison to the copolymers analyzed.

5.1.7 Experimental

5.1.7.1 Electrochemical Measurements

5.1.7.1.1 Sample Preparation and Electrochemical Crosslinking

Different substrates were employed for electrochemical measurements (Au slides and 5 μm – Pt IDE) and for chemical doping (float-glass slides). Information about substrate and their cleaning procedure is reported 3.3. Sample preparation was performed by spin-coating (WS-400-6NPP-LITE, *Laurell Technologies*) the polymers from 10 mg/mL chloroform solution at room temperature. Samples employed for chemical doping were casted at 1000 rpm/s, ACE 50 whereas samples for electrochemical characterization were casted at 2000 rpm, ACE 50. After spin-coating the samples were dried under vacuum and were subjected to thermal annealing for 1 h at 150°C. Electrochemical crosslinking was performed by three subsequent CV cycles in 0.1 M CH_3CN/NBu_4PF_6. at a scan-rate of 20 mV/s, the electrochemical window employed for crosslinking was adapted for each polymer, in the case of PVTPA the crosslinking potential window was from -0.35 to + 0.9 V vs Fc/Fc^+ whereas in the case of PVTPA-*co*-PS from -0.35 to + 0.8 V vs Fc/Fc^+.

5.1.7.1.2 Cyclic Voltammetry

All electrochemical experiments were performed with an Autolab PGSTAT204 potentiostat (*Metrohm*) at room temperature in 0.1 M CH_3CN/NBu_4PF_6 under an Argon atmosphere. A three-electrode air-tight cell endowed with a Pt counter electrode (surface area higher or comparable to the one of the WE), Ag/AgCl and pseudo-reference electrode and Au WE were employed. More detailed information about the electrochemical set-up is reported section 3.1.1.1. All potential values are referenced to the Fc/Fc^+ internal. The active area of the polymer analysis was of ~0.8 cm^2.

5.1.7.1.3 Chronoamperometry

Chronoamperometry experiments were performed on ec-PVTPA and ec-PVTPA-*co*-PS by completely discharging the films at a potential value of -0.1 V vs Ag/AgCl for a duration time of 60 s and by subsequently applied the target charging potential for 120 s. The target potentials are measured from the lower to the more positive value, every 0.1 V from + 0.5 V to +1.2 V *vs* Ag/AgCl in the case of ec-PVTPA and between + 0.5 V to +1.1 V *vs* Ag/AgCl for ec-PVTPA-*co*-PS copolymers. The total oxidative charge (q+) at certain potentials of polarization by chronoamperometry is determined by integrating the current measured by application of a target potential for a time necessary for the current to asymptotically reach zero (120 s) as follows:

$$\int_{to}^{t} I(t)dt \qquad (5.2)$$

Charge from cyclic voltammetry is determined by integrating the current measured during the forward oxidation scan and by dividing by the scan-rate (v):

$$\frac{\int_{Eo}^{E} I(E)dE}{v} \qquad (5.3)$$

5.1.7.1.4 *In-Situ* Conductance

In-situ conductance experiments were performed using a three-electrode set-up electrochemical cell endowed with 5-µm Pt IDE electrodes (DropSens), an Autolab PGSTAT204 potentiostat (Metrohm), a µSTAT400 (Dropsens) and a conductivity interface CIP2 (*Heka*). Detailed description of the experimental set-up for *in-situ* conductance are reported in 3.1.1.2.2. All measurements were performed, unless specified, under Argon atmosphere in 0.1 M CH_3CN/NBu_4NPF_6 with a scan-rate of 10 mV/s, and by applying a drain potential of 10 mV between the combs. All potential values are referenced to the Fc/Fc^+ internal standard.

5.1.7.2 Electrogravimetric Measurements

5.1.7.2.1 Sample Preparation

The resonator surface was coated with the active material, PVTPA and PVTPA-*co*-PS 50-50, respectively, by spin-coating (5 mg/mL $CHCl_3$, 2000 rpm, ACE 50). The films were further subjected to electrochemical crosslinking by three subsequent cycles of oxidation in 0.1 M CH_3CN/NBu_4PF_6, in the potential window 0 – 1.2 V vs Ag/AgCl, yielding ec-PVTPA and ec-PVTPA-*co*-PS 50-50 respectively. After electrochemical crosslinking the films were rinsed with acetonitrile and EQCM measurements were performed by 5 subsequent CV cycles at a scan-rate of 50 mV/s in the potential window 0-1.1 V vs Ag/AgCl; 3 M KCl, to equilibrate the film composition. An average film thickness of ~70 nm was determined by profilometry, by analyzing the height change relative to a scratch.

5.1.7.2.2 EQCM

QCM is coupled to cyclic voltammetry, namely EQCM, to analyze the global electrochemical behavior and mass uptake resulting from the electrochemical doping of ec-crosslinked PVTPA and PVTPA-*co*-PS polymers films. Gold coated 9 MHz quartz resonators (AWS, Valencia, Spain) with surface area (S=0.2 cm^2) were employed as working electrode (WE) for EQCM characterization. A standard three-electrode electrochemical cell (AWS) endowed with Au-coated quartz resonator (9 MHz-AWS, Valencia, Spain) as WE, an Ag/AgCl (3 M KCl saturated with AgCl) as reference electrode (RE9, and a platinum grid as counter electrode (CE). The cell was connected to a Yokogawa frequency counter and a, Autolab PGSTAT100 potentiostat. Electrochemical crosslinking and all electrogravimetric measurements were performed using CH_3CN/NBu_4PF_6 0.1M as electrolyte. The solvent and

salt were electrochemical grade and were not subjected to previous purification before usage.

The simultaneous frequency shift (Δf) of the quartz resonator WE during CV experiments was tracked. The latter was converted into mass response Δm *(*mass change per unit area) according to Sauerbrey equation $\Delta f=-C_f \Delta m$. It is important to remind that the application of the Sauerbrey equation is only valid for sufficiently thin and rigid films, electroacoustic measurements (EQCM-D) are necessary to correct the sensitivity factor of the resonator. In the case of 9 MHz resonators employed the value of C_f used for calculations was $16.7 \cdot 10^7$ $g^{-1}cm^{-2}Hz$.[20] For the data treatment, in comparison to the experimental results, the fifth equilibration cycle was employed.

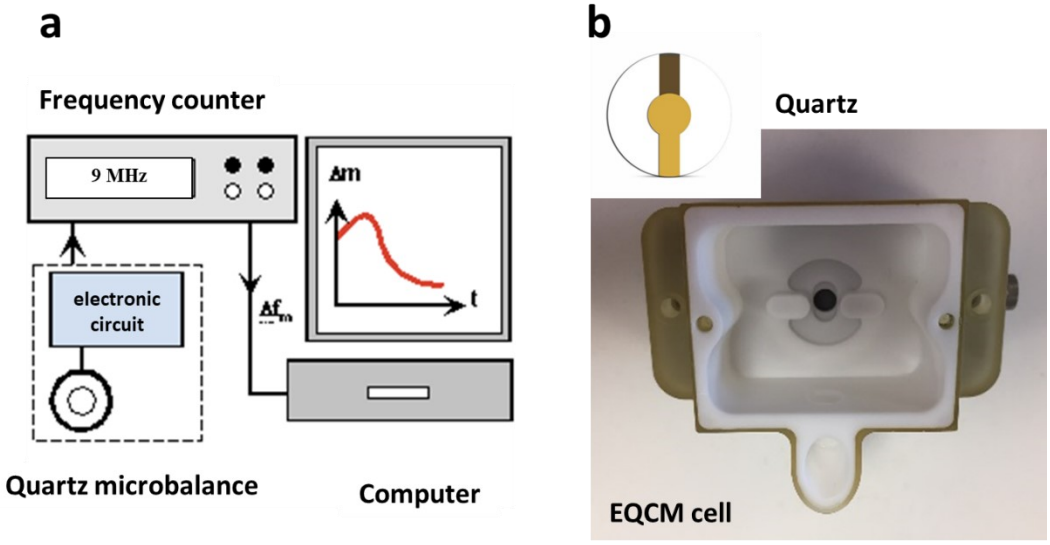

Figure 5.19: (a) QCM experimental setup. (b) EQCM cell and picture of the quartz resonator employed. Measurements were performed in Paris, Sorbonne University at the LISE institute under supervision of Prof. H. Perrot and Dr. O. Sel.

5.1.7.2.3 Ac-electrogravimetry

As previously mentioned, EQCM gives information about the absolute change in frequency at the electrode upon an electrochemical process, which can be correlated to the mass variation. EQCM is however limited to a global mass exploration. Indeed, no kinetic information about the species involved in the charge compensation can be extrapolated. *Ac*-electrogravimetry of electrochemically crosslinked ec-PVTPA and ec-PVTPA-*co*-PS was performed in complementarity to EQCM measurements, to study the transfer mechanism of different species directly and indirectly involved in the charge compensation upon electrochemical doping.

After determining the global mass change by EQCM (1.1.6), *ac*-electrogravimetric measurements were performed with the same cell configuration and three-electrode combination as for EQCM. The complete experimental setup for *ac*-electrogravimetry is shown in Figure 5.18. A four-channel frequency response analyser (FRA, *Solartron 1254*)

and a lab-made potentiostat (*SOTELEM-PGSTAT*) were employed. The QCM was used under dynamic regime, the coated working electrode with ec-PVTPA and ec-PVTPA-*co*-PS 50-50 were polarized at selected potentials, in the region of electroactivity of the film. A sinusoidal potential perturbation with small amplitude (50 mV) was superimposed to the applied potential. The frequency was variated in the following range: 10 mHz <f< 63 kHz. The frequency change Δf_m associated with the mass response (Δm_f) at the coated WE was determined by QCM simultaneously with the electrochemical charge response (Δq). The obtained results are directed by the FRA and the electrogravimetric transfer function ($\Delta m/\Delta E(\omega)$) as well as the charge/potential transfer function ($\Delta q/\Delta E(\omega)$) are obtained simultaneously at the given potential and frequency modulation f (pulsation $\omega=2\pi f$). The theoretical transfer functions $\Delta m/\Delta E(\omega)_{theo}$ as well as $\Delta q/\Delta E(\omega)_{theo}$ can be calculated by equations:

$$\frac{\Delta C_i}{\Delta E}(\omega)=\frac{G_i}{(j\omega d_f)+K_i} \qquad (5.4)$$

$$\frac{\Delta m}{\Delta E}(\omega)=-d_f \sum_i M_i \frac{G_i}{(j\omega d_f)+K_i} \quad \text{(i=ions and non-ions)} \qquad (5.5)$$

$$\frac{\Delta q}{\Delta E}(\omega)=F d_f \sum_i \frac{G_i}{(j\omega d_f)+K_i} \quad \text{(i=ions)} \quad (5.6)$$

where ΔC_i represents the change of the concentration of each species (ions and free solvent) in the film and d_f the film thickness (~70 nm), K_i and G_i are the partial derivatives of the flux (J_i) with respect to concentration and the potential, respectively. Reconstruction of the single contribution to the mass is done by integration of equation (5.5), the sum of the single contributions gives the reconstruction of the global mass. The latter is compared with the values obtained by EQCM measurements on the same film.

Finally, the characteristic parameters: frequency of transfer (f_i), transfer resistance (Rt_i) and the instantaneous capacitance (C_i) of each species are determined.

$$f_i=\frac{K_i}{2\pi d_f} \quad (5.7)$$

$$Rt_i=\frac{\pm 1}{F G_i} \quad (5.8)$$

$$C_i=\frac{-F d_f G_i}{K_i} \quad (5.9)$$

More detailed information about theory and experimental set-up as well as for data interpretation for *ac*-electrogravimetry are provided in section 3.1.1.2.4.

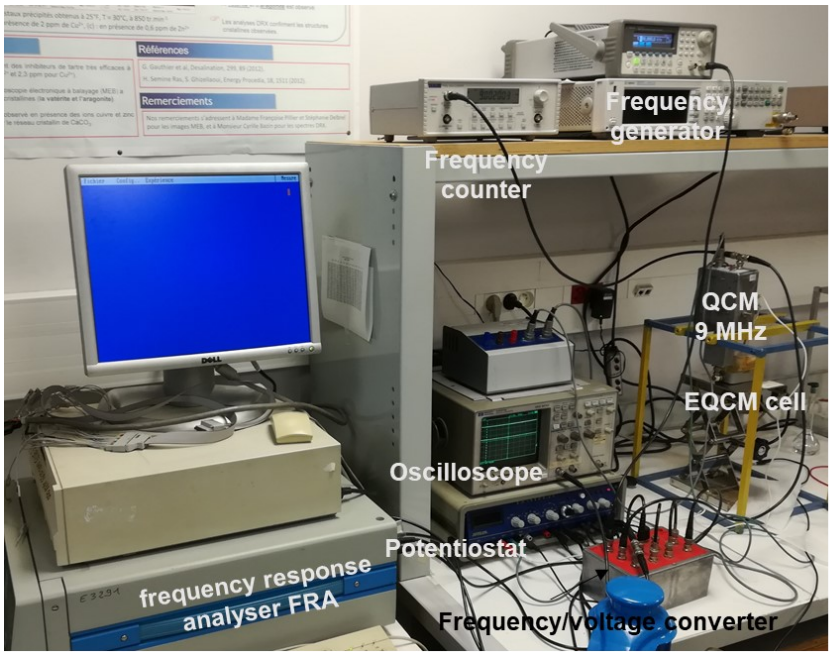

Figure 5.20: Ac-electrogravimetry setup. Measurements were performed in Paris, Sorbonne University at the LISE institute under supervision of Prof. H. Perrot and Dr. O. Sel.

5.2 Electrochemical and Conductivity Study of Crosslinkable Redox Polymers based on Arylamines and Carbazole Architectures

5.2.1 Introduction and Objectives

Since their discovery, conducting polymers have attracted the attention of the scientific community due to their intrinsic electronic conductivity upon doping. Many applications of conducting polymers (CPs), including hole transport layers (HTLs) in optoelectronic devices as well as electrochemical energy storage applications, require in fact efficient transport of charges through an active polymer layer. The nature of charge carriers and the interpretation of conductivity behaviors of doped conjugated polymers is therefore matter of interest and has been subject of many investigations ever since the discovery of high conductivities in these materials. Experimentally it remains however non-trivial to find the optimum doping level to reach maximum conductivities upon chemical doping of redox polymers, furthermore conductivities typically remain rather low[51] in comparison to conjugated systems such as poly(3-hexylthiophene)[52] and poly(ethylenedioxythiophene)[53].

In this section we present a work on the concomitant trigger of crosslinking and electronic conductivity upon electrochemical and chemical oxidation of a class of redox polymers endowed with triarylamine and carbazole pendant units, leading to crosslinked architectures. The experimental results here reported can also be found in the publication *J. Mater. Chem. C* **2020**, *8*, 15393–15405.[54] The structure of the polymers, namely polyvinyltriphenylamine (PVTPA), polyvinylphenylcarbazole (PVPhCbz) and polyvinylcarbazole (PVCbz) including structural information is provided in Figure 5.1. Upon oxidation of the triarylamine and carbazole redox units crosslinked polymer thin films can be generated with dimeric redox-active units *N,N,N',N'*-tetraphenylbenzidine (TPB), *9,9'-diphenyl-9H,9'H-3,3'*-bicarbazole (BPhCbz) and *9,9'-diethyl-9H,9'H-3,3'*-bicarbazole (BCbz), respectively. An analysis of the doping behavior of such systems is very important for applications where the system is employed in a doped state, for example during the charging/discharging process in batteries or where the materials are employed in highly doped states e.g., in hole-transport layers (HTLs) or transparent electrodes in perovskite solar cells and organic light emitting diodes. *In-situ* UV-Vis-NIR spectroelectrochemistry and *in-situ* conductance are performed to follow the trends in conductance as a function of polarization potential in correlation to the evolution of the neutral (N), radical cation ($R^{+\bullet}$) and dication state (D^{2+}), respectively.[55] Based on previous results[36] the chemical and electrochemical doping experiments are interpreted within the mixed valence conductivity model and the differences encountered between the polymers are discussed in terms of

planarization of the redox pendant units passing from TPA to Cbz and consequently intermolecular interactions.

Further, based on *in-situ* electrochemical results, optimization of chemical doping with the strong oxidant $FeCl_3$ was performed on PVTPA, PVCbz and PVPhCbz thin polymer films, with the aim to generate conducting transparent films with increased chemical and thermal stability to be employed in HTLs and transparent electrodes in optoelectronic applications. In general, conductivity of HTL is very important in defining the device performance, allowing efficient charge transport, lower ohmic-drops and improved device efficiency.[56] In this context, increased conductivity can be achieved for example by *p*-type doping of the HTL. This approach, aimed to achieve higher mobilities and improved device performance have been reported for example on the arylamine derivative *2,2',7,7'*-tetrakis(*N,N*-p-dimethoxyphenylamino)-*9,9'*-spirobifluorene (Spiro-OMeTAD) using different types of dopants including F4TCNQ[57], ionic liquid[58] as well as the low cost dopant $FeCl_3$.[59] Side chain triarylamine and carbazole polymers, including PVTPA and especially PVCbz, also known under the abbreviation PVK, have been employed as hole transport materials, and different works can be found reporting their chemical doping. In this chapter we also want to emphasize the importance of performing electrochemical and chemical doping studies in parallel, to target chemical doping especially in mixed-valence films and to achieve higher conductivities. The importance and success of this approach aspect has also being underlined by other recent literature in this field.[52,60]

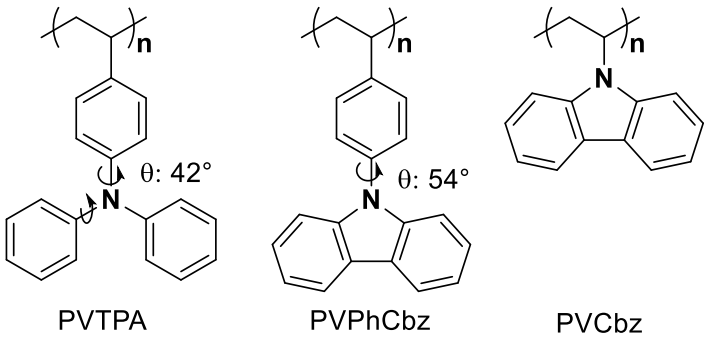

Figure 5.21: Structure of PVTPA, PVPhCbz and PVCbz including dihedral angles (θ). Carbazole structure is planar (for fused rings θ ~0°).[61,62]

The syntesis of PVTPA and PVPhCbz polymers was performed by Dr. Luca Scapinello and Philipp Sliskovic, respectively. Part of the results presented in this chapter have been gathered by the M.Sc. Yushi Lu and M.Sc. Claire Schlewitz in the context of their master thesis and research internship, respectively. Theoretical calculations were performed by Prof. Carmen Ruiz Delgado and the PhD student Sergio Gámez from the University of Malaga.

5.2.2 Electrochemical Crosslinking and Characterization of *ec*-PVTPA, *ec*-PVPhCbz and *ec*-PVCbz

5.2.2.1 Electrochemical Crosslinking of PVTPA, PVPhCbz and PVCbz

Thin films of PVTPA, PVPhCbz and PVCbz were deposited by spin-coating on an electrode surface, and were subjected to electrochemical oxidation to obtain crosslinked electroactive films. In Figure 5.22 (a) three successive voltametric cycles of oxidation performed at a scan-rate of 20 mV/s in 0.1 M CH_3CN/NBu_4NPF_6 are shown. In the first forward cycle of the voltammetric experiment, indicated with a dashed line, all films show an irreversible oxidation peak, which is assigned to the one-electron oxidation of the redox active pendant unit to the radical cation state. The peak potentials for the irreversible oxidation indicated as E_{cl}, are at 0.63 V for PVTPA, 0.84 V for PVPhCbz and 0.79 V for PVCbz, respectively. As described in the previous chapters, the crosslinking reaction involves the one-electron oxidation of the redox units generating highly reactive radical cations, due to the high spin density localized at the phenyl para position in triarylamines and the position 3 of the carbazole units. The species undergo an irreversible dimerization generating N,N,N′,N′-tetraphenylbenzidine (TPB) in the case of PVTPA and 3-3´-bicarbazole (BCbz) in the case of PVPhCbz and PVCbz, respectively. The as-generated films will be accordingly indicated as *ec*-PVTPA, *ec*-PVPhCbz and *ec*-PVCbz.

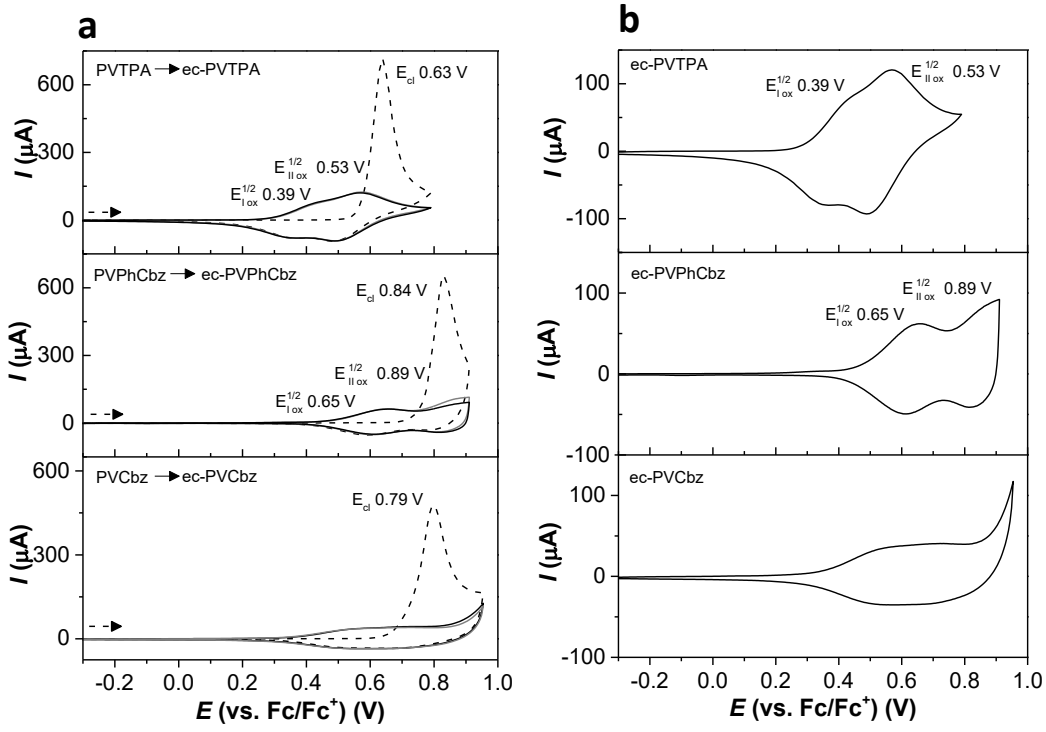

Figure 5.22: (a) CV pattern for three subsequent oxidative cycles of PVTPA, PVPhCbz and PVCbz thin polymer films registered in 0.1 M Bu_4NPF_6/CH_3CN with a scan rate of 20 mV·s^{-1}. First cycle indicated with dashed line, second cycle with a gray line and third cycle with a continuous black line. After the first cycle ec-PVTPA, ec-PVPhCbz and ec-PVCbz are generated. (b) Third oxidation cycle. Adapted with permission from ref. [54]. Copyright 2020 RSC.

5.2.2.2 Electrochemical Characterization of *ec*-PVTPA, *ec*-PVPhCbz and *ec*-PVCbz

The third voltammetric cycle presented in Figure 5.22 (b) shows for all polymers a decrease of the oxidation onset, resulting from the increased conjugation following the coupling reaction after the first oxidation cycle. The CV patterns of the generated *ec*-PVTPA and *ec*-PVPhCbz show two reversible and partially overlapping oxidation peaks which are assigned to the one electron oxidation to the radical cation at half-wave potentials $E_{1/2}$ of 0.39 V ($TPB^{+\bullet}$) and of 0.65 V ($BPhCbz^{+\bullet}$). At more positive potential values, the following one electron oxidation to the dication state with a $E_{1/2}$ of 0.53 V (TPB^{2+}) and 0.89 V ($BPhCbz^{2+}$) can be identified for *ec*-PVTPA and *ec*-PVPhCbz, respectively. In comparison to the other polymers, in the case of ec-PVCbz a broad reversible oxidation signal is found up to potentials of 0.9 V, with characteristics more typical of conjugated systems such as P3HT instead of two well defined redox peaks.[28,63]

Based on literature results, we expect that the oxidation and coupling of the redox pendant groups in acetonitrile stops at the level of dimerization, and no superior oligomers are generated.[64–66] The dimerization of redox-active pendants in the polymer films occurs both inter- and intra-polymer chains and results in crosslinked networks.[4,17] The crosslinking reaction leads to an increased stability towards dissolution, in particular for solvents such as acetone and THF for which the pristine films are completely soluble. No significant variations in the CV shape are observed between the second and all following subsequent voltammetric cycles, suggesting that the coupling reaction might be concluded after the first oxidation sweep. Should the oxidation reaction not stop at the dimerization of the redox units, in analogy to an electrodeposition process, we would expect with an increase in the number of oxidation cycles also a progressive shift of the film oxidation onset to less positive potential values. This phenomenon was not observed here.

5.2.3 *In-situ* Electrochemical Characterization of *ec*-PVTPA, *ec*-PVPhCbz and *ec*-PVCbz

Electrogenerated *ec*-PVTPA, *ec*-PVPhCbz and *ec*-PVCbz films were characterized by *in-situ* UV-Vis-NIR and *in-situ* conductance measurements to provide further insight about electrochemical doping and aiming to optimize and understand the simultaneous chemical crosslinking of the films, as typically employed in HTLs application.

5.2.3.1 *ec*-PVTPA

In-situ UV-Vis-NIR spectroelectrochemistry and *in-situ* conductance of *ec*-PVTPA during the forward cycle of oxidation via cyclic voltammetry are presented in Figure 5.23. The neutral crosslinked polymer film shows an absorption maximum at 352 nm at -0.4 V which is characteristic of neutral TPB (Figure 5.23 (c), blue spectra).[5] The increase in the oxidation potential above 0.26 V is associated with the development of two new bands

appearing at 476 nm and 1083 nm, which can be assigned to the HOMO–SOMO and SOMO–LUMO transitions of the radical cation.[5,54,67] The intensity of these bands reaches a maximum at 0.53 V after which a band with an absorption maximum of 741 nm starts forming, while the neutral band reaches its minimum. The band at 741 nm is – in accordance with literature – assigned to the dication TPB^{2+} species. Two sets of isosbestic points are encountered: at 395 nm for $TPB/TPB^{+\bullet}$, and at 378 nm, 425 nm, 529 nm and 995 nm for the redox couple $TPB^{+\bullet}/TPB^{2+}$. It can be observed how the onset for the peak-trend in Figure 5.23 (d) for the forward oxidation cycle also corresponds to the conductance onset in Figure 5.23 (f). The conductance profile in the forward cycle is characterized by a bell-shape with a maximum at 0.57 V and a shoulder around 0.42 V, a base-line conductance is measured up to 0.2 V and above 0.8 V. This behavior can be explained by mixed-valence conductivity, and is typically found in redox polymers.[68] Indeed, the polymer conductance only starts increasing above 0.2 V due to the electron hopping between neutral and radical cation species. The first conductance shoulder is reached at 0.42 V in close correspondence to the half-wave potential for the first oxidation ($E^{1/2}$ ($TPB/TPB^{+\bullet}$) in the CV (Figure 5.23 (f)). The conductance further increases reaching its highest value at 0.57 V which is about the half-wave potential for the second oxidation ($E^{1/2}$ ($TPB^{+\bullet}/TPB^{2+}$)). Upon further increasing the potential the conductance decreases, as at some point only TPB^{2+} species are available, i.e., no more sites for electron hopping. This conductance behavior was already described by Yurchenko *et al.*[36] in terms of two distinct but partially overlapped conductance regimes, with equal intensity of the conductance maxima, where hopping takes place between the two redox couples of TPB.[28,51]

Interestingly, in comparison to the results reported by Yurchenko *et al.,*[36] our data show a broader and hardly resolved conductance regime with a higher conductance registered for the $TPB^{+\bullet}/TPB^{2+}$ redox couple in comparison to one of $TPB/TPB^{+\bullet}$. We suggest that these differences might arise from the slightly different chemical nature of the two polymers under study. Whereas in our case the TPA redox units are directly connected to a polyvinyl backbone, in the case of Yurchenko et al. the pendant TPA units were linked via oxydimethylene spacers to a polystyrene backbone. We suggest that the different extent of interactions between the redox units in the two polymer films might result in the variations of the local environments of the redox centers, giving rise to slightly different ranges of redox potentials [30,51,69–71] and, consequently, of the observed differences in the conductance profiles. Similar observations are also found in the case of PVTPA-*co*-PS by decreasing the amount of TPA in the polymer composition (section 5.1.4.2).

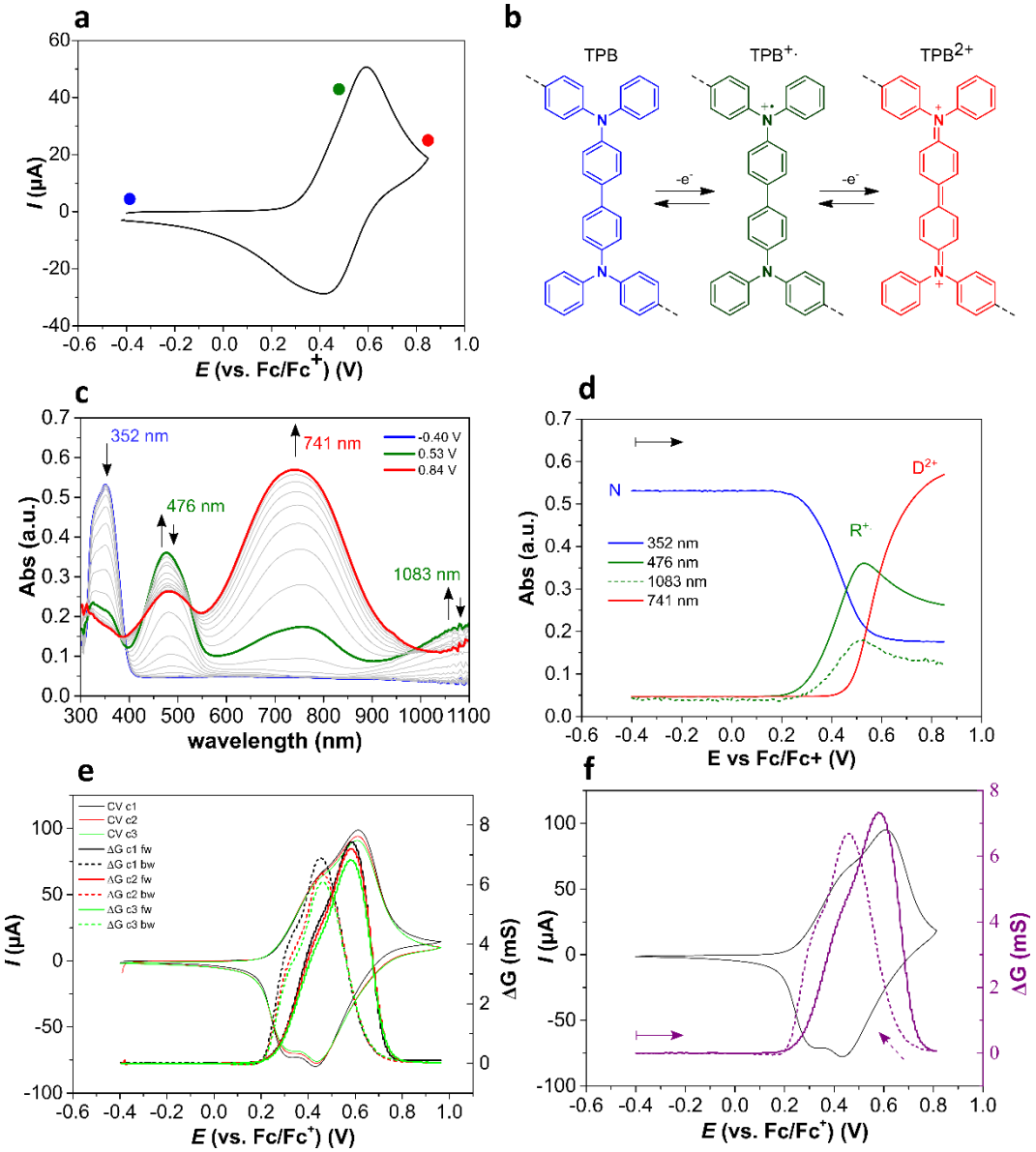

Figure 5.23: In-situ spectroelectrochemistry of ec-PVTPA thin film on ITO electrode, scan-rate 20 mV/s in 0.1 M CH_3CN/NBu_4PF_6 (a) CV cycle; (b) representation of the structures of TPB in the radical cation and dication state; (c) UV-Vis-NIR spectra registered during the forward scan; (d) peak-evolution of representative species in the forward scan. (e) Three subsequent in-situ conductance cycles of ec-PVTPA up to 1 V vs Fc/Fc⁺ (f) single cycle up to +0.8 V vs Fc/Fc⁺. Pt-IDE 5µm; 20 mV/s in 0.1 M CH_3CN/NBu_4PF_6. Neutral state indicated in blue, radical cation in green and dication state in red. Picture adapted with permission from ref. [54]. Copyright 2020 RSC.

5.2.3.2 *ec*-PVPhCbz

Figure 5.24 summarizes the *in-situ* UV-Vis NIR spectroelectrochemistry and *in-situ* conductance measurements which were registered during the oxidative doping of *ec*-PVPhCbz in the forward cycle. In Figure 5.24 (c), absorption spectra at different doping levels are presented, the neutral state of *ec*-PVPhCbz is characterized by a λ_{max} of 326 nm, whereas the radical cation state has two characteristic bands at 426 nm and 1047 nm, respectively, and the dication state presents a λ_{max} of 758 nm. Isosbestic points for the redox couple BPhCbz/$BPhCbz^{+\bullet}$ are found at 355 nm and for the $BPhCbz^{+\bullet}$/ $BPhCbz^{2+}$ at 466 nm

and 995 nm.[72] The proposed UV-Vis-NIR spectroscopic assignment is also supported by EPR data in the literature. [52,73] In Figure 5.24 (c) the absorption spectra for the neutral state (-0.3 V, blue) after the first oxidation (0.61 V, green) and at a fully oxidised state (1.05 V, red) are reported. The peak evolution for the different doped states in Figure 5.24 (d) shows the increase in absorption of the radical cation state (green curves, 426 and 1047 nm) together with the absorption decrease of the neutral band starting from 0.42 V which coincides with the onset of the *in-situ* conductance and the oxidation onset.

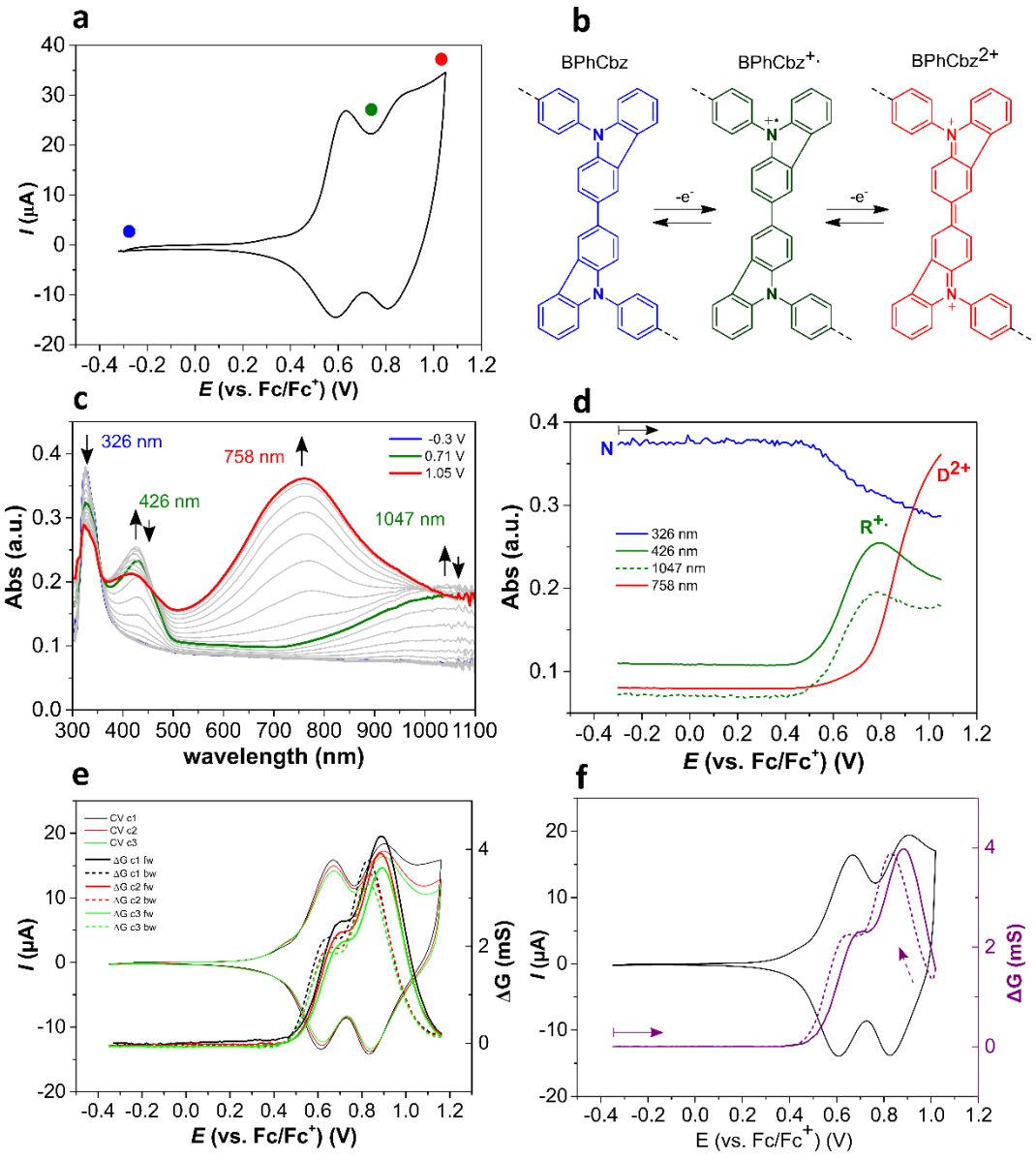

Figure 5.24: In-situ spectroelectrochemistry of ec-PVPhCbz thin film on 5μm Pt-IDE electrode, (a) CV cycle; (b) representation of the structures of BPhCbz in the radical cation and dication state; (c) UV-Vis-NIR spectra registered during the forward scan; (d) peak-evolution of representative species in the forward scan. (e) Three subsequent in-situ conductance cycles of ec-PVPhCbz up to.1.2 V vs Fc/Fc⁺. (f) In-situ conductance up to.1.0 V vs Fc/Fc⁺. Measurements performed with Pt-IDE 5μm at 20 mV/s in 0.1M CH_3CN/NBu_4PF_6. Neutral state indicated in blue, radical cation in green line and dication in red. Picture adapted with permission from ref. [54]. Copyright 2020 RSC.

The maximum absorption of radical cation is reached at 0.80 V, the potential value at which the dication band intensity also starts to increase. This potential value correlates well with the relative minimum between the two conductance maxima in the *in-situ* conductance plot (purple curve, Figure 5.24 (f)). The behaviour of ec-PVPhCbz is overall very similar to the one of ec-PVTPA film with bell-shaped conductance and presence of two defined mixed conducting regimes and higher conductance when $BPhCbz^{+\bullet}$/ $BPhCbz^{2+}$ species are present.

Another interesting observation concerns the lower conductance associated to electron hopping between $N/R^{+\bullet}$ and $R^{+\bullet}/D^{2+}$ found for ec-PVTPA and ec-PVPhCbz. In both cases the conductance for the second conductance regime is around twice as high as the first one. Similar findings are also described for oligothiophenes in the literature. [74,75] The results could be explained by a different electron diffusion coefficient for the different species ($N/R^{+\bullet}$)< ($R^{+\bullet}$ /D^{2+}). Another possible explanation could be the convolution of the second peak with the first one due to the small peak-to-peak separation, which corresponds to only 140 mV in the case of *ec*-PVTPA, and which is 210 mV for *ec*-PVPhCbz. We assume that convolution of the two peaks could lead to the higher maximum conductance observed for the second oxidation regime.

5.2.3.3 *ec*-PVCbz

In-situ UV-Vis-NIR spectra registered during the forward CV cycle of *ec*-PVCbz are presented in Figure 5.25 (c, d). In accordance with the other two polymers, we assign the following redox states: 326 nm to the neutral polymer; broad bands around 400 nm and above 1000 nm to the radical cation and another broad band with a maximum at 761 nm to the dication. In this case only a single isosbestic point at 966 nm is visible. With respect to the two other polymers, the spectroscopical variation between the different redox states seems to be less pronounced. This becomes also evident from the peak-evolution in Figure 5.25 (d). In the case of *ec*-PVCbz the radical cation bands (green curves, 402 nm and 999 nm) do not decrease in intensity after the first oxidation is completed but seem to reach saturation for higher potentials. These absorption variations also relate well with the *in-situ* conductance measurement, Figure 5.25 (d). By increasing the polymer oxidation level, the conductance slowly starts increasing above 0.18 V as radical cations are generated (development of the 402 and 999 nm bands, green curves). Above 0.7 V the radical cation absorption saturates and in correspondence to the slope change in the dication band at 761 nm (red curve), the film reaches its maximum conductance. This maximum conductance is maintained throughout the entire potential window explored (up to 1.1 V).

Despite the polymers' structural similarities, it is striking that *ec*-PVCbz shows a significantly different conductance profile compared to *ec*-PVTPA and *ec*-PVPhCbz.

Whereas two conductance regimes with corresponding maxima could be identified for *ec*-PVTPA and *ec*-PVPhCbz, the conductance trend in the case of ec-PVCbz shows a broad region of high conductance. Such a conductance plateau is usually reported for conjugated polymers, and has not been reported for redox systems so far.[28,51] Further, in analogy to conjugated systems the voltammogram of ec-PVCbz appears featureless (Figure 5.26 (a)).

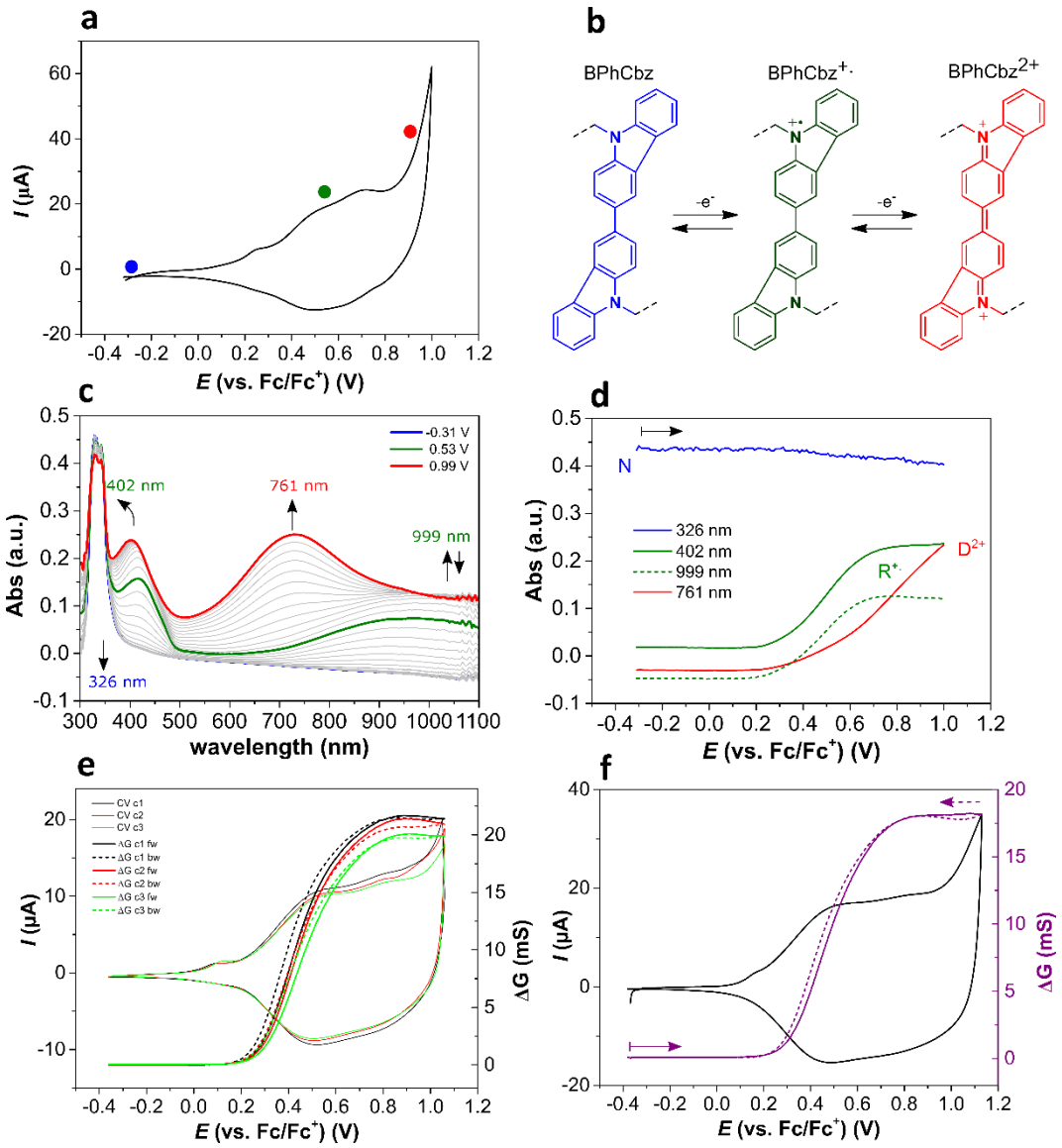

Figure 5.25: In-situ spectroelectrochemistry of ec-PVCbz thin film on 5µm Pt-IDE electrode, scan-rate 20 mV/s in 0.1M CH_3CN/NBu_4PF_6. (a) CV cycle; (b) representation of the structures of BPhCbz in the radical cation and dication state; (c) UV-Vis-NIR spectra registered during the forward scan; (d) peak-evolution for the forward oxiation scan. (e) In-situ conductance of ec-PVCbz three subsequent cycles up to 1 V vs Fc/Fc⁺ (f) single cycle up to +1.15 V vs Fc/Fc⁺. Measurements performed with Pt-IDE 5µm at 20 mV/s in 0.1M CH_3CN/NBu_4PF_6. Neutral state indicated in blue, radical cation in green and dication in red. Picture adapted with permission from ref. [54]. Copyright 2020 RSC.

The CV of *ec*-PVCbz was compared to the one of the molecular counterpart, N-ethylcarbazole (Figure 5.26 (a)). It can be observed how the two broad redox waves of ec-PVCbz CV signal correlate in potential values with the first and second oxidation of the dimer of N-ethylcarbazole registered during the CV experiment. The electrolysis of N-ethylcarbazole was also conducted with similar conditions with respect to the voltammetric experiment of the polymer to verify the possible formation of higher order oligomers considering the peculiar and capacitive shape of the ec-PVCbz cyclic voltammogram. For this purpose, a 2.5 mM solution of N-ethylcarbazole was dissolved in 0.1 M CH_3CN/Bu_4NPF_6 electrolyte solution, and potentiostatic oxidation was carried out in an electrochemical cell endowed with a Pt counter electrode, Au working electrode and a saturated calomel electrode as reference electrode in a salt bridge for 3 hours under N_2 atmosphere. The electrolysis solution was then dried, and the reaction mixture was purified through column chromatography. Ethyl-acetate: hexane in ratio 1:9 was employed as eluent; as cation exchange resin sodium poly-styrenesulfonate was added for electrolyte separation. Separation of the reaction mixture was correlated to one single product. The latter was characterized via ^{1}H-NMR (Figure 5.27) and was recognized as the dimerization product: *9,9'*-diethyl-*9H,9'H-3,3'*-bicarbazole.

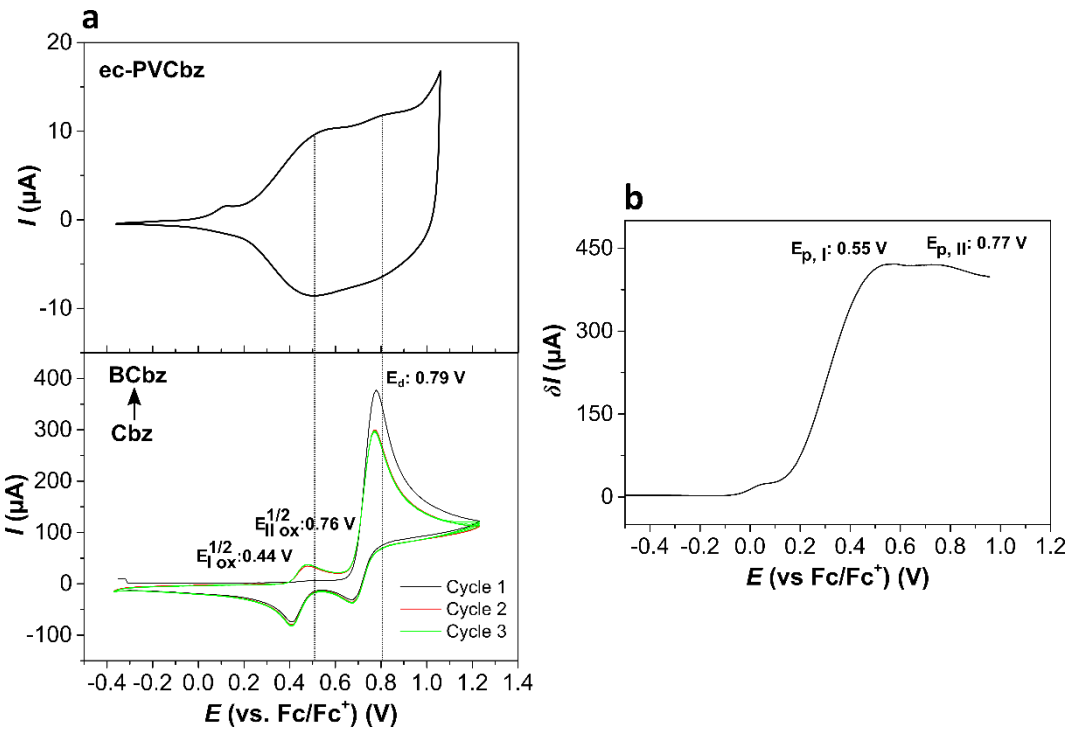

Figure 5.26: (a) (top) CV of ec-PVCbz in 0.1 M Bu_4NPF_6/CH_3CN, scan rate 20 mV/s and (bottom) CV of N-ethyl carbazole (0.5 mM) in 0.1 M Bu_4NPF_6/CH_3CN, scan rate 150 mV/s; Au working electrode. b) Differential Pulse Voltammetry of ec-PVCbz in in 0.1 M Bu_4NPF_6/CH_3CN at 20 mV/s. dE: 25 mV. Picture adapted with permission from ref. [54]. Copyright 2020 RSC.

The electrolysis of N-ethylcarbazole also confirms literature results which claim the formation of only dimeric species and no higher oligomers with the experimental conditions

employed.[76,77] The CV and differential pulsed voltammetry (DPV) of *ec*-PVCbz was also compared to the one registered for oxidation of N-Ethylcarbazole in 0.1 M CH_3CN/NBu_4PF_6, showing a similar pattern and correlation with peak potentials (Figure 5.26 (a)). An onset potential of 0.26 V corresponding to a HOMO of -5.36 eV was measured for *ec*-PVCbz.

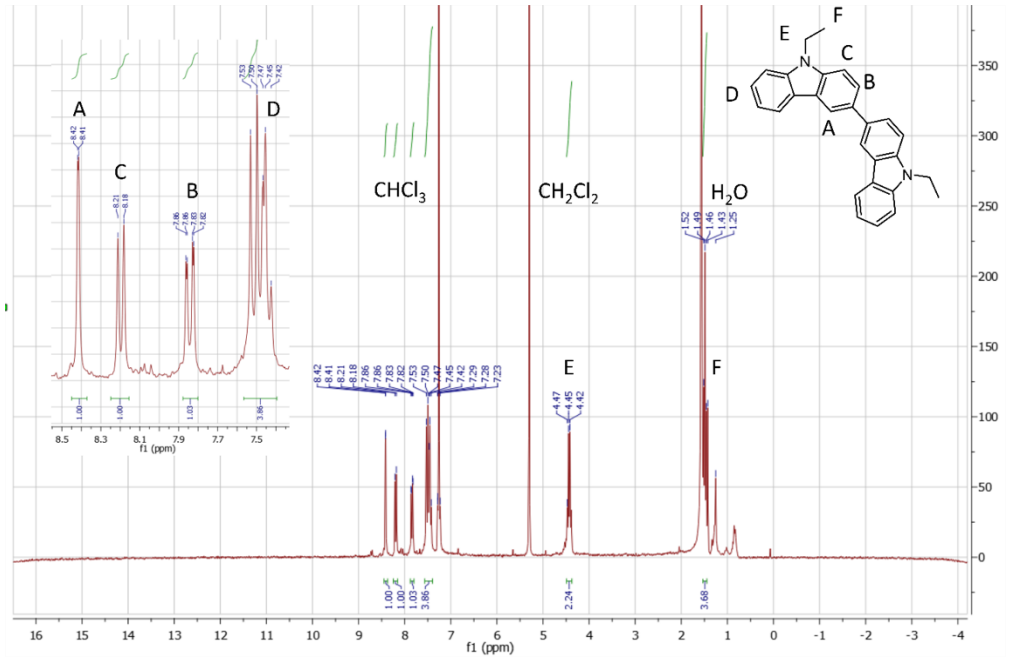

Figure 5.27: 1H-NMR of electrolysis product of N-Ethylcarbazole: 9,9'-diethyl-9H,9'H-3,3'-bicarbazole.

In contrast to the bell-shape behavior previously observed, electrochemical doping experiments of *ec*-PVCbz films present a conductance plateau maintained over the whole range of potentials analyzed (Figure 5.25 (f)). This is remarkable due to the structural similarities between the three polymers, all characterized by pendant dimeric redox units that can be reversibly oxidized in two redox steps. Such plateau conductivity has so far only been observed in conjugated polymer films, such as poly(3-hexylthiophene) (P3HT) and PEDOT.[6,28,78,79]

Electron hopping between polymer chains generally constitutes the rate determining step for charge transport in conducting polymers.[28,51] In this context, high conducting states can for example be achieved by favoring the spatial proximity of the redox units for an efficient electron tunneling and by a low reorganization energy.[51,68,80,81] π–dimers and π-stacks are known to favor interchain transport of charge carriers in conjugated polymers.[51,69,82–84] It was recently found that an effective π-π stacking constitutes the bottle-neck to enhance electrical performance of conducting polymers allowing for good percolation channels, rather than high crystallinity and high order.[85,86] Zozoulenko et al. analyzed the charge percolation efficiency in different PEDOT:Tosylate morphologies,

showing how samples with relatively low order but with good π-π connections between the polymer chains present more efficient connections for charge hopping than disjunct crystallites in highly crystalline samples.[85] Similar considerations resulted in a very recent work from our group; in which we report remarkably high conductivities in simply spin-coated disordered P3HT films using an *ex-situ* electrochemical doping approach.[52] The employment of units favoring π-stacking should therefore also in the case of redox polymers as in the case of PVCbz herein reported, be favored to promote increased electron hopping and conductivity.[54]

5.2.3.4 π-π stacking in Crosslinked Dimers

To provide more insight in the difference between the systems, we carried out DFT calculations to investigate the ability for π-dimer formation and π-π aggregates comparing pure BPhCbz and BCbz dimer systems. Since TPA is characterized by a propeller-like structure and endowed with dihedral angles of 42°, with limited ring planarization and low tendency to π-stacking[62], its dimer TPB was therefore not taken into consideration.

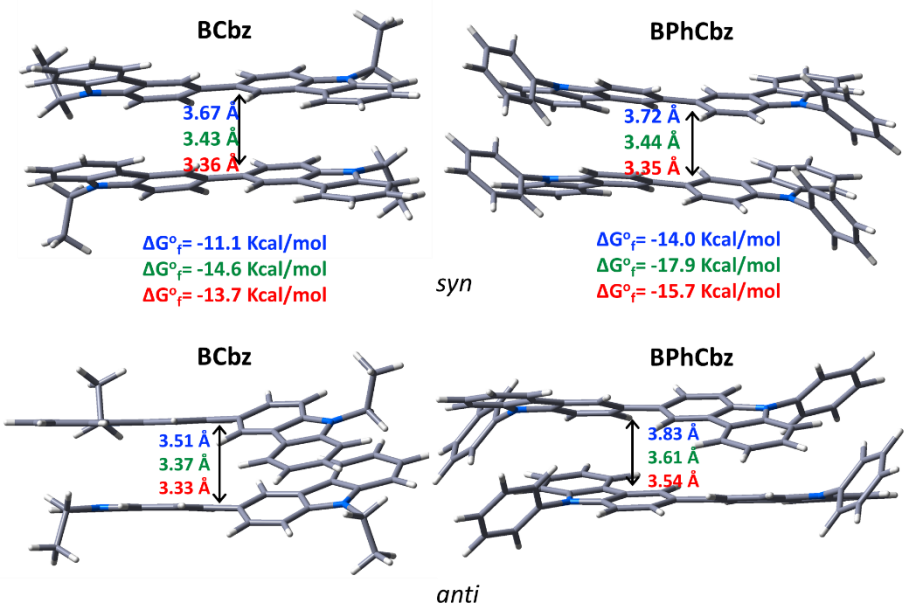

*Figure 5.28: Lateral views of the DFT-computed global minimum structure π-dimers of BCbz and BPhCbz in a (top) syn-configuration and (bottom) anti-configuration. The shortest C-C distances between the monomers and the free energy of formation values (at 298 K) calculated at the ωB97XD/6-31G** level in acetonitrile are also shown (blue, green and red values denoted the neutral, radical cation and dication states, respectively). Calculations performed by Prof. C. Ruiz Delgado and S. Gamez. Picture adapted with permission from ref. [54]. Copyright 2020 RSC.*

Two different cofacial arrangements of the BPhCbz and BCbz moieties were considered: a parallel (*syn*) and an antiparallel (*anti*) conformation (Figure 5.28). The negative Gibbs free energy values reveal the favourable formation of π-π aggregates in the neutral, radical cation and dication states, both in the BPhCbz and BCbz systems. The *anti*-conformation is found to be 2-3 Kcal/mol more stable than the parallel *syn* model, with

similar energies found for BPhCbz and BCbz systems. Smaller intermolecular π-stacking distance and a higher cofacial overlap are calculated for BCbz compared to BPhCbz (Figure 5.28). The DFT calculated Mülliken atomic charges on each Cbz unit of the π-dimer aggregates of BCbz and BPhCbz.

A stronger interaction between the BCbz units is further corroborated by the experimental spectroscopic data previously reported: the absence of an isosbestic point and the merging of the radical cation and dication bands might suggest overall less defined distinction between the redox states (Figure 5.25 (c)). Also the electrochemical characterization of ec-PVCbz does point in this direction (Figure 5.26 (b)). The CV in is rather featureless and capacitive as if constituted by several broad overlapping redox waves.

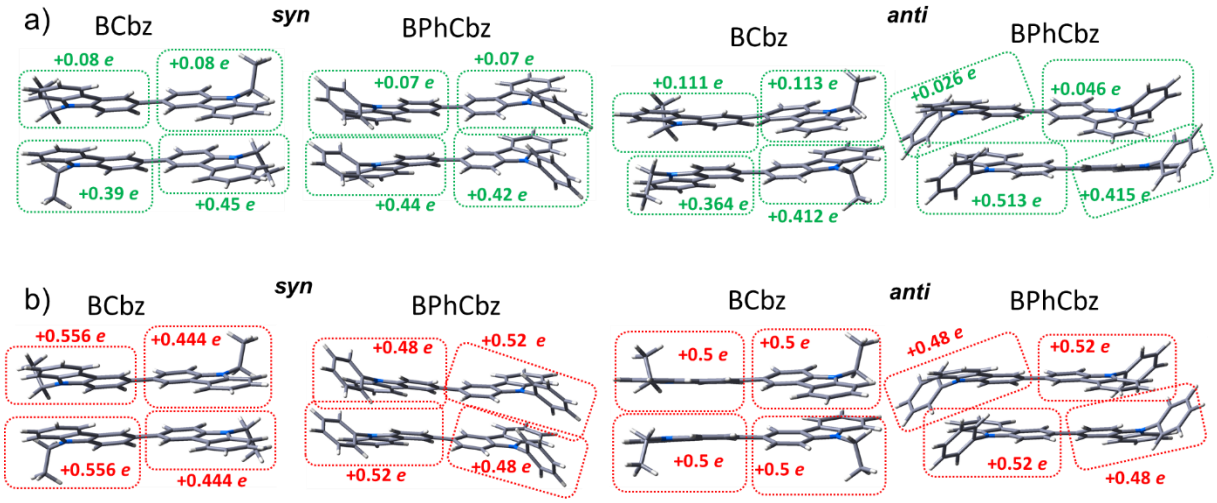

*Figure 5.29: DFT-calculated Mülliken atomic charges (ωB97XD/6-31G** level in acetonitrile) on each Cbz unit of the π-dimer aggregates of BCbz and BPhCbz in a syn (left) or anti (right) configuration for the radical cation (a) and dication (b) states. Calculations performed by Prof. C. Ruiz Delgado and S. Gamez. Picture adapted with permission from ref. [54]. Copyright 2020 RSC.*

It is common to find that the shapes of CVs are strongly dependent on intermolecular interactions.[63] Reciprocal interactions, differences in the spatial distribution of the redox centers and a distribution of species with different E^0 can give rise to peak widths at half-height that can differ by up to several hundreds of mV from the theoretically expected value of 90.6 mV for the one electron exchange of surface confined species at RT. [30,51,69–71] In this context, the featureless CV and wider electrochemical window of ec-PVCbz with respect to the other polymers analyzed in the manuscript could be described as a result of the conspicuous intermolecular interactions which might arise from a more efficient π-stacking, as evidenced by DFT calculations.

One could consider the redox polymers, despite the limited conjugation length of the dimers, as a network of close interacting dimers which generate a band of closely spaced states with slightly different energies. These could be considered as several close redox

states and conductivity in accordance with Heinze description.[28] as a sequence of electron hopping between several mixed valence-states very close in energy. Analogous considerations were proposed by Zotti et al.[87] to describe the plateau conductivity found for octathiophene and decathiophene oligomers despite their limited conjugation. In the previous chapter, the effect of the degree of interactions between redox units resulting from their dilution in PVTPA-*co*-PS copolymers endowed by different contents of triphenylamine (TPA) redox active units and of non-redox active polystyrene (PS) units was analyzed. It was previously found that variations of the redox active content in the polymer strongly affects the conductivity profile of the species. More specifically, a decrease in the potential region where the polymer is electroactive was found, with also decreased capacitive characteristic of the voltammogram. The experimental observation herein presented, together with the findings in the previous chapter, represents a good description for the mixed valence conductivity model. Indeed, it may well represent the situation where multiple following redox states at different energies are present and associated to subsequent hopping possibilities between different subsequent units. These results are also supported by recent studies in which the effects of chain to chain interactions in conducting polymers on their conductivity profile are analyzed.[80,81,85] In the case of π-conjugated polymers, a much higher ensemble of possibilities concerning energies for the different redox states is expected, as different effective conjugations are present, further it must be considered that the progressive removal of electrons influences the energy of further oxidation reactions.

5.2.4 Chemical Oxidation: Simultaneous Crosslinking and Doping

The simultaneous chemical crosslinking and doping of PVTPA, PVPhCbz and PVCBz thin films was conducted by a sequential solution doping method. The low cost oxidizing agent $FeCl_3$ (anhydrous) was used because of the high standard oxidation potential of 1.47 V vs Fc/Fc^+ of the Fe(III)/Fe(II) redox couple in acetonitrile.[59]-[88] $FeCl_3$ has already been used to polymerize and dope triarylamines and carbazoles in the literature. [6,77,89–91] Furthermore, chemical oxidation with $FeCl_3$ and electrochemical oxidation lead to similar oxidation products which is important for a direct comparison between chemically and electrochemically oxidized samples in this study.[76,77,92] All chemical oxidation measurements reported in the study were performed in a nitrogen filled glovebox. Thin films of the polymers were covered with 50 µL of the oxidant in acetonitrile, which is an orthogonal solvent for the polymers, and excess of dopant was removed by spincoating. The doping process was controlled by varying the concentration of the dopant: (0.1 to 4 mg/mL in case of PVTPA and 1 to 10 mg/mL for PVPhCbz and PVCbz) as well as the exposure time. To follow the chemical doping process, and to identify the nature of charge carriers accountable

for the measured conductivities of each film, UV-Vis-NIR spectra were recorded for comparing the results with the ones obtained by *in-situ* spectroelectrochemistry data.

Conductivity data of PVTPA (Figure 5.30 (a)), PVPhCbz (Figure 5.32 (a)) and PVCbz (Figure 5.34 (a)) films doped with $FeCl_3$ solutions for 10 s are presented in the following. Maximum conductivities of $(1.0 \pm 0.1)\cdot10^{-3}$ S/cm and $(6.8 \pm 1.1)\cdot10^{-4}$ S/cm for PVTPA and PVPhCbz (b) are registered upon doping with 2 mg/mL and 5 mg/mL solutions, respectively upon exposure of the samples with the oxidizing solutions for 10s. By analyzing the dependency of the conductivity of PVTPA and PVPhCbz on the $FeCl_3$ concentration, a bell shape trend is observed, with conductivity decreasing after reaching the maximum. The results upon chemical oxidation match well with the *in-situ* conductance results registered for the electrochemically crosslinked polymers and are in good correlation with *in-situ* spectroelectrochemical data. On the other hand, PVCbz is the polymer presenting the highest conductivities and gives values up to 10^{-2} S/cm for $FeCl_3$ concentrations in a large concentration range, from 3 to 10 mg/mL (Figure 5.34 (a)). The data obtained by chemical oxidation are also in this case in good agreement with the wider range of potential of higher conductance found for electrochemically crosslinked film upon electrochemical doping (Figure 5.25). For all three polymers maximum conductivities measured for films after 60 s doping time were similar but were reached already at lower oxidant concentrations. This concentration dependency suggests a diffusion-controlled process.[93] The evolution of conductivities as function of dopant concentration for different exposures times well evidences this phenomenon, as one can see in Figure 5.31 (a) in the case of PVTPA. Direct comparison of absorption data upon chemical doping with *in-situ* conductance results, show for all systems a very good correlation between doping level and conductivity as for electrochemical doping (Figure 5.30 (d); Figure 5.32 (d) and Figure 5.34 (d)). Indeed, maximum conductivity upon chemical doping is associated with an absorption pattern like the one registered for potential values associated with maxima in the *in-situ* conductance and a mixed valence behaviour of conductivity.

5.2.4.1 PVTPA Chemical Crosslinking and Doping

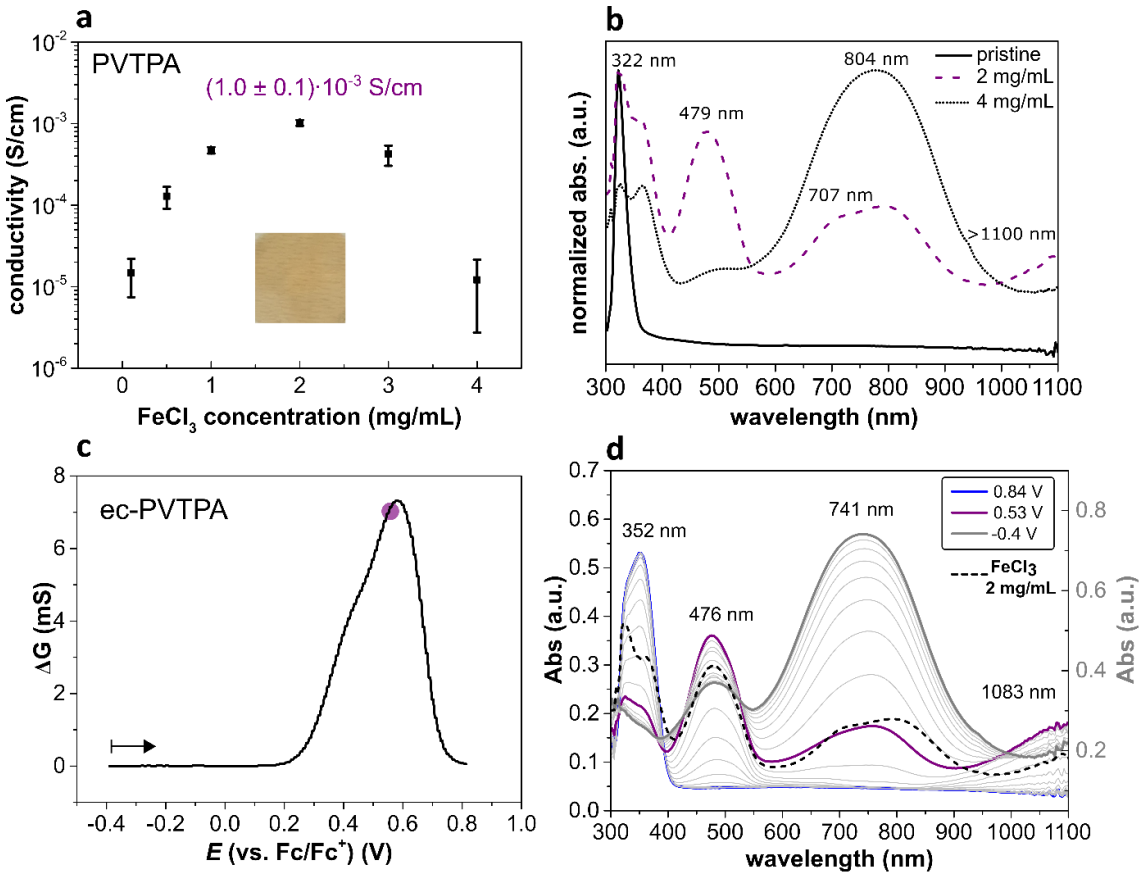

Figure 5.30: Sequential doping of a PVTPA film with $FeCl_3/CH_3CN$ solutions with different concentrations (0.1; 0.5; 1; 2; 3 and 4 mg/mL) for 10 s. (a) conductivity data and inset of a 1 cm^2 film doped with 2 mg/mL $FeCl_3$ solution at maximum conductivity, (b) UV-Vis-NIR absorption spectra for as-casted PVTPA film (black continuous line); at maximum conductivity (2 mg/mL; purple dashed line) and at 4 mg/mL (dotted black line). (c) Forward in-situ conductance cycle with characteristic "bell-shape" from Figure 5.23, (d) UV-Vis-NIR spectroelectrochemistry of ec-PVTPA with absorption at +0.53 V (purple line, at max conductance) in comparison to the absorption spectra registered at maximum conductivity (2 mg/mL; 10 s) upon chemical doping (black dashed-line). Picture adapted with permission from ref. [54]. Copyright 2020 RSC.

In case of PVTPA (Figure 5.30 (b)) the pristine polymer exhibits a neutral band with a maximum of 322 nm, this fits very well with the absorption wavelength reported for the pure triphenylamine (TPA) compound.[5] At 2 mg/mL $FeCl_3$ concentration one can distinguish bands with maxima at 479, 707, 804 and > 1100 nm which hint, upon comparison with spectroelectrochemical data, to a successful crosslinking and in particular, to the concurrent presence of TPB units in a radical cation and dication state within the polymer film. At the highest concentration of 5 mg/mL a small band at 479 nm and a more distinct band around 804 nm are visible and the absorption pattern well resembles the one obtained upon electrochemical doping at high potentials. In all doped samples, a peak maximum at 360 nm is observed which is associated with the absorption of the dopant $FeCl_3$,[5,94] which overall hampers band assignments to the polymer species in this wavelength range, in particular in the case of the neutral dimerized species: TPB, BPhCbz and BCbz.

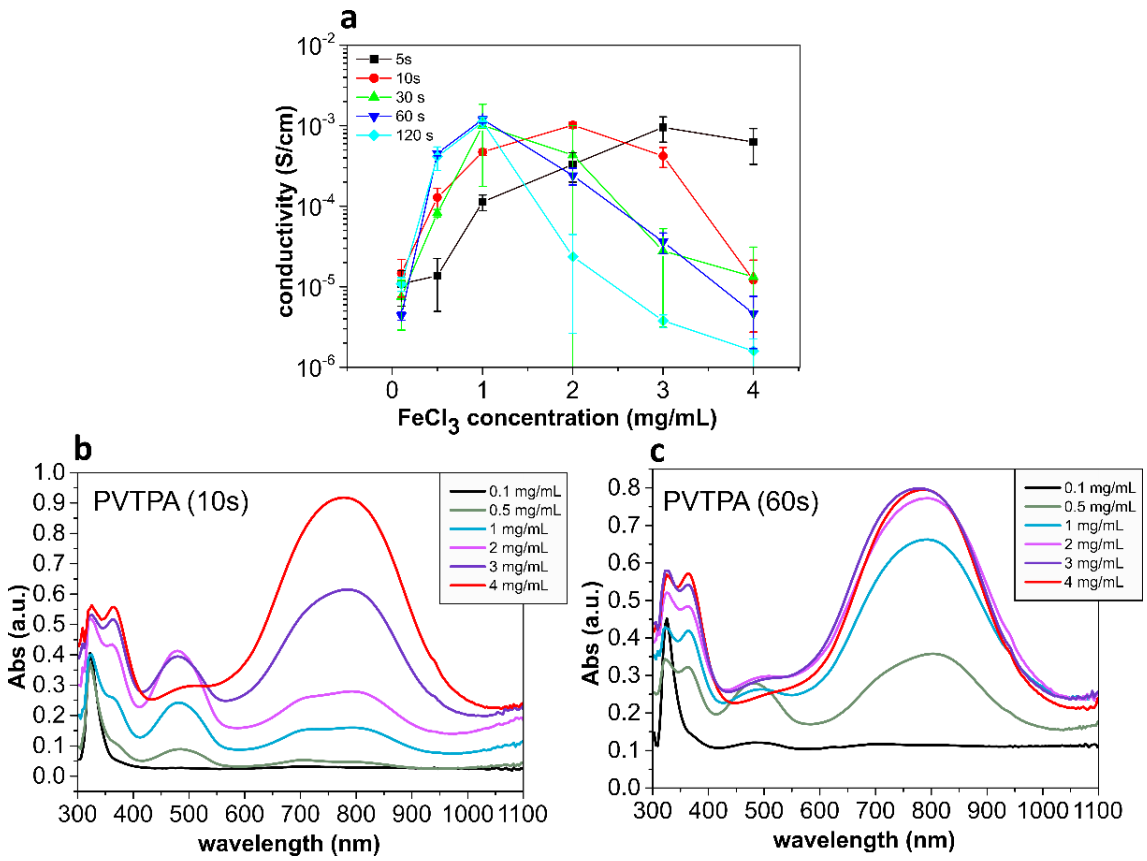

Figure 5.31: (a) Sequential doping of a PVTPA film with $FeCl_3/CH_3CN$ solutions with different concentrations (0.1; 0.5; 1; 2; 3 and 4 mg/mL) and for different doping times. UV-Vis-NIR of sequentially doped PVTPA films with $FeCl_3/CH_3CN$ for (b) 10 s and (c) 60 s. The correlated conductivity data are presented in a.

5.2.5 PVPhCbz Chemical Crosslinking and Doping

PVPhCbz (Figure 5.32) is also characterized by a similar absorption behavior as PVTPA in relation to conductivity which fits very well the *in-situ* conductance results, hinting to a strong dependency on the doping level and a mixed valence conductivity mechanism. In the case of the doped film, the band at 797 nm, which, upon comparison with spectroelectrochemical data is assigned to the dications state of BPhCbz units is dominant.

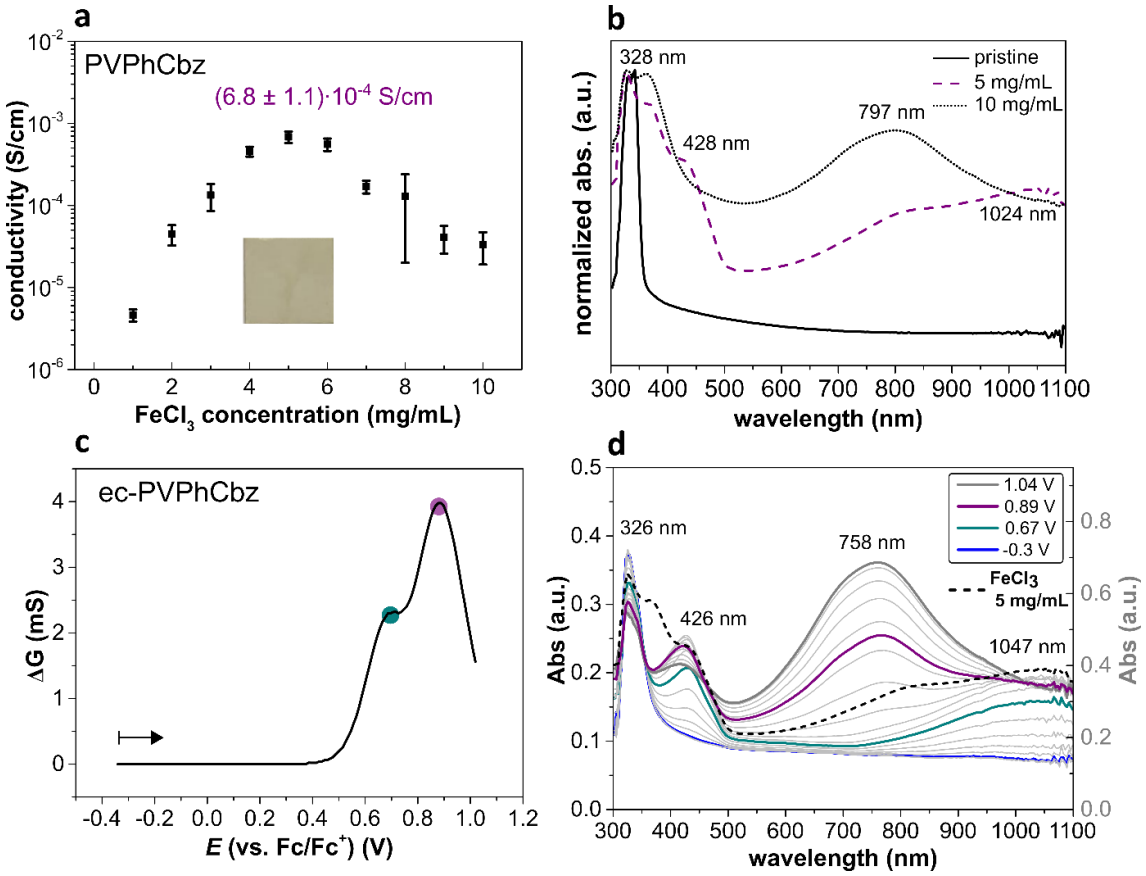

Figure 5.32: Sequential doping of a PVPhCbz film with $FeCl_3/CH_3CN$ solutions with different concentrations (1-10 mg/mL) for 10 s. (a) conductivity data and inset of a 1 cm^2 film doped with 5 mg/mL $FeCl_3$ solution at maximum conductivity, (b) UV-Vis-NIR absorption spectra for as-casted PVPhCbz film (black continuous line); at maximum conductivity (5 mg/mL; purple dashed line) and at 10 mg/mL (dotted black line). (Bottom) (c) Forward in-situ conductance cycle with characteristic "bell-shape" from Figure 5.24. (d) UV-Vis-NIR spectroelectrochemistry of ec-PVPhCbz with absorption at +0.67 V (green line, first relative max) and at 0.89 V (purple line, second and absolute max) in comparison to the absorption spectra registered at maximum conductivity (5 mg/mL; 10 s) upon chemical doping (black dashed-line). Picture adapted with permission from ref. [54]. Copyright 2020 RSC.

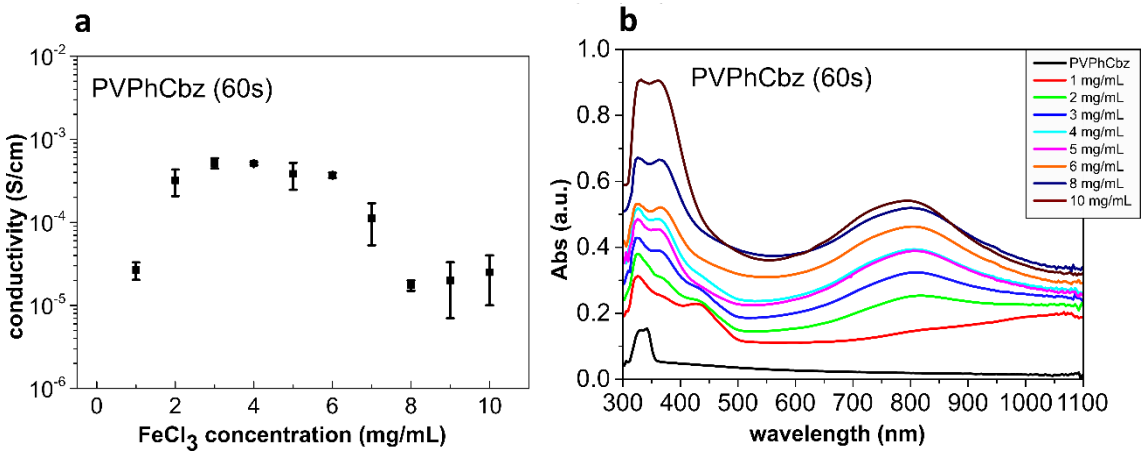

Figure 5.33: (a) Chemical crosslinking and doping of PVPhCbz films with $FeCl_3/CH_3CN$ for 60 s exposure time with $FeCl_3/CH_3CN$ for 10 s. Electronic conductivity and (b) corresponding UV-Vis-NIR absorption spectra. Adapted from Yushi Lu Master Thesis (2018).

The neutral polymer film has an absorption maximum of 328 nm.[22] The highest conductivity was registered for the 5 mg/mL doped sample where the characteristic film absorption presents maxima at 428 nm, 797 nm, and 1024 nm, i.e., for a concurrent presence of radical cations and dications, as evidenced upon overlay of absorption spectra with spectroelectrochemical data (Figure 5.32 (d)). The complete set of absorption and conductivity data measured upon 60 s exposure to the dopant are reported in Figure 5.33, showing also in this case a strong dependency of the conductivity with doping times and dopant concentration, with conductivity values obtained for lower dopant concentrations in comparison to the doping dataset obtained at shorter contact times.

5.2.5.1 PVCbz Chemical Crosslinking and Doping

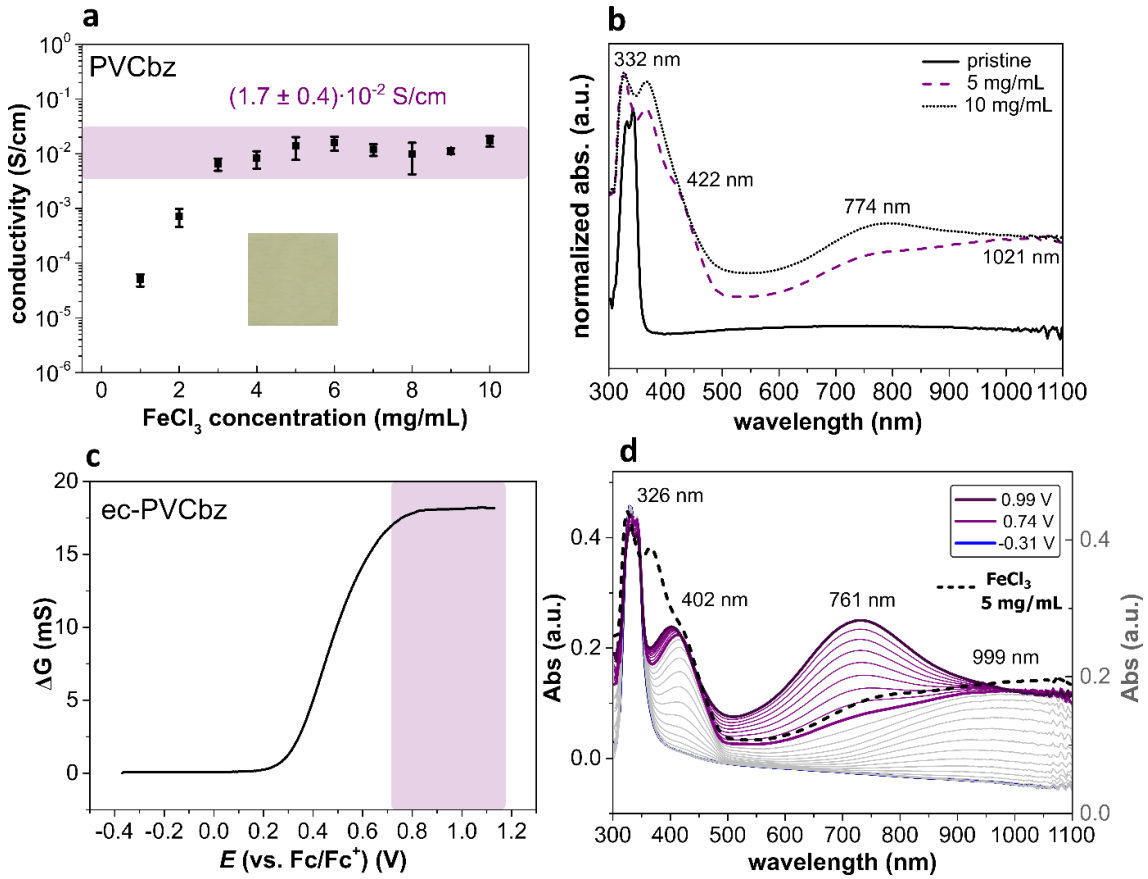

Figure 5.34: Sequential doping of a PVCbz film with $FeCl_3/CH_3CN$ solutions with different concentrations (1-10 mg/mL) for 10 s. (a) conductivity data and inset of a 1 cm^2 film doped with 5 mg/mL $FeCl_3$ solution at maximum conductivity, (b) UV-Vis-NIR absorption spectra for as-casted PVCbz film (black continuous line); at maximum conductivity (5 mg/mL; purple dashed line) and at 10 mg/mL (dotted black line). (Bottom) (c) Forward in-situ conductance cycle with plateau conductance behavior from Figure 5.25, (d) UV-Vis-NIR spectroelectrochemistry of ec-PVTPA with absorption at potential values more positive than 0.74 V (purple line, reaching the plateau region)) in comparison to the absorption spectra registered at maximum conductivity (5 mg/mL; 10 s) upon chemical doping (black dashed-line). Picture adapted with permission from ref. [54]. Copyright 2020 RSC.

In the case of PVCbz doping (Figure 5.34 (b)), the absorption of the neutral polymer has a maximum at 332 nm. The conductivity values do not show significant variations above 3 mg/mL over the whole concentration range explored, also the absorption behavior is quite similar. One can identify a band around 422 nm, as well as a rather broad band above 600 nm with a shoulder around 770 nm in the films doped with 5 and 10 mg/mL. The spectra show overall less pronounced variations when compared with the ones registered for chemically doped PVTPA and PVPhCbz, similarly as for *in-situ* spectroelectrochemical results (Figure 5.34 (d)). It can be noted that the films are overall quite transparent which could be useful for application as transparent electrode. In analogy to *in-situ* conductance results, high conductivity values are maintained over a wider range of concentrations, making the performance of this material less dependent from the doping level with respect to the case of PVTPA and PVPhCbz previously described.

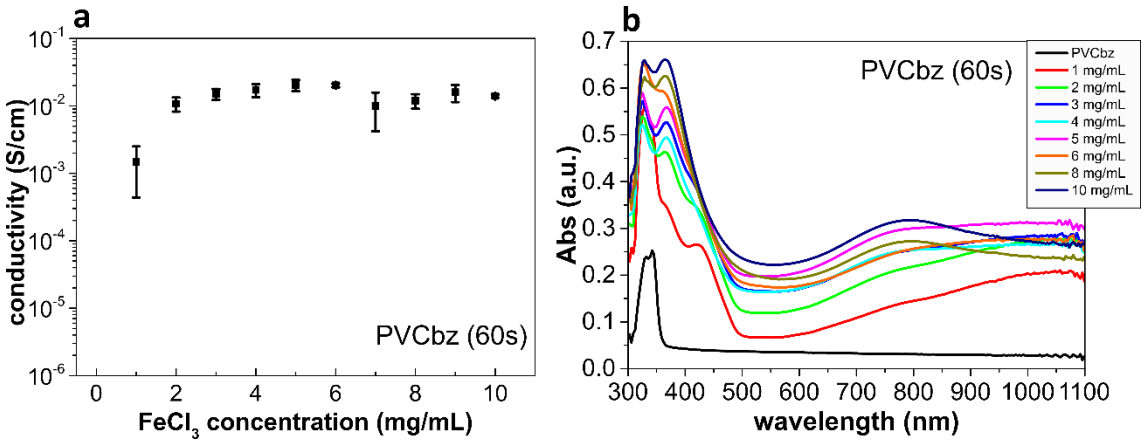

Figure 5.35: (a) Chemical crosslinking and doping of PVCbz films with $FeCl_3/CH_3CN$ for 60 s exposure time with FeCl3/CH3CN for 10 s. Electronic conductivity and (b) corresponding UV-Vis-NIR absorption spectra.

5.2.5.2 Chemical Oxidation in Air

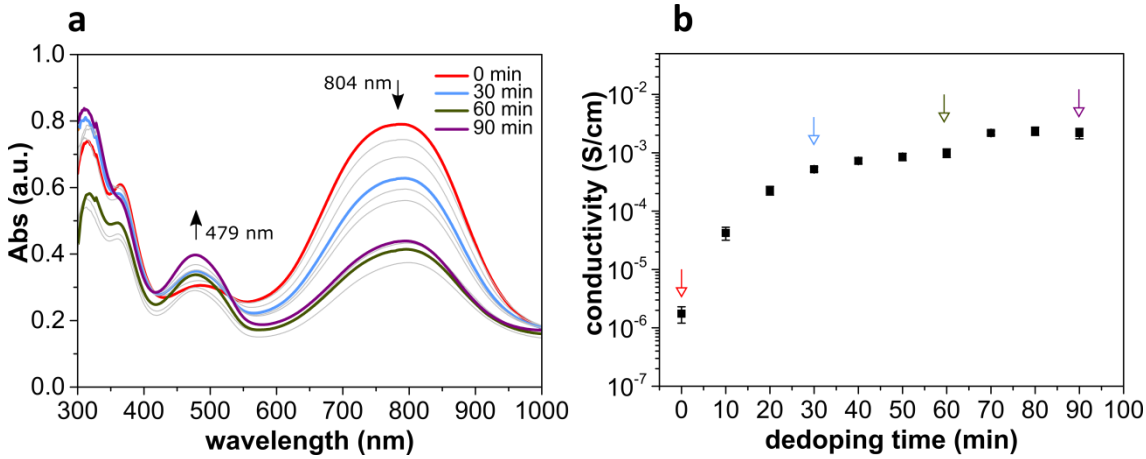

Figure 5.36: Development of a doped PVTPA film (doped with 4 mg/mL $FeCl_3/CH_3CN$ for 1 min) at time 0 min, when exposed to air. De-doping in air is followed by UV-Vis-NIR (a) and additionally conductivity measurements were performed (b). Adapted from Yushi Lu Master Thesis (2018).

All chemical doping experiments presented in the manuscript were performed in a nitrogen filled glovebox to allow for a reliable comparison between conductivities and related absorption spectra. To show the impact of air exposure and the necessity of performing measurements in an inert environment, the development of a sequentially doped PVTPA film (4 mg/mL solution for 60 s) is presented, the gathered data are presented in Figure 5.36. The film was then exposed to air and UV-Vis-NIR absorption spectra and electronic conductivities were measured every 10 min in order to follow their variation in correlation to the exposure time to air.

It is found that upon contact with air the film absorption progressively changes, as the dication band with maximum at 804 nm bleaches with concomitant increase in intensity of the characteristic radical cation band with maximum at 479 nm. After 60 min of air exposure, a coexistence of radical cation and dication species becomes visible and stable. While the starting conductivity is low, after 60 min conductivity values as high as $2 \cdot 10^{-3}$ S/cm are reached which are comparable to the highest conductivities for samples measured in the glovebox when exposed to 2 mg/ml $FeCl_3/CH_3CN$ for 10 s. UV-vis-NIR measurements after dedoping indicate a coexistence of radical cation and dication species which is optimal for high conductivities. The results are particularly interesting and could be exploited, for the employment of conducting transparent layers in air.

5.2.6 Comparison

For a better correlation of the experimental results between doped electrochemically crosslinked samples and simultaneously chemically doped and crosslinked samples, characteristic absorption maxima are reported in Table 5.5.

	EC Doped Films			Chemically Doped Films		
species	$\lambda_{max\ N}$ **(nm)**	$\lambda_{max\ R}^{+\bullet}$ **(nm)**	$\lambda_{max\ D}^{2+}$ **(nm)**	$\lambda_{max\ N}$ **(nm)**	$\lambda_{max\ R}^{+\bullet}$ **(nm)**	$\lambda_{max\ D}^{2+}$ **(nm)**
TPA	-	-	-	322	-	-
TPB	352	476; 1083	741	-	479; >1100	804
PhCbz	-	-	-	328		
BPhCbz	342	429; 1004	751	-	428; 1024	797
Cbz				332		
BCbz	326	402; 999	761	-	422; 1021	777

Table 5.5: Characteristic UV-Vis-NIR absorption maxima upon electrochemical doping (second oxidation cycle) of ec-PVTPA, ec-PVPhCbz and ec-PVCbz and chemical oxidation by $FeCl_3$ of PVTPA, PVPhCbz and PVCbz.

Upon comparison of the electrochemical results with the spectroscopical and conductivity study of chemically doped PVTPA and PVPhCbz films, we find that the doping with $FeCl_3$ dopant leads to highly conducting states only when charge carriers of different oxidation

states are concurrently present. This is the case of PVTPA and PVPhCbz films when doped with 2 and 5 mg/mL respectively, where the highest conductivities of the two polymer films are registered in the case of 10 s exposure time to the oxidant solutions (Figure 5.30 (a), Figure 5.31 (a) and Figure 5.32 (a)).

As previously mentioned, for a direct comparison, we superimposed the absorption of the chemically oxidized samples at their maximum conductivity with the ones registered during the spectroelectrochemical measurements. Both PVTPA and PVPhCbz samples are characterized by the simultaneous presence of radical cation and dication species in their highest conductivity state. By comparing the film absorption maxima of the different states of oxidation obtained by chemical and electrochemical doping, the absorption peak maxima are well comparable between chemically and electrochemically oxidized samples. The maxima after $FeCl_3$ doping reveals only a slight blue shift with respect to electrochemically doped samples (Table 5.5); for example, in the case of PVTPA the maximum of absorbance for the dication level is found at 741 nm upon electrochemical doping (*ec*-PVTPA) whereas at 804 nm in by oxidation with $FeCl_3$. Similar observations were also found for polaron and bipolaron band positions in various conjugated polymers and are generally discussed in terms of polaron / bipolaron-anion distance resulting from different counterions. In our case the differences observed might arise from the slightly larger thermochemical radius r of $FeCl_4^-$ (r = 3.35 Å) compared to PF_6^- (r = 2.4 Å) as counter-anions.[60,95,96]

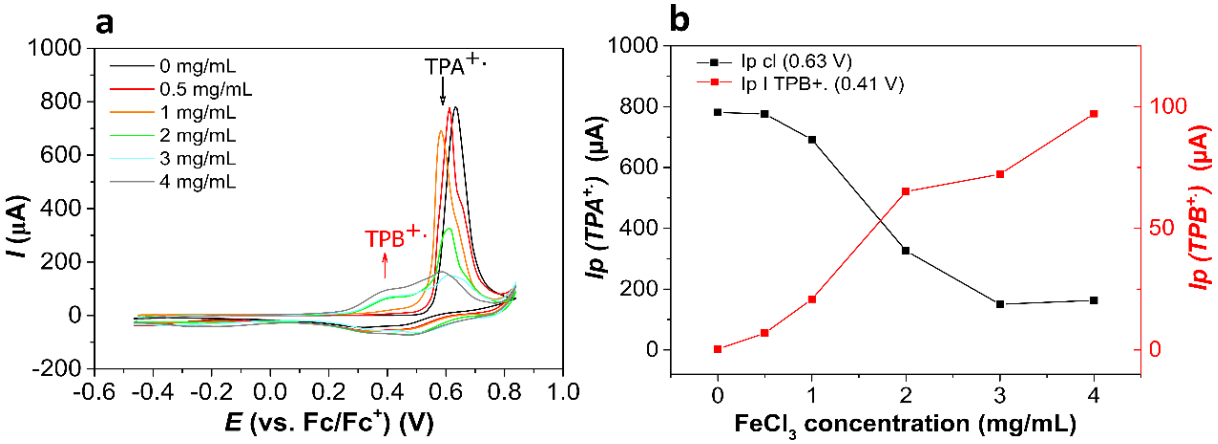

Figure 5.37: "Post-chemical doping" electrochemical characterization of sequentially doped PVTPA films. (a) CV of chemically oxidized samples (after 10s $FeCl_3/CH_3CN$ at different concentrations indicated), in CH_3CN/NBu_4PF_6 (0.1 M) at 20 mV/s. The first cycle is shown to visualize remaining non-crosslinked TPA units still present in the films. (b) Extracted CV peak currents for the first forward CV cycle at the cross-linking peak at 0.63 V (black) and the first oxidation of TPB (red) units at 0.41 V. Picture adapted with permission from ref. [54]. Copyright 2020 RSC.

It must be taken into consideration that in the case of chemical doping a portion of the film with incomplete crosslinking could be present. An additional voltammetric characterization was for this purpose performed on chemically doped and crosslinked PVTPA samples and which hints in this direction (Figure 5.37). With increasing the oxidant concentration, the intensity of the crosslinking peak (+0.64 V) progressively decreases,

whereas the $TPB^{+\bullet}$ peak current increases. Additionally, also in the case of the low conducting 4 mg/mL oxidized sample, the $TPA^{+\bullet}$ peak in the voltammetric experiment can still be observed. The presence of un-dimerized neutral monomers, even when the majority of the film is in its dication state, can be explained by the lower oxidation potential of the dimeric species for oxidation with respect to the monomer, resulting in their favoured oxidation with respect to new dimerization.

Overall higher oxidant concentrations would be necessary to trigger the crosslinking and doping of PVPhCbz and PVCbz film, which seems to be in accordance with the higher oxidation potential of PVPhCbz (0.84 V) with respect to PVTPA (0.63 V). The standard oxidation potential of $FeCl_3$ is ca. +1.47 V *vs.* Fc/Fc^+ [88], allowing for the thermodynamical feasibility of the oxidation of the polymer films. Further, diffusion of the oxidant through the polymer film must be taken into consideration as well. Chemical doping of PVTPA and PVPhCbz and the conductivity profiles can be well compared with the *in-situ* experiments and the conductivity behavior can be explained by mixed valence conductivity. [28,68] As already discussed, the model predicts that for localized electroactive systems conductivity is sustained by the electron hopping between redox units in different states of oxidation. The highest conductivity for a certain redox event is found at its half-wave potential. In this situation the highest probability for electron hopping is found to be when exactly half of the redox states for the redox reactions are occupied.[28,51,75,97] A model of mixed conductivity is given below (Figure 5.38).

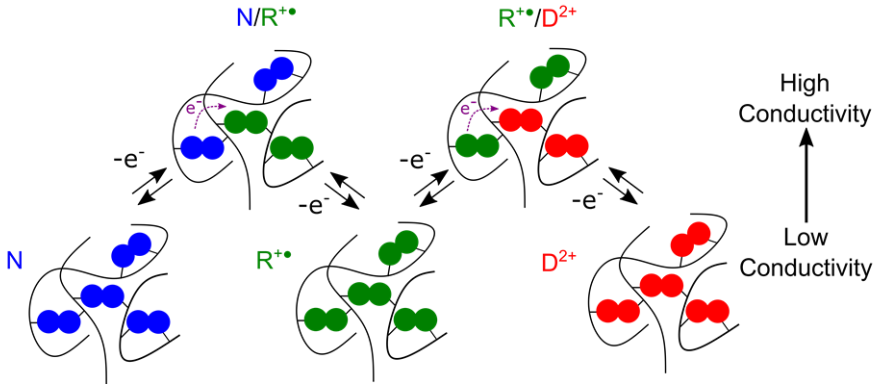

Figure 5.38: Representation of the mixed-valence conductivity mechanism between dimeric species in the neutral (N, blue), radical cation (R+•, green) and dication (D2+, red) states with maximum conductivity obtained in mixed valence states N/ R+•,and R+•/D2+. Picture adapted with permission from ref. [54]. Copyright 2020 RSC.

Remarkably, the conductivity of PVCbz after $FeCl_3$ doping results in maximum conductivities as high as $2{\cdot}10^{-2}$ S/cm which are maintained over different levels of oxidation of the polymer. Also, the conductivities obtained with the described doping procedure for PPhCbz and PVTPA with 10^{-3} S/cm are high for this class of polymers. Compared to literature the conductivity values are higher than the ones reported for chemically doped PVCbz.[13,98–100]. Kanega et al. reached conductivities up to $6{\cdot}10^{-4}$ S/cm al.[98] upon oxidation

with $SbCl_5$, while Block et al.[100] reported 10^{-5} S/cm by doping to BCz radical cations (stoichiometric determination) with tris(4-bromophenyl)ammoniumyl hexachloroantimonate. One possible reason for these lower values could be that the doping in these studies only resulted in the generation of radical cations, as demonstrated by optical absorption and EPR characterization. The experimental data suggest on the other hand, that the highest conductivity values should only be reached when also a portion of the redox active units are oxidized to the dication level. This result emphasizes the importance of performing electrochemical and chemical doping studies in parallel as it helps to target the doping process towards the highest conducting state of the system.

To highlight the relevance of the results herein gathered, conductivity values of other redox polymers from literature widely employed for electrochemical energy storage or optoelectronic applications are reported: polymers bearing the redox-active unit 2,2,6,6-tetramethylpiperidinyloxyl (TEMPO) as pendant can reach maximum conductivies as high as $8.5 \cdot 10^{-3}$ S/cm upon electrochemical doping.[101,102] Tetrathiafulvalene (TTF) based redox polymers did show conductivities up to $2.3 \cdot 10^{-3}$ S/cm upon doping with tetracyanoquinodimethane.[103,104] Further, TPA based films for optical applications showed upon doping maximum conductivities of the order 10^{-3}-10^{-2} S/cm.[9,57,58] Finally, also in the case of chemical doping of the n-type polymer PNDI2OD-T2 values of 10^{-3}-10^{-2} S/cm are found, i.e. in a similar order of magnitude.[105,106]

In general, redox polymers present conductivities which are orders of magnitude lower than those reachable by conjugated systems. However, also the chemical nature might play a role: while PVCbz can give $2.1 \cdot 10^{-2}$ S/cm as reported here, the conjugated carbazole analoga poly(3,6-N-alkylcarbazole) give maximum conductivities of 1 S/cm[43,78,108] which is still orders of magnitude smaller than classical polythiophenes such as P3HT or PEDOT with conductivities ranging from hundreds to thousands of S/cm.

5.2.7 Conclusions

In this chapter a study on electronic conductivity upon chemical and electrochemical oxidation of polyvinyltriphenylamine (PVTPA) and polyvinylcarbazole (PVPhCbz and PVCbz) redox polymer films was presented. The oxidative dimerization of the electroactive units is performed on solution casted films and results in the polymer crosslinking. Upon exposure with $FeCl_3$ solutions highly conducting films are obtained with maximum conductivities ranging from 10^{-3} to 10^{-2} S/cm. The increased chemical stability resulting from crosslinking together with the transparency of the conducting layers makes them interesting candidates for optoelectronic applications as HTLs or transparent electrodes.

It was found that doping of PVTPA and PVPhCbz gives bell-shaped conductivity profiles with a maximum conductivity only observed when radical cations and dications are

both present with the pure neutral and fully oxidized samples only giving very low conductivities. Crosslinked and doped PVCbz films on the other hand do maintain the highest conductivity over a broad doping range of 400 mV (from 0.7 to 1.1 V) and a range of doping concentrations. This is also the region when dication species are concurrently present with radical cations. The bell-shape conductivity profile also implies that for chemical doping the exact doping concentration must be found, while the plateau-conductivity is overall less sensitive to the doping conditions. *In-situ* electrochemistry with conductance and spectroscopy have been performed prior to identify the right doping regimes to be targeted upon chemical doping. Further, it is also found that cross-communication allowing three-dimensional electronic connectivity for hopping is strongly affecting the conductivity profile, as evidenced in the case of doping PVCbz. DFT calculations hint to a pronounced tendency of the bicarbazole units to form π-stacks, and, in the case of BCbz smaller intermolecular π-stacking distances are calculated in comparison to BPhCbz. A more efficient π-stacking between neighboring units may explain the broad region of high conductivity, further, neighboring interactions result in significant variations in the electrochemical and potential dependent conductivity profile of the molecules. Summarizing, designing redox polymers with efficient spatial interactions which allow for good hopping connectivity could lead to broader regions of conductivities, similarly to conjugated polymers, with the advantage of their superior redox activity and processability.

5.2.8 Experimental

5.2.8.1 Structural Characteristics of Polymers

Polymer	$\bar{M}n$ [g/mol]	$\bar{M}w$ [g/mol]	PDI
PVCbz	19 400	64 300	3.3
PVPhCbz	2 260	3 900	1.7
PVTPA	29 000	48 000	1.6

Table 5.6: Overview of number and weight average molecular weights and PDI for PVCbz, PVPhCbz and PVTPA determined by SEC experiments in THF at 30°C. Synthesis of PVTPA was performed by Dr. L. Scapinello. PVPhCbz was synthesized by Philipp Sliskovic, commercial PVCbz (Sigma Aldrich) was employed as purchased.

5.2.8.2 Sample Preparation: Thin-Film Deposition

Different substrates were employed for electrochemical measurements (ITO-coated glass slides, Au slides and Pt 5 µm IDE) and for chemical doping (float-glass slides). Information about substrate and their cleaning procedure is reported in section 3.3. Sample preparation was performed via spin-coating (WS-400-6NPP-LITE, *Laurell Technologies*) the polymers from 10 mg/mL chloroform solution at room temperature. Samples employed for chemical

doping were casted at 1000 rpm s^{-1}, ACE 50 whereas samples for electrochemical characterization were casted at 2000 rpm, ACE 50. After spin-coating the samples were dried under vacuum and were subjected to thermal annealing for 1 h at 150°C. Typical film thicknesses of the chemically doped samples were ~90–100 nm and of the samples employed for electrochemical characterization were ~50 nm determined by Atomic Force Microscopy (Dimension Icon, *Bruker*).

5.2.8.3 Electrochemical Methods

All electrochemical experiments were performed with an Autolab PGSTAT204 potentiostat (*Metrohm*) at room temperature in 0.1 M CH_3CN/NBu_4PF_6 under an Argon atmosphere. A three-electrode air-tight cell endowed with a Pt counter electrode (surface area higher or comparable to the one of the WE), Ag/AgCl and pseudo-reference electrode and Au WE were employed. All potential values are referenced to the Fc/Fc^+ internal. The electrochemically active area was ~0.8 cm^2. More detailed information about the electrochemical set-up is reported in section 3.1.1.1.

5.2.8.3.1 Electrochemical Crosslinking

Electrochemical crosslinking was performed by three subsequent CV cycles in 0.1 M CH_3CN/NBu_4PF_6. at a scan-rate of 20 mV/s, the electrochemical window employed for crosslinking was adapted for each polymer; in the case of PVTPA the film was cycled between 0 - +1.2 V *vs.* Ag/AgCl whereas for PVPhCbz and PVCbz the electrochemical window of crosslinking was 0 - +1.3 V *vs.* Ag/AgCl. Electrochemically crosslinked samples are indicated as ec-PVTPA; ec-PVPhCbz and ec-PVCbz, respectively.

5.2.8.3.2 Differential Pulse Voltammetry (DPV)

Differential-Pulse-Voltammetry experiments were performed at a scan-rate of 20 mV/s and with a modulation amplitude of 25 mV and the same experimental set-up as the one employed for CV measurements.

5.2.8.4 *In-situ* Electrochemical Methods

5.2.8.4.1 *In-situ* Conductance

In-situ conductance experiments were performed using a three-electrode adapted electrochemical cell endowed with 5-µm Pt IDE electrodes (DropSens), an Autolab PGSTAT204 potentiostat (Metrohm), a µSTAT400 (Dropsens) and a conductivity interface CIP2 (*Heka*). Detailed description of the experimental set-up for *in-situ* conductance are reported in section 3.1.1.2.2. All measurements were performed, unless specified, under Argon atmosphere in 0.1 M CH_3CN/NBu_4NPF_6 with a scan-rate of 20 mV/s, and by applying

a drain potential of 20 mV between the combs. All potential values are referenced to the Fc/Fc^+ internal standard.

5.2.8.4.2 In-situ UV-Vis-NIR Spectroelectrochemistry

In-situ UV-Vis-NIR spectroelectrochemistry were performed using an Autolab PGSTAT204 potentiostat (Metrohm) and a Zeiss UV−vis spectrometer endowed with a MCS621 Vis II spectrometer cassette and a CLH600F lamp. The measurements were conducted in a custom-made three-electrodes quartz cell employing a Pt wire as counter electrode (CE), an AgCl coated Ag wire as (pseudo)reference electrode (RE) and polymer-coated 5µm interdigitated (IDE) Pt electrodes (Dropsens) as working electrode (WE). The measurements were performed under Ar atmosphere and all the potential values were referenced to the formal potential of the $Fc|Fc^+$ redox couple. *In-situ* spectroelectrochemical measurements were conducted with a scan rate of 20 mV s^{-1}. Further Information about the experimental set-up and procedure are found in section 3.1.1.2.1.

5.2.8.5 Chemical Doping

Chemical doping and the related characterization (UV-Vis-NIR and conductivity measurements) were performed in a nitrogen filled glovebox to avoid de-doping effects otherwise observed. Chemical doping was performed by exposing the substrates to anhydrous iron(III) chloride ($FeCl_3$) in acetonitrile as dopant solutions. The doping process was controlled by varying the concentration of the dopant and its exposure time. The excess of dopant was removed from the sample by spinning at 3000 rpm for 1 min with a Delta 6RC spin coater (*Suess MicroTec*). Immediately after doping, the sheet resistivites of the polymer films were measured using the four- point-probe technique (Signatone SP4 probe head, linear arrange- ment of tips, spacing = 1 mm, and Keithley 2636B *SourceMeter*). The samples were also analysed by UV-Vis-NIR spectroscopy.

5.2.8.6 Computational Methods

Theoretical calculations and their interpretation were performed by S. Gaméz and Prof. C. R. Delgado from the University of Malaga. The molecular geometries of the neutral and charged species of dimers TPB, BPhCbz and BCbz were optimized in acetonitrile (using the PCM method)[109] at the Density Functional Theory (DFT) level using the GAUSSIAN16 program. Two different hybrid functionals were tested, such as the hybrid generalized gradient approximation (GGA) functional [110,111] and the long-range corrected hybrid functional CAM-B3LYP[112], together with the 6-31G** basis set.[113] Interestingly, the two B3LYP and CAM-B3LYP functionals predict the same behaviour in the description of the structural and electronic properties of TPB, BPhCbz and BCbz dimers. Cofacial π-dimers of BPhCbz and BCbz in *anti* and *syn* configurations were calculated at the neutral, radical

cation and dication states to illustrate the intermolecular interactions between neighbouring redox units. In this regard, the long-range-corrected functional of Head-Gordon and coworkers ωB97XD[114] (which includes empirical dispersion) was used, together with the 6-31G** basis set. All geometrical parameters were allowed to vary independently, and no imaginary frequencies were observed, which ensures the finding of the global minimum energy.

5.2.9 Appendix to 5

5.2.9.1 Synthesis of Polyvinylphenylcarbazole (PVPhCbz)

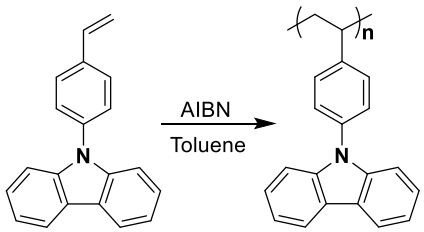

Scheme 5.3: Synthetic route yielding PVPhCbz.Synthesis performed by Philipp Sliskovic.

To a stirred solution of 9-(4-Vinylphenyl)-9H-carbazole (500 mg, 1.86 mmol, 1 eq.) in freshly distilled toluene (freeze-pump-thaw degassed 3 times) AIBN was added (freshly recrystallized from MeOH) (10 mg, 0.02 mmol, 0.01 eq.). The reaction mixture was then heated to 70°C for 12 hours. The polymer was precipitated from cold methanol; 300 mg of raw product are obtained. The polymer is dissolved in THF and filtered using disposable syringe filters with a pore size of 0.45 µm; 150 mg of polymer are finally obtained. SEC *vs.* PS standards (THF, 30◦C): M_n= 2 260 g/mol; M_w = 3 900 g/mol; PDI = 1.7. The synthesis of PVPhCbz was performed by Philipp Sliskovic and was adapted from ref. [115–117].

5.2.9.2 Polyvinylcarbazole (PVCbz)

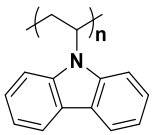

PVCbz was purchased from Sigma Aldrich and used as received. SEC *vs.* PS standards was performed by Philipp Sliskovic in THF at 30 ℃: M_n= 19 400 g/mol; M_w = 64 300 g/mol; PDI = 3.3.

5.2.10 References

[1] M. Skompska, L. M. Peter, *J. Electroanal. Chem.* **1995**, *383*, 43–52.
[2] M. I. Mangione, R. A. Spanevello, D. Minudri, P. Cavallo, L. Otero, F. Fungo, *Electrochim. Acta* **2018**, *263*, 585–595.
[3] M. Zhao, H. Zhang, C. Gu, Y. Ma, *J. Mater. Chem. C* **2020**, *8*, 5310–5320.
[4] P. Taranekar, T. Fulghum, D. Patton, R. Ponnapati, G. Clyde, R. Advincula, *J. Am. Chem. Soc.* **2007**, *129*, 12537–12548.
[5] O. Yurchenko, D. Freytag, L. Zur Borg, R. Zentel, J. Heinze, S. Ludwigs, *J. Phys. Chem. B* **2012**, *116*, 30–39.
[6] P. Reinold, K. Bruchlos, S. Ludwigs, *Polym. Chem.* **2017**, *8*, 7351–7359.
[7] E. J. W. Crossland, P. Cunha, S. Scroggins, S. Moratti, O. Yurchenko, U. Steiner, M. A. Hillmyer, S. Ludwigs, *ACS Nano* **2010**, *4*, 962–966.
[8] N. Tsukamoto, J. Ha, H. Sato, K. Strzelec, *Int. J. Polym. Mater. Polym. Biomater.* **2004**, *53*, 799–807.
[9] N. Mizoshita, S. Inagaki, *Adv. Funct. Mater.* **2018**, *28*, 1803116–1803124.
[10] M. S. Driver, J. F. Hartwig, *J. Am. Chem. Soc.* **1996**, *118*, 7217–7218.
[11] A. Baba, K. Onishi, W. Knoll, R. C. Advincula, **2004**, DOI 10.1021/jp047965f.
[12] P. L. T. Boudreault, S. Beaupré, M. Leclerc, *Polym. Chem.* **2010**, *1*, 127–136.
[13] J. M. Reyna-González, P. Roquero, E. Rivera, *Des. Monomers Polym.* **2009**, *12*, 233–245.
[14] L. Jin, B. Hu, Z. Liu, X. Zhang, M. Mo, C. Li, *J. Electrochem. Soc.* **2018**, *165*, 155–162.
[15] W. T. Neo, Q. Ye, S. J. Chua, J. Xu, *J. Mater. Chem. C* **2016**, *4*, 7364–7376.
[16] H. J. Yen, G. S. Liou, *Polym. Chem.* **2018**, *9*, 3001–3018.
[17] G. Jiang, C. Huang, A. Baba, R. Advincula, *Macromol. React. Eng.* **2012**, *6*, 153–159.
[18] P. Yang, P. Sun, W. Mai, *Mater. Today* **2016**, *19*, 394–402.
[19] J. Agrisuelas, C. Gabrielli, J. J. García-Jareño, H. Perrot, O. Sel, F. Vicente, *Electrochim. Acta* **2015**, *164*, 21–30.
[20] W. Gao, O. Sel, H. Perrot, *Electrochim. Acta* **2017**, *233*, 262–273.
[21] M. Skompska, A. R. Hillman, *J. Electroanal. Chem.* **1997**, *433*, 127–134.
[22] V. Carlier, M. Skompska, C. Buess-Herman, *J. Electroanal. Chem.* **1998**, *456*, 139–152.
[23] K. Bruchlos, Influence of Morphology on Electrochemical Redox Processes in Semiconducting Polymers, Stuttgart University, **2019**.
[24] M. Behl, E. Hattemer, M. Brehmer, R. Zentel, *Macromol. Chem. Phys.* **2002**, *203*, 503–510.
[25] G. Wypych, *Handbook of Polymers*, Elsevier, **2016**.
[26] T. G. Fox, S. Loshaek, *J. Polym. Sci.* **1955**, *15*, 371–390.
[27] F. R. Mayo, F. M. Lewis, *J. Am. Chem. Soc.* **1944**, *66*, 1594–1601.
[28] J. Heinze, B. A. Frontana-Uribe, S. Ludwigs, *Chem. Rev.* **2010**, *110*, 4724–4771.
[29] G. Inzelt, *Monographs in Electrochemistry*, **2008**.
[30] P. J. Peerce, A. J. Bard, *J. Electroanal. Chem.* **1980**, *114*, 89–115.
[31] A. J. Bard, L. R. Faulkner, V. S. Bagotsky, *Electrochemical Methods Fundamentals of Electrochemistry*, **2001**.
[32] G. Zotti, G. Schiavon, *Synth. Met.* **1989**, *31*, 347–357.
[33] E. Sezer, J. Heinze, *Electrochim. Acta* **2006**, *51*, 3668–3673.

[34] D. Ofer, R. M. Crooks, M. S. Wrighton, *J. Am. Chem. Soc.* **1990**, *112*, 7869–7879.
[35] G. Salinas, J. A. Del-Oso, P. J. Espinoza-Montero, J. Heinze, B. A. Frontana-Uribe, *Synth. Met.* **2018**, *245*, 135–143.
[36] O. Yurchenko, J. Heinze, S. Ludwigs, *ChemPhysChem* **2010**, *11*, 1637–1640.
[37] C. Gabrielli, J. J. García-Jareño, M. Keddam, H. Perrot, F. Vicente, *J. Phys. Chem. B* **2002**, *106*, 3182–3191.
[38] H. Goubaa, F. Escobar-Teran, I. Ressam, W. Gao, A. El Kadib, I. T. Lucas, M. Raihane, M. Lahcini, H. Perrot, O. Sel, *J. Phys. Chem. C* **2017**, *121*, 9370–9380.
[39] M. D. Levi, C. Lopez, E. Vieil, M. A. Vorotyntsev, *Electrochim. Acta* **1997**, *42*, 757–769.
[40] C. Visy, J. Kankare, *J. Electroanal. Chem.* **1998**, *442*, 175–188.
[41] E. Sezer, M. Skompska, J. Heinze, *Electrochim. Acta* **2008**, *53*, 4958–4968.
[42] S. Bruckenstein, A. R. Hillman, *J. Phys. Chem.* **1991**, *95*, 10748–10752.
[43] C. Gabrielli, J. J. Garcia-Jareo, H. Perrot, *Electrochim. Acta* **2001**, *46*, 4095–4103.
[44] M. Ue, A. Murakami, S. Nakamura, *J. Electrochem. Soc.* **2002**, *149*, A1385.
[45] Y. H. Zhao, M. H. Abraham, A. M. Zissimos, *J. Org. Chem.* **2003**, *68*, 7368–7373.
[46] W. Plieth, A. Bund, U. Rammelt, S. Neudeck, L. M. Duc, in *Electrochim. Acta*, Pergamon, **2006**, pp. 2366–2372.
[47] C. Gabrielli, J. J. García-Jareño, M. Keddam, H. Perrot, F. Vicente, *J. Phys. Chem. B* **2002**, *106*, 3182–3191.
[48] C. Gabrielli, M. Keddam, H. Perrot, M. C. Pham, R. Torresi, *Electrochim. Acta* **1999**, *44*, 4217–4225.
[49] C. M. G. Bach, J. R. Reynolds, *J. Phys. Chem.* **1994**, *98*, 13636–13642.
[50] A. R. Hillman, S. J. Daisley, S. Bruckenstein, *Electrochem. commun.* **2007**, *9*, 1316–1322.
[51] T. M. Swager, *Macromolecules* **2017**, *50*, 4867–4886.
[52] D. Neusser, C. Malacrida, M. Kern, Y. M. Gross, J. van Slageren, S. Ludwigs, *Chem. Mater.* **2020**, *32*, 6003–6013.
[53] M. Goll, A. Ruff, E. Muks, F. Goerigk, B. Omiecienski, I. Ruff, R. C. González-Cano, J. T. Lopez Navarrete, M. Carmen Ruiz Delgado, S. Ludwigs, *Beilstein J. Org. Chem.* **2015**, *11*, 335–347.
[54] C. Malacrida, Y. Lu, K. Dirnberger, S. Gámez-Valenzuela, M. C. Ruiz Delgado, S. Ludwigs, *J. Mater. Chem. C* **2020**, *8*, 15393–15405.
[55] T. M. Swager, *Macromolecules* **2017**, *50*, 4867–4886.
[56] H. Xu, H. Xu, F. Yuan, D. Zhou, X. Liao, L. Chen, Y. Chen, Y. Chen, *J. Mater. Chem. A* **2020**, *8*, 11478–11492.
[57] Y.-S. Liu, S. Guo, J. Feng, Y.-F. Liu, Y.-G. Bi, D. Yin, X.-L. Zhang, H.-B. Sun, *Opt. Lett.* **2019**, *44*, 4817–4820.
[58] J. Liu, W. Liu, E. Aydin, G. T. Harrison, F. H. Isikgor, X. Yang, A. S. Subbiah, S. De Wolf, *ACS Appl. Mater. Interfaces* **2020**, *12*, 23874–23884.
[59] X. Gu, Y. Li, Y. Mu, M. Zhang, T. Lu, P. Wang, *RSC Adv.* **2018**, *8*, 9409–9413.
[60] A. I. Hofmann, R. Kroon, S. Zokaei, E. Järsvall, C. Malacrida, S. Ludwigs, T. Biskup, C. Müller, *Adv. Electron. Mater.* **2020**, 2000249.
[61] G. M. Tang, R. H. Chi, W. Z. Wan, Y. T. Wang, Y. Z. Cui, S. W. Ng, *J. Chem. Res.* **2017**, *41*, 79–81.
[62] P. Blanchard, C. Malacrida, C. Cabanetos, J. Roncali, S. Ludwigs, *Polym. Int.* **2019**, *68*, 589–606.
[63] K. Bruchlos, D. Trefz, A. Hamidi-Sakr, M. Brinkmann, J. Heinze, A. Ruff, S.

Ludwigs, *Electrochim. Acta* **2018**, *269*, 299–311.
[64] R. F. Nelson, R. H. Philp, *J. Phys. Chem.* **1979**, *83*, 713–716.
[65] R. Reynolds, L. L. Line, R. F. Nelson, *J. Am. Chem. Soc.* **1974**, *96*, 1087–1092.
[66] R. F. Nelson, R. N. Adams, *J. Am. Chem. Soc.* **1968**, *90*, 3925–3930.
[67] P. Rapta, J. Lukkari, J. Tarábek, M. Salomäki, M. Jussila, G. Yohannes, M. L. Riekkola, J. Kankare, L. Dunsch, *Phys. Chem. Chem. Phys.* **2004**, *6*, 434–441.
[68] C. E. D. Chidsey, R. W. Murray, *J. Phys. Chem.* **1986**, *90*, 1479–1484.
[69] R. Takita, C. Song, T. M. Swager, *Org. Lett.* **2008**, *10*, 5003–5005.
[70] R. G. Compton, M. E. Laing, A. Ledwith, I. I. Abu-Abdoun, *J. Appl. Electrochem.* **1988**, *18*, 431–440.
[71] N. Kurapati, P. Pathirathna, R. Chen, S. Amemiya, *Anal. Chem.* **2018**, *90*, 13632–13639.
[72] C. L. Ramírez, M. I. Mangione, S. G. Bertolotti, E. M. Arbeloa, A. R. Parise, *J. Photochem. Photobiol. A Chem.* **2018**, *365*, 199–207.
[73] M. Lapkowski, J. Zak, K. Karon, B. Marciniec, W. Prukala, *Electrochim. Acta* **2011**, *56*, 4105–4111.
[74] T. Benincori, S. Gámez-Valenzuela, M. Goll, K. Bruchlos, C. Malacrida, S. Arnaboldi, P. R. Mussini, M. Panigati, J. T. López Navarrete, M. C. Ruiz Delgado, et al., *Electrochim. Acta* **2018**, *284*, 513–525.
[75] H. John, R. Bauer, P. Espindola, P. Sonar, J. Heinze, K. Müllen, *Angew. Chemie - Int. Ed.* **2005**, *44*, 2447–2451.
[76] K. Karon, M. Lapkowski, *J. Solid State Electrochem.* **2015**, *19*, 2601–2610.
[77] S. Mallick, S. Maddala, K. Kollimalayan, P. Venkatakrishnan, *J. Org. Chem.* **2019**, *84*, 73–93.
[78] M. Wieland, C. Malacrida, Q. Yu, C. Schlewitz, L. Scapinello, *Flex. Print. Electron.* **2020**, *5*, 014016.
[79] G. Salinas, B. A. Frontana-Uribe, *ChemElectroChem* **2019**, 1–14.
[80] R. Shomura, K. Sugiyasu, T. Yasuda, A. Sato, M. Takeuchi, *Macromolecules* **2012**, *45*, 3759–3771.
[81] D. Lee, T. M. Swager, *J. Am. Chem. Soc.* **2003**, *125*, 6870–6871.
[82] Y. Harima, X. Jiang, Y. Kunugi, K. Yamashita, A. Naka, K. K. Lee, M. Ishikawa, *J. Mater. Chem.* **2003**, *13*, 1298–1305.
[83] K. M. Knoblock, C. J. Silvestri, D. M. Collard, *J. Am. Chem. Soc.* **2006**, *128*, 13680–13681.
[84] T. Sakai, T. Satou, T. Kaikawa, K. Takimiya, T. Otsubo, Y. Aso, *J. Am. Chem. Soc.* **2005**, *127*, 8082–8089.
[85] N. Rolland, J. F. Franco-Gonzalez, R. Volpi, M. Linares, I. V. Zozoulenko, *Phys. Rev. Mater.* **2018**, *2*, 1–9.
[86] S. Wang, S. Fabiano, S. Himmelberger, S. Puzinas, X. Crispin, A. Salleo, M. Berggren, *Proc. Natl. Acad. Sci. U. S. A.* **2015**, *112*, 10599–10604.
[87] B. G. Zotti, G. Schiavon, A. Berlin, *Adv. Mater.* **1993**, *5*, 551–554.
[88] B. Kratochvil, R. Long, *Anal. Chem.* **1970**, *42*, 43–46.
[89] M. Li, *Chem. - A Eur. J.* **2019**, *25*, 1142–1151.
[90] C. Su, Y. Ye, L. Xu, C. Zhang, *J. Mater. Chem.* **2012**, *22*, 22658–22662.
[91] A. Maity, M. Biswas, *J. Appl. Polym. Sci.* **2006**, *100*, 819–824.
[92] T. V. Richter, C. H. Braun, S. Link, M. Scheuble, E. J. W. Crossland, F. Stelzl, U. Würfel, S. Ludwigs, *Macromolecules* **2012**, *45*, 5782–5788.
[93] P. Reiser, L. Müller, V. Sivanesan, R. Lovrincic, S. Barlow, S. R. Marder, A. Pucci,

W. Jaegermann, E. Mankel, S. Beck, *J. Phys. Chem. C* **2018**, *122*, 14518–14527.
[94] C. Chevrot, E. Ngbilo, K. Kham, S. Sadki, *Synth. Met.* **1996**, *81*, 201–204.
[95] V. Vijayakumar, Y. Zhong, V. Untilova, M. Bahri, L. Herrmann, L. Biniek, N. Leclerc, M. Brinkmann, *Adv. Energy Mater.* **2019**, *9*, 1–12.
[96] Z. Liang, Y. Zhang, M. Souri, X. Luo, A. M. Boehm, R. Li, Y. Zhang, T. Wang, D. Y. Kim, J. Mei, et al., *J. Mater. Chem. A* **2018**, *6*, 16495–16505.
[97] E. F. Dalton, N. A. Surridge, J. C. Jernigan, K. O. Wilbourn, J. S. Facci, R. W. Murray, *Chem. Phys.* **1990**, *141*, 143–157.
[98] H. Kanega, Y. Shirota, H. Mikawa, *J. Chem. Soc. Chem. Commun.* **1984**, 158–159.
[99] J. V. Grazulevicius, P. Strohriegl, J. Pielichowski, K. Pielichowski, *Prog. Polym. Sci.* **2003**, *28*, 1297–1353.
[100] H. Block, M. A. Cowd, S. M. Walker, *Polymer (Guildf).* **1977**, *18*, 781–785.
[101] C. Karlsson, T. Suga, H. Nishide, *ACS Appl. Mater. Interfaces* **2017**, *9*, 10692–10698.
[102] L. Rostro, S. H. Wong, B. W. Boudouris, *Macromolecules* **2014**, *47*, 3713–3719.
[103] Y. Ren, J. S. Moore, *Polym. Chem.* **2015**, *6*, 8325–8330.
[104] T. Shimizu, T. Yamamoto, *Chem. Commun.* **1999**, 515–516.
[105] D. Trefz, A. Ruff, R. Tkachov, M. Wieland, M. Goll, A. Kiriy, S. Ludwigs, *J. Phys. Chem. C* **2015**, *119*, 22760–22771.
[106] Y. M. Gross, D. Trefz, C. DIngler, D. Bauer, V. Vijayakumar, V. Untilova, L. Biniek, M. Brinkmann, S. Ludwigs, *Chem. Mater.* **2019**, *31*, 3542–3555.
[107] S. T. Wellinghoff, Z. Deng, J. F. Reed, S. A. Jenekhe, *Mol. Cryst. Liq. Cryst.* **1985**, *118*, 403–412.
[108] S. Wakim, B. R. Aïch, Y. Tao, M. Leclerc, *Polym. Rev.* **2008**, *48*, 432–462.
[109] J. Tomasi, M. Persico, *Chem. Rev.* **1994**, *94*, 2027–2094.
[110] C. Lee, W. Yang, R. G. Parr, *Phys. Rev. B* **1988**, *37*, 785–789.
[111] A. D. Becke, *J. Chem. Phys.* **1993**, *98*, 1372–1377.
[112] T. Yanai, D. P. Tew, N. C. Handy, *Chem. Phys. Lett.* **2004**, *393*, 51–57.
[113] W. J. Hehre, K. Ditchfield, J. A. Pople, *J. Chem. Phys.* **1972**, *56*, 2257–2261.
[114] J. Da Chai, M. Head-Gordon, *Phys. Chem. Chem. Phys.* **2008**, *10*, 6615–6620.
[115] N. B. McKeown, S. Badriya, M. Helliwell, M. Shkunov, *J. Mater. Chem.* **2007**, *17*, 2088–2094.
[116] F. Monnier, M. Taillefer, *Angew. Chemie* **2009**, *121*, 7088–7105.
[117] H. P. Shi, L. Xu, Y. Cheng, J. Y. He, J. X. Dai, L. W. Xing, B. Q. Chen, L. Fang, *Spectrochim. Acta - Part A Mol. Biomol. Spectrosc.* **2011**, *81*, 730–738.

6 Conclusions and Prospectives

Electrodeposition is an efficient and straight-forward method for the obtainment of functional electroactive surfaces due to the simplicity of the experimental set-ups, the reduction of material waste, the possibility to work at low temperatures, as well as due to the superior stability and insolubility of the deposited films.[1–4] Conjugated monomers of small dimensions, such as thiophene, pyrrole, aniline etc. have been traditionally employed due to their accessibility and marked reactivity; the employment of such simple and small molecules is associated with high oxidation potentials that can lead to uneven film growth and film overoxidation, limiting film performance and electroactivity. In addition, films obtained by electrodeposition of conventional monomers are associated with the formation of highly polydisperse polymer chains associated with a wide range of oxidation potentials.[1,2]

In this thesis the electrochemical reactivity of different classes of redox molecules of optoelectronics interest was analyzed and exploited to crosslink by oxidative dimerization precursor systems endowed with multiple dimerization sites. The so-generated electroactive films show well-defined and controlled π-conjugation and result in a well-defined redox behavior, which can be directly related to the one of the dimer of the starting redox unit. This dissertation was subdivided in two main sections, the first of which deals with the electrochemical deposition from solution of different multimeric systems of optoelectronic interest upon oxidation, whereas in the second section of the thesis, electrochemically triggered dimerization was exploited to crosslink previously casted thin-films of redox-active polymers.

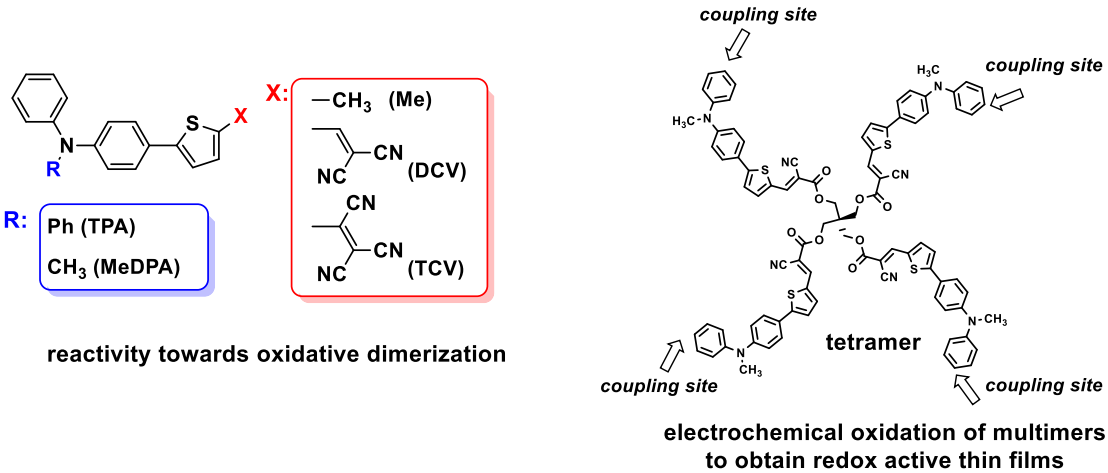

Figure 6.1: Structure of TPA and MeDPA based chromophores and multimer whose oxidative behavior was analyzed.

In the first section of this dissertation, we reported the reactivity towards dimerization of a set of D-π-A push-pull molecules based on similar molecular architectures, consisting of a small push-pull system with an arylamine donor block, triphenylamine (TPA) and

methyldiphenylamine (MeDPA), respectively, connected to an acceptor group through a thienyl linker. The aim of the study was to provide additional understanding of the dimerization ability of arylamine-based systems, in particular, of linear D-π-A push-pull systems. Indeed, whereas the redox behavior upon oxidation of simple arylamines is generally known and well-characterized, the functionalization of their structure with π-conjugated blocks, such as in the case of D-π-A push-pull molecules, can result in significant changes in the molecular reactivity. In the literature it has been generally observed that an elongation of the π-system and the substitution of reactive para terminals could leads to a stabilization of the radical cation state in comparison to unsubstituted triarylamines. Although, no studies in the context of D-π-A push-pull systems are reported.[1,5–7]

The analysis of the molecular reactivity towards dimerization and the dependency of the molecular structure, is therefore interesting considering the ubiquitous employment of this class of D-π-A push-pull systems in organic photovoltaics.[8] The results should provide additional knowledge and rationalization of the electrochemical behavior of these systems for the synthesis of new stable compounds. Secondly, it is aimed to identify suitable dimerizing units on the basis of emerging approaches employing crosslinking of two arylamine or carbazole units in multimer-systems to prepare functional films for electro-optic applications.[4,9]

The list of molecules investigated in this thesis are reported in Figure 6.2. The following structure-property relationships were analyzed with regards to radical-cation reactivity:

- the substitution of triphenylamine (TPA) (molecules **1**-**3**) with a methyl diphenylamine (MeDPA) (molecules **4**-**6**) donor unit;
- the nature and electron withdrawing character of the acceptor unit.

In all cases a thienyl unit is used as π-linker. Compounds **1** (TPA-TMe) and **4** (MeDPA-TMe) are synthesized to analyze the effect of introduction of an acceptor unit in comparison to compounds **2, 3, 5** and **6**. The strength of the acceptor unit is increased in the order dicyanovinyl (DCV) (chromophores **2** and **5**) and tricyanovinyl (TCV) (chromophores 3 and **6**) respectively. The structure-properties relationships in relation to chromophores' electrochemical behaviour was studied by electrochemical methods, *in-situ* UV-Vis spectroelectrochemical experiments and TD-DFT calculations. The latter were carried out by S. Gámez and Prof. C. Ruiz Delgado from the university of Malaga. Synthesis of the chromophores was performed in the group of P. Blanchard from the university of Angers and by D. Gepperth, my colleague from the chair of structure and properties of polymeric materials at the university of Stuttgart.

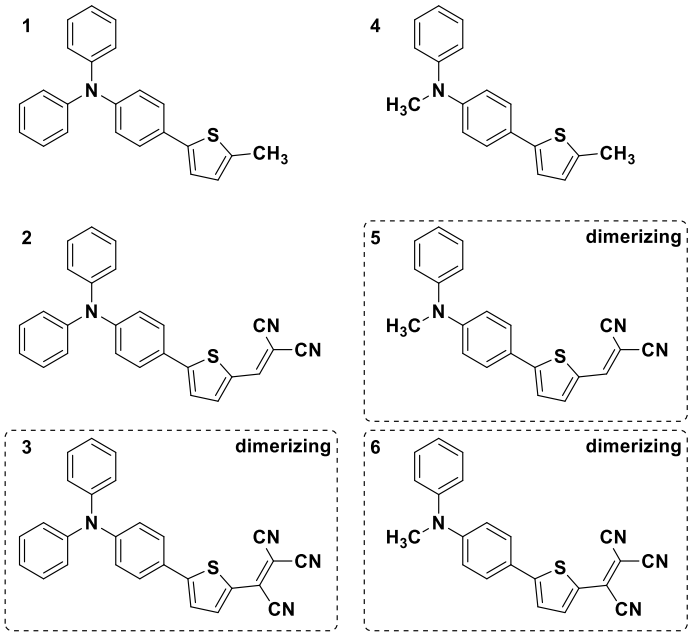

*Figure 6.2: Structure of chromophores **1**-**6** highlighting compounds **3**, **5** and **6** which were observed to undergo dimerization when electrochemically oxidized in 0.1 M CH_2Cl_2 / NBu_4PF_6.*

Figure 6.2 reports the structure of the analyzed chromophores and highlights the ones undergoing irreversible dimerization upon electrochemical oxidation; the respective DPV experiments upon oxidation for the different chromophores are shown in Figure 6.3. In general, experimental results indicate that the replacement of a Ph with a Me unit in the arylamine-based push-pull molecules significatively effects the reactivity of the compounds, we found that Me substituted chromophores tend to be more reactive towards oxidative dimerization than the Ph substituted ones. Further, it is generally observed that the introduction of an acceptor unit results in a shift towards more positive oxidation potentials; with highest oxidation potentials found for TCV containing chromophores, followed by DCV substituted chromophores and a concurrent increase of the compounds reactivity. As summary we report Figure 6.3, in which it can be observed how the oxidation signals of the dimers of the dimerizing compounds upon backward oxidation sweep are associated with more pronounced change in current, for Me-substituted chromophores (right side), in particular for TCV substituted compound **6**.

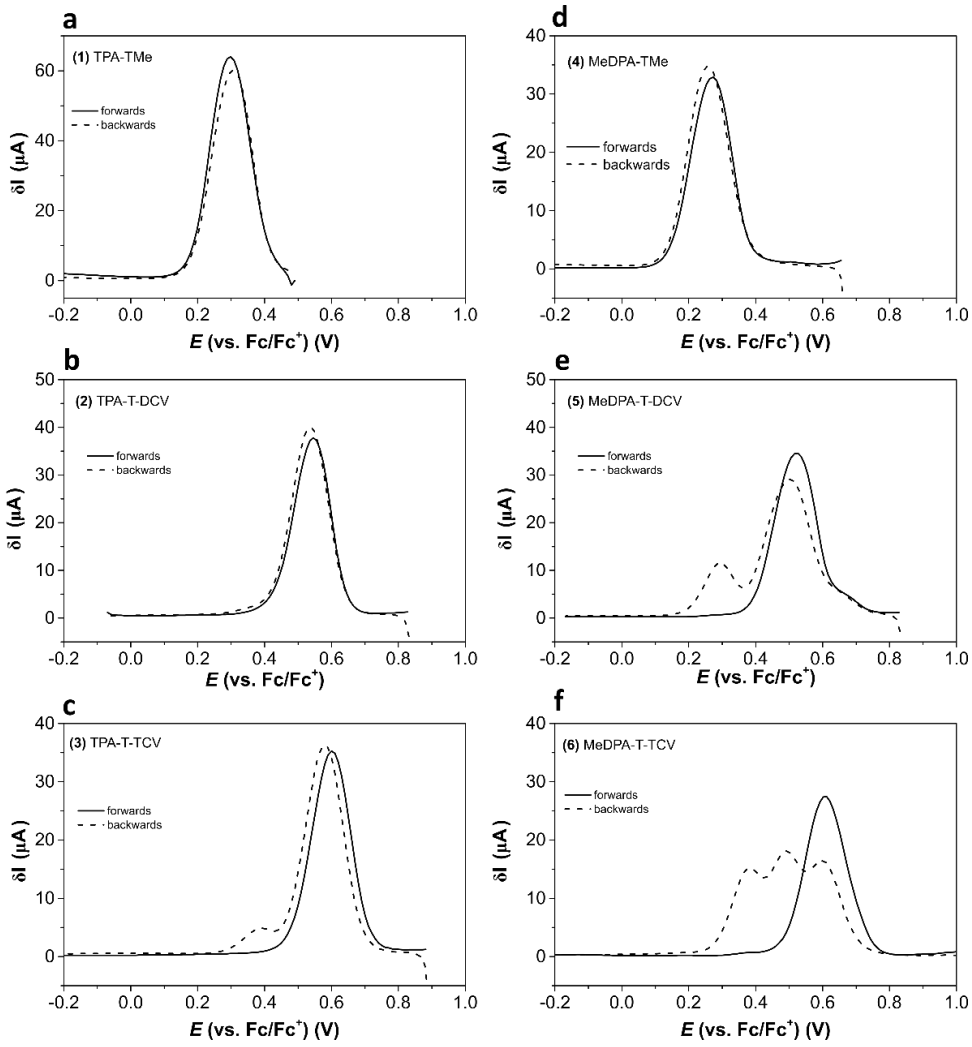

*Figure 6.3: Differential pulse voltammetry of compounds **1**-**6** in 0.1 M CH_2Cl_2/NBu_4PF_6; scan-rate 20 $m{\cdot}Vs^{-1}$; Au electrode. Modulation amplitude employed is 25 mV.*

Dimerization of compounds **3**, **5** and **6** is confirmed by DPV and *in-situ* UV-Vis-NIR spectroelectrochemical experiments. TD-DFT vertical transition of the chromophores and their dimers in different states of charge confirm the band assignment and charged species generation upon comparison with spectroelectrochemical results.

Theoretical calculations were performed to rationalize the observed reactivity in the chromophore series. It was found that spin-density alone (Mülliken) is not enough to predict dimerization behavior in the series, but rather steric hindrance and geometrical factors must also be taken in consideration, in contrast to general discussions of reactivity which can be found in the literature for dimerization of substituted arylamines and electropolymerization of conjugated monomers.[1,6,10] Further, for the first time correlations between the closed-shell nature of the dimeric-dication state was correlated with the dimerization ability of arylamine compounds. As similar findings are encountered also for other benzidine dications in the literature, we suggest a future extension of the study and correlation also to other conjugated compounds employed for electrodeposition. Finally, the dimerization

ability of arylamine-based chromophores is exploited to electrodeposit electroactive films of **Tetra-5**, generating stable films with reversible redox and electrochromic behavior, the latter will be developed and tested in BHJ solar cells.

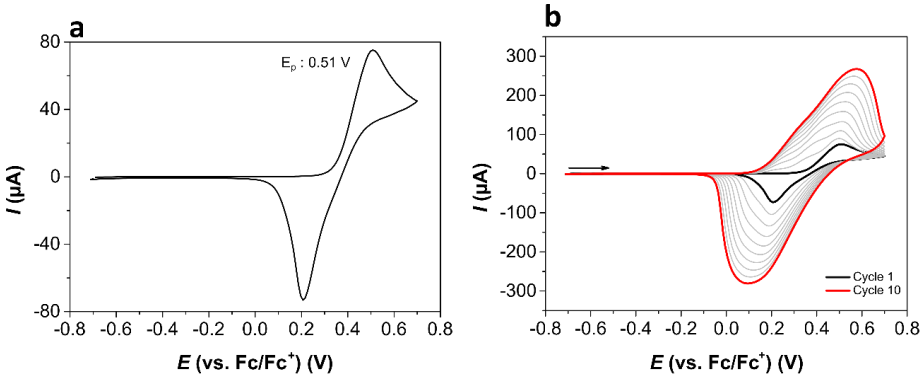

Figure 6.4: (a) I cycle of electrodeposition of Tetra-5 and (b) complete electrodeposition pattern in CH_2Cl_2/NBu_4PF_6 0.1 M, ITO electrode; scan-rate 50 mV/s. Adapted with permission from ref. [11] (Wiley 2019).

Experimental results and calculations above discussed can be found in the publication *ChemElectroChem* **2019**, 1–15.

As a second example of oxidation of multimers to deposit electroactive functional surfaces, the electrochemical characterization of a set of chiral molecules endowed with a 2,2'-biindole architecture with oligothiophene terminals modified through different π-spacers was conducted in a collaboration with the group of T. Benincori from the university of Como.

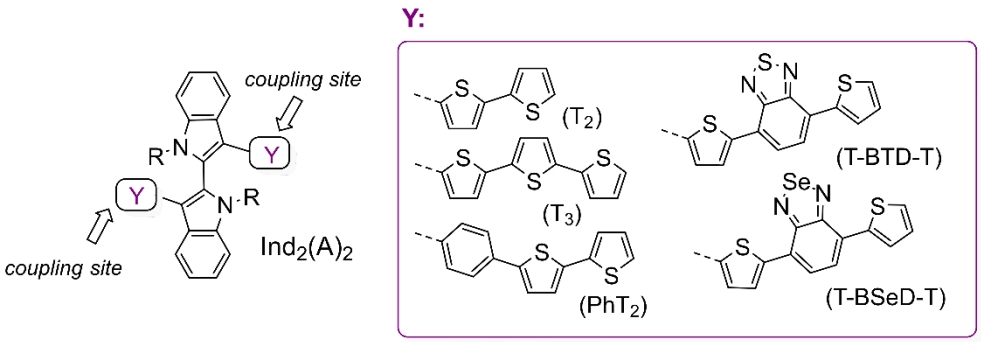

electrochemical oxidation of multimers to obtain redox active thin films

Figure 6.5: Structure of atropoisomeric oligomers endowed with two coupling sites, with referment to chapter 4.2.

The molecular structure of the investigated compounds is reported in Figure 6.5; the redox behavior of these molecules, endowed with symmetric oligothienyl terminals which are linked through an internal indole core, is the one characteristic of interacting equivalent redox moieties. For all molecules the oxidative cyclic voltammetry (CV) patterns are characterized by multiple peaks, in Figure 6.6 the experimental results on compounds **1-3**

are reported, analogous behavior is encountered for compounds **4** and **5**. Considering the structural differences between the molecules, a first couple of peaks (A, B) is observed for the first oxidation. Supported by previous calculations,[22] and because no oligomerization is possible by oxidation around this first set of peaks (Figure 6.6 (a), (c) and (e)), the oxidations associated with these two signals (A, B) are assigned to the activation at the level of the more electron-rich indole moieties with only partial delocalization on the oligo-thiophene system. That suggests that the two peaks belong to the two interacting radical cations which are localized on both indole centers, *i.e.,* two indole-oligothiophene partially interacting redox sites. As example, a scheme for the oxidation steps of compound Ind_2T_6 is reported in Figure 6.7.

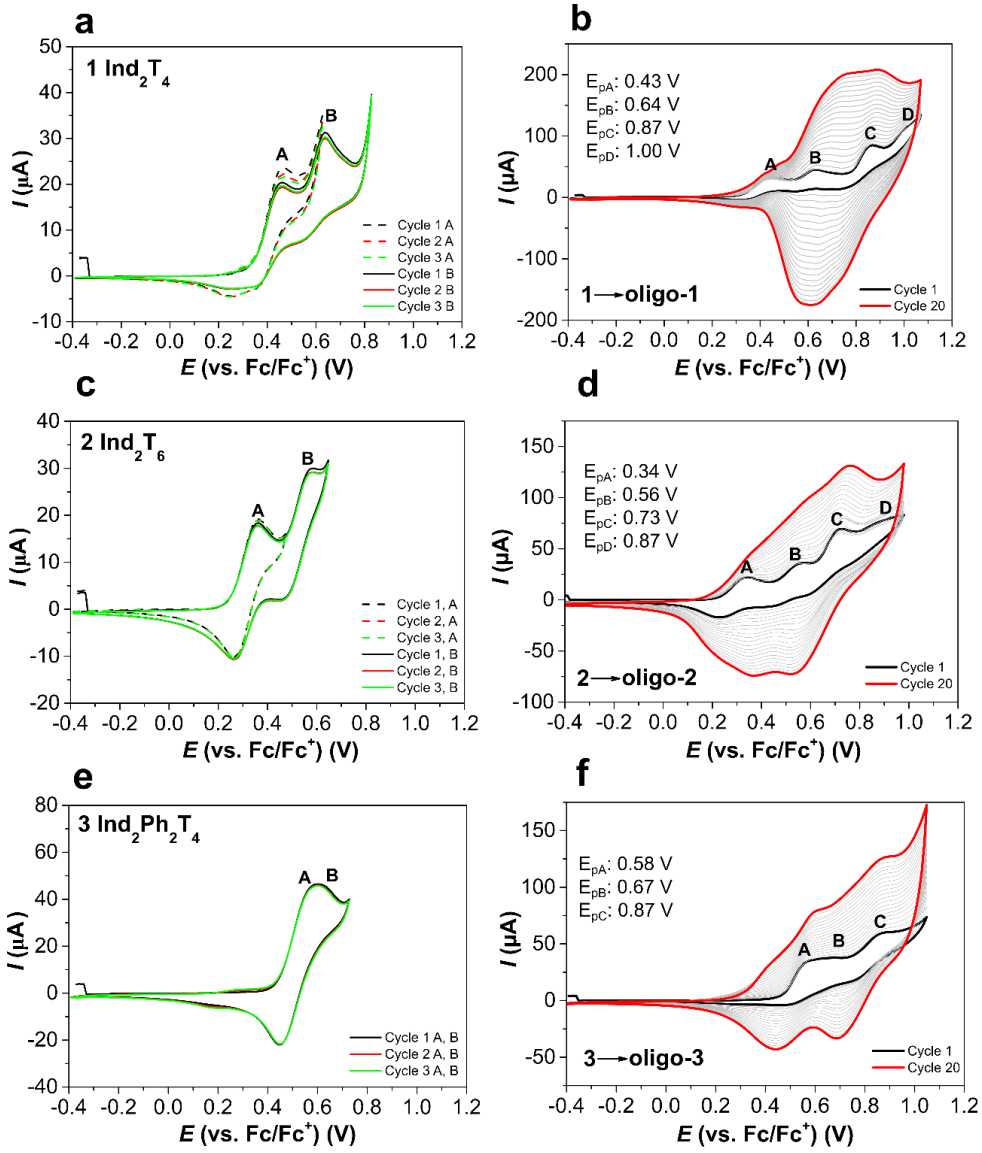

*Figure 6.6: Cyclic voltammetry of molecules **1** (a), **2** (c) and **3** (e) in CH_2Cl_2/NBu_4PF_6 0.1 M at a scan-rate of 20 mV/s; multiple cycles around the first (A) and second (B) peaks of oxidation are shown. Electrodeposition of **1** (b), **2** (d) and **3** (f) by multiple cycling around the III (C) and IV (D) oxidation peaks at a scan-rate of 20 mV/s and a monomer concentration of 0.5 mM; ITO electrode.*

In all systems a second couple of peaks (C, D) is registered by polarizing the working electrode (WE) at more positive potentials, the latters can be attributed to the activation of the thienyl terminals. Indeed, oxidation at the levels of these two peaks in CH_2Cl_2 is followed by the electrodeposition of electroactive films upon multiple cycling (Figure 6.6 (b), (d) and (f)). The coupling of the so generated radical cations at the free α-thienyl positions generates oligomers of higher order which nucleate on the electrode surface, and the so obtained films show well-defined π-conjugation.

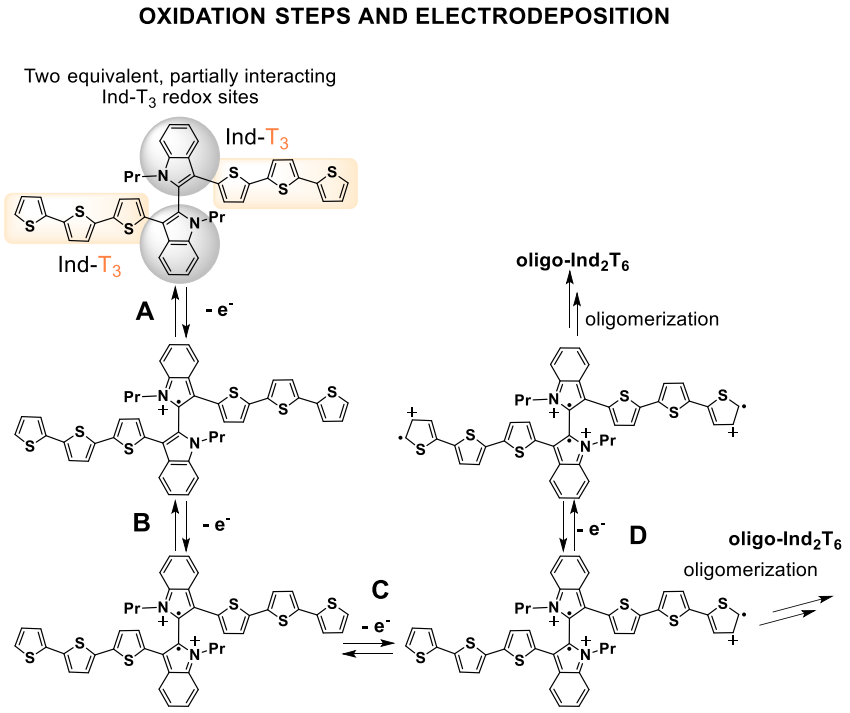

Figure 6.7: Exemplification of the oxidation scheme for compound ***2*** *(**Ind₂T₆**) leading to electrodeposition of* ***oligo-2****.*

Structure-property relationships as function of the different π-spacers were analysed, modifications of the interaction of the two partially interacting redox moieties was observed for the different compounds, resulting in different peak-to-peak separations. All molecules could be successfully electrodeposited generating stable electroactive films which could be repeatedly charged and discharged between their neutral and oxidised states in a highly reversible way. In general, the position and topology of the bands at different states of charge are dominated by the oligothienyl moieties. The analysis of *in-situ* conductance and of UV-Vis-NIR spectroelectrochemistry also hints to the fact that the biindole scaffold plays only a marginal role in determining charge transport and absorption properties within the system (Figure 6.8).

After analysing the charging behaviour and assigning the charge speciation as function of the potential by combined electrochemical methods for electrdeposited racemic films of compounds **1**-**5**, the enantiodiscrimination ability of an enantiopure oligomeric films

of Ind_2T_6 was demonstrated with *(S)-(−)-* or *(R)-(+)*-N,N′-dimethyl-1-ferrocenylethylamine chiral probes. A peak potential separation of ~40 mV between the two antipodes was reproducibly measured, specularly for the two enantiomeric films. As outlook, the chiral discriminating ability of these systems and their reversible electrochromic behaviour could be exploited for developing chiral electrochromic devices.

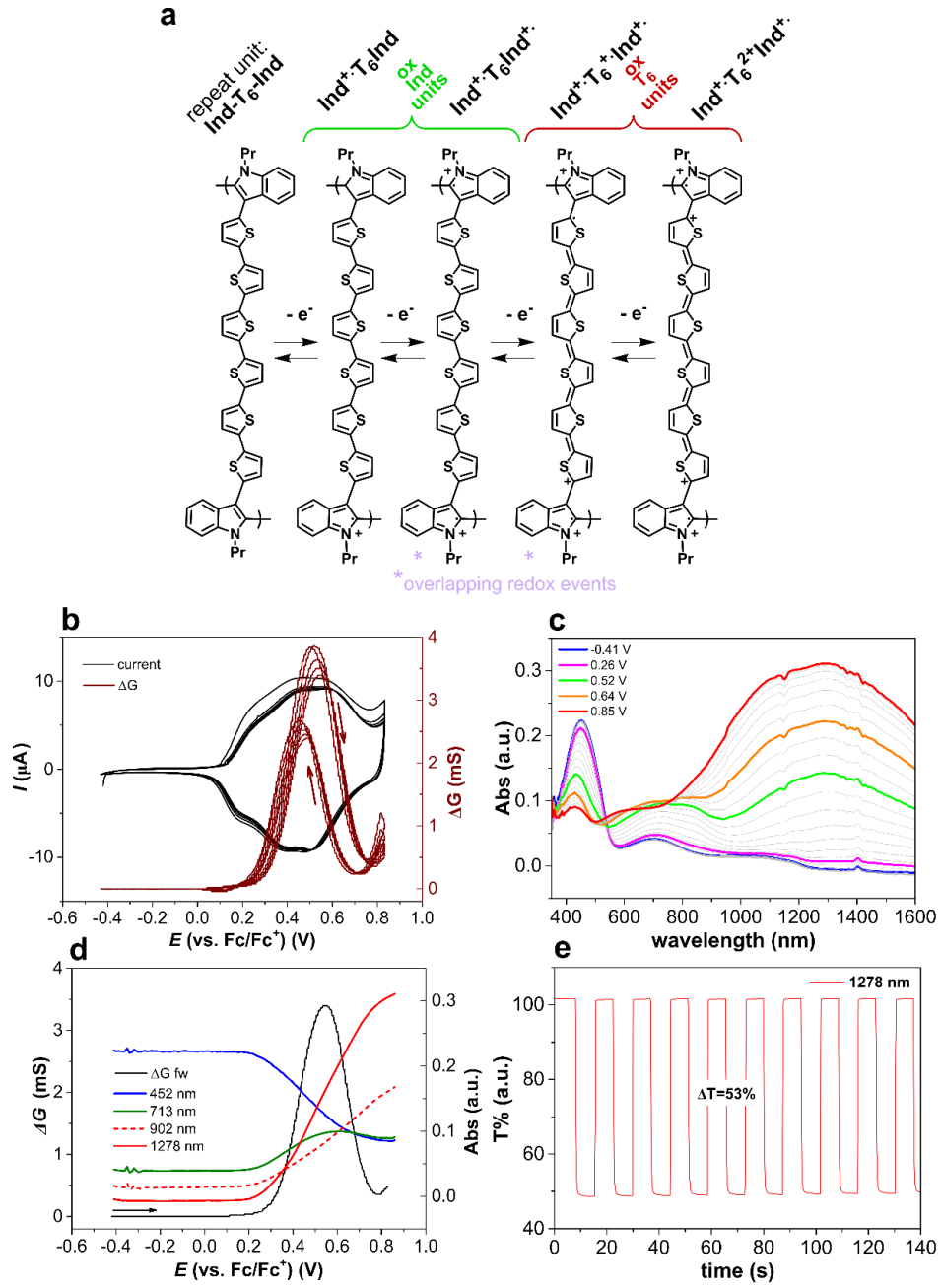

Figure 6.8: (a) General representation of the different states of charge of ***oligo-2****. In the case of oligomerization products every repeat unit will be oxidized simultaneously. The first oxidation is localized on the more electron-rich biindolic core, in two oxidation steps. Further oxidation involves radical cation and dication formation localized on oligothienyl terminals. Picture adapted from ref [1]. Copyright Wiley 2021. (b) In-situ conductance multiple oxidation cycles. (c) UV-Vis-NIR spectroelectrochemical measurements registered during the forward oxidation cycle of* ***olgo-2*** *(ITO electrode) (d) In-situ conductance (5th cycle) over-imposed to peak-trend registered for the forward*

oxidation; measurements registered with a scan-rate of 20 mV/s in 0.1 M CH_2Cl_2/NBu_4PF_6, (Pt 5-µm IDE). Picture adapted from ref [12]. Copyright Wiley 2021.

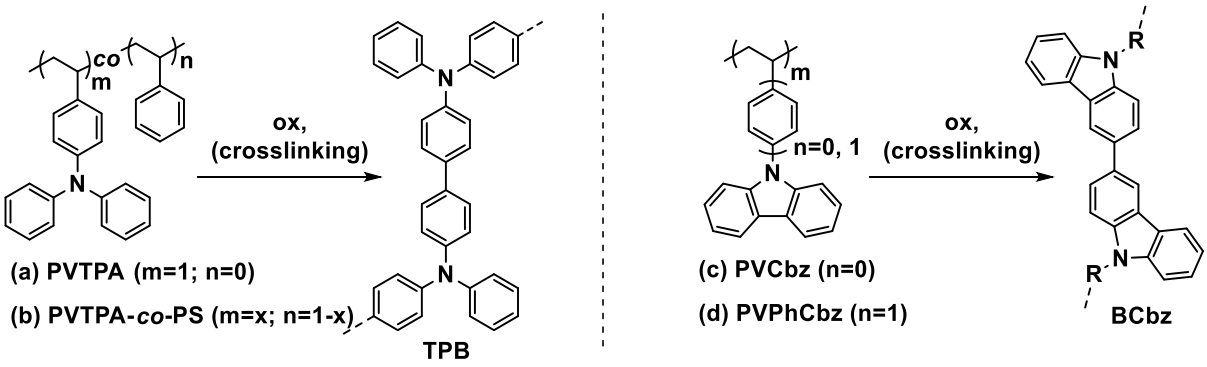

Figure 6.9: PVTPA, PVTPA-co-PS, PVCbz and PVPhCbz (left) and of the dimerization products tetraphenylbenzidine (TPB) and biscarbazole (BCbz) (right).

In the second part of the thesis, insight of oxidative crosslinking as a post-solution deposition step to obtain electroactive films is provided. The dimerizing ability of triarylamine (TPA) and carbazole (Cbz) in the form of redox-active pendant units on a saturated polymer backbone as crosslinkers was studied upon oxidation. Electrochemical and doping behaviors of the crosslinked polymer films were analyzed by *in-situ* electrochemical methods (*in-situ* conductance and *in-situ* UV-Vis spectroelectrochemistry). Additionally, electrochemical quartz crystal microbalance (EQCM) and *ac*-electrogravimetry were performed upon electrochemical doping of the films, providing specific contributions and kinetic information about the species involved in the charge-compensation process. Initially, the effect of variation of the polymer film composition in terms of the number of redox units with respect to electrochemical, potential dependent conductance and ion transport properties was investigated by comparing films of the PVTPA homopolymer with PVTPA-*co*-PS copolymers containing different PVTPA-PS ratios. More precisely, 50-50, 30-70, 20-80 and 10-90 ratios were analyzed respectively. Variations in the CV profiles of electrochemically crosslinked films were observed modifying the redox active content of the polymer films. These included a variation of the total oxidative charge, of the peak positions, which was observed to shift towards more positive potential values, and a narrowing of the window of electroactivity as the amount of TPA redox unit in the film decreases.

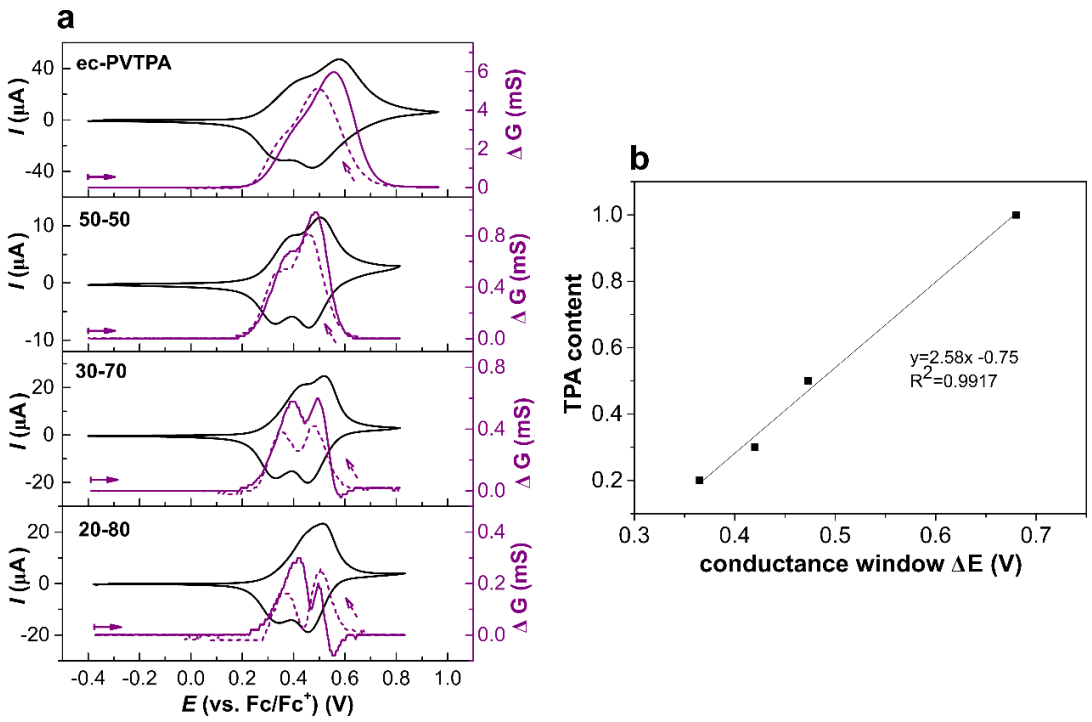

Figure 6.10: (a) In-situ conductance of ec-PVTPA and ec-PVTPA-co-PS with different PVTPA-PS ratios. Measurements performed in 0.1 M CH_3CN/NBu_4PF_6; scan-rate 10 mV/s; Pt 5 µm-IDE; II cycle. (b) average conductance window from forward and backward scan reported as function of TPA content in the polymers.

We also found that in the case of electrochemically crosslinked copolymers bearing a low PVTPA content (20-80 and 10-90), a shift in the peak position and shape is observed by varying the scan-rate. We claim that observed variation in peak shape and shift towards more positive potentials could be explained by the increased resistance of the polymer films, which could hinder the radical cation formation, as the amount of non-polar PS units in the polymer film increases.[34] The decrease in the amount of redox units in the ec-PVTPA-*co*-PS copolymers is also accompanied by a decrease in the potential region of electroactivity of the polymer and to the capacitive characteristics of the voltammogram. We could observe a direct relationship between the conductivity region (and electroactivity) of the polymers and the number of redox units in the film. The *in-situ* conductance pattern of all electrochemically crosslinked films follows a mixed valence conductivity behavior, with two maxima of conductance encountered for the oxidation TPB/$TPB^{+\bullet}$ and $TPB^{+\bullet}$/ TPB^{2+}, respectively. In the case of polymers with reduced PVTPA content, the two conductance regimes are well separated, whereas in the case of the homopolymer, overlap between the two conductance regimes is found (Figure 6.10).

The charge compensation properties upon oxidation of electrochemically crosslinked arylamine-based polymers, ec-PVTPA and ec-PVTPA-*co*-PS in 0.1M CH_3CN/NBu_4PF_6 was analyzed through classical and advanced EQCM, and the effect of film composition on the transfer of ions and solvents upon oxidation was analyzed. In Figure

6.11 are reported EQCM measurements coupled with CV, the results indicate a mass uptake upon oxidation and two regimes are observed in the mass change, with good correlation with the oxidation steps TPB/$TPB^{+\bullet}$ and $TPB^{+\bullet}$/ TPB^{2+}. The calculation of f(Δm/Δq) (g mol^{-1}) from EQCM data, gives in both cases molar mass values for the species higher than the one of the sole anion PF_6^-. The participation of other species in addition to the single anion was further investigated by *ac*-electrogravimetry. This latter indicates that the species transfer at electrode | electrolyte interface is dominated by anions and solvent moving in the same flux direction, for both ec-PVTPA and ec-PVTPA-*co*-PS 50-50.

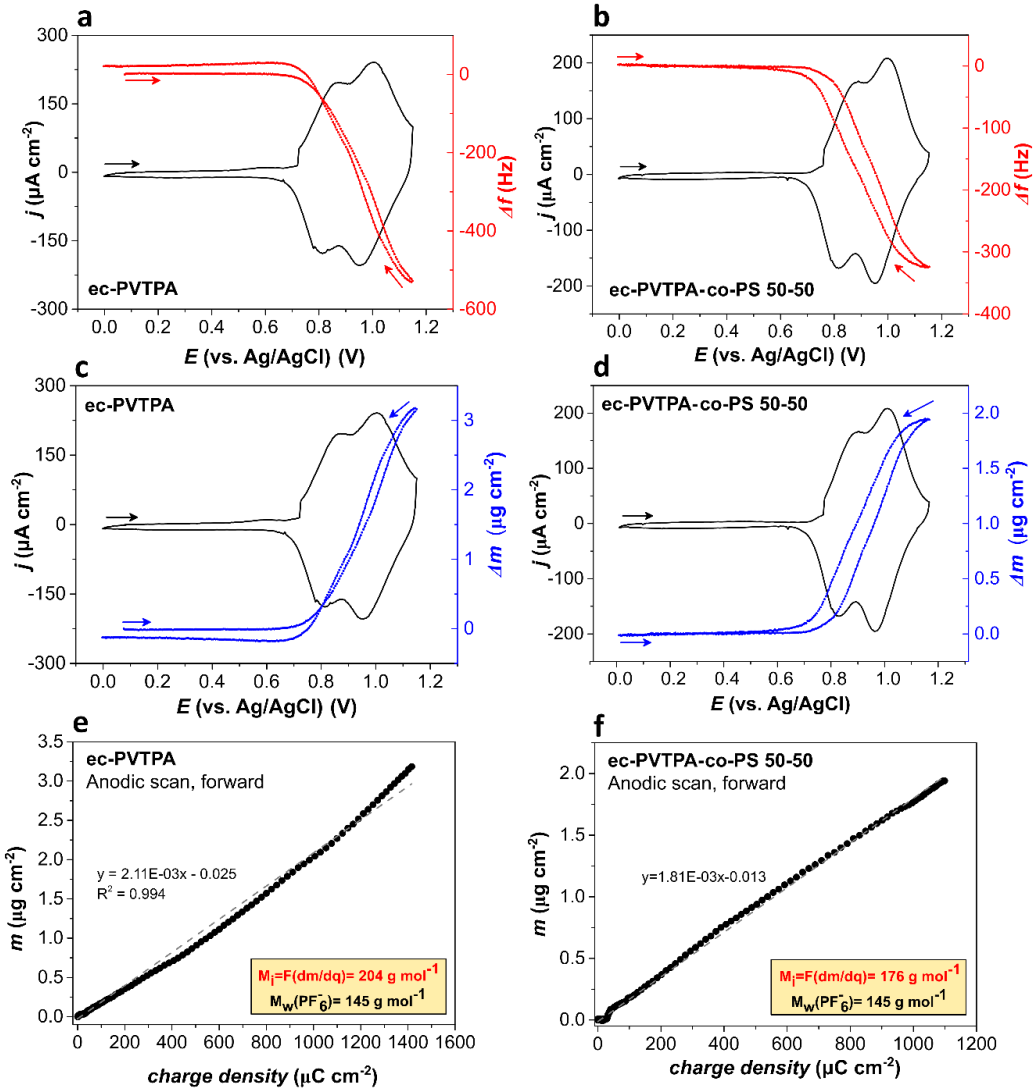

Figure 6.11: Cyclic Voltammetry of (left side) ec-PVTPA and (right side) ec-PVTPA-co-PS combined with QCM Δf_m (a ,b red curves); global mass changed from EQCM (c, d blue curves). F(dm/dq) obtained as the slope of the mass change vs. charge density (e, f) plot. Scan-rate 50 mVs^{-1} in CH_3CN/NBu_4PF_6 0.1 M; 5th cycle.

Good correlation of the mass change by *ac*-electrogravimetry reconstruction and by EQCM is found. Characteristic parameters from ac-electrogravimetric measurements including the transfer resistance Rt_i, the frequency f_i and the instantaneous capacitance Ct_i were determined for solvent and anion for both homopolymer and copolymer. The

frequency f_i is related to the transfer kinetics of the species, whereas the transfer resistance, Rt_i is related to the ease/difficulty of their transfer.

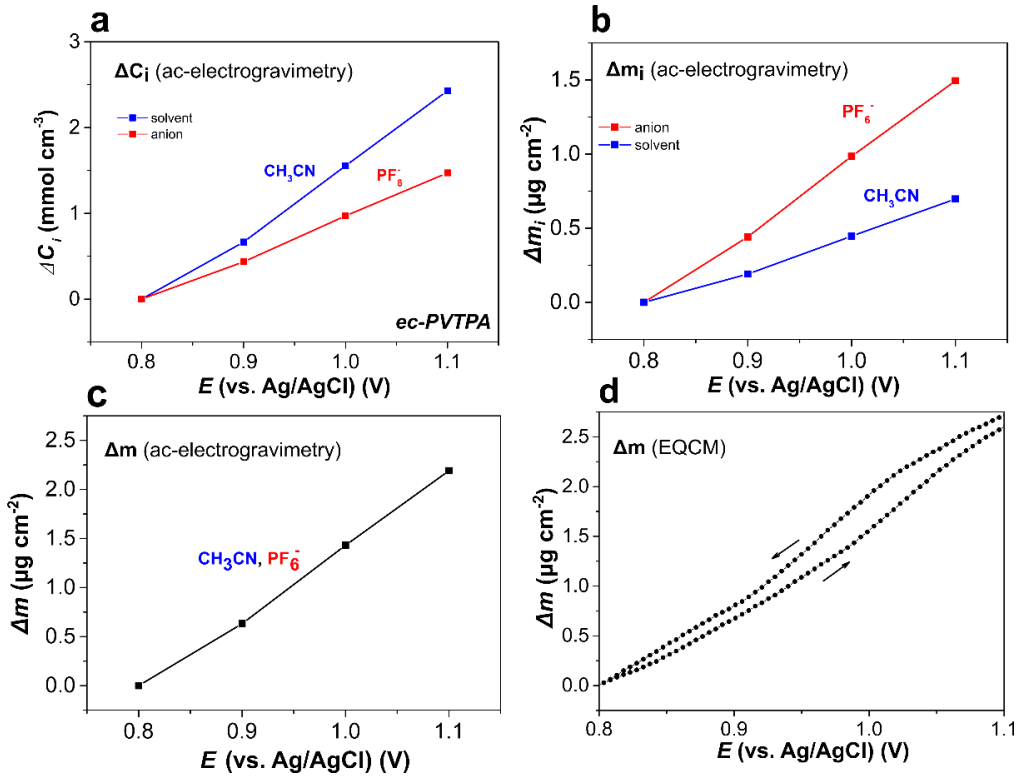

Figure 6.12: Change of concentration ΔC_i (a) and mass Δm_i (b) for the single species involved in the charge compensation, and (c) global mass change Δm for ec-PVTPA reconstructed from ac-electrogravimetry upon oxidation. Global mass change from EQCM (d) for comparison.

We found a more facile anion and solvent transfer at the electrode|electrolyte interface for the homopolymer ec-PVTPA in comparison to the copolymer ec-PVTPA-*co*-PS 50-50. The observed results could be attributed to the less polar nature of the polymer due to the presence of PS units. The modification of the polymer structure with PS units shows an effect on the transport characteristics of the species involved at the film|electrolyte interface but not on their nature. In general, the homopolymer ec-PVTPA shows for both electronic conductivity and ion transfer superior performance in comparison to the copolymers analyzed. In general, a significant influence of the polymer structure on transport characteristics is found in terms of different physico-chemical properties such as redox response, potential-dependent conductivity, and ion transport at the film|electrolyte interface.

The concomitant crosslinking and doping with the strong oxidant $FeCl_3$ of spin-coated crosslinkable redox polymer films was also performed and optimized, in particular, we reported a study on electronic conductivity upon chemical and electrochemical oxidation of polyvinyltriphenylamine (PVTPA) and polyvinylcarbazole (PVPhCbz and PVCbz) redox polymer films.

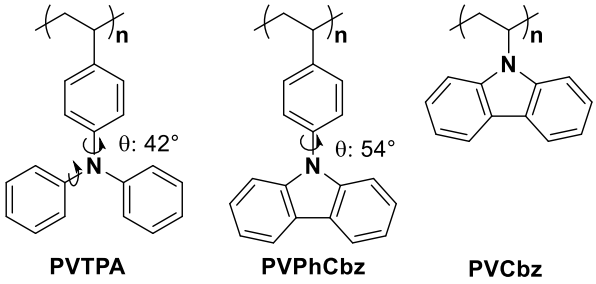

Figure 6.13: Structure of PVTPA, PVPhCbz and PVCbz including dihedral angles (θ). Carbazole structure is planar (for fused rings θ ~0°).[12,13]

The oxidative dimerization of the electroactive units is performed on solution casted films and results in the polymer crosslinking. Upon exposure with $FeCl_3$ solutions highly conducting films are obtained with maximum conductivities ranging from 10^{-3} to 10^{-2} S/cm. The increased chemical stability resulting from crosslinking together with the transparency of the conducting layers makes them interesting candidates for optoelectronic applications as HTLs or transparent electrodes. It was found that doping of PVTPA and PVPhCbz gives bell-shaped conductivity profiles with a maximum conductivity only observed when radical cations and dications are both present with the pure neutral and fully oxidized samples only giving very low conductivities. Crosslinked and doped PVCbz films on the other hand do maintain the highest conductivity over a broad doping range of 400 mV (from 0.7 to 1.1 V) and a range of doping concentrations. This is also the region when dication species are concurrently present with radical cations. The bell-shape conductivity profile also implies that for chemical doping the exact doping concentration must be found, while the plateau-conductivity is overall less sensitive to the doping conditions. *In-situ* electrochemistry with conductance and spectroscopy have been performed prior to identify the right doping regimes to be targeted upon chemical doping.

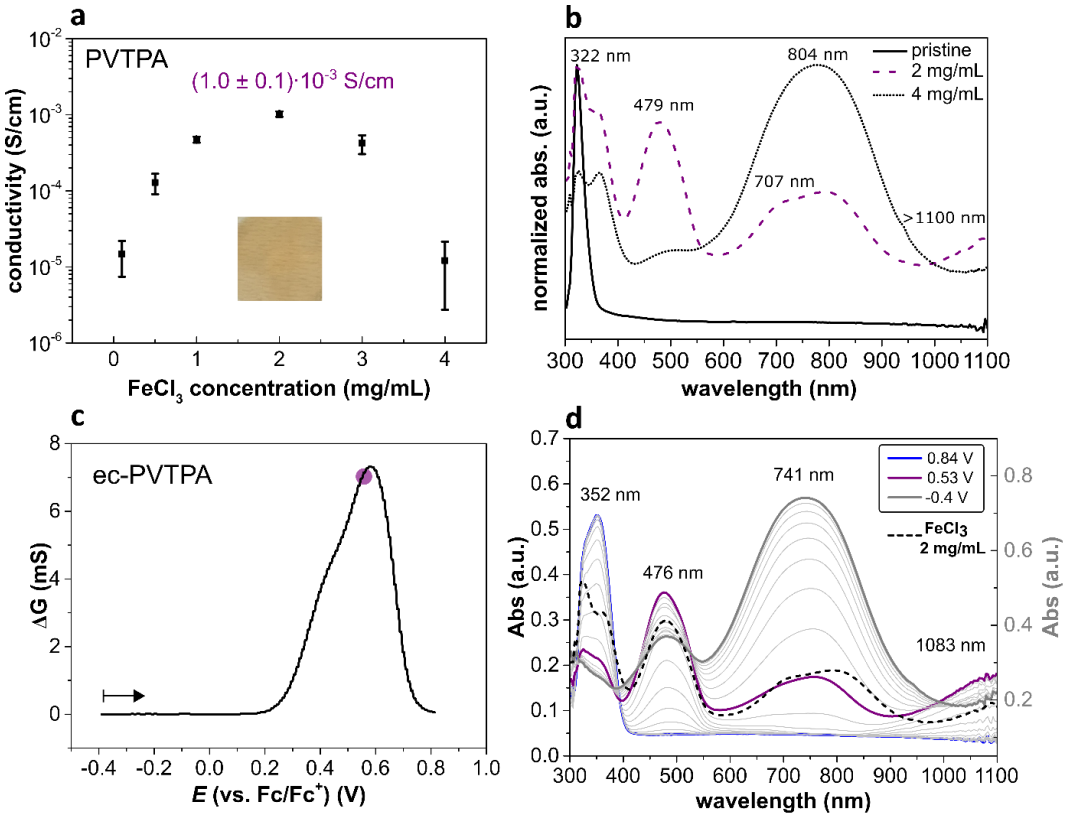

Figure 6.14: Sequential doping of a PVTPA film with $FeCl_3/CH_3CN$ solutions with different concentrations (0.1; 0.5; 1; 2; 3 and 4 mg/mL) for 10 s. (a) conductivity data and inset of a 1 cm^2 film doped with 2 mg/mL $FeCl_3$ solution at maximum conductivity, (b) UV-Vis-NIR absorption spectra for as-casted PVTPA film (black continuous line); at maximum conductivity (2 mg/mL; purple dashed line) and at 4 mg/mL (dotted black line). (c) Forward in-situ conductance cycle with characteristic "bell-shape". (d) UV-Vis-NIR spectroelectrochemistry of ec-PVTPA with absorption at +0.53 V (purple line, at max conductance) in comparison to the absorption spectra registered at maximum conductivity (2 mg/mL; 10 s) upon chemical doping (black dashed-line). Picture adapted with permission from ref. [13]. Copyright 2020 RSC.

Further, it is also found that cross-communication allowing three-dimensional electronic connectivity for hopping is strongly affecting the conductivity profile, as evidenced in the case of doping PVCbz. DFT calculations hint to a pronounced tendency of the bicarbazole units to form π-stacks, and, in the case of BCbz smaller intermolecular π-stacking distances are calculated in comparison to BPhCbz. A more efficient π-stacking between neighboring units may explain the broad region of high conductivity. Similarly to what observed for ec-PVTPA-*co*-PS copolymers, neighboring interactions result in significant variations in the electrochemical and potential dependent conductivity profile of the molecules.

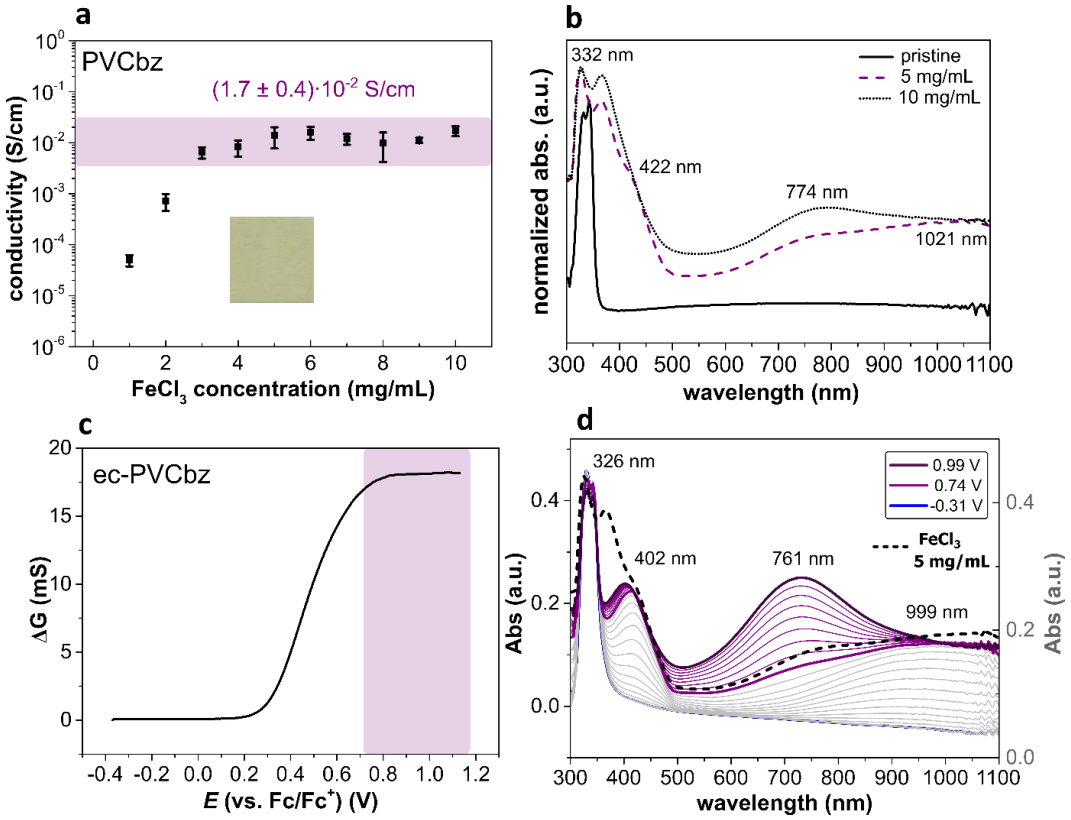

Figure 6.15: Sequential doping of a PVCbz film with $FeCl_3/CH_3CN$ solutions with different concentrations (1-10 mg/mL) for 10 s. (a) conductivity data and inset of a 1 cm^2 film doped with 5 mg/mL $FeCl_3$ solution at maximum conductivity, (b) UV-Vis-NIR absorption spectra for as-casted PVCbz film (black continuous line); at maximum conductivity (5 mg/mL; purple dashed line) and at 10 mg/mL (dotted black line). (Bottom) (c) Forward in-situ conductance cycle with plateau conductance behavior. (d) UV-Vis-NIR spectroelectrochemistry of ec-PVTPA with absorption at potential values more positive than 0.74 V (purple line, reaching the plateau region)) in comparison to the absorption spectra registered at maximum conductivity (5 mg/mL; 10 s) upon chemical doping (black dashed-line). Picture adapted with permission from ref. [13]. Copyright 2020 RSC.

The increased chemical stability resulting from crosslinking, together with the transparency and “high” conductivity of the resulting doped layers makes them interesting candidates for hole transport layers and transparent electrodes in optoelectronics applications. The reported crosslinking and doping procedure are currently under test for PVCbz and PVTPA thin layers used as HTLs in perovskite solar cells.

6.1.1 References

[1] J. Heinze, B. A. Frontana-Uribe, S. Ludwigs, *Chem. Rev.* **2010**, *110*, 4724–4771.

[2] P. Taranekar, T. Fulghum, D. Patton, R. Ponnapati, G. Clyde, R. Advincula, *J. Am. Chem. Soc.* **2007**, *129*, 12537–12548.

[3] G. Jiang, C. Huang, A. Baba, R. Advincula, *Macromol. React. Eng.* **2012**, *6*, 153–159.

[4] M. I. Mangione, R. A. Spanevello, D. Minudri, P. Cavallo, L. Otero, F. Fungo, *Electrochim. Acta* **2018**, *263*, 585–595.

[5] R. F. Nelson, R. H. Philp, *J. Phys. Chem.* **1979**, *83*, 713–716.

[6] E. T. Seo, R. F. Nelson, J. M. Fritsch, L. S. Marcoux, D. W. Leedy, R. N. Adams, *J. Am. Chem. Soc.* **1966**, *88*, 3498–3503.

[7] O. Yurchenko, D. Freytag, L. Zur Borg, R. Zentel, J. Heinze, S. Ludwigs, *J. Phys. Chem. B* **2012**, *116*, 30–39.

[8] J. Roncali, P. Leriche, P. Blanchard, *Adv. Mater.* **2014**, *26*, 3821–3838.

[9] M. Zhao, H. Zhang, C. Gu, Y. Ma, *J. Mater. Chem. C* **2020**, *8*, 5310–5320.

[10] S. C. Creason, J. Wheeler, R. F. Nelson, *Coupling Rates of 4-Substituted Triphenylaminium Ions*, **1972**.

[11] C. Malacrida, A. H. Habibi, S. Gámez-Valenzuela, I. Lenko, P. S. Marqués, A. Labrunie, J. Grolleau, J. T. López Navarrete, M. C. Ruiz Delgado, C. Cabanetos, P. Blanchard and S. Ludwigs, ChemElectroChem, **2019**, 6, 4215–4228.

[12] C. Malacrida, L. Scapinello, R. Cirilli, S. Grecchi, A. Penoni, T. Benincori, S. Ludwigs, *ChemElectroChem* **2021**, *8*, 3250–3261.

[13] C. Malacrida, Y. Lu, K. Dirnberger, S. Gámez-Valenzuela, M. C. Ruiz Delgado, S. Ludwigs, *J. Mater. Chem. C* **2020**, *8*, 15393–15405.